PHYSIK-DEPARTMENT

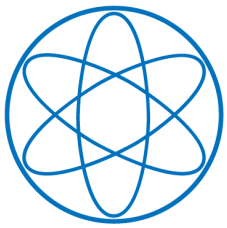

The Potential of Neganov-Luke Amplified Cryogenic Light Detectors and the Scintillation-Light Quenching Mechanism in $CaWO_4$ Single Crystals in the Context of the Dark Matter Search Experiment CRESST-II

Dissertation von
Sabine Roth

TECHNISCHE UNIVERSITÄT
MÜNCHEN

TECHNISCHE UNIVERSITÄT MÜNCHEN

Physik Department
Lehrstuhl E15 für Experimentalphysik und Astroteilchenphysik

The Potential of Neganov-Luke Amplified Cryogenic Light Detectors and the Scintillation-Light Quenching Mechanism in $CaWO_4$ Single Crystals in the Context of the Dark Matter Search Experiment CRESST-II

Sabine B. Roth

Vollständiger Abdruck der von der Fakultät für Physik der Technischen Universität München zur Erlangung des akademische Grades eines

Doktors der Naturwissenschaften (Dr. rer. nat.)

genehmigten Dissertation.

Vorsitzender:		Univ.-Prof. Dr. Alejandro Ibarra
Prüfer der Dissertation:	1.	Univ.-Prof. Dr. Franz Freiherr von Feilitzsch (i.R.)
	2.	Priv.-Doz. Dr. Andreas Ulrich

Die Dissertation wurde am 26.08.2013 bei der Technischen Universität München eingereicht und durch die Fakultät für Physik am 25.09.2013 angenommen.

Abstract

Experimental observations from cosmology as well as various aspects in theoretical particle physics point to the existence of unknown types of particles not included in the standard model of particle physics. Actually, this so-called dark matter is demonstrated to account for the by far dominating mass component - compared to baryonic matter - of our universe. One type of particle candidates - proposed by theoretical particle physics - fulfilling all of the requirements for dark matter are the so-called WIMPs, weakly interacting massive particles. For most kinds of WIMPs predicted by theory, a mass range of roughly $\mathcal{O}$(10GeV) to more than $\mathcal{O}$(1TeV) as well as a weak interaction with baryonic matter via low-energetic nuclear-recoil production of only $\mathcal{O}$(10keV) to $\mathcal{O}$(100keV) with rates of less than 0.1 events per kg and day are expected. Directly detecting and characterizing dark matter particles is one of the key problems of present-day astroparticle physics. The CRESST experiment (Cryogenic Rare Event Search with Superconducting Thermometers) aims at the direct detection of WIMP-nucleus scattering events in the target crystals (scintillating $CaWO_4$ single crystals) of a modularized cryogenic detector. In order to achieve an efficient particle identification, i.e., a discrimination of background events induced by, e.g., electron, γ or neutron interactions in the detector, the so-called phonon-light technique is employed. The phonon-light technique is based on the detection of the different amounts of scintillation light produced for different interacting particles by a separate cryogenic light detector. The particle-dependent production of scintillation light is referred to as the light-quenching effect and is quantified by the so-called Quenching Factors. For example, the Quenching Factor of $\sim 10\%$ for Oxygen recoils corresponds to the reduction of the amount of scintillation light produced for Oxygen recoils compared to the amount of scintillation light produced for electron/γ-events in $CaWO_4$. As the energy detected in the light channel of the CRESST experiment for particles in the energy region expected for WIMP-nucleus interactions maximally amounts to a few 100eV (for electron/γ-events), very efficient light detectors with excellent resolution in the low-energy region are required for an efficient discrimination of background events. In addition, in order to correctly identify the type of interacting particle, the knowledge of the particle-dependent Quenching Factors in $CaWO_4$ is a prerequisite. Within the present work, both of these issues were addressed.

First, the investigation of the potential of Neganov-Luke amplified light detectors for an optimization of the light detection in the CRESST experiment is presented. By introducing a well-motivated new fabrication technique, one major drawback of Neganov-Luke light detectors, the decreasing amplification over time, causing a detector response varying over time, can be resolved. This is confirmed by experiments performed within the present work. Additionally, the up to now unknown improvement of the energy-dependent detector resolution in the low-energy region, which is important for the dark matter search, is studied and can be explained consistently. For the example of a realized Neganov-Luke detector, the drastic improvement of the background suppression that could be achieved in a CRESST-like detector module is calculated on the basis of the experimentally determined improvement of the energy-dependent detector resolution. This result underlines the great potential of the application of Neganov-Luke amplified light detectors for the dark matter search with CRESST.

In the second part, a comprehensive, microscopic model for the light generation and quenching in $CaWO_4$ as developed within the present work is presented. This model describes the light generation and quenching observed for different interacting particles on the basis of the temporal and spatial evolution of fundamental excitations (self-trapped excitons, STEs) generated in a $CaWO_4$ crystal for different modes of excitation. Within this model, the light-quenching effect as well as the shape of the non-exponential scintillation-light decay-time spectrum that can be observed for particle-induced energy depositions in $CaWO_4$, are consistently explained on the basis of STE-STE quenching via the Förster interaction. This model is experimentally validated by correctly predicting the decay-time spectra observed under ion-beam excitation leading to *quenched* light generation as well as under two-photon excitation with a N_2 laser leading to *unquenched* light generation. The results of the experiments which were performed at the tandem accelerator of the MLL (Maier-Leibnitz-Laboratorium) in Garching can be employed to determine free parameters of the model. A first, preliminary calculation of Quenching Factors for different interacting particles in $CaWO_4$ already reveals that, with the developed model, experimentally observed features such as the energy-, temperature-, and crystal-dependency of the Quenching Factors are all explained as well as correctly predicted. Thus, this model if not only able to describe the observed light-yield quenching on a microscopic basis, but, furthermore, after all model parameters are determined, it provides the possibility to theoretically calculate and predict energy-dependent Quenching Factors for different interacting particles. Such Quenching Factors, in turn, deliver the basis of the particle identification and, thus, the basis of the background suppression for the dark matter search with the CRESST experiment. Hence, the developed model essentially contributes to a better understanding and further improvement of the background-suppression capability not only of the CRESST experiment, but also of future dark matter experiments where new detector materials (e.g., $CaMoO_4$, Ti:Al_2O_3 or YO_3) have to be selected and characterized, e.g., with special emphasis on search for light WIMPs.

Zusammenfassung

Durch experimentelle Beobachtungen aus der Kosmologie sowie diverse Hinweise aus der theoretischen Teilchenphysik kann auf die Existenz unbekannter Teilchen, die nicht im Standardmodell der Teilchenphysik enthalten sind, geschlossen werden. Diese sogenannte Dunkle Materie stellt - im Gegensatz zur baryonischen Materie - den überwiegenden Teil der Masse unseres Universums dar. Potenzielle Kandidaten für die Dunkle Materie, die von der theoretischen Teilchenphysik vorausgesagt werden, sind die sogenannten WIMPs (Weakly Interacting Massive Particles). Für nahezu alle Arten dieser theoretisch vorhergesagten WIMPs wird eine Masse im Bereich von $\mathcal{O}$(10GeV) bis hin zu mehr als $\mathcal{O}$(1TeV), sowie eine schwache Wechselwirkung mit baryonischer Materie durch die Erzeugung niederenergetischer Kernrückstöße von lediglich $\mathcal{O}$(10keV) bis $\mathcal{O}$(100keV) bei einer Wechselwirkungsrate von weniger als 0.1 Ereignissen pro kg und Tag erwartet. Der direkte Nachweis und die Charakterisierung der Teilchen der Dunklen Materie gehören zu den Kernproblemen der heutigen Astroteilchenphysik. Das CRESST-Experiment (Cryogenic Rare Event Search with Superconducting Thermometers) hat den direkten Nachweis von durch WIMPs verursachten Kernrückstoßereignissen in den Target-Kristallen (szintillierende $CaWO_4$-Einkristalle) eines modular aufgebauten Tieftemperaturdetektors zum Ziel. Um eine effektive Teilchenidentifikation zu ermöglichen, d.h. um eine Unterdrückung von Untergrundereignissen durch Wechselwirkungen von beispielsweise Elektronen, γ-Teilchen oder Neutronen in dem Detektor zu erreichen, wird die sogenannte Phonon-Licht-Technik angewendet. Die Phonon-Licht-Technik basiert auf dem Nachweis der unterschiedlichen Mengen an Szintillationslicht, die für verschiedene wechselwirkende Teilchen erzeugt werden, mithilfe eines separaten kryogenen Lichtdetektors. Die teilchenartabhängige Erzeugung von Szintillationslicht wird als Licht-Quenching-Effekt bezeichnet und wird durch die sogenannten Quenching-Faktoren quantifiziert. Beispielsweise entspricht der Quenching-Faktor von Sauerstoffkernrückstößen von ca. 10% der Reduktion des nachgewiesenen Szintillationslichts für Sauerstoffkernrückstöße im Vergleich zu einem Elektron-/γ-Ereignis gleicher Energie. Da im CRESST-Experiment die im Lichtkanal nachgewiesene Energie für Wechselwirkungen in der Energieregion, in der von WIMPs verursachte Kernrückstöße erwartet werden, maximal wenige 100eV beträgt (Elektron-/γ-Ereignisse), werden sehr effektive Lichtdetektoren mit ausgezeichneter Energieauflösung bei niedrigen Energien benötigt, um bestmöglich Untergrundereignisse zu unterdrücken. Zudem ist die Kenntnis der teilchenartabhängigen Quenching-Faktoren in $CaWO_4$ eine Grundvoraussetzung, um die Art eines wechselwirkenden Teilchens korrekt festlegen zu können. In der vorliegenden Arbeit werden beide vorgenannten Aspekte eingehend behandelt.

Zuerst wird das Potenzial von Neganov-Luke-verstärkten Lichtdetektoren vorgestellt, mit denen der Lichtnachweis im Rahmen des CRESST-Experiments optimiert werden kann. Einer der großen Nachteile von Neganov-Luke-Lichtdetektoren, die mit der Zeit abnehmende Signalverstärkung, welche eine sich mit der Zeit ändernde Detektorantwort verursacht, kann behoben werden, indem eine wohlmotivierte, neue Fertigungstechnik für derartige Lichtdetektoren eingeführt wird. Dieser Umstand wird durch Experimente belegt, die im Rahmen der vorliegenden Arbeit durchgeführt wurden. Zusätzlich wird die Verbesserung der energieabhängigen Detektorauflösung im Bereich kleiner nachgewiesener Energien, die gerade für die Suche nach Dunkler Materie wichtig sind, durch die Anwendung des

Neganov-Luke-Effekts untersucht und konsistent erklärt. Unter Verwendung der experimentell bestimmten, energieabhängigen Verbesserung der Energieauflösung eines Neganov-Luke-Detektors, der im Zuge der vorliegenden Arbeit hergestellt wurde, wird beispielhaft die deutliche Verbesserung der Untergrundunterdrückung, die in einem CRESST-Detektormodul erzielt werden könnte, berechnet. Dieses Ergebnis untermauert das große Potenzial, das die Anwendung von Neganov-Luke-verstärkten Lichtdetektoren für die Suche nach Dunkler Materie mit dem CRESST-Experiment hat.

Als zweiter Aspekt wird ein umfassendes, mikroskopisches Modell für die Lichtentstehung und das Licht-Quenching in $CaWO_4$ vorgestellt, wie es in der vorliegenden Arbeit entwickelt wurde. Dieses Modell beschreibt die Lichtentstehung und das Quenching, welche bei unterschiedlichen wechselwirkenden Teilchen beobachtet werden, auf Basis der zeitlichen und räumlichen Entwicklung der fundamentalen Anregungen (self-trapped excitons, STEs), die in einem $CaWO_4$-Kristall für verschiedene Arten der Anregung entstehen. Im Rahmen des Modells wird der Licht-Quenching-Effekt und die nicht-exponentielle Pulsform des Szintillationslicht-Zerfallsspektrums, die bei von Teilchen verursachten Energieeinträgen in $CaWO_4$ beobachtet werden, konsistent durch ein STE-STE-Quenching vermöge der Förster-Wechselwirkung erklärt. Das Modell wird experimentell validiert, indem die *gequenchten* Lichtzerfallsspektren, die bei der Anregung mit einem Ionenstrahl beobachtet werden können, und die *ungequenchten* Lichtzerfallsspektren, die bei der Zwei-Photonen-Anregung mit einem N_2-Laser beobachtet werden können, korrekt vorhergesagt werden. Die Ergebnisse dieser Experimente, die am MLL-Tandem-Beschleuniger (Maier-Leibnitz-Laboratorium) in Garching durchgeführt wurden, können verwendet werden, um freie Parameter des Modells festzulegen. Eine erste, vorläufige Berechnung der Quenching-Faktoren für verschiedene in $CaWO_4$ wechselwirkende Teilchen zeigt bereits, dass mit dem entwickelten Modell experimentell beobachtete Charakteristika der Quenching-Faktoren, wie die Energie- und Temperaturabhängigkeiten sowie die Abhängigkeit vom verwendeten Kristall, umfassend erklärt und vorhergesagt werden. Das Modell ist also nicht nur in der Lage, den beobachteten Licht-Quenching-Effekt auf Basis mikroskopischer Effekte zu erklären, sondern erlaubt darüber hinaus, nach der Festlegung aller Modellparameter, die energieabhängigen Quenching-Faktoren für verschiedene wechselwirkende Teilchen theoretisch zu berechnen und vorherzusagen. Die derart bestimmbaren Quenching-Faktoren wiederum sind unabdingbar für die Teilchenidentifikation und damit für die Untergrundunterdrückung bei der Suche nach Dunkler Materie mit dem CRESST-Experiment. Damit trägt das entwickelte Modell wesentlich zu einem besseren Verständnis und einer weiteren Verbesserung der Untergrundunterdrückung im CRESST-Experiment bei. Dieser Beitrag lässt sich zudem auch auf zukünftige Experimente zur Suche nach Dunkler Materie übertragen, wozu neue Detektormaterialien (z.B. $CaMoO_4$, Ti:Al_2O_3 oder YO_3) ausgewählt und charakterisiert werden müssen, beispielsweise im Hinblick auf eine Suche nach leichten WIMPs.

Contents

Part I

Direct Dark Matter Search

Chapter 1

Motivation: Direct Detection of Dark Matter Particles

Strong evidence from cosmology (see, e.g., [1]) as well as from indirect observations (see, e.g., [2]) points to the existence of large amounts of non-luminous, dark matter in our universe. The currently most stringent limits can be retrieved from new results from the Planck collaboration, indicating that $\sim 26.8\%$ of the mass and energy content of our universe is made of dark matter [1]. Besides these experimental indications for the existence of non-baryonic dark matter, theoretical particle physics predicts several particles beyond the Standard Model of Elementary Particle Physics that could constitute this dark matter in our universe [3]. Among them is the so-called WIMP (weakly interacting massive particle) for which several candidates as, e.g., the so-called LSP, the lightest supersymmetric particle (that is stable), are suggested from supersymmetry. For most kinds of WIMPs, a mass in the range from roughly $\mathcal{O}(10\text{GeV})$ to more than $\mathcal{O}(1\text{TeV})$ as well as a weak interaction with baryonic matter via the production of nuclear recoils is predicted. Under the assumption of a spin-independent WIMP-nucleon interaction, a proportionality of the scattering cross section on A^2 is expected (with A being the mass number of the target nucleus) [4]. Direct dark-matter search-experiments, as the CRESST experiment (Cryogenic Rare Event Search with Superconducting Thermometers) [5], are exactly aimed at detecting such rare WIMP-nucleon scattering events. Due to the weak interaction and low expected event rate (WIMP event rates of less than 0.1 events per kg and day are expected), low energy thresholds (of $\mathcal{O}(1\text{keV})$ to $\mathcal{O}(10\text{keV})$), low-background environments, large target masses as well as an excellent background-suppression technique to discriminate, e.g., events caused by natural radioactivity, are required to allow for a direct detection and identification of dark matter particles. Various direct detection experiments exist fulfilling these requirements by being located in underground laboratories, employing, e.g., cryogenic detectors offering low energy thresholds (compare section I/2.2), and detecting two signals (phonon/charge, see, e.g., [6] or phonon/light, see, e.g., [5]) for each energy deposition in their respective target material to achieve an event-by-event background discrimination.

Results from such experiments are generally indicated in the WIMP-nucleon cross-section vs. WIMP-mass plane where the accumulated exposure of an experiment (in kg days) and the number of potential events observed translate either into a limit that can be set, excluding the parameter space above with a certain confidence level, or into regions of the parameter space favored by the experimental observations. The current best limit is

provided by the Xenon100 experiment [7], with a minimal cross section of $\sim 2 \cdot 10^{-45}$cm at a WIMP mass of $\sim 55 \frac{\text{GeV}}{c^2}$. However, recent results from various experiments, as, e.g., results from the analysis of the data recorded with the Si detectors in the CDMS-II experiments (Cryogenic Dark Matter Search), favor a low-mass WIMP with, e.g., for the CDMS-II Si-data, a best fit value at a cross section of $\sim 1.9 \cdot 10^{-41}\text{cm}^2$, at a WIMP mass of $\sim 8.6 \frac{\text{GeV}}{c^2}$ [6]. This result as well as various limits and best fit values from several direct dark matter search experiments are presented in the WIMP-nucleon cross-section vs. WIMP-mass plane in figure 1.1, as a zoom into the low-mass WIMP region. Within the context of the present work, especially the latest results from the CRESST-II experiment (pink regions) should be noticed: Within the last period of data-taking of the CRESST experiment, more events in the potential signal region for the dark matter search were observed than can be explained with known sources of backgrounds. Thus, also for the CRESST experiment, the parameter region favored due to attributing the observed excess signal to WIMP-nucleus scattering events is shown. The indicated areas correspond to best fit values of $\sim 6.6 \cdot 10^{-41}\text{cm}^2$ for a WIMP mass of $\sim 9.3 \frac{\text{GeV}}{c^2}$ and of $\sim 2.2 \cdot 10^{-42}\text{cm}^2$ for a WIMP mass of $\sim 21.1 \frac{\text{GeV}}{c^2}$, respectively [5].

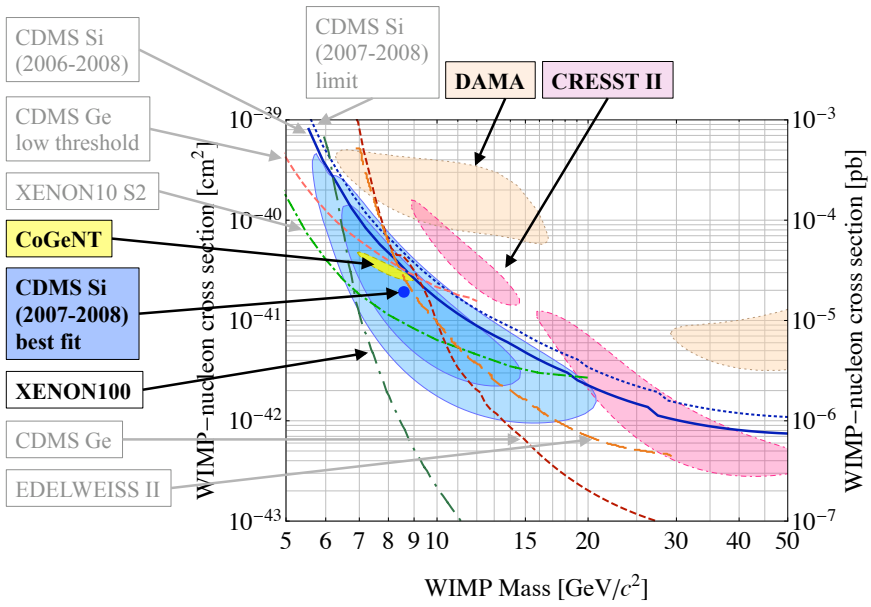

Figure 1.1: Spin-independent WIMP-nucleon cross section versus WIMP mass: Experimental limits and possible signal regions for various dark matter experiments. A zoom into the low-mass WIMP region is shown. Figure adopted from [6].

From figure 1.1, it can be seen that the current status of the dark matter search raises several questions as, on the one hand, the results of several experiments point to the existence of low-mass WIMPs, whereas other experiments, especially the limit set by the Xenon100 experiment, rule out most of the parameter space favored by these results (the Xenon100 limit is shown as dashed-dotted, dark-green line in figure 1.1). It should be noted, as reported in [8], that, e.g., by assuming isospin-dependent coupling of the dark matter particles with nucleons, the tension between the CDMS-II results obtained with Si [6] and the Xenon100 limit [7] can be reduced, but not completely resolved. Thus, it can

be concluded that, clearly, the need for further investigations arises to clarify the low-mass WIMP scenario in particular as well as the complete WIMP enigma in general.

Chapter 2

Dark Matter Search with the CRESST-II Experiment

The dark matter search experiment CRESST-II is aimed at the direct detection of elastic WIMP-nucleon scattering events in scintillating $CaWO_4$ single crystals. In order to enable the rare event search, the CRESST experiment is located in the underground laboratory of the Laboratori Nazionali del Gran Sasso in Italy. In the following, a short introduction to the detector design and working principle of CRESST detectors is given. Thereafter, the background suppression employing the so-called phonon-light technique - which will be addressed within the present work - is presented.

For details on the latest results obtained with CRESST-II, see [5] and, for further details of the CRESST experiment, as , e.g., the complete setup, see [9].

2.1 CRESST Detectors

The CRESST experiment employs cryogenic detector modules operated at mK temperatures for the dark matter search. One CRESST detector module consists of a scintillating $CaWO_4$ crystal of $\sim$ 300g which is used as target for the WIMP search and a separate cryogenic light detector (with a SOS - Silicon-On-Sapphire - light-absorber substrate), both enclosed in a scintillating and reflective housing. In a particle interaction in the $CaWO_4$ crystal, most of the energy deposited is converted into phonons. To detect these phonons, the $CaWO_4$ target crystal, in the following referred to as the phonon detector, is equipped with a Tungsten transition edge sensor (W-TES) for read out of the phonon signal. The scintillation light which is also produced in the particle interaction is detected by the light detector which is likewise equipped with a W-TES for read out of the phonon signal caused in the SOS substrate by absorbed scintillation-light photons. In figure 2.1 a), a photograph of an opened CRESST-II detector module is shown. In figure 2.1 b), the basic working principle of a TES is indicated: The super-to-normal conducting transition of a W-TES can be seen (resistance of the TES versus temperature). The TES is temperature-stabilized within its transition region. An energy deposition in the absorber of the cryogenic detector ($CaWO_4$ crystal or SOS substrate) leads to the production of thermal and non-thermal phonons. These phonons induce an increase of the temperature of the TES. Thus, the energy deposition in the absorber of the cryogenic detector leads to an increase of the temperature of the TES which, as indicated in figure 2.1 b), in turn, leads to an increase of the resistance of the TES. The resistance change of the TES is

read out with a so-called SQUID (Superconducting Quantum Interference Device) which, basically, is a highly sensitive magnetometer and can be used to detect extremely small current changes. For details on the working principle of cryogenic detectors, see, e.g., [10], and on the TES design and read out, see, e.g., [9].

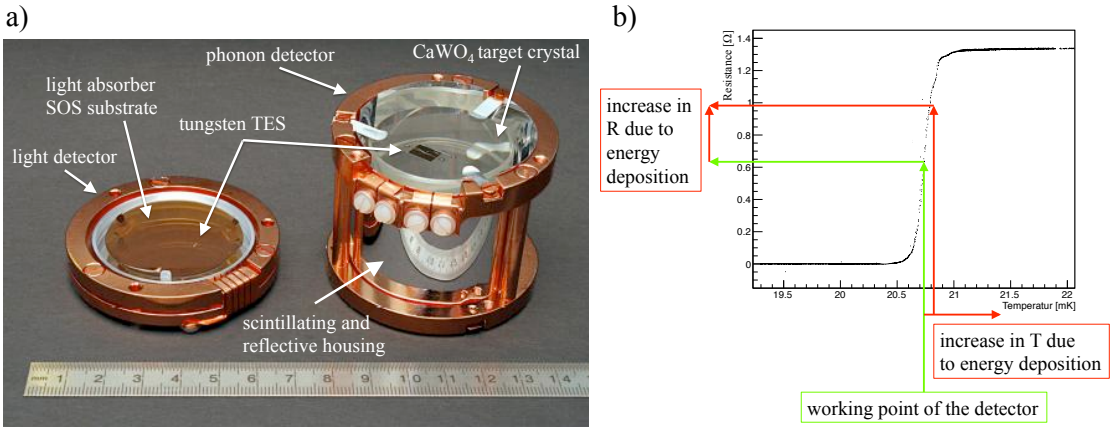

Figure 2.1: Panel a): Photograph of an opened CRESST-II detector module consisting of the $CaWO_4$ crystal utilized as target for the dark matter search and the separate cryogenic light detector (SOS substrate). Both detectors are equipped with TESs for signal read out. Panel b): Working principle of a TES-based signal read out. Shown is the super-to-normal conducting transition of a W-TES. The green arrows indicate the working point of the TES at which it is temperature-stabilized. Due to an energy deposition in the absorber of the cryogenic detector, the TES temperature is increased, leading to an increased resistance which can be read out with a SQUID.

2.2 The Phonon-Light-Technique

As can be deduced from the description of CRESST detector modules in section I/2.1, for each interaction of a particle of type *part* in the $CaWO_4$ crystal depositing the energy E_{part} there, two coincident signals are recorded: The energy detected as phonons in the $CaWO_4$ crystal, i.e., in the phonon detector, E_{det}, as well as the energy detected in the light detector in the form of produced scintillation-light photons, $L_{det}^{part}(E_{det})$. As indicated by the superscript *part* in $L_{det}^{part}(E_{det})$, it is observed that different amounts of scintillation light are generated and, hence, detected for different interacting particles such as, e.g., e^-/γ-particles, α-particles or the different nuclear recoils, Oxygen, Calcium and Tungsten ions, when depositing the same energy in the phonon detector. This circumstance is generally referred to as light-quenching effect and is the basis of the identification of the type of the interacting particle with the phonon-light technique (see, e.g., [5, 11]). From experiments, the basic trend is observed that, the heavier the interacting particle, the more quenched, i.e., reduced, the amount of scintillation light produced.

The differences in the detected amount of scintillation light $L_{det}^{part}(E_{det})$ for different interacting particles (e.g., $part \in \{e^-, \gamma, \alpha, \mathrm{O}, \mathrm{Ca}, \mathrm{W}\}$) for which the energy E_{det} is detected in the phonon detector are used as discrimination criterion for background suppression. It should be noted that E_{det} does not correspond to the total energy deposited by the

particle in the crystal, E_{part}, as a fraction of this energy is converted into scintillation light and is, thus, not detected in the phonon detector. In addition, it is important to take into account that, even for electron and γ-particle interactions for which the relatively largest amount of scintillation light is produced, only a small fraction of the total energy deposited in the $CaWO_4$ crystal is detected as scintillation light in the light detector. The typical fraction of the energy deposited that is detected in the light detector for a γ-particle (mean value of all investigated modules [12]), can be determined to amount to 1.86% at mK temperatures [12].

However, for particle identification, not the absolute amount of scintillation light detected is of interest, but its relative amount for different interacting particles. For this reason, in the context of the CRESST experiment, the convention of defining the light yield detected for 122keV γ-particles (from a calibration with a ^{57}Co source), $LY^{\gamma}_{det}(122\text{keV})$, as unity is used [5]. This definition is equivalent to gauging the energy scale of the light detector with the convention that the amount of energy detected in the light detector for 122keV γ-interactions, $L^{\gamma}_{det}(122\text{keV})$, corresponds to 122keV_{ee} (ee for electron equivalent, compare, e.g., [13]):

$$L^{\gamma}_{det}(122\text{keV}) \;=:\; 122\text{keV}_{ee} \tag{2.1}$$

$$\Leftrightarrow LY^{\gamma}_{det}(122\text{keV}) \;:=\; 1 \tag{2.2}$$

Using these definitions, the light yield for an interacting particle of type *part* for which the energy E_{det} is detected in the phonon channel is given by:

$$LY^{part}_{det}(E_{det}) \;=\; \frac{L^{part}_{det}(E_{det})}{E_{det}} \tag{2.3}$$

With this definition, electron recoils have a light yield of roughly unity whereas other interacting particles, such as nuclear recoils, are assigned a light yield smaller than unity. This reduction in light yield is quantified by the introduction of the so-called Quenching Factors [5]. The Quenching Factor $QF^{part}(E_{det})$ describes the relative amount of scintillation light created for a particle of type *part* for which the energy E_{det} is detected in the phonon detector compared to the amount of scintillation light created for an electron/γ-event of the same detected energy. It should be noted that the Quenching Factor is not a quantity that can be assigned to a single event recorded for one interacting particle of type *part*, but corresponds to the mean of the light yield of particles of type *part* compared to the mean of the light yield for electron recoils depositing the same energy. Thus, the Quenching Factors for different interacting particles (e.g., *part* $\in \{e^-, \gamma, \alpha, \text{O}, \text{Ca}, \text{W}\}$) of type *part* can be defined by:

$$QF^{part}(E_{det}) := \frac{\overline{LY^{part}_{det}(E_{det})}}{\overline{LY^{\gamma}_{det}(E_{det})}} = \frac{\overline{L^{part}_{det}(E_{det})}}{\overline{L^{\gamma}_{det}(E_{det})}} \tag{2.4}$$

where E_{det} is the energy detected in the phonon channel and the values for the light yield $\overline{LY^{part}_{det}}$ or amount of scintillation light $\overline{L^{part}_{det}}$ have to be understood as mean values at the respective detected energy E_{det}. Although, in equation 2.4 an explicit energy dependency is allowed for the Quenching Factor, it is assumed, in general, to be independent of energy [14]. This assumption leads to the following definition:

$$QF^{particle} := \frac{\overline{LY^{particle}_{det}(E_{det})}}{\overline{LY^{\gamma}_{det}(E_{det})}} = \frac{\overline{L^{particle}_{det}(E_{det})}}{\overline{L^{\gamma}_{det}(E_{det})}} \tag{2.5}$$

Hence, the Quenching Factor of a particle of type *part* defined in this way specifies the mean light yield expected for interactions of particles of type *part*. This circumstance is illustrated in more detail in figure 2.2 where data recorded with one CRESST detector module is depicted in the light-yield vs. E_{det} (energy detected in the phonon channel) plane (black dots). The differently colored bands indicated in the figure (yellow/turquois, pink and grey bands) correspond to the light-yield bands where events caused by α-particles, O and W ions, respectively, are expected. The mean of these bands is defined by the Quenching Factors (relative to the mean of the electron/γ band) and the widths of these bands are defined by the light-detector resolution for the respectively detected amount of scintillation light[1] (in terms of energy) [14].

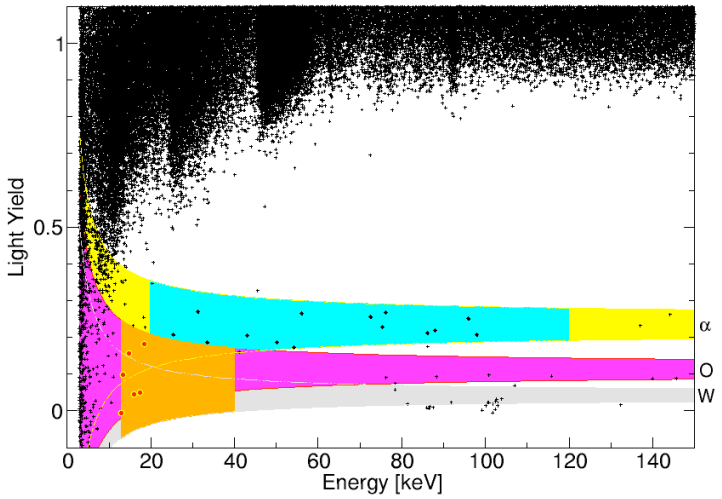

Figure 2.2: Data from one CRESST detector module in the light-yield energy plane: The large amount of events for light yields of roughly unity corresponds to electron recoils (γ and e^- interactions). Events with smaller light yields can be assigned to the interaction of other particles in the $CaWO_4$ crystal as follows: The yellow/turquois band indicates the region where events due to α-particles are expected, the pink and grey bands relate to the regions of expected Oxygen and Tungsten recoils, respectively. The widths of the bands are chosen such that 80% of the respective events are expected inside the shaded regions whereas 10 % of the events are expected above and below, respectively. The orange region corresponds to the acceptance region for the WIMP search as used in [5]. Figure adopted from [5]. Copyright (2013) by Springer Science+Media.

Additionally indicated in figure 2.2 is the region of interest for the dark matter search (orange region). This region indicates the light-yield energy range where events from WIMP-nucleon scattering are expected to show up, i.e., the acceptance region for the dark matter search. As WIMPs are expected to produce nuclear recoils in their interaction with baryonic matter (compare chapter I), the acceptance region comprises the nuclear recoil bands: O- and W-recoil event-bands (as indicated in figure 2.2) and the Ca-recoil event-band (which is between the O- and W-event bands, not indicated in figure 2.2). The lower limit of this region on the x-axis (i.e., with respect to energy detected in the phonon detector), $\sim$ 13keV, is defined by the overlap of the nuclear recoil bands with the electron/γ event-band, such that, for the complete data set, one electron-recoil event

[1] For details on the determination of the energy-dependent light detector resolution in CRESST, see [14].

in the acceptance region has to be expected [5]. The upper limit of this region on the x-axis (i.e., with respect to energy detected in the phonon detector), $\sim$ 40keV, is defined by the limited event rate (see [5] for details). The upper and lower limits of this region on the y-axis (i.e., with respect to energy detected in the light detector) are defined by the resolution of the light detector for energies corresponding to the mean light yields of the O- and W-event bands, respectively.

From figure 2.2 and the presented explanations, it becomes clear that in order to define the acceptance region for the WIMP search as well as to correctly identify the type of the interacting particle (or the recoil it produced), two requirements arise:

- On the one hand, the values of the Quenching Factors have to be known, as otherwise, the regions in the light-yield energy plane where events induced by different interacting particles are expected, cannot be identified. For the CRESST experiment, the following Quenching Factors[2] (see table 2.1) were determined and used for the analysis of the data from the last run [5]:

$QF^{e^-/\gamma}$	$:= 100\%$
QF^{α}	$\sim 22\%$
QF^{O}	$(10.4^{+0.5}_{-0.5})\%$
QF^{Ca}	$(6.38^{+0.62}_{-0.65})\%$
QF^{W}	$(3.91^{+0.48}_{-0.43})\%$
QF^{Pb}	$\sim 1.4\%$

Table 2.1: Quenching Factors as used and determined in the dark matter analysis of the latest CRESST-II run [5].

  It should be noted that these values were determined by experiments only and that, up to this point, no comprehensive understanding of the underlying physics exists. In addition, it should be taken into account, that the Quenching Factors stated in table 2.1, are assumed to exhibit no dependency on the energy of the primary interacting particle.

- On the other hand, in order to achieve an efficient background suppression, i.e., to clearly identify the type of interacting particle, light detectors with excellent energy resolution within the energy region of the acceptance region are required. This implies that the resolution of the light detector defines (besides other influences as, e.g., the counting statistics of photons being produced for particles of the same type and energy) the widths of the bands. It should be noted that, as discussed above, for electron/γ events only about 1.86% of the energy is detected in the light detector. Hence, for electron/γ-events with energies between $\sim$ 13keV and $\sim$ 40keV (region of interest), an energy of only about 240eV to 740eV is detected in the light detector. Thus, taking additionally the Quenching Factors (table 2.1) into account, which define the reduction of the light yield of different interacting particles compared to the light yield of electron/γ-events, it becomes clear, that the "light-energy" region of interest for the dark matter search comprises the region from $\sim$ 740eV down to

[2]The errors quoted for Quenching Factors that were determined previously in independent measurements are integrated in the dark matter analysis as Gaussian errors [5].

0eV. Hence, for an efficient background suppression with the CRESST-II experiment, light detectors with excellent energy resolution at very low energies are required.

From this discussion it becomes clear that, in order to achieve an efficient background suppression and particle identification with the CRESST-II experiment, on the one hand, the knowledge of the Quenching Factors for different interacting particles is mandatory, and that, on the other hand, light detectors with optimized energy resolution in the low-energy region are required.

Both of these requirements are addressed within the present work. In the first part of this thesis, the investigation of the application of the so-called Neganov-Luke effect for the improvement of the light-detector performance is presented. In the second part, the developed comprehensive, microscopic model which offers a detailed understanding of the Quenching Factors as well as allows to theoretically predict Quenching Factors for different interacting particles is described.

Part II

Cryogenic Composite Light Detectors with Neganov-Luke Amplification

Chapter 1

Motivation and Overview

As discussed in section I/2.2, the background suppression with the phonon-light technique, as employed in the CRESST experiment, is based on the identification of the interacting particle via the relative amount of scintillation light created in its energy-deposition process. A graphical illustration of the application of the phonon-light technique can be found in figure 2.2 (in section I/2.2) where the events recorded with one CRESST detector module are depicted in the light-yield energy plane: Each event is represented by its corresponding light yield, i.e., the relative amount of energy detected in the light detector in the form of scintillation-light photons (relative to the mean amount of scintillation light detected for 122keV γ-particles), and the energy detected in the phonon detector in the form of phonons. Thus, as can be seen from figure 2.2 (in section I/2.2), in order to identify the type of the interacting particle (or the type of nuclear recoil produced in the interaction process), two requirements can be formulated:

- On the one hand, the knowledge of the relative amount of scintillation light created for different interacting particles is essential for the identification of the type of the interacting particle. The observation that different amounts of scintillation light are created for the interaction of different particles in $CaWO_4$ is referred to as the light-quenching effect and is quantified by the so-called Quenching Factors (the light-quenching effect is discussed in detail in part III of this thesis). Thus, the Quenching Factor which is attributed to a type of particle defines the position of the mean of the light-yield band in the light-yield energy plane for interacting particles of this type, i.e., the mean vertical position where events caused by interacting particles of the regarded type are expected in the light-yield energy plane.

- On the other hand, in order to clearly identify the type of an interacting particle, i.e., to assign the light yield of a recorded event to one of the light-yield bands defined by the Quenching Factors, an efficient detection of the created scintillation light with high resolution is required. The widths of the light-yield bands indicated in figure 2.2 (section I/2.2) represent the uncertainty of the assignment of a recorded event to one type of interacting particle, i.e., to one Quenching Factor. The more scintillation light is detected and the higher the resolution of the light detector, the more accurate the assignment of the recorded event to one Quenching Factor. In other words, the more scintillation light is detected and the higher the resolution of the light detector, the smaller the widths of the light-yield bands, i.e., the more accurate the identification of the type of interacting particle. It should be noted that, of course, the minimum widths of these bands are limited by the Poisson statistics of the creation and detection process of the scintillation light. This implies that, even for a

light detector with "perfect" single photon detection, an uncertainty of the created and detected amount of scintillation light remains, due to the statistical variation in the creation and absorption process of scintillation-light photons. In addition, it should be noted that, for particle interactions in the $CaWO_4$ crystal with energies in the range interesting for the dark matter search ($\sim$ 13keV to $\sim$ 40keV, see region indicated in orange in figure 2.2 in section I2.2 and [5]), the absolute amounts of energy recorded in the light detector, i.e., the absolute amounts of scintillation light detected (in eV), are very small: Taking into account that, in a typical CRESST detector module, only about 1.86% of the energy of an electron recoil event is detected as scintillation light in the light detector [12], it can be deduced that for an electron event of 13keV (40keV), an energy of only about 242eV (744eV) is detected in the light detector. However, for nuclear recoil events (as expected for interactions of dark matter particles in the $CaWO_4$ crystal, see section I/1), the light-quenching effect additionally reduces the amount of light produced and, thus, detected. Thus, employing the Quenching Factor of, e.g., Tungsten recoils, as used in the last CRESST analysis (see table 2.1 in section I/2.2), it can be calculated that, for W recoils of 13keV (40keV), an energy of only about 9.5eV (29eV) is detected in the light detector. Thus, in the context of the CRESST experiment, the light-detector resolution at very low energies is important.

From this discussion, it can be deduced that one possibility to improve the particle identification with the phonon-light technique in the CRESST experiment, i.e., the background suppression for the dark matter search, is the improvement of the energy resolution of the light detector in the low-energy range. Within the present work, this issue is addressed by investigating the potential of the application of the so-called Neganov-Luke effect [15, 16] to cryogenic light detectors and by investigating the achieved improvement of the detector resolution.

The basic applicability of the Neganov-Luke effect for the improvement of the signal-to-noise ratio of a light detector was already extensively studied and proved in [17, 18]. In [17, 18], an improvement of the signal-to-noise ratio by a factor of $\sim$ 9 as well as an improvement of the energy resolution of the light detector at an energy of $\sim$ 615eV by $\sim$ 10% was achieved. However, on the one hand, no statement on the improvement of the detector resolution at even smaller energies - as interesting for the dark matter search - was made. On the other hand, a decrease of the amplification with time was observed, constituting a potential obstacle for the application of Neganov-Luke detectors in a dark matter search-experiment as CRESST which requires a long-term, stable detector response. Although in [17, 18], a method was developed to regenerate the detector and, thus, restore the originally achieved amplification, the drift of the light-detector signal-height between such regeneration events, nonetheless, would have to be corrected. Such a correction introduces additional uncertainties into the determination of the amount of scintillation light detected and is, thus, not advantageous.

Therefore, within the present work, on the one hand, a new fabrication method for Neganov-Luke amplified light detectors is suggested and tested experimentally. This method is designed to overcome the decrease of the signal amplification with time. On the other hand, the energy-dependent resolution of a light detector built according to the suggested method is investigated to clarify the achievable improvement of the particle identification and, thus, of the background-suppression capability of CRESST detector

modules by the application of the Neganov-Luke effect.

Hence, in the following, at first, a short introduction to the design of cryogenic composite light detectors as well as of a calibration method for light detectors using light pulses from a LED (from [17, 18]) is given (see chapter II/2). The introduction of this calibration method is important as it allows for an absolute calibration of the light-detector response also in the low-energy range interesting for the dark matter search as well as the determination and investigation of the energy-dependent absolute resolution of light detectors.

Thereafter, in chapter II/3, the signal amplification via the application of the Neganov-Luke effect is explained. The setup of a realized cryogenic composite light detector with Neganov-Luke amplification, built according to the suggested fabrication method (with the goal to overcome the discussed decrease of the amplification with time), is presented. Using this detector, experiments were performed with which the new design of the detector was tested with regard to achieved improvements of the signal stability with time. Additionally, the energy-dependent resolution of the light detector with and without Neganov-Luke amplification was investigated. The results from these experiments are presented and discussed. A physical interpretation of the observed variation of the dependency of the detector resolution on the energy and the applied voltage is presented. In the end, the potential improvement of the energy-dependent particle identification in a CRESST detector module is quantified that could be achieved using this light detector with applied Neganov-Luke voltage compared to the employment of this light detector without Neganov-Luke voltage. The great potential of the application of Neganov-Luke detector for the improvement of the background suppression in the CRESST experiments is discussed.

Chapter 2

Cryogenic Composite Light Detectors and Calibration Method for Light Detectors

In this chapter, the composite detector design for cryogenic light detectors is presented (see section II/2.1) as well as a calibration method for light detectors using light pulses from a LED is introduced (see section II/2.2). In section II/2.3, the application of this calibration method to a cryogenic composite detector is presented and the obtained results are discussed. The accuracy of the calibration method is demonstrated.

2.1 Cryogenic Composite Light Detectors

The cryogenic light detectors investigated in the present work are built according to the composite design which is introduced in the following. Thereafter, a realized composite light detector is presented.

2.1.1 Composite Detector Design

For a short description of the basic design and working principle of cryogenic detectors, see section I/2.1. For the composite detector design, the TES is produced on a separate small crystal substrate which is then attached to the absorber of the detector, i.e., in the case of the light detectors built within the present work, a thin, high-purity Si substrate, by glueing. In figure 2.1, a sketch of the principle design can be seen:

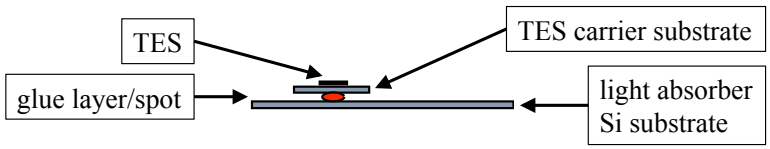

Figure 2.1: Sketch of the composite detector design applied for light detectors.

For details on the composite detector design, a discussion of its advantages compared to the production of the TES directly on the absorber of a cryogenic detector as well as for a thermal detector model for cryogenic composite detectors, see [19, 20]. In the context

of the application of the Neganov-Luke effect to cryogenic detectors, the employment of the composite detector design especially offers the advantage that the TES and the absorber substrate are electrically decoupled from each other. This is desirable as, for the employment of the Neganov-Luke effect, a voltage is applied across the absorber (for details, see section II/3.1) which, if the TES would not be electrically decoupled, could disturb the signal generation in the TES.

2.1.2 Realized Composite Detector

In figure 2.2, a photograph of a realized composite light detector (detector *571-7*) can be seen. In addition, a sketch of the employed TES design which basically corresponds to the design of the light-detector TESs as applied in the CRESST experiment[1] (compare, e.g., [21]) is shown:

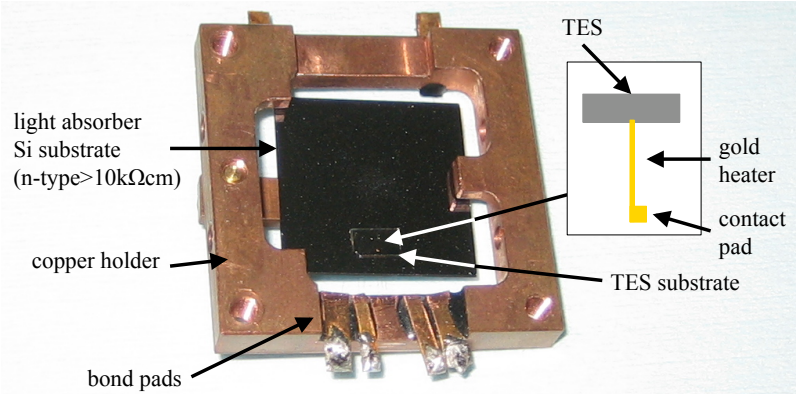

Figure 2.2: Photograph of a realized composite light detector with a CRESST-like TES design: Additionally shown is the sketch of the TES design utilized.

The TES (0.3x1.0)mm^2 consists of an Ir-Au bilayer evaporated onto a small (3x5x0.3)mm^3 Si substrate (for details on Ir-Au TESs, see, e.g., [22]). The absorber substrate is a Si n-type substrate with a specific resistance $>$ 10kΩcm of (20x20x0.38)mm^3. Measurements with this detector will be presented in section II/2.3.

2.2 Calibration Method

The LED calibration method was introduced in [17, 18] where it is described in detail. In the following, only a short summary of the method and its employment within the present work is given. Light pulses from a pulsed blue InGaN-LED[2] (peak wavelength at $\sim$ 430nm, chosen to approximately match the spectral range of the $CaWO_4$ light emission, $\sim$ 440nm, see section III/5.1.2) at room temperature are guided onto the detector at mK temperatures (in a He_3/He_4 dilution refrigerator) with the help of a glass fiber. By varying the pulse height of the LED pulses[3], a spectrum with various peaks, P_n ($n = 1, 2, \ldots$),

[1] The TESs of CRESST light-detectors are additionally equipped with Al phonon collectors to enlarge the phonon collection area.

[2] LED430-06, Roithner Lasertechnik GmbH, Wien, Austria. Peak wavelength: 430nm, half width: 20nm.

[3] The LED was operated with rectangular voltage pulses from a function generator: Dual-Channel Arbitrary/Function Generator AM300, Rhode und Schwarz, München, Germany.

corresponding to different pulse heights of the LED light-pulses can be recorded. Readout of the light-detector signal is realized with a SQUID (Superconducting Quantum Interference Device). In the analysis of the recorded data (pulses from the light detector, the analysis is performed analogously to the one described in [22]), each peak (containing, e.g., 2000 pulses of the nominal same respective pulse height each) is fitted with a Gaussian. In this way, each peak P_n is assigned a peak position $x(P_n)$, corresponding to a specific amount of energy deposited in the light-detector substrate, and a peak width, $\sigma_{tot}(P_n)$, corresponding to the 1-σ resolution of the light detector at the respective energy (both quantities in analog-to-digital converter-channels, i.e., ADC channels). As described in [17, 18], it can be assumed that the total resolution of the light detector, σ_{tot}, can be described by two independent contributions: A constant contribution σ_0, comprising, e.g., the electronic noise component of the signal, and the energy-dependent contribution, σ_{ph}, corresponding to the Poisson counting statistics of the creation and detection process of the detected photons from the LED (or from the $CaWO_4$ crystal). Using this assumption, the pulse height x registered in the light detector for a number of N detected photons as well as the corresponding resolution, $\sigma_{tot}(x)$, of the light detector can be expressed as (see [17, 18]):

$$x = a \cdot N \tag{2.1}$$

$$\sigma_{ph} = a \cdot \sqrt{N} \tag{2.2}$$

$$\sigma_{tot}^2 = \sigma_0^2 + \sigma_{ph}^2 \tag{2.3}$$

$$\Rightarrow \sigma_{tot} = \sqrt{\sigma_0^2 + a^2 \cdot N} = \sqrt{\sigma_0^2 + a \cdot x} \tag{2.4}$$

where a denotes the scaling factor between the pulse height x of the light-detector signal and the number N of detected photons. Equation 2.2 describes the Poisson counting statistics for the number of N detected photons. As indicated by equation 2.4, in this way, a relationship between the resolution σ_{tot} and the pulse height x of the light detector is achieved. By fitting equation 2.4 to the experimentally determined pulse-height resolution set (from the LED calibration measurement), $(x(P_n), \sigma_{tot}(P_n))$ with $n = 1, 2, \ldots$, the values for the scaling factor a as well as the constant noise term σ_0 can be determined. If these parameters are known, equation 2.1 can be used to calculate the number of photons detected for each peak, P_n. Thus, as the energy per photon, $E_{ph} = 2.9\text{eV}$, is known, the response of the light detector can be calibrated and the energy-dependent resolution of the light detector can be expressed in terms of energy. The relationship of the energy detected in the light detector, E, to the pulse height, x, can be expressed by:

$$E = \frac{E_{ph}}{a} \cdot x \tag{2.5}$$

Hence, it can be seen that, the larger the scaling factor a, the smaller the energy detected corresponding to the same pulse height x or, in other words, the larger the scaling factor a, the larger the pulse height x that is recorded for the same amount of energy (compare also equation 2.1).

Thus, performing a measurement campaign with different LED pulse-heights, an energy calibration and the energy-dependent resolution of the investigated light detector can be determined. It should be noted that, employing such a calibration scheme, small energy depositions, as they are interesting in the context of the CRESST experiment (compare

section II/1) can be realized, as well as the complete area of the light detector can be tested (by illuminating the complete absorber area[4]).

2.3 Application of the Calibration Method

A LED calibration as described in section II/2.2 with the light detector *571-7* (see section II2.1.2) was performed. In addition to the LED calibration, a spectrum with events recorded for a ^{55}Fe source was recorded. It should be noted that an aperture was used in between the ^{55}Fe source and the light detector so that only a small area of the light absorber was exposed to the ^{55}Fe source, whereas the photons from the LED were illuminating the complete area of the Si absorber.

2.3.1 Results and Discussion

From the data recorded with the LED calibration, the $(x(P_n), \sigma_{tot}(P_n))$ $(n = 1, 2, \ldots)$ parameter set is determined and fitted using equation 2.4. The following values for the parameters σ_0 and a were determined from the fit (in ADC channels of the SQUID response):

$$a = (2.31 \pm 0.07)\text{ADC channels} \tag{2.6}$$

$$\sigma_0 = (8.78 \pm 0.23)\text{ADC channels} \tag{2.7}$$

It should be noted that the errors stated correspond to the statistical uncertainties from fit results. This is also the case for all other uncertainties stated within the following discussion.

Using the values determined for a and σ_0 as well as the energy calibration that can be performed with the help of the scaling factor a, the energy calibration can be performed and the energy-dependent resolution of the light detector can be determined. Defining the energy threshold, E_{th}^{LED} of the detector as the 5σ width of the constant noise term σ_0 (compare, e.g., [17, 18]), E_{th} can be determined from the LED calibration to amount to:

$$E_{th}^{LED} = (55.1 \pm 2.2)\text{eV} \tag{2.8}$$

In figure 2.3, the LED calibration performed, i.e., the $(x(P_n), \sigma_{tot}(P_n))$ $(n = 1, 2, \ldots)$ set in ADC channels (left y-axis and lower x-axis) is shown as blue markers (error bars of the data points correspond to the statistical uncertainties of the fits of the Gaussian to the peaks P_n). The right y-axis as well as the upper x-axis depict the result of the energy calibration. In addition, the result of the fit of equation 2.4 (section II/2.2) to the data is shown as a red line.
From figure 2.3, it can be seen that the assumed dependency of the light-detector resolution on the amount of energy detected (compare equation 2.4 in section II/2.2) delivers a satisfying description of the data. This observation already points to the applicability of the LED calibration method for the determination of the energy calibration as well as of the energy-dependent detector resolution. However, to finally validate the LED calibration method, the energy calibration obtained can be tested using the measurement performed with the ^{55}Fe source, as described in the following.

[4]This is in contrast to the calibration with, e.g., an x-ray source with aperture.

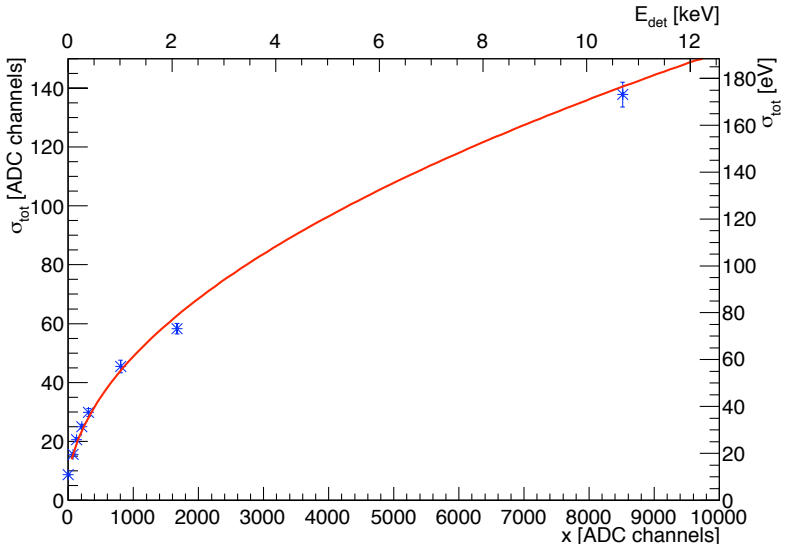

Figure 2.3: LED calibration performed with detector *571-7*: The 1σ widths of the peaks recorded in the LED calibration are plotted versus their positions (blue markers and error bars). The left y-axis and the lower x-axis correspond to the size of these quantities in ADC channels, i.e., as measured. The right y-axis corresponding to $\sigma_{tot}(E_{det})$, the energy-dependent detector resolution and the upper x-axis corresponding to the energy E_{det} in the light detector, depict the result of the energy calibration. In addition, the result of the fit of equation 2.4 (in section II/2.2), i.e., of the LED calibration, is shown as a red line.

2.3.2 Accuracy of the Calibration Method

In addition to the determination of the energy threshold of the detector, from the LED calibration, the ADC channel for which the mean of the Mn-K$_{alpha}$ line (5.89keV) from the ^{55}Fe source, $x^{LED}(E(\text{Mn-K}_{alpha}))$, is expected as well as the width of this line, $\sigma_{tot}^{LED}(E(\text{Mn-K}_{alpha}))$, can be predicted:

$$x^{LED}(E(\text{Mn-K}_{alpha})) = (4691.69 \pm 142.17)\text{ADC channels} \tag{2.9}$$

$$\sigma_{tot}^{LED}(E(\text{Mn-K}_{alpha})) = (104.47 \pm 2.22)\text{ADC channels} \tag{2.10}$$

These predictions can be compared to the results obtained from the analysis of the measurement using the ^{55}Fe source: From this measurement, the following peak position, $x^{Fe}(E(\text{Mn-K}_{alpha}))$, and 1σ width, $\sigma_{tot}^{Fe}(E(\text{Mn-K}_{alpha}))$, of the Mn-K$\alpha$ line can be determined:

$$x^{Fe}(E(\text{Mn-K}_{alpha})) = (4643.09 \pm 1.52)\text{ADC channels} \tag{2.11}$$

$$\sigma_{tot}^{Fe}(E(\text{Mn-K}_{alpha})) = (32.0 \pm 1.53)\text{ADC channels} \tag{2.12}$$

Additionally to the events caused by the x-rays from the ^{55}Fe source, random triggers were used to acquire empty baselines. These empty baselines can be employed to determine the 5σ width of the baseline noise. As, e.g., discussed in [18], the 5σ width of the baseline noise can be regarded as the energy threshold, E_{th}, of the detector. Using the information obtained from the Mn-K$_\alpha$ line to calibrate the energy scale, the energy threshold of the detector can be expressed in terms of energy:

$$E_{th} = (63.6 \pm 1.0)\text{eV} \tag{2.13}$$

Comparing the values predicted from the LED calibration to the values determined from the measurement with the ^{55}Fe source, several observations can be made:

- The mean of the line of the Mn-Kα line, as predicted by the LED calibration and as determined from the recorded spectrum, are in very good agreement. Thus, the method employed to obtain an energy calibration from the measurements of various peaks from a LED is validated. Therefore, also the energy-dependent resolution of the light detector in the LED-calibration measurement has to be valid.

- However, comparing the widths of the Mn-Kα line, as predicted by the LED calibration and as determined from the recorded spectrum, it can be seen that they clearly deviate from each other. Regarding this deviation, it should be recalled that the photons from the LED were used to irradiate the complete detector surface whereas the detector area illuminated by the x-rays from the ^{55}Fe source was strongly diminished by using an aperture. Due to the thin substrate of the light detector and the accordingly large surface-to-volume ratio, rather large deviations of the signal heights for energy depositions at different positions of the detector can be expected (see, e.g., discussion in [18]). Thus, as, by the ^{55}Fe source only a very small area of the detector was illuminated, all of the recorded Mn-Kα events were produced at nearly the same position. Hence, for these events, the position-dependnecy of the detector response does not contribute to the broadening of the peak in the spectrum. For the events recorded in the LED calibration, however, the energy-dependent response of the detector contributes to the broadening of the peaks observed in the spectrum and, thus, to the energy-resolution of the detector, as the complete detector area was illuminated with the photons from the LED. Therefore, the observed difference in the determined and predicted width of the Mn-Kα line can be explained consistently and does not indicate any invalidity of the LED calibration method. Instead, this observation motivates the employment of light pulses (illuminating the complete detector area) for the characterization of light detectors in the context of the CRESST experiment as, in the CRESST experiment, also the complete area of the light detector substrate is exposed to the scintillation light generated in particle interactions in the $CaWO_4$ crystal.

- In addition, it should be noted that the described different impact of the position-dependency of the detector response onto the width of the peak observed in the ^{55}Fe calibration and onto the width determined with the LED calibration can also produce a deviation of the mean values of the predicted and determined position of the Mn-Kα peak. Dependent on the position of the area illuminated by the x-rays from the ^{55}Fe source and the detector response for this special position (which can be smaller or larger than the mean detector response of the complete detector), a positive or negative deviation of the measured Mn-Kα peak position from the position predicted by the LED calibration can be expected.

- Comparing the values determined for the energy thresholds from the ^{55}Fe calibration and the LED calibration, on the one hand, the described effect of the position dependency of the detector response has to be considered (as the energy-peak-position relationship of the Mn-Kα line is used for the conversion of the width of the noise peak into energy). However, on the other hand, also the different methods used to determine the respective values have to be taken into account: The value for the energy threshold obtained from the LED calibration is determined with the help of

the fit of the complete data set recorded in the LED calibration (compare figure 2.3 in section II/2.3.1). The value for the energy threshold obtained from the ^{55}Fe calibration, however, is determined by using the information of the widths of the noise peak and the Mn-Kα peak only, i.e., by extrapolating the energy-position relationship obtained from the 5.89keV Mn-Kα peak down to a few tens of eV. Thus, the value determined from the ^{55}Fe calibration can be expected to be afflicted with a significantly larger systematic uncertainty than the value determined from the LED calibration. From these considerations it can be deduced that the two values determined, i.e., $E_{th}^{LED} = (55.1 \pm 2.2)$eV and $E_{th}^{LED} = (63.6 \pm 1.0)$eV (statistical uncertainties only), most likely agree with each other. The value obtained from the LED calibration is regarded is more reliable, especially taking the position dependency of the detector response into account.

Thus, in conclusion, it can be stated that the application of the LED calibration method for the characterization of light detectors (especially in the context of the CRESST experiment) is validated and well-motivated. This method will also be employed to characterize the detector response and energy-dependent resolution of Neganov-Luke amplified light detectors (see chapter II/3).

Chapter 3

Neganov-Luke Amplified Cryogenic Composite Light Detectors

In this chapter, the investigation of the potential of Neganov-Luke amplified light detectors for the improvement of particle identification, i.e., background suppression, employing the phonon-light technique in the CRESST experiment is presented. In section II/3.1, a short introduction to the Neganov-Luke effect as well as an overview of the results obtained for Neganov-Luke amplified cryogenic detectors in the context of the CRESST experiment from the literature is given. In section II/3.2, a new fabrication method of Neganov-Luke amplified light detectors, dedicated to resolve the problem of the decreasing signal height with time (compare discussion in chapter II/1) is presented. A cryogenic light detector built according to the new fabrication method is investigated concerning the amplification stability with time as well as concerning its voltage- and energy-dependent energy resolution by using the LED calibration method introduced in section II/2.2. The measurements and results obtained are discussed and interpreted in section II/3.3. Consequences that can be drawn from the gained understanding of the underlying physics effects are presented. In section II/3.4, the potential of the observed energy-dependent improvement of the light-detector resolution for the particle identification and, thus, for the background suppression in the CRESST experiment is discussed.

3.1 The Neganov-Luke Effect

3.1.1 Working Principle

The Neganov-Luke effect is based on the amplification of the phonon signal in the semiconducting absorber of a cryogenic detector by drifting the electron-hole pairs created in the energy-deposition process of a particle in an electric field applied across the absorber [15, 16]. The electric field is generated by a so-called Neganov-Luke voltage, V_{NL}, which is applied across the absorber of the cryogenic detector via electrodes deposited on adjacent sides of the absorber of the cryogenic detector. The charge carriers deposit the energy they gain in their drift process in the electric field in the form of phonons in the absorber of the detector and, thus, amplify the phonon signal in the detector. Hence, if the summed drift length l_d of the electron and hole of one electron-hole pair initially created with energy E_{eh} corresponds to the distance between the electrodes d, i.e., if both charge carriers are

collected at the electrodes, the thermal gain $G_t(V_{NL})$ per one electron-hole pair is given by $G_t(V_{NL}) = 1 + \frac{e \cdot V_{NL}}{E_{eh}}$, where e corresponds to the electron charge. The thermal gain is the factor, the amount of phonons generated has to be multiplied with in order to account for the extra phonons generated by the application of the Neganov-Luke effect. As the signal height in a cryogenic detector (based on the detection of phonons for signal read out, compare section I/2.2) is assumed to be proportional to the energy deposited in the absorber in the form of phonons, also the signal height per one electron-hole pair has to be multiplied with the thermal gain, $G_t(1\,eh)(V_{NL})$. Thus, if all charge carriers created in the primary energy deposition-process by a particle with energy E_{part} in the absorber of the cryogenic detector are collected at the electrodes, the thermal gain achieved for the overall signal height in the detector corresponds to

$$G_t(V_{NL}) = 1 + \frac{e \cdot V_{NL}}{\epsilon} \tag{3.1}$$

where ϵ denotes the mean energy that an electron-hole pair obtained in the energy-deposition process of the primary interacting particle. In the case of the cryogenic light detectors investigated in the present work, it can be assumed that for each photon of the LED (or the $CaWO_4$ crystal) with an energy of $E_{ph} \approx 2.9$eV, one electron-hole pair is created, i.e., that the mean energy per electron-hole pair, ϵ, corresponds to the energy of one photon (compare [17, 18] and references therein). As discussed in [17, 18], the theoretically achievable gain, defined by equation 3.1 can be reduced by two effects.

- On the one hand, charge carriers can accumulate below the electrodes, partially compensating the applied Neganov-Luke voltage and, thus, leading to a reduced effective voltage $V_{NL}^{eff}(t)$ existent within the absorber of the cryogenic detector [23]. It should be noted that, following [17, 18], the effective, reduced voltage $V_{NL}^{eff}(t)$ is assumed to be possibly dependent on time t as the accumulation process of charge carriers below the electrodes is a time-dependent process.

- On the other hand, the charge carriers can become captured by electron traps (existing in every real crystal lattice) in their drifting process, thus, reducing the mean drift distance l_d of an electron-hole pair in comparison to the distance between the electrodes, i.e., $l_d < d$ [23]. It should be noted that the mean drift distance results from the averaging of the lengths traveled by the fraction of electron-hole pairs collected at the electrodes and by the fraction of electron-hole pairs for which at least one charge carrier was trapped in the drift process, reducing the drift distance for this electron-hole pair. Hence, a reduced average drift length does not correspond to a reduced drift length for all electron-hole pairs, but to the incomplete collection of all charge carriers.

The thermal gain under consideration of these effects is reduced to:

$$G_t^{eff}(V_{NL}^{eff}(t)) = 1 + \frac{e \cdot V_{NL}^{eff}(t)}{\epsilon} \cdot \frac{l_d}{d} \tag{3.2}$$

3.1.2 Current Status of Achieved Improvements and Open Questions

As can be deduced from this discussion, for the employment of the Neganov-Luke effect, it is required that electrodes are deposited onto the light-detector substrate to enable the application of the Neganov-Luke voltage. For the composite Neganov-Luke light detector

realized and investigated within the present work, the basic design was adopted from [17, 18]. The differences between the applied basic designs are that, within the present work, a structured CRESST-like TES was employed as well as that the fabrication of the electrodes was altered as will be discussed in section II/3.2. A sketch of this designs as employed within the present works is shown in figure 3.1.

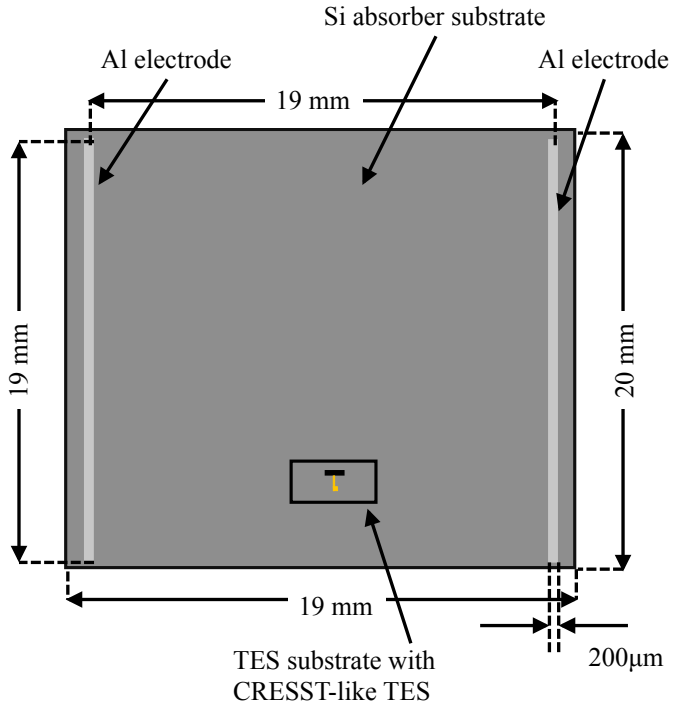

Figure 3.1: Sketch of the design of a Neganov-Luke amplified light detector as utilized within the present work and as adopted from [17, 18]: The top view onto the light detector is depicted.

As can be seen from figure 3.1, two Al electrodes are deposited close to the edges of one surface of the light-detector substrate. In this way, the Neganov-Luke voltage is applied homogeneously almost across the complete area of the light detector while maintaining a large part of the light-detector absorber uncovered, which can then be used for light detection. In [17, 18], with Neganov-Luke detectors built according to this design, an improvement of the signal-to noise ratio of the light-detector signal at an applied Neganov-Luke voltage of 100V by a factor of ~ 9 was achieved and an improvement of the light-detector resolution at $\sim$ 615eV by $\sim$ 10% was observed. However, as discussed in chapter II/1, a decrease of the amplification with time is observed: For an applied Neganov-Luke voltage of 50V, the pulse height of a LED light-pulse is observed to decrease by a factor of ~ 1.4 during a measurement time of $\sim$ 1.1h (see figure 6.17 in [18], energy-deposition rate during this measurement: $\sim 50\frac{\text{keV}}{\text{s}}$) [18]. In [17, 18], this reduction of the pulse height is attributed to space charges building up below the contacts, reducing the effective Neganov-Luke voltage and, thus, the observable amplification with time. To account for this decrease, a regeneration method (flushing with long LED pulses without applied Neganov-Luke voltage) was developed and successfully applied. It is estimated that, in a dark matter search experiment like CRESST in a low-background environment with reduced energy-deposition rate, one regeneration process at most every 24h would have to be applied [17]. How-

ever, as discussed in [17], the need for a correction of the pulse height to account for the decreasing amplification between such regeneration procedures still exists. Such a correction of the pulse height introduces an additional uncertainty into the determination of the amount of scintillation light detected in the dark matter search which is not advantageous.

From this presentation of the results and the understanding achieved for Neganov-Luke detectors in [17, 18], it becomes clear that, in order to finally clarify the applicability and the potential of Neganov-Luke amplified light detectors for the dark matter search with CRESST, two open questions should be addressed:

- On the one hand, a prevention of the accumulation of charge carriers below the electrodes is strived for as, then, no decrease of the amplification with time is expected to occur (see sections II/3.2 and II/3.3.1).
- On the other hand, the energy-dependent resolution of a Neganov-Luke amplified light detector in the energy region which is interesting in the context of the dark matter search has to be investigated to clarify the influence of the Neganov-Luke amplification on the efficiency of the particle identification with the phonon-light technique (see sections 3.3.2 and 3.4).

These open questions were investigated within the present work as presented in the following.

3.2 New Fabrication Method of Neganov-Luke Amplified Light Detectors

In the following, a new fabrication method for the electrodes of Neganov-Luke amplified light detectors is suggested which is expected to overcome the observed decrease of the pulse height with time. As already discussed in [17, 18], most probably, electron and hole traps within the band gap of the Si absorber of the light detector in the region below the electrodes, can be identified as the cause of the observed decrease of the amplification in time as this decrease is attributed to an accumulation of charge carriers below the electrodes.

In more detail, it can be deduced that, in order to generate the observed decrease of the amplification with time, i.e., a reduction of the effective voltage within the light-absorber substrate, a spatial concentration of electron and hole traps below the electrodes has to exist. This can be concluded as, if only traps homogeneously distributed within the absorber substrate existed, charge carriers would be trapped homogeneously distributed within the complete substrate so that no resulting effective counter-voltage within the substrate could built up. On the basis of this interpretation of the observed decrease of the amplification with time, in the present work, it is suggested that the required increased trap density below the electrodes is caused by an increased defect (impurity) density below the electrodes which is created in the production process of the electrodes. The process applied for the production of the aluminum electrodes of the Neganov-Luke detectors reported in [17, 18] as well as in the present work involves the following steps (for a more detailed description of the process, see, e.g., [18]):

- A negative photolithographic process defining the regions on the Si substrate where the electrodes are deposited on.

- The introduction of the absorber substrate into a ultra-high vacuum (UHV) system.
- A short Ar ion etching step which is performed to remove the natural oxide layer present on the Si substrate. This step is performed in order to achieve a semiconductor-metal contact with ohmic behavior as well defined as possible. It should be noted that, as discussed in [17, 18], concerning the type of the contact achieved with this method (i.e., if the contact behaves ohmic or Schotty-like), uncertainties remain. In this context, it should be noted that often different amplifications are observed for forward or reversed bias of the Neganov-Luke voltage [17, 18]. This points to an undefined Schottky-like behavior of the contacts as, in principle, the applied voltage polarities should be indistinguishable as both contacts are nominally identical. Also this observation is attempted to be addressed via the newly introduced fabrication method within the present work (see below).
- The deposition of the Al layer of the electrodes in the same UHV system (in [17, 18] with a thickness of $\sim$ 2kÅ by electron-beam evaporation, in the present work with a thickness of $\sim$ 5kÅ by Ar-sputtering with a Kaufmann-source).
- A lift-off process of the photolithographic mask.

From this description of the production process of the electrodes, it can be deduced that a destruction of the Si crystal structure below the electrodes is introduced by the Ar etching step as well as by the deposition of Al by sputtering (in the sputtering process, rather high-energetic Al atoms impinge onto the Si surface). Hence, in addition to the destruction of the crystal structure of the Si absorber below the Al electrodes, it can also be expected that a fraction of the Al atoms is implanted into the Si substrate. There, in general, the Al atoms occupy predominantly interstitial lattice sites without an annealing step (as is applied for intentional doping of Si). Furthermore, Si and Al are known to exhibit a non-neglibible solubility within each other [24], even at room temperature. Thus, it can be expected that a fraction of the Al atoms deposited onto the Si surface diffuses into the Si substrate and vice a versa (in fact, the diffusion of Al into Si is a well known process to occur, potentially shortening blocking contacts by so-called junction spiking).

Thus, after the production process as described above, it can be expected that, on the one hand, Al impurities are introduced into the Si absorber below the electrodes and, on the other hand, that the crystal structure of the Si absorber is damaged below the electrodes. This is clearly not beneficial as Al is known to introduce acceptor levels $\sim$ 0.069eV above the valence-band edge in Si whereas Si vacancies in Si (defects of the crystal structure) are known to introduce deep acceptor levels $\sim$ 0.34eV below the conduction-band edge (compare, e.g., [25]). Hence, it can be deduced that a fabrication method for the Al electrodes has to be employed that either avoids the production of defects from the beginning or, at least, allows to heal the defects produced in the electrode-production process afterwards. In addition, as, in any case, it can be expected that Al diffuses into the Si substrate (if no blocking layer is utilized), the contact area below the Al electrodes can be assumed to be p^+-doped (Al acts as p^+-dopant in Si [25]). This circumstance should be capitalized to produce contacts with mostly ohmic character by employing Si p-type substrates [26] instead of Si n-type substrates, as were utilized, e.g, in [17, 18].

On the basis of this discussion and the consequences drawn, within the present work, an extended production process for the Al electrodes is suggested using Si p-type substrates:

In principle, the complete production process as described above is adopted, however, after the lift-off process, an additional step, a forming-gas annealing procedure is applied. With this annealing step, on the one hand, a metallization of the Al-Si contact (alloying of the contact [26]) as well as a, at least, partial annealing of the defects of the Si crystal structure below the electrodes is attempted to be achieved.

For the realization of a Neganov-Luke detector fabricated according to the suggested method, Al electrodes were deposited onto a Si p-type substrate of (20x20x0.525)mm^3 with a specific resistivity $< 6k\Omega cm$ following the procedure described above. The annealing step was conducted using a forming-gas mixture of 95% N_2, 5% H_2, a ramping rate of 6°C/minute, a final annealing temperature and time duration of annealing of 400°C for half an hour and a ramping rate of 6°C/minute back down to room temperature[1]. As the last step of the light-detector production, a Tungsten TES sputtered onto a small Al_2O_3 substrate of (3x5x0.33)mm^3 (for a description of the W-TES production process as well as the utilized deposition system, see [20]) and structured as depicted in figure 3.1 (in section II/3.1) was glued onto the absorber substrate. The produced detector is labeled as *0202-6*. In figure 3.2, the super-to-normal conducting transition of the utilized W-TES is shown (recorded for a bias current of $1\mu A$):

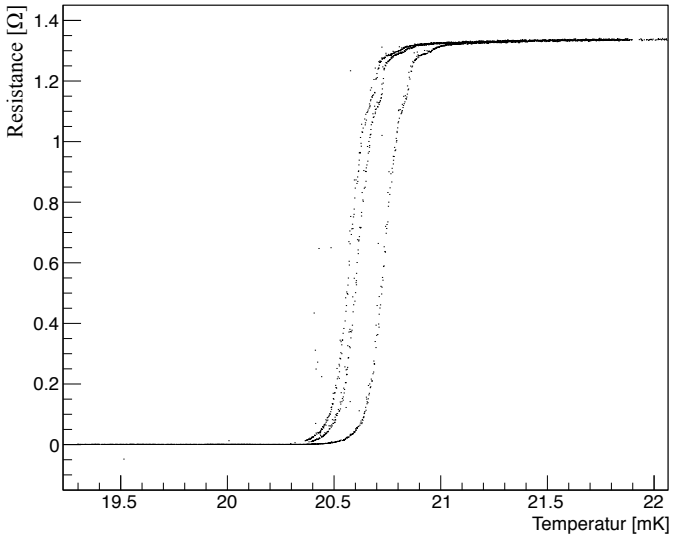

Figure 3.2: Super-to-normal conducting transition of the W-TES of detector *0202-6* recorded for a bias current of $1\mu A$: The transition temperature amounts to $\sim$ 20.6mK with a width of only $\sim$ 0.2mK. The fact that multiple shapes of the transition are visible can be attributed to the weak thermal coupling of the detector and, thus, of the TES to the copper holder on which the heater and thermometer utilized for the transition measurement were located. For details on the measurement of superconducting transition curves, see, e.g., [18].

Unfortunately, it was observed that, in the annealing step, impurities (most probably metal impurities) were deposited onto the surface of the Si absorber (visible as weak coloring of the surface under certain angles of observation). These impurities prevented the

[1]This procedure was assessed in collaboration with Dr.-Ing. L. Nebrich, Fraunhofer Institut für Modulare Festkörper-Technologien EMFT, NMD, München, Germany. The annealing procedure was performed by Dr. habil. A. Erb, crystal laboratory, Technische Universität München, Germany.

application of high voltages (larger than $\sim$ 90eV) and resulted in a rather low amplification observed for detector *0202-6* which is attributed to the effect of a reduced drift length due to carrier trapping as described in section II/3.1. Nonetheless, detector *0202-6* could be employed for measurements to investigate the open questions raised in the context of the application of the Neganov-Luke amplification. These measurements as well as the results are described and discussed in the following.

3.3 Performed Measurements and Results

In order to investigate the two questions raised in the context of the applicability of the Neganov-Luke effect for the dark matter search with the CRESST experiments (compare section II/3.1), with detector *0202-6* (described in section II/3.2), the following measurements (combination of two campaigns, $MC1$ and $MC2$) were performed:

- A measurement at an applied Neganov-Luke voltage of $V_{NL} = 40\text{V}$ for $\sim$ 2.7h for which an LED pulse-height was monitored. The mean energy-deposition rate during this measurements was $\sim 40\frac{\text{keV}}{\text{s}}$. Hence, the conditions of this measurement can be approximately compared to the measurement in [18] (described in section II/3.1) for which a decreasing amplification over time was observed.
- LED calibration with electrically shortened contacts, i.e., $V_{NL} = 0\text{V}$ applied Neganov-Luke voltage. For each of the two measurement campaigns, one "0V" LED-calibration was performed in order to provide a reference point for the assessment of the achieved amplification and energy-resolution of the detector response with applied Neganov-Luke voltage. As will be discussed below, due to relating all measurements to their respective "0V"-measurement, the results obtained from the two campaigns can be combined as they describe the intrinsic behavior of the detector.
- LED calibrations for applied Neganov-Luke voltages of $V_{NL} = +10\text{V}, \pm 20\text{V}, +40\text{V}, -60\text{V}, -80\text{V}$ were performed. It should be noted that the measurements performed at $V_{NL} = -60\text{V}, -80\text{V}$ were performed in $MC2$ while all other measurements were performed in $MC1$. For these LED calibrations, the same pulse heights of the LED pulses as in the respective "0V" measurements were utilized. Thus, every peak P_n in the spectrum recorded for applied Neganov-Luke voltage can be assigned to a peak in the spectrum recorded in the respective "0V" measurement.

The recorded data was analyzed in analogy to the description in [22]. In the following, the results of these measurements are presented and discussed.

3.3.1 Amplification Stability with Time

In figure 3.3, the amplitudes of the LED pulses (blue markers, determined, applying a standard-event fit, see [22]) recorded with detector *0202-6* at an applied Neganov-Luke voltage of $V_{NL} = 40\text{V}$, are shown versus time. In addition, a fit of a straight line to the amplitudes of the pulses versus time is depicted as solid, red line.
From figure 3.3, it can be seen that, in contrary to the results reported in [17, 18] (decrease of the signal height by a factor of $\sim$ 1.4 after $\sim$ 1.1h), the signal height, i.e., the amplification of the signal, is constant over the complete measurement time of $\sim$ 2.7h (for a comparable energy-deposition rate). The fit with the straight line reveals a gradient of less than 0.4% of the absolute value of the pulse height, being statistically consistent with

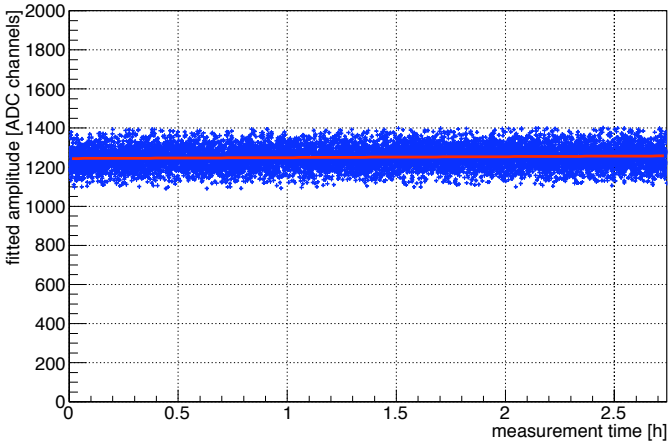

Figure 3.3: Fitted amplitudes (blue markers) of the light-detector signals for one LED pulse-height recorded with detector *0202-6* at $V_{NL} = 40$V monitored for ~ 2.7h. In addition, a fit of a straight line to the distribution of events is depicted as solid, red line.

a constant pulse height. Thus, it can be deduced that the interpretation of the decrease of the amplification observed in [17, 18] as well as the consequences drawn for the fabrication method of the Neganov-Luke electrodes within the present work are correct.

3.3.2 Voltage- and Energy-Dependent Light Detector Resolution

Concerning the analysis of the data recorded in the two measurements campaigns ($MC1$ and $MC2$), it should be noted that both measurement campaigns were performed using the same SQUID, the same settings for the detector read out as well as the same working point of the detector. In the following, it will become clear that this agreement of the measurement conditions allows to utilize the results obtained in both measurements together in a combined analysis (concerning the amplification and energy-resolution of the detector). Actually, it should be noted that the measurement performed with detector *571-7* (see section II2.3.1) was, in turn, performed with a different SQUID, however, the gain of the different SQUID systems utilized is almost identical. Thus, in fact, also the values for the constant noise term, σ_0 as well as for the scaling factor a, determined for detector *571-7*, can be used for a comparison of the "0V" measurements.

"0V" LED-Calibration Measurements

At first the respective "0V" LED calibrations of the measurement campaigns $MC1$ and $MC2$ are analyzed, yielding the scaling factors a^{MC1} and a^{MC2} as well as the constant noise terms σ_0^{MC2} and σ_0^{MC1} (in ADC channels), respectively, in analogy to sections II/2.2 and II/2.3.1. The following values (in ADC channels) were determined:

$$a^{MC1} = 0.493 \pm 0.009 \tag{3.3}$$

$$\sigma_0^{MC1} = 7.12 \pm 0.12 \tag{3.4}$$

$$a^{MC2} = 0.476 \pm 0.007 \tag{3.5}$$

$$\sigma_0^{MC2} = 11.56 \pm 0.09 \tag{3.6}$$

From these values, the following, respective (5σ) energy thresholds (compare section II/2.3.1) of detector *0202-6* in the respective measurement campaign can be determined:

$$E_{th}^{LED\,MC1} = (209.4 \pm 5.3)\text{eV} \tag{3.7}$$

$$E_{th}^{LED\,MC2} = (351.8 \pm 5.6)\text{eV} \tag{3.8}$$

It should be noted that all of these values, i.e., also the values determined in ADC channels (equations 3.3 to 3.6), can directly be compared to each other, due to the fact that the same SQUID and same read out settings have been utilized.

Comparing the values determined for the constant noise terms of detector *0202-6* (equations 3.4 and 3.6) in the two measurement campaigns, it can be seen that the determined values differ from each other. This disagreement is related to an enhanced electronic noise level observed in measurement campaign $MC2$ compared to $MC1$. However, as will be deduced in the following, this disagreement does not prevent the utilization of measurements from both campaigns in one combined analysis.

In addition, these values can be compared to the value for the constant noise term determined in section II2.3.1 for detector *571-7* (equation 2.7). It can be seen that the constant noise term determined for detector *0202-6* in $MC1$ is even smaller than the corresponding value determined for the measurement with detector *571-7*. Taking into account the rather small energy threshold achieved with detector *571-7* (exhibiting the larger constant noise term), this indicates that the electronic noise conditions in $MC1$ were actually very good.

However, from equations 3.7 and 3.8, it can be seen that the corresponding determined energy thresholds of detector *0202-6* are rather large, especially when comparing these values to the result obtained for detector *571-7* (see section II/2.3.1). This observation already points to the fact that the signal generation in detector *0202-6* was not nearly as efficient as the signal generation in detector *571-7*. In fact, the rather large energy thresholds determined for detector *0202-6* are mainly attributed to the contamination and related enhanced defect density and potentially enlarged heat capacity (due to the impurities) of the absorber substrate of detector *0202-6* (compare discussion in section II/3.2). This interpretation of the enlarged energy threshold of detector *0202-6* compared to detector *571-7* will be confirmed when comparing the determined scaling factors of the two detectors.

Nonetheless, at first, the two scaling factors determined for detector *0202-6* should be compared to each other: From equations 3.3 and 3.5, it can be be seen that the two scaling factors - which relate the generated pulse height to the number of photons detected (compare equation 2.1 in section II/2.2) - are in agreement with each other (within the error margins). Actually, this observation is important as it illustrates that the response of detector *0202-6* to energy depositions was the same, in both measurement campaigns, regardless of the different energy thresholds. Thus, it can be deduced that all measurements recorded for detector *0202-6* can be used together for a combined analysis. Of course, the different reference points from the "0V" LED calibration for the constant noise term have to be taken into account, as will be shown in the analysis of the data with applied Neganov-Luke voltage.

Thus, as already indicated above, the scaling factors of detector *0202-6* can be compared

to the scaling factor obtained for detector *571-7* (equation 2.6 in section II/2.3.1). A large difference between the the values determined for the respective detectors can be observed: The scaling factor of detector *571-7* is almost a factor of 5 larger than the scaling factors determined for detector *0202-6*. As can be deduced from the discussion of equation 2.5 in section II/2.2, a larger scaling factor results in a larger pulse height recorded with the detector for the same energy deposition. Thus, using only the information delivered by the scaling factor, it becomes clear that detector *571-7* exhibited pulse heights roughly 5 times larger than the corresponding pulse heights recorded with detector *0202-6*. Taking into account that the respectivelly used SQUID systems exhibit the same gain, this difference can, in fact, be attributed to the signal generation in the detectors. From this observation it can be deduced that, in fact, the conversion of detected energy into observable signal height with detector *0202-6* was much less efficient. Thus, as already indicated above, within the present work, the comparably small scaling factors a^{MC1} and a^{MC2} are mainly attributed to the enlarged impurity density and heat capacity of the absorber substrate of detector *0202-6* created in the annealing step.

From this discussion, it can be concluded that, on the one hand, the energy thresholds of detector *0202-6* in both measurement campaigns were rather large due to the impurities deposited on the absorber substrate and differ from each other. Nonetheless, it can be observed that the scaling factors determined in both measurement campaigns comply with each other. Within the present work, a conclusive explanation of these observations can be given underlining that the detector response at 0V applied Neganov-Luke voltage is well understood and can be used as a basis for the investigations of the detector response with applied Neganov-Luke voltage which will be presented in the following. In addition, it was discussed that the absolute values of the determined scaling factors are small, which is attributed to the large impurity density on the surface of the detector.

Applied Neganov-Luke Voltage: Analysis of the LED Calibrations Performed

In order to analyze the LED calibrations performed at an applied Neganov-Luke voltage V_{NL}, at first, an idealized, theoretical expectation of the impact of the application of a Neganov-Luke voltage on the relationship of the widths of the recorded peaks, $\sigma_{tot,V_{NL}}$, and the peak positions, $x_{V_{NL}}$ is discussed. As discussed in section II/2.2 and utilized in the analysis of the "0V" LED measurements above, without applied Neganov-Luke voltage, the following relationship between the widths of the peaks and their positions is assumed (see equation 2.4 in section II/2.2):

$$\sigma_{tot,0\mathrm{V}} = \sqrt{\sigma_{0,0\mathrm{V}}^2 + a \cdot x_{0\mathrm{V}}} \tag{3.9}$$

For applied Neganov-Luke voltage, however, an amplification of the signal height corresponding to the effective thermal gain is observed (compare section II/3.1). This amplification factor, labeled $A(V_{NL})$ in the following, can be determined from the LED calibrations as the mean value for all LED peaks P_n recorded ($n = 1, \ldots, M$). Thus, the peak position at an applied Neganov-Luke voltage can be described by:

$$x_{V_{NL}}(P_n) = x_{0\mathrm{V}}(P_n) \cdot A(V_{NL}) \tag{3.10}$$

$$A(V_{NL}) = \frac{1}{M} \cdot \sum_{n=1}^{M} \frac{x_{V_{NL}}(P_n)}{x_{0\mathrm{V}}(P_n)} \tag{3.11}$$

Thus, in an idealized, theoretical approach, i.e., neglecting any other influences of the applied Neganov-Luke voltage onto the signal generation (e.g., assuming, that no additional contant noise is generated, i.e., that $\sigma_{0,V_{NL}} = \sigma_{0,0\mathrm{V}}$), the relationship between the peak width $\sigma_{tot,V_{NL}}$ and the peak position $x_{V_{NL}}$ can be expressed by:

$$\sigma^{ideal}_{tot,V_{NL}} = \sqrt{\sigma^2_{0,0\mathrm{V}} + a \cdot x_{V_{NL}}} = \sqrt{\sigma^2_{0,0\mathrm{V}} + a \cdot A_{V_{NL}} \cdot x_{0\mathrm{V}}} \tag{3.12}$$

where the scaling factor a is the same as in the "0V" measurement as this factor describes the detector response to an amount of deposited energy in the absorber substrate[2]. As all parameters of equation 3.12 are known (either from the corresponding "0V" measurement or determined from the amplified pulse heights for applied Neganov-Luke voltage), this idealized, theoretical expectation of the energy-dependent detector resolution for applied Neganov-Luke voltage can be compared to the recorded data. Such a comparison is shown in figure 3.4. In panel a) of figure 3.4, the LED calibration of the "0V" measurement of the measurement campaign $MC1$ is shown (blue markers and error bars correspond to the data points), additionally the fit of equation 3.10 to the data is indicated as solid, red line. In panel b) of figure 3.4, the LED calibration at 40V is shown (black markers and error bars correspond to the data points). The idealized description of the detector resolution according to equation 3.9 is shown as solid, red line. Clearly, it can be seen that the idealized model does not reproduce the data in a satisfying way. Additionally, in green, the fit to the data using an extended model for the energy-dependent light-detector resolution is shown. It can be seen that this function describes the data nicely. The results from this fit were used to perform the energy calibration for the 40V measurement (see y-axis on the right-hand side and upper x-axis). This model is presented and discussed in the following.
For the LED calibrations performed with applied Neganov-Luke voltage, it was found that a model for the energy-dependent light-detector resolution extended by two terms had to be used to reliably fit the data. The following formula was used:

$$\sigma^{new}_{tot,V_{NL}} = \sqrt{\sigma^2_{0\,0\mathrm{V}} + \sigma^2_{1,V_{NL}} + a \cdot A(V_{NL}) \cdot x_{0\mathrm{V}} + b(V_{NL}) \cdot x_{0\mathrm{V}} + c(V_{NL}) \cdot x^2_{0\mathrm{V}}} \tag{3.13}$$

where $\sigma_{1,V_{NL}}$ simply corresponds to an additional constant noise term due to the application of the Neganov-Luke voltage (compare, e.g., [18]).

Applied Neganov-Luke Voltage: Interpretation of the Deduced Model

Thus, two terms were introduced, with the following motivation and interpretation (where N corresponds to the number of photons per LED pulse, compare section II/2.2):

- $\sigma_{cc,V_{NL}} := \sqrt{b(V_{NL}) \cdot x} \propto \sqrt{N}$: This term is introduced to account for the incomplete *charge collection* and the therewith connected incomplete drift lengths of some of the charge carriers. This process introduces an additional uncertainty for the total amount of energy deposited in the absorber substrate as the number of charge carriers trapped as well as their respective drift lengths (before they get trapped) can vary. As it is assumed that, for each photon absorbed, one electron-hole pair is created, the process of charge collection can be described by Poisson counting-statistics (compare, e.g., [27]). For very small energies, this term is expected to

[2] By applying the Neganov-Luke effect, simply the amount of energy deposited in the detector is enlarged, however, the scaling factor is not affected.

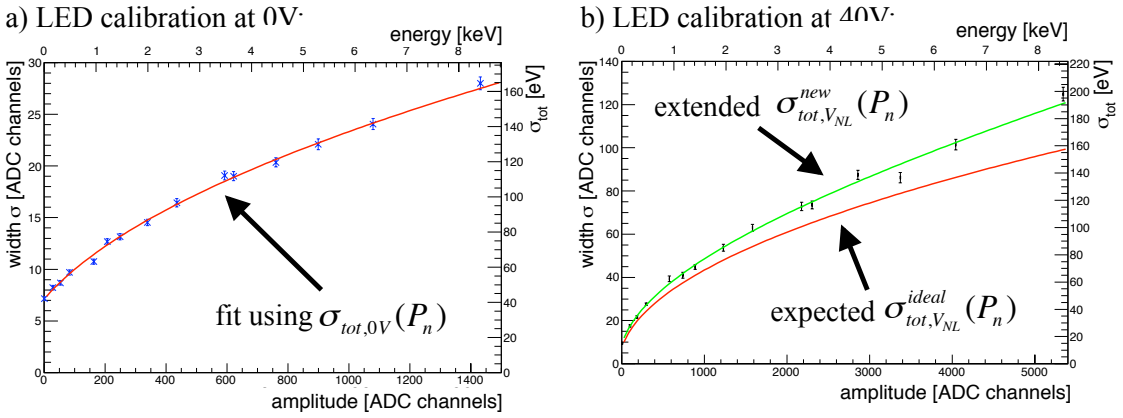

Figure 3.4: LED calibration performed with detector *0202-6*: In panel a), the LED calibration without applied Neganov-Luke voltage (blue markers) is shown, in panel b), the LED calibration for an applied Neganov-Luke voltage of 40V is shown. The 1σ widths of the peaks recorded in the LED calibration are plotted versus their positions (blue markers and error bars). The left y-axis and the lower x-axis correspond to the size of these quantities in ADC channels, i.e., as measured. The right y-axis corresponding to $\sigma_{tot}(E_{det})$, the energy-dependent detector resolution and the upper x-axis corresponding to the energy E_{det} in the light detector, depict the result of the energy calibration. In addition, the result of the fit of equation 2.4 (section II/2.2), i.e., of the LED calibration, is shown as red line.

be small as, most probably, most of the charge carriers are not drifted at all, but immediately recombine with their partner. For increasing voltages applied, at first, this term should become larger as an increasing number of charge carriers is effectively drifted. However, above a certain threshold voltage, $V_{NL}^{th,\,cc}$, this term can be expected to decrease again. This should be the case when, effectively, more than half of the charge carriers are drifted through the complete substrate and reach the electrodes.

- $\sigma_{rc,\,V_{NL}} := \sqrt{c(V_{NL}) \cdot x^2} \propto N$: This term is introduced to account for the possibility for an electron and a hole to encounter each other and, then, to recombine with each other, instead of being drifted through the Silicon absorber-substrate and generating phonons (*recombining charges*). Thus, also this process introduces an additional uncertainty for the total amount of energy deposited in the absorber substrate. However, this process can be assumed to depend on the squared Poisson statistics as it describes the probability of an encounter of two charge carriers which were, in principle, not produced by the same photon. This effect is expected to decrease with increasing voltage as already, for very small voltages, an efficient separation of two charge carriers can be achieved.

Thus, the application of equation 3.12 for the description of the energy-dependent light-detector resolution for applied Neganov-Luke voltage is well motivated. It should be noted that the parameters $b(V_{NL})$ and $c(V_{NL})$ introduced to describe these effects have to be dependent on voltage as they correspond to physics effects which depend on voltage. In addition, it should be noted that these parameters describe intrinsic properties of the investigated detector and can, hence, be expected to correspond to each other, also for the two different measurement campaigns. In figure 3.4, the determined values for $b(V_{NL})$

(panel a) and $c(V_{NL})$ (panel b) are depicted versus the respective applied Neganov-Luke voltage.

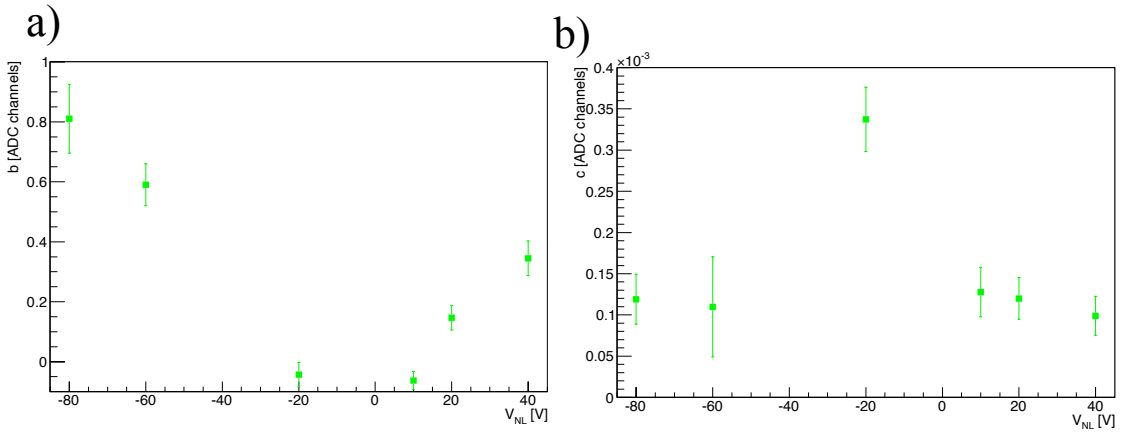

Figure 3.5: Parameters $b(V_{NL})$ (panel a) and $c(V_{NL})$ (panel b) of the model utilized to describe the energy-dependent light-detector resolution for applied Neganov-Luke voltage: Parameter $b(V_{NL})$ describes the impact of the incomplete charge carrier collection on the energy resolution of the light detector. It can be seen that, for the voltage range tested within the present work, this parameter increases. Parameter $c(V_{NL}$ describes the impact of recombining charge carriers on the energy resolution of the light detector. It can be seen that this parameter strongly decreases for increasing voltage and that the overall size of this parameter is very small.

From figure 3.5, it can be seen that the experimentally determined voltage-dependency of the parameters $b(V_{NL})$ and $c(V_{NL})$ nicely complies to the the expected voltage-dependency as described above. This agreement supports the presented interpretation of the impact of the application of a Neganov-Luke voltage on the energy-dependent detector resolution. As can be seen from figure 3.5 a), the parameter $b(V_{NL})$, describing the impact of the incomplete charge collection increases monotonically within the voltage range that could be tested within the present work. Thus, within the developed interpretation, this implies that significantly less than half of the generated electron-hole pairs are drifted until they reach the electrodes (compare discussion above). This prediction can be tested as, using the determined amplification factor (equation 3.11), and the fact that this amplification factor corresponds to the effective thermal gain $G_t^{eff}(V_{NL}^{eff})$ as defined by equation 3.2 (in section II/3.1), where no time dependency of V_{NL}^{eff} has to be considered (compare section II/3.3.1). From these considerations, the effective, reduced drift length l_d can be determined. For the example of an applied Neganov-Luke voltage, an effective drift length of only $l_d(-80\text{V}) = 2.87\text{nm}$ can be determined. This very small value for the effective drift length, on the one hand, points to the fact that only a few electrons and holes reach the electrodes, i.e., that the vase majority of the charge carriers become trapped in their drift process. This interpretation is in perfect agreement with the observation of the enlarged impurity density on the surface of the absorber, as discussed above (compare section II/3.2). On the other hand, the short drift length determined for $V_{NL} = -80\text{V}$, also indicates, that, in the voltage range investigated, $V_{NL} < V_{NL}^{th,cc}$ as the threshold voltage for complete charge carrier collection as defined above. Therefore, within the investigated voltage range, a monotonically rising parameter $b(V_{NL})$ is expected, as is observed.

In analogy to the "0V" measurement, the results of fits to the LED calibration data using equation 3.13 can be employed to allow for an energy calibration of the detector response. An example for the obtained energy calibration can already be seen in figure 3.4, panel b), when inspecting the upper x-axis and right y-axis.

Actually, the energy calibration performed in this way can be used to test the validity of the suggested interpretation and modeling of the energy-dependent detector resolution with applied Neganov-Luke voltage: As indicated at the beginning of section II3.3, in each measurement of one measurement campaign, the same pulse heights of the LED were utilized to perform the LED calibration. Thus, if the deduced modeling of the energy-dependent detector resolution is correct, the different energy calibrations obtained for the different Neganov-Luke voltages have to deliver the same energy for the corresponding peaks of the LED calibrations. Hence, the determined energies for each peak P_n by the different energy calibrations can be compared to each other, as is depicted for peak P_5 of each LED calibration in figure 3.6:

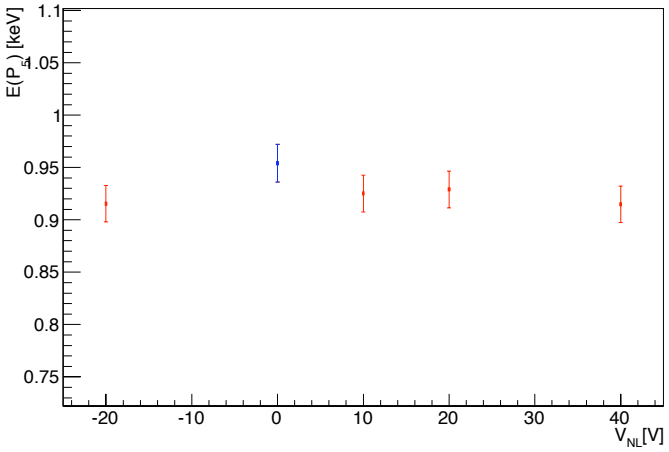

Figure 3.6: Peak position (in terms of energy) of peak P_5 of all measurements performed in measurement campaign $MC1$: On the x-axis, the applied Neganov-Luke voltage is shown, on the y-axis, for pulse P_5 of the LED calibrations, the respective assigned energy in keV is shown. The blue marker labels the "0V" measurement.

Indeed, from figure 3.6, a satisfying agreement (within the error margins,) of the determined energies can be seen, validating the performed LED calibration using equation 3.13.

Using these energy calibrations as well as the mathematical description of the energy-dependent resolution of the light detector (equation 3.9 without applied Neganov-Luke voltage and equation 3.13 with applied Neganov-Luke voltage) determined from the measurements, the energy-dependent resolution of the detector for different applied voltages as well as without applied voltage can be compared. Such a comparison is shown in figure 3.7 for the example of the measurements without Neganov-Luke voltage applied as well as with +10V and +40V from $MC1$:
In figure 3.7, clearly, the impact of the described degradation of the resolution at large energies (due to the additional broadening caused by the applied Neganov-Luke voltage) can be seen. However, the most important observation that can be made is that, in the

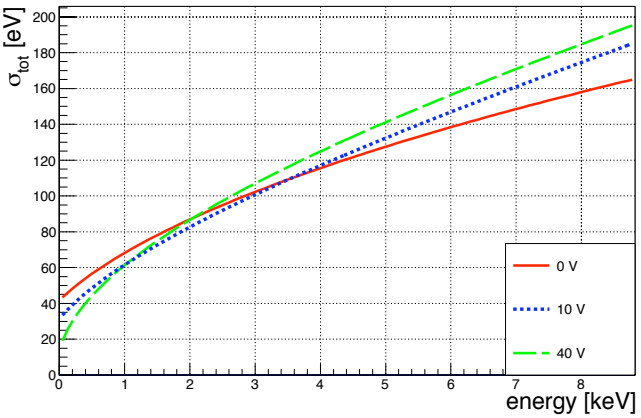

Figure 3.7: Energy-dependent resolution of the investigated light detector determined as described in the main text: The energy resolution without applied Neganov-Luke voltage is depicted as solid red line. The energy resolution with an applied Neganov-Luke voltage of +10V is depicted as dotted blue line. The energy-dependent resolution with an applied Neganov-Luke voltage of +40V is depicted as dashed, green line.

low-energy region up to a few 100eV which is interesting in the context of the dark matter search (see section 1), the energy resolution is significantly improved, even at the small Neganov-Luke voltages tested.

Hence, with these measurements, it could be demonstrated that, by employing the Neganov-Luke amplification for cryogenic light detectors, a significant improvement of the energy resolution in the low-energy region which is important for the dark matter search can be achieved. In addition, an understanding of the impact of the Neganov-Luke effect on the energy-dependent resolution was gained.

3.4 Implications for the Background Suppression with the CRESST Experiment

In order to illustrate the great potential of Neganov-Luke amplified light detectors for the improvement of the background-suppression technique in the CRESST experiment, a simple calculation is performed as depicted in figure 3.8.
Shown are the calculated 80% event bands of the light-yield energy plane for electron/γ-events (dotted black area), Oxygen (upper-left to lower-right red dashed area) and Tungsten (upper-right to lower-left blue dashed area) recoils (compare section II/2.2). For the determination of the widths of the event bands, on the one hand (panel a), the energy-dependent resolution of detector *0202-6* without applied Neganov-Luke voltage was used. On the other hand (panel b), the energy-dependent resolution of detector *0202-6* determined for an applied Neganov-Luke voltage of +40V was assumed. For the calculations it was assumed that, for electron/γ events, a mean amount of 2% of the deposited energy is detected asf scintillation light in the light detector (see section II/2.2.4). For the Oxygen and Tungsten recoil bands, reduced light yields according to the Quenching Factors as utilized in the CRESST experiment were employed (compare table 2.1 in section I/2.2). In

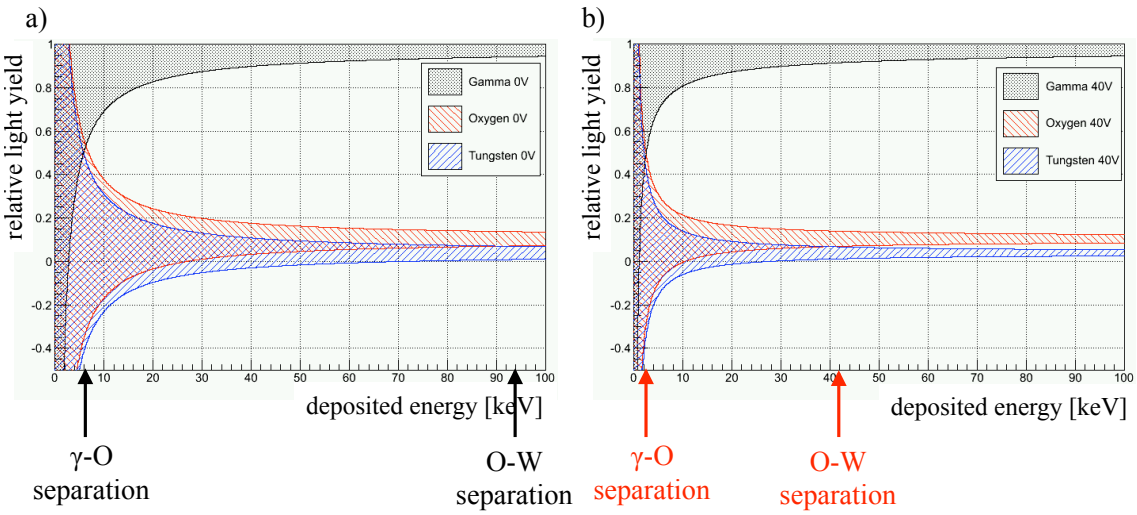

Figure 3.8: Calculated 80% light-yield bands for electron, Oxygen and Tungsten recoils in $CaWO_4$, assuming experimentally determined energy-dependent light-detector resolutions: In panel a), the results obtained utilizing the light-detector resolution without applied Neganov-Luke voltage are shown. In panel b), the corresponding results obtained for the energy-dependent light-detector resolution for +40V applied Neganov-Luke voltage are shown. Additionally indicated (black and red arrows) are the energies for which a separation of the different light-yield bands can be observed.

addition, in figure 3.8, the energies from which on a separation of the electron/γ light-yield band and the Oxygen light-yield band as well as of the Tungsten and Oxygen light-yield bands can be observed. Clearly the beneficial impact of the improved light-detector resolution at low energies on the signal identification is visible.

In conclusion, it can be stated that, on the one hand, the successful application of the new fabrication method for Neganov-Luke amplified light detectors and the achieved constant amplification over time was shown. On the other hand, with the experiments and investigations performed within the present work, the potential improvement of the background discrimination based on the phonon-light technique with the CRESST experiment by the application of Neganov-Luke amplified light detectors could be demonstrated.

Part III

Scintillation-Light Quenching in $CaWO_4$

Chapter 1

Motivation and Overview

1.1 Motivation

Inorganic scintillators are nowadays widely used for the detection of ionizing radiation. Applications cover a large range from, e.g., high energy physics (the electromagnetic calorimeter of CMS [28] is made of $PbWO_4$) to imaging in medical diagnostics (e.g., in positron emission tomography, BGO (bismuth germanate) is used, see [29] for other examples). A lot of effort was already undertaken to understand and optimize the scintillation-light output in the context of these applications (see, e.g., [30]). Especially, investigations concerning the optimization of fast response (decay) times[1], radiation hardness or the light yield[2] have been carried out. However, concerning rare event searches[3] [40], another property of these materials is of essential importance: The dependency of the light output on the type of interacting particle. This circumstance is referred to as scintillation-light quenching and is described by a so-called Quenching Factor (as presented in I/2.2). The observed quenching of the light signal is used for identifying the type of interacting particle and, thus, for discriminating background events against the searched for rare events (e.g., potential Dark Matter nuclear recoils, as depicted in figure 2.2). For this purpose, cryogenic detectors made of inorganic scintillators as, e.g., $CaWO_4$, are often employed as target with a two-channel read-out (compare the CRESST-II detector modules, presented in section I/2.1). A phonon (heat) detection channel delivers the primary information on the energy deposited by an interacting particle and a simultaneously operated light-detection channel offers the possibility of particle identification on an event-by-event basis. In addition, for many scintillators, varying light-pulse shapes for different interacting particles can be observed, see, e.g., [41].

Many investigations concerning either the wavelength-spectra or the decay-time spectra of the light output of inorganic scintillators under different excitations exist. However, a conclusive explanation on a microscopic basis for the light-yield quenching in combination with the varying shapes of the scintillation-light pulses under excitation by different par-

[1] Fast response times are in most cases desirable as scintillation detectors are often operated in the counting regime.

[2] For references, see, e.g., [31] on a systematical investigation of the scintillation efficiency of alkali and alkali earth compounds, or [32] concerning the effect of material defects and trap levels on the scintillator performance in complex oxides.

[3] Neutrino-less double-beta decay search [33, 34]: E.g., CANDLES with CaF_2 [35] or LUCIFER with ZnSe [36]; and direct Dark Matter searches [37, 38]: E.g. CRESST-II with $CaWO_4$ [5] or ROSEBUD with (amongst others) BGO [39].

ticles is still missing. In the following, an approach to conclusively explain all observed features within one model is presented. This model contains a full description of the scintillation-light generation process in $CaWO_4$ (including, e.g., defect centers) and can also be used for the evaluation and optimization of the performance of self-grown $CaWO_4$ crystals.

1.2 Overview of the Proposed Model

In the course of this work, a consistent description of the generation of scintillation light and the reduction of the scintillation efficiency (i.e., the light quenching) for different projectiles in $CaWO_4$ single crystals on a microscopic basis was developed. This model does not only provide a closed explanation of the light generation and quenching in $CaWO_4$, but also delivers a mathematical formulation for the calculation of decay-time spectra and the light yield of $CaWO_4$ under excitation by different particles. In addition, it is suggested that the model offers the possibility to predict energy- and temperature-dependent Quenching Factors as well as light-pulse shapes, for any type of interacting particle in various other self-activated inorganic scintillators in combination with rather easily realizable experiments.

The presentation of the suggested model can be divided into three major aspects: The theoretical model (see chapter III/3), the conducted experiments to test and validate the model (see chapter III/4) and the analysis of the experimental data yielding the determination of remaining free model parameters as well as the validation of the model (see chapter III/5).

Before the developed theoretical model is presented, a review of established knowledge of the scintillation-light generation and the light-quenching in $CaWO_4$ is given in chapter III/2. The new **theoretical model** presented in chapter 3 includes

- A description of the basic production process of scintillation-light in a $CaWO_4$ single crystal: The intrinsic scintillation light in $CaWO_4$ single crystals is generated by de-excitation of one type of luminescence centers, which leads to a purely exponential decay-time spectrum. Extrinsic scintillation light is generated by defects in the lattice, also leading to purely exponential decay-time spectra. Included in the model are radiative, non-radiative as well as migration processes of the fundamental excitations in $CaWO_4$.

- A discussion of the differences in the process of energy loss of different interacting particles and resulting differences in the efficiency of creating excited luminescence centers and their spatial distribution. For the description of the spatial distribution of the ionization-density generated by different primary interacting particles, a model is developed and the parameters of this model are determined with the help of simulations with the programs SRIM (The Stopping and Range of Ions in Matter) [42] and CASINO (monte CArlo SImulation of electroNs in sOlids) [43]. Unfortunately, it becomes evident that the available simulation programs do not provide all the information required to completely calculate and determine the spatial distribution of the particle-induced ionization-denstiy. The remaining uncertainties are dealt with in chapter III/5.

- The introduction of the light-quenching mechanism for interacting particles in $CaWO_4$ on the basis of exciton-exciton self-interactions. Introducing such an interaction possibility leads to a dependency of the light-generation efficiency not only on the total amount of created excitations, but also on their (position-dependent) density distribution.

Additionally to predicting the amount of scintillation light produced by different interacting particles, this model also provides information on the decay-time spectra of the scintillation-light output, dependent on the type of interacting particle. Hence, this model links macroscopic quantities like the observed light quenching and the shape of the decay-time evolution of the scintillation light to the microscopic quantity of the ionization-density distribution created in $CaWO_4$ by interacting particles.

To determine the free parameters of the model as well as to test and validate the model, **experiments** were conducted. Wavelength spectra and decay-time spectra (for selected wavelengths) of $CaWO_4$ crystals under different excitations were acquired. As excitation source, a N_2-gas laser, leading to two-photon excitation, and the tandem accelerator, for the production of pulsed ion beams (oxygen and iodine), were used. In addition, the temperature of the $CaWO_4$ crystal could be varied between room temperature and $\sim$ 20K. These experiments are presented in chapter III/4.

The analysis of the data obtained in the experiments in the context of the developed model is presented in chapter III/5. With this analysis, the values of the free parameters of the model are determined and the description of the light generation and quenching by the developed model is validated.

The model is finally used for the calculation of Quenching Factors (QFs) in $CaWO_4$ for different particles, especially for electron and nuclear recoils. The calculated QFs can be compared to various experimentally determined Quenching Factors (chapter III/6). In this context, also the so-called phonon-quenching and gamma-quenching are discussed. In addition, a short comparison with two existing models for the light-yield quenching in $CaWO_4$ is presented as well as limitations and further improvements of the developed model are addressed. The implications of the developed model, i.e., of the gained understanding and description of the light generation and quenching in $CaWO_4$, are discussed.

Chapter 2

Light Production and Quenching in $CaWO_4$

As basis the for the understanding the light-generation mechanism in $CaWO_4$ single crystals, first a compilation of important properties of $CaWO_4$ is presented. Then, the established model of light-generation in $CaWO_4$ is reviewed and the observed light-yield quenching for $CaWO_4$ under different excitations is discussed. Limitations of the existing models and features of the light output of $CaWO_4$ which are not explained by these models are referred to.

2.1 Basic Properties of $CaWO_4$

2.1.1 Crystal Structure of $CaWO_4$

$CaWO_4$ single crystals exhibit the so-called sheelite crystal structure of the body-centered tetragonal space group ($I4_1/a$), see figure 2.1. The primitive unit cell consists of four

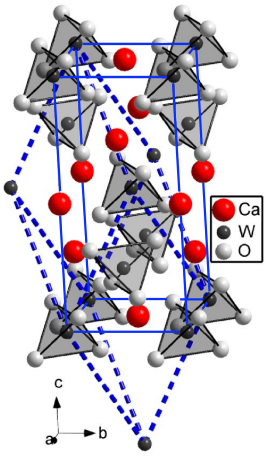

Figure 2.1: Crystal structure of $CaWO_4$: The tetrahedrons correspond to $[WO_4]^{2-}$ oxyanion complexes whereas the red spheres show the positions of Ca^{2+} cations. The solid lines show the tetragonal, the dashed lines the primitive unit cell. Figure adopted from [44]. Copyright (2013) by the American Physical Society.

$CaWO_4$ molecules [44]. The lattice parameters are $a = 5.243(2)$Å and $c = 11.376(3)$Å (see

[44] and references therein). In this crystal structure, the distance between neighboring Tungsten atoms, $d_{\text{W-W}} \approx 3.87$Å, is the same in all directions[1], leading to a highly symmetric position of W ions [46]. The crystal structure is described as highly ionic between the metal cations $Ca^{+\alpha}$ and the (approximately) tetrahedrical $WO_4^{-\alpha}$ anions (almost perfect T_d symmetry), where $\alpha \approx 2$ [45]. The crystal structure can be described by an ordered sub-lattice of $[WO_4]^{2-}$ complexes, ionically bound to Ca^{2+} cations [47]. The character of the bonding within the $WO_4^{-\alpha}$ anions is primarily covalent, exhibiting a splitting into σ and π bindings [44, 45].

2.1.2 Electronic Structure of $CaWO_4$: Ground State

The electronic structure of an idealized, undisturbed $CaWO_4$ single crystal lattice can be described by several approaches. The strong ionic character of $CaWO_4$ justifies the application of molecular orbital calculations as a starting point. In such a framework, the energy levels of the crystal solid are approximated by the corresponding energy levels of the molecular compounds. Applying density functional theory leads to a band-structure representation of the electronic levels in the system. The corresponding bands can be characterized concerning their type, gradient, symmetry and band-gap energy.

Molecular Orbital Theory

A representation of calculated energy levels of the main contributions of W and O ions for two primitive unit cells of $CaWO_4$ can be seen in figure 2.2 a) [48]. Also indicated is the band-gap energy E_{gap} as calculated in [48] for this supercell of 1x1x2 unit cells of $CaWO_4$. A corresponding schematic diagram of the crystal-field spitting and hybridization of the molecular orbits of the $WO_4^{-\alpha}$ anion ($\alpha \approx 2$) is shown in figure 2.2 b). The initially discrete molecular orbitals are broadened into energy bands in the solid [45]. This representation indicates that the upper states of the valence band are mostly constituted from O 2p (π and σ) states whereas the lowest levels of the conduction band show largely W 5d character. The topmost band of the conduction band consists of Ca 3d states [45].

Density Functional Theory

To further characterize the electronic band structure of $CaWO_4$, the ground-state total energy and the electron density can be calculated using density functional theory (see [45])[2]. The total density of states $N^T(E)$ per unit cell of $CaWO_4$, as evaluated in [45], is displayed in figure 2.3 a). Included are the upper-core, valence-band, and conduction-band states. The zero level of energy is chosen as the upper edge of the last occupied state. All core-level energy-states show relatively small chemical shifts and are, thus, very little influenced by the crystal structure. In figures 2.3 b), c), d), and e), the atomic contributions of O, Ca and W orbitals to the density of states of the valence and conduction band are displayed. Again, the zero of energy is chosen as upper edge of the last occupied state. Due to the nearby (heavy) W ions, the 2p O orbitals experience strong crystal-field splitting into σ and π states [45], while the W 5d states are split into e- and t_2-like states [45]. It can be seen that the valence-band's upper edge is dominated by Oxygen contributions (in more detail, the 2p π orbital [45]) whereas the conduction band's lower edge

[1] The Ca and the W ions exhibit S_4 point symmetry [45].

[2] In [45], only one-electron energies are taken into account. No exciton energy-levels have been used there.

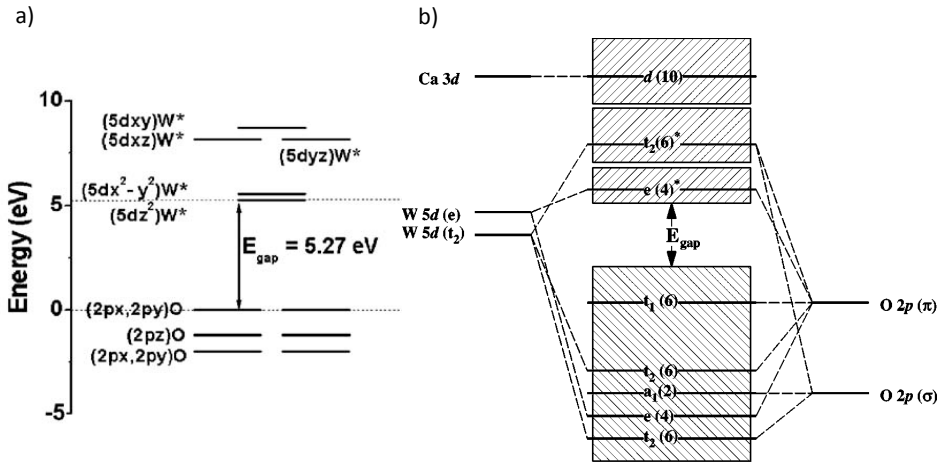

Figure 2.2: Schematic drawing of the electronic level system of a $WO_4^{-\alpha}$ anion ($\alpha \approx 2$): a) main contributions of W and O ions to the crystal orbitals for a supercell of 1x1x2 primitive unit cells (figure reprinted from [48], Copyright (2013) with permission from Elsevier), b) crystal-field splitting and hybridization of the molecular orbitals of a $WO_4^{-\alpha}$ anion ($\alpha \approx 2$), numbers in parentheses indicate the degeneracy of each state. The shaded boxes indicate the broadening of the discrete states by neighboring molecules in the solid. Figure adopted from [45]. Copyright (2013) by the American Physical Society.

primarily consists of Tungsten contributions (in more detail, the 5d e orbital [45]). The bandwidth of the valence band amounts to about 5eV, the width of the lower conduction band is about 1eV. The additional upper conduction band which is dominated by Ca 3d states starts about 2eV above the conduction-band edge.

Electronic Band Structure

From the calculations of the density of states, a band-structure diagram for $CaWO_4$, as shown in figure 2.4, can be deduced [45]. The minimum bandgap of $CaWO_4$ is at the Γ point of the Brillouin zone, indicating that $CaWO_4$ is a direct band gap material. The dispersion of the valence band is relatively small. The width of the O 2p π states constituting the top of the valence band is only 0.5eV per band [49]. The entire valence band (including the W 5d t_2 contributions) is quite wide. In addition, the splitting of the conduction band into two sub-bands, as already indicated in figure 2.2 b) (the W 5d states and the Ca 3d states, respectively), can be seen. The width of the lower conduction band (lCB) can be determined to $E_{width-lCB} \approx 1$eV.

Band Gap Energy

On the basis of the calculations in [45], the band-gap energy of $CaWO_4$ can be determined to be $E_{gap} \approx 4.09$eV. However, this value can just be taken as an estimate as band-gap energies calculated from density-functional theory are known to be underestimated (see [45] and references therein). Theoretically calculated and experimentally determined values for the band-gap energy[3] can also be found in other references. In the following, a

[3]The experimental value is usually assigned by extrapolation of a linear fit to the fundamental absorption edge.

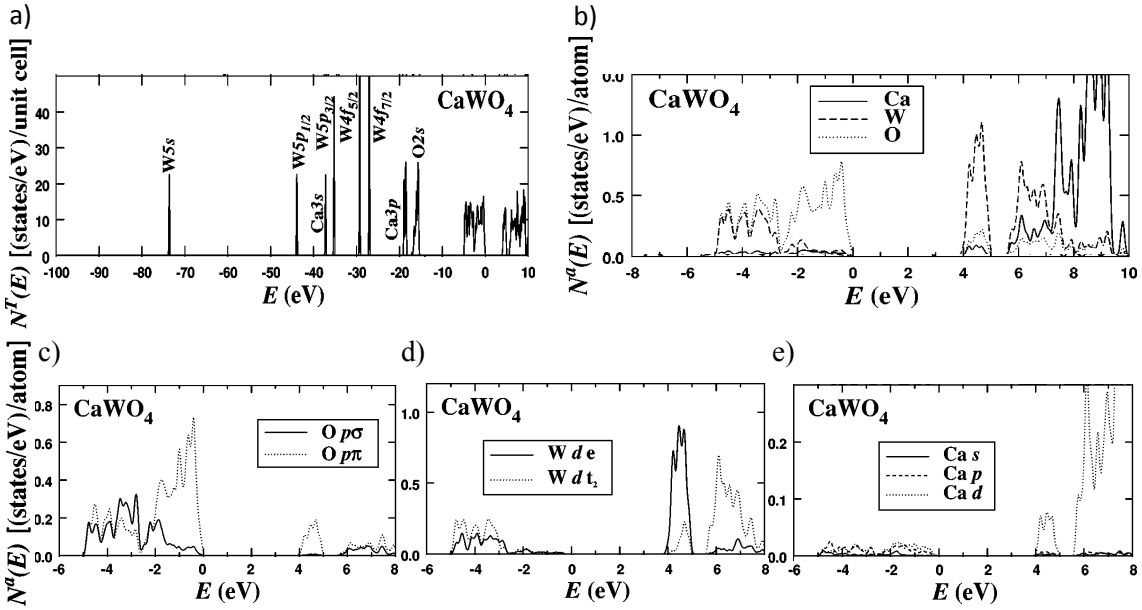

Figure 2.3: Density of states in $CaWO_4$ from [45]: a) total density of states for upper-core, valence and conduction band, core states labeled according to their dominant orbital behavior; b) partial densities on an expanded scale, showing the individual contributions of Ca, O and W to the valence and conduction band; partial densities are weighted by the respective ionic charges within the applied muffin-tin spheres of the calculations [45]; c), d) and e) partial densities of states as in b), showing the individual contributions of O, W and Ca in more detail. For all figures: Zero energy level at upper edge of last occupied band. Figures adopted from [45]. Copyright (2013) by the American Physical Society.

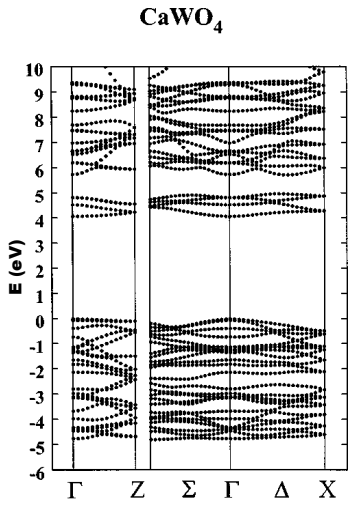

Figure 2.4: Band-structure diagram for $CaWO_4$. The band dispersions are plotted along the three symmetry directions of the body-centered-tetragonal Brillouin zone. Figure adopted from [45]. Copyright (2013) by the American Physical Society.

few examples of band-gap energies assigned to different $CaWO_4$ samples are given:

- An experimental and theoretical study of undoped $CaWO_4$ powders, grown with the micro-wave assisted hydrothermal method, is described in [50]: $E_{gap} = 4.7$eV ± 0.05eV.
- $CaWO_4$ crystalline and distorted thin films, synthesized following a soft chemical method are investigated (theoretically and experimentally) in [48]: $E_{gap} = 5.27$eV (crystalline sample[4]).
- Two samples from $CaWO_4$ single crystals grown with the Czochralski technique are studied in [51]. The focus of this investigation is the (temperature-dependent) spectral shape of the scintillation-light output under one- and two-photon excitation[5]: $E_{gap} = 5.2\text{eV} \pm 0.3\text{eV}$.
- A sample of a $CaWO_4$ single crystal grown in Russia was examined in [52] by studying the photoluminescence and thermoluminescence spectra under electron excitation[6]: $E_{gap} = 4.8$eV.

From these examples, it can be seen that the determined values for the band-gap energy of $CaWO_4$ roughly range from 4.7eV to 5.3eV. The mean value determined from these data yields a band-gap energy for pure $CaWO_4$ single crystals of ~ 5.0eV. Thus, in the following, the value, $E_{gap} = 5.0$eV for the band-gap energy of $CaWO_4$, will be adopted and used throughout this work.

Summary of the Electronic Structure of a $CaWO_4$ Single Crystal

In summary, it can be stated that the undisturbed, unexcited electronic configuration of $CaWO_4$ can be described by a filled valence band of t_1 symmetry (O 2p π-character) and an empty $\sim$ 1eV wide conduction band of e symmetry (mainly W 5d e-character) [45]. This configuration corresponds to filled one-electron states below the band gap, i.e., a $t_1^6 e^0$ electron-configuration [45]. Above this conduction band (W 5d e-character), a second conduction band (mainly Ca 3d character), $\sim$ 2eV higher in energy, can be found. The minimum gap separating the valence and the e-conduction band can be found in the middle of the Brillouin zone and can be determined to ~ 5.0eV.

2.1.3 Deformation of the Electronic Structure due to Defects

In every real crystal structure, irregularities and impurities can be found. For $CaWO_4$ single crystals, the major deviations from a perfect single crystal structure are reported to be due to deformed W-O bonds[7], Mo impurities[8] (substituting a W ion) or O deficiencies

[4] For the structurally disordered sample, a value of $E_{gap} = 4.15$eV has been determined experimentally. This value is not taken into account here as the undisturbed electronic structure of $CaWO_4$ is of interest.

[5] The lower bound of 4.9eV corresponds to the (extrapolated) onset of the two-photon-excitation threshold. The upper limit of 5.5eV accounts for a possible suggested shift of the two-photon excitation spectrum towards lower energies (relative to the band gap) due to strong electron-phonon coupling [51].

[6] This value is actually the energy of a sharp edge in the excitation spectrum. This could be interpreted as the band-gap energy as the observed behavior is characteristic for the excitation within the intrinsic Urbach absorption edge [52].

[7] Deformations can occur close to impurities or, in general, can be caused by defects in the crystalline structure.

[8] Due to its chemical similarity to Tungsten, molybdenium is known to be one of the major contaminants in the raw material used for $CaWO_4$ production [32].

[32, 48]. Measured impurity densities (density of chemical impurities) of different $CaWO_4$ crystals show typical occurrences of single elements of the order of 1 to 10ppm (parts per million) and maximum occurrences of single elements of the order of $\sim$ 100ppm (see, e.g., [53] or appendix B in [54]). In total, the maximum impurity densities typically are in the range of roughly 50 to 400ppm. Such disturbances of the regular lattice, like impurities or deformed unit cells, can give rise to symmetry-breaking processes of the lattice, known to promote the creation of intermediary energy levels within the forbidden band gap [55]. An example of energy levels, as obtained from molecular orbital calculations for a distorted primitive unit cell, of $CaWO_4$ can be seen in figure 2.5: For the level scheme in a), a regular unit cell was considered whereas, for the level scheme in b), one of the W ions was shifted 0.3Å away from one of its attached O ions, thus, increasing the corresponding bond length. It can be seen that breaking the predominant T_d-symmetry leads to the creation of electronic levels within the band gap while maintaining the character (symmetry and type) of the energy levels constituting the band edges of the valence and conduction bands. The same holds true for the energy-level scheme of unit cells distorted by an Oxygen vacancy [32]. Also for Mo impurities, the structure of the energy levels constituting the valence- and conduction-band edges can be assumed to be identical [56, 57, 45]. The introduction of, e.g., Bi impurities changes the character of the respective energy levels (see [58]). For deformed $[WO_4]^{2-}$ complexes, different values for experimentally determined band gaps are reported. Experimentally and theoretically determined deviations from the undisturbed band gap range from $\sim$ 0.3eV [50] to $\sim$ 1.2eV [48]. For $CaMoO_4$, a band gap of 4.6eV is reported [45]. Thus, deviations of the band-gap energy for unit cells incorporating Mo in $CaWO_4$ in comparison to the undisturbed band gap can be expected to be $\sim$ 0.4eV.

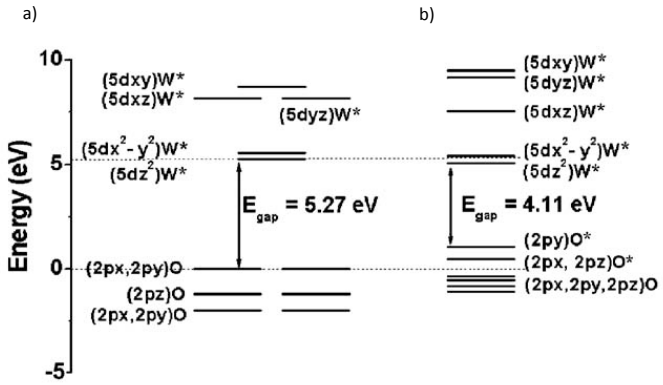

Figure 2.5: Main contributions of W and O ions to the crystal orbitals for one primitive unit cell of $CaWO_4$: a) undisturbed, regular primitive unit cell, b) distorted unit cell where one W-O bond was elongated by 0.3Å. Reprinted figure [48], Copyright (2013), with permission from Elsevier.

Defects, as the above mentioned Mo impurities or Oxygen vacancies, are known to introduce deep electron traps[9] into the electronic structure of $CaWO_4$ which are stable up to room temperature or even above [32]. As will be shown below, the existence of such traps is clearly not beneficial for an efficient transfer of energy to the intrinsic scintillation centers in $CaWO_4$ (see sections III/2.2 and III/3.1.4). Hence, the introduction of impurities or

[9]The nature of deep hole traps in $CaWO_4$, as, e.g., induced by stable radiation damage (remaining coloration of the crystal), is not yet clear [32].

disordered unit-cells should, of course, be avoided right from the beginning, e.g., by using the purest raw materials possible for the crystal production or by application of thermal treatment of the crystals for annealing of structral defects. However, as mentioned above, any real single crystal incorporates defects. One attempt to overcome this restriction is the use of dopants. Concerning the suppression of deep electron traps due to Oxygen vacancies in isostructural $PbWO_4$, doping with La^{3+} is reported to be beneficial [32]: La, replacing the Pb cation (or, for $CaWO_4$, the Ca^{2+} cation), can act as an electron donor and, thus, supplies the lattice with additional electrons to fill deep traps. The especially interesting feature of La doping (in comparison to doping with other rare earth elements) is that it is known to compensate for the electron deficiencies without introducing additional energy levels within the forbidden band gap[10] of $PbWO_4$ [49]. A similar mechanism is suggested for La-doped[11] $CaWO_4$ [32, 59].

2.1.4 Electronic Structure of $CaWO_4$: Excited State

Energy deposition in a $CaWO_4$ single crystal typically leads to excited electrons in the conduction bands and holes in the valence band[12]. These charge carriers relax via energy-loss processes (like, e.g., creation of further ionization and phonon emission) to the respective band edges to form the energetically lowest, excited electronic-state. In the following, the electronic configuration -for a perfect crystal lattice- adopted after this relaxation process will be described.

Hole Relaxation and Self-Trapping

In $CaWO_4$, holes being created deep within the valence band are supposed to show quite high mobility during their relaxation process to the band edge as the entire valence band in which they reside is quite wide ($\sim$ 5eV) [49], see figure 2.4. However, when they are relaxed to the band edge, the small dispersion of the valence band edge causes efficient auto-localization of the hole[13] preferentially in the 2p π orbital (see figure 2.2) of the $[WO_4^\star]^{2-}$ complex (see, e.g., [49, 32]). The localization-process of the hole is accompanied by a trigonal Jahn-Teller distortion of the electronic structure of the tetrahedron with a Jahn-Teller energy[14] of $E_{JT-h} \approx 0.63$eV [60]. This distortion corresponds to a spatial reconfiguration of the unit cell (deformation) and a redistribution of the charge [50]. This deformation is accompanied by the creation of defined energy levels within the band gap near the top of the valence band, shifted by the Jahn-Teller energy and, thus, leads to the formation of self-trapped holes (STHs) in $CaWO_4$ [32]. Due to the thermal trap depth[15]

[10] This behavior can be ascribed to the electronic structure of La: If La is stripped off its $5d^1$ electron, the closed shell configuration [Xe] $6s^2$ remains. This configuration exhibits the same number of valence electrons (also in the s-orbital) as the replaced Ca.

[11] It is already known that La^{3+} doping of $CaWO_4$ reduces radiation-induced absorption of the crystal ([32] and references therein).

[12] For a more detailed discussion of the energy-loss process of a particle and other possible excitations and intermediary steps in the energy-distribution process, see section III/3.1.1.

[13] The smaller the dispersion width of a band, the smaller the localization energy that has to be overcome by the carrier in the self-trapping process ([49] and references therein).

[14] The Jahn-Teller energy corresponds to the energy difference of the new level within the band gap and the undisturbed band edge.

[15] The thermal trap depth corresponds to the energy that has to be overcome to thermally activate detrapping of the hole, i.e., to enable hopping of the hole to neighboring $[WO_4]^{2-}$ complexes. The energy required for such a hop can be identified with the energy of the saddle point of the disturbed potential between two neighboring $[WO_4]^{2-}$ complexes [60] and can, thus, be smaller than the Jahn-Teller energy.

of roughly 0.33eV [32] to 0.42eV [49], STHs are stable up to temperatures of roughly 150-175K. This could also be deduced from the occurrence of a thermoluminescence peak at these temperatures. The observed thermoluminescence is attributed to the onset of tunneling of STHs, leading to recombination with electrons localized in deep electron traps[16] [32]. Thus, at room temperature, STHs exhibit a certain mobility. The typical detrapping time can be determined to be $\sim$ 50ms [32]. This is more than three orders of magnitude larger than the typical decay time of the scintillation light of $CaWO_4$ at room temperature which is of the order of 10μs (see the following section III/2.2). Hence, regarding the scintillation mechanism in $CaWO_4$, STHs can be considered to be stable and immobile even at room temperature.

Electron Relaxation

Excitation of an electron can lead to a primary occupation of a state either in the lower or in the upper conduction band (see figure 2.4). Only electrons excited into the upper conduction band can be considered as free charge carriers in the crystal [45]. This identification can be deduced from experimental observations:

- Photoconductivity in $CaWO_4$ crystals is reported to be observable for excitation energies larger than 6.2eV while the band-gap energy is only $\sim$ 5.0eV [47].
- An offset of $\sim$ 2.2eV is measured between the band-gap energy and the onset of the excitation of thermoluminescence [49]. This indicates that only electrons being excited into the upper conduction band are mobile and can efficiently migrate to defects where they get localized in deep traps.

Hence, electrons excited into the upper conduction band migrate through the crystal until they are relaxed (via ionization and/or phonon production) into the lower conduction band. There, they can either directly get trapped by existing deep electron traps, directly get localized at $[WO_4^\star]^{2-}$ complexes distorted by a STH to form self-trapped excitons (for more details, see section III/2.1.5) or undergo a migration-period until they get either trapped or localized[17] (for a discussion of this migration process, see section III/2.1.5). Experimental indications pointing to a mobility of electrons in $CaWO_4$ will be discussed below in section III/2.2.3 in the context of the scintillation-light pulse-shape.

Electrons directly excited into the lower conduction band cannot move freely through the lattice, but are localized at the respective $[WO_4^\star]^{2-}$ complex where usually also the created hole resides and forms a STH [61]. As will be explained below in section III/2.1.5, this implies that most electrons excited into the lower conduction band directly form excitons without an intermediate migration stage. For this reason, the lower conduction band is sometimes called the excitonic band [61].

Electronic Structure and Transition Selection Rules

Electrons and holes relaxed to the band edge correspond to the lowest energetic electron configuration $t_1^5e^1$ (see figure 2.6 b). For this configuration, group theory predicts four

[16] These deep electron traps are supposed to be stable at least up to room temperature, see section III/2.1.3.

[17] In $CaWO_4$, self-trapping of electrons in a non-disturbed lattice is not known to occur [49].

excited states[18]: Two singlet and two triplet many-electron states: $^1T_1$, $^1T_2$ and $^3T_1$, $^3T_2$, respectively [45, 62]. Of course, the transition of electrons from the $t_1^6e^0$ ground state with $^1A_1$ symmetry into an excited state (singlet or triplet state) underlies electric and magnetic selection rules (see, e.g., [47]). Regarding possible transitions between these energy levels, only the transition $^1A_1 \rightarrow {}^1T_2$ is electric dipole allowed and, thus, expected to account for the fundamental absorption edge of $CaWO_4$ [62, 57]. The transition $^1A_1 \rightarrow {}^1T_1$ is only magnetic dipole allowed and is, therefore, not expected to contribute significantly to the absorption process of photons [62]. The transitions $^1A_1 \rightarrow {}^3T_1/\ {}^3T_2$ are in principle spin-forbidden. However, de-excitation of the system could be accomplished via the reverse transitions: $^3T_1/{}^3T_2 \rightarrow {}^1A_1$, as these transitions become partially allowed by reduction of the degeneracy of the $^3T_1$ and $^3T_2$ levels. The reduction of degeneracy is caused by spin-orbit coupling and Jahn-Teller splitting induced by the STH at the $[WO_4^\star]^{2-}$ complex [62, 63]. As indicated in [63] for the example of $PbWO_4$, the energy ordering of the sub-levels created by such splitting cannot be deduced from group theory predictions. Actually, arguments can be found[19] that the lowest-lying energy levels contributing to the de-excitation of the system originate mainly from the $^3T_2$ state (see [62]). In figure 2.6, a sketch of such an energy-level scheme including the possible transitions between the different states can be seen: On the left hand side, the excitation of a $[WO_4]^{2-}$ complex (in T_d symmetry) is depicted. On the right hand side, the level scheme arising from the hole self-trapping process leading to the shifted STH state and the Jahn-Teller and spin-orbit splitting of the $^3T_2$ level (JT-SO-$^3T_2$ states) can be seen.
Thus, it can be assumed (and is adopted and used in the following) that radiative de-excitation of the system can only occur via partially allowed transitions from JT-SO-$^3T_2$ split states to the STH state[20] (see, e.g., [62]). As these transitions are only partially allowed, the corresponding lifetimes of these excited states are rather large (see section III/2.2.3). As will be shown later (see section III/2.2.3) and as indicated in figure 2.6 (for the $^3T_2$ level), the energy gap, ΔE_{split}, between these split states is of the order of $\sim$ 1meV [57].

2.1.5 Self-Trapped Excitons in $CaWO_4$

Creation of Self-Trapped Excitons (STEs)

Figure 2.7 depicts a schematic representation of a typical STE-formation process. It is widely accepted that electrons in $CaWO_4$ relaxed to the conduction-band edge ($^3T_2$ level) of a $[WO_4^\star]^{2-}$ complex (hosting a STH within the band gap) align with the STHs to form self-trapped (Frenkel-) excitons, STEs (see, e.g., [65, 41]).

[18] Of course, also energetically lower-lying states in the valence band and energetically higher-lying states in the conduction band can contribute to transitions. However, for the scintillation mechanism, the transitions between the energetically closest-lying states of valence and conduction band are of interest as excited charge carriers typically relax to the band edges before recombining. For transitions between other states, see, e.g., [47].

[19] As pointed out in [62], the energetically lowest-lying state that is expected to be created by the symmetry-breaking process of the $^3T_1$ level should exhibit ^1E symmetry [62]. The transition $^1E \rightarrow {}^1A_1$ would yield polarized scintillation light in contrast to the observation of unpolarized scintillation light [62]. Due to this experimental indication, a significant contribution of this transition to the de-excitation in $CaWO_4$ can be ruled out [62].

[20] Another level-mixing scheme is suggested in [64, 63] for $PbWO_4$ where it is assumed that pseudo-Jahn-Teller interaction leads to a mixing of $^3T_1$ and $^3T_2$ states resulting in a more complicated structure of the energetically lowest-lying excited states.

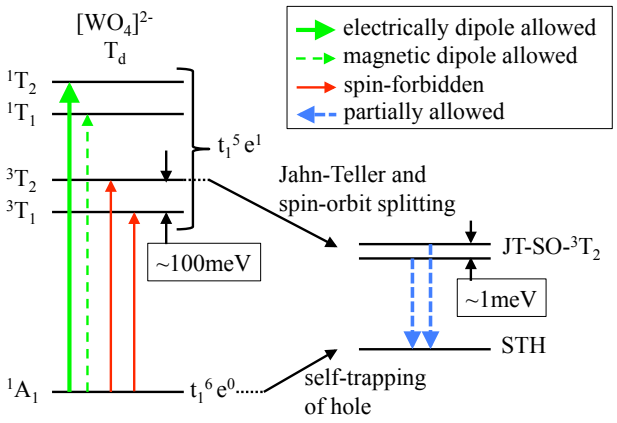

Figure 2.6: Ordering of the energy levels in a $[WO_4]^{2-}$ molecule: Left hand side: During excitation of an electron into the lower conduction band (as obtained from molecular orbital theory [57]). Right hand side: After self-trapping of the hole which leads to the splitting of the $^3T_2$ state by Jahn-Teller and spin-orbit coupling (JT-SO-$^3T_2$). Vertical arrows (see legend) symbolize absorption and emission transitions between the energy levels. Additionally, the spin-orbit splitting of the $^3T_2$ level of the order of $\sim$ 1meV [57] is indicated.

As indicated in figure 2.7, the process leading to the creation of a STE occurs in several steps. The excitation of an electron (by photon absorption or ionization by a particle) leads to an electron in the conduction band and a hole in the valence band. The hole self-traps (creation of hole level within the band gap) and induces a distortion of the electronic configuration of the $[WO_4^\star]^{2-}$ complex yielding a potential well (JT-SO-$^3T_2$ states) for the electron in the conduction band. The electron relaxes to the conduction-band edge ($^3T_2$ level) from which a transition to the ground state is spin-forbidden (see section III/2.1.4). Further relaxation of the electron into the potential well corresponds to trapping of the electron by the STH and, thus, to formation of an STE. The STE exhibits a rather large lifetime ($\sim$ 10μs at room temperature) as the transition between the JT-SO-$^3T_2$ states and the ground state is only partially allowed (see section III/2.1.4).

The character of the energetically lowest state of the STE is supposed to reflect the type of the electronic states constituting it: In particular, the state of the STE mainly corresponds to the triplet state $^3T_2$ of the $t_1^5e^1$ configuration (see section III/2.1.4). As the triplet state $^3T_2$ experiences spin-orbit splitting into energetically closely-lying states (see figure 2.6), it is suggested that the corresponding STE state should also exhibit splitting into energetically closely-lying energy levels with a comparable energy-splitting of the order of $\Delta E_{split} \approx$ 1meV. Due to the strong electron-phonon coupling in $CaWO_4$ [66], at room temperature, these levels are subject to huge broadening leading to an intense overlap between them (see [66] and the discussion in section III/2.2).

Experimental evidence for the creation of STEs in $CaWO_4$ can, e.g., be found in [65] where time- and wavelength-resolved, transient optical absorption spectra were measured for $CaWO_4$ at 100K. The electron and hole component of the STE can each be detected through their respective typical excited-state absorption (ESA) energies:

- $E_{ESA-e} \approx$ 2.5eV for electrons, corresponding to a transition from the bottom of the

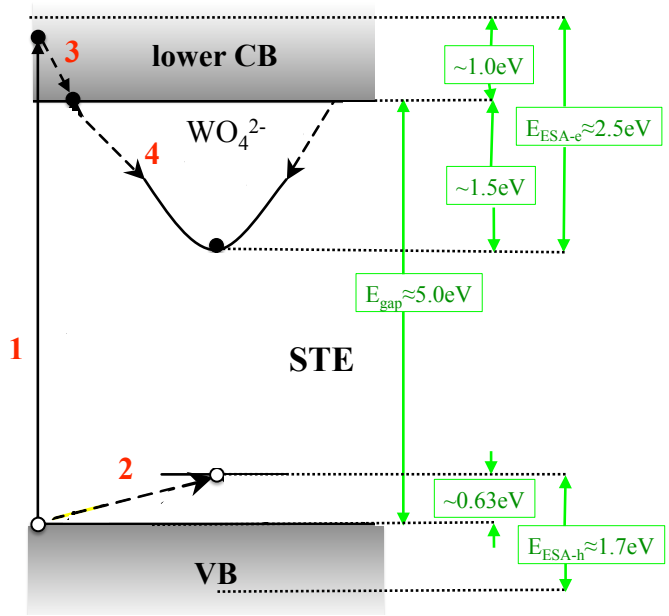

Figure 2.7: Schematic representation of the STE-formation process in a $[WO_4]^{2-}$ complex: Open circles represent holes, closed circles electrons. Black arrows represent the following processes, respectively: **1** - excitation of the electron from the valence band (VB) into the lower conduction band (CB): $^1A_1 \rightarrow {}^1T_2$ (into the energetically higher-lying singlet state, see figure 2.6); **2** - self-trapping process of the hole yielding hole and electron energy-levels within the band gap; **3** - relaxation of the electron to the band edge, i.e., the energetically lowest-lying (spin-orbit split) triplet state: $^1T_2 \rightarrow {}^3T_2$; **4** - formation of the STE through trapping of the electron by the STH, i.e., distortion of the energetically lowest-lying states of the conduction-band edge into a potential well for the electron. In reality, the processes labeled as **3** and **4** occur simultaneously. Green arrows and labels indicate energy differences and are explained in the main text.

potential well (distorted $^3T_2$ state) to the t_2 states of the conduction band[21] (upper edge of the lower conduction band, see figure 2.2 b)

- $E_{ESA-h} \approx 1.7$eV for holes, corresponding to the excitation of an electron from within the valence band[22] into the Jahn-Teller shifted STH-state [66, 60]

The corresponding energies can also be found in figure 2.7 indicated by green arrows. Proof that these components are involved in the scintillation process is provided by the fact that their lifetimes show the same temporal behavior as the decay-time of the scintillation light of $CaWO_4$. Additionally, a weaker spectral component centered at 1.3eV with a lifetime of $\sim$ 20ns was detected in the transient absorption spectrum. This component can be assigned to electrons that are participating in a delayed formation of STEs as the time structure of this ESA coincides with the delayed rise of a fraction of the lumines-

[21] In principle, this transition would be parity forbidden. However, due to mixing with the d-orbital of the metal cation, the transition gets partially allowed [66].

[22] No information on the energy levels in the valence band from where electrons are excited could be found. However, from the rather large energy of $E_{ESA-h} = 1.7$eV in contrast to the Jahn-Teller energy of the STH, $E_{JT-h} = 0.63$eV, it can at least be deduced that the respective electron levels cannot be the ones constituting the valence-band edge.

cence decay-time spectrum[23] (for a more detailed discussion of this observation, see section III/2.2). In contrast to these delayed STEs, very fast trapping times, $\sim 200 \pm 50$fs, are reported in [61] for electrons excited directly into the excitonic band (lower conduction band), indicating direct creation of STEs without intermediate STH production.

From the ESA energy for the electron component of the STE, $E_{ESA-e} \approx 2.5$eV [65], in combination with the width of the lower conduction band (see, e.g., [45] and figure 2.3), $E_{width-lCB} \approx 1$eV, the trap depth of electrons in the STE, $E_{STE-e-trap}$, can be estimated to

$$E_{STE-e-trap} = E_{ESA-e} - E_{width-lCB} \approx 1.5\text{eV}, \tag{2.1}$$

corresponding to the difference in energy of the undisturbed conduction-band edge and the depth of the potential well for the electron in the STE. This trap depth of electrons in the STE as well as the width of the lower conduction band are both indicated in figure 2.7 by green arrows. Together with the band-gap energy of $E_{gap} = 5.0$eV of the undisturbed lattice (see section III/2.1.2) and the Jahn-Teller energy of the STH, $E_{JT-h} = 0.63$eV (see section III/2.1.4), a rough estimate of the energy stored in the STE, E_{STE}, can be given:

$$E_{STE} = E_{gap} - E_{STE-e-trap} - E_{JT-h} \approx 2.9\text{eV}. \tag{2.2}$$

The band-gap energy as well as the Jahn-Teller energy of the STH are both depicted in figure 2.7 by green arrows.

Mobility of Self-Trapped Excitons: Diffusion Coefficient, Diffusion Length and Migration Time

As can be seen from equation 2.2, a huge energy difference of ~ 2.1eV exists between the minimum energy needed to create a STE, $E_{gap} = 5.0$eV, and the energy of the STE, $E_{STE} \approx 2.9$eV. Especially at low temperatures, this leads to a strong localization of the exciton at the respective $[WO_4]^{2-}$ group and, thus, to the identification of the exciton as a self-trapped Frenkel exciton. Due to this huge energy difference, it could be expected that these STEs exhibit no mobility at all, even at room temperature. However, as shown in [67], the shape of the respective energy-potential curves (see figure 2.8) of the ground state and the excited exciton state[24] allow for a thermally activated hopping-type migration of the STE from one neighboring $[WO_4]^{2-}$ to another already at low temperatures (~ 10K, see the following discussion).
Due to the flat slope of the potential curve of the STE excited states, a small thermal activation energy (excitation to an energetically higher-lying vibrational state), $\Delta E_{ex-mobility}$, is sufficient to create an overlap between the energy-potential curve of the STE and the ground state of the neighboring $[WO_4]^{2-}$ group, enabling its excitation indicated by the upward arrow [67] (see figure 2.8). This "resonance" permits the transfer of the excitation to the next $[WO_4]^{2-}$ group which can be interpreted as thermally activated hopping of the STE. This corresponds to a random-walk migration of the STE through the crystal lattice [67]. Such a thermally activated random-walk migration can be described by a temperature-dependent diffusion coefficient $D(T)$ [67, 68]:

$$D(T) = D_0 \cdot e^{(-\frac{\Delta E_{ex-mobility}}{k_B \cdot T})} \tag{2.3}$$

[23] The rest of the electrons, the major part, seems to directly form STEs (see [65] and the discussion in section III/2.2).

[24] In [67], the shapes of the potential curves are inferred from the shapes of the excitation and emission energy-spectra.

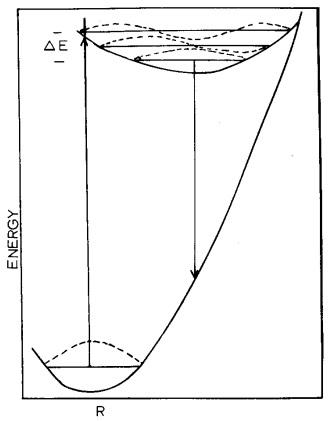

Figure 2.8: Schematic drawing of a configuration-coordinate diagram of a STE in $CaWO_4$: Shown is the steep slope of the potential curve of the ground state (lower parabola) from which excitation of the $[WO_4]^{2-}$ can take place (upward arrow), and the flat slope of the excited states curve (upper parabola). Excitation of the $[WO_4]^{2-}$ can occur, e.g., via photon absorption by the electron or ionization induced by a moving particle. Additionally, different energy levels are exemplarily indicated: The ground state and two vibrational levels (excited states) of the STE and the lowest level of its electronic ground state. ΔE corresponds to the activation energy that has to be overcome to transfer the STE from one $[WO_4]^{2-}$ to another (in the text the notation $\Delta E_{ex-mobility}$ is used). Reprinted with permission from [67], AIP Publishing LLC.

where $\Delta E_{ex-mobility}$ is the activation energy, k_B the Boltzmann constant, T the temperature and D_0 is the constant value reached in the high-temperature limit. As discussed in more detail in appendix A.1, STEs residing at regular unit cells or at disturbed unit cells are supposed to exhibit slightly different activation energies, $\Delta E_{ex-mobility,\text{reg}} \approx 4.5\text{meV}$ and $\Delta E_{ex-mobility,\text{dist}} \approx 6.9\text{meV}$ [67], but the same constant $D_0 \approx 1.2 \cdot 10^{-7} \frac{\text{cm}^2}{s}$ [68]. Thus, STEs residing at regular $[WO_4]^{2-}$ groups or at distorted $[WO_4]^{2-}$ groups can be assigned slightly different temperature-dependent diffusion coefficients:

$$D_{\text{STE reg}}(T) = 1.2 \cdot 10^{-7} \frac{\text{cm}^2}{s} \cdot e^{(-\frac{4.5\text{meV}}{k_B \cdot T})} \tag{2.4}$$

$$D_{\text{STE dist}}(T) = 1.2 \cdot 10^{-7} \frac{\text{cm}^2}{s} \cdot e^{(-\frac{6.9\text{meV}}{k_B \cdot T})} \tag{2.5}$$

The following discussion of the exciton mobility is presented for STEs at regular unit cells. Of course, the same calculations can be performed for STEs at distorted unit cells.

Following [68], STEs in $CaWO_4$ can be assigned a typical, temperature-dependent diffusion-length $l_{\text{diff reg}}(T)$ during their (also temperature-dependent) lifetime $\tau_{\text{STE reg}}(T)$:

$$l_{\text{diff reg}}(T) = \sqrt{2 \cdot \tau_{\text{STE reg}}(T) \cdot D_{\text{STE reg}}(T)} = \sqrt{2 \cdot \tau_{\text{STE reg}}(T) \cdot D_0 \cdot e^{(-\frac{\Delta E_{\text{ex-mobility, reg}}}{k_B T})}} \tag{2.6}$$

With this equation, a diffusion length of ~ 13.5nm at room temperature can be calculated. At temperatures $\lesssim 4.6$K, migration of excitons during their typical lifetime is suppressed as the diffusion length becomes smaller than the distance between two neighboring $[WO_4]^{2-}$ complexes ($d_{\text{W-W}} = 3.87$Å , see section III/2.1.1). For a more detailed description of the

determination of these values, see appendix A.2. Due to the highly symmetric position of $[WO_4]^{2-}$ groups in the crystal structure (section III/2.1.1), no directional dependencies of the exciton mobility in $CaWO_4$ are expected.

As described in [68], the migration of a STE in the $CaWO_4$ lattice can be characterized as nearest neighbor random-walk. In such a model, a typical (temperature-dependent) hopping time $t_{h\ \mathrm{reg}}(T)$ needed for one energy-transfer step can be assigned to the migrating exciton:

$$t_{h\ \mathrm{reg}}(T) = \frac{d^2_{\mathrm{W\text{-}W}}}{6 \cdot D_{\mathrm{STE\ reg}}(T)} \tag{2.7}$$

where $d_{\mathrm{W\text{-}W}}$ is the lattice spacing between neighboring tungstate complexes (see section III/2.1.1) and $D_{\mathrm{STE\ reg}}(T)$ is the temperature-dependent diffusion-coefficient. If the density, C_{defects}, of disturbed unit cells (defects) in a $CaWO_4$ is known, from this hopping time a resulting energy-transfer rate from regular units cells to defects can be calculated [68]. The inverse of this transfer rate corresponds to the migration time $\tau_{\mathrm{mig,\ reg.\rightarrow dist.}}(T)$ for STEs from regular units cells to disturbed unit cells:

$$\tau_{\mathrm{mig,\ reg.\rightarrow dist.}}(T) = \frac{t_{h\ \mathrm{reg}}(T)}{C_{\mathrm{defects}}} \tag{2.8}$$

Of course, also STE migration back from the distorted unit cell (defect) to a regular unit cell is possible. In this case, the "defect density" specifying the density of available final states for this process (regular unit cells) is $(1 - C_{\mathrm{defects}}) \approx 1$. Thus, the corresponding migration time, $\tau_{\mathrm{mig,\ dist.\rightarrow reg.}}(T)$, for STEs from defect states (distorted unit cells) to regular unit cells should be given directly by the corresponding hopping time $t_{h\ \mathrm{dist}}(T)$. For the calculation of this hopping time, the diffusion coefficient for STEs at distorted cells has to be used.

2.1.6 Electronic Structure of Excited Defects

In the following, a few comments on the electronic structure of excited unit cells incorporating typical defects (as discussed above in section III/2.1.3) are presented. Different states after the relaxation of excited electrons are discussed:

- An electron from a distorted unit cell gets excited, but is trapped or localized somewhere else in the lattice:
  This leads to a single hole remaining at the distorted unit cell. As discussed in section III/2.1.3, distorted unit cells exhibit a very similar electronic configuration as regular unit cells. Thus, it can be expected that the hole at the distorted unit cell also undergoes self-trapping. This leads to a STH and the corresponding potential well in the conduction band. This potential well corresponds to an empty, very deep electron trap within the band gap. As the mobility of STHs can be neglected on typical timescales of the scintillation-light production, such STHs can be considered as stable and as removed from the STE-production process.

- An electron from a regular unit cell is excited and gets trapped - during its relaxation process - in the energetically lower-lying electron level of a distorted, not excited unit cell:
  This leads to an electron located in the potential well of the conduction band at a distorted unit cell, without a hole (or STH) present in the valence band. As discussed

above in section III/2.1.3, these trapped electrons are immobile at room temperature and at all lower temperatures. Thus, these electrons can be considered as removed from the STE-creation process.

- An electron from a distorted unit cell gets excited, remaining at (or migrating back to) the distorted unit cell:
  As discussed in section III/2.1.3, for deformed $[WO_4]^{2-}$ complexes, Mo impurities, and Oxygen vacancies, a similar electronic configuration as for undisturbed unit cells can be expected. Thus, it is supposed that excitation of such unit cells also leads to STH creation followed by STE formation. However, the electron and hole energy-levels (from which the STE originates) are closer to each other due to the distortion of the unit cell: Experimentally determined variations of the band gap due to deformation of the unit cell amount to $\Delta E_{gap} \approx 0.3 - 1.2$eV (see section III/2.1.3). Thus, the electronic levels taking part in the STE-creation process are already deformed, even before the hole gets self-trapped. The additional deformation of the energy levels due to the Jahn-Teller distortion (see the discussion of hole relaxation and self-trapping) can be expected to be less severe, but nonetheless present. Hence, the decreased band gap of distorted unit cells can be expected to lead to a reduction of the STE energy by a maximum amount of ΔE_{gap} compared to STEs at regular unit cells. Thus, for deformed unit cells, probably STE energies ranging from minimal ~ 1.9eV up to the energy of STEs at regular unit cells, $E_{STE} = 2.9$eV, could be expected.

- A distorted unit cell gets excited in the course of energy transfer by exciton migration:
  As just discussed, it is expected that a STE with reduced energy is created at such excited, distorted unit cells.

In summary, excitation of distorted unit cells is expected to lead either to STE formation there or to trapped charge carriers being efficiently removed from the STE-creation process. In accordance with the discussion of STEs at regular unit cells, also the energy levels of STEs at deformed unit cells should experience (temperature-dependent) broadening due to strong electron-phonon coupling in the $CaWO_4$ lattice.

2.2 Established Knowledge on the Light Generation in $CaWO_4$

In this section, a generally accepted model describing the scintillation-light generation in $CaWO_4$ single crystals is presented. For a typical example of an emission spectrum of $CaWO_4$ excited by 31eV photons at 8K[25], see figure 2.9 a). Typical examples of light pulse-shapes at 295K under different excitations can be seen in figure 2.9 b).
In the following, at first, the generally accepted mechanism to produce the scintillation light at and around the peak wavelength of the spectrum (~ 420nm) is presented. Thereafter, the origin of the asymmetric shape of the spectrum and, thus, of the scintillation light at larger wavelengths, $\lambda \gtrsim 500$nm, is discussed. Further, a review of the temperature dependency of the decay time of the scintillation light as well as of the light yield of $CaWO_4$ is given. Finally, an overview of experimentally determined Quenching Factors, specifying the varying amount of light output for different interacting particles is presented.

[25] Data extracted from figure 1 in [46] using DataThiefIII [69].

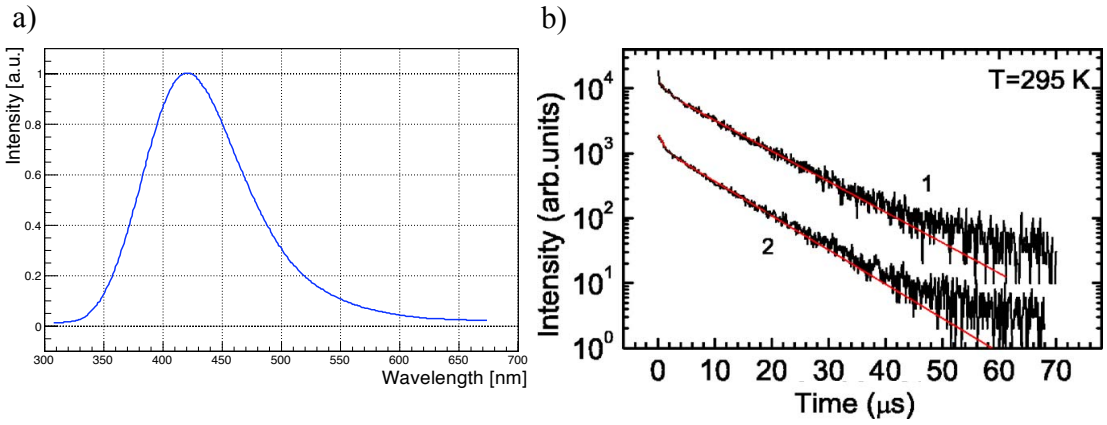

Figure 2.9: Panel a) Typical luminescence spectrum of a $CaWO_4$ single crystal measured at a temperature of 8K (data adopted from [46]). Excitation was realized with 31eV photons from HASYLAB (DESY) [46]. Panel b) Typical scintillation-light pulse-shape of a $CaWO_4$ single crystal at $T = 295$K. Curve 1: Excitation by a γ-particle; Curve 2: Excitation by an α-particle; Red lines: Respective best fit obtained for a simple pulse-shape model using two exponentials [41]. Figure b) adopted from [41]. Copyright (2013) by John Wiley & Sons Inc.

2.2.1 Scintillation Mechanism in $CaWO_4$

After excitation of a $CaWO_4$ crystal, STEs at regular and distorted unit cells as well as separated STHs and trapped electrons can be found (see discussion in section III/2.1.4). The major part of the emission spectrum (i.e., the high-energy part of the spectrum, see figure 2.9 a) is well described by the radiative recombination of (Frenkel-type) STEs at regular $[WO_4]^{2-}$ complexes [62, 67, 57, 32]. Thus, $CaWO_4$ can be identified as self-activated, intrinsic scintillator[26] [70] containing an intrinsic scintillation center in every (regular, non-defective) unit cell. Luminescence photons resulting from the recombination of STEs ($E_\gamma = E_{STE} \approx 2.9$eV) are Stokes-shifted by $\sim$ 2eV compared to the band-gap energy, $E_{gap} = 5.0$eV. This large Stokes shift and the broad emission spectrum (see figure 2.9 a) show that the excitons are, in fact, self-trapped before emitting photons [45].

The character and type of the involved energy levels as well as their energy ordering and distances can be inferred from the discussion in section III/2.1.5. This leads to a schematic representation of the potential curves of the energy levels involved in the excitation and relaxation processes of STEs at regular $[WO_4]^{2-}$ complexes as shown in figure[27] 2.10. The potential curves of the ground state of the system involved in the excitation process are shown in red: The $^1A_1$ state (valence-band edge, zero of energy) and the $^1T_2$ state (conduction-band edge[28]) with the energy gap $E_{gap} = 5.0$eV between them. The STH state and the two excited electron states resulting from Jahn-Teller and spin-orbit splitting of the $^3T_2$ level (indicated as JT-SO-$^3T_2$ in figure 2.10) can be seen in blue. The

[26] For a general classification of inorganic scintillators, see appendix A.3.

[27] The only feature discussed in section III/2.1, but not indicated in figure 2.10 is the overlap of the STH-potential curve with neighboring $[WO_4]^{2-}$ complexes allowing for thermally activated hopping of the STH.

[28] Although the singlet levels are energetically lower this definition is adapted here. As discussed in section III/2.1.4, the fundamental absorption of $CaWO_4$ is expected to occur due to the $^1A_1 \rightarrow {}^1T_2$ transition.

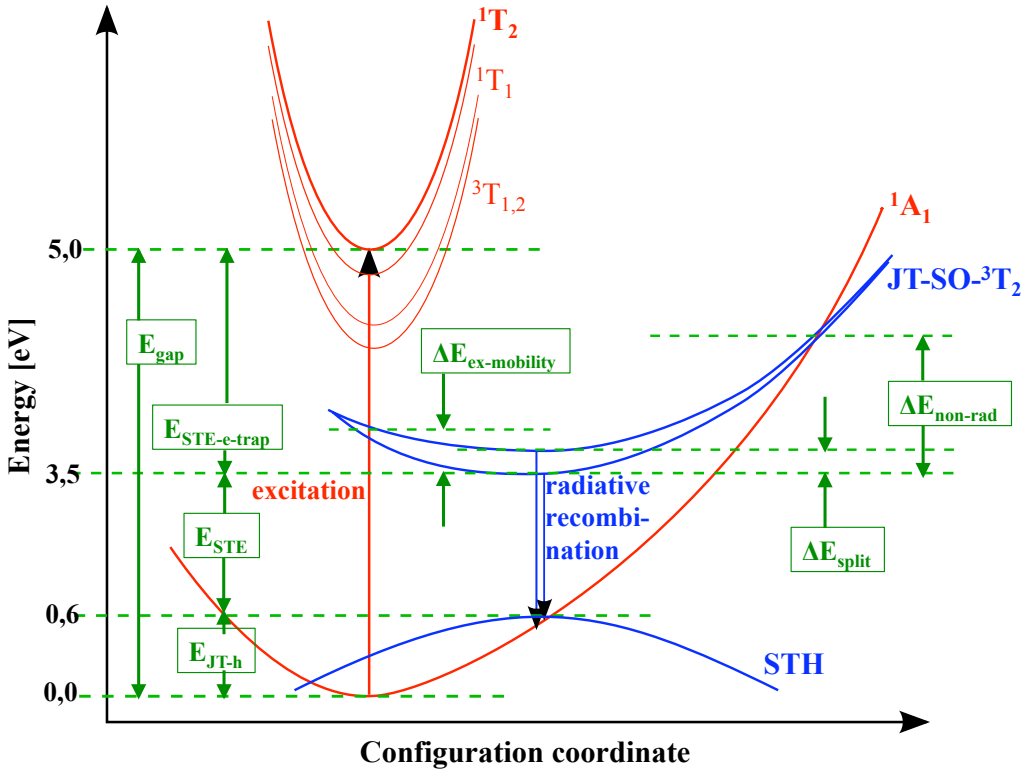

Figure 2.10: Scheme of potential-energy curves of a $[WO_4]^{2-}$ complex during excitation and recombination of a STE: The zero of energy is identified with the ground state of the system. The energy (y-) axis scaling is only a qualitative representation. Curves shown in red correspond to levels involved in the excitation process (upward red arrow): The electronic ground-state configuration $^1A_1$ and the empty singlet and triplet states $^1T_{1,2}$ and $^3T_{1,2}$. Curves shown in blue indicate levels involved in the de-excitation process (radiative recombination corresponds to downward arrows): The STH level depicts the self-trapped hole level of the STE, the levels indicated as JT-SO-$^3T_2$ corresponds to the Jahn-Teller and spin-orbit split states of the electron of the STE. Corresponding energies and energy differences are labeled in green. For a more detailed description, see main text.

deformation of the unit cell due to the self-trapping process of the exciton is represented by the horizontal shift (along the configuration coordinate) of these levels compared to the ground states. This shift corresponds to the deformation energy stored in the lattice for an excited STE. Excited electrons and holes relaxed to these states constitute the STEs with an energy of $E_{STE} \approx 2.9$eV. The STH state is Jahn-Teller shifted by $\Delta E_{JT-h} \approx 0.63$eV in relation to the valence-band edge. The JT-SO-$^3T_2$ states experience an energy shift of $E_{STE-e-trap} \approx 1.5$eV in relation to the undisturbed conduction-band edge. The two JT-SO-$^3T_2$ states are separated from each other by an energy ΔE_{split} (order of magnitude $\sim$ 1meV). Also indicated is the "resonance" of the JT-SO-$^3T_2$ states and the ground state of the $[WO_4]^{2-}$ group enabling excitation (upward arrow in red) of a neighboring $[WO_4]^{2-}$ with the resulting energy barrier of $\Delta E_{ex-mobility} \approx 4.5$meV for exciton migration (compare figure 2.8). Additionally, the overlap of the JT-SO-$^3T_2$ states and the ground state can be seen on the right hand side, illustrating radiation-less recombination of STEs under phonon emission. The corresponding energy barrier that has to be overcome to realize this process is $\Delta E_{non-rad} \approx 0.32$eV (see [41] and section III/2.2.3). The downward arrows in

blue indicate recombination of STEs under photon emission. If de-excitation of the STE occurs via this process, the energy stored in the deformation of the unit cell (horizontal shift compared to ground state) is released as phonons.

From this representation, it becomes clear that the probabilities for the different processes (radiative, non-radiative recombination and migration) to contribute to the lifetime of STEs in $CaWO_4$ are highly dependent on temperature. At 0K the radiative de-excitation from the energetically lower-lying JT-SO-$^3T_2$ state represents the only remaining possibility. For increasing temperature, successively, it becomes possible for STEs to (thermally activated) overcome the respective energy barriers. Thus, recombination from the energetically higher-lying JT-SO-$^3T_2$ state and exciton migration to neighboring unit cells become possible until non-radiative return to the ground-state is also enabled. The temperature dependencies of these processes are reflected in the temperature-dependent changes of the emission spectrum, of the decay time and of the light yield, as will be presented in the following.

2.2.2 Wavelength Spectrum of the Scintillation Light

Energy deposition in a $CaWO_4$ single crystal with energies $\gtrsim$ 7eV (by photons or particles[29]) typically leads to a broad emission spectrum, ranging from roughly 300nm to 700nm with a maximum at about 420nm ($\sim$ 2.95eV)[30]. This broad and mostly featureless spectrum is usually decomposed into two sub-spectra (like, e.g., two Gaussians, see chapter 5 in [54]) as shown exemplarily in figure 2.11: Scintillation-light spectra of a CRESST crystal ("Conrad") under photon excitation $E_{exc} \approx$ 30eV at 8K and 302K are shown in black (pictures from [54]). The complete fit functions for both temperatures are depicted as dashed, red lines whereas the respective two individual sub-spectra (Gaussians) are shown in green. The temperature dependencies of the respective integral intensities (total, blue and green Gaussian integrals) are depicted in figure 2.12. The high energetic band is attributed to the radiative de-excitation of regular $[WO_4]^{2-}$ complexes and therefore called the intrinsic emission: Blue spectrum, peak position at $\sim$ 445nm/440nm (8K/302K), FWHM of $\sim$ 90nm/100nm (8K/302K). The low-energetic band is assigned to the radiative de-excitation of disturbed $[WO_4]^{2-}$ complexes (defects as, e.g., Oxygen vacancies, see section III/2.1.3) and, thus, called the extrinsic emission: Green spectrum, peak position at $\sim$ 510nm/520nm (8K/302K), FWHM of $\sim$ 150nm/170nm (8K/302K). The share of the total integrated scintillation light contained in the intrinsic component (blue) is $\sim$ 70% at both temperatures,[31] [54], however, varies for intermediate temperatures as can be seen in figure 2.12.
From this example, three main features of the wavelength spectra of scintillation light of $CaWO_4$ single crystals can be identified:

- The overall shape of the spectrum is very broad:
  Light production in $CaWO_4$ is the result of the recombination of an electron and a

[29] Here, it is referred to the common case of excitation with particles or photons with energies $\gtrsim$ 7eV. Excitation with energies $\lesssim$ 7eV, but $\gtrsim$ 5eV leads to electrons excited only into the lower conduction band which are directly localized at the corresponding $[WO_4^\star]^{2-}$ complexes (see section III/2.1.4). Excitation with even smaller energies ($\lesssim$ 5eV) can lead to selective excitation of defects as these exhibit smaller band-gap energies (see section III/2.1.3).

[30] The position of the maximum is crystal-dependent and will be discussed below.

[31] As discussed in [54], the crystal "Conrad" contains a relatively large amount of Oxygen vacancies. For this reason, the green component of the spectrum is relatively strong and the maximum is green shifted.

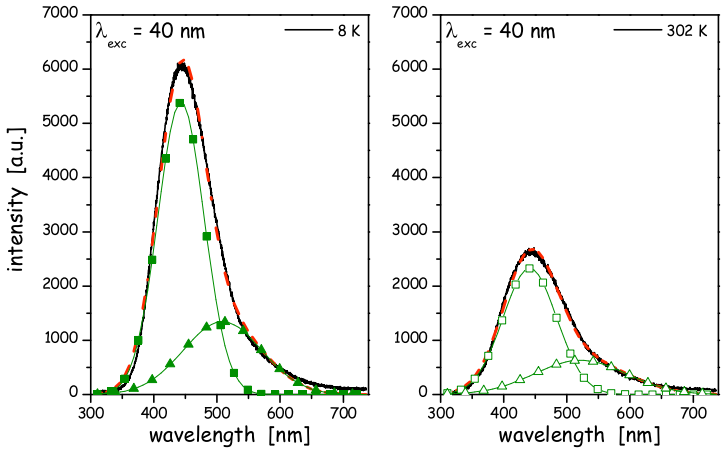

Figure 2.11: Luminescence spectra of a $CaWO_4$ single crystal (CRESST crystal "Conrad", see [54]) measured at a temperature of 8K (left) and 302K (right) under VUV excitation with $\sim$ 30eV photons: Both spectra were fitted with the sum of two Gaussians (red, dashed lines). Rectangles correspond to the intrinsic (blue) component of the spectra, triangles to the extrinsic (green) component of the spectra. Closed symbols refer to the measurement at 8K, open ones to the measurement at 302K. Figure reprinted with permission from [54].

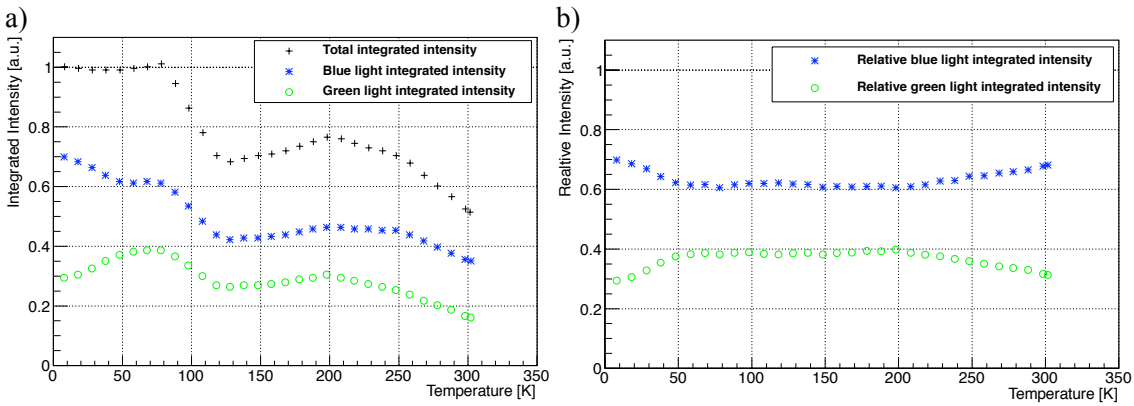

Figure 2.12: Temperature dependency of the total integral intensity and of the spectral decomposition of the scintillation-light spectra of crystal Conrad for temperatures between 8K and 302K (see also figure 2.11): In figure a), the integrated intensities (scaled to unity for the 8K measurement) of the total spectrum (black crosses), the intrinsic component (blue asterisks) and the extrinsic component (green circles) are depicted. In figure b), the same data displayed as temperature-dependent relative intensities of the intrinsic (blue asterisks) and extrinsic (green circles) component can be seen. Data taken from figure 5.17 in [54].

hole bound in a STE (see section III/2.2.1). Radiative de-excitation of the STE is accompanied by phonon production induced by the relaxation of the large deformation of the unit cell (caused by the strong self-trapping process). Due to the strong electron-phonon coupling in the $CaWO_4$ lattice, this yields, even at very low temperatures, a strong broadening of the emitted spectrum[32]. Moreover, the STE pos-

[32]In principle, no phonons would be available in the lattice for broadening at very low temperatures. As,

sesses several closely-lying excited energy states that are, at elevated temperatures, strongly mixed and, thus, cause additional broadening. Hence, the scintillation-light production-process is a multi-level and multi-phonon process leading to strong, temperature-dependent broadening[33] of the produced scintillation-light spectrum.

- The spectrum exhibits a clearly visible asymmetric shape:
  The asymmetry is assigned to the contribution of several (usually two) types of scintillation centers to the emission: Undisturbed, regular $[WO_4]^{2-}$ centers are assumed to produce the blue, intrinsic scintillation light. Disturbed, defective (or deformed) $[WO_4]^{2-}$ centers are expected to produce less-energetic, green, extrinsic scintillation light [62, 57, 46]. As discussed in sections III/2.2.1 and III/2.1.6, excitation of both types of scintillation centers is assumed to lead to STE creation and, thus, to excitonic scintillation-light production. Hence, both spectra should experience the large broadening just discussed. The assumption that defective centers (with smaller band gaps) lead to the generation of the green scintillation-light component is justified by the observation of light spectra under selective excitation: If excitation is realized with, e.g., photons of energies smaller than the band-gap energy of $CaWO_4$, predominantly defective centers are excited. Light spectra recorded under such excitation (at low temperatures) show a strong green shift (see, e.g., [54], measurements at 4.2K). In general, it can be deduced that the position of the maximum of the light spectrum depends on the amount of defect centers in the crystal.

- The relative intensities of the green and blue light component as well as the total integrated intensity are temperature dependent:
  The temperature-related change in the light yield will be discussed below in the framework of a phenomenological model (section III/2.2.4). For the variation of the composition of the spectrum (blue and green components) with temperature, no explanation could be found in the literature. However, this feature will be discussed and be explained within the model developed here (see, e.g., figure 5.6 in section III/5.2.2).

Due to the identification of undisturbed, regular $[WO_4]^{2-}$ centers as source of the blue light and defective (or deformed) $[WO_4]^{2-}$ centers as source of the green light, in the following, these centers will be referred to as blue centers and green centers, respectively. The scintillation light produced by blue centers is referred to as blue or intrinsic scintillation light (wavelength region around $\sim$ 420nm), the light produced by green centers as green or extrinsic scintillation light (wavelength region around $\sim$ 500nm).

2.2.3 Decay-Time Spectrum of the Scintillation Light

Dominant Features of the Decay-Time Spectrum

The decay-time spectrum of the scintillation light of $CaWO_4$ exhibits different shapes (and integrated intensities, i.e., light yields, see section III/2.2.5) for excitation with different particles, as already indicated in figure 2.9 b). In many references (see, e.g., [41]), excitation is performed with particles, e.g., γ- or α-particles. Decay-time spectra obtained under

however, phonons are produced in the de-excitation process itself, even at, e.g., 8K, a strong broadening of the emitted spectrum is observed.

[33] For a quantitative approach to determine the temperature-dependent impact of phonon interaction with the emitting $[WO_4]^{2-}$ center, see [51].

such excitations are commonly described by a superposition of one fast component (decay times of the order of $\sim 1\mu$s at room temperature [41]) and one slow component (decay times of the order of $\sim 9\mu$s at room temperature [41]) whereas the origin of the different components is not completely clear up to now. In most cases, decay times are determined with a fit of the sum of two exponentials to the data: $f(t) = y_0 + \sum_{i=1}^{2} A_i \cdot e^{-\frac{t}{\tau_i}}$ [46]. In table 2.1, the results of such fits from [41] for excitation with γ- and α-particles at different temperatures are presented. It has to be noted that the fit with two exponentials delivers only a phenomenological description of the pulse shape, as will be shown in sections III/3.2 and III/4.7. Thus, the fit results of the decay times and amplitudes can only be regarded as estimations[34].

	5.5MeV α-particles (^{241}Am source)					
T [K]	A_1 [%]	τ_1 [μs]	A_2 [%]	τ_2 [μs]	$\frac{A_1\cdot\tau_1}{A_1\cdot\tau_1+A_2\cdot\tau_2}$ [%]	$\frac{A_2\cdot\tau_2}{A_1\cdot\tau_1+A_2\cdot\tau_2}$ [%]
295	40	1.0(2)	60	8.6(3)	7	93
77	50	3.2(3)	50	16.6(4)	16	84
4.2	98	1.0(2)	2	330(40)	13	87
0.02	98.4	1.2(2)	1.6	340(40)	18	82
	1.2 MeV γ-particles (^{60}Co source)					
295	30	1.4(2)	70	9.2(3)	6	94
77	60	2.1(3)	40	17.6(3)	15	85
4.2	<99	0.9(2)	0.5	480(60)	27	73
0.02	<99	1.0(2)	0.4	500(60)	33	67

Table 2.1: Results of the fits with the sum of two exponentials $f(t) = y_0 + \sum_{i=1}^{2} A_i \cdot e^{-\frac{t}{\tau_i}}$ to scintillation-light pulses of a $CaWO_4$ crystal obtained from α- and γ-excitation at different temperatures (from [41]). The two last columns showing the relative intensities of the components were calculated to allow for an easier comparison of the relative weights of the fast (labeled 1) and slow (labeled 2) component of the scintillation light.

From this example, different conclusions can be drawn:

- The light-pulse shapes for different interacting particles differ from each other, with respect to the fitted decay times and relative weights of the two components.
- The slow decay time τ_2 increases strongly with decreasing temperature whereas the fast decay time τ_1 does not change significantly.
- For all regarded pulses, the slow decay time (τ_2) delivers the strongly dominating fraction of the integral of each pulse.

In general, it is accepted that the slow decay time can be assigned to the recombination of STEs (holes in the STH and electrons in the JT-SO-$^3T_2$ levels) at intrinsic (undisturbed) $[WO_4]^{2-}$ complexes, i.e. at blue centers (see, e.g., [41]). Hence, the scintillation light

[34] In addition, the time resolution used for recording in [41] delivers only very few data points for the fast decay time, especially at low temperatures, as can be seen in figures 2 and 3 in [41].

emitted with the slow decay time corresponds to the blue component of the scintillation-light spectrum. The relatively slow decay time of this component supports this assumption: Radiative de-excitation from the triplet levels of the STE is supposed to exhibit relatively long lifetimes due to the fact that this transition is only partially allowed (see section III/2.1.4). The strong temperature dependency of this component (compare values in table 2.1) is discussed below. The origin of the fast component is not yet agreed upon. Different suggestions to explain the observation of the fast component can be found in the iterature (see discussion in chapter III/6), however, up to now no conclusive model exists. The occurrence of the fast decay time as well as the until now unexplained variation of the fitted decay times for different interacting particles will be addressed within in the developed model (see chapter III/3). This model offers a new approach to explain all these features consistently (see section III/5).

Temperature Dependency of the Slow Decay Time

As can already be seen from the values listed in table 2.1, the slow decay-time component of $CaWO_4$ exhibits a strong temperature dependency. In figure 2.13, more detailed data [41] on the slow decay-time component of $CaWO_4$ (under α-particle excitation, determined with a two exponential fit), can be found. For the explanation of this dependency, often a three-level model, assuming the existence of two emitting levels (the two JT-SO-$^3T_2$ states) and one ground level (the STH state), is used [41]. The fit of this model to the data is indicated in figure 2.13 as red line.

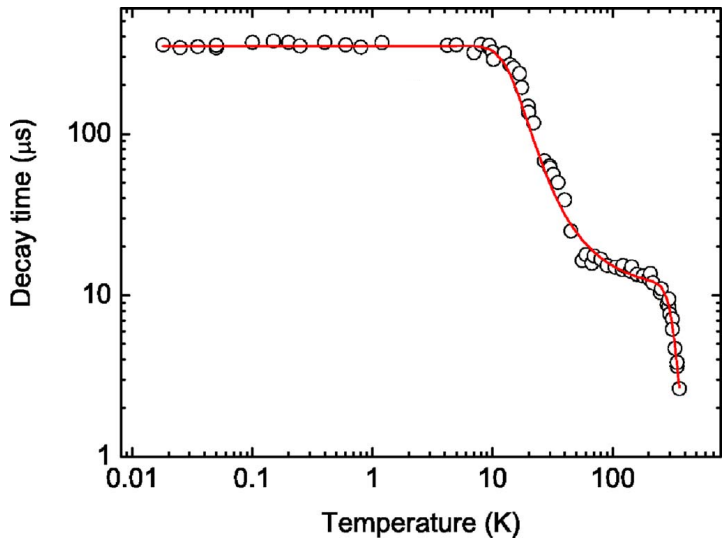

Figure 2.13: Temperature dependency of the slow decay time of the scintillation light of $CaWO_4$ under 5.5MeV ^{241}Am α-particle excitation (see values in table 2.1): Circles correspond to data points, the red line to the fit of a three-level model to the data. Picture taken from [41]. Figure adopted from [41]. Copyright (2013) by John Wiley & Sons Inc.

As can be seen, this model reproduces the dominant features of the temperature dependency of the slow (intrinsic) decay-time component of the $CaWO_4$ scintillation light nicely: The plateau at low temperatures ($\lesssim 10K$) corresponds to the purely radiative decay of the energetically lowest-lying emitting level. The decrease of the decay time with increas-

ing temperature (for 10K $\lesssim T \lesssim$ 200K) can be assigned to the increased probability of radiative decay from the energetically higher-lying emitting energy level. The decrease of the decay time observed for temperatures $\gtrsim$ 250K can be assigned to the occurrence of non-radiative decay (thermal quenching) from both emitting levels. For a more detailed discussion of the model and for the fit results of the parameters, see appendix A.4.

Within such a model, the temperature dependency of the slow decay-time component is described well, however, neither the differences among the values obtained under different particle excitations nor the origin and the variation of the fast decay-time component are explained. In addition, the possibility and impact of exciton migration on the observed decay time is not considered. All these features will be addressed in the model developed in the course of this work (see chapter III/3).

Rise Time of the Scintillation-Light Pulse

According to [65] and [71, 61], the main fraction of STEs created in $CaWO_4$ after excitation with photons or particles is produced very fast on a typical time scale of 200 ± 50fs. However, a fraction of the STEs ($\gtrsim$ 15%) is produced by a delayed recombination process (typical time scales of 20ns (measurement at 100K) [65] to 40ns (measurement at 300K) [71, 61]) of electrons in the conduction band and STHs. A more detailed discussion of these measurements can be found in appendix A.5. Due to these two different production processes of STEs in $CaWO_4$, the scintillation light produced by the respective STEs also exhibits a partial, very fast rise ($\sim$ 200fs, partial amplitude $\lesssim$ 85%) and a partial, delayed rise (of the order of a few 10ns) [65, 71]. An interpretation of these observations and the temperature-dependency of this effect is offered within the developed model in section III/3.1.2.

2.2.4 The Scintillation-Light Yield

Temperature-Dependency of the Light Yield

An example for the dependency of the light yield of a $CaWO_4$ crystal on temperature [41, 46] is shown in figure 2.14:
It can clearly be seen that the light yield increases strongly with decreasing temperature ($\gtrsim$ 10K). From these measurements, a relative gain in light yield at low temperature ($T \lesssim$ 9K) compared to the light yield at room temperature by a factor of 1.8 can be determined [46]. Two different temperature regions can be identified where strong changes in the light yield are observed: For temperatures above $\sim$ 250K as well as for the temperature region between $\sim$ 200K and $\sim$ 10K, the light yield varies strongly. Below $\sim$ 10K, the light yield is roughly constant. In the literature, often a phenomenological model is used to explain the observed temperature dependency of the light yield of scintillators (see, e.g., [46]). Such a model for $CaWO_4$ is presented and discussed in appendix A.6. Within this model, the decrease of the light yield for elevated temperatures ($T \gtrsim$ 250K) is usually attributed to the so-called thermal quenching, i.e., the occurrence of a non-radiative decay channel for excitations of scintillation centers. The additional increase of the light yield for lower temperatures (10K $\lesssim T \lesssim$ 200K) is assumed to be the result of the decreasing mobility of excitations initially created in the scintillator: The smaller the mobility of produced excitations, the lower the probability that these excitations are captured by quenching centers where they are dissipated without producing scintillation light [46]. All

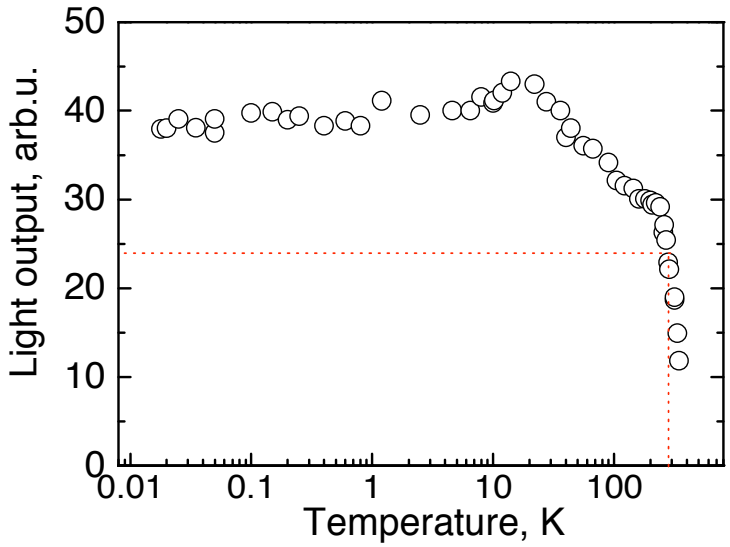

Figure 2.14: Temperature dependency of the light yield of the scintillation light of $CaWO_4$ using ^{241}Am α-particle excitation: Circles correspond to data points, the dashed, red lines indicate the light yield determined at room temperatures (295K). Picture adopted from from [46]. Copyright (2013) by John Wiley & Sons Inc.

these processes are considered and integrated in the model developed within this work in more detail (see chapter III/3).

The enhancement of the light-yield curve observed at $\sim$ 20K (see figure 2.14) is sometimes (see, e.g., [72]) attributed to a technical aspect in the light-detection process. The following argumentation is usually used: The lower the temperature, the larger the main (slow) decay time of the scintillation light of $CaWO_4$ (compare section III/2.2.3). It is suggested that the elongated decay time at low temperature leads to an incomplete collection of all scintillation photons and, thus, to an artificially smaller detected amount of scintillation light [72]. This possible explanation cannot be ruled out by basic arguments. However, another explanation of the peak of the light output at $\sim$ 20K will be given within the developed model in section III/3.2.1.

Absolute Light Yield and Detection Efficiency in CRESST Detector Modules

In the following, the value of the absolute light yield of $CaWO_4$, defined as the total amount of scintillation light escaping the crystal compared to the total amount of energy deposited in the crystal, is discussed. This value can vary significantly for different crystal samples: Of course, the light yield depends on the quality of the investigated sample, in terms of the contained defect density. In addition, the amount of scintillation light escaping a $CaWO_4$ crystal is also known to be highly dependent on the exact shape and surface treatment (polishing or roughening) of the investigated sample[35] (see, e.g., [73] and [74]).

[35] $CaWO_4$ exhibits a high probability of internal reflection of scintillation light due to its high refractive index $n \approx 1.95$ [73]. Therefore, the geometrical shape as well as roughening or polishing of the surface greatly influence the amount of light escaping the crystal.

Direct determination of the absolute light yield of a $CaWO_4$ crystal cannot be performed easily. However, if the detection efficiency of the setup used for the light detection can be determined and if, for the light detector used an absolute energy calibration, can be performed, the absolute light yield of the investigated crystal can be estimated. Such a method was applied in [12] to the detection of $CaWO_4$ scintillation light in several CRESST detector modules at mK temperatures:

- The mean fraction of deposited energy (for 727keV γ-rays of ^{212}Bi) detected with the light detector in a CRESST detector module amounts to 1.86% (mean value of all investigated modules [12]).
- The mean detection efficiency for the $CaWO_4$ scintillation light in the light detector of these CRESST detector modules[36] is determined to be 31% [12].

With these values, an absolute light yield of $CaWO_4$ at mK temperatures of 6.0% for γ-interactions can be estimated. This value is in very good agreement with the low-temperature value of 6.1%, estimated in appendix A.6. As discussed above, the light yield of $CaWO_4$ for temperatures $\lesssim$ 10K appears to be constant and the gain in light yield for a decrease in temperature from room temperature to 9K amounts to 1.8. Hence, an absolute light yield for $CaWO_4$ under γ-irradiation at room temperature of $\frac{6.0\%}{1.8} = 3.3\%$ can be estimated.

The following values for the absolute light yield of $CaWO_4$ under γ irradiation can be estimated:

$LY^{\gamma}_{abs}(T \lesssim 10\text{K})$	6.0%
$LY^{\gamma}_{abs}(T = 295\text{K})$	3.3%

Table 2.2: Absolute light yield LY^{γ}_{abs} of $CaWO_4$ crystals as employed in the CRESST experiment. LY^{γ}_{abs} is defined as fraction of deposited energy (for γ-irradiation) escaping the crystal in form of scintillation photons.

2.2.5 Light-Yield Quenching for Different Interacting Particles

As already indicated in section I/2.1, the amount of scintillation light generated in $CaWO_4$ by different interacting particles varies strongly. This effect is commonly referred to as light-yield quenching and is described with the help of the Quenching Factor as defined in equation I/2.5. The Quenching Factor describes the reduction in light yield for different interacting particles compared to the light yield for e^-/γ events of the same energy[37]. The knowledge of the Quenching Factor is particularly important in the context of the Dark Matter search experiments CRESST and EURECA in which the different light yields

[36] For a short discussion on a possible dependency of the detection efficiency in CRESST detector modules on the position of the energy deposition within the $CaWO_4$ crystal, see appendix A.7.

[37] In the context of the CRESST experiment, this energy has to be identified with the energy detected in the phonon channel E_{det}. This energy is not identical to the energy of the interacting particle as part of the energy leaves the crystal in form of scintillation photons. Due to the light-yield quenching effect, for different particles, a different amount of energy is transformed into scintillation light. Thus, for different particles of the same primary energy a different fraction of the primary energy, remains in the crystal and is detected by the phonon channel. This fact is referred to as phonon-quenching and is discussed in more detail in section III/6.1.1.

produced by different interacting particles are used for the important issue of background discrimination on an event-by-event basis (see section I/2.1).

Many different experiments have already been performed to determine the Quenching Factors for different interacting particles in $CaWO_4$ (see, e.g., [75, 76, 77] and references therein). In the following, see table 2.3, a selection of results obtained with different methods, at different energies of the interacting particles and at different measurement temperatures are presented.

	$QF^{e^-/\gamma}$		$:= 100\%$
CRESST*, $T \approx 10$mK	QF^{α}	($20\text{keV} \lesssim E_{det} \lesssim 120\text{keV}$)	$\sim 22\%$
	QF^{O}	($100\text{keV} \lesssim E_{det} \lesssim 300\text{keV}$)	$(10.4\pm0.5)\%$
	QF^{Pb}	($E_{det} \approx 103\text{keV}$)	$\sim 1.4\%$
NSF**, $T \approx 20$mK	QF^{O}	($240\text{keV} \leq E_{det} \leq 300\text{keV}$)	$(10.3\pm0.1)\%$
	QF^{Ca}	($240\text{keV} \leq E_{det} \leq 300\text{keV}$)	$(6.3\pm0.4)\%$
MPI***, $T \approx 300$K	QF^{Ca}	($E = 18\text{keV}$)	$(6.38^{+0.62}_{-0.65})\%$
	QF^{W}	($E = 18\text{keV}$)	$(3.91^{+0.48}_{-0.43})\%$
JM****, $T \approx 300$K	QF^{O}	($1095\text{keV} \leq E \leq 2209\text{keV}$)	$(7.8\pm0.3)\%$
	QF^{Ca}	($452\text{keV} \leq E \leq 943\text{keV}$)	$(6.3\pm1.6)\%$
	QF^{W}	($E = 100\text{keV}$)	$(< 3.0)\%$ (2σ)

Table 2.3: Quenching Factors determined with different methods for different energies of the interacting particle (E = energy of the particle, E_{det} = energy detected in the phonon channel of a CRESST-II-like cryogenic detector module) and at different measurement temperatures. *: Values directly determined in the CRESST-II experiment [5]. **: Values determined in a dedicated experiment [77] at the neutron scattering facility of the Maier-Leibnitz-Laboratorium, Garching. ***: Values determined in a dedicated experiment [78] at the Max-Planck-Institut für Physik, München. ****: Values determined in a dedicated experiment [75, 76] at the neutron scattering facility of the Maier-Leibnitz-Laboratorium, Garching.

As can be seen from the values listed in table 2.3, the Quenching Factors for different particles vary strongly, thus, enabling the employment of the light signal as discrimination parameter in rare event searches as, e.g., the direct Dark Matter search with the CRESST experiment. In addition, it can be seen that the values determined at different temperatures or with different energies of the interacting particles partly differ from each other. Up to now, no theoretical model explaining the observed light-yield quenching or the observed differences of measured values for a Quenching Factor on a microscopic basis exists. With currently available models, the strength of the observed light-yield quenching for different particles can only be described on a phenomenological basis (see discussion in section III/6.2). However, the new model developed within this thesis (presented in chapter III/3) will allow to completely explain and even to calculate Quenching Factors for different kinds of interacting particles in $CaWO_4$ on a theoretical basis.

Chapter 3

Comprehensive Model Developed in this Thesis

In this chapter, the model developed for the scintillation-light production and quenching in $CaWO_4$ under particle excitation is presented. This model delivers a comprehensive explanation of the efficiency of the scintillation-light generation in $CaWO_4$ for different modes of excitation on a microscopic basis. In particular, the observed light-quenching effect for different interacting particles in $CaWO_4$ is explained by the model and can be assessed quantitatively. The model is based on the temporal evolution of the population of fundamental excitations (self-trapped excitons, STEs) created by an energy deposition in a $CaWO_4$ single crystal. Within the model, the produced amount of scintillation light due to the energy deposition, e.g., by an interacting particle, can be associated with the pulse shape of the produced scintillation-light which reflects the lifetime and temporal evolution of the STE population.

In section III/3.1, the different microscopic processes involved in the generation, excitation and de-excitation of STEs for an interacting particle in $CaWO_4$ are presented. As starting point, the energy-deposition processes for different interacting particles that lead to the production of ionization are presented. In the developed model included are the microscopic description of the formation process and the determination of the spatial distribution of STEs created in the energy-deposition process by the primary interacting particle and by all of its recoil particles. The particle-induced initial, spatial distribution of STEs is determined with the help of simulations with the programs SRIM [42] and CASINO [43] on the basis of a geometrical model developed for the energy-loss process of interacting particles. Different microscopic processes that are considered to be involved in the excitation and de-excitation of STEs in $CaWO_4$ are presented where it will become clear that the STE-STE interaction process which is included in the model is particularly important in the context of the light-quenching effect. At the end of section III/3.1, a summary of the first part of the model describing the spatial and temporal evolution of the STE population in $CaWO_4$ is given.

In section III/3.2, the processes of the scintillation-light generation by the described STE population are discussed. At first, a qualitative discussion of the temperature-dependent impact of the different microscopic STE excitation and de-excitation processes onto the scintillation-light generation is presented. In addition, a mathematical model for the shape and temperature dependencies of the wavelength spectra of the scintillation light is intro-

duced. The basic mathematical relationship between the generated scintillation light and the STE populations as well as their temporal evolution is presented and discussed. From this discussion, it can be seen that the introduced STE-STE interaction mechanism for densely created STEs, in comparison to spatially separated STEs, is assumed to induce the observed light-yield quenching for heavy, charged particles. Therefore, the description of the model is split into two parts: At first, the model for the light generation by STEs created via a *rare excitation mode*, i.e., STEs created far away from each other, is discussed. In this case, it is assumed that the STEs cannot interact with each other and, hence, the produced scintillation light is labeled as *unquenched*. Thereafter, the light-generation mechanism described by the complete model, i.e., including the possibility of the STE-STE interaction is discussed. This complete model describes the light generation by a STE population created by a *dense excitation mode*, i.e., correlated and closely located STEs as, e.g., created by a recoiling nucleus. The high densities of STEs created, e.g., by recoiling nuclei, allow for the STE-STE interaction mechanism and, thus, as will be discussed, lead to a reduced light output. Therefore, the scintillation light produced by densely created STEs is labeled as *quenched*.

In section III/3.3, a summary of the complete model is given. A discussion and concept for the experimental determination of free parameters of the model as well as a concept for the model validation are presented.

Within the developed model, the existence of two different STE populations is assumed: *Blue STEs* at intrinsic centers (undisturbed $[WO_4]^{2-}$ complexes, see section III/2.2.2) and *green STEs* at defect centers (defective, disturbed $[WO_4]^{2-}$ complexes, see section III/2.2.2). In the following, the term *blue scintillation light* is used for the scintillation light generated by the radiative decay of blue STEs at intrinsic centers whereas the term *green scintillation light* is used for the scintillation light generated in the radiative decay of green STEs at defect centers. Defect centers correspond to any type of $[WO_4]^{2-}$ complexes with a disturbed energy-level scheme at the band edge, as, e.g., a $[WO_4]^{2-}$ complex containing a Mo atom, an Oxygen vacancy or a deformed crystal structure (see section III/2.1.3). All of these disturbed $[WO_4]^{2-}$ complexes are assumed to generate green-shifted (less energetic) scintillation light compared to undisturbed scintillation centers (compare section III/2.2.2). However, for $[WO_4]^{2-}$ complexes containing, e.g., a La impurity, the energy-level scheme at the band edge should not be influenced (see section III/2.1.3). Hence, such complexes are assumed to contain blue STEs when excited and, thus, to yield blue light generation.

The presented discussion covers a temperature range from room temperature, 300K, down to mK. In general, it is assumed that the excitation of a $CaWO_4$ crystal is performed with photons or particles depositing a minimum energy larger than the band gap of the material ($E_{gap} = 5.0$eV, see section III/2.1.2). Hence, no selective excitation of states within the band gap, i.e., no selective excitation of defect centers (see section III/2.1.3), is assumed to occur.

3.1 Exciton Generation, Excitation and De-Excitation in $CaWO_4$

3.1.1 Energy-Deposition Processes of Different Interacting Particles

In the following, the energy-deposition processes for different interacting particles are reviewed with special focus on the respective efficiencies in creating ionization (electrons in the conduction band and corresponding holes in the valence band). Two different energy thresholds are important in this context:

- The **ionization-threshold energy**: $E_{i-th} = 2.35 \cdot E_{gap} = 11.75\text{eV}$ (see, e.g., [46, 79] and appendix A.6).
  This energy threshold corresponds to the typical mean energy needed to create an electron-hole pair in $CaWO_4$, i.e., to excite an electron into the conduction band, in a particle interaction. For particles, e.g., electrons, with energies lower than this threshold energy, typically no further ionization takes place[1] [79]. This feature can, e.g., be recognized from the occurrence of a minimum in the luminescence quantum-yield for excitation with photons of different energies: For photon energies higher than the ionization threshold, the quantum yield starts to increase again indicating the beginning of the multiplication of secondary electron-hole pair creation (see, e.g., figure 1 in [80]).

- The minimum **displacement energies** for the different nuclei in the crystal lattice: $E_{disp-O} = 28\text{eV}$ (Oxygen), $E_{disp-Ca} = 25\text{eV}$ (Calcium), $E_{disp-W} = 25\text{eV}$ (Tungsten) [42].
  The displacement energy corresponds to the minimum energy required to be transferred to a nucleus of the lattice in a collision in order to remove it from its lattice site. Hence, for collisions with less energy transfer, the knocked-on nucleus of the crystal lattice is only excited (e.g., oscillations are excited), but no recoiling nucleus traversing the crystal is produced.

Deposition of Energy by the Primary Particle

Taking the two energy thresholds defined for electron- and nuclear-recoil production into account, the energy-loss processes for different interacting particles can be classified. Depending on the type of the primary particle and its energy E_{part}, several (dominant) possibilities for the interaction with the $CaWO_4$ lattice, i.e., the energy-deposition process, occur. A detailed discussion of the different energy-loss processes for different primary interacting particles, as, e.g., electrons, neutrons or heavy, charged particles, is presented in appendix B.1.

From this discussion, it can be seen that an interaction in $CaWO_4$ (and, in general, in inorganic scintillators) is always followed by an avalanche of secondary excitations. In principle, three major types of energy deposition by the different primary particles can be identified and will be considered in the following:

- Electronic stopping: The production of ionization, i.e., the excitation of electrons into the conduction band (creating corresponding holes in the valence band). This

[1] Of course, photons with energies larger than the band gap, but less than the ionization threshold can be absorbed and produce electron-hole pairs.

process can occur for a typical mean energy transfer to electrons of the $CaWO_4$ lattice larger than the ionization threshold.

- Nuclear stopping: The production of nuclear recoils and vacancies (or replacement collisions), i.e., energy stored in lattice defects. This process can occur for an energy transfer larger than the respective displacement energy to a nucleus of the $CaWO_4$ lattice.

- The direct production of phonons by the primary particle.

In the context of the scintillation-light generation in $CaWO_4$, only the fraction of energy deposited in ionization $F_{ioniz}(E_{part})$ is of interest as excited luminescence centers (STEs) can only be created by electrons in the conduction band and holes in the valence band (see section III/2.2). Here, ionization is defined as the fraction of energy transferred to the electrons of the $CaWO_4$ crystal. As can be seen from the overview presented in appendix B.1, this fraction is different for different interacting particles and also depends on the energy deposited by the primary particle. To determine this fraction for different interacting particles, different methods which are presented in the following are applied.

It has to be noted that, from this point on, in the following, the term E_{part} denotes the total energy *deposited* by the primary particle *part* in a $CaWO_4$ crystal. Hence, e.g., for an electron depositing only part of its energy in a Compton scattering event (and leaving the crystal with the remaining energy), E_{part} only refers to the amount of energy transferred to the excited electron and hole and not to the initial total energy of the primary electron. As discussed above, for particles with energies smaller than the ionization-threshold E_{i-th} (except photons), no further ionization is assumed to take place. Hence, the following discussion is carried out for particles that deposit energies $E_{part} \geq E_{i-th}$.

Fraction of Energy Deposited in Ionization by Electrons

From the above discussion of the dominant energy-loss processes of electrons (and, thus, also for x-rays and γ-particles primarily exciting electrons), it can be concluded that the total energy deposited by the primary particle is converted into ionization. Therefore, it is assumed that, for electrons, x-rays and γ-particles in the primary interaction with the $CaWO_4$ crystal, the total energy of the primary particle is deposited into ionization: $F_{ioniz}(E_{el}) = F_{ioniz}(E_{\gamma}) = F_{ioniz}(E_{\text{X-ray}}) = 100\%$.

Fraction of Energy Deposited in Ionization by Heavy Charged Particles

For nuclear recoils, α-particles or other heavy, charged particles, the fraction of energy deposited in ionization is less than 100% due to the direct production of phonons and lattice defects in the nuclear stopping process. The respective contributions of the electronic and nuclear stopping processes to the total energy loss of heavy, charged particles in matter are described by the Lindhard theory [81] and the Bethe-Bloch formula (see, e.g., [82] and [83]). For the simplest case of a target material consisting of one element (with proton number Z_{mat}) and an interacting particle (with proton number Z_{part}), three major regions depending on the particle energy E_{part} can be identified [81]:

- **Regime 1**: Low energies with an upper bound characterized by the critical energy E_c with $v_{part} \lesssim v_c := 0.015 \cdot v_0 \cdot Z^{\frac{2}{3}}$, where v_{part} is the velocity of the particle, v_c

is the critical velocity, $v_0 = \frac{e^2}{\hbar}$ is the Bohr velocity[2] and $Z^{\frac{2}{3}} = (Z_{part}^{\frac{2}{3}} + Z_{mat}^{\frac{2}{3}})$ [81]. The stopping process is dominated by nuclear stopping as, at these velocities, the electrons of the material can follow the induced electric field of the particle passing by. The contribution of electronic stopping is small and assumed to be proportional to the velocity of the interacting particle v_{part} [81]. In this regime, the interacting particle keeps most of its electrons bound.

- **Regime 2**: Intermediate energies with an upper bound characterized by the energy E_1 with $v_{part} \lesssim v_1 = v_0 \cdot Z_{part}^{\frac{2}{3}}$, where v_1 is an estimate for the the mean electron velocity of the interacting particle. The contribution by nuclear stopping decreases and the contribution of electronic stopping increases roughly proportional to $E_{part}^{\frac{1}{2}}$ or, respectively, proportional to v_{part} [81]. At the maximum velocity of this regime, it is assumed that the ion is fully stripped off its bound electrons. At this energy, also the maximum electronic stopping occurs, represented by the occurrence of the so-called Bragg peak.

- **Regime 3**: High energies of the interacting particle, i.e. $v_0 \cdot Z_{part}^{\frac{2}{3}} = v_1 \lesssim v_{part}$. The electronic stopping starts to decrease again, however, it is still the dominant energy-loss process of the interacting particle. In this regime, it is assumed that the interacting particle is stripped off its bound electrons. The contribution of electronic stopping is described with the Bethe-Bloch formula [82, 83].

Adopting these definitions, a very rough estimate of the corresponding energy regimes for Ca, O and W ions interacting in $CaWO_4$ can be performed, under the assumption that Z_{mat} is given by the mean proton number of $CaWO_4$: $Z_{CaWO_4} = \frac{Z_{Ca}+Z_W+4\cdot Z_O}{6} = 21$. The resulting energies and velocities (% of the velocity of light, c) are shown in table 3.1.

	O	Ca	W
$E_{part} \lesssim E_c$	dominated by nuclear stopping		
$\frac{v_c}{c}$	0.13%	0.16%	0.28%
E_c [MeV]	0.012	0.050	0.651
$E_c \lesssim E_{part} \lesssim E_1$	nuclear and electronic stopping		
$\frac{v_1}{c}$	2.91%	5.37%	12.84%
E_1 [MeV]	6.33	53.75	1428.39
$E_1 \lesssim E_{part}$	dominated by electronic stopping		

Table 3.1: Energy regions of different dominant energy-loss processes for O, Ca and W ions interacting in $CaWO_4$: Estimation on the basis of the different velocity regimes, defined in [81].

From these values, it can be seen that, in the energy region of interest for the dark matter search (energy depositions less than 100keV, see section I/2.2), the energy-loss processes of nuclear recoils are mostly dominated by nuclear stopping.

In order to determine the fraction $F_{ioniz}(E_{part})$ of the energy of the primary particle

[2]The Bohr velocity corresponds to the velocity of the electron of a hydrogen atom in the classical atomic model by Bohr. It can be obtained by equalizing the centrifugal force and the gravitational force for the quantized orbits postulated by Bohr.

that is deposited in ionization (directly by the primary particle and by the induced nuclear recoils), simulations with the program SRIM (The Stopping and Range of Ions in Matter) [42] were performed. A discussion of the simulations and their analysis can be found in appendix B.3.2. SRIM delivers the fraction of energy deposited in ionization by the chosen primary particle and the individual contributions of the ionization created directly by the primary particle and of the ionization created by recoiling nuclei of the target material. In figure 3.1, the fraction $F_{ioniz}(E_{part})$ of the energy E_{part} for O (dotted, black line), Ca (dashed, green line) and W (solid, red line) ions in an energy range from 100eV to 50MeV as calculated with the SRIM software is shown.

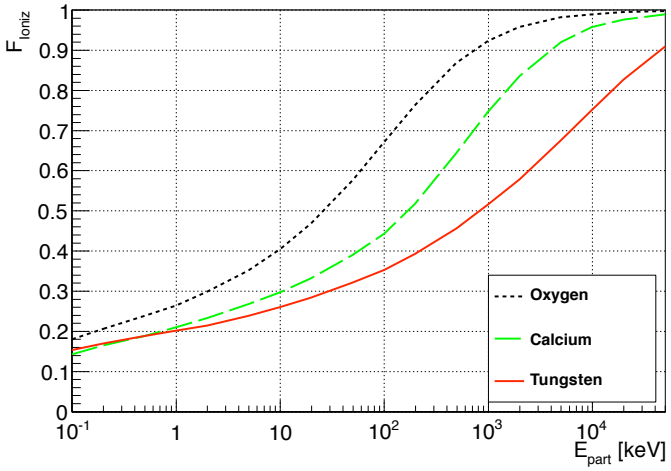

Figure 3.1: Fraction of energy deposited in ionization for O (dotted, black line), Ca (dashed, green line) and W (solid, red line) ions interacting in $CaWO_4$ (semi-logarithmic plot): Calculated with the SRIM software (for details, see appendix B.3.2).

Summary: Energy Deposition in Ionization by Different Particles

From this discussion of the energy-deposition processes of different interacting particles, the following assumptions used as basis for the model describing the light generation and quenching in $CaWO_4$ are derived:

- Interacting electrons (as well as photons, x-rays and γ-particles) deposit a fraction of $F_{ioniz}(E_{part}) = 100\%$ of their energy into ionization.
- Interacting heavy, charged particles (such as ions or nuclear recoils) deposit an energy- and particle-dependent fraction $F_{ioniz}(E_{part})$ of their energy in ionization. This fraction is determined with the help of SRIM simulations.

In table 3.2, examples for the fraction of energy deposited in ionization for electrons as well as O, Ca and W ions of 1keV, 10keV, 100keV and 1MeV are shown ($F_{ioniz}(E_{part})$ for O, Ca and W ions calculated with SRIM). It can be seen that, e.g, for Oxygen ions of 10keV, only $\sim$ 4keV, i.e., $\sim$ 40%, of the energy are converted into ionization while for 10keV electrons it is assumed that the complete energy of 10keV is converted into ionization. However, this difference is not yet enough to explain the reduction in light yield observed for Oxygen ions in comparison to electrons which amounts to roughly a factor of 10 (see Quenching Factors in table 2.3, section III/2.2.5).

	e^-	O	Ca	W
$F_{ioniz}(E_{part} = 1\text{keV})$	100%	26.4%	20.9%	19.9%
$F_{ioniz}(E_{part} = 10\text{keV})$	100%	40.3%	29.6%	25.8%
$F_{ioniz}(E_{part} = 100\text{keV})$	100%	66.8%	44.3%	35.2%
$F_{ioniz}(E_{part} = 1\text{MeV})$	100%	92.2%	74.5%	51.3%

Table 3.2: Fraction of energy deposited in ionization for different interacting particles in $CaWO_4$.

All of the processes described are assumed to be independent of temperature. Hence, the values for the fraction of energy deposited in ionization as determined with the SRIM simulations are adopted for the complete temperature range under consideration (mK up to room temperature).

3.1.2 Primary Excitation of Luminescence Centers in $CaWO_4$

Production of Low Energetic Electrons and Holes

The next step in the light-generation process is the conversion of ionization (high- and low-energetic electrons and holes) into low-energetic electrons and holes which cannot create any further ionization. As already indicated in the discussion of the energy-loss process of electrons and holes in section III/3.1.1, it is assumed that a mean energy of $E_{eh} = 2.35 \cdot E_{gap} = 11.75\text{eV}$ is needed to create an electron in the conduction band and a hole in the valence band. Therefore, it is assumed that a mean number of electrons (in the conduction band) and holes (in the valence band), $N_{eh}(E_{part})$, depending on the type and energy of the primary particle are created:

$$N_{eh}(E_{part}) = \frac{F_{ioniz}(E_{part}) \cdot E_{part}}{E_{eh}} = \frac{F_{ioniz}(E_{part}) \cdot E_{part}}{2.35 \cdot E_{gap}} = \frac{F_{ioniz}(E_{part}) \cdot E_{part}}{11.75\text{eV}} \quad (3.1)$$

This process is assumed to be independent of temperature. As described in section III/2.1.4, the holes in the valence band undergo a self-trapping process (phonon production) and form STHs (self-trapped holes), preferably at the $[WO_4]^{2-}$ complexes where they were created. In the considered temperature range, these STHs can be assumed to be immobile (on the time scale of the lifetime of self-trapped excitons, see section III/2.1.4). The electrons in the conduction band relax via phonon emission to the band edge.

Electron Mobility: The Exciton-Formation Process

As starting point for the discussion of the STE-formation process, $N_{eh}(E_{part})$ electrons relaxed to the band edge of the conduction band and an equal number of STHs inducing potential wells for electrons in the conduction band are considered. In principle, the influence of electron traps due to defects in the crystal structure has to be taken into account. However, in this section, as a first step, only the recombination of electrons with STHs is discussed whereas the capture process of electrons by traps and its influence on the STE-formation process is presented in section III/3.1.2.

Rise Time of the Scintillation Light

As discussed in section III/2.2.3, the scintillation light of $CaWO_4$ exhibits two different rise times: A fraction F_{dr} ($\sim$ 15% at 300K [71]) of the scintillation light exhibits a delayed rise time τ_{dr} (temperature-dependent, 40ns at room temperature [71]) whereas the main part of the scintillation light $(1 - F_{dr})$ exhibits a very fast rise ($\sim 200 \pm 50$fs [71]). The delayed rise time was observed to decrease with decreasing temperature (in [65], a delayed rise time of only 20ns is reported for a measurement performed at 100K).

These observations indicate a split production process of STEs in $CaWO_4$ (compare discussion in appendix A.5 and [71, 65]): It can be assumed that the main part of the scintillation light $(1-F_{dr})$ exhibiting the fast rise time is produced by the fraction $(1-F_{dr})$ of the STE population that was created in a very fast process (on a timescale of the fast rise time of the scintillation light). The fraction F_{dr} of the scintillation light is produced by a fraction F_{dr} of the STE population that was created in a delayed formation process (on a timescale of the delayed rise time of the scintillation light). This interpretation of the results can be explained theoretically with a diffusion-controlled recombination of the electrons with STHs to STEs.

Diffusion-Controlled Recombination of Electrons and STHs

A detailed presentation of a simplified model for the diffusion-controlled recombination process of electrons and STHs to STEs as well as of the approximations performed, can be found in appendix B.2.1. A summary of this model is presented in the following:

In a diffusion-controlled recombination process, it is assumed that electron-STH pairs with a distance shorter than the radius $R^0_{eSTH}(T)$ ("black sphere" radius) recombine immediately to a STE[3]. Recombination of electron-STH pairs with a distance larger than $R^0_{eSTH}(T)$ is controlled by the diffusion process of electrons versus the immobile[4] STHs. The "black sphere" radius can be identified with the so-called Onsager radius which is defined as the distance of two charged particles for which the energy of the Coulomb interaction (in a dielectric medium with relative electric permittivity ϵ_r) is equal to the thermal energy[5] $k_B \cdot T$ [84]. The "black sphere" (Onsager) radius of immediate recombination is given by:

$$R^0_{eSTH}(T) := \frac{e^2}{4 \cdot \pi \cdot \epsilon_0 \cdot \epsilon_r \cdot k_B \cdot T} \tag{3.2}$$

with ϵ_0 as the vacuum permittivity. As presented in detail in appendix B.2.1, using $R^0_{eSTH}(T)$ and a (simplified) differential equation describing the temporal evolution of the population of electrons in the conduction band (compare [85] for a general model), it can be deduced that the fraction of electrons recombining immediately with STHs to STEs,

[3]This radius is labeled as "black sphere" radius as the process of recombination of two particles within such a "black sphere" is not specified further, but is only characterized by the assumption that the probability for recombination is 100% and that the process is faster than any other process considered.

[4]In section III/2.1.4, it is explained that, within the temperature range considered, STHs in $CaWO_4$ can be assumed to be immobile.

[5]k_B is the Boltzmann constant and T is the temperature.

$F_{im-rec}(T)$, is proportional to:

$$F_{im-rec}(T) \propto (R^0_{eSTH}(T))^3 \cdot C_{STH} \propto \frac{(R^0_{eSTH}(T))^3}{V^{diff}_{e(CB)}} \tag{3.3}$$

where $C_{STH} = \frac{1}{V^{diff}_{e(CB)}}$ is defined as the density of STHs in the volume $V^{diff}_{e(CB)}$ that is probed by the electrons in their diffusion process (for a discussion of the assumption that $V^{diff}_{e(CB)}$ and C_{STH} are not dependent on temperature, see appendix B.2.2). In addition, it can be seen that, within this simplified model, the temporal evolution of the delayed recombining electron population in the conduction band is described by an exponential function with decay constant $\frac{1}{k_{dr}(T)}$. This diffusion controlled, delayed recombination rate of these electrons, $k_{dr}(T)$, is proportional to (compare appendix B.2.1):

$$k_{dr}(T) \propto D_{e(CB)}(T) \cdot R^0_{eSTH}(T) \cdot C_{STH} \tag{3.4}$$

where $D_{e(CB)}(T)$ is the diffusion coefficient of electrons in the conduction band.

Inspecting equations 3.3 and 3.4 and taking the temperature dependency of the electron diffusivity (see appendix B.2.2) as well as of the "black sphere" radius (see equation 3.2) into account, the following conclusions can be drawn:

- The fraction of immediately recombining electron-STH pairs, $F_{im-rec}(T)$, i.e., the fraction of STEs that is created immediately, is expected to be proportional to T^{-3}. Hence, the fraction of immediately recombining electron-STH pairs increases strongly with decreasing temperature.
- For the recombination rate $k_{dr}(T)$, of the fraction $(1-F_{im-rec}(T))$ of delayed recombining electron-STH pairs, at elevated temperatures, a dependency of $k_{dr}(T) \propto T^{-\frac{3}{2}}$, at low temperatures, a dependency of $k_{dr}(T) \propto T^{\frac{3}{2}}$ can be expected (compare appendix B.2.3). Hence, the fraction of STEs that is created in the delayed, diffusion controlled process is expected to exhibit a temperature-dependent rise time $\frac{1}{k_{dr}(T)}$.

Resulting STE-Formation Process

From the discussion above, it can be concluded that, in the simplified model for the electron-STH pair recombination, the temporal development of the STE-formation process via the two recombination processes mentioned, can be expressed qualitatively by:

$$\begin{aligned} N^{form\, e^- STH}_{STE}(E_{part}, T, t) = \Theta(t) \cdot (1 - F_{dr}(T)) \cdot N_{eh}(E_{part}) + \\ + \Theta(t) \cdot F_{dr}(T) \cdot k_{dr}(T) \cdot e^{-k_{dr}(T) \cdot t} \cdot N_{eh}(E_{part}) \end{aligned} \tag{3.5}$$

where $N^{form\, e^- STH}_{STE}(E_{part}, T, t)$ is the change in the number of STEs due to the recombination of electrons and STHs. $\Theta(t)$ is the Heaviside step function, $F_{dr}(T)$ corresponds to the fraction of STEs produced by the delayed (diffusion-controlled) recombination process and $(1 - F_{dr}(T))$ corresponds to the fraction of STEs produced in the immediate recombination process. It has to be noted that, up to this point, no electron-capture processes by electron traps are included.

Comparison with the Observed Time Dependency of the Scintillation Light

This mathematical model for the STE-formation process, based on the simplified model for the electron-STH pair recombination, nicely complies with the observed composition of the rise time of the scintillation light of $CaWO_4$ (compare to the discussion of the observed rise time of $CaWO_4$ scintillation light at the beginning of this section): The fraction $(1 - F_{dr}(T))$ of STEs can be assumed to produce the fast rising part of the scintillation light. And the fraction $F_{dr}(T)$ of STEs can be assumed to produce the part of the scintillation light with a delayed rise time $\tau_{dr}(T) = \frac{1}{k_{dr}(T)}$.

As discussed above, at room temperature, the fraction of scintillation light exhibiting an immediate (very fast) rise time is of the order of $\sim 85\%$ [71]. Hence, at room temperature, the fraction $(1 - F_{dr}(T))$ of immediately recombining STEs can be expected to be of the order of $\sim 85\%$. In addition, it has to be noted that the fraction of immediately recombining STEs, $(1 - F_{dr}(T))$, is expected to exhibit a strong temperature dependency proportional to T^{-3} (compare discussion in appendix B.2.3). Taking into account this strong temperature dependency, it can be expected that, for temperatures below 100K, the fraction of delayed recombining STEs is very small[6]. Therefore, in the following, it is assumed that, for temperatures below 100K, the fraction of delayed recombining electrons can be neglected:

$$F_{dr}(T \lesssim 100\text{K}) \approx 0 \tag{3.6}$$

$$1 - F_{dr}(T \lesssim 100\text{K}) \approx 1 \tag{3.7}$$

The rise time of the fraction of scintillation light produced delayed is reported to amount to ~ 40ns at room temperature [71] and ~ 20ns at 100K [65]. Combining these observations with the discussion of the expected temperature dependency of the electron-STH pair recombination-process (see appendix B.2.3), it is deduced that the delayed recombination time of STEs, exhibits a net decrease from room temperature, $\tau_{dr}(T = 300K) \approx 40$ns down to 100K, $\tau_{dr}(T = 100K) \approx 20$ns, with a possible minimum in between (compare appendix B.2.3).

Efficiency of the Production of Self-Trapped Excitons

Impact of Electron Traps Contained in the Crystal Lattice

In a real crystal lattice containing electron traps, the electrons relaxed to the band edge of the conduction band cannot only recombine with STHs to STEs, but can also get captured by electron traps[7]. Hence, dependent on where an electron is located after its relaxation process to the band edge (either close to a STH, close to an electron trap or neither in the direct vicinity of a STH nor an electron trap), different possibilities occur: The electron can either immediately get captured by a STH and form a STE, immediately get captured by

[6] From the transient absorption measurements at a temperature of 100K presented in [65], the absorptivity of the fraction of delayed recombining electrons can be compared to the absorptivity of the fraction of electrons recombining immediately to STEs. Assuming that the absorptivity of both electron populations is roughly the same, from the ratio of the integrated optical densities (estimated on the basis of figure 2 in [65]), it can be deduced that the delayed recombining fraction of electrons at 100K is at least 3 orders of magnitude smaller than the immediately recombining fraction of electrons.

[7] As discussed in section III/2.1.3, these electron traps are produced by the same centers that are assumed to produce the green scintillation light.

an electron trap or migrate through the crystal until it is captured in a delayed process by a STH or an electron trap. Electrons captured by STHs or electron traps can be regarded as immobile as the respective potential wells (of the STHs and of the electron traps) are too deep to allow thermal disintegration of the respective configuration (compare sections III/2.1.5 and III/2.1.3). Therefore, electrons captured by electron traps can be considered as being removed from the STE-formation process, i.e., be considered as lost electrons. In each of the capture processes, the energy difference of the electron at the conduction-band edge and in the potential well (of a STH or of an electron trap) is released as phonons.

In analogy to the electron-capture process by STHs, the electron-capture process by electron traps can be modeled with a diffusion-controlled recombination process (compare to the discussion above and appendices B.2.1 to B.2.3). In appendix B.2.4, the impact of the existence of electron traps, interpreted as additional recombination partners for electrons (in addition to the STHs), in such a model is discussed. From this discussion, it can be seen that the total fraction of electrons captured by electron traps, F_{e^-traps}, and the fraction captured by STHs, $F_{STH} = (1 - F_{e^-traps})$, (in the immediate and delayed processes combined) only depends on the ratio of the relative occurrences of electron taps and STHs in the volume $V_{e(CB)}^{diff}$ probed by the electron in its diffusion process[8]:

$$F_{e^-traps} = \frac{C_{\text{defects}}}{C_{STH} + C_{\text{defects}}} \not\propto T \tag{3.8}$$

$$F_{STH} = (1 - F_{e^-traps}) = \frac{C_{STH}}{C_{STH} + C_{\text{defects}}} \not\propto T \tag{3.9}$$

Resulting Model for the STE-Formation Process and its Efficiency

Hence, within the simplified model developed for the recombination of electrons with STHs and electron traps, the total (integrated) number of electrons and holes that yield the formation of STEs, $N_{STE}^{form\,e^-STH}$, is assumed to be independent of temperature and can be written as

$$N_{STE}^{form\,e^-STH}(E_{part}) = (1 - F_{e^-trap}) \cdot N_{eh}(E_{part}) \tag{3.10}$$

Thus, if, e.g., the defect density C_{defects} and the volume $V_{e(CB)}^{diff}$, i.e., the volume probed by the electrons in their diffusion process, would be known, this fraction could be calculated.

The major part of these STEs, $N_{im\,STE}^{form\,e^-STH}(E_{part}, T, t)$ (for $T \lesssim 100$K, $(1 - F_{dr}(T)) \approx 1$), is produced in a very fast process, in the following denoted as immediate creation process (compare equation 3.5). The radiative decay of these **immediately created STEs** delivers the **fast rising part of the scintillation light**. The part $N_{del\,STE}^{form\,e^-STH}(E_{part}, T, t)$ of the STE population is produced in a **delayed process** with a (temperature-dependent) exponential rise time $\tau_{dr}(T)$ (compare to the discussion below equation 3.7). There, $\tau_{dr}(T)$ is determined by the diffusion-controlled recombination with STHs and electron traps. The radiative decay of these STEs leads to the **delayed emission** of a fraction of scintillation

[8]The volume $V_{e(CB)}^{diff}$ probed by the electron in its migration process can still be assumed to be independent of temperature as the only recombination processes considered are provided by the recombination with STHs or electron traps. Hence, the electron migrates until it is captured.

light with a rise time of $\tau_{dr}(T)$ ($\sim$ 40ns at room temperature and $\sim$ 20ns at 100K):

$$N_{STE}^{form\,e^-STH}(E_{part},t) = N_{del\,STE}^{form\,e^-STH}(E_{part},T,t) + N_{im\,STE}^{form\,e^-STH}(E_{part},T,t) \quad (3.11)$$

$$N_{im\,STE}^{form\,e^-STH}(E_{part},T,t) = \Theta(t)\cdot(1-F_{e^-trap})\cdot(1-F_{dr}(T))\cdot N_{eh}(E_{part})$$

$$N_{del\,STE}^{form\,e^-STH}(E_{part},T,t) = \Theta(t)\cdot(1-F_{e^-trap})\cdot\frac{F_{dr}(T)}{\tau_{dr}(T)}\cdot e^{-\frac{t}{\tau_{dr}(T)}}\cdot N_{eh}(E_{part})$$

Type of Primarily Produced STEs

Due to the immobility of the STHs[9], it can be deduced that STEs are mainly created at those $[WO_4]^{2-}$ complexes that get excited in the process of primary energy deposition and further ionization. As, however, the typical density of defective (green light emitting) $[WO_4]^{2-}$ centers should be in the range of a few 10ppm to a few 100ppm, the statistical probability of directly exciting such a defect center should be very small[10]. Hence, in the following, it is assumed that only intrinsic scintillation centers and, thus, only blue STEs are directly excited in the process of energy deposition and ionization. However, as can be seen from the wavelength spectra recorded for $CaWO_4$ crystals under different modes of excitation and at different temperatures, the scintillation-light spectrum is always a composition of green and blue light[11] (see, e.g., figure 2.12 in section III/2.2.2). Therefore, at least one process leading to the excitation of green STEs has to exist. This fact will be discussed in more detail in section III/3.1.3.

Spatial Distribution of the Produced Ionization and STEs

Besides the differences in the amount of energy deposited in ionization for different interacting particles in $CaWO_4$, another important difference in the energy-deposition process exists: The spatial distribution of the ionization, i.e. the **density of the excited STEs** differs significantly for different interacting particles.

The differences in the spatial distribution of the created ionization can, e.g., be recognized from the different track lengths of different particles of the same energy in their respective energy-loss processes in $CaWO_4$: Here, the track length l_{track} is defined as the length of the track of the primary particle and not as the penetration depth into the material. This length can be determined with simulations using the program SRIM [42] (The Stopping and Range of Ions in Matter) for heavy, charged interacting particles (ions)

[9] On the time scale of the lifetime of self-trapped excitons, STHs are assumed to be immobile (see section III/2.1.4).

[10] The defect density should not directly be equated with the impurity density ($\sim$ 50ppm to 400ppm, see section III/2.1.3) as, on the one hand, certain impurities (e.g., La doping) do not disturb the lattice structure in a way that centers emitting green light are formed. On the other hand, defect centers also include deformed $[WO_4]^{2-}$ complexes which are not caused by an impurity or vacancy, but by a deformed unit cell. In general, it is assumed that most of the deformed $[WO_4]^{2-}$ complexes are created due to the existence of impurities (disturbance of the lattice structure by foreign atoms). Hence, it can be expected that the number of deformed unit cells should be roughly of the same order of magnitude as the number of impurities.

[11] This is true for all modes of non-selective excitation, i.e., excitations with individual primary particle energies of at least the energy of the band gap of $CaWO_4$. However, also for selective excitation (only extrinsic scintillation centers are excited in the primary energy-deposition process) above a temperature of $\sim$ 5K, a composite wavelength spectrum is observed (see, e.g., [86]). Only for temperatures below $\sim$ 5K, selective excitation of green centers is observed to lead to selective emission, i.e., the production of green scintillation light only (see, e.g., chapter 5 in [54]).

and with the program CASINO [43] (monte CArlo SImulation of electroNs in sOlids) for electrons. For details on the simulations, see appendix B.3.2. As an example, the track lengths l_{track} for electrons as well as O, Ca and W ions in $CaWO_4$ determined from the simulations are shown in figure 3.2 for the energy range from 100eV to 1MeV.

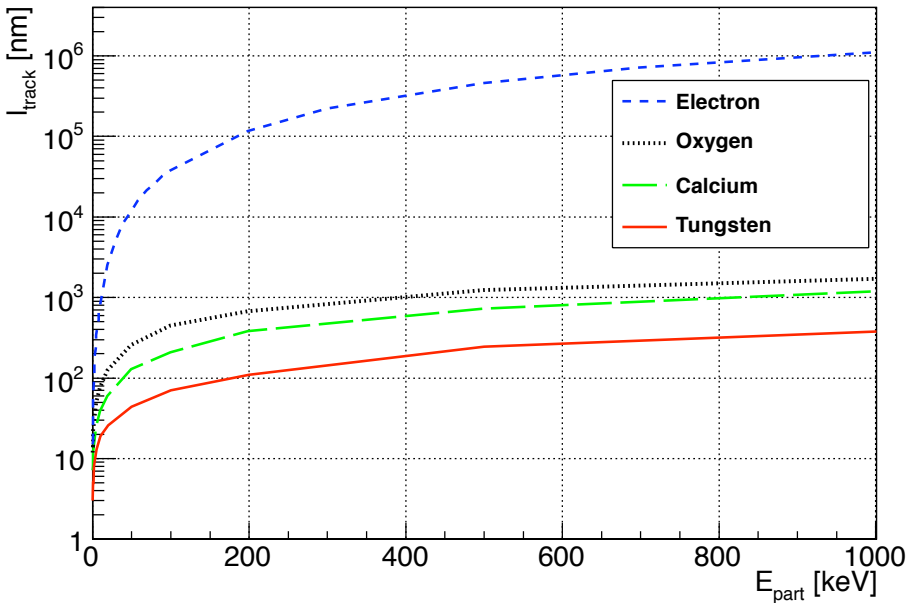

Figure 3.2: Mean track lengths for different primary interacting particles in $CaWO_4$: Electrons (dashed, blue line), O (dotted, black line), Ca (dashed, green line), and W (solid, red line) ions (semi-logarithmic scale). These track lengths were calculated from the data delivered by the SRIM program for ions and the CASINO program for electrons (for details on the simulations, see appendix B.3.2).

However, it has to be noticed that not only the length of the track of the primary particle differs for different particles of the same energy, but that also the total volume of energy deposition, e.g., the radial extent, as well as the spatial distribution of the created STEs within this volume are different. When comparing the various energy-deposition processes as described in section III/3.1.1 for different interacting particles, it is evident that the volume of energy deposition and the position-dependent density of the produced STEs have to differ for different particles. In the following, a brief, qualitative discussion of the differences in size and density of the excited volumes for electrons and nuclear recoils is given.

Basic Considerations Concerning Initially Generated Ionization Densities for Different Interacting Particles:

In order to allow for a description of the ionization distribution initially created by different interacting particles, the following basic observations regarding the energy-loss processes of these particles are capitalized:

- Electrons, photons, γ-particles or other kind of ionizing radiation:
  - It is assumed, as discussed in more detail in appendix B.1, that all of these particles deposit 100% of their energy in ionization. Hence, the energy-loss

process of all of these particles involves only the transfer of the energy of the primary particle onto electrons (and holes) of the target material.

- Thus, if the ionization distribution for electrons (and holes) with energies less than the energy of the primary particle as well as the position, energy and number of electrons (and holes) produced by the primary particle are known, then the ionization distribution produced by the primary particle can be deduced.
- It should be noted that the energy-loss process of a hole is, in principle, assumed to be the same as the one of an electron with the same energy (compare appendix B.1).

- Heavy, possibly charged, interacting particles such as ions[12] or neutrons:
  - As discussed in appendix B.1, the interaction of neutrons with the crystal lattice is expected to be described by the production of a nuclear recoil in the crystal lattice, i.e., by the production of a O, Ca or W ion. The produced nuclear recoil (O, Ca or W ion) undergoes the energy-loss process as described for all other heavy, charged particles.
  - For other primary heavy, charged particles (including O, Ca and W ions), a cascade of recoiling electrons (directly created ionization) and nuclear recoils of the crystal lattice (O, Ca and W recoil ions) are produced in the energy-loss process of the primary particle with energy E_{part} (compare appendix B.1).
  - Hence, the determination of the ionization distribution for a heavy, charged primary particle of energy E_{part} can be divided into two parts: The determination of the ionization created directly by the primary interacting particle (or by the primarily created nuclear recoil for neutrons) and the determination of the ionization created by the potentially produced recoil ions, i.e., O, Ca and W ions with energies $\leq E_{part}$.
  - Thus, if the ionization distribution produced directly by the primary particle and the ionization distribution for O, Ca and W ions with energies less than the energy of the primary particle, E_{part}, as well as the position, energy and number of these nuclear recoils are known, then the total ionization distribution produced in the energy-loss process of the primary particle can be deduced.
  - Of course, the respectively created ionization densities by the primary particle and by its recoil ions can exhibit an overlap in space. These overlap regions are taken into account within the model as discussed below.

Hence, the ionization density produced by an arbitrary interacting particle can be attributed to the ionization densities produced by recoil particles of the $CaWO_4$ lattice, i.e., by electrons, O, Ca and W ions, except for the ionization produced directly by an interacting heavy, charged particle. Therefore, in the following, the initially created ionization-density distribution for all possible recoil particles in $CaWO_4$ as primary interacting particles is discussed. The determination of the resulting ionization-density distribution for

[12] Within the model developed here, the phrase "ion" is also used for initially neutral interacting atoms as no major difference in the energy-loss processes of atoms and ions of the same species and type are expected due to the large ionization potential of a solid material such as $CaWO_4$. Already after the first few collisions of the particle with the electrons and nuclei of the target material, the primary particle is expected to carry an effective, energy-dependent charge state, independent of its original charge state (see, e.g., [87]).

different primary interacting particles on the basis of this information is presented in appendices B.3.6 and B.3.7.

Qualitative Discussion of the Initially Generated Ionization Densities for Electrons:

Electrons are expected to excite secondary electrons into the conduction band in individual collisions with electrons of the target material. The energy distribution of the produced electrons follows a Landau distribution (see, e.g., [88] as well as figure 3.4), i.e., the majority of these electrons possesses very small energies whereas a small number of the created electrons is high-energetic. Electrons with energies less than the ionization threshold energy, $E_{i-th} = 11.75\text{eV}$ (compare section III/3.1.1), cannot produce any further ionization whereas electrons with higher energies[13] can create further ionization, i.e., excite further electrons into the conduction band which lose and distribute their energy in an analogous way as the primary electron. Of course, when producing such high-energetic secondary electrons, an overlap of the low-energetic electrons created by the primary electron and created by secondary high-energetic electrons can exist, leading to an enhanced ionization density at the respective position along the primary electron track. A graphical representation of this description can be found in figure 3.3.

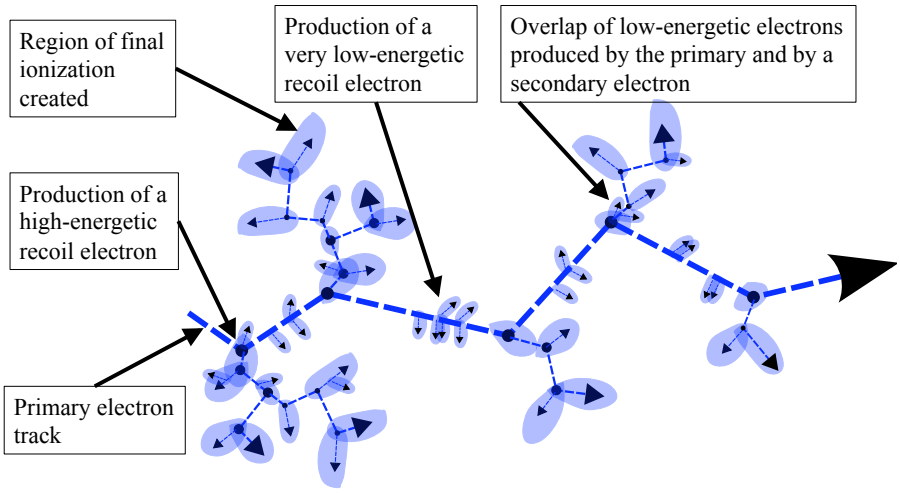

Figure 3.3: Graphical illustration of the ionization-density distribution created by an electron as the primary interacting particle in $CaWO_4$: The thick, dashed, blue line corresponds to the track of the primary electron. The black dots along its track mark positions where high-energetic electrons are created that possess enough energy to create further ionization. The filled, blue areas correspond to the regions where electrons and/or holes with energies less than the ionization threshold are created, i.e., particles that cannot create any further ionization. Thus, these regions correspond to the final distribution of the created ionization.

As is depicted in figure 3.3, it is expected that an electron deposits its energy quite homogeneously distributed over a relatively *large volume* (combination of the areas filled in blue in figure 3.3) through individual collisions with electrons of the target material.

[13] Typically, secondary electrons with energies up to a few 100eV are created along the track of the primary electron. However, also collisions with an energy transfer up to the complete energy of the primary electron are possible.

Qualitative Discussion of the Initially Generated Ionization Densities for Nuclear Recoils:

In contrast, for nuclear recoils (O, Ca and W ions), compact cascades of displacement atoms/ions [42], directly produced phonons, nuclear recoils and continuously produced ionization along relatively *short tracks* are created. Therefore, the volume where ionization is produced can be divided into several parts: The volume excited directly by the primary particle and the individual regions excited by the produced nuclear recoils. These regions are considered as being separated from each other, except for a very small overlap region where the track of the produced nuclear recoil starts. In this region, the ionization created by the primary particle and by the recoiling atoms overlap. The energy distribution of the electrons produced directly by the primary particle can be expected to follow a Landau distribution (see, e.g., [88]), i.e. the majority of the created electrons are low-energetic electrons (which cannot be regarded as starting their own separate energy-deposition tracks) while only a few high-energetic electrons are produced. In figure 3.4, a qualitative, graphical representation of the expected energy distribution of the created electrons is presented. The dashed, blue rectangles indicate the assumed division into low-energetic and high-energetic electrons.

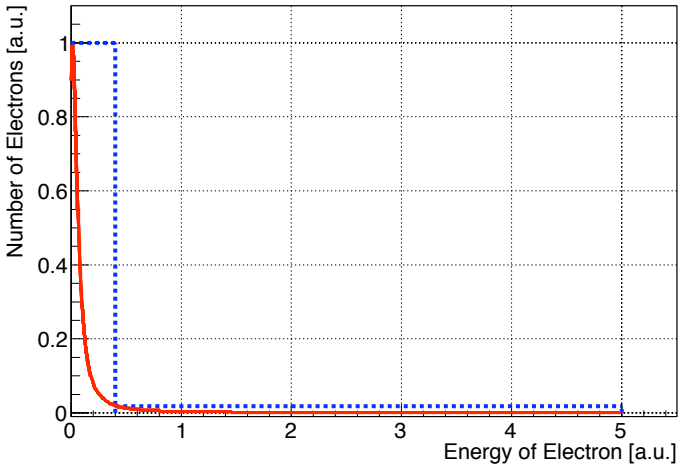

Figure 3.4: Qualitative, graphical representation of the number of electrons created in the energy-loss process of a particle in dependency of their energy: This dependency is assumed to be describable by a Landau distribution (solid, red line). For visualization of the assumed division of the electrons into low-energetic and high-energetic electrons, dashed, blue rectangles are indicated.

Within the model developed, the following qualitative description of the energy deposition by these electrons around the track of the interacting particle is used (compare "core and penumbra" model in [89]): The large number of low-energetic electrons deposit their energy close to the track of the interacting particle within a small, cylindrical inner volume, the "core" volume. The high-energetic electrons potentially escape this inner volume, dependent on the direction of their movement[14] and deposit at least a fraction of their energy within a separate, outer volume[15] (each high-energetic electron in a separate

[14]The direction of the movement of the electrons has to be regarded relative to the track direction of the interacting particle (from perpendicular to nearly parallel to the track of the interacting particle).

[15]The high-energetic electrons that escape the inner volume can, of course, also deposit part of their energy within the inner volume.

volume outside of the inner volume). These high-energetic electron tracks outside the inner volume correspond to separated, thinly ionized volumes extending far beyond the thin inner cylinder. The sum of all these thinly ionized, outer volumes corresponds to the "penumbra" volume in [89]. A graphical representation of this description can be found in figure 3.5. As can be seen from figure 3.5, it is expected that heavy, charged particles,

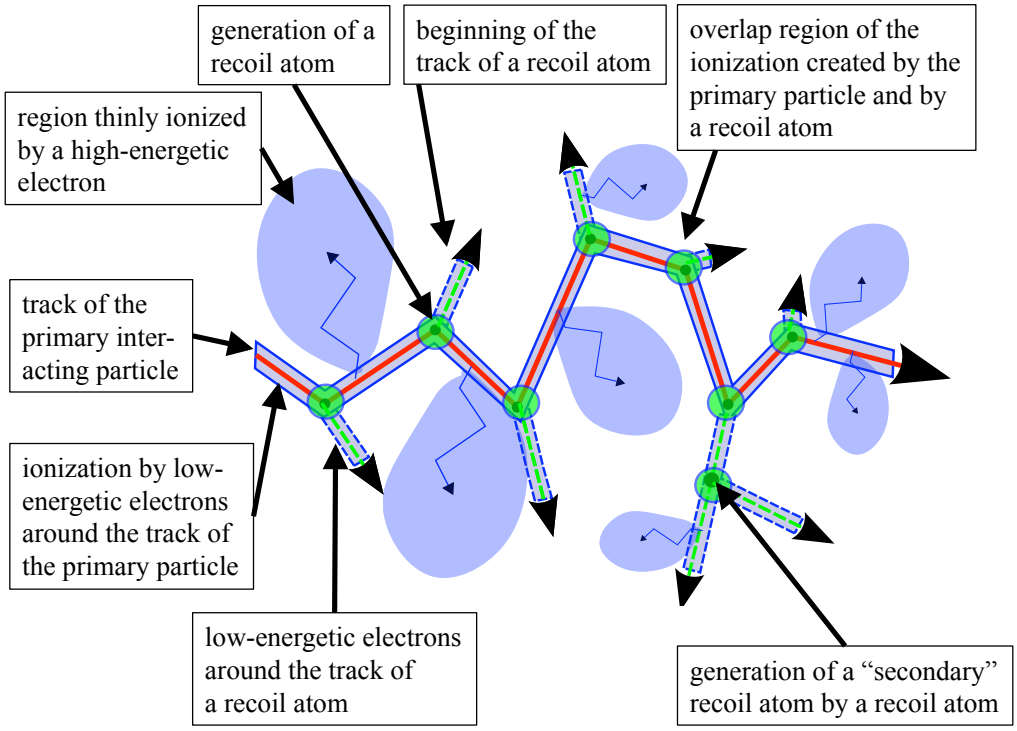

Figure 3.5: Graphical illustration of the ionization-density distribution created by a heavy, charged primary interacting particle in $CaWO_4$: The solid, red line corresponds to the track of the primary particle. The dots along its track mark positions where recoil atoms are created. The filled, blue region directly around the track of the primary interacting particle (and around the tracks of its recoil atoms) corresponds to the "core" region, i.e., the region where the low-energetic electrons (ionization) are located that are continuously produced by the primary interacting particle. Additionally indicated are a few high-energetic electrons that escape this dense "core" region leading to individual, comparably large regions that are thinly ionized. The circular regions filled in green at the positions of the production of recoil atoms indicate the "overlap" region of the ionization produced directly by the primary particle and the ionization produced directly by the recoil atom.

such as nuclear recoils, deposit their energy distributed within a relatively small volume (compared to an electron of the same energy) which is divided into several sub-volumes: Some with very high (core volumes) and others with low ionization densities (penumbra volumes).

Relationship between Ionization Density Produced and Energy Deposited by an Interacting Particle:

Within the model developed, the different extents of the excited volumes and the produced excitation densities are quantified by the position-dependent parameter $\rho_{ioniz}(E_{part}, \mathbf{x})$

which is the produced ionization density at the position $\mathbf{x} = (x, y, z)^T$ (in $\frac{eV}{nm^3}$, where the superscript T indicates that the vector is transposed) within the volume $V_{ex}(E_{part})$ excited in the energy-loss process of the particle *part* depositing the energy E_{part}. The following relationship between $\rho_{ioniz}(E_{part}, \mathbf{x})$ and the amount of energy deposited in ionization, $E_{part} \cdot F_{ioniz}(E_{part})$, holds:

$$E_{part} \cdot F_{ioniz}(E_{part}) = \int\limits_{V_{ex}(E_{part})} \rho_{ioniz}(E_{part}, \mathbf{x})\, d\mathbf{x} \tag{3.12}$$

Hence, in order to describe the ionization produced by one primary interacting particle, the density of energy deposited in ionization has to be known for each point in the target material that is excited in the process of energy loss of the primary particle and of the created secondary (recoil) particles.

Outline of the Developed Approach to Determine the Ionization Density:

The approach developed within this work to determine the spatial distribution of the ionization, $\rho_{ioniz}(E_{part}, \mathbf{x})$, and, hence, the produced STE-density distribution generated by an interacting particle in $CaWO_4$, $n_{bSTE}^{form\,0}(E_{part}, \mathbf{x})$, can be divided into three parts:

1. The first step is the development of a physical and mathematical model for the distribution of the ionization generated along the track of a primary particle as well as along the tracks of its recoil particles. This model describes the extent and geometrical distribution of the ionization generated.

2. The second part involves performing and analyzing simulations with the programs SRIM [42] and CASINO [43]. These simulations deliver information on the amount of energy deposited in ionization directly by the primary interacting particle (along its track) and on the production of recoil particles (position of production, type and energy of the recoil particle) along the track of the primary particle.

3. The third step corresponds to the determination of the energy- and particle-dependency of the radial extent of the excited volumes around the tracks of the primary interacting particle as well as of its recoil particles as this information is not delivered by the performed simulations.

Combining this information, a mathematical description of the initially produced ionization density and of the extent of the excited volume where this density is distributed is achieved for different interacting particles. To convert the ionization distribution determined in this way, $\rho_{ioniz}(E_{part}, \mathbf{x})$, as well as the amount of energy deposited in ionization $E_{part} \cdot F_{ioniz}(E_{part})$ into the density distribution $n_{bSTE}^{form\,0}(E_{part}, \mathbf{x})$ and the number, $N_{bSTE}^{0}(E_{part})$, of the initially produced blue STEs, the following relationships have to be used (compare equations 3.1 and 3.11):

$$N_{bSTE}^{0}(E_{part}) = \frac{(1 - F_{e^- trap})}{2.35 \cdot E_{gap}} \cdot E_{part} \cdot F_{ioniz}(E_{part}) \tag{3.13}$$

$$n_{bSTE}^{form\,0}(E_{part}, \mathbf{x}) = \frac{(1 - F_{e^- trap})}{2.35 \cdot E_{gap}} \cdot E_{part} \cdot \rho_{ioniz}(E_{part}, \mathbf{x}) \tag{3.14}$$

where the denominator, $2.35 \cdot E_{gap} = 2.35 \cdot 5.0\text{eV}$, corresponds to the mean energy needed to excite one electron into the conduction band in $CaWO_4$ and the numerator, $1 - F_{e^- trap}$,

indicates that the fraction F_{e^-trap} of the produced electrons gets captured by electron traps and, hence, cannot create STEs. As can be seen from equation 3.14, the produced STE density is directly proportional to the generated ionization density. Therefore, in the following description of the determination of the ionization density, the expressions $\rho_{ioniz}(E_{part}, \mathbf{x})$ and $n_{bSTE}^{form\,0}(E_{part}, \mathbf{x})$ are used synonymously.

It should be noted that the description and modeling of the STE density produced by an interacting particle was carried out with the goal to fulfill the following three requirements:

- The developed description should express the *typical* STE-density distribution created by a particle, i.e. it should allow to average over a large number of simulated energy-loss processes for such a particle to calculate the corresponding mean STE-density distribution.
- The developed description should be expressible in a simple mathematical formulation to allow the utilization of the described spatial distribution of the initially created STEs within the model for the light generation in $CaWO_4$ (section III/3.2.4)[16].
- As will be discussed in section III/3.3.2, to determine the free model parameters and to validate the complete model, experiments using ion-beam excitation of a $CaWO_4$ crystal were performed. For the analysis of these experiments in the context of the model, the initially created STE density has to be known for the employed ions. The ions used in the experiments were Oxygen and Iodine ions with an energy of roughly 35MeV. Hence, in order to enable the determination of the STE density initially created by these two ions, the STE density for the possible recoil ions (O, Ca and W ions) with energies up to $\sim$ 35MeV have to be determined. Therefore, the method to determine the STE density for recoiling particles was applied to recoil atoms with energies up to 35MeV. The maximum energy used was 50MeV.

In the following, first the underlying concept of determining the ionization distribution generated by interacting particles in $CaWO_4$ is introduced. Then, the geometrical model used to describe the geometrical distribution of the STE density generated by an interacting particle is introduced. Thereafter, a short overview of the data delivered by the simulations as well as of the method developed to determine as many of the parameters of the geometrical model as possible from the data delivered by the simulations (details on the simulations and developed methods can be found in appendix B.3).

Basic Concept for the Determination of the Particle-Induced Ionization Distribution:

The goal is to obtain a mathematical description of the spatial distribution of the ionization generated by a primary interacting particle within an energy region including the recoil energies interesting for the direct dark matter search (energy deposits of only a few keV, see section III/2.2) up to $\sim$ 50MeV (energies of the ions used in the experiments to determine the model parameters and validate the model, see chapter III/4). The basic idea capitalized is the self-similarity of the energy-loss process of a higher-energetic primary

[16] In section III/3.2.4, it will become clear that a simple mathematical description of the STE density enables an analytical formulation of the decay-time spectrum of the produced photons. This was regarded as desirable as the resulting formulas will be used to fit experimentally acquired light-pulse shapes (see chapter III/5).

particle with energy E_{part}: If the ionization density produced directly by the primary particle as well as by all possible recoil particles with energies $E_{rec} \lesssim E_{part}$ is known, then the total ionization density produced in the complete energy-loss process of the higher-energetic primary particle can be determined. Hence, the idea was to built up a database in a bottom-up approach containing the information on the ionization densities created for recoil particles within an energy region starting from an energy of 20eV (at such small energies, the probability to produce further recoil particles is very small, compare to E_{i-th} and E_{disp} defined in section III/3.1.1) up to the largest energy regarded, i.e., $\sim$ 50MeV. In order to cover the complete energy range, simulations and calculations at certain supporting points (energies of the recoil particles) were performed. A mathematical description of the produced ionization density was determined such that this description can be interpolated for energies between the supporting points. In this way, the calculation of the ionization distribution for all energies considered was enabled.

Geometrical Model for the Spatial Distribution of the Initially Created Blue STE Population:

In the following, the geometrical model as well as its interpretation developed to determine the ionization density with the help of the data delivered by the simulations is presented. For the description of the produced ionization, a cylindrical coordinate system around the track of the primary interacting particle is introduced with the coordinates $\mathbf{x} := (\rho, \varphi, z)^T$ (relative to the track of the regarded particle, T indicates the transposition of the vector). Hence, in the following, the z-direction corresponds to the coordinate along the summed-up track of the respectively regarded particle and *not* to one of the cartesian coordinates of the crystal. In analogy, the coordinates ρ and φ are defined as relative to the track direction. This assignment implies that the starting point of the track of a particle at $z = 0$nm can be located at any position $\mathbf{x}_0 := (x, y, z)^T$ within the crystal volume and does *not* indicate that the track of a particle starts, e.g., at the surface of the crystal volume. Within the developed model, the ionization density $\rho_{ioniz}(E_{part}, \mathbf{x})$ and, hence, the STE density $n_{bSTE}^{form\,0}(E_{part}, \mathbf{x})$ generated in the energy-deposition process of an interacting particle is described using a combination of two different mathematical models. Depending on the type and energy of the interacting primary particle, either just one of these two models or a combination of both of these models (for different sub-volumes of the complete excited volume) are used. In the following, these two models are introduced for the example of a heavy, charged particle (such as nuclear recoil, i.e., O, Ca or W ion) as primary interacting particle. The model used for electrons can be found in appendix B.3.1.

The two models introduced are labeled *PIT* (*P*rimary *I*onization *T*rack) and *Rec* (*Rec*oil) and describe the ionization produced along and around the track of the primary interacting particle and along and around the tracks of its recoil ions, respectively. Both of the developed models are based on the description of the energy-distribution of the created electrons as depicted in figure 3.4: A particle (primary particle or recoil atom generated by the primary particle) produces ionization in the form of a few high- and a large number of low-energetic electrons along its track. Therefore, the volume and the distribution of the ionization created along and around the track of a heavy, charged particle can be divided into two parts:

- The fraction of ionization deposited in the form of low-energetic electrons, $F^{in}(E_{part})$, is expected to be deposited within an inner, cylindrical volume directly around the

track of the interacting particle (compare figure 3.5). Of course, also high-energetic electrons that escape the inner volume can produce ionization there. This ionization is also included in the fraction $F^{in}(E_{part})$. A comparably small radius $r^{in}(E_{part})$ (of the order of 0.2 to 0.5nm) is assigned to this inner cylinder reflecting that the low-energetic electrons have only very short ranges, i.e., very small penetration depths $d_{max}(E_{part})$ (compare to the discussion in appendix B.3.10). Therefore, the density of the ionization generated within the inner volume is expected to be high.

- The fraction of ionization $F^{out}(E_{part}) = 1 - F^{in}(E_{part})$ created by the few high-energetic electrons generated that escape the inner dense volume of energy deposition is assumed to be distributed over several thinly ionized large volumes around the track of the interacting particle (compare figure 3.5). To describe the extent of this excited volume in a simple mathematical approach, it is assumed that these individual, thinly ionized volumes can be represented by one united, thinly ionized volume centered around the inner (densely ionized) volume. Thus, within the developed model, the volume excited by the few high-energetic electrons (in their energy-deposition process outside the inner volume) is described as a hollow cylinder around the inner volume. This outer volume, a hollow cylinder, contains the fraction $F^{out}(E_{part}) = 1 - F^{in}(E_{part})$ and stretches from $r^{in}(E_{part})$ to a comparably large radius $r^{out}(E_{part})$ (of the order of 1 to 10nm) reflecting the thin distribution of the ionization by individual electrons as well as the comparably large ranges of high-energetic electrons. Therefore, the density of the ionization generated in the outer volume is expected to be small.

Hence, within both geometrical models which are introduced in the following, the excited volume (where ionization is produced) around the track of an interacting particle (primary particle or one of its recoils) is assumed to be composed of two cylindrical volumes with different ionization densities (compare, e.g., the "core and penumbra" model in [89]): A thin core region directly around the track with a high ionization density (due to the large number of low-energetic electrons) and a large volume around this central (core) cylinder with a much lower ionization density (due to the small number of high-energetic electrons that can escape the central high-density volume).

Model "PIT":

The model "*PIT*" describes the distribution of energy deposited in ionization in a cylinder (divided into an inner and an outer volume) around the track of the primary interacting particle, called the *P*rimary *I*onization *T*rack, *PIT*. This volume contains *all ionization generated directly by the primary particle as well as the ionization generated by recoil particles within an "overlap region", corresponding to the first 1nm of their track*[17]. Within

[17]It should be noted that this description has to be regarded as self-similar description, i.e., consider the recoil atom which is produced by the primary particle as primary particle itself, then "secondary" recoils produced by this "primary" recoil induce overlap regions with the "primary" recoil track. If such an overlap occurs within the first nm of the "primary" recoil track, then this ionization also overlaps with the *PIT* of the real primary particle. Apart from this potential overlap region within the first nm of the "primary" recoil track between the "secondary" recoil tracks and the *PIT* no other overlap possibility is assumed. This assumption is applied as the probability for such an overlap to occur can be expected to be small. Due to the three-dimensional degree of freedom for the direction of the particle tracks in the crystal, the probability that the track of the "secondary" recoil atom (produced along the track of the "primary" recoil atom) leads back to volume of the *PIT* is very small.

the *PIT* model included is the variation of the produced ionization density in the direction of the track of the primary interacting particle: Such a variation reflects the energy-dependency of the electronic stopping-power of a heavy, charged particle, i.e., the efficiency of producing ionization which strongly depends on the energy of the interacting particle and, hence, on the position z along its track (compare, e.g., table 3.2). As will be shown when discussing the results of the simulations, this variation can be expressed by an exponential dependency of the ionization density on the coordinate z along the track. Hence, mathematically, this variation of the ionization density in z-direction can be described by an exponential function with decay constant $\alpha_{PIT}(E_{part})$ $\left[\frac{1}{\text{nm}}\right]$ (the same for inner cylinder and outer hollow cylinder). Within the inner volume and the outer volume of the *PIT*, no variation of the generated ionization in ρ- and φ-direction is assumed. For a graphical representation of this model, see figure 3.6 below.

Model "Rec":

The model "*Rec*" describes the *distribution of the energy deposited in ionization in small cylindrical slices of* $\Delta l_{min} = 1nm$ *length along the track of a recoiling particle.* Therefore, this model as well as all corresponding parameters are labeled *"Rec"*. The division of the recoil tracks into these small volumes is required for the method developed within the present work to determine the typical ionization-density distribution created by all recoil particles of one primary interacting particle, i.e., to calculate the average of the ionization-density distributions created by all recoil particles for each of the simulated primary ions of one type and energy (for details, see below). Hence, the volume excited in the complete energy-loss process of a primary particle contains a large number of such small volumes described by the model *Rec*: The track of each individual of the several recoil atoms produced by one primary particle is divided into 1nm long slices along the respective recoil track (the same method is utilized for the tracks of "secondary" recoils produced by the "primary" recoil). In analogy to the *PIT* model, each of these small volumes described by the model *Rec* is divided into an inner cylinder and an outer hollow cylinder. It should be noticed that the first of these 1nm long slices corresponds to the "overlap region" with the ionization produced by the primary particle (for a graphical representation, see figure 3.6 below) and is, hence, not treated as an individual *Rec* volume as it is already included in the *PIT*. Within the model *Rec*, no dependency of the produced ionization (within the inner and outer volume, respectively) on any of the cylindrical coordinates $\mathbf{x} = (\rho, \varphi, z)^T$ is assumed: Within the inner volume of one of these 1nm long slices, the energy deposited in ionization is assumed to be distributed homogeneously and, within the outer volume of one of these 1nm long slices, the energy deposited in ionization is assumed to be distributed homogeneously, however, not with the same density. The inner and outer radii as well as the partitioning of the ionization into the inner and outer volumes of all of the *Rec* volumes produced in the energy-deposition process of one primary particle are assigned the same values. Hence, these geometrical parameters have to reflect the mean behavior of all of the recoil particles produced by one primary interacting particle. This method to model the ionization density produced by all of the recoil particles was chosen in order to simplify the determination as well as the mathematical description of the combined ionization-density distribution generated by all of the recoil particles.

In figure 3.6, a qualitative, graphical representation of the two models for the example of a heavy, charged particle as primary interacting particle is presented.

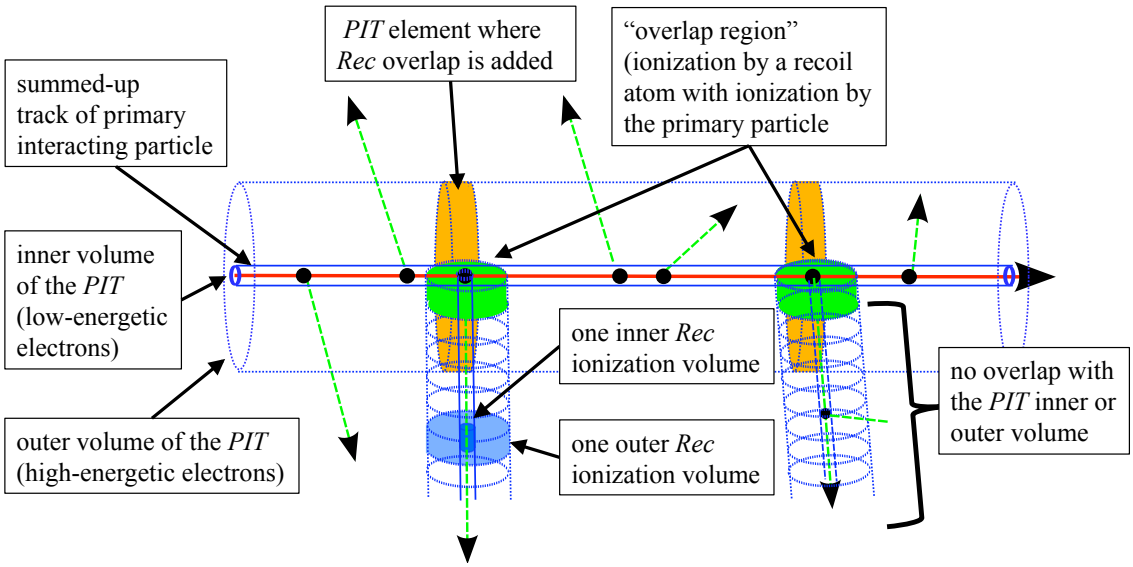

Figure 3.6: Qualitative, graphical representation of the two models *PIT* and *Rec* used to describe the distribution of the energy deposited in ionization by an interacting particle: The summed-up track of the primary interacting particle is shown as solid, red line. Inner and outer volume of the primary ionization track, *PIT*, are indicated by full blue and dotted blue cylindrical shapes around the track of the primary particle, respectively. Additionally, the ionization tracks caused by two of the recoiling atoms are shown. The described division of the volume excited by a recoil into 1nm long slices is displayed by the cylindrical slice (filled in blue, also sub-divided into an inner (dark blue) and an outer (lighter blue) cylindrical volume). The "overlap region" of the ionization produced by the recoil and by the primary particle, as defined in the developed model, is indicated as a horizontal, filled, green cylinder, respectively. The energy deposited within this first slice of the recoil track is added to the *PIT* at the position where the recoil was produced (indicated by the vertical cylinder filled in orange). Note that, as indicated, all other recoil volumes are assumed to exhibit no overlap with any other excited volume.

As can be seen from figure 3.6, this description of the process of generating ionization and distributing the generated ionization involves the division of the total excited volume $V_{ex}(E_{part})$ into several individual smaller sub-volumes: These are the *PIT* volume, i.e., the excited volume around the track of the primary interacting particle as well as many *Rec* volumes, i.e., the 1nm long slices of the excited volumes around the tracks of the various recoil atoms generated. Each of these sub-volumes is divided into an inner cylinder and an outer hollow cylinder. Hence, all of these sub-volumes combined constitute the complete excited volume where the sub-volumes are defined such that no overlap between them exists (compare figure 3.6).

Mathematical Description of the Spatial Distribution of the Initially Created Blue STE Population

In the following, the mathematical formulation of the two models is presented. As can be deduced from the description above, all of the parameters used to describe the extent of the different volumes, e.g., the radii, as well as the partitioning of the generated ionization between those volumes are dependent on the type and energy of the primary interacting particle. These dependencies reflect the different underlying energy-deposition

processes and ionization distributions generated by different interacting particles with different amounts of energy deposited. In order to improve the readability of the formulas, the dependency of the parameters on the energy and the type of the primary particle is not displayed explicitly in the formulas. However, it should be kept in mind that all of these parameters and, hence, also the numbers and densities of STEs created within the different volumes are, of course, dependent on the type and the energy of the primary interacting particle.

Model "PIT":

The parameters and volumes described by the model *PIT* can be summarized as presented in table 3.3.

parameter	meaning
$z = 0$ [nm]	starting point of the track of the primary interacting particle
$z = l_{track}(E_{part})$ [nm]	end point of the track of the primary interacting particle
$\alpha_{PIT}(E_{part})$ $\left[\frac{1}{\text{nm}}\right]$	decay constant describing the variation of the ionization density along the track (dependency on the z-coordinate)
$\rho = r^{in}_{PIT}(E_{part})$ [nm]	radius of the inner cylinder of the *PIT* and inner radius of the outer hollow cylinder of the *PIT*
$\rho = r^{out}_{PIT}(E_{part})$ [nm]	outer radius of the outer hollow cylinder of the *PIT*
$V_{PIT}(E_{part})$ [nm^3]	total volume of the *PIT*
$V^{in}_{PIT}(E_{part})$ [nm^3]	inner volume of the *PIT*
$V^{out}_{PIT}(E_{part})$ [nm^3]	outer volume of the *PIT*
$E_{ioniz,PIT}(E_{part})$ [eV]	total energy deposited in ionization within the *PIT* (by the primary particle and by recoil atoms in the "overlap region")
$F^{in}_{PIT}(E_{part})$	fraction of $E_{ioniz,PIT}(E_{part})$ deposited in $V^{in}_{PIT}(E_{part})$
$F^{out}_{PIT}(E_{part})$	fraction of $E_{ioniz,PIT}(E_{part})$ deposited in $V^{out}_{PIT}(E_{part})$
$E^{in}_{ioniz,PIT}(E_{part})$ [eV]	energy deposited in the inner volume of the *PIT*
$E^{out}_{ioniz,PIT}(E_{part})$ [eV]	energy deposited in the outer volume of the *PIT*
$N_{bSTE,PIT}(E_{part})$	total number of blue STEs initially created in the *PIT*
$N^{in}_{bSTE,PIT}(E_{part})$	number of blue STEs initially created in $V^{in}_{PIT}(E_{part})$
$N^{out}_{bSTE,PIT}(E_{part})$	number of blue STEs initially created in $V^{out}_{PIT}(E_{part})$

Table 3.3: Parameters used to describe the distribution of the energy deposited in ionization and the distribution of the initially created blue STE population within the primary ionization track *PIT*.

For the description of the division of the total energy, $E_{ioniz,PIT}(E_{part})$ (deposited in ionization in the *PIT* volume), between the inner and outer *PIT* volumes, the following

relationships can be used:

$$F_{PIT}^{in} + F_{PIT}^{out} = 1 \tag{3.15}$$

$$E_{ioniz,PIT}^{in} = E_{ioniz,PIT} \cdot F_{PIT}^{in} \tag{3.16}$$

$$E_{ioniz,PIT}^{out} = E_{ioniz,PIT} \cdot F_{PIT}^{out} = E_{ioniz,PIT} \cdot (1 - F_{PIT}^{in}) \tag{3.17}$$

Using equation 3.13, the initial numbers of blue STEs created in the inner and in the outer volume of the PIT, respectively, can be expressed by:

$$N_{bSTE,PIT}^{in} = \frac{(1 - F_{e^-trap})}{2.35 \cdot E_{gap}} \cdot E_{ioniz,PIT}^{in} \tag{3.18}$$

$$N_{bSTE,PIT}^{out} = \frac{(1 - F_{e^-trap})}{2.35 \cdot E_{gap}} \cdot E_{ioniz,PIT}^{out} \tag{3.19}$$

$$\Rightarrow N_{bSTE,PIT} = N_{bSTE,PIT}^{in} + N_{bSTE,PIT}^{out} = \frac{(1 - F_{e^-trap})}{2.35 \cdot E_{gap}} \cdot E_{ioniz,PIT} \tag{3.20}$$

The volumes (inner cylinder and outer hollow cylinder) in which the distribution of the initially produced blue STE populations is described by the model PIT are defined by:

$$V_{PIT}^{in} := \left\{ \mathbf{x} = \begin{pmatrix} \rho \\ \varphi \\ z \end{pmatrix} \in \mathbb{R}^3; \begin{pmatrix} \rho \\ \varphi \\ z \end{pmatrix} \in [0, r_{PIT}^{in}] \times [0, 2\pi] \times [0, l_{track}] \right\} \tag{3.21}$$

$$V_{PIT}^{out} := \left\{ \mathbf{x} = \begin{pmatrix} \rho \\ \varphi \\ z \end{pmatrix} \in \mathbb{R}^3; \begin{pmatrix} \rho \\ \varphi \\ z \end{pmatrix} \in [r_{PIT}^{in}, r_{PIT}^{out}] \times [0, 2\pi] \times [0, l_{track}] \right\} \tag{3.22}$$

$$V_{PIT} = V_{PIT}^{in} + V_{PIT}^{out} \tag{3.23}$$

Hence, the density of blue STEs produced in the inner volume of the PIT, $V_{PIT}^{in}(E_{part})$, which is assumed to depend only on the z-coordinate within the volume (variation along the track), can be expressed by:

$$\begin{aligned} n_{bSTE}^{form\,0}(z)\Big|_{\mathbf{x}\in V_{PIT}^{in}} &:= n_{bSTE}^{form\,0}(\mathbf{x})\Big|_{\mathbf{x}\in V_{PIT}^{in}} = \\ &= N_{bSTE,PIT}^{in} \cdot \frac{1}{(r_{PIT}^{in})^2 \cdot \pi} \cdot \frac{\alpha_{PIT}}{(1 - e^{-\alpha_{PIT} \cdot l_{track}})} \cdot e^{-\alpha_{PIT} \cdot z} \\ N_{bSTE,PIT}^{in} &= \int\limits_{V_{PIT}^{in}} n_{bSTE}^{form\,0}(\mathbf{x})\ \rho\ d\rho d\varphi dz \end{aligned}$$

Using the definition of a position-independent density of blue STEs in the inner volume of the PIT, $n_{bSTE,in,PIT}^{form\,0}$, this expression can be simplified:

$$n_{bSTE,in,PIT}^{form\,0} := N_{bSTE,PIT}^{in} \cdot \frac{1}{(r_{PIT}^{in})^2 \cdot \pi} \cdot \frac{\alpha_{PIT}}{(1 - e^{-\alpha_{PIT} \cdot l_{track}})} \tag{3.24}$$

$$n_{bSTE}^{form\,0}(z)\Big|_{\mathbf{x}\in V_{PIT}^{in}} = n_{bSTE,in,PIT}^{form\,0} \cdot e^{-\alpha_{PIT} \cdot z} \tag{3.25}$$

In analogy, the blue STE density $n^{form\,0}_{bSTE,out,PIT}$ within the outer volume of the *PIT*, $V^{out}_{PIT}(E_{part})$, can be expressed with a position-independent density of blue STEs:

$$n^{form\,0}_{bSTE,out,PIT} := N^{out}_{bSTE,PIT} \cdot \frac{1}{((r^{out}_{PIT})^2 - (r^{in}_{PIT})^2) \cdot \pi} \cdot \frac{\alpha_{PIT}}{(1 - e^{-\alpha_{PIT} \cdot l_{track}})} \tag{3.26}$$

$$n^{form\,0}_{bSTE}(z)\Big|_{\mathbf{x} \in V^{out}_{PIT}} := n^{form\,0}_{bSTE}(\mathbf{x})\Big|_{\mathbf{x} \in V^{out}_{PIT}} = n^{form\,0}_{bSTE,out,PIT} \cdot e^{-\alpha_{PIT} \cdot z} \tag{3.27}$$

$$N^{out}_{bSTE,PIT} = \int\limits_{V^{out}_{PIT}} n^{form\,0}_{bSTE}(\mathbf{x})\ \rho\ d\rho d\varphi dz$$

Model "Rec":

As discussed above, within the model *Rec*, the distribution of the ionization generated by recoil atoms within 1nm long slices along their ionization tracks is described (except for the first nm which is incorporated in the *PIT* model). Hence, one of the described volumes stretches from the position $z = z^0_{Rec}$ to $z = z^0_{Rec} + 1$nm along the recoil track. As indicated above, for each of these slices (for all recoils of one primary particle), the same radii and partitioning of the ionization between the inner and the outer volume, as well as a homogeneous distribution of the ionization within each of the cylindrical volumes are assumed. Thus, *no dependency of the geometrical distribution of the generated ionization on the position z^0_{Rec} along the recoil track* remains. Hence, within the total volume excited by one primary particle always the same radii and partitioning of the ionization in *Rec* volumes are used, regardless from which recoil track and from which position within this recoil track such a 1nm slice is cut. Therefore, the z-coordinates of these volumes can be transformed:

$$z \in [z^0_{Rec}, z^0_{Rec} + 1] \rightarrow z \in [0, 1] \qquad \text{[nm]}$$

The only difference between these volumes remaining is the different amount of energy deposited in each of these volumes, i.e., the correspondingly different number of blue STEs contained within these volumes. It should be noted that, in this way, still the variation of the ionization density in the direction of the recoil track is included[18] (with a 1nm-binning of the z-coordinate of the recoil track). Therefore, in the following, all parameters differing for different slices of the recoil tracks (the amount of the energy deposited and, thus, the number and density of generated blue STEs) are labeled additionally with an integer number i attached to the label $Rec[i]$ to indicate the differences for different slices of recoil tracks.

With these considerations, the parameters and volumes of one slice of a recoil track, $Rec[i]$, described by the model *Rec* can be summarized as presented in table 3.4.

For the description of the partitioning of the total energy, $E_{ioniz,Rec[i]}(E_{part})$, deposited in ionization in one of the recoil volumes $V_{Rec}(E_{part})$ between the inner and outer volume,

[18] Compare to the model *PIT*: Here this variation of the density of the produced ionization and, hence, of the initially created density of blue STEs is included as a continuous variation described by an exponential function in z-direction.

parameter	meaning
$z \in [0,1]$ [nm]	dimension of one of the *Rec* volumes in z-direction, $Rec[i]$
$\rho = r^{in}_{Rec}(E_{part})$ [nm]	radius of the inner cylinder of the *Rec* volumes and inner radius of the outer hollow cylinder of the *Rec* volumes
$\rho = r^{out}_{Rec}(E_{part})$ [nm]	outer radius of the outer hollow cylinder of the *Rec* volumes
$V_{Rec}(E_{part})$ [nm^3]	total *Rec* volume (1nm slice of a recoil track)
$V^{in}_{Rec}(E_{part})$ [nm^3]	inner *Rec* volume (1nm slice of a recoil track)
$V^{out}_{Rec}(E_{part})$ [nm^3]	outer *Rec* volume (1nm slice of a recoil track)
$E_{ioniz,Rec[i]}(E_{part})$ [eV]	total energy deposited in ionization within the volume $Rec[i]$ (*by the recoil atom* and by its recoil atoms within their "overlap regions")
$F^{in}_{Rec}(E_{part})$	fraction of $E_{ioniz,Rec[i]}(E_{part})$ deposited in $V^{in}_{Rec}(E_{part})$
$F^{out}_{Rec}(E_{part})$	fraction of $E_{ioniz,Rec[i]}(E_{part})$ deposited in $V^{out}_{Rec}(E_{part})$
$E^{in}_{ioniz,Rec[i]}(E_{part})$ [eV]	energy deposited in the inner volume of $Rec[i]$
$E^{out}_{ioniz,Rec[i]}(E_{part})$ [eV]	energy deposited in the outer volume of $Rec[i]$
$N_{bSTE,Rec[i]}(E_{part})$	total number of blue STEs initially created in the volume $Rec[i]$
$N^{in}_{bSTE,Rec[i]}(E_{part})$	number of blue STEs initially created in $V^{in}_{Rec}(E_{part})$
$N^{out}_{bSTE,Rec[i]}(E_{part})$	number of blue STEs initially created in $V^{out}_{Rec}(E_{part})$

Table 3.4: Parameters of the model *Rec* used to describe the distribution of the energy deposited in ionization and the distribution of the initially created blue STE population within a 1nm long slice $Rec[i]$ of the track of one recoil atom of the primary interacting particle.

the following relationships can be used:

$$F^{in}_{Rec} + F^{out}_{Rec} = 1 \tag{3.28}$$

$$\Rightarrow E^{in}_{ioniz,Rec[i]} = E_{ioniz,Rec[i]} \cdot F^{in}_{Rec} \tag{3.29}$$

$$\Rightarrow E^{out}_{ioniz,Rec[i]} = E_{ioniz,Rec[i]} \cdot F^{out}_{Rec} = E_{ioniz,Rec[i]} \cdot (1 - F^{in}_{Rec}) \tag{3.30}$$

Using equation 3.13, the respective initial numbers of blue STEs created in the inner and outer volumes of the slice $Rec[i]$ of a recoil track can be expressed by:

$$N^{in}_{bSTE,Rec[i]} = \frac{(1 - F_{e^- trap})}{2.35 \cdot E_{gap}} \cdot E^{in}_{ioniz,Rec[i]} \tag{3.31}$$

$$N^{out}_{bSTE,Rec[i]} = \frac{(1 - F_{e^- trap})}{2.35 \cdot E_{gap}} \cdot E^{out}_{ioniz,Rec[i]} \tag{3.32}$$

$$\Rightarrow N_{bSTE,Rec[i]} = N^{in}_{bSTE,Rec[i]} + N^{out}_{bSTE,Rec[i]} = \frac{(1 - F_{e^- trap})}{2.35 \cdot E_{gap}} \cdot E_{ioniz,Rec[i]} \tag{3.33}$$

The volumes (inner cylinder and outer hollow cylinder) for which the model *Rec* describes

the distribution of the initially produced blue STE populations, are defined by:

$$V_{Rec}^{in} := \left\{ \mathbf{x} = \begin{pmatrix} \rho \\ \varphi \\ z \end{pmatrix} \in \mathbb{R}^3; \begin{pmatrix} \rho \\ \varphi \\ z \end{pmatrix} \in [0, r_{Rec}^{in}] \times [0, 2\pi] \times [0, 1] \right\} \tag{3.34}$$

$$V_{Rec}^{out} := \left\{ \mathbf{x} = \begin{pmatrix} \rho \\ \varphi \\ z \end{pmatrix} \in \mathbb{R}^3; \begin{pmatrix} \rho \\ \varphi \\ z \end{pmatrix} \in [r_{Rec}^{in}, r_{Rec}^{out}] \times [0, 2\pi] \times [0, 1] \right\} \tag{3.35}$$

$$V_{Rec} = V_{Rec}^{in} + V_{Rec}^{out} \tag{3.36}$$

From these expressions for the sub-volumes of the slice $Rec[i]$ of a recoil track, it can be seen that the geometrical parameters used are assumed to be the same for all slices of all recoil tracks generated by one primary interacting particle (no dependency on i).

Hence, the density of blue STEs produced in the inner volume of the slice $Rec[i]$, $V_{Rec}^{in}(E_{part})$ which is assumed to be independent of the position within the volume, is given by:

$$n_{bSTE,in,Rec[i]}^{form\,0} := n_{bSTE,i}^{form\,0}(\mathbf{x})\Big|_{\mathbf{x}\in V_{Rec}^{in}} = N_{bSTE,Rec[i]}^{in} \cdot \frac{1}{(r_{Rec}^{in})^2 \cdot \pi \cdot 1\text{nm}} \tag{3.37}$$

$$N_{bSTE,Rec[i]}^{in} = \int\limits_{V_{Rec}^{in}} n_{bSTE,i}^{form\,0}(\mathbf{x})\ \rho\ d\rho d\varphi dz$$

In analogy, the density of blue STEs produced in the outer volume of the slice $Rec[i]$, $V_{Rec}^{out}(E_{part})$, can be expressed by:

$$n_{bSTE,out,Rec[i]}^{form\,0} := n_{bSTE,i}^{form\,0}(\mathbf{x})\Big|_{\mathbf{x}\in V_{Rec}^{out}} = N_{bSTE,Rec[i]}^{out} \cdot \frac{1}{((r_{Rec}^{out})^2 - (r_{Rec}^{in})^2) \cdot \pi \cdot 1\text{nm}} \tag{3.38}$$

$$N_{bSTE,Rec[i]}^{out} = \int\limits_{V_{Rec}^{out}} n_{bSTE,i}^{form\,0}(\mathbf{x})\ \rho\ d\rho d\varphi dz$$

It can be recognized that the STE densities described by equations 3.37 and 3.38 do not contain any dependency on the position within the respective volumes besides the limitations of the volumes. This reflects the assumed homogeneous distribution of the ionization within the individual volumes. On the other hand, it can be seen that these densities can differ for different slices of recoil tracks ($Rec[i]$) if the number of blue STEs deposited in these slices, $N_{bSTE,Rec[i]}$, differs, i.e., if a different amount of energy, $E_{ioniz,Rec[i]}(E_{part})$, was initially deposited within these slices.

Parameters Required for the Description of the Initially Created STE density

From the mathematical formulation of the two models, the parameters required to describe the distribution of the STE density initially created by one interacting particle can be determined:

- The length of the track of the primary interacting particle: $l_{track}(E_{part})$.
- The number of STEs generated within the total PIT volume, i.e., the amount of energy deposited in ionization in the total PIT volume (compare equation 3.20): $E_{ioniz,PIT}(E_{part})$.

- The decay constant describing the variation of the ionization density along the track, i.e., within the inner and outer PIT volumes: $\alpha_{PIT}(E_{part})$.
- The partitioning of the ionization between inner and outer PIT volume: $F^{in}_{PIT}(E_{part})$.
- The inner and outer radii of the PIT volumes: $r^{in}_{PIT}(E_{part})$ and $r^{out}_{PIT}(E_{part})$.
- The number of STEs generated within each of the recoil volumes, i.e., the respective energy deposited within each of the Rec volumes (compare equation 3.33): $E_{ioniz,Rec[i]}(E_{part})$.
- The partitioning of the ionization between inner and outer Rec volumes: $F^{in}_{Rec}(E_{part})$.
- The inner and outer radii of the Rec volumes: $r^{in}_{Rec}(E_{part})$ and $r^{out}_{Rec}(E_{part})$.

Performed Simulations and Delivered Data:

In the following, an overview of the performed simulations as well as a short description of the analysis method developed for the data delivered by the simulations is presented. It should be noted that, due to the fact that no information on the energy of the electrons created in the energy-deposition process of a heavy, charged particle is given by the simulations, the radii as well as the partitioning of the ionization between inner and outer volumes of the PIT and the Rec volumes cannot be determined directly from the simulations[19]. A short introduction of the method used to obtain estimates for the values of these parameters is presented. Details on the simulations, their analysis as well as on the determination of the radial parameters can be found in appendices B.3.2 to B.3.10.

As already indicated, to determine the ionization densities produced by electrons and ions interacting in $CaWO_4$, two different programs were used:

- In order to simulate the energy-loss process of electrons interacting in $CaWO_4$, the program CASINO [43] was used.
- In order to simulate the energy-loss process of heavy, charged particles, such as nuclear recoils interacting in $CaWO_4$, the program SRIM [42] was used.

Employing these programs, simulations of the energy-loss processes of electrons, O, Ca and W ions at supporting points distributed over the complete energy range considered were performed. All of these simulations were, of course, performed using a large number of simulated events in order to obtain sufficient statistics and to allow averaging of the deduced results. For ions, 10000 particles each, with energies of 20eV, 50eV 100eV, 200eV, etc. up to 1MeV and 2000 particles each, with energies of 2MeV, 5MeV, etc. up to 50MeV were simulated. For electrons 10000 particles, each, with energies of 20eV, 40eV, 60eV, etc. up to 200eV, with energies of 300eV, 400eV, etc. up to 1keV, with energies of 2keV, 3keV, etc. up to 10keV, with energies of 20keV, 30keV, etc. up to 100keV and 1000 particles each, with energies of 200keV, 300keV, 500keV, 700keV and 1MeV were simulated. The information gained by these simulations can be used for two purposes: On the one hand, the data delivered by the simulations is used to built up a database containing the

[19] As discussed in appendix B.3.9, a similar problem exists for the radial parameters of the ionization distribution created by electrons. Thus, also for electrons as primary interacting particle, the values of the radial parameters have to be assessed independently of the performed simulations. The developed method is discussed in appendix B.3.9

information of the ionization density generated by the simulated particles for the case they are considered as recoil particles of another primary interacting particle. As the major fraction of recoil particles produced are low-energetic (for electrons, see, e.g., discussion before figure 3.4, for ions, see appendix B.3.10), the low-energy region was sampled with a higher accuracy whereas, for higher energies, a decreased coverage was used. On the other hand, of course, these simulations automatically deliver the information on the ionization density produced by the simulated particles for the case they are considered as primary interacting particle themselves.

Details on the programs, the chosen settings and the utilized output files can be found in appendix B.3.2. From the overview presented there, it can be seen that the following information was retrieved from the data delivered by the simulations:

- For each simulated particle, a list of positions where a recoil particle was produced (in cartesian coordinates within the crystal, $\mathbf{x} := (x, y, z)^T$). For ions, this is a list of nuclear recoils produced which contains the information about the position, type and energy of the produced nuclear recoils. For electrons, this is a list of "secondary" electrons produced which contains the information about the position and energy of the produced electrons.

- From this information for each simulated particle, the track of the primary particle as well as the total length of the track can be obtained (by summing up the distances between collisions where recoil ions/electrons are produced[20]). Averaging the total lengths of the tracks of all simulated particles (for one type and one energy), the mean length of the track $l_{track}(E_{part})$ of such a particle can be obtained.

- In analogy, the mean penetration depth $d_{max}(E_{part})$, into the initial direction of movement of the simulated primary particle can be obtained.

- For each simulated ion, additionally, the electronic stopping $S_{el}(x, y, z)$ (in $\frac{\text{eV}}{\text{nm}}$) for the primary interacting particle at each position along its track where a nuclear recoil is produced is given.

- For all simulated ions of one type and one energy, the mean total amount of ionization created by the primary particle alone and created by all of its recoil particles combined can be determined.

It should be noted that, for ions, no information on the energy of the produced electrons is given. In addition, it should be taken into account that, within the CASINO simulations of electrons as primary particles, only low-energetic electrons are produced, i.e., the production of high-energetic electrons with large energy transfer from the primary electron to a recoil electron is suppressed. Instead, the low-energetic electrons that would be created by such a high-energetic recoil electron are "directly produced" by the primary electron (compare, e.g., [90]).

Basic Concept of the Method Developed for the Analysis of the Simulations:

The concept for the analysis of the data delivered by the simulations is based on the

[20]The distance travelled by the primary particle after the last collision listed is also considered in the analysis of the simulations. For details, see appendix B.3.2.

self-similarity of the energy-loss process by the primary interacting particle and its recoil particles: Hence, the analysis of the simulations is performed iteratively, starting with the determination of the ionization-density distribution of the lowest-energetic particles. The information gained in this way on the ionization distribution generated by the regarded particle as recoil particle can then be used as input for the determination of the ionization-density distribution created by recoils of a higher-energetic particle. A detailed description of the complete method developed can be found in appendix B.3.4 for O, Ca and W ions as primary interacting particles. A graphical representation of this method is presented in appendix B.3.5. In appendices B.3.6 and B.3.7, the application of this method to heavy, charged particles as well as to electrons and γ-particles as primary interacting particles is explained.

Within the developed method, the resulting ionization distribution created by, e.g., a heavy, charged particle, as determined from the simulations, is represented in the following way: The complete ionization distribution is divided into the fraction deposited within the PIT volume and the fraction of ionization produced outside of the PIT volume by recoil particles. The ionization distribution within the PIT can then be characterized by an exponential function describing the dependency of the energy deposited in ionization within the PIT volume along the track of the primary interacting particle. The ionization distribution generated by recoil particles is described by a histogram containing the occurrences of energy depositions (in eV per nm) within each of the small Rec volumes excited. With such a description, the amount of energy deposited within the PIT volume ($E_{ioniz,PIT}(E_{part})$) and within each of the Rec ($E_{ioniz,Rec[i]}(E_{part})$) volumes is determined. Additionally, the information on the length of the primary particle track, $l_{track}(E_{part})$, and on the decay constant, $\alpha_{PIT}(E_{part})$, of the ionization-density along the track are delivered.

However, up to this point, no information on the radial distribution of the ionization densities is gained. As discussed in appendix B.3.8, the corresponding parameters, e.g., $r^{in}_{PIT}(E_{part})$, $r^{out}_{PIT}(E_{part})$ and $F^{in}_{PIT}(E_{part})$ for the PIT volume of a heavy, charged primary interacting particle, cannot be determined from the simulations. The method developed within the present work to, nonetheless, obtain estimates for these values for all of these parameters (for arbitrary heavy, charged particles and for electrons as primary interacting particles) is presented in detail in the appendices B.3.9 and B.3.10. This method can be divided into two steps: As a first step, a model for the energy- and particle-dependency of the radial parameters is presented (separately for heavy, charged particles and for electrons as primary interacting particles). Then, a concept to determine these parameters for one type and energy of a primary interacting particle in $CaWO_4$ (for one ion and for one electron with a defined energy each) is developed: For electrons, the information on the light yield of 100keV electrons at low temperatures is used to adjust the radial parameters for a 100keV electron as primary interacting particle (see also section III/6.1.1). For heavy, charged particles, the scintillation-light pulse-shape recorded for ^{127}I ions ($\sim$ 35MeV) within the present work (see chapter III/4 for a description of the experiments) can be used to adjust the radial parameters for I ions with $\sim$ 35MeV as primary interacting particles (see section III/5.3). Using the determined values of the radial parameters for the regarded primary interacting particles in combination with the assumed energy- and particle-dependencies, the values of these parameters can be determined for any heavy, charged particle and for electrons with an energy roughly between 1keV and several MeV.

Thus, using the described geometrical model in combination with the simulations, their analysis and the determination of the radial parameters, a complete description of the ionization-density distribution, $\rho_{ioniz}(E_{part}, \mathbf{x})$, generated by a primary interacting particle of type *part* with energy E_{part} in $CaWO_4$ is achieved. In the following discussion of the model for the light generation and quenching in $CaWO_4$, it is assumed that the ionization density $\rho_{ioniz}(E_{part}, \mathbf{x})$ produced by an energy deposition in the crystal can be determined with the described method and is, hence, a known parameter of the model.

Summary of Primary STE-Formation Processes

An overview of the processes discussed up to this point is shown in figure 3.7.

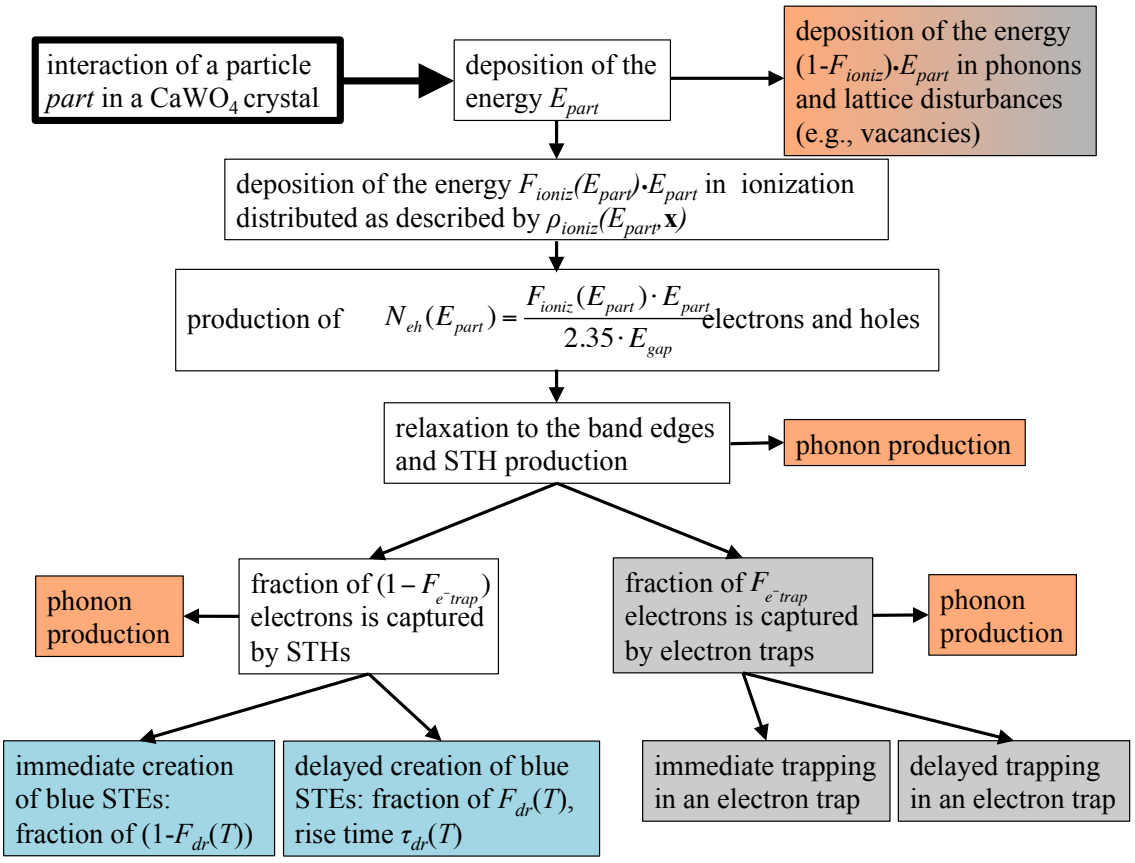

Figure 3.7: Overview over the processes of energy deposition that lead to the creation of blue STEs: Orange boxes indicate processes in which phonons are produced. Grey boxes correspond to processes in which energy is stored in the lattice in the form of lattice disturbances (vacancies, trapped electrons and single STHs). Blue boxes correspond to the production of blue STEs.

Within the model, it is assumed that, for a particle depositing the energy E_{part}, a fraction of $F_{ioniz}(E_{part})$ is converted into ionization which is distributed in the excited volume V_{ex} according to the ionization-density distribution $\rho_{ioniz}(E_{part}, \mathbf{x})$. This fraction of the deposited energy as well as its spatial distribution are determined with the help of the described geometrical model, the simulations and the analysis method developed. The integral of the ionization density $\rho_{ioniz}(E_{part}, \mathbf{x})$ over the excited volume V_{ex}, i.e., the

fraction of energy deposited into ionization, can be expressed as:

$$\int_{V_{ex}} \rho_{ioniz}(E_{part}, \mathbf{x}) d\mathbf{x} = F_{ioniz}(E_{part}) \cdot E_{part} \tag{3.39}$$

Due to the mean energy needed to create an electron-STH pair, the possible capture processes of electrons by electron traps (lost electrons) and the low density of defect (green) centers, it is assumed that initially a total number $N_{bSTE}^{form\, e^- STH}(E_{part})$ of purely blue STEs is produced. These STEs are distributed within the volume V_{ex} according to the position-dependent density $n_{bSTE}^{form\, e^- STH}(E_{part}, \mathbf{x})$. Using equations 3.1 and 3.10, the number and density of the initially created blue STEs are given by:

$$N_{bSTE}^{form\, e^- STH}(E_{part}) = (1 - F_{e^- trap}) \cdot N_{eh}(E_{part}) = (1 - F_{e^- trap}) \cdot \frac{F_{ioniz}(E_{part}) \cdot E_{part}}{11.75\text{eV}} \tag{3.40}$$

$$n_{bSTE}^{form\, e^- STH}(E_{part}, \mathbf{x}) = \frac{(1 - F_{e^- trap}) \cdot \rho_{ioniz}(E_{part}, \mathbf{x})}{2.35 \cdot E_{gap}} = \frac{(1 - F_{e^- trap}) \cdot \rho_{ioniz}(E_{part}, \mathbf{x})}{11.75\text{eV}} \tag{3.41}$$

The size of the fraction $F_{e^- trap}$ of electrons captured by electron traps depends on the density of defects in the respective $CaWO_4$ crystal and is assumed to be independent of temperature.

A fraction $F_{dr}(T)$ of these STEs is produced in a delayed recombination process. Using the simplified diffusion-controlled recombination model (see the discussion at the beginning of this section as well as appendix B.2), this delayed process can be described by an exponential rise time $\tau_{dr}(T)$. Hence, the time-dependent number $N_{bSTE}^{form\, e^- STH}(E_{part}, T, t)$ (which, if integrated, corresponds to the total number of produced blue STEs, $N_{bSTE}^{form\, e^- STH}(E_{part})$, see equation 3.40) and density $n_{bSTE}^{form\, e^- STH}(E_{part}, T, \mathbf{x}, t)$ of blue STEs created by the particle *part* depositing the energy E_{part} are given by:

$$\begin{aligned}
&\int_{-\infty}^{+\infty} N_{bSTE}^{form\, e^- STH}(E_{part}, T, t)\, dt = N_{bSTE}^{form\, e^- STH}(E_{part}) \\
&N_{bSTE}^{form\, e^- STH}(E_{part}, T, t) = \\
&= \Theta(t) \cdot \frac{(1 - F_{e^- trap}) \cdot F_{ioniz}(E_{part}) \cdot E_{part}}{2.35 \cdot E_{gap}} \cdot \left[(1 - F_{dr}(T)) + \frac{F_{dr}(T)}{\tau_{dr}(T)} \cdot e^{-\frac{t}{\tau_{dr}(T)}} \right]
\end{aligned} \tag{3.42}$$

$$\begin{aligned}
&\int_{-\infty}^{+\infty} n_{bSTE}^{form\, e^- STH}(E_{part}, T, \mathbf{x}, t)\, dt = n_{bSTE}^{form\, e^- STH}(E_{part}, \mathbf{x}) \\
&n_{bSTE}^{form\, e^- STH}(E_{part}, T, \mathbf{x}, t) = \\
&= \Theta(t) \cdot \frac{(1 - F_{e^- trap}) \cdot \rho_{ioniz}(E_{part}, \mathbf{x})}{2.35 \cdot E_{gap}} \cdot \left[(1 - F_{dr}(T)) + \frac{F_{dr}(T)}{\tau_{dr}(T)} \cdot e^{-\frac{t}{\tau_{dr}(T)}} \right]
\end{aligned} \tag{3.43}$$

where the time scale $\tau_{dr}(T)$ of the delayed process as well as the fraction of STEs created in the delayed process $F_{dr}(T)$ are temperature-dependent parameters with

$$\begin{aligned}
F_{dr}(T \leq 100\text{K}) &\approx 0 \\
\tau_{dr}(T \approx 300\text{K}) &\approx 40\text{ns}.
\end{aligned}$$

as discussed above (see equations 3.6 and 3.7).

3.1.3 Processes Involved in the Excitation and De-Excitation of STEs

In the following, the different processes involved in the excitation and de-excitation of the populations of intrinsic (blue) and extrinsic (green) luminescence centers as well as their temperature dependencies are discussed. These populations and their densities are denoted by $N_b(E_{part}, T, t)$ and $n_b(E_{part}, T, \mathbf{x}, t)$, respectively, for the blue STEs and by $N_g(E_{part}, T, \mathbf{x}, t)$ and $n_g(E_{part}, T, \mathbf{x}, t)$, respectively, for the green STEs. It is important to notice that the up to now discussed formation processes $N_{bSTE}^{form\,e^-STH}(E_{part}, T, t)$ and $n_{bSTE}^{form}(E_{part}, T, \mathbf{x}, t)$ (see previous section) describe the change in time of the blue STE population $N_b(E_{part}, T, t)$ and its density $n_b(E_{part}, T, \mathbf{x}, t)$ due to the excitation during the energy-deposition process.

Starting from the population $n_b(E_{part}, T, \mathbf{x}, t)$ of blue STEs created in the energy-deposition process (see section III/3.1.2), at first the two mechanisms considered to be responsible for the excitation of defect centers (green STEs) are presented. One consequence of the excitation of green STEs is the emergence of a possibility to (re-)excite intrinsic luminescence centers, i.e., blue STEs. Thereafter, the different possibilities for the de-excitation of intrinsic and defective luminescence centers are discussed: The radiative and non-radiative recombination of the STEs (photon and phonon production), the STE-migration process and the newly introduced possibility of exciton-exciton interaction. At the end of this section, a summary of the considered processes is presented.

In the following, the dependencies of the numbers and densities of STEs on the particle energy E_{part} and the temperature T will no longer be expressed explicitly in order to improve the readability, e.g., $n_b(E_{part}, T, \mathbf{x}, t) =: n_b(\mathbf{x}, t)$. Nonetheless, it has to be kept in mind that the fraction of energy deposited in ionization and its position-dependent distribution differ for different interacting particles and primary particle energies. In addition, the temporal development of STE populations differs for different temperatures due to the temperature dependencies of the involved processes.

Excitation of Extrinsic Luminescence Centers

As discussed in section III/3.1.2, it is assumed that only blue STEs are excited directly in the energy-deposition process. However, as already mentioned, the scintillation-light spectrum of $CaWO_4$ is observed to be composed of blue and green scintillation light. Within the model developed here, two different processes are considered for the excitation of green STEs, i.e., STEs at defective (extrinsic) scintillation centers:

Migration of Blue STEs to Defect Centers

Green STEs can be excited by the migration of blue STEs from intrinsic centers to defect centers. As the migration process of blue STEs is described by the migration time $\tau_{\mathrm{mig,\ b\to g}}(T)$ (see section III/2.1.5), the formation process of green STEs ($n_{gSTE}^{form\,mig:b\to g}(\mathbf{x}, t)$)

by migration of blue STEs can be expressed as:

$$n_{gSTE}^{form\,mig:b\rightarrow g}(\mathbf{x},t) = \frac{1}{\tau_{\mathrm{mig,\ b\rightarrow g}}(T)} \cdot n_b(\mathbf{x},t) \tag{3.44}$$

$$\tau_{\mathrm{mig,\ b\rightarrow g}}(T) = \frac{t_{\mathrm{hb}}(T)}{C_{gC}} = \frac{t_{\mathrm{hb}}(T)}{C_{\mathrm{defects}}} \tag{3.45}$$

with the hopping time $t_{\mathrm{hb}}(T)$ needed for one energy-transfer step in the migration process (see equation 2.7 in section III/2.1.5) and the density of green centers $C_{\mathrm{gC}} = C_{\mathrm{defects}}$ which corresponds to the density of defect centers, as explained at the beginning of this chapter. It has to be noted that, at very low temperatures ($T \lesssim 5\mathrm{K}$), no migration of blue STEs at all (not even to the neighboring $[WO_4]^{2-}$ complex) during their lifetime is possible (see section III/2.1.5).

Reabsorption of Blue Photons at Defect Centers

Green STEs can be excited by reabsorption of a fraction F_{abs} of blue photons (produced by radiative decay of blue STEs) at defect centers. This excitation mechanism of defect centers needs to be introduced as, even at very low temperatures ($T \lesssim 5\mathrm{K}$), still a non-negligible fraction of the produced scintillation light can be assigned to excited green centers (see, e.g., figure 2.12 in section III/2.2.2, at 8K, a fraction of $\sim 29\%$ of the scintillation light is green). As the radiative decay process of blue STEs is described by the radiative decay time $\tau_{rb}(T)$ (see equation 3.54), the formation process of green STEs ($n_{gSTE}^{form\,abs}(\mathbf{x},t)$) by reabsorption of blue photons can be expressed as:

$$n_{gSTE}^{form\,abs}(\mathbf{x},t) = F_{abs} \cdot \frac{1}{\tau_{rb}(T)} \cdot n_b(\mathbf{x},t) \tag{3.46}$$

The possibility to excite green STEs by reabsorption of blue photons corresponds to the assumption that the absorption spectrum of defect centers exhibits an overlap with the energy spectrum of the blue photons (intrinsic scintillation), i.e., with the range from roughly 3.5eV (350nm) to 2.5eV (500nm) (compare, e.g., figure 2.11 in section III/2.2.2). This assumption can be justified by a model for the electronic structure of defect centers indicating a significantly smaller band gap in comparison to intrinsic centers (see discussion in appendix B.4.1) as well as by investigations of the absorption spectrum of $CaWO_4$ described in literature (see discussion in appendix B.4.2). From these theoretical and experimental indications, it can be deduced that defect centers, in fact, show absorption in the wavelength region of the intrinsic $CaWO_4$ scintillation-light emission. Therefore, the suggested mechanism of exciting defect centers via the absorption of blue scintillation light (produced at the intrinsic scintillation centers) is well-motivated.

It has to be noted that no temperature dependency of the fraction F_{abs} of blue photons absorbed at defect centers is assumed. This approximation is supported by the results obtained in [86]: The transmission spectra of a $CaWO_4$ sample in the wavelength region from 240nm (5.2eV) to 1000nm (1.24eV) measured at room temperature and at liquid nitrogen temperature (77K) show practically no difference in the energy region of the intrinsic blue scintillation light. Therefore, it is assumed that the efficiency of the absorption of blue photons at defect centers (which can be assumed to dominate the absorbance in this wavelength region, see discussion in appendix B.4.2), does not depend on temperature. However, of course, this fraction should depend on the density of defects present in the

respective $CaWO_4$ crystal.

Combined Excitation of Green STEs

Hence, within the developed model, it is assumed that green centers can be excited either by the migration of blue STEs to defect centers or by the absorption of blue photons at defect centers. Therefore, it can be concluded that the combined excitation of green centers, i.e., the total formation of green STEs, $n_{gSTE}^{form}(\mathbf{x},t)$, can be expressed as:

$$\begin{aligned}\left[\frac{\partial n_g(\mathbf{x},t)}{\partial t}\right]_{ex} &= n_{gSTE}^{form\,mig:b\rightarrow g}(\mathbf{x},t) + n_{gSTE}^{form\,abs}(\mathbf{x},t) = \\ &= \left(\frac{1}{\tau_{\text{mig, b}\rightarrow\text{g}}(T)} + F_{abs}\cdot\frac{1}{\tau_{rb}(T)}\right)\cdot n_b(\mathbf{x},t) \end{aligned} \tag{3.47}$$

where the fraction F_{abs} of blue photons absorbed at defect centers is assumed to be independent of temperature, but dependent on the density of defects in the respective $CaWO_4$ crystal. Due to the temperature dependency of the STE migration, at very low temperatures ($T \lesssim 5$K), the only process considered for the excitation of green STEs is the absorption of blue photons at defect centers.

Excitation of Intrinsic Luminescence Centers

As a consequence of the possibilities to excite green STEs by migration of blue STEs and by reabsorption of blue photons, also the reverse processes, i.e., the excitation of blue STEs by migration of green STEs or by reabsorption of green photons, have to be discussed.

Migration of Green STEs to Intrinsic Centers

As discussed in section III/2.1.5, the migration of green STEs to intrinsic scintillation centers can, in fact, be observed[21] with a temperature-dependent efficiency of the energy transfer from defect to intrinsic centers [67, 68]. It has to be noted that this migration corresponds to a transfer of the excitation from a defect center (less energy stored in the self-trapping process of the STE) to an intrinsic center (more energy stored in the self-trapping process of the STE). Within the model developed here, the possibility of this migration process to occur is supposed to be permitted due to the deformation energy already stored in the unexcited defective unit cell of a green center (compare to the discussion of the electronic structure of defect centers in appendix B.4.1).

Of course, the respective migration time $\tau_{\text{mig, g}\rightarrow\text{b}}(T)$ is determined by the corresponding hopping time $t_{\text{hg}}(T)$ for green STEs (see section III/2.1.5). For the migration of green STEs to intrinsic centers, the number density of final states C_{bC}, i.e., the probability to

[21] In [67, 68], it is reported that excitation by photons with energies below the band gap (e.g., 4.7eV in [67]), assumed to selectively excite defect centers, leads to the emission of purely green light at 10K and, at room temperature, to an emission spectrum (blue and green light) similar to the one obtained with 5.2eV photons (energy larger than the band gap). Excitation with the 5.2eV photons at 10K, on the other hand, leads to the same emission spectrum as at room temperature, with the only difference that the room-temperature spectrum is slightly more broadened. These observations are interpreted in [67] as indication for a thermally activated STE migration from defect centers (green STEs) to intrinsic centers (blue STEs).

reach an intrinsic (blue) center after one migration step, can be assumed to be approximately one $C_{bC} \approx 1$. This can be assumed as, due to the small number density of defect centers (C_{defects} in the range from a few 10ppm to a few 100ppm), defect centers can be assumed to be surrounded by intrinsic, undisturbed centers. Hence, already after one hop, the green STE has migrated from a defect center to an intrinsic center. Therefore, the formation process of blue STEs ($n_{bSTE}^{form\,mig:g\to b}(\mathbf{x},t)$) by migration of green STEs to intrinsic centers can be expressed as:

$$n_{bSTE}^{form\,mig:g\to b}(\mathbf{x},t) = \frac{1}{\tau_{\text{mig, g}\to\text{b}}(T)} \cdot n_g(\mathbf{x},t) \tag{3.48}$$

$$\tau_{\text{mig, g}\to\text{b}}(T) = \frac{t_{\text{hg}}(T)}{C_{bC}} \approx t_{\text{hg}}(T) \tag{3.49}$$

where, for the calculation of the hopping time of green STEs $t_{\text{hg}}(T)$, of course, the diffusion coefficient for green STEs (see equation 2.5 in section III/2.1.5) has to be used. As the diffusivity of green STEs is non-negligible (see diffusion coefficient of green STEs in section III/2.1.5), the process of exciting blue STEs by migration of green STEs has to be included into the time-dependent description of the blue STE population and its density.

Reabsorption of Green Photons at Intrinsic Centers

As discussed in section III/2.1.2, the band gap of intrinsic scintillation centers in $CaWO_4$, i.e., of the undisturbed lattice, is determined to be $E_{gap} \approx 5.0$eV. On the other hand, e.g., from figure 2.11 (section III/2.2.2), it can be deduced that the emission spectrum of green light stretches roughly from 350nm (3.5eV) to 700nm (1.8eV). Hence, no overlap of the green STE emission-spectrum and the absorption spectrum of intrinsic scintillation centers should exist. Therefore, the possibility to excite an intrinsic scintillation center, i.e., a blue STE, by absorption of a green photon can be neglected.

Resulting Excitation of Blue STEs

Hence, within the model developed in the present work, it is assumed that blue STEs can - in addition to their primary formation in the energy-deposition process (see equation 3.43 in section III/3.1.2) - be repopulated by green STEs migrating from defect centers to intrinsic centers. Hence, the complete blue STE-formation process (excitation of blue STEs) can be expressed by:

$$\begin{aligned}\left[\frac{\partial n_b(\mathbf{x},t)}{\partial t}\right]_{ex} &= n_{bSTE}^{form\,mig:g\to b}(\mathbf{x},t) + n_{bSTE}^{form\,e^-STH}(E_{part},T,\mathbf{x},t) = \\ &= \frac{1}{\tau_{\text{mig, g}\to\text{b}}(T)} \cdot n_g(\mathbf{x},t) + \\ &+ \Theta(t) \cdot \frac{(1-F_{e^-trap}) \cdot \rho_{ioniz}(E_{part},\mathbf{x})}{2.35 \cdot E_{gap}} \cdot \left[(1-F_{dr}(T)) + \frac{F_{dr}(T)}{\tau_{dr}(T)} \cdot e^{-\frac{t}{\tau_{dr}(T)}}\right]\end{aligned} \tag{3.50}$$

Due to the temperature dependency of the STE migration (compare section III/2.1.5), for very low temperatures ($T \lesssim 5$K), it is assumed that no re-excitation of the blue STE population by migration of green STEs can take place.

Radiative and Non-Radiative Recombination of Excitons

As discussed in section III/2.2, for blue and green STEs the possibilities of radiative and non-radiative recombination occur (see, e.g., figure 2.10 in section III/2.2). In the following, the model and terminology used to describe the radiative and non-radiative decay processes are explained for blue STEs. An analogous description can be used for green STEs as it is assumed that, for excited defect centers, the energy-level structure at the band edge is, in principle, the same (see discussion in appendix B.4.1). However, it has to be kept in mind that the values of most parameters are different for blue and green STEs. The reason for these differences as well as probable deviations that have to be expected are discussed at the end of this section.

Radiative Recombination of Blue STEs

Due to the deformation of unit cells containing STEs (caused by the self-trapping process of the holes), the lowest energy level of the electron in the STE, $^3T_2$, is assumed to be split into two closely-lying energy levels: The two Jahn-Teller and spin-orbit split states JT-SO-$^3T_2$ (compare section III/2.2.1) with an energy splitting of D_b (order of magnitude $\sim$ 1meV). Within the model, it is assumed that radiative recombination of a STE can occur from both of these states, the ground state (level 1_b) and the first excited state (level 2_b) of STEs. Both of these states emerge from the triplet state $^3T_2$ so that radiative decay becomes partially allowed by the symmetry-breaking process due to the Jahn-Teller and spin-orbit splitting. Radiative recombination times from these levels can be assumed to be relatively long, due to the only partial allowance.

The assumption of two active radiative levels is needed as, otherwise, assuming only one active level for the radiative decay of STEs, the radiative recombination rate would exhibit no temperature dependency. However, this would be in contradiction with the observed scintillation efficiency of $CaWO_4$ at room temperature, as is discussed in detail in appendix B.5. From this discussion, it becomes clear that the radiative decay time has to exhibit a temperature dependency, i.e., it has to decrease for increasing temperature. This temperature dependency can, e.g., be modeled with the existence of two active radiative levels with different recombination rates[22] as, e.g., the two JT-SO-$^3T_2$ states. The relative populations of these levels are determined by thermal equilibrium, i.e. the populations of the two levels can populate and de-populate each other in phonon-assisted processes. This interaction between the two levels implies that the scintillation light produced by the radiative decay of these two levels exhibits one combined exponential radiative recombination time. The relative populations of the two levels and, thus, their respective contributions to the radiative decay are temperature dependent (determined by the available phonon population). Due to the postulated increase of the radiative recombination time for decreasing temperature, it is assumed in the following that the radiative recombination time τ_{L1b} of the energetically lower-lying *level* 1_b is larger than the radiative recombination time τ_{L2b} of the energetically higher-lying *level* 2_b. For decreasing temperature, i.e., decreasing phonon-assisted excitation of *level 2*, such a configuration leads to an enhanced probability

[22] This configuration, in principle, complies to the one suggested in a commonly used three-level model. The three-level model is often used to describe the temperature dependency of the slow decay time of wolframates or molybdades (see, e.g., [41] and references therein) and is presented in appendix A.4 for $CaWO_4$.

of the electron of the STE to reside in *level 1$_b$*. Hence, for decreasing temperature, the probability of radiative decay from *level 1$_b$* is increasing and, therefore, the effective radiative recombination time is dominated by τ_{L1b}, i.e., increasing for decreasing temperature.

To obtain a mathematical description of the effective radiative recombination time $\tau_{rb}(T)$ of the blue STE population $n_b(\mathbf{x},t)$, an analogous approach as in the three-level model (see appendix A.4) can be used[23]. With the notation that the blue STE population of *level 1$_b$* is described by $n_{b-L1}(\mathbf{x},T,t)$ with a radiative recombination time τ_{L1b} and the same notation for *level 2$_b$*, the total blue STE population $n_b(\mathbf{x},t)$ and the condition of thermal equilibrium of the two levels can be expressed as:

$$n_b(\mathbf{x},t) = n_{b-L1}(\mathbf{x},T,t) + n_{b-L2}(\mathbf{x},T,t) \tag{3.51}$$

$$n_{b-L2}(\mathbf{x},T,t) = n_{b-L1}(\mathbf{x},T,t) \cdot e^{-\frac{D_b}{k_B \cdot T}} \tag{3.52}$$

$$\Rightarrow n_b(\mathbf{x},t) = n_{bSTE-L1}(\mathbf{x},T,t) \cdot \left(1 + e^{-\frac{D_b}{k_B \cdot T}}\right) \tag{3.53}$$

with D_b corresponding to the energy splitting between the two levels. The change in the total blue STE population by radiative decay from the two levels can be described by the combined, temperature-dependent radiative recombination time $\tau_{rb}(T)$:

$$\frac{1}{\tau_{rb}(T)} := \frac{\frac{1}{\tau_{L1b}} + \frac{1}{\tau_{L2b}} \cdot e^{-\frac{D_b}{k_B \cdot T}}}{1 + e^{-\frac{D_b}{k_B \cdot T}}} \tag{3.54}$$

$$\begin{aligned}\left[\frac{\partial n_b(\mathbf{x},t)}{\partial t}\right]_{rad} &= -\frac{1}{\tau_{L1b}} \cdot n_{b-L1}(\mathbf{x},T,t) - \frac{1}{\tau_{L2b}} \cdot n_{b-L2}(\mathbf{x},T,t) = \\ &= -\frac{1}{\tau_{rb}(T)} \cdot n_b(\mathbf{x},t)\end{aligned} \tag{3.55}$$

It can be seen that the value of D_b (of the order of 1meV) as well as the relative values of the radiative recombination times τ_{L1b} and τ_{L2b} determine the temperature for which a change in behavior of the total radiative recombination time $\tau_{rb}(T)$ can be observed.

Non-Radiative Recombination of Blue STEs

In addition to the radiative recombination, the non-radiative recombination of STEs is possible, as discussed in section III/2.2.1. This non-radiative recombination process is assumed to be responsible for the observed change in light yield at temperatures $\gtrsim$ 200K (compare figure 2.14 in section III/2.2.4). This effect is therefore often called thermal quenching. Following N.F. Mott et al. [91], the non-radiative recombination process can be described as a thermally activated process in which the electron of the STE overcomes the energy barrier ΔE_b so that recombination of the electron and the STH under phonon-emission with a non-radiative rate constant K_{nrb} is possible. Hence, the size of the energy barrier ΔE_b is connected to the temperature from which on (for higher temperatures)

[23] However, it has to be noticed that, in comparison to the three-level model, the sum of the radiative and non-radiative recombination rates cannot be equated with the total recombination rate of STEs as, here, also other processes (as, e.g., STE migration) influencing the lifetime of the blue and green STE populations are considered. Therefore, the values of the decay rates determined with the three-level model (see appendix A.4) cannot be adopted as these values were determined assuming no other de-excitation processes for STEs as well as only one type of scintillation center.

thermal quenching is effective. This energy barrier has been determined for $CaWO_4$ by different authors with different methods to amount to ~ 0.34eV [92], ~ 0.32eV [41] and ~ 0.30eV [93]. In the following, a mean value of $\Delta E_b = 0.32$eV will be adopted[24]. As the energy barrier for the occurrence of the non-radiative process ΔE_b is much larger than the energy barrier separating the two emitting JT-SO-$^3T_2$ levels, D_b, the approximation that the same value for ΔE_b can be used for both energy levels is justified (compare [41] and figure 2.10 in section III/2.2.1). Hence, it can be assumed that the change of the total blue STE population $n_b(\mathbf{x}, t)$ via non-radiative recombination can be described with a temperature-dependent non-radiative decay time $\tau_{nrb}(T)$:

$$\left[\frac{\partial n_b(\mathbf{x},t)}{\partial t}\right]_{non-rad} = -\frac{1}{\tau_{nrb}(T)} \cdot n_b(\mathbf{x},t) \tag{3.56}$$

$$\frac{1}{\tau_{nrb}(T)} := K_{nrb} \cdot e^{-\frac{\Delta E_b}{k_B \cdot T}} \tag{3.57}$$

Due to the temperature dependency of the non-radiative recombination time, i.e., the thermal quenching, it is concluded that, for temperatures $\lesssim 200$K, the contribution of the non-radiative recombination to the total change of the blue STE population can be neglected.

Radiative and Non-Radiative Recombination of Green STEs

As discussed in appendix B.4.1, the structure of the energy-level scheme of excited defect centers (green STEs) is assumed to be the same as that of intrinsic centers. Therefore, in principle, the complete description of the radiative and non-radiative recombination processes of green STEs can be adopted from the one for blue STEs. The only differences occur in the expected values of the parameters used for the description (compare to the discussion in appendix B.4.1):

- The radiative recombination times τ_{L1g} and τ_{L2g} for green STEs are expected to be faster than the radiative recombination times for blue STEs τ_{L1b} and τ_{L2b}.

- The energy splitting between the two emitting levels for green STEs, D_g, is expected to be of the same order of magnitude as for blue STEs (1meV), however, does not necessarily have to exhibit the same value.

- The energy barrier for the non-radiative recombination of green STEs, ΔE_g, is expected to be smaller compared to the energy barrier ΔE_b for STEs at intrinsic centers.

With these assumptions, the change of the green STE population $n_g(\mathbf{x}, t)$ via the radiative and non-radiative recombination processes can be expressed with the same mathematical

[24] The values determined in literature were assigned either on the basis of the temperature dependency of the slow scintillation-light component or of the temperature dependency of the scintillation-light yield. As will be shown within the discussion of the model, it is assumed that both of these features are dominated by the behavior of the blue light component. Therefore as well as due to the argumentation outlined in section III/3.2.1, the values for ΔE reported in literature are assumed to correspond to the energy barrier for blue STEs, i.e., to ΔE_b.

model as developed for the blue STEs (compare equations 3.55, 3.54 and 3.56, 3.57):

$$\left[\frac{\partial n_g(\mathbf{x},t)}{\partial t}\right]_{rad} = -\frac{1}{\tau_{L1g}} \cdot n_{g-L1}(\mathbf{x},T,t) - \frac{1}{\tau_{L2g}} \cdot n_{g-L2}(\mathbf{x},T,t) = \\ = -\frac{1}{\tau_{rg}(T)} \cdot n_g(\mathbf{x},t) \tag{3.58}$$

$$\frac{1}{\tau_{rg}(T)} := \frac{\frac{1}{\tau_{L1g}} + \frac{1}{\tau_{L2g}} \cdot e^{-\frac{D_g}{k_B \cdot T}}}{1 + e^{-\frac{D_g}{k_B \cdot T}}} \tag{3.59}$$

$$\left[\frac{\partial n_g(\mathbf{x},t)}{\partial t}\right]_{non-rad} = -\frac{1}{\tau_{nrg}(T)} \cdot n_g(\mathbf{x},t) \tag{3.60}$$

$$\frac{1}{\tau_{nrg}(T)} := K_{nrg} \cdot e^{-\frac{\Delta E_g}{k_B \cdot T}} \tag{3.61}$$

with the combined radiative recombination time $\tau_{rg}(T)$ for green STEs and the non-radiative recombination time $\tau_{nrg}(T)$ of green STEs (for both emitting levels) as well as the non-radiative rate constant K_{nrg}. An estimation for the value of the energy barrier ΔE_g is presented in appendix B.7 (on the basis of discussions presented in section III/3.2.1).

Exciton Migration

As already indicated in the discussion of the excitation processes of blue and green STEs (see equations 3.50 and 3.47), the possibility for STEs to migrate within the crystal is contained in the model. Three different cases have to be considered: The migration of a blue STE to a defect center with the migration time $\tau_{\text{mig, b}\to\text{g}}(T)$, the migration of green STEs to an intrinsic centers with the migration time $\tau_{\text{mig, g}\to\text{b}}(T)$ and the migration of a blue STE to another intrinsic center with the migration time $\tau_{\text{mig, b}\to\text{b}}(T)$. As already discussed in the context of the excitation of intrinsic centers by migration of green STEs, due to the low defect density (roughly 50ppm to a few 100ppm), the probability for the presence of two neighboring defect centers is negligible. Hence, the possibility for green STEs to directly migrate to another defect center is not considered within the model.

The migration process of blue STEs to defect centers as well as the migration process of green STEs to intrinsic centers have already been discussed in the context of the excitation of blue and green STEs. Therefore, in the following, only the mathematical expressions for the change of the respective STE population induced by the migration process will be given. The notation is still that the density of defect centers, i.e., of green centers, is labeled as $C_{\text{gC}} = C_{\text{defects}}$ and the hopping time of blue (green) STEs is labeled as $t_{\text{hb}}(T)$ ($t_{\text{hg}}(T)$) (see equation 2.7 in section III/2.1.5). The hopping times are determined by the distance between two scintillation centers ($d_{\text{W-W}} = 3.87$Å , see section III/2.1.1) and the respective diffusion coefficients of blue (regular) STEs, $D_{\text{bSTE}}(T)$ (see equation 2.4 in section III/2.1.5), and green (disturbed) STEs, $D_{\text{gSTE}}(T)$ (see equation 2.5 in section III/2.1.5).

The change in the blue STE population $n_b(\mathbf{x},t)$ due to the migration of blue STEs to

defect centers can be expressed as:

$$\left[\frac{\partial n_b(\mathbf{x},t)}{\partial t}\right]_{mig} = -\frac{1}{\tau_{\text{mig, b}\to\text{g}}(T)} \cdot n_b(\mathbf{x},t) \tag{3.62}$$

$$\tau_{\text{mig, b}\to\text{g}}(T) = \frac{t_{h\text{b}}(T)}{C_{\text{defects}}} = \frac{d^2_{\text{W-W}}}{6 \cdot D_{\text{bSTE}}(T) \cdot C_{\text{defects}}} \tag{3.63}$$

$$D_{\text{bSTE}}(T) = D_{\text{STE reg}}(T) = 1.2 \cdot 10^{-7} \frac{\text{cm}^2}{s} \cdot e^{(-\frac{4.5\text{meV}}{k_B \cdot T})} \tag{3.64}$$

The change in the green STE population $n_g(\mathbf{x},t)$ due to the migration of green STEs to intrinsic centers can be expressed as:

$$\left[\frac{\partial n_g(\mathbf{x},t)}{\partial t}\right]_{mig} = -\frac{1}{\tau_{\text{mig, g}\to\text{b}}(T)} \cdot n_g(\mathbf{x},t) \tag{3.65}$$

$$\tau_{\text{mig, g}\to\text{b}}(T) \approx t_{\text{hg}}(T) = \frac{d^2_{\text{W-W}}}{6 \cdot D_{\text{gSTE}}(T)} \tag{3.66}$$

$$D_{\text{gSTE}}(T) = D_{\text{STE dist}}(T) = 1.2 \cdot 10^{-7} \frac{\text{cm}^2}{s} \cdot e^{(-\frac{6.9\text{meV}}{k_B \cdot T})} \tag{3.67}$$

It can be seen that the values (and temperature dependencies) of the diffusion coefficients of blue and green STEs are adopted from literature (see discussion and references in section III/2.1.5). These values are assumed to be adoptable for the model developed here as they have been determined in [67] using equivalent assumptions concerning the migration processes from defect to intrinsic centers and vice versa. This implies that the (temperature-dependent) migration times of blue and green STEs (equations 3.63 and 3.66) can be calculated, apart from the density of defects, C_{defects}, which is a crystal dependent parameter influencing the blue STE migration time.

The last case considered, i.e., the migration of a blue STE to another (unexcited) intrinsic center, does not change the number of blue STEs, but only their spatial distribution. The impact of this effect will only be discussed qualitatively within the model. Nonetheless, the relevance and temperature dependency of this process can be specified by the migration time $\tau_{\text{mig, b}\to\text{b}}(T)$ and the diffusion length $l_{\text{diff b}}(T)$ of blue STEs (compare section III/2.1.5): Under the assumption that the majority of neighboring centers is of the intrinsic type, the migration of a blue STE to another (neighboring) intrinsic center is completely determined by the respective hopping time of blue STEs $t_{h\text{b}}(T)$:

$$\tau_{\text{mig, b}\to\text{b}}(T) \approx t_{h\text{b}}(T) = \frac{d^2_{\text{W-W}}}{6 \cdot D_{\text{bSTE}}(T)} \tag{3.68}$$

To the blue STEs in $CaWO_4$ can be assigned a typical, temperature-dependent diffusion-length $l_{\text{diff b}}(T)$ during their (also temperature-dependent) lifetime $\tau_{ltb}(T)$ (compare equation 2.6 in section III/2.1.5):

$$l_{\text{diff b}}(T) = \sqrt{2 \cdot \tau_{ltb}(T) \cdot D_{\text{bSTE}}(T)} \tag{3.69}$$

It has to be noted that, for low temperatures ($T \lesssim 5\text{K}$), where no diffusion of STEs is expected to occur (compare discussion in section III/2.1.5), all of these migration processes can be neglected.

Exciton-Exciton Interaction

Additionally to the possibilities to induce a change of the STE populations discussed up to now, also an interaction between STEs is considered within the model. The mechanism suggested is a Förster dipole-dipole energy transfer. Such an interaction was already proposed, e.g., in [85] where the theory of scintillator non-linearity and non-proportionality is discussed in general and used for the interpretation of scintillation-light decay-time spectra of $CaWO_4$ measured via $\sim$ 90eV photon excitation [94]. In principle, such an interaction possibility is also the basis of the qualitative description of the light-yield quenching with Birks' saturation law (see, e.g., [95] for the interpretation of Quenching Factors of $CaWO_4$ using Birks' law). A comparison of the model developed here with the mentioned investigations and models is presented in section III/6.2.

Förster Dipole-Dipole Energy Transfer

The Förster interaction describes a non-radiative energy transfer between closely located neutral dipoles, where the dipoles can, e.g., be identified with excitations in a scintillator [96]. If the two dipoles are positioned closely enough to each other, the energy of one of the dipoles is transferred to the other dipole resulting in a non-radiative recombination of the first one and the excitation of the other one. This energy transfer can, e.g., be described as virtual photon exchange[25]. The dipole excited by the transferred energy relaxes again to its ground state under phonon emission. The strength of the interaction depends on the distance ρ of the dipoles, where $|\rho| = R_{d-d}$ denotes the so-called Förster radius: The Förster radius is defined as the distance of two dipoles for which the recombination rate due to Förster energy transfer is equal to the recombination rate of the dipoles by all other means (as, e.g., by the radiative recombination process) [96]. Thus, it can be concluded that, for higher densities of dipoles, the probability for Förster energy transfer increases. The value of the Förster radius R_{d-d} is a material-specific parameter which depends on the overlap of the emission spectrum and the absorption spectrum of the involved dipoles and is typically of the order of a few nm [96]. Assuming the interaction of two dipoles of the same type j, the Förster radius R_{d-d} is proportional to[26] (see, e.g., [97]):

$$R_{d-d}(T) \propto \left(\frac{F_{j\,rad}(T)}{n_{mat}^4} \cdot \int S_{em,j}(\lambda, T) \cdot S_{abs,j}(\lambda, T) \cdot \lambda^6 d\lambda \right)^{\frac{1}{6}} \tag{3.70}$$

with the spectral distribution of the emission spectrum $S_{em,j}(\lambda, T)$ and of the absorption spectrum $S_{abs,j}(\lambda, T)$ of the dipoles[27] j and the refractive index n_{mat} of the material. $F_{j\,rad}(T)$ corresponds to the fraction of dipoles that would decay radiatively assuming the absence of the Förster interaction [97], i.e. $F_{j\,rad}(T)$ corresponds to the radiative branching ratio of the dipoles[28]. The integration has to be performed over the wavelength (λ)

[25] It has to be noted that no real photon is emitted by one dipole and absorbed by the other. The probability for a real photon emission and consecutive absorption process by two different excited scintillation centers usually can be neglected due to the typically (for energy depositions by individual particles) low number of simultaneously excited scintillation centers.

[26] The proportionality constant includes dimensions leading to the dimension of a length for the result.

[27] It should be noted that the spectral distributions are no absolute spectra, but refer to the normalized shapes of the spectra as the efficiency of the radiative emission and, hence, the spectral integral of the emission spectrum are contained in the factor $F_{j\,rad}(T)$.

[28] This definition of the Förster radius does not include the efficiency of the absorption by the dipoles. In analogy to the radiative branching ratio of the dipole, a factor containing this efficiency can also be

region of the absorption spectrum [96]. The shape of the absorption and emission spectra and, hence, also their overlap integral as well as the radiative branching ratio can, of course, depend on temperature (T), leading to a possible temperature dependency of the Förster radius $R_{d-d} = R_{d-d}(T)$.

Due to the definition of the Förster radius $R_{d-d}(T)$, the rate of reaction (Förster energy-transfer), $K_{d-d}(T, \rho)$, of two dipoles of the same type j at a distance ρ to each other can be expressed as [97, 85]:

$$K_{d-d}(T, \rho) = \frac{1}{\tau_{lt\,j}(T)} \cdot \left(\frac{R_{d-d}(T)}{\rho} \right)^6 \tag{3.71}$$

$$\Rightarrow \frac{K_{d-d}(T, \rho = R_{d-d}(T))}{k_{lt\,j}(T)} = 1 \tag{3.72}$$

where $\tau_{lt\,j}(T)$ denotes the intrinsic lifetime and $k_{lt\,j}(T) := \frac{1}{\tau_{lt\,j}(T)}$ denotes the intrinsic recombination rate of the dipoles j determined by all processes of de-excitation, except the Förster interaction[29] [97]. Equation 3.72 provides the definition of the Förster radius.

As is demonstrated in appendix B.6.1 with the help of some generally accepted approximations (e.g., randomly oriented dipoles) and the Förster reaction rate depending on the distance ρ (equation 3.71), an expression for the time-dependent Förster (dipole-dipole) interaction rate $\beta_{d-d}(T, t)$ can be obtained. Therefore, the impact of the Förster interaction on the temporal evolution of the population (density) of the dipoles $n_j(\mathbf{x}, t)$ can be expressed as (compare [85]):

$$\left[\frac{\partial n_j(\mathbf{x}, t)}{\partial t} \right]_{d-d} = -\beta_{d-d}(T, t) \cdot n_j^2(\mathbf{x}, t) \tag{3.73}$$

$$\beta_{d-d}(T, t) = \frac{2}{3} \cdot \pi^{\frac{3}{2}} \cdot R_{d-d}^3(T) \cdot \frac{1}{\sqrt{\tau_{lt\,j}(T) \cdot t}} \tag{3.74}$$

Hence, under the approximations introduced in appendix B.6.1, the recombination rate of interacting dipoles due to the Förster energy transfer is determined by the Förster radius $R_{d-d}(T)$, the intrinsic lifetime of the dipoles $\tau_{lt\,j}(T)$ (in absence of the Förster interaction) and the initial distribution of the density of the dipoles $n_j(\mathbf{x}, t = 0)$.

From equation 3.74, it can be seen that, for short times t, the impact of this interaction mechanism on the population of the dipoles is large whereas, for large times t, the impact on the population of dipoles is small ($\propto \frac{1}{\sqrt{t}}$). For a large initial density of dipoles at $t = 0$, a fast and strong reduction of the number of dipoles takes place (in each interaction process, one dipole is destroyed). The larger the density at the beginning, the faster and, hence, the more efficient the reduction of the number of dipoles. However, at larger times, the probability for this interaction to occur decreases to zero, independent of the initial density of dipoles. This is caused by the autocorrelation of this interaction mechanism which implies that the density of dipoles (which controls the impact of the Förster

included: Compare, e.g. [96], where the overlap integral is performed over the emission spectrum of the emitting species and the spectral absorptivity of the absorbing species.

[29] The lifetime and recombination rate determined by all other means of de-excitation are denoted as "intrinsic", in order to distinguish it from the "effective" lifetime of dipoles which is additionally affected by the Förster interaction (corresponding to an extrinsic impact on the individual dipoles).

interaction) is reduced with time not only by the decay via all other means (radiative, non-radiative and migration), but also due to the destruction via the Förster interaction.

This implies that the *effective lifetime* of the dipoles (considering *all* means of depopulation, i.e., also *including* the Förster interaction) is shortened for small times t, due to the additional recombination of dipoles via the Förster interaction. The efficiency of this process, i.e., the extent of the shortening of the lifetime, depends on the initial density of the dipoles. For large times t, the lifetime of the dipoles converges against their *intrinsic lifetime* $\tau_{lt\,j}(T)$ (determined by all means of depopulation *except* the Förster interaction), independently of the initial density of the dipoles.

Identifying the dipoles in the description of the Förster interaction with STEs in $CaWO_4$, this interaction mechanism can, in principle, be easily transferred to the case of interacting STEs. However, at first, the different interaction possibilities arising from the existence of blue and green STEs have to be discussed.

Green STEs and the Förster Interaction

As discussed in the context of the migration process of green STEs (discussion above equation 3.65), it can be assumed that green STEs (excited defect centers) are, in first-order approximation, surrounded by intrinsic centers, i.e., potentially blue STEs. Therefore, the interaction of green STEs with other green STEs is neglected. In addition, due to the small number density of defect centers, also for blue STEs, the probability of energy transfer to a green STE is correspondingly small. Hence, only the possibility of energy transfer from a green STE to a blue STE has to be considered. However, also for this interaction possibility, the probability to occur can be assumed to be negligible due to the short lifetime of green STEs (see, e.g., section III/3.1.4) and, additionally, for the fraction of green STEs produced by absorption of blue photons, due to their isolated positions (for a detailed discussion and explanation, see appendix B.6.2).

Nonetheless, it should be noted that the intensity and the decay-time spectrum of the green light component (produced by the radiative decay of green STEs) are influenced by the introduction of the Förster interaction between blue STEs. This is a result of the assumed excitation mechanism of green STEs via the radiative decay or migration of blue STEs. Due to this dependency, changes in the effective lifetime of blue STEs, as introduced by the Förster interaction (additional reduction of the blue STE number for dense populations of blue STEs), effect also the temporal evolution of the green STE population and, hence, the green light production. For a more detailed discussion, see section III/3.2.4.

Interaction of Blue STEs via Förster Energy-Transfer

From the discussion above, it can be seen that only the Förster interaction between two blue STEs is considered within the model. In such an interaction, one blue STE recombines by transferring its energy to a second blue STE. The second STE gets either excited ($STE_b^\star$) or (intermediately) broken-up into an electron-hole pair which is assumed to recombine afterwards to an STE again. It is assumed that the excited STE as well the

created electron-hole pair relax via emission of phonons to non-excited blue STEs:

$$\begin{aligned} \mathrm{STE}_b + \mathrm{STE}_b \rightarrow \mathrm{STE}_b^\star \quad &\Rightarrow \quad \mathrm{STE}_b^\star \rightarrow \mathrm{STE}_b + \text{phonons} \\ \mathrm{STE}_b + \mathrm{STE}_b \rightarrow e^- + h \quad &\Rightarrow \quad e^- + h \rightarrow \mathrm{STE}_b + \text{phonons} \end{aligned}$$

Hence, as a result of such a reaction of two blue STEs, one STE is destroyed and phonons are generated. The change of the blue STE population due to the Förster interaction between two blue STEs can, in analogy to equation 3.74, be expressed using the Förster radius $R_{d-d}(T)$ for blue STEs in $CaWO_4$ (compare equation 3.70) and the intrinsic lifetime $\tau_{ltb}(T)$ of blue STEs (in the absence of the Förster interaction) as:

$$\left[\frac{\partial n_b(\mathbf{x},t)}{\partial t}\right]_{d-d} = -\frac{2\cdot\pi^{\frac{3}{2}}}{3}\cdot\frac{R_{d-d}^3(T)}{\sqrt{\tau_{ltb}(T)\cdot t}}\cdot n_b^2(\mathbf{x},t) \tag{3.75}$$

$$R_{d-d}(T) \propto \left(\frac{F_{b\,rad}(T)}{n_{CaWO_4}^4}\cdot\int S_{em,b}(\lambda,T)\cdot S_{abs,b}(\lambda,T)\cdot\lambda^6 d\lambda\right)^{\frac{1}{6}} \tag{3.76}$$

where $S_{em,b}(\lambda,T)$ and $S_{abs,b}(\lambda,T)$ correspond to the emission and absorption spectra, $F_{b\,rad}(T)$ corresponds to the radiative branching ratio of blue STEs in $CaWO_4$ and n_{CaWO_4} corresponds to the refractive index of $CaWO_4$. The determination and the temperature dependency of the intrinsic lifetime $\tau_{ltb}(T)$ as well as of the radiative branching ratio $F_{b\,rad}(T)$ of blue STEs in $CaWO_4$ are discussed in detail in section III/3.3. A presentation of values of the Förster radius in $CaWO_4$ already determined as well as a discussion of the expected temperature dependency is presented in the following:

Values Determined for the Förster Radius in $CaWO_4$

In literature [98, 94], values for the Förster radius in $CaWO_4$ determined with excitation by fast (fs to ps) photon-pulses (photon energy 89.84eV) generated with a FEL (free-electron laser) can be found. A discussion of the method used to determine the Förster radius in these references as well as a comparison with the model developed here can be found in section III/6.2. The values determined amount to 2.6nm (at 300K) in [98] and to 4.34nm (at 8K) and 2.93nm (at 300K) in [94]. In [94], it is stated that the differences between the values obtained for the two temperatures are still within the error margins. Hence, it can be expected that the Förster radius in $CaWO_4$ is within the range of roughly 2 to 4nm.

Temperature Dependency of the Förster Radius in $CaWO_4$

As can be seen from equation 3.76, the temperature-dependent Förster radius for the STE-STE interaction is determined by the overlap integral of the emission and absorption spectra of blue STEs in $CaWO_4$ as well as by the radiative branching ratio for blue STEs.

In appendix B.6.3, a quantitative discussion of the temperature dependency of the overlap integral of the emission and absorption spectrum of blue STEs in $CaWO_4$ can be found. As a basis for the discussion, measurements of emission spectra preformed within the present work and measurements of the transient absorption spectra of STEs in $CaWO_4$ from [65] are used. From this discussion, it can be concluded that, indeed, an overlap of the emission and absorption spectra of blue STEs in $CaWO_4$ at mK temperatures up to room temperature exists. The overlap integral of these spectra could change slightly

with varying temperature as both spectra can be expected to get sharper for decreasing temperature and are not centered around the same central wavelengths.

Probably much more important for the temperature dependency of the Förster radius of blue STEs in $CaWO_4$ is the change of the radiative branching ratio with temperature. With the parameters of the model determined in section III/5.2.2, the radiative branching ratio for blue STEs in $CaWO_4$ within the developed model can be determined to amount to $\sim 42\%$ at room temperature and $\sim 100\%$ at low temperatures ($T \lesssim 5K$).

From these considerations of the temperature dependencies of the radiative branching ratio and the overlap integral of the emission and absorption spectrum in $CaWO_4$, a very rough estimate of the relative change of the Förster radius with temperature (from mK to room temperature) can be obtained. The approximations used are explained in appendix B.6.4. Using equation 3.76, the ratio of the Förster radii at room temperature and $T \lesssim 5$K can be calculated to amount to $\frac{R_{d-d}(T=300K)}{R_{d-d}(T\lesssim 5K)} \approx 0.86$.

Using this very rough estimate, it is expected that the Förster radius in $CaWO_4$ at mK temperatures is larger than the Förster radius at room temperature, corresponding to an increase of the impact of the Förster interaction with decreasing temperature. It should be noted that this estimate can most probably only deliver a trend and does not necessarily quantify the real change of the Förster radius with temperature. Nonetheless, the basic prediction of an increasing Förster radius for decreasing temperature is in good agreement with the trend shown by the values determined for the Förster radius at 300K (2.93nm) and 8K (4.34nm) in [94].

Impact of the Förster Interaction on the Light Generation

As can be seen from equation 3.75, the Förster interaction delivers an additional non-radiative decay channel for blue STEs which depends on the density of the STE population. Hence, it can be expected that, the higher the density of STEs (as, e.g., in nuclear recoil tracks), the larger the impact of this additional decay channel. The more STEs decay via the Förster interaction, the smaller the efficiency of the competing process of producing scintillation light, i.e., the smaller the light yield. It should be noted that the dependency of the impact of the Förster interaction on the density of STEs is not linear, but quadratical (compare equation 3.75). In addition, it can already be deduced that the Förster interaction of blue STEs should lead to a (significant) shortening of their effective lifetime for short times t after the initial energy deposition process. For large times t, the STE lifetime is expected to converge to its intrinsic value (determined by all other decay channels except the Förster interaction). Hence, for large times t after the initial creation of the STE population, it is expected that the lifetime of STEs always shows the same value, independently from the initially created STE density.

In addition, it should be noted that the Förster radius is a purely material- and temperature-dependent parameter. It does not depend on the way the STEs were generated, but only on the density of the created STE population.

Summary of the Considered Processes

In figure 3.8, a graphical overview of all processes leading to changes in the density of blue and green STEs is presented, starting at the point where the initial blue STE population is produced (compare figure 3.7 in section III/3.1.2):

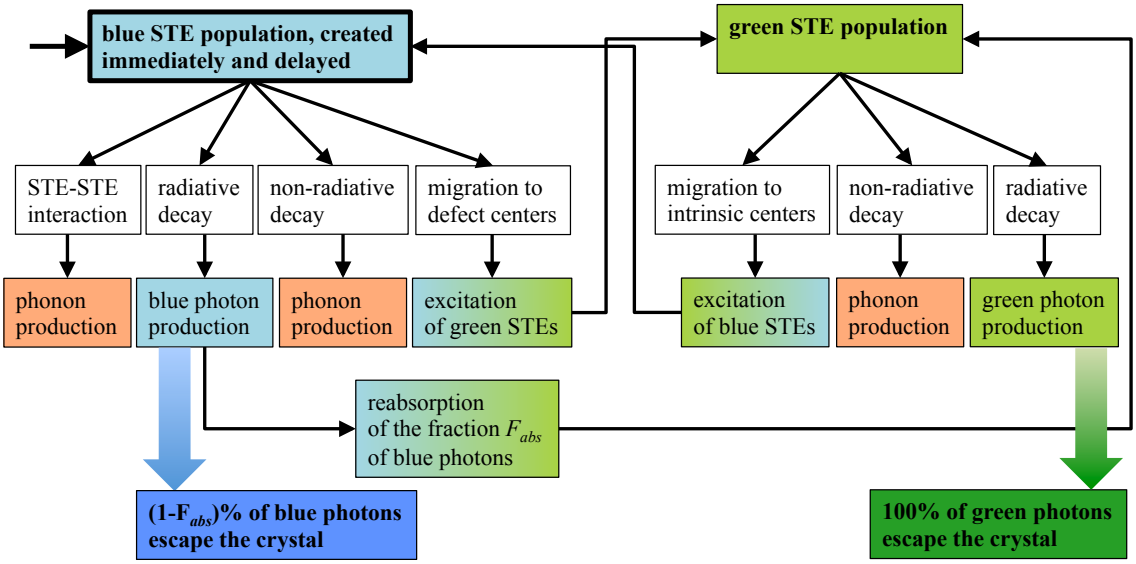

Figure 3.8: Overview over the processes involved in the excitation and de-excitation of the blue and green STE populations: Blue boxes correspond to blue STEs and photons. Green boxes indicate the green STEs and photons. Boxes in red correspond to processes in which phonons are produced.

As already indicated in figure 3.8, within the model the total number of photons that escape the crystal can be expressed as sum of the fraction of non-absorbed blue light $(1 - F_{abs}) \cdot L_b(E_{part}, T)$ and 100% of the produced green light $L_g(E_{part}, T)$. A detailed discussion of the temperature-dependent light generation on the basis of this model is presented in chapter III/3.2.

The mathematical formulation of the excitation and de-excitation processes of the populations of blue and green STEs, respectively, in combination with the initial "extrinsic" creation process of blue STEs (discussed in section III/3.1.2), is given by :

Excitation Processes of Blue STEs

$$\begin{aligned}\left[\frac{\partial n_b(\mathbf{x},t)}{\partial t}\right]_{ex} &= n_{bSTE}^{form\,mig:g\to b}(\mathbf{x},t) + n_{bSTE}^{form\,e^-STH}(E_{part},T,\mathbf{x},t) = \\ &= +\frac{1}{\tau_{\text{mig, g}\to\text{b}}(T)} \cdot n_g(\mathbf{x},t) + \\ &\quad + \Theta(t) \cdot \frac{(1 - F_{e^-trap}) \cdot \rho_{ioniz}(E_{part},\mathbf{x})}{2.35 \cdot E_{gap}} \cdot \left[(1 - F_{dr}(T)) + \frac{F_{dr}(T)}{\tau_{dr}(T)} \cdot e^{-\frac{t}{\tau_{dr}(T)}}\right]\end{aligned} \tag{3.77}$$

De-Excitation Processes of Blue STEs

$$\begin{aligned}\left[\frac{\partial n_b(\mathbf{x},t)}{\partial t}\right]_{de-ex} &= \left[\frac{\partial n_b(\mathbf{x},t)}{\partial t}\right]_{rad} + \left[\frac{\partial n_b(\mathbf{x},t)}{\partial t}\right]_{non-rad} + \left[\frac{\partial n_b(\mathbf{x},t)}{\partial t}\right]_{mig} + \\ &+ \left[\frac{\partial n_b(\mathbf{x},t)}{\partial t}\right]_{d-d} = \\ &= -\left(\frac{1}{\tau_{rb}(T)} + \frac{1}{\tau_{nrb}(T)} + \frac{1}{\tau_{\text{mig, b}\to\text{g}}(T)}\right)\cdot n_b(\mathbf{x},t) - \\ &- \frac{2\cdot\pi^{\frac{3}{2}}}{3}\cdot\frac{R^3_{d-d}(T)}{\sqrt{\tau_{ltb}(T)\cdot t}}\cdot n_b^2(\mathbf{x},t)\end{aligned} \tag{3.78}$$

Excitation Processes of Green STEs

$$\begin{aligned}\left[\frac{\partial n_g(\mathbf{x},t)}{\partial t}\right]_{ex} &= n_{gSTE}^{form\,mig:b\to g}(\mathbf{x},t) + n_{gSTE}^{form\,abs}(\mathbf{x},t) = \\ &= +\left(\frac{1}{\tau_{\text{mig, b}\to\text{g}}(T)} + F_{abs}\cdot\frac{1}{\tau_{rb}(T)}\right)\cdot n_b(\mathbf{x},t)\end{aligned} \tag{3.79}$$

De-Excitation Processes of Green STEs

$$\begin{aligned}\left[\frac{\partial n_g(\mathbf{x},t)}{\partial t}\right]_{de-ex} &= \left[\frac{\partial n_g(\mathbf{x},t)}{\partial t}\right]_{rad} + \left[\frac{\partial n_g(\mathbf{x},t)}{\partial t}\right]_{non-rad} + \left[\frac{\partial n_g(\mathbf{x},t)}{\partial t}\right]_{mig} = \\ &= -\left(\frac{1}{\tau_{rg}(T)} + \frac{1}{\tau_{nrg}(T)} + \frac{1}{\tau_{\text{mig, g}\to\text{b}}(T)}\right)\cdot n_g(\mathbf{x},t)\end{aligned} \tag{3.80}$$

For the definitions and mathematical formulations of the different parameters, see the respective subsections of the current section and section III/3.1.2 (for the "extrinsic" creation process for blue STEs).

3.1.4 Complete Model for the Generation, Excitation and De-Excitation of STEs

In figure 3.9, a graphical representation of the complete model for STE evolution is shown, including all processes considered for the generation, excitation and de-excitaiton of STEs in $CaWO_4$.

Definition of the Lifetimes of Blue and Green STEs

On the basis of this summary, the concept of the lifetimes of STEs can finally be defined. As already indicated in the discussion of the Förster interaction (section III/3.1.3), the definition of two different *lifetimes* for those STEs which experience the Förster interaction is required:

- The *intrinsic lifetime* of STEs, $\tau_{ltb}(T)$ and $\tau_{ltg}(T)$, respectively, is defined as the lifetime of STEs due to all de-excitation mechanisms *except* the Förster interaction, i.e., the lifetime a single STE in $CaWO_4$ would exhibit due to the de-excitation by radiative, non-radiative and migration processes with no other STE present with which an interaction would be possible. This intrinsic lifetime is also the one that

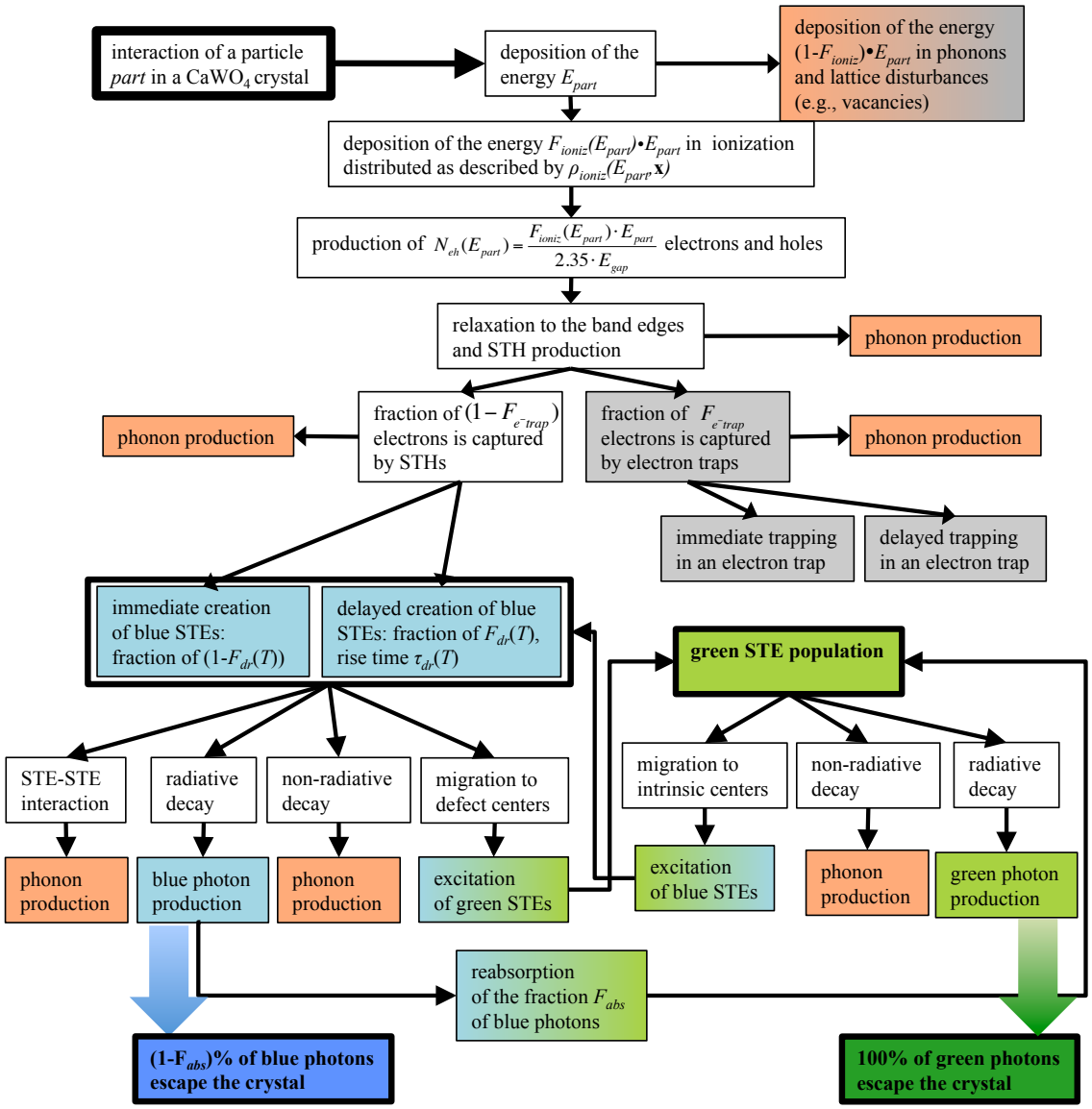

Figure 3.9: Complete model of the STE generation, excitation and de-excitation in $CaWO_4$. Red boxes indicate processes in which phonons are produced. Grey boxes correspond to processes in which energy is stored in the lattice in the form of lattice disturbances (vacancies, trapped electrons and single STHs). Blue boxes correspond to blue STEs and photons. Green boxes indicate green STEs and photons.

has to be used for the calculation of the Förster interaction (see definition and explanation of the Förster interaction in section III/3.1.3).

$$\frac{1}{\tau_{ltb}(T)} = \frac{1}{\tau_{rb}(T)} + \frac{1}{\tau_{nrb}(T)} + \frac{1}{\tau_{\mathrm{mig,\ b\to g}}(T)} \tag{3.81}$$

$$\frac{1}{\tau_{ltg}(T)} = \frac{1}{\tau_{rg}(T)} + \frac{1}{\tau_{nrg}(T)} + \frac{1}{\tau_{\mathrm{mig,\ g\to b}}(T)} \tag{3.82}$$

- The *effective lifetime* of STEs is defined as the time-dependent lifetime of STEs

including the the time-dependent Förster interaction. Due to the time dependency of the impact of the Förster interaction, this lifetime can no longer be expressed mathematically as a simple sum of individual processes, but is the result of the combined impact of all considered processes on the population of STEs, including the Förster interaction. This concept of an *extrinsic* lifetime is introduced to clarify the impact of the Förster interaction on the lifetime of STEs.

As can be seen from equation 3.80, for green STEs, the definition of the *intrinsic* lifetime (equation 3.82) contains *all* de-excitation mechanisms considered for green STEs. Hence, for green STEs, this *intrinsic* lifetime equals their *effective* lifetime. It should be noted that, due to the different excitation mechanisms that are included in the model, also the effective lifetimes do not correspond to the total time dependency of the STE populations. This dependency is described by the set of solutions of the complete differential equations for the STE populations. The final differential equations for the STE populations are presented in the following, their solutions will be discussed in chapter III/3.2.

From the definition of the intrinsic lifetimes (equations 3.81 and 3.82), it can already be recognized that the intrinsic lifetime of a STE population can never be larger than any of the times describing the respective radiative, non-radiative and migration processes. This implies, e.g., that the intrinsic lifetime of green STEs always has to be shorter than the migration time of green to blue STEs: $\tau_{ltg}(T) \leq \tau_{\text{mig, b}\rightarrow\text{g}}(T)$. As discussed in section III/3.1.3, the migration time of green STEs can be calculated for any temperature,. Hence, an upper limit for the green STE lifetime can already be expressed. In table 3.5, values of the migration time of green STEs to blue STEs, $\tau_{\text{mig, g}\rightarrow\text{b}}(T)$, calculated with equation 3.66 (section III/3.1.3) for a few example temperatures T are given:

T [K]	300	100	20	10	5
$\tau_{\text{mig, g}\rightarrow\text{b}}(T)$	2.72ns	4.63ns	114ns	6.32μs	18.7ms

Table 3.5: Examples of the migration time for green STEs to intrinsic centers for different temperatures T: As explained in the main text, at the respective temperatures, these values (calculated with equation 3.66, section III/3.1.3) constitute upper limits for the lifetime of green STEs.

Combining these considerations with the observation that, at any temperature, a considerable amount of green light is produced (see, e.g., section III/3.2.1), already allows to draw a conclusion concerning the order of magnitude of the radiative recombination time of green STEs: The fact that, at any temperature, a considerable amount of green scintillation light is produced implies that, at any temperature, a considerable number of green STEs decay radiatively. This circumstance, however, indicates, that the radiative decay time of green STEs has to be roughly of the same order of magnitude as the migration time of green STEs or even faster as the radiative decay has to compete with the process of migration. Hence, this implies, that the radiative decay time at, e.g., room temperature has to be of the order of a few to a few tens of ns or, e.g., at 20K has to be of the order of a few to a few hundreds of ns. Such a short radiative decay time, however, is in perfect agreement with the model for the electronic structure of defect centers (see appendix B.4.1). This model predicts a considerably shorter radiative decay time for green STEs than for blue STEs (as will be shown in section III/5.2.2, for blue STEs, a lifetime and radiative decay time at room temperature (and at 20K) of a few to a few tens of μs (a few tens of μs at 20K) can be determined).

Definition of the Branching Ratios of Blue and Green STEs

From the definitions of the *intrinsic* lifetimes of blue and green STEs, the different branching ratios (radiative, migrating and non-radiative) of the blue and green STE populations can be defined (compare, e.g., [91]). The radiative branching ratio $F_{b\,rad}(T)$ of blue STEs, for example, is defined as the fraction of blue STEs that decays radiatively. These fractions are, of course, temperature dependent as they are determined by the respective ratio of the corresponding process time (e.g., $\tau_{rb}(T)$ for the radiative recombination of blue STEs) to the total intrinsic lifetime of the respective STE population (e.g., $\tau_{ltb}(T)$ for the blue STE population). Hence, the branching ratios can be calculated by:

$$F_{b\,rad}(T) = \frac{\tau_{ltb}(T)}{\tau_{rb}(T)} \qquad \text{and} \qquad F_{g\,rad}(T) = \frac{\tau_{ltg}(T)}{\tau_{rg}(T)} \tag{3.83}$$

$$F_{b\,mig}(T) = \frac{\tau_{ltb}(T)}{\tau_{\text{mig, b}\to\text{g}}(T)} \qquad \text{and} \qquad F_{g\,mig}(T) = \frac{\tau_{ltg}(T)}{\tau_{\text{mig, g}\to\text{b}}(T)} \tag{3.84}$$

$$F_{b\,nrad}(T) = \frac{\tau_{ltb}(T)}{\tau_{nrb}(T)} \qquad \text{and} \qquad F_{g\,nrad}(T) = \frac{\tau_{ltg}(T)}{\tau_{nrg}(T)} \tag{3.85}$$

The branching ratios defined in this way denote, e.g., the efficiency with which a blue STE generates a blue photon. As the defined branching ratios cover all possibilities of de-excitation for the blue and green STEs, respectively, that are considered in the model, the natural condition, that the sum of all these fractions (for blue and for green STEs, respectively) equals unity is complied.

Differential Equations for the Populations of Blue and Green STEs

With the definition of the *intrinsic* lifetimes of blue and green STEs, the complete set of differential equations describing the temporal evolution of the blue and green STE populations within the model can be written as:

$$\begin{aligned}\frac{\partial n_b(\mathbf{x},t)}{\partial t} = & -\frac{1}{\tau_{ltb}(T)}\cdot n_b(\mathbf{x},t) - \frac{2\cdot\pi^{\frac{3}{2}}}{3}\cdot\frac{R_{d-d}^3(T)}{\sqrt{\tau_{ltb}(T)\cdot t}}\cdot n_b^2(\mathbf{x},t) + \frac{1}{\tau_{\text{mig, g}\to\text{b}}(T)}\cdot n_g(\mathbf{x},t) + \\ & + n_{bSTE}^{form\,e^-STH}(E_{part},T,\mathbf{x},t)\end{aligned} \tag{3.86}$$

$$\frac{\partial n_g(\mathbf{x},t)}{\partial t} = -\frac{1}{\tau_{ltg}(T)}\cdot n_g(\mathbf{x},t) + \left(\frac{1}{\tau_{\text{mig, b}\to\text{g}}(T)} + F_{abs}\cdot\frac{1}{\tau_{rb}(T)}\right)\cdot n_b(\mathbf{x},t) \tag{3.87}$$

where the formation process of blue STEs, $n_{bSTE}^{form\,e^-STH}(E_{part},T,\mathbf{x},t)$, due to the recombination of electrons and STHs is not displayed explicitly to underline that this process describes the generation of STEs due to the "extrinsic" process of electron-STH pair recombination (extrinsic to the STE population) as well as to improve the readability of the equation.

Regarding this system of coupled differential equations, already several observations can be made:

- The Förster interaction is the only process considered that depends on the density of the STE populations. Neglecting the Förster interaction, the same set of differential equations (including all other processes considered) can be used for the integral numbers of STEs, $N_b(t)$ and $N_g(t)$, instead of their densities $n_b(\mathbf{x},t)$ and $n_g(\mathbf{x},t)$.

- The Förster interaction is the only mechanism considered that induces a difference in the temporal evolution of the STE populations for different interacting particles (which produce different densities of STEs): The higher the initially produced STE density, the larger the impact of the Förster interaction on the temporal evolution of the STE populations. Hence, for short times t after the energy deposition, it can be deduced that, the larger the initially produced STE densities, the faster and the more efficient the non-radiative decay of STEs via the Förster interaction. For long times t after the energy deposition, the effective lifetime of the STEs converges against the temporal evolution of STEs in absence of the Förster interaction, independently of the initially created STE density.

- The Förster interaction is the only de-excitation mechanism considered that causes a difference in the fraction of radiatively decaying STEs for different STE densities as the radiative process has to compete with the Förster interaction.

- It is assumed that, due to the low defect density, green STEs can only be excited by migration or radiative decay of blue STEs (compare section III/3.1.2). Hence, the influence of the Förster interaction on the lifetime and radiative branching ratio of blue STEs also leads to a reduction of excited green STEs. As the coupling of the two STE populations defined by the differential equations 3.86 and 3.87 is linearly dependent on the density of the two STE populations, it can be deduced that changes in the blue STE population induced by the Förster interaction affect the green STE population correspondingly (linearly propagated).

In section III/3.2, the system of coupled, inhomogeneous, non-linear differential equations will be used to determine a temperature-dependent model for the scintillation-light generation in $CaWO_4$ for different interacting particles depositing different amounts of energies.

3.2 Scintillation-Light Generation and Quenching in $CaWO_4$

3.2.1 Temperature-Dependent Light Yield and Spectral Composition

As a basis for the quantitative discussion of the temperature dependency of the amount of generated light and its spectral composition, the measurement of wavelength-dependent scintillation-light spectra reported in [54] are used. In [54], excitation was performed with ~ 30eV photons which are absorbed within a thin surface layer, i.e., in a comparably compact volume. Hence, it can be expected that STEs close to each other are created where the extent of the density of STEs depends on the focussing and intensity of the incident photon beam[30].

As discussed in section III/3.1.4, the spectral composition of the scintillation light and, thus, also its change with temperature are not expected to depend on the mode of primary excitation. The change in the total light yield with temperature, however, is expected to depend on the mode of primary excitation. In addition, it should be noted that the blue-to-green light ratio as well as the absolute amount of scintillation light are supposed to depend on the density of defect centers and are, thus, crystal-dependent parameters.

[30] The chosen settings of the focussing and beam intensity are not stated in [54] as, for the investigations performed there, the values of these parameters were not relevant.

Hence, the discussion of the temperature dependency of the spectral composition as well as of the amount of scintillation light generated on the basis of the measurements performed in [54] can only be adopted qualitatively for other crystals and other modes of excitation.

The results of the measurements of the light yield and its spectral composition obtained in [54] are displayed in figure 3.10. In [54], the spectral decomposition was performed by fitting the sum of two Gaussians to the wavelength spectra recorded for temperatures between 8K and 302K. It should be noted that the $CaWO_4$ crystal used there (denoted crystal Conrad), contained many defect centers leading to a rather large amount of green scintillation light compared to other $CaWO_4$ crystals [54]. In addition to the results from [54] (black, blue and green markers), six temperature regions in which changes in the temperature dependencies of the depicted parameters occur are indicated by dashed, vertical red lines (labeled with roman numbers, same regions for panel a and b).

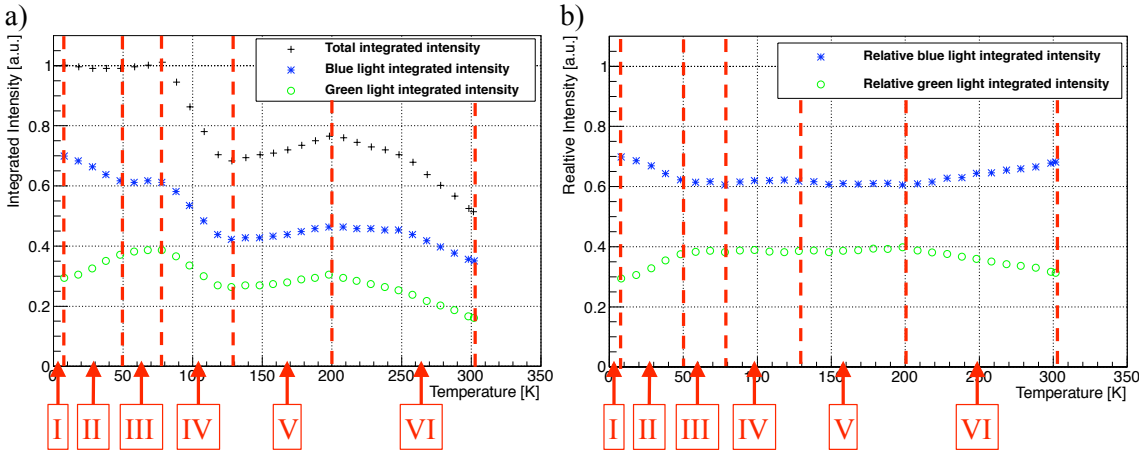

Figure 3.10: Temperature dependency of the integral intensity and of the spectral composition of the scintillation-light spectra of crystal Conrad for temperatures between 8K and 302K: In figure a), the integrated intensities (scaled to unity for the 8K measurement) of the total spectrum (black crosses), the intrinsic component (blue asterisks) and the extrinsic component (green circles) are depicted. In figure b), the same data, as relative intensities of the intrinsic (blue asterisks) and extrinsic (green circles) component are displayed (data adopted from figure 5.17 in [54].). In addition to the results, six temperature regions in which changes in the temperature dependencies of the depicted parameters (integrated intensity and relative intensities of green and blue light) occur are indicated by dashed, vertical red lines (labeled with roman numbers, same regions for panel a and b).

Influence of the Different Processes Included in the Model

Within the model developed here, the indicated temperature regions and changes of the total integrated light yield as well as of the spectral composition are identified with temperature-dependent influences of different processes onto the scintillation-light production, i.e., onto the temporal evolution of the STE populations. Starting at very low temperatures ($T \lesssim 5$K), for increasing temperature, in every temperature region, other processes (e.g., STE migration) are assumed to become possible, due to the increase in thermal energy, allowing to overcome the potential-energy barriers of the different processes:

- Region I (0K to $\sim$ 5K): Only radiative recombination from the energetically lower-lying radiative levels (for blue STEs τ_{L1b}, for green STEs τ_{L1g}, see section III/3.1.3) as well as the Förster interaction (for blue STEs R_{d-d}, see section III/3.1.3) are possible. Excitation of green STEs and, hence, green photon production is only caused by absorption of the fraction F_{abs} of blue photons (see section III/3.1.3). The integrated total intensity of scintillation light depends on the number of STEs produced in the primary energy-deposition process, i.e., on the number of electron-STH pairs that recombine to STEs, $N_{bSTE}^{form\,e^-STH}(E_{part})$ (see section III/3.1.2), and on the impact of the Förster interaction controlled by the produced ionization density, $\rho_{ioniz}(E_{part}, \mathbf{x})$ (see section III/3.1.2).

- Region II ($\sim$ 5K to $\sim$ 50K): With increasing temperature, first the migration from blue to green STEs becomes possible ($\tau_{\mathrm{mig,\ b\to g}}(T)$ with an energy barrier $\Delta E_{bSTE,mig} = 4.5$meV, see section III/3.1.3) leading to an increase of excited green STEs and, hence, to an increase of produced green light. Still, the only non-radiative process is the Förster interaction of blue STEs. Therefore, the integrated total intensity of light stays roughly the same. For further increasing temperature, also migration from green to blue STEs ($\tau_{\mathrm{mig,\ g\to b}}(T)$ with an energy barrier $\Delta E_{gSTE,mig} = 6.9$meV, see section III/3.1.3) becomes possible, so that, at $\sim$ 50K, a steady state of the efficiencies of the two migration processes is reached. Within this temperature region, also the radiative recombination from the respective second emitting energy levels of blue and green STEs becomes possible leading to a decrease of the effective radiative decay times[31] ($\tau_{rb}(T)$, $\tau_{rg}(T)$ with energy barriers D_b, D_g of the order of 1meV, see section III/3.1.3).

- Region III ($\sim$ 50K to $\sim$ 70K): The respective radiative recombination and migration processes of blue and green STEs become faster with roughly the same temperature dependency so that the steady state of the efficiencies of the migration processes from blue to green and green to blue STEs persists. Therefore, no changes of the integrated amount of light nor of its spectral composition are observed.

- Region IV ($\sim$ 70K to $\sim$ 130K): Onset of the non-radiative recombination process of green STEs ($\tau_{nrg}(T)$ with an energy barrier ΔE_g, see section III/3.1.3). Therefore, the total integrated intensity of the scintillation light decreases. The relative intensities of blue and green light roughly stay the same. Hence, still a steady state of the efficiencies of the migration processes is expected to persist. Due to these migration processes, the additional recombination process for green STEs (non-radiative decay) analogously affects the evolution of the blue STE population.

- Region V ($\sim$ 130K to $\sim$ 200K): A weak increase in the integrated total light intensity can be observed. Within the developed model, this increase can either be explained by a further decreasing radiative decay time which could induce an increasing amount of STEs decaying radiatively or by a decrease of the Förster radius within this temperature region (see section III/3.1.3) which would also lead to an enhanced radiative efficiency. In fact, also a combination of both effects is possible. In addition, it can be seen that the relative intensities of blue and green light roughly stay the same. Therefore, still a steady state of the efficiencies of the migration processes is expected to persist.

[31] This fact can, e.g., be recognized from figure 2.13 in section III/2.2.3, where it can be seen that the slow decay time of $CaWO_4$ starts to decrease for temperatures $T \gtrsim 10$K.

- Region VI ($\sim$ 200K to $\sim$ 300K): Onset of the non-radiative recombination of blue STEs ($\tau_{nrb}(T)$ with an energy barrier $\Delta E_g = 0.32$eV, see section III/3.1.3), leading to a decreasing integrated amount of light. In addition, the onset of this additional recombination process leads to a decrease in the lifetime of blue STEs. Due to the small activation energies of the migration processes, it is assumed that the migration times start to saturate, i.e., to converge against their final values within this temperature region. The same can be assumed for the radiative decay times of blue and green STEs as well as for the non-radiative decay time of the green STE population. Therefore, the decrease in the lifetime of blue STEs leads to an effective decrease of the efficiency in migration of blue to green STEs whereas the efficiency of the migration of green to blue STEs is assumed to stay roughly constant. This leads to a decreasing efficiency in exciting green STEs via migration which results in a decreasing relative intensity of green light.

In addition to the features of the data presented in figure 3.10, in figure 2.14 (in section III/2.2.4, temperature dependent light-yield measurements using ^{241}Am α-particle excitation from [46]), another feature can be recognized: At $\sim$ 20K, the total integrated light yield exhibits a weakly pronounced, global maximum. Within the model developed here, this small excess and the slightly decreasing light yield for temperatures $T \lesssim 20$K can be connected to the diffusion length of blue STEs at these temperatures. It is suggested that, below 20K, the diffusion length of the blue-to-blue STE migration process ($l_{\text{diff, b}}(T)$ and $\tau_{\text{mig, b}\to\text{b}}(T)$, compare section III/3.1.3) becomes smaller than the Förster radius at this temperature. This would imply that blue STEs can no longer efficiently escape the STE-STE interaction by migration and that the influence of this process increases until no migration at all is possible ($T \lesssim 5$K, see section III/2.1.5). Hence, within the model, for temperatures $T \lesssim 5$K, neither for the integrated total intensity of the scintillation light nor for the spectral composition of the scintillation light any temperature-dependency is expected[32].

It can be seen that, within the developed model, the two regions of major decrease of the integrated amount of light (for increasing temperature) are characterized by the impact of the non-radiative recombination channels for green STEs (region IV) and blue STEs (region VI). The reason why the non-radiative decay of green STEs is assumed to start at lower temperatures than the one of blue STEs is that, due to the intrinsic deformation of defect centers the thermal activation energy needed for green STEs to recombine non-radiatively can be expected to be smaller. For a more detailed discussion of the expected influence of the deformation of the unexcited defect-center unit-cell on its electronic structure and, hence, on the heights of the energy barriers connected to the various recombination processes of green STEs, see appendix B.4.1.

Shape and Decomposition of the Wavelength Spectrum

From the discussion of the temperature-dependent composition of the scintillation light, it can be seen that, at any temperature T within the considered range, the total wavelength

[32] The only parameter that could still induce a change is the Förster radius. However, as the temperature dependency of the Förster radius is based on the radiative branching ratio (which is expected to be unity at these temperatures) and the phonon interaction of emitting and absorbing energy levels of the STEs (widths of the emission and absorption spectra), which is expected to have ceased at such low temperatures, no significant change of the Förster radius below 5K is expected.

spectrum $S_{em,tot}(T,\lambda)$ of the emitted scintillation light of $CaWO_4$ is describable by the sum of two individual sub-spectra, $S_{em,b}(T,\lambda)$ (blue scintillation light) and $S_{em,g}(T,\lambda)$ (green scintillation light). As discussed in section III/2.2.2, these individual sub-spectra are strongly broadened even at very low temperatures and exhibit additional broadening for increasing temperature due to the electron-phonon coupling in the $CaWO_4$ crystal lattice. In literature, often a mathematical model using the sum of two Gaussians, one for each sub-spectrum, to describe the shape of the total wavelength spectrum can be found (see, e.g., [54] and references therein).

However, within the developed model, it is assumed that a large fraction of the green scintillation light is generated by reabsorption of produced blue photons at green scintillation centers (see section III/3.1.4). In general, however, the probability of reabsorption of the intrinsic (blue) light by extrinsic states (the defect centers within the band gap) of a light-emitting material, can be expected to be larger for higher-energetic photons in comparison to lower-energetic photons (of the intrinsic, blue light spectrum) [99]. The pronounced absorption of higher-energetic photons of the intrinsic light, however, leads to the creation of a sharper cutoff at the short wavelength side (larger energies) of the intrinsic scintillation-light spectrum in comparison to its long wavelength side (smaller energies) [99]. Therefore, within the developed model, the shape of the blue scintillation-light spectrum cannot be described by a symmetric Gaussian distribution. To mathematically model the expected asymmetric shape of the blue scintillation-light spectrum within the model, an exponentially modified Gaussian, i.e., a convolution of a Gaussian distribution with a truncated exponential function, is used:

$$\begin{aligned} S_{em,b}(T,\lambda) &= \left(\frac{A_b(T)}{\sqrt{2\cdot\pi}\cdot\sigma_b(T)} \cdot e^{-\frac{(\lambda-\mu_b(T))^2}{2\cdot\sigma_b^2(T)}} \right) * \left(\Theta(\lambda-\mu_b(T)) \cdot \frac{1}{\lambda_{abs}(T)} \cdot e^{-\frac{\lambda-\mu_b(T)}{\lambda_{abs}(T)}} \right) \\ &= \frac{A_b(T)}{2\cdot\lambda_{abs}(T)} \cdot e^{-\frac{\lambda-\mu_b(T)}{\lambda_{abs}(T)}} \cdot e^{\left(\frac{\sigma_b(T)}{\sqrt{2}\cdot\lambda_{abs}(T)}\right)^2} \cdot \left\{ 1 + erf\left(\frac{\lambda-\mu_b(T)}{\sqrt{2}\cdot\sigma_b(T)} - \frac{\sigma_b(T)}{\sqrt{2}\cdot\lambda_{abs}(T)} \right) \right\} \end{aligned} \tag{3.88}$$

with the parameters $A_b(T)$, $\sigma_b(T)$ and $\mu_b(T)$ corresponding to the intensity, the width and the mean of the Gaussian. The parameter $\lambda_{abs}(T)$ corresponds to the decay constant of the exponential and is used to model the asymmetry of the spectrum induced by the reabsorption process. It has to be noted that equation 3.88 only offers a mathematical model for the shape of the spectrum and that the parameters appearing in equation 3.88 do not reflect the underlying physical quantities. For example, the parameter $\mu_b(T)$ does not correspond to the maximum or the mean of the blue light component.

For the physical interpretation of the shape of the total blue spectrum, three parameters can be used:

- The integral of the complete function, $I_b(T)$ (which is given by the intensity $A_b(T)$ of the Gaussian[33]).
- The mean of the complete function[34] which is given by $m_b(T) = \mu_b(T) + \lambda_b(T)$. The

[33] This identity is caused by the chosen normalization of the Gaussian and the exponential.

[34] The mean of an exponentially modified Gaussian can, in general, be calculated as the sum of the mean of the Gaussian μ and of the parameter describing the exponential decay λ. The mean, $m = \mu + \lambda$, corresponds to the center of gravity of the distribution.

mean of the complete function (equation 3.88) corresponds to the mean wavelength of the blue photons, i.e., using $\overline{E}_{Pb}(T) = \frac{h \cdot c}{m_b(T)}$ for the mean energy of the blue photons.

- The width of the complete function delivered by the square root of the variance of the complete function, $\sigma_{tot,b}(T) = \sqrt{\mathrm{Var}_{tot}(S_{em,b}(T,\lambda))} = \sqrt{\sigma_b^2(T) + \lambda_b^2(T)}$.

The lower energetic (green) scintillation light generated by the extrinsic (defect) centers, on the other hand, is assumed to be able to traverse the $CaWO_4$ crystal undisturbed. Hence, within the model, it is assumed that, in the $CaWO_4$ crystal, no absorption centers for green photons exist (compare section III/3.1.3). Therefore, in the following, the green scintillation light spectrum is mathematically modeled by a Gaussian distribution:

$$S_{em,g}(T,\lambda) = \frac{A_g(T)}{\sqrt{2 \cdot \pi} \cdot \sigma_g(T)} \cdot e^{-\frac{(\lambda - \mu_g(T))^2}{2 \cdot \sigma_g^2(T)}} \tag{3.89}$$

with the parameters $A_g(T)$, $\sigma_g(T)$ and $\mu_g(T)$ corresponding to the intensity, the width and the mean of the Gaussian. The mean of the green light component corresponds to the mean of the Gaussian $m_g(T) = \mu_g(T)$ and the width of the complete green spectrum simply corresponds to the 1-σ width of the Gaussian distribution $\sigma_{tot,g}(T) = \sigma_g(T)$. The integral of the green light component corresponds to the intensity of the Gaussian $I_g(T) = A_g(T)$.

Therefore, within the developed model, the complete function $S_{em,tot}(T,\lambda)$ used to described the shape of the scintillation-light spectrum of $CaWO_4$ is given by the sum of the blue and green sub-spectra (see equations 3.88 and 3.89, respectively):

$$S_{em,tot}(T,\lambda) = S_{em,b}(T,\lambda) + S_{em,g}(T,\lambda) \tag{3.90}$$

In section III/5.1, wavelength spectra of $CaWO_4$ scintillation light recorded within this work (at $\sim$ 300K and $\sim$ 20K) are analyzed using the developed mathematical model. From this analysis it can be seen that the most significant change of the shape of the spectra with temperature is a variation of the width of the spectra with temperature. From the measurements performed in [51] covering a temperature region from 8K to 300K, it can be seen that for temperatures $T \lesssim 50$K, the width of the total spectrum remains constant (within the measurement uncertainties in [51]). For higher temperatures, the width of the total spectrum increases. Following [51] (and references therein), the temperature-dependency of the width of the emission spectrum of $CaWO_4$ can be modeled using a formula describing the impact of the temperature-dependent electron-phonon coupling in $CaWO_4$. As, within the model developed here, the two sub-spectra of the blue and the green scintillation light are regarded separately, this relationship is applied to each of the individual sub-spectra separately. The dependency of the widths of the spectra on temperature T and on the energy of the involved phonons $E_{phonon}^{CaWO_4}$ can be described by the following formulas (compare [51]):

$$\sigma_{tot,b}(T) = \sigma_{tot,b}^0 \cdot \sqrt{\coth\left(\frac{E_{phonon}^{CaWO_4}}{2 \cdot k_b \cdot T}\right)} \tag{3.91}$$

$$\sigma_{tot,g}(T) = \sigma_{tot,g}^0 \cdot \sqrt{\coth\left(\frac{E_{phonon}^{CaWO_4}}{2 \cdot k_b \cdot T}\right)} \tag{3.92}$$

where $\sigma^0_{tot,b} = \sigma_{tot,b}(T = 0\text{K})$ and $\sigma^0_{tot,g} = \sigma_{tot,g}(T = 0\text{K})$ correspond to the widths of the respective sub-spectra at 0K. The energy and, hence, the mode of the phonons interacting primarily with the respective emitting STEs can be determined to be the same for blue and green STEs (see section III/5.1, analysis of measurements performed within the present work). The energy of the interacting phonon mode determined within the present work amounts to $\sim$ 43meV for both, the blue and the green sub-spectrum, respectively. This value is in good agreement with the values obtained in [51] for the complete spectrum of two investigated $CaWO_4$ crystals ($\sim$ 42meV and $\sim$ 45meV, respectively). This phonon mode can be identified with an internal vibration mode of the $[WO_4]^{2-}$ tetrahedra [51] (see, e.g., [50]). This identification supports the interpretation of the temperature-dependent broadening as a process induced by the interaction of the electrons of the STEs (at $[WO_4]^{2-}$ complexes) with the phonons of the lattice.

In addition, from the analysis of the measurements performed within this work (section III/5.1), it can be seen that the mean values of the blue and the green sub-spectra show only a minor temperature dependency. This is in good agreement with measurements in [51], where the temperature-dependent change of the mean wavelength of the complete scintillation-light spectrum of two $CaWO_4$ crystals is analyzed: For a temperature change from room temperature down to 8K, a variation of the peak position of the total spectrum by only $\sim$ 1% to 3% (dependent on the crystal) is observed. In addition, it can be seen that, for temperatures below $\sim$ 50K, the peak position remains completely constant (within the measurement uncertainties in [51]).

3.2.2 Scintillation-Light Generation

Within the developed model for the evolution of the STE population in $CaWO_4$ (section II/3.1), the solutions $n_b(\mathbf{x}, t)$ and $n_g(\mathbf{x}, t)$ of the system of differential equations (equations 3.86 and 3.87 in section III/3.1.4) describe the temporal evolution of the STE populations produced by an interacting particle depositing the energy E_{part} at temperature T. The temporal evolution of the produced scintillation light that escapes the crystal, i.e., the decay-time spectrum of the photons $P_{tot}(E_{part}, T, t)$, is then given by the sum of the decay-time spectra of the green and blue photons that escape the crystal. As can be seen from the overview of the model for the STE evolution, no possibility for the absorption of green photons within a $CaWO_4$ crystal is included in the model. Hence, it is expected that all of the green photons produced, $P_g(E_{part}, T, t)$, escape the crystal. The number of blue photons escaping the crystal, $P_b(E_{part}, T, t)$, corresponds to the fraction of blue photons produced that is not absorbed at defect centers ($(1 - F_{abs})$, compare figure 3.8 in section III/3.1.4). The decay-time spectra of the blue and the green photons, $P_b(E_{part}, T, t)$ and $P_g(E_{part}, T, t)$, can be calculated as the integral of the radiatively decaying density of the blue and green STE populations, respectively, over the complete excited volume V_{ex}:

$$P_{tot}(E_{part}, T, t) = P_b(E_{part}, T, t) + P_g(E_{part}, T, t) \tag{3.93}$$

$$P_b(E_{part}, T, t) = (1 - F_{abs}) \cdot \int\limits_{V_{ex}} \frac{1}{\tau_{rb}(T)} \cdot n_b(\mathbf{x}, t) d\mathbf{x} \tag{3.94}$$

$$P_g(E_{part}, T, t) = \int\limits_{V_{ex}} \left[\frac{1}{\tau_{rg}(T)} \cdot n_g(\mathbf{x}, t) \right] d\mathbf{x} \tag{3.95}$$

The complete number of photons $P_{tot}(E_{part},T) = P_b(E_{part},T) + P_g(E_{part},T)$ escaping the crystal for a particle depositing the energy E_{part} (at temperature T) is then simply given by the integral in time over the decay-time spectrum of the produced photons:

$$P_{tot}(E_{part},T) = \int_{-\infty}^{+\infty} \left[P_b(E_{part},T,t) + P_g(E_{part},T,t)\right] dt = \int_{-\infty}^{+\infty} P_{tot}(E_{part},T,t)dt \quad (3.96)$$

In addition, the ratio of the generated (and escaping) number of blue-to-green photons, $R_{b-g}(T)$, can be expressed:

$$R_{b-g}(T) := \frac{P_b^{nq}(E_{part},T)}{P_g^{nq}(E_{part},T)} \quad (3.97)$$

As discussed in section III/3.1.4, this ratio is expected to be independent of the used mode of excitation, i.e., to be independent of the density of generated STEs and, thus, also independent of the energy deposited by the interacting particle. Therefore, it is assumed, as indicated in equation 3.97, that the ratio of the numbers of escaping blue-to-green photons only depends on the temperature T (for the justification of this assumption, see section III/3.2.4).

In analogy to the decay-time spectra and numbers of photons produced, the decay-time spectra $L_b(E_{part},T,t)$ and $L_g(E_{part},T,t)$ as well as the complete amount of blue and green scintillation light $L_{tot}(E_{part},T) = L_b(E_{part},T) + L_g(E_{part},T)$ (in units of energy, [eV]) can be calculated. To convert the number of blue and green photons into energy emitted as scintillation light, the mean energies of blue and green photons (see section III/3.2.1), $\overline{E}_{Pb}(T)$ and $\overline{E}_{Pg}(T)$, respectively, can be used. The scintillation-light decay-time spectra and the integrated amount of scintillation light escaping the crystal can be expressed as:

$$\begin{aligned}
L_{tot}(E_{part},T,t) &= L_b(E_{part},T,t) + L_g(E_{part},T,t) \\
L_b(E_{part},T,t) &= \overline{E}_{Pb}(T) \cdot (1 - F_{abs}) \cdot \int_{V_{ex}} \frac{1}{\tau_{rb}(T)} \cdot n_b(\mathbf{x},t)d\mathbf{x} \\
L_g(E_{part},T,t) &= \overline{E}_{Pg}(T) \cdot \int_{V_{ex}} \frac{1}{\tau_{rg}(T)} \cdot n_g(\mathbf{x},t)d\mathbf{x} \\
L_{tot}(E_{part},T) &= \int_{-\infty}^{+\infty} \left[L_b(E_{part},T,t) + L_g(E_{part},T,t)\right] dt \\
&= L_b(E_{part},T) + L_g(E_{part},T)
\end{aligned} \quad (3.98)$$

In the following, most of the times, the decay-time spectra of photons, e.g., $P_b(E_{part},T,t)$, the ratio of the numbers of blue-to-green photons $R_{b-g}(T)$ as well as the integrated total amount of the scintillation light in energy, $L_{tot}(E_{part},T)$, will be used as these are the parameters often determined in experiments: A measurement of the decay-time spectrum performed with a photomultiplier delivers the relation of photons per time. From a measurement of the wavelength spectrum of the scintillation light with a spectrometer, the ratio of the numbers of blue-to-green photons can be determined. And a light-yield measurement often directly specifies the integrated amount of detected energy.

Hence, it can be seen that, both, the temperature-, particle- and crystal[35]-dependent total amount $L_{tot}(E_{part}, T)$ as well as the decay-time spectrum of photons $P_{tot}(E_{part}, T, t)$ can be described within the model developed here using the same set of parameters, only dependent on the microscopic processes involved in the STE generation, excitation and de-excitation.

With equations 3.93 to 3.96, the dependency of the amount of produced scintillation light as well as of its decay-time spectrum on the temporal development of the STE populations (differential equations 3.86 and 3.87 in section III/3.1.4) is described. Hence, it can be deduced that the observable decay time of the scintillation light is described by the temporal evolution of the STE populations[36]. Hence, taking into account the discussion of the differential equations for the STE populations in section III/3.1.3, already several qualitative conclusions concerning the scintillation-light production for different interacting particles can be drawn:

- The larger the initially produced STE density, the shorter the effective lifetime of STEs for short times t after the energy deposition and, hence, the shorter the observable decay time of the scintillation light. For large times t after the initial energy deposition, the effective lifetime of STEs, and hence, the observable decay time of the scintillation light converges always against the evolution of a STE population in absence of the Förster interaction, independently of the initially created STE density.

- The differences in the amount of scintillation light produced for different interacting particles, i.e., the different Quenching Factors (see section III/2.2.5), can be explained by a combination of two effects:

  - The fraction of deposited energy that leads to STE production, i.e., the fraction of energy deposited in ionization $F_{ioniz}(E_{part})$, is different for different interacting particles (compare section III/3.1.2).
  - The initially produced STEs are distributed differently within the excited crystal volume (according to $n_{bSTE}^{form\,e^-STH}(E_{part}, T, \mathbf{x}, t)$) for different interacting particles. Due to the different densities, the Förster interaction leads to different efficiencies in producing scintillation light, even for the same number of initially produced STEs (competition of the radiative recombination with the non-radiative reduction of the number of STEs via the Förster interaction).

- A non-linear dependency of the total amount of scintillation light produced for different STE densities on temperature is predicted. This is evident when the change of the amount of scintillation light produced by a population of spatially separated STEs (no Förster interaction) and by a population of densely created STEs (with Förster interaction) is compared for a temperature change from room temperature to a temperature below $\sim$ 5K:

  - Below $\sim$ 5K, the only processes considered leading to changes in the STE populations are the radiative decay and the Förster interaction, whereas, at

[35] Some parameters depend on the defect density and are, thus, dependent on the individual investigated crystal.

[36] This deduction will be shown and discussed in the following two sections.

room temperature, all processes considered within the model are assumed to be active (see discussion in section III/3.2.1).

- Hence, for the spatially separated STE population, the change in the efficiency of producing scintillation light is only induced by the extinction of the migration and non-radiative recombination processes.
- For the densely created STE population, however, additionally, the increase of the Förster radius with decreasing temperature has to be considered. The increasing Förster radius leads to an enhanced quenching effect for decreasing temperatures.

Therefore, the change in the amount of produced scintillation light with temperature is not of the same extent, i.e., not linearly proportional to temperature, when comparing the amount of light produced by the two populations.

- The amount of the excited green STEs and, hence, of the produced green light is determined by the blue STE population and its temporal behavior. This implies that, independently of the initially produced blue STE density, i.e., for all kinds of different particles or primary modes of (non-selective) excitation of the $CaWO_4$ crystal, always the same ratio of blue-to-green scintillation light can be expected[37].

Hence, it can be seen that, within the model, the light-quenching effect that can be observed for different interacting particles in $CaWO_4$ is assumed to be a result of the different efficiencies in generating ionization in combination with the non-radiative recombination (quenching) due to the Förster interaction of the blue STE population.

In order to calculate the amount of generated light $L_{tot}(E_{part}, T)$ for an interacting particle depositing the energy E_{part} at temperature T, the system of differential equations 3.86 and 3.87 (section III/3.1.4) has to be solved and the various free parameters have to be determined. However, this system of inhomogeneous, coupled, non-linear equations cannot be solved analytically whereas, in absence of the Förster interaction, the system becomes linear and can be solved analytically. The strategy used within this thesis, to approximate solutions for the complete system is based on the approach that two cases will be distinguished and discussed successively:

- The **unquenched model**, containing all processes described except the Förster interaction. This model can be expressed analytically without any approximations.
- The **complete, quenched model**, containing all processes described. For this complete model, an approximation - derived from the results for the unquenched model - is presented which allows to derive an analytical solution.

[37] This is true for the assumption made that the distribution of defect centers is uniform within the whole crystal volume. Nonetheless, also for a non-uniform distribution, the differences in the ratio of blue-to-green light due to different positions of the primary energy deposition can be expected to be small as the main amount of green scintillation light is assumed to be produced by reabsorption of blue photons at defect centers. This process, however, should be independent of the position of the primary energy deposition.

3.2.3 Model Without Exciton-Exciton Interaction: Unquenched

The Basic Unquenched Model

The unquenched model describes the temporal evolution of STEs in absence of the Förster interaction, i.e., of STEs that can be assumed to be spatially separated and, thus, independent from each other. Therefore, any dependency on the spatial distribution of STEs within the model vanishes and the resulting differential equations only depend linearly on the STE densities. Using the following relationships of the numbers of STEs, $N_b^{nq}(t)$ and $N_g^{nq}(t)$, and their densities, $n_b^{nq}(\mathbf{x},t)$ and $n_g^{nq}(\mathbf{x},t)$,

$$N_b^{nq}(t) = \int\limits_{V_{ex}} n_b^{nq}(\mathbf{x},t)d\mathbf{x}$$

$$N_g^{nq}(t) = \int\limits_{V_{ex}} n_g^{nq}(\mathbf{x},t)d\mathbf{x}$$

the differential equations can directly be expressed as differential equations of the number of STEs instead of their densities. The superscript *nq* indicates that no reduction of the number of STEs, i.e., *no quenching* of their number due to the Förster interaction is considered within this model. Then, the decay-time spectra of the photons produced that escape the crystal, $P_b^{nq}(E_{part},T,t)$ and $P_g^{nq}(E_{part},T,t)$ (equations 3.94 and 3.95), can directly be expressed using the numbers of STEs:

$$P_b^{nq}(E_{part},T,t) = (1-F_{abs})\cdot\frac{1}{\tau_{rb}(T)}\cdot N_b^{nq}(t) \tag{3.99}$$

$$P_g^{nq}(E_{part},T,t) = \frac{1}{\tau_{rg}(T)}\cdot N_g^{nq}(t) \tag{3.100}$$

The resulting system of coupled, inhomogeneous and linear differential equations that has to be solved can be expressed as:

$$\frac{\partial N_b^{nq}(t)}{\partial t} = -\frac{1}{\tau_{ltb}(T)}\cdot N_b^{nq}(t) + \frac{1}{\tau_{\text{mig, g}\to\text{b}}(T)}\cdot N_g^{nq}(t) + N_{bSTE}^{form\,e^-STH}(E_{part},T,t) \tag{3.101}$$

$$\frac{\partial N_g^{nq}(t)}{\partial t} = -\frac{1}{\tau_{ltg}(T)}\cdot N_g^{nq}(t) + \left(\frac{1}{\tau_{\text{mig, b}\to\text{g}}(T)} + F_{abs}\cdot\frac{1}{\tau_{rb}(T)}\right)\cdot N_b^{nq}(t) \tag{3.102}$$

where $N_{bSTE}^{form\,e^-STH}(E_{part},T,t)$ corresponds to the so-called source term and describes the temperature- and time-dependent formation of STEs out of the number of $N_{eh}(E_{part})$ initially generated electron-hole pairs (compare equation 3.43 in section III/3.1.2):

$$\begin{aligned} N_{bSTE}^{form\,e^-STH}&(E_{part},T,t) = \\ &= \Theta(t)\cdot\frac{(1-F_{e^-trap})\cdot F_{ioniz}(E_{part})\cdot E_{part}}{2.35\cdot E_{gap}}\cdot\left[(1-F_{dr}(T)) + \frac{F_{dr}(T)}{\tau_{dr}(T)}\cdot e^{-\frac{t}{\tau_{dr}(T)}}\right] = \\ &= \Theta(t)\cdot(1-F_{e^-trap})\cdot N_{eh}(E_{part})\cdot\left[(1-F_{dr}(T)) + \frac{F_{dr}(T)}{\tau_{dr}(T)}\cdot e^{-\frac{t}{\tau_{dr}(T)}}\right] \end{aligned} \tag{3.103}$$

The solutions of this system of differential equations, $N_b^{nq}(t)$ and $N_g^{nq}(t)$, can be obtained by first solving the homogeneous case ($N_{bSTE}^{form\,e^-STH}(E_{part},T,t)=0$) and then expanding the solution via the variation of constants.

Using the resulting solutions as well as equations 3.99 and 3.100, the decay-time spectra of the photons generated by a population of spatially separated (non-quenched) STEs can be expressed as:

$$P_b^{nq}(E_{part},T,t) = \Theta(t)\cdot\frac{(1-F_{abs})\cdot(1-F_{e^-trap})\cdot N_{eh}(E_{part})}{\tau_{rb}(T)}\cdot \\ \cdot\left[\frac{\frac{1}{\tau_{ltg}(T)}-\frac{1}{\tau_1(T)}}{\frac{1}{\tau_2(T)}-\frac{1}{\tau_1(T)}}\cdot\left((1-F_{dr}(T))\cdot e^{-\frac{t}{\tau_1(T)}}+\frac{F_{dr}(T)}{1-\frac{\tau_{dr}(T)}{\tau_1(T)}}\cdot\left\{e^{-\frac{t}{\tau_1(T)}}-e^{-\frac{t}{\tau_{dr}(T)}}\right\}\right)+\right. \\ \left.+\frac{\frac{1}{\tau_2(T)}-\frac{1}{\tau_{ltg}(T)}}{\frac{1}{\tau_2(T)}-\frac{1}{\tau_1(T)}}\cdot\left((1-F_{dr}(T))\cdot e^{-\frac{t}{\tau_2(T)}}+\frac{F_{dr}(T)}{\frac{\tau_{dr}(T)}{\tau_2(T)}-1}\cdot\left\{e^{-\frac{t}{\tau_{dr}(T)}}-e^{-\frac{t}{\tau_2(T)}}\right\}\right)\right] \tag{3.104}$$

$$P_g^{nq}(E_{part},T,t) = \Theta(t)\cdot\frac{(1-F_{e^-trap})\cdot N_{eh}(E_{part})}{\tau_{rg}(T)}\cdot\frac{\frac{1}{\tau_{\text{mig, b}\to\text{g}}(T)}+F_{abs}\cdot\frac{1}{\tau_{rb}(T)}}{\frac{1}{\tau_2(T)}-\frac{1}{\tau_1(T)}}\cdot \\ \cdot\left[(1-F_{dr}(T))\cdot\left\{e^{-\frac{t}{\tau_1(T)}}-e^{-\frac{t}{\tau_2(T)}}\right\}+\frac{F_{dr}(T)}{1-\frac{\tau_{dr}(T)}{\tau_1(T)}}\cdot\left\{e^{-\frac{t}{\tau_1(T)}}-e^{-\frac{t}{\tau_{dr}(T)}}\right\}-\right. \\ \left.-\frac{F_{dr}(T)}{\frac{\tau_{dr}(T)}{\tau_2(T)}-1}\cdot\left\{e^{-\frac{t}{\tau_{dr}(T)}}-e^{-\frac{t}{\tau_2(T)}}\right\}\right] \tag{3.105}$$

where $\tau_1(T)$ and $\tau_2(T)$ are defined as:

$$\frac{1}{\tau_1(T)} := \frac{1}{2}\cdot\left(\frac{1}{\tau_{ltb}(T)}+\frac{1}{\tau_{ltg}(T)}\right)- \\ -\frac{1}{2}\cdot\sqrt{\left(\frac{1}{\tau_{ltg}(T)}-\frac{1}{\tau_{ltb}(T)}\right)^2+4\cdot\frac{1}{\tau_{\text{mig, g}\to\text{b}}(T)}\cdot\left(\frac{1}{\tau_{\text{mig, b}\to\text{g}}(T)}+F_{abs}\cdot\frac{1}{\tau_{rb}(T)}\right)} \tag{3.106}$$

$$\frac{1}{\tau_2(T)} := \frac{1}{2}\cdot\left(\frac{1}{\tau_{ltb}(T)}+\frac{1}{\tau_{ltg}(T)}\right)+ \\ +\frac{1}{2}\cdot\sqrt{\left(\frac{1}{\tau_{ltg}(T)}-\frac{1}{\tau_{ltb}(T)}\right)^2+4\cdot\frac{1}{\tau_{\text{mig, g}\to\text{b}}(T)}\cdot\left(\frac{1}{\tau_{\text{mig, b}\to\text{g}}(T)}+F_{abs}\cdot\frac{1}{\tau_{rb}(T)}\right)} \tag{3.107}$$

From equations 3.104 and 3.105, it can already be seen, that the times $\tau_1(T)$ and $\tau_2(T)$ have the character of observable rise and/or decay times of the produced photons, i.e., of the scintillation light. This observation as well as the size of these rise and decay times will be discussed in detail in the following sections.

The integrated number of photons escaping the crystal and, using the mean photon energies $\overline{E}_{Pb}(T)$ and $\overline{E}_{Pg}(T)$, also the integrated amount of blue and green scintillation-light

(in energy) can be expressed as (see equations 3.96 and 3.98):

$$P_b^{nq}(E_{part},T) = (1-F_{abs}) \cdot \frac{(1-F_{e^-trap}) \cdot N_{eh}(E_{part})}{\tau_{rb}(T)} \cdot \frac{\tau_1(T) \cdot \tau_2(T)}{\tau_{ltg}(T)} \tag{3.108}$$

$$P_g^{nq}(E_{part},T) = \frac{(1-F_{e^-trap}) \cdot N_{eh}(E_{part})}{\tau_{rg}(T)} \cdot \tau_1(T) \cdot \tau_2(T) \left(\frac{1}{\tau_{\text{mig, b}\rightarrow\text{g}}(T)} + \frac{F_{abs}}{\tau_{rb}(T)} \right) \tag{3.109}$$

$$L_b^{nq}(E_{part},T) = \overline{E}_{Pb}(T) \cdot P_b^{nq}(E_{part},T)$$
$$L_g^{nq}(E_{part},T) = \overline{E}_{Pg}(T) \cdot P_g^{nq}(E_{part},T)$$

Using the branching ratios of the blue and green STE populations, defined in section III/3.1.3 (equations 3.83, 3.84 and 3.85), the integral numbers of blue and green photons escaping the crystal, respectively, can be expressed as:

$$P_b^{nq}(E_{part},T) = (1-F_{e^-trap}) \cdot N_{eh}(E_{part}) \cdot (1-F_{abs}) \cdot \cdot \frac{F_{b\ rad}(T)}{1-F_{g\ mig}(T) \cdot (F_{b\ mig}(T) + F_{abs} \cdot F_{b\ rad}(T))} \tag{3.110}$$

$$P_g^{nq}(E_{part},T) = (1-F_{e^-trap}) \cdot N_{eh}(E_{part}) \cdot [F_{b\ mig}(T) + F_{abs} \cdot F_{b\ rad}(T)] \cdot \cdot \frac{F_{g\ rad}(T)}{1-F_{g\ mig}(T) \cdot (F_{b\ mig}(T) + F_{abs} \cdot F_{b\ rad}(T))} \tag{3.111}$$

With these relationships, the ratio $R_{b-g}(T)$ of the numbers of blue-to-green photons escaping the crystal (compare equation 3.97 in section III/3.2.2) can be expressed as:

$$R_{b-g}(T) := \frac{P_b^{nq}(E_{part},T)}{P_g^{nq}(E_{part},T)} = \frac{F_{b\ rad}(T)}{F_{g\ rad}(T)} \cdot \frac{(1-F_{abs})}{(F_{b\ mig}(T) + F_{abs} \cdot F_{b\ rad}(T))} \tag{3.112}$$

As discussed in section III/3.2.2, this ratio is expected to be independent of the used mode of excitation, i.e., to be independent of the density of generated STEs. Therefore, this parameter is not assigned the superscript nq.

The total amount of scintillation light and the total number of photons escaping the crystal can be expressed as:

$$L_{tot}^{nq}(E_{part},T) = (1-F_{e^-trap}) \cdot N_{eh}(E_{part}) \cdot \cdot \frac{\overline{E}_{Pb}(T) \cdot (1-F_{abs}) \cdot F_{b\ rad}(T) + \overline{E}_{Pg}(T) \cdot (F_{b\ mig}(T) + F_{abs} \cdot F_{b\ rad}(T)) \cdot F_{g\ rad}(T)}{1-F_{g\ mig}(T) \cdot (F_{b\ mig}(T) + F_{abs} \cdot F_{b\ rad}(T))} \tag{3.113}$$

$$P_{tot}^{nq}(E_{part},T) = (1-F_{e^-trap}) \cdot N_{eh}(E_{part}) \cdot \cdot \frac{(1-F_{abs}) \cdot F_{b\ rad}(T) + (F_{b\ mig}(T) + F_{abs} \cdot F_{b\ rad}(T)) \cdot F_{g\ rad}(T)}{1-F_{g\ mig}(T) \cdot (F_{b\ mig}(T) + F_{abs} \cdot F_{b\ rad}(T))} \tag{3.114}$$

In order to explain the deduced general solutions (valid for the complete temperature range considered, equations 3.104 and 3.105) and the meaning of the parameters $\tau_1(T)$ and $\tau_2(T)$, the temperature-dependent behavior of these formulas can be analyzed: In the following, three different temperatures are considered in detail. At these temperatures, the influence of different processes can be neglected or has to be considered, depending on the thermal energy barriers and temperature-dependencies of the individual processes (see sections III/3.1.2 and III/3.2.1):

- $T \lesssim 5\text{K}$: For this temperature region, only the radiative decay of STEs has to be considered. The fraction of STEs generated in the initial delayed recombination process of electrons and STHs can be neglected: $F_{dr}(T \lesssim 100\text{K}) \approx 0$ (see equation 3.6 and the corresponding discussion in section III/3.1.2).

- $T = 20\text{K}$: For this temperature, only the radiative decay and the migration of STEs have to be considered. The fraction of STEs generated in the initial delayed recombination process of electrons and STHs can be neglected: $F_{dr}(T \lesssim 100\text{K}) \approx 0$.

- $T = 300\text{K}$: For this temperature, all processes considered in the unquenched model, i.e., the radiative decay, the migration, the non-radiative decay as well as the delayed formation of STEs, have to be taken into account. Hence, this model corresponds to the complete unquenched model.

Model for Temperatures Below 5K

Within the unquenched model, in this temperature region, the only de-excitation processes that are considered to be active are the radiative recombination processes of the blue and green STEs from their lower-lying energy levels (compare discussion in section III/3.2.1). Thus the lifetimes of blue and green STEs (compare equations 3.81 and 3.82, in section III/3.1.3) correspond to the radiative decay times from the lower-lying energy levels of the STEs, τ_{L1b} and τ_{L1g} (compare section III/3.1.3), respectively:

$$\begin{aligned} \tau_{\text{mig, b}\to\text{g}}(T \lesssim 5\text{K}) &\gg \tau_{rb}(T \lesssim 5\text{K}) & \tau_{\text{mig, g}\to\text{b}}(T \lesssim 5\text{K}) &\gg \tau_{rg}(T \lesssim 5\text{K}) \\ \tau_{nrb}(T \lesssim 5\text{K}) &\gg \tau_{rb}(T \lesssim 5\text{K}) & \tau_{nrg}(T \lesssim 5\text{K}) &\gg \tau_{rg}(T \lesssim 5\text{K}) \\ \Rightarrow \tau_{ltb}(T \lesssim 5\text{K}) &\approx \tau_{rb}(T \lesssim 5\text{K}) \approx \tau_{L1b} & \Rightarrow \tau_{ltg}(T \lesssim 5\text{K}) &\approx \tau_{rg}(T \lesssim 5\text{K}) \approx \tau_{L1g} \end{aligned}$$

Therefore, the branching ratios describing the de-excitation processes of the STE populations (see equations 3.83 to 3.85 in section III/3.1.3) are given by:

$$\begin{aligned} \Rightarrow F_{b\ rad}(T \lesssim 5\text{K}) &\approx F_{g\ rad}(T \lesssim 5\text{K}) \approx 1 \\ \Rightarrow F_{b\ nrad}(T \lesssim 5\text{K}) &\approx F_{g\ nrad}(T \lesssim 5\text{K}) \approx F_{b\ mig}(T \lesssim 5\text{K}) \approx F_{b\ mig}(T \lesssim 5\text{K}) \approx 0 \end{aligned}$$

Inserting the relationships for the lifetimes and recombination times of STEs into the definitions of the rise and decay times $\tau_1(T)$ and $\tau_2(T)$ (equations 3.106 and 3.107), it can already be seen that $\tau_1(T \lesssim 5\text{K})$ corresponds to the lifetime of blue STEs and $\tau_2(T \lesssim 5\text{K})$ corresponds to the lifetime of green STEs:

$$\begin{aligned} \frac{1}{\tau_1(T \lesssim 5\text{K})} \approx \frac{1}{2} \cdot \left(\frac{1}{\tau_{ltb}(T \lesssim 5\text{K})} + \frac{1}{\tau_{ltg}(T \lesssim 5\text{K})} \right) - \\ - \frac{1}{2} \cdot \sqrt{\left(\frac{1}{\tau_{ltg}(T \lesssim 5\text{K})} - \frac{1}{\tau_{ltb}(T \lesssim 5\text{K})} \right)^2 + 0} = \frac{1}{\tau_{ltb}(T \lesssim 5\text{K})} \approx \frac{1}{\tau_{L1b}} \\ \frac{1}{\tau_2(T \lesssim 5\text{K})} \approx \frac{1}{2} \cdot \left(\frac{1}{\tau_{ltb}(T \lesssim 5\text{K})} + \frac{1}{\tau_{ltg}(T \lesssim 5\text{K})} \right) + \\ + \frac{1}{2} \cdot \sqrt{\left(\frac{1}{\tau_{ltg}(T \lesssim 5\text{K})} - \frac{1}{\tau_{ltb}(T \lesssim 5\text{K})} \right)^2 + 0} = \frac{1}{\tau_{ltg}(T \lesssim 5\text{K})} \approx \frac{1}{\tau_{L1g}} \end{aligned}$$

As for temperatures $T \lesssim 5\text{K}$, no migration of STEs is expected to occur, the only excitation mechanism for blue STEs that has to be considered is the (extrinsic) generation of blue STEs in the energy deposition process. Concerning this formation process, within the developed model, it is assumed that the fraction of STEs generated in the delayed formation process for temperatures below 100K can be neglected (see section III/3.1.2):

$$F_{dr}(T \lesssim 100\text{K}) = 0$$

Hence, the only excitation process for blue STEs remaining for temperatures below 5K, is constituted by the immediate generation of $(1 - F_{e^- trap}) \cdot N_{eh}(E_{part})$ blue STEs (compare equation 3.103). For green STEs, on the other hand, the only excitation mechanism that has to be considered for $T \lesssim 5\text{K}$, is the absorption of blue photons at defect centers (no migration).

Therefore, the coupled system of differential equations as well as its solutions $P_b^{nq}(E_{part}, T \lesssim 5\text{K}, t)$ and $P_g^{nq}(E_{part}, T \lesssim 5\text{K}, t)$ are strongly simplified and can be expressed as:

$$\frac{\partial N_b^{nq}(t)}{\partial t} = -\frac{1}{\tau_{L1b}} \cdot N_b^{nq}(t) + \Theta(t) \cdot (1 - F_{e^- trap}) \cdot N_{eh}(E_{part}) \tag{3.115}$$

$$\frac{\partial N_g^{nq}(t)}{\partial t} = -\frac{1}{\tau_{L1g}} \cdot N_g^{nq}(t) + F_{abs} \cdot \frac{1}{\tau_{L1b}} \cdot N_b^{nq}(t) \tag{3.116}$$

$$P_b^{nq}(E_{part}, T \lesssim 5\text{K}, t) = \Theta(t) \cdot \frac{(1 - F_{abs}) \cdot (1 - F_{e^- trap}) \cdot N_{eh}(E_{part})}{\tau_{L1b}} \cdot e^{-\frac{t}{\tau_{L1b}}} \tag{3.117}$$

$$P_g^{nq}(E_{part}, T \lesssim 5\text{K}, t) = \Theta(t) \cdot \frac{F_{abs} \cdot (1 - F_{e^- trap}) \cdot N_{eh}(E_{part})}{\tau_{L1g} - \tau_{L1b}} \cdot \left\{ e^{-\frac{t}{\tau_{L1b}}} - e^{-\frac{t}{\tau_{L1g}}} \right\} \tag{3.118}$$

The integrated number of blue and green photons, $P_b(E_{part}, T)$ and $P_g(E_{part}, T)$, as well as the total number of photons, $P_{tot}(E_{part}, T)$, and total amount of scintillation light, $L_{tot}^{nq}(E_{part}, T \lesssim 5\text{K})$, can then be expressed as (compare equations 3.110 to 3.114, except 3.112):

$$\begin{aligned}
P_b^{nq}(E_{part}, T \lesssim 5\text{K}) &= (1 - F_{abs}) \cdot (1 - F_{e^- trap}) \cdot N_{eh}(E_{part}) \\
P_g^{nq}(E_{part}, T \lesssim 5\text{K}) &= F_{abs} \cdot (1 - F_{e^- trap}) \cdot N_{eh}(E_{part}) \\
P_{tot}^{nq}(E_{part}, T \lesssim 5\text{K}) &= P_b^{nq}(E_{part}, T \lesssim 5\text{K}) + P_g^{nq}(E_{part}, T \lesssim 5\text{K}) = \\
&= (1 - F_{e^- trap}) \cdot N_{eh}(E_{part})
\end{aligned} \tag{3.119}$$

$$L_{tot}^{nq}(E_{part}, T \lesssim 5\text{K}) = (1 - F_{e^- trap}) \cdot N_{eh}(E_{part}) \cdot \left[\overline{E}_{Pb}(T) \cdot (1 - F_{abs}) + \overline{E}_{Pg}(T) \cdot F_{abs} \right] \tag{3.120}$$

Hence, the ratio of the number of blue photons to green photons escaping the crystal $R_{b-g}(T \lesssim 5\text{K})$ is given by (see equation 3.112):

$$R_{b-g}(T \lesssim 5\text{K}) = \frac{P_b^{nq}(E_{part}, T \lesssim 5\text{K})}{P_g^{nq}(E_{part}, T \lesssim 5\text{K})} = \frac{1 - F_{abs}}{F_{abs}} \tag{3.121}$$

From these mathematical expressions for the decay-time spectra as well as for the amount and the composition of the produced scintillation light, several conclusions for the light generation and observable characteristics of the decay-time spectra at temperatures $T \lesssim 5K$

can be drawn:

a) Pulse Shape of the Blue Scintillation Light for $T \lesssim 5K$:

For the unquenched blue photon component, a *purely exponential decay* with a decay time corresponding to the radiative decay time from the energetically lower-lying level of the blue STE is predicted (decay-time spectrum from equation 3.117). Hence, the radiative decay time τ_{L1b} of blue STEs can be determined with a measurement of the decay-time spectrum of the blue photons below for temperatures $T \lesssim 5$K. The observable decay time of the blue scintillation light for temperatures $T \lesssim 5$K should correspond to τ_{L1b}.

b) Pulse Shape of the Green Scintillation Light for $T \lesssim 5K$:

The decay-time spectrum of the unquenched green photon component (equation 3.118) is described by an *exponentially rising and exponentially decaying pulse* with time constants corresponding to the radiative decay from the energetically lower-lying levels τ_{L1b} and τ_{L1g}. Using only equation 3.118, it cannot be determined which time corresponds to the rise or to the decay time. However, as discussed theoretically in section III/3.1.3, within the developed model it is expected that the radiative decay time of green STEs is much shorter than the one of blue STEs. In addition, e.g., in [67], it is reported that the decay time of green scintillation light generated by a selective excitation mode[38] at a temperature of $\sim$ 7K exhibits the same (slow) decay time as the scintillation light generated by a non-selective excitation mode. Therefore, within this model, it is proposed that, for temperatures $T \lesssim 5$K, the radiative decay time of green STEs can be identified with the rise time of the green scintillation-light pulse. Hence, the decay time of the green scintillation-light pulse corresponds to the radiative decay time of blue STEs. Thus, it can be deduced that, with a detailed measurement of the decay-time spectrum of the green scintillation-light component for temperatures below 5K, the radiative decay time of green STEs from their energetically lower-lying level τ_{L1g} can be determined as the rise time of the light pulse.

c) Amount of Scintillation Light Generated and its Spectral Composition for $T \lesssim 5K$:

- The ratio of blue-to-green light is only determined by the amount of blue photons absorbed at green centers, F_{abs} (compare equation 3.121). Hence, a measurement of the wavelength spectrum (and its decomposition into the blue and green light component) at a temperature below 5K, allows the determination of F_{abs}.

- The (unquenched) total amount of photons produced by the deposited energy E_{part} is only determined by the fraction of electron-STH pairs that do not recombine to STEs, i.e., by the fraction of electrons that get trapped, F_{e^-trap} (compare equations 3.119 and 3.120). Hence, for a temperature below 5K and a known amount of energy deposited (producing spatially separated STEs), the fraction of electrons captured by electron traps, F_{e^-trap} can be determined if one of the following two measurements are performed:

[38] For the excitation of the $CaWO_4$ crystal, photons with an energy of 4.7eV were used in [67]. These photons can be expected to be absorbed at defect centers only (see discussion in appendix B.4.2). As almost no migration of STEs is possible at a temperature of $\sim$ 7K, most of the generated scintillation light can be ascribed to the radiative decay of STEs at defect centers, i.e., to the radiative decay of green STEs.

- Either the total number of photons emitted by the crystal is measured,
- or the total amount of scintillation light (in units of energy) emitted by the crystal as well as the wavelength spectrum of the scintillation light is measured (to determine the mean photon energies $\overline{E}_{Pb}(T \lesssim 5\text{K})$ and $\overline{E}_{Pg}(T \lesssim 5\text{K})$ and relative contributions of blue and green photons).

The conclusions for the pulse shapes of the scintillation light deduced for temperatures below ~ 5K will be revisited and validated within the discussion of the scintillation-light pulse-shape for temperatures below ~ 5K in the quenched model (see discussion of figure 3.13 in section III/3.2.4).

Model for a Temperature of ~ 20K

As discussed in section III/3.2.1, for temperatures between $\sim$ 5K and $\sim$ 70K (regions II and III in figure 3.10), additionally to the radiative recombination of STEs, also their respective migration processes have to be considered. The influence of the non-radiative recombination processes is still assumed to be negligible. The temperature of 20K was chosen as an example as, within this work, experiments were conducted at this temperature. Hence, in the following, a temperature of 20K is considered, although it should be kept in mind that the statements made are valid for the temperature range from $\sim$ 5K to $\sim$ 70K.

At 20K, the radiative recombination process of both types of STEs is expected to be determined by a temperature-dependent mixture of radiative decay from the ground levels (with τ_{L1b} and τ_{L1g}) of the STEs and their first excited states (with τ_{L2b} and τ_{L2g}, compare section III/3.1.3). The migration processes can be described by the respective temperature-dependent migration times ($\tau_{\text{mig, b}\to\text{g}}(T)$ and $\tau_{\text{mig, g}\to\text{b}}(T)$, see section III/3.1.3). Thus, at a temperature of 20K, the intrinsic lifetimes of the STE populations can be expressed as (compare equations 3.81 and 3.82, in section III/3.1.3):

$$\begin{aligned}
\tau_{nrb}(T) &\gg \tau_{rb}(T) & \tau_{nrg}(T) &\gg \tau_{rg}(T)\\
\frac{1}{\tau_{rb}(T)} &:= \frac{\frac{1}{\tau_{L1b}} + \frac{1}{\tau_{L2b}} \cdot e^{-\frac{D_b}{k_B \cdot T}}}{1 + e^{-\frac{D_b}{k_B \cdot T}}} & \frac{1}{\tau_{rg}(T)} &:= \frac{\frac{1}{\tau_{L1g}} + \frac{1}{\tau_{L2g}} \cdot e^{-\frac{D_g}{k_B \cdot T}}}{1 + e^{-\frac{D_g}{k_B \cdot T}}}\\
\tau_{\text{mig, b}\to\text{g}}(T) &\approx \frac{d^2_{\text{W-W}}}{6 \cdot D_{\text{bSTE}}(T) \cdot C_{\text{defects}}} & \tau_{\text{mig, g}\to\text{b}}(T) &\approx \frac{d^2_{\text{W-W}}}{6 \cdot D_{\text{gSTE}}(T)}\\
\Rightarrow \frac{1}{\tau_{ltb}(T)} &\approx \frac{1}{\tau_{rb}(T)} + \frac{1}{\tau_{\text{mig, b}\to\text{g}}(T)} & \Rightarrow \frac{1}{\tau_{ltg}(T)} &\approx \frac{1}{\tau_{rg}(T)} + \frac{1}{\tau_{\text{mig, g}\to\text{b}}(T)}
\end{aligned} \tag{3.122}$$

Therefore, the branching ratios describing the de-excitation processes of the STE populations at a temperature of 20K (see equations 3.83 to 3.85 in section III/3.1.3) are given by:

$$\begin{aligned}
F_{b\ nrad}(T) &\approx 0 & F_{g\ nrad}(T) &\approx 0\\
F_{b\ rad}(T) &= \frac{\tau_{ltb}(T)}{\tau_{rb}(T)} & F_{g\ rad}(T) &= \frac{\tau_{ltg}(T)}{\tau_{rg}(T)}\\
F_{b\ mig}(T) &= \frac{\tau_{ltb}(T)}{\tau_{\text{mig, b}\to\text{g}}(T)} & F_{g\ mig}(T) &= \frac{\tau_{ltg}(T)}{\tau_{\text{mig, g}\to\text{b}}(T)}\\
F_{b\ rad}(T) + F_{b\ mig}(T) &\approx 1 & F_{g\ rad}(T) + F_{g\ mig}(T) &\approx 1
\end{aligned}$$

In the definitions of the observable decay and rise time $\tau_1(T)$ and $\tau_2(T)$ (equations 3.106 and 3.107), respectively, formally nothing changes in comparison to the general formulas:

$$\frac{1}{\tau_{1/2}(T)} := \frac{1}{2}\cdot\left(\frac{1}{\tau_{ltb}(T)}+\frac{1}{\tau_{ltg}(T)}\right)\mp \\ \mp\frac{1}{2}\cdot\sqrt{\left(\frac{1}{\tau_{ltg}(T)}-\frac{1}{\tau_{ltb}(T)}\right)^2+4\cdot\frac{1}{\tau_{\text{mig, g}\to\text{b}}(T)}\cdot\left(\frac{1}{\tau_{\text{mig, b}\to\text{g}}(T)}+F_{abs}\cdot\frac{1}{\tau_{rb}(T)}\right)} \tag{3.123}$$

where the upper (lower) sign refers to $\tau_1(T)$ ($\tau_2(T)$), respectively. However, it should be noted that the lifetimes of the STEs at 20K, $\tau_{ltb}(T=20K)$ and $\tau_{ltg}(T=20K)$, contain only contributions of the radiative and migration processes.

At this point of the discussion, the changes of the observable decay and rise times, $\tau_1(T)$ and $\tau_2(T)$, respectively, due to the introduction of the additional migration processes can be reviewed: For temperatures $T \lesssim 5$K, the time $\tau_1(T)$ corresponds to the intrinsic lifetime of blue STEs, $\tau_{ltb}(T \lesssim 5\text{K})$, and the time $\tau_2(T)$ corresponds to the intrinsic lifetime of green STEs, $\tau_{ltg}(T \lesssim 5\text{K})$. From equation 3.123, it can be seen that by introducing the migration processes, the time $\tau_1(T)$ becomes larger than the lifetime of blue STEs (subtraction of the migration term for the inverse of $\tau_1(T)$). On the other hand, $\tau_2(T)$ becomes smaller than the lifetime of green STEs (addition of the additional migration term for the inverse of $\tau_2(T)$). To roughly quantify these changes, in equation 3.123, the size of the additionally introduced term (second term under the square root) has to be compared to the size of the first term under the square root, i.e., the order of magnitudes of the two terms have to be compared:

$$\mathcal{O}\left[\left(\frac{1}{\tau_{ltg}(T)}-\frac{1}{\tau_{ltb}(T)}\right)^2\right] \quad \text{and} \quad \mathcal{O}\left[\frac{4}{\tau_{\text{mig, g}\to\text{b}}(T)}\cdot\left(\frac{1}{\tau_{\text{mig, b}\to\text{g}}(T)}+F_{abs}\cdot\frac{1}{\tau_{rb}(T)}\right)\right]$$

Taking into account that the lifetime of green STEs is much smaller than the lifetime of blue STEs (see sections II/ 3.1.3 and appendix B.4), and that, for each STE population both, the migration and radiative processes, have to be roughly of the same order of magnitude as the intrinsic lifetime of the respective STEs[39], the following relationships for $T = 20$K can be derived:

$$\tau_{ltg}(T) \ll \tau_{ltb}(T) \qquad \Rightarrow \qquad \frac{\tau_{ltg}(T)}{\tau_{ltb}(T)} \ll 1$$
$$\mathcal{O}(\tau_{rb}(T)) \approx \mathcal{O}(\tau_{\text{mig, b}\to\text{g}}(T)) \approx \mathcal{O}(\tau_{ltb}(T))$$
$$\mathcal{O}(\tau_{rg}(T)) \approx \mathcal{O}(\tau_{\text{mig, g}\to\text{b}}(T)) \approx \mathcal{O}(\tau_{ltg}(T))$$

[39] Otherwise these processes would affect neither the temporal development nor the spectral composition of the scintillation light (compare discussion in section III/3.2.1).

With these relationships, the order of magnitudes of the two terms can be estimated:

$$\mathcal{O}\left[\left(\frac{1}{\tau_{ltg}(T)}-\frac{1}{\tau_{ltb}(T)}\right)^2\right]\approx\mathcal{O}\left[\frac{1}{\tau_{ltg}^2(T)}\right]$$

$$\mathcal{O}\left[\frac{4}{\tau_{\text{mig, g}\to\text{b}}(T)}\cdot\left(\frac{1}{\tau_{\text{mig, b}\to\text{g}}(T)}+F_{abs}\cdot\frac{1}{\tau_{rb}(T)}\right)\right]\approx\mathcal{O}\left[\frac{1}{\tau_{ltg}(T)}\cdot\left(\frac{2}{\tau_{ltb}(T)}\right)\right]=$$

$$=\mathcal{O}\left[\frac{1}{\tau_{ltg}^2(T)}\cdot\frac{\tau_{ltg}(T)}{\tau_{ltb}(T)}\right]\ll\mathcal{O}\left[\frac{1}{\tau_{ltg}^2(T)}\right]$$

$$\Rightarrow\mathcal{O}\left[\left(\frac{1}{\tau_{ltg}(T)}-\frac{1}{\tau_{ltb}(T)}\right)^2\right]\gg\mathcal{O}\left[\frac{4}{\tau_{\text{mig, g}\to\text{b}}(T)}\cdot\left(\frac{1}{\tau_{\text{mig, b}\to\text{g}}(T)}+F_{abs}\cdot\frac{1}{\tau_{rb}(T)}\right)\right]$$

From this relationship it can be seen that the additional term due to the migration processes introduces only a relatively small change of the observable rise and decay times, $\tau_1(T)$ and $\tau_2(T)$, compared to the lifetimes of blue and green STEs, $\tau_{ltb}(T)$ and $\tau_{ltg}(T)$. Nonetheless, it should be noted that at a temperature of 20K, the rise and decay times are no longer exclusively determined by the lifetimes of the STE populations, but also by the extent of their interdependency, i.e., of their mutual excitation mechanisms.

For a temperature of 20K (as well as for the complete temperature range from $\sim$ 5K to $\sim$ 70K), the fraction of blue STEs generated in the delayed formation process can be neglected.

$$F_{dr}(T\lesssim 100\text{K})=0$$

Using all of these considerations, the coupled system of differential equations, at a temperature of 20K, can be expressed as:

$$\frac{\partial N_b^{nq}(t)}{\partial t}=-\frac{1}{\tau_{ltb}(T)}\cdot N_b^{nq}(t)+\frac{1}{\tau_{\text{mig, g}\to\text{b}}(T)}\cdot N_g^{nq}(t)+\Theta(t)\cdot(1-F_{e^-trap})\cdot N_{eh}(E_{part}) \tag{3.124}$$

$$\frac{\partial N_g^{nq}(t)}{\partial t}=-\frac{1}{\tau_{ltg}(T)}\cdot N_g^{nq}(t)+\left(\frac{1}{\tau_{\text{mig, b}\to\text{g}}(T)}+F_{abs}\cdot\frac{1}{\tau_{rb}(T)}\right)\cdot N_b^{nq}(t) \tag{3.125}$$

The solutions for the decay-time spectra of the photons are given by:

$$P_b^{nq}(E_{part},T,t)=\Theta(t)\cdot\frac{(1-F_{abs})\cdot(1-F_{e^-trap})\cdot N_{eh}(E_{part})}{\tau_{rb}(T)}\cdot\frac{\frac{1}{\tau_{ltg}(T)}-\frac{1}{\tau_1(T)}}{\frac{1}{\tau_2(T)}-\frac{1}{\tau_1(T)}}\cdot$$
$$\cdot\left[e^{-\frac{t}{\tau_1(T)}}+\frac{\frac{\tau_{ltg}(T)}{\tau_2(T)}-1}{1-\frac{\tau_{ltg}(T)}{\tau_1(T)}}\cdot e^{-\frac{t}{\tau_2(T)}}\right] \tag{3.126}$$

$$P_g^{nq}(E_{part},T,t)=\Theta(t)\cdot\frac{(1-F_{e^-trap})\cdot N_{eh}(E_{part})}{\tau_{rg}(T)}\cdot\frac{\frac{1}{\tau_{\text{mig, b}\to\text{g}}(T)}+F_{abs}\cdot\frac{1}{\tau_{rb}(T)}}{\frac{1}{\tau_2(T)}-\frac{1}{\tau_1(T)}}\cdot$$
$$\cdot\left[e^{-\frac{t}{\tau_1(T)}}-e^{-\frac{t}{\tau_2(T)}}\right] \tag{3.127}$$

The number of blue and green photons escaping the crystal, $P_b^{nq}(E_{part},T)$ and $P_g^{nq}(E_{part},T)$, at a temperature of 20K, can then be derived as:

$$P_b^{nq}(E_{part},T) = (1-F_{abs})\cdot(1-F_{e^-trap})\cdot N_{eh}(E_{part})\cdot \cdot \frac{F_{b\ rad}(T)}{1-F_{g\ mig}(T)\cdot(F_{b\ mig}(T)+F_{abs}\cdot F_{b\ rad}(T))}$$

$$P_g^{nq}(E_{part},T) = (1-F_{e^-trap})\cdot N_{eh}(E_{part})\cdot[F_{b\ mig}(T)+F_{abs}\cdot F_{b\ rad}(T)]\cdot \cdot \frac{F_{g\ rad}(T)}{1-F_{g\ mig}(T)\cdot(F_{b\ mig}(T)+F_{abs}\cdot F_{b\ rad}(T))}$$

Comparing these expressions with equations 3.110 and 3.111 (section III/3.2.2), describing the general case, it can be seen that the expressions for a temperature of 20K are formally the same. However, it has to be noted, that the branching ratios of the STEs are different due to their temperature dependencies and due to two deviations: On the one hand, the branching ratios can, in principle, exhibit a temperature dependency, on the other hand, at a temperature of 20K, only the radiative and migration processes and not the non-radiative recombination processes are included. Using the relationships of the branching ratios of the green and blue STEs ($F_{b\ rad}(T)+F_{b\ mig}(T)\approx 1$ and $F_{g\ rad}(T)+F_{g\ mig}(T)\approx 1$), the total number of photons escaping the crystal $P_{tot}^{nq}(E_{part},T)$ as well as the total amount of scintillation light produced, $L_{tot}^{nq}(E_{part},T)$, can be expressed as:

$$P_{tot}^{nq}(E_{part},T) = (1-F_{e^-trap})\cdot N_{eh}(E_{part}) \tag{3.128}$$

$$L_{tot}^{nq}(E_{part},T) = (1-F_{e^-trap})\cdot N_{eh}(E_{part})\cdot \cdot \frac{\overline{E}_{Pb}(T)\cdot(1-F_{abs})\cdot F_{b\ rad}(T)+\overline{E}_{Pg}(T)\cdot(F_{b\ mig}(T)+F_{abs}\cdot F_{b\ rad}(T))\cdot F_{g\ rad}(T)}{1-F_{g\ mig}(T)\cdot(F_{b\ mig}(T)+F_{abs}\cdot F_{b\ rad}(T))} \tag{3.129}$$

The ratio of the numbers of blue and green photons escaping the crystal, $R_{b-g}(T)$ (see equation 3.112 in section III/3.2.2) at a temperature of 20K, can be expressed as:

$$R_{b-g}(T) = \frac{F_{b\ rad}(T)}{F_{g\ rad}(T)}\cdot\frac{(1-F_{abs})}{1-F_{b\ rad}(T)\cdot(1-F_{abs})} \tag{3.130}$$

From these expressions for the decay-time spectra and for the amount and composition of the produced scintillation light, several conclusions concerning the light generation and observable characteristics of decay-time spectra at a temperatures of 20K (and the complete temperature region between $\sim$ 5K and $\sim$ 70K) can be drawn:

a) Pulse Shape of the Blue Scintillation Light at 20K:

- In equation 3.126, describing the pulse shape of the blue light component, the first term in the square brackets corresponds to the pulse shape of the blue light at temperatures $T \lesssim 5$K (except for the scaling factor, compare equation 3.117). This term describes a purely exponential decay with decay time $\tau_1(T)$, which roughly corresponds to the lifetime of blue STEs.

- The second term in the square brackets in equation 3.126, is positive as, $\tau_1(T) \gg \tau_{ltg}(T)$ and $\tau_{ltg}(T) \gtrsim \tau_2(T)$.

- Hence, this second, positive term describes a fraction of the generated amount of blue scintillation light which exhibits the decay time $\tau_2(T)$. The extent of this fraction is described by the size of the scaling factor in front of the exponential function.

- In order to estimate the impact of this second term, the relationships $\tau_1(T) \gg \tau_{ltg}(T)$ and $\tau_2(T) \gtrsim \tau_{ltg}(T)$ (compare discussion above) can be used: Considering these correlations, it can be seen that the scaling factor in front of the exponential function of the second term is very small and, thus, also the pulse height and partial integral of this second term in comparison to the first term in square brackets (compare also to the discussion at the end of this section and in appendix B.8).

Hence, it can be deduced that at a temperature of 20K, the pulse shape of the blue scintillation light produced can approximately be described by a single exponential decay[40] with decay time $\tau_1(T)$.

b) Pulse Shape of the Green Scintillation Light at 20K:

- Comparing equation 3.127, describing the pulse shape of the green scintillation light at 20K, to the pulse shape of the green light for temperatures $T \lesssim 5$K (equation 3.118), it can be seen that the basic shape of the decay-time spectrum does not change. The decay-time spectrum is described by a pulse exhibiting a purely exponential rise with $\tau_2(T)$ and a purely exponential decay with $\tau_1(T)$.

- The only differences are that the decay and rise times, $\tau_1(T)$ and $\tau_2(T)$, are no longer exactly identical to the lifetimes of the STE populations, $\tau_{ltb}(T)$ and $\tau_{ltg}(T)$, respectively, and that the scaling factor in front of the exponential pulse shape has changed. This fact is discussed in more detail in the following paragraph (in the context of the amount and composition of the scintillation light generated).

c) Amount of Scintillation Light Generated and its Spectral Composition at 20K:

- The ratio of blue-to-green photons emitted, $R_{b-g}(T)$ (equation 3.130), no longer only depends on the fraction of blue photons absorbed at defect centers, but also on the efficiencies (i.e., the branching ratios) of the migration processes.

- The exact dependencies become clear, when inspecting equation 3.130 describing the ratio of the number of emitted blue-to-green photons:
  The factor $F_{b\ rad}(T) \cdot (1 - F_{abs})$ appearing in the numerator and denominator describes the integrated fraction of blue STEs that decay radiatively (with an efficiency according to the radiative branching ratio $F_{b\ rad}(T)$) and that can escape the crystal, $(1 - F_{abs})$. It should be noted, that some of these radiatively decaying blue STEs were excited by migration of green STEs to intrinsic centers. Hence, the complete denominator of the second term of equation 3.130 $(1 - F_{b\ rad}(T) \cdot (1 - F_{abs}))$, corresponds to the integrated number of blue STEs that either did decay radiatively but were absorbed at defect centers or did not decay radiatively (i.e. migrated to green centers). This number is equal to the integrated number of green STEs that is generated within the complete light-production process. It has to be mentioned that not all of these green STEs decay radiatively, but some of them migrate back to intrinsic centers. This explains the denominator of the first term of equation

[40] Quantitative estimations of the impact of the second term are given in section III/5.2.2.

3.130, the multiplication of the integrated number of green STEs with their radiative branching ratio, $F_{g\ rad}(T)$, i.e., the efficiency of green STEs to produce green photons.

- As can be seen from equation 3.128, describing the total number of photons produced, this number does not change in comparison to temperatures below $\sim$ 5K. The total number of photons produced is only determined by the fraction of electrons that gets captured in electron traps (F_{e^-trap}) and is, hence, removed from the STE formation process (compare section III/3.1.2). This relationship reflects the fact that, within the unquenched model, for temperatures below $\sim$ 70K no non-radiative recombination processes for STEs are assumed to occur.

- However, as just discussed, the relative contributions of blue and green photons to the total number of photons change. Hence, although no non-radiative recombination process of STEs is introduced, the total amount of scintillation light (in energy) changes from $T \lesssim 5$K to $T = 20$K, according to the modified ratio of blue-to-green photons and the temperature-dependent mean energies of blue and green photons (compare equations 3.120 and 3.129).

- As discussed in section III/3.2.1, the mean energy of a blue or a green photon is found to be roughly constant within the complete temperature range considered from mK to room temperature (compare to section III/3.2.1 and to the results of measurements performed within the present work, section III/5.1). Hence, no additional change of the energy leaving the crystal in form of scintillation photons due to varying mean photon energies has to be expected.

The conclusions concerning the pulse shapes of the blue and green scintillation light component will be validated experimentally by measurements of the scintillation light generated by a spatially separated population of initially produced STEs at a temperature of $\sim$ 20K (see sections III/3.3.2 and III/5.2).

Model for Room Temperature

With these explanations and considerations of the decay-time spectra and of the total amount of scintillation light generated at very low temperatures ($T \lesssim 5$K) as well as at intermediate temperatures ($T = 20$K, or, more general, 5K $\lesssim T \lesssim$ 70K), the complete model for the complete temperature range analyzed (mK to $\sim$ 300K) can be revisited. As can be seen from the discussion in section III/3.2.1, the complete model only has to be utilized for the description of the light generation processes for temperatures between $\sim$ 200K and $\sim$ 300K (region IV in figure 3.10, section III/3.2.1). Hence, for a temperature of 300K (which was chosen as experiments were performed at this temperature within this work), the model as well as the mathematical formulations, exactly as described at the beginning of this section (equations 3.101 and 3.102), have to be used. As the mathematical expressions are already stated there, they are not repeated here.

Comparing the differential equations describing the complete model (equations 3.101 and 3.102) to the model for a temperature of 20K (see equations 3.124 and 3.125), it can be seen that, at 300K, additionally, the non-radiative recombination processes of blue and green STEs as well as the delayed initial formation of a fraction of blue STEs ($F_{dr}(T)$) have to be considered. In addition, it should be noted that, of course, the radiative recombination

and migration times of the STE populations become faster according to their respective temperature dependencies. Hence, the intrinsic lifetimes of the STE populations are now determined by all three processes, the radiative, the non-radiative recombination, and the migration process, competing with each other:

$$\frac{1}{\tau_{ltb}(T)} = \frac{1}{\tau_{rb}(T)} + \frac{1}{\tau_{nrb}(T)} + \frac{1}{\tau_{\text{mig, b}\rightarrow\text{g}}(T)} \tag{3.131}$$

$$\frac{1}{\tau_{ltg}(T)} = \frac{1}{\tau_{rg}(T)} + \frac{1}{\tau_{nrg}(T)} + \frac{1}{\tau_{\text{mig, g}\rightarrow\text{b}}(T)} \tag{3.132}$$

In analogy, of course, also the branching ratios of the blue and green STE populations are influenced:

$$F_{b\,rad}(T) = \frac{\tau_{ltb}(T)}{\tau_{rb}(T)} \qquad \text{and} \qquad F_{g\,rad}(T) = \frac{\tau_{ltg}(T)}{\tau_{rg}(T)} \tag{3.133}$$

$$F_{b\,mig}(T) = \frac{\tau_{ltb}(T)}{\tau_{\text{mig, b}\rightarrow\text{g}}(T)} \qquad \text{and} \qquad F_{g\,mig}(T) = \frac{\tau_{ltg}(T)}{\tau_{\text{mig, g}\rightarrow\text{b}}(T)} \tag{3.134}$$

$$F_{b\,nrad}(T) = \frac{\tau_{ltb}(T)}{\tau_{nrb}(T)} \qquad \text{and} \qquad F_{g\,nrad}(T) = \frac{\tau_{ltg}(T)}{\tau_{nrg}(T)} \tag{3.135}$$

Before discussing the solutions of the differential equations of the complete model (equations 3.104 and 3.105), first, a discussion of the relationships between the different times involved, the radiative, non-radiative and migration times as well as the lifetimes and the decay and rise times of the scintillation-light pulses, $\tau_1(T)$ and $\tau_2(T)$, is presented.

From the discussion of the temperature dependency of the generated scintillation light and its spectral composition (see section III/3.2.1), the following conclusions for the lifetimes of the STEs as well as for the different recombination and migration times of blue and green STEs at room temperature ($T = 300$K) can be drawn:

- At room temperature, the scintillation light is a composition of blue and green scintillation light. Hence, it can be deduced that, for both STE populations, the radiative decay channel has to represent a successfully competing recombination process. Therefore, the radiative recombination time has to be roughly of the same order of magnitude as the total intrinsic lifetime of the respective STE population[41].

- Comparing the temperature dependencies of the radiative and migration times for each STE population separately (see e.g., section III/3.1.3), it can be seen that they exhibit the same basic temperature-dependent behavior (exponentially decreasing with increasing temperature). Additionally, it can be noticed that the thermal energy barriers of these processes (the radiative decay from the energetically higher-lying level as well as the migration process) are assumed to be very similar (D_b and D_g of the order of 1meV, see section III/3.1.3, as well as $\Delta E_{mig\ b} = 4.5$meV and $\Delta E_{mig\ g} = 6.9$meV, see section III/3.1.3). Taking also into account that, at a temperature of $\sim$ 20K, the radiative and the migration times should be of the same order of

[41] Otherwise, if, e.g., the radiative decay time of blue STEs would be much larger than the total intrinsic lifetime of blue STEs, this would imply that the lifetime of blue STEs would be dominated by one or both of the other two process and, hence, that the blue STE population would dominantly migrate to defect centers and/or recombine non-radiatively.

magnitude[42] (for each STE population separately, compare to the discussion of the model for $\sim$ 20K), it can be deduced that, for all temperatures $T \gtrsim 20$K, these times should always be roughly of the same order of magnitude (for each STE population separately). Therefore, the migration time has to be roughly of the same order of magnitude as the total intrinsic lifetime of the respective STE population[43].

- The onset of the non-radiative recombination process of green STEs (at $\sim$ 70K) as well as the one of blue STEs (at $\sim$ 200K) are both inducing a permanent reduction of the amount of scintillation light produced (compare figure 3.10 in section III/3.2.1). Hence, it can be deduced that, at temperatures larger than the respective onset temperatures, the non-radiative recombination processes are efficiently reducing the respective STE populations. Therefore, the non-radiative recombination time has to be roughly of the same order of magnitude as the total intrinsic lifetime of the respective STE population.

From this discussion it can be seen that, for a temperature of 300K, the following approximate relationships can be formulated:

$$\mathcal{O}\left(\tau_{rb}(T)\right) \approx \mathcal{O}\left(\tau_{\text{mig, b}\rightarrow\text{g}}(T)\right) \approx \mathcal{O}\left(\tau_{nrb}(T)\right) \approx \mathcal{O}\left(\tau_{ltb}(T)\right)$$
$$\mathcal{O}(\tau_{rg}(T)) \approx \mathcal{O}(\tau_{\text{mig, g}\rightarrow\text{b}}(T)) \approx \mathcal{O}(\tau_{nrg}(T)) \approx \mathcal{O}(\tau_{ltg}(T))$$

Considering additionally, that the radiative decay time of the green STE population is expected to be at least two orders of magnitude smaller than the radiative recombination time of blue STEs (compare discussion in appendix B.4.1), it can be deduced that also at a temperature of 300K:

$$\tau_{ltg}(T) \ll \tau_{ltb}(T) \qquad \Rightarrow \qquad \frac{\tau_{ltg}(T)}{\tau_{ltb}(T)} \ll 1$$

Using these correlations, the same conclusions as in the discussion of the model for $T \sim 20$K concerning the relationships of the times $\tau_1(T)$ and $\tau_2(T)$ (equations 3.106 and 3.107) with the intrinsic lifetimes $\tau_{ltb}(T)$ and $\tau_{ltg}(T)$ of the blue and green STE populations, can be drawn: The time $\tau_1(T)$ is expected to be slightly larger than the lifetime of the blue STE population, $\tau_{ltb}(T)$. The time $\tau_2(T)$ is expected to be slightly smaller than the lifetime of the green STE population, $\tau_{ltg}(T)$. Therefore, it can be deduced that, also at 300K, the following relationships are valid:

$$\tau_2(T) \lesssim \tau_{ltg}(T) \ll \tau_{ltb}(T) \lesssim \tau_1(T) \tag{3.136}$$

Using the information on the migration time of green STEs (compare section III/3.1.4) at 300K as well as equation 3.132, an estimate of the order of magnitude of the time $\tau_2(T)$

[42] Otherwise, no influence of the migration processes onto the evolution of the STE populations, i.e., on the produced scintillation light, should be observable.

[43] It should be noted that this conclusion can be drawn on the basis of the observable change of the blue-to-green photon ratio at temperatures $\gtrsim$ 5K, i.e., on the basis of the observed onset temperatures of the migration process and the radiative recombination process (from the higher lying level). The onset temperature of the migration process, however, is expected to be dependent on the defect density: The less defects are contained in the crystal lattice, the larger migration lengths, i.e., longer migration times, are needed until efficient migration from blue STEs to green STEs can be observed (compare section III/2.1.5). Hence, the smaller the defect densities, the larger the expected onset temperature of the migration process and, hence, the larger the temperature at which the migration and radiative times are expected to be of roughly the same order of magnitude.

at 300K can be obtained:

$$\begin{aligned} \tau_{\text{mig, g}\to\text{b}}(T) &= 2.72\text{ns} \\ \Rightarrow \tau_{ltg}(T) &\lesssim \tau_{\text{mig, g}\to\text{b}}(T) = 2.72\text{ns} \\ \Rightarrow \mathcal{O}\left(\tau_2(T)\right) &\approx \mathcal{O}\left(1\text{ns}\right) \end{aligned}$$

Additionally, it can be taken into account that the formation time of the fraction of delayed created STEs, $\tau_{dr}(T)$ (compare section III/3.1.2), at 300K is assumed to be known:

$$\tau_{dr}(T = 300\text{K}) \approx 40\text{ns}$$

Inspecting the expressions for the general solutions of the blue and green decay-time spectra (equations 3.104 and 3.105 in the description of the basic unquenched model), it can be seen that the shape of the scintillation light generated, i.e., its exponential decay-time constants, are given by the three times $\tau_1(T)$, $\tau_2(T)$ and $\tau_{dr}(T)$. Considering the expressions derived above and, in addition, that the observed decay-time spectra of the $CaWO_4$ scintillation light at 300K are reported to always contain a slow component (of the order of $\sim 9\mu$s, see section III/2.2.3), it can be concluded that this slow decay time can only be assigned to the time $\tau_1(T = 300K)$. Therefore, the following relationships are expected to hold at 300K:

$$\begin{aligned} \tau_1(T) &\approx 9\mu\text{s} \\ \mathcal{O}\left(\tau_{ltb}(T)\right) &\approx \mathcal{O}\left(9\mu\text{s}\right) \\ \tau_2(T) \lesssim \tau_{ltg}(T) < &\tau_{dr}(T) \ll \tau_{ltb}(T) \lesssim \tau_1(T) \end{aligned} \tag{3.137}$$

Hence, it can be seen that, at 300K, the lifetime of blue STEs (and therefore also $\tau_{rb}(T)$, $\tau_{nrb}(T)$ and $\tau_{\text{mig, b}\to\text{g}}(T)$) is expected to be roughly of the order of 9μs. The lifetime of green STEs (and therefore also $\tau_{rg}(T)$, $\tau_{nrg}(T)$ and $\tau_{\text{mig, g}\to\text{b}}(T)$) is expected to be roughly of the order of 3ns.

Using all of these considerations, several conclusions for the decay-time spectra of the blue and green photons generated (equations 3.104 and 3.105) as well as for the total amount of light (equation 3.113) and the ratio of the numbers of blue photons to green photons (equation 3.112) produced at 300K can be drawn:

a) Pulse Shape of the Blue Scintillation Light at 300K:

- The first term in square brackets of the formula for $P_b^{nq}(E_{part}, T, t)$ (second line of equation 3.104) corresponds to the first term of the decay-time spectrum of the blue light at 20K (see equation 3.126): Blue scintillation light is generated with a decay time of $\tau_1(T)$ roughly corresponding to the lifetime of blue STEs.
- However, at 300K, only the fraction $(1 - F_{dr}(T))$ of the blue STEs is produced immediately[44] so that only the corresponding fraction of the scintillation light $(1 - F_{dr}(T))$ exhibits the purely exponential decay with $\tau_1(T)$.
- The fraction $F_{dr}(T)$ of the STEs, on the other hand, is produced in a delayed recombination process so that the corresponding fraction of the scintillation light exhibits

[44]This fraction is expected to be of the order of $\sim 85\%$, i.e., to be the larger fraction (compare section III/3.1.2).

a delayed rise with $\tau_{dr}(T)$ before decaying with the decay time $\tau_1(T)$. It should be noted that the expression for the scaling factor in front of the exponentially rising and decaying pulse, $\frac{F_{dr}(T)}{1-\frac{\tau_{dr}(T)}{\tau_1(T)}}$, causes the integral in time over this pulse shape to be equal to $F_{dr}(T)$.

- Analogously, the second term in square brackets in the formula for $P_b^{nq}(E_{part}, T, t)$ (third line of equation 3.104) can be interpreted. Again, the observation can be made that this term corresponds to the second term of the decay-time spectrum of the blue light at 20K (see equation 3.126).

- The following pulse shape is described by this second term in square brackets: The fraction $(1 - F_{dr}(T))$ exhibits a purely exponential decay with decay time $\tau_2(T)$ corresponding roughly to the lifetime of green STEs. The fraction $F_{dr}(T)$ exhibits a rise time $\tau_2(T)$ corresponding roughly to the lifetime of green STEs and a decay time[45] of $\tau_{dr}(T)$.

- Hence, the pulse shape of the second term is expected to be the sum of the (larger) purely exponentially decaying fraction $(1 - F_{dr}(T))$ with the very fast decay time $\tau_2(T)$ and of the (smaller) exponentially rising $(\tau_2(T))$ and decaying $(\tau_{dr}(T))$ fraction $F_{dr}(T)$.

- Taking now additionally the scaling factors in front of the first and the second term into account (second and third line of equation 3.104), the same argumentation as for the model at 20K can be used: As the lifetime of green STEs, $\tau_{ltg}(T)$, is supposed to roughly correspond to $\tau_2(t)$ and as $\tau_2(T) \ll \tau_1(T)$, it can be seen that the pulse height and partial integral of the second term compared to the first term is expected to be very small (compare also to the discussion at the end of this section and in appendix B.8).

Hence, it can be concluded that, within the model developed, the unquenched blue light component at 300K can be expected to be dominated by the first term in the formula for $P_b^{nq}(E_{part}, T, t)$ (second line of equation 3.104). This implies that the pulse shape should be describable by a (larger) fraction $(1 - F_{dr}(T))$ exhibiting a purely exponential decay with $\tau_1(T) \approx 9\mu$s and a (smaller) fraction exhibiting the same decay time $\tau_1(T)$ and a rise time of $\tau_{dr}(T) \approx 40$ns.

b) Pulse Shape of the Green Scintillation Light at 300K:

- The first term in square brackets in the formula for $P_g^{nq}(E_{part}, T, t)$ (second line of equation 3.105) directly corresponds to the pulse shape of the green scintillation light at 20K (except for the scaling factor $(1-F_{dr}(T))$ in front of this term, compare equation 3.127): A pulse shape exponentially rising with $\tau_2(T)$ corresponding roughly to the lifetime of green STEs, $\tau_{ltg}(T)$, and exponentially decaying with $\tau_1(T)$ corresponding roughly to the lifetime of blue STEs, $\tau_{ltb}(T)$. This part of the green light pulse corresponds to the (larger) fraction of immediately created STEs, $(1-F_{dr}(T))$.

[45] Note that, for the second term of $P_b^{nq}(E_{part}, T, t)$ describing the delayed rise, in contrary to the first term of $P_b^{nq}(E_{part}, T, t)$, the assignment of rise and decay times switches as the lifetime of green STEs is expected to be smaller than the delayed formation time of STEs.

- The part of the green light pulse corresponding to the delayed creation of STEs is split into two parts: The first one (second term of equation 3.105) rising with $\tau_{dr}(T)$ and decaying with $\tau_1(T)$, the second one (third term of equation 3.105), the negative one, rising with $\tau_2(T)$ and decaying with $\tau_{dr}(T)$.

- Taking again the relationships and orders of magnitude of the different involved times into account, it can be seen that the last term of equation 3.105 (third term) should be much smaller than the second term of equation 3.105. This implies that the pulse shape of the green scintillation light at 300K should be dominated by the first and the second term of equation 3.105.

- Considering the first term of equation 3.105, it becomes clear that this term can be interpreted as the recombination of green STEs (on a timescale of $\tau_2(T)$ which roughly corresponds to $\tau_{ltg}(T)$) which were excited by blue STEs (on a timescale of $\tau_1(T)$ which roughly corresponds to $\tau_{ltb}(T)$).

- Taking additionally into account that the rise time $\tau_2(T)$ ($\mathcal{O}$(1ns)) of the (larger) fraction $(1 - F_{dr}(T))$ of this pulse shape is expected to be much shorter than its decay time $\tau_1(T)$ ($\mathcal{O}(10\mu s)$), it can be seen that this fraction of green scintillation light can approximately be described by a purely exponential decay with the decay time $\tau_1(T)$.

- Using this approximation the resulting pulse shape can be described by a fraction $(1 - F_{dr}(T))$ with a purely exponential decay $(\tau_1(T))$ and a fraction $F_{dr}(T)$ with an exponentially rising $(\tau_{dr}(T))$ and decaying pulse shape $(\tau_1(T))$.

- Comparing this approximated pulse shape to the pulse shape of the blue scintillation-light component, it can be seen that both pulse shapes agree with each other (except for the different scaling factors in front of the square brackets).

Hence, it can be concluded that, within the model developed, the unquenched green light component at 300K is expected to be dominated by the first two terms in the formula for $P_g^{nq}(E_{part}, T, t)$ (second line of equation 3.105). Taking into account that the lifetime of green STEs is expected to be very short compared to the one of blue STEs, the pulse shape of the green scintillation light is expected to agree with the pulse shape of the blue scintillation light at 300K (except for the different scaling factors in front of the square brackets).

c) Amount of Scintillation Light Generated and its Spectral Composition at 300K:

- The ratio of the number of blue photons to green photons produced is described by equation 3.112. Comparing this formula to the formula deduced for a temperature of 20K (equation 3.130), it can be seen that the mathematical description does not change. It should be noted that the branching ratios of the different processes of course change for a temperature of 300K compared to a temperature of around 20K as, at 300K, also the non-radiative recombination processes are possible. The impact of these additional decay channels onto the ratio of the number of blue photons to green photons produced can already be seen in figure 3.10 (section III/3.2.1) and the successive discussion of the regions IV, V and VI indicated in this figure. The basic interpretation of this formula presented in the discussion of the model for temperatures around 20K, however, is nonetheless also valid at 300K.

- As can be seen from equation 3.114 describing the integrated number of photons produced at 300K, this formula can not be simplified as is the case for the expression at 20K (equation 3.128)[46].
- At 300K, the total amount of scintillation light and the total number of photons generated, described with equations 3.113 and 3.114, can also not be expressed in a more simplified form.
- Nonetheless, the equations describing the integrated number of blue photons (equation 3.110) and the integrated number of green photons (equation 3.111) escaping the crystal can be interpreted within the model developed:
  - The term $(1 - F_{e^- trap}) \cdot N_{eh}(E_{part})$ in both formulas corresponds to the number of STEs generated out of the number $N_{eh}(E_{part})$ of electron-hole pairs produced in the energy-deposition process.
  - In both formulas, the second term (fraction in the respective second line) corresponds to the total efficiency of the respective STE population to generate light, i.e., to decay radiatively (including the possibility that, e.g., STEs which migrated "away" can migrate back and again get the chance to decay radiatively).
  - The factor $(1 - F_{abs})$ in the expression for the number of blue photons escaping the crystal reflects the fact that the fraction F_{abs} of blue photons is absorbed at defect centers and can, hence, not leave the crystal.
  - The factor $[F_{b\ mig}(T) + F_{abs} \cdot F_{b\ rad}(T)]$ in the expression for the number of green photons corresponds to the number of green STEs that get excited in the course of the de-excitation of blue STEs.

Conclusions for the Unquenched Model

a) Basic Pulse Shapes:

Inspecting the solutions obtained for the unquenched model at different temperatures, it can be seen that, within the complete temperature range considered, **the pulse shape of the unquenched blue scintillation-light component is dominated by a purely exponential decay[47] with decay time** $\tau_1(T)$. Additionally, it can be seen that, within the complete temperature range considered, the expression for **the unquenched green scintillation-light component is dominated by an exponentially rising ($\tau_2(T)$) and exponentially decaying ($\tau_1(T)$) pulse shape.** The rise time of the green scintillation-light pulse is always given by $\tau_2(T)$ which roughly corresponds to the lifetime of green STEs, $\tau_{ltg}(T)$. The decay time of the blue as well as of the green scintillation-light pulse is given by $\tau_1(T)$, which roughly corresponds to the lifetime of blue STEs, $\tau_{ltb}(T)$.

[46] For the model at 20K, the relationships $F_{b\ rad}(T) + F_{b\ mig}(T) \approx 1$ and $F_{g\ rad}(T) + F_{g\ mig}(T) \approx 1$ could be used to simplify the expression for the total number of photons produced.

[47] At room temperature, in principle, additionally the term corresponding to the delayed creation of STEs has to be considered. However, as mentioned in the discussion of the decay-time spectrum at room temperature, the integral of this term is determined by the fraction of delayed recombining electron-STH pairs, $F_{dr}(T)$. This fraction is strongly decreasing with decreasing temperature and is, even at room temperature, expected to amount to only $\sim 15\%$.

b) Excitation of Green STEs by the Blue STE Population:

Using this description of the pulse shapes, it can be deduced that the pulse shape of the green scintillation-light component can be interpreted as the excitation of green STEs by a fraction of blue STEs ($F_{b\ mig}(T) + F_{abs} \cdot F_{b\ rad}(T)$)[48] with a time constant $\tau_1(T)$ and a de-excitation of green STEs with a time constant $\tau_2(T)$. This implies that the decay time $\tau_2(T)$ can be assigned to the temporal evolution of the green STE population in absence of a time-dependent excitation. Mathematically, the excitation by blue STEs can be expressed by a convolution of the time-dependent green STE population (described by $\Theta(t) \cdot e^{-\frac{t}{\tau_2(T)}}$) with the time-dependent blue STE population (described by $\Theta(t) \cdot e^{-\frac{t}{\tau_1(T)}}$). This behavior is also reflected in the description of the basic excitation and de-excitation mechanisms of STEs (compare section III/3.1.3).

c) Effective Unquenched Lifetimes of STEs:

In the presented interpretation of the observable pulse shapes of the scintillation light, the decay time $\tau_{\mathbf{1}}(\mathbf{T})$ can be identified with the **effective unquenched lifetime of blue STEs** which contains the intrinsic lifetime $\tau_{ltb}(T)$ of blue STEs, as well as the influence of all mutual excitation processes of the blue and green STE populations. In analogy, $\tau_{\mathbf{2}}(\mathbf{T})$ can be identified with the **effective unquenched lifetime of green STEs**, containing the intrinsic lifetime $\tau_{ltg}(T)$ of green STEs, as well as the impact of all mutual excitation processes of blue and green STEs on this lifetime.

d) Fractions of Scintillation Light Exhibiting a Faster Exponential Decay Time:

From the determined expressions for the decay-time spectra of blue and green photons (equations 3.104, 3.105, 3.117, 3.118,3.126 and 3.127), it can be deduced that the dominating fractions of the blue and the green light components (within the complete temperature range considered) exhibit the same, single exponential decay behavior with the same slow decay time $\tau_1(T)$. However, as can be seen from the exact expressions for the decay-time spectra of the blue and the green light components, small fractions of both scintillation-light components exhibit faster decay times. The impact of these (smaller) fractions can be estimated as calculated in detail in appendix B.8 and as is summarized in the following[49]:

→ *Scintillation light influenced by delayed created STEs with $\tau_{dr}(T)$ (see discussion below equation 3.7 in section III/3.1.2):*
At temperatures $T \gtrsim 100$K, a fraction $F_{dr}(T)$ of the blue as well as of the green light, is produced by delayed created STEs (STE creation with $\tau_{dr}(T)$). **For both components, the blue and the green light, the fraction $F_{dr}(T)$ rises with $\tau_{dr}(T)$ and decays with the slow decay time $\tau_1(T)$** (same, slow decay time as the dominant fraction of the blue and the green light). The following parameters describe this fraction (compare section III/3.1.2):

[48] This fraction is given by the fraction of blue STEs that is absorbed at and migrates to defect centers: ($F_{b\ mig}(T) + F_{abs} \cdot F_{b\ rad}(T)$), compare equation 3.112.

[49] To estimate the relevance of these fractions, the respective terms in the formulas for the decay-time spectra can be integrated and these integrals can be compared to the integrals of the slowly decaying main fractions. In appendix B.8, the calculation as well as the explanation of the respective integrals are presented.

integral of this fraction: $F_{dr}(T)$ ($\sim 15\%$ at 300K)
$(1 - F_{dr}(T))$ increasing strongly with decreasing temperature, $(1 - F_{dr}(T)) \propto T^{-3}$,
$\tau_{dr}(300K) \approx 40$ns, $\tau_{dr}(100K) \approx 10$ns

→ *Blue scintillation light with a decay time faster than $\tau_1(T)$:*
A very small fraction of the blue scintillation light (determined by the ratio of $\frac{\tau_{ltg}(T)-\tau_2(T)}{\tau_1(T)-\tau_{ltg}(T)} \ll 1$, compare equation B.62 in appendix B.8) exhibits a faster exponential decay (subdivided into two parts: one part with decay time $\tau_2(T)$ and one part with decay time $\tau_{dr}(T)$). This fraction is very small (for all temperatures considered, compare appendix B.8). **Hence, this fast decaying fraction of the blue light, can be neglected in comparison to the dominating fraction of blue light decaying with $\tau_1(T)$.**

→ *Green scintillation light with a decay time faster than $\tau_2(T)$:*
At temperatures $T \gtrsim 100$K, a very small fraction of the green light (determined by the ratio of $\frac{\tau_2(T)}{\tau_1(T)}$, compare appendix B.8) exhibits the fast decay time $\tau_{dr}(T)$. This fraction can be neglected within the complete temperature range considered, as the relationship $\frac{\tau_2(T)}{\tau_1(T)} \ll 1$ is always valid. **Hence, this fast decaying fraction of green light can be neglected in comparison to the dominating fraction of the green light rising with $\tau_2(T)$ and decaying with $\tau_1(T)$.**

e) Validation of these considerations:

These conclusions will be **validated experimentally**, by measurements of the decay-time spectra of the blue and green scintillation-light components of $CaWO_4$ generated by a spatially separated population of STEs (see sections III/4.7.2 and III/5.2). In addition, using the completed model (all parameters of the model determined on the basis of experiments, see section III/5.2.2), it can be calculated that the fractions of the unquenched scintillation light exhibiting a faster decay time are at least three orders of magnitude smaller than the integrated fractions with the slow decay time $\tau_1(T)$.

These considerations show that, within the complete temperature range considered, both components of the unquenched scintillation light, the blue as well as the green light components, are completely dominated by a single exponential decay with slow decay time $\tau_1(T)$. No significant amount of the blue nor the green scintillation light exhibits a decay time faster than $\tau_1(T)$. Hence, it can be deduced that, within the model developed, the fast component of the scintillation light of $CaWO_4$ observed under particle excitation (compare section III/2.2.3, fast initial decay of the scintillation light for, e.g., α- and γ-particles) cannot be explained by the green scintillation-light component. Within the developed model this fast component can be explained by the interacting of blue STEs via the Förster interaction as will be discussed in the next section.

3.2.4 Model with Exciton-Exciton Interaction: Complete Model Including Quenching

In the following, the model for the light generation and quenching including the Förster interaction is presented. This model has to be applied as soon as STEs are generated close enough to each other as is, e.g., the case in nuclear recoil tracks. These STEs can no

longer be regarded as independent from each other and the interaction between STEs via the Förster interaction has to be considered. The understanding acquired and the insight gained into the processes of the light generation as well as the inter-dependencies of the blue and green STE populations within the unquenched model, will be used to develop approximations for the general system of differential equations describing the quenched model.

It should be noted that the description of the temporal evolution of the quenched STE populations and, hence, of the generated decay-time spectra of the scintillation light, depends on the density of the initially created blue STEs. The density of the initially generated blue STEs, however, depends on the distribution of the energy deposited in ionization by the primary interacting particle and, hence, on the type and energy of the respective primary interacting particle (compare section III/3.1.2). Therefore, at first, a general expression for the decay-time spectra of the produced blue and green photons is derived still containing the general expression for the dependency on the distribution of the initially created blue STE population. Thereafter, the geometrical model developed within this thesis for the description of the initial STE distribution generated by an interacting particle (compare section III/3.1.2), is inserted into this general expression. This yields an explicit (analytical) expression for the quenched decay-time spectrum of the generated scintillation light by an interacting particle in $CaWO_4$.

The Basic Quenched Model

The basic quenched model describes the temporal evolution of STEs under consideration of the Förster interaction. As discussed in section III/3.1.3, the impact of the Förster interaction depends on the density of the STEs. Hence, the differential equations describing the model first have to be solved for the densities of the STE populations $n_b(\mathbf{x},t)$ and $n_g(\mathbf{x},t)$ and then be integrated over the excited volume V_{ex} to obtain the decay-time spectrum of the produced photons, as described in section III/3.2.2. The differential equations that have to be solved can be expressed as:

$$\begin{aligned}\frac{\partial n_b^q(\mathbf{x},t)}{\partial t} = & -\frac{1}{\tau_{ltb}(T)}\cdot n_b^q(\mathbf{x},t) - \frac{2\cdot\pi^{\frac{3}{2}}}{3}\cdot\frac{R_{d-d}^3(T)}{\sqrt{\tau_{ltb}(T)\cdot t}}\cdot(n_b^q(\mathbf{x},t))^2 + \frac{1}{\tau_{\text{mig, g}\to\text{b}}(T)}\cdot n_g^q(\mathbf{x},t) + \\ & + n_{bSTE}^{form\,e^-STH}(E_{part},T,\mathbf{x},t) \qquad (3.138)\\ \frac{\partial n_g^q(\mathbf{x},t)}{\partial t} = & -\frac{1}{\tau_{ltg}(T)}\cdot n_g^q(\mathbf{x},t) + \left(\frac{1}{\tau_{\text{mig, b}\to\text{g}}(T)} + F_{abs}\cdot\frac{1}{\tau_{rb}(T)}\right)\cdot n_b^q(\mathbf{x},t) \qquad (3.139)\end{aligned}$$

where the superscript q indicates that these are the differential equations and solutions of the quenched model. The initial, external excitation of blue STEs, $n_{bSTE}^{form\,e^-STH}(E_{part},T,\mathbf{x},t)$, is given by (compare equation 3.77 in section III/3.1.3):

$$\begin{aligned}& n_{bSTE}^{form\,e^-STH}(E_{part},T,\mathbf{x},t) \qquad =\\ & = +\Theta(t)\cdot\frac{(1-F_{e^-trap})\cdot\rho_{ioniz}(E_{part},\mathbf{x})}{2.35\cdot E_{gap}}\cdot\left[(1-F_{dr}(T)) + \frac{F_{dr}(T)}{\tau_{dr}(T)}\cdot e^{-\frac{t}{\tau_{dr}(T)}}\right] \qquad (3.140)\end{aligned}$$

With the definition of the initially generated density $n_{bSTE}^{form\,0}(E_{part}, \mathbf{x})$ of blue STEs the external initial formation process of STEs can be expressed as:

$$n_{bSTE}^{form\,0}(E_{part}, \mathbf{x}) = \frac{(1 - F_{e^-trap}) \cdot \rho_{ioniz}(E_{part}, \mathbf{x})}{2.35 \cdot E_{gap}} \tag{3.141}$$

$$n_{bSTE}^{form\,e^-STH}(E_{part}, T, \mathbf{x}, t) = +\Theta(t) \cdot n_{bSTE}^{form\,0}(E_{part}, \mathbf{x}) \cdot \left[(1 - F_{dr}(T)) + \frac{F_{dr}(T)}{\tau_{dr}(T)} \cdot e^{-\frac{t}{\tau_{dr}(T)}}\right] \tag{3.142}$$

As already indicated in section III/3.2.2, this system of differential equations (equations 3.138 and 3.139) cannot be solved analytically. In the following, the approach used to obtain approximations for the solutions of this system of differential equations is presented.

However, to finally obtain the strived for decay-time spectra of the blue and green photons escaping the crystal, $P_b^q(E_{part}, T, t)$ and $P_g^q(E_{part}, T, t)$, the distribution of the initially produced blue STEs has to be known so that the integration over space, i.e. over the excited volume V_{ex}, can be performed (compare equations 3.94 and 3.95, section III/3.2.2):

$$P_b^q(E_{part}, T, t) = (1 - F_{abs}) \cdot \int\limits_{V_{ex}} \frac{1}{\tau_{rb}(T)} \cdot n_b^q(\mathbf{x}, t) d\mathbf{x} \tag{3.143}$$

$$P_g^q(E_{part}, T, t) = \int\limits_{V_{ex}} \frac{1}{\tau_{rg}(T)} \cdot n_g^q(\mathbf{x}, t) d\mathbf{x} \tag{3.144}$$

Using the approximate solutions derived for $n_b^q(\mathbf{x}, t)$ and $n_g^q(\mathbf{x}, t)$, solutions of this volume integral for two special cases of the initially produced STE distribution will be presented later in this section.

Derived Approximate Solution for the Quenched Model

In the following, first the applied approximations and assumptions (paragraph *a*, containing five features) are explained. Thereafter, the conclusions that can be drawn from applying these approximations to the *unquenched* model (paragraph *b*) are presented. This intermediate step is performed in order to derive the impact of the approximations on the mathematical description of the model. Then (paragraph *c*), the conclusions that can be drawn from the approximated unquenched model are transferred to the quenched model and the approximated formulation of the quenched model is derived. In the final paragraph *d*, the analytical solution of the approximated differential equation for the quenched blue STE population is presented and discussed.

a) Applied Approximations and Assumptions:

1. As already expressed by the formulation of the differential equations of the quenched model, it is assumed that the Förster interaction only has to be considered for blue STEs interacting with each other (compare discussion of the Förster interaction in section III/3.1.3 and appendix B.6.2). For green STEs, no interaction via the Förster interaction is considered.

2. In the following, the approximation is made that, independently of temperature, **the initial delayed formation process of the blue STEs is neglected**. Hence, it

is assumed that, within the complete temperature range considered, the complete primary excitation of STEs can be described by the immediate formation process: This corresponds to the assumption that $F_{dr}(T) \stackrel{!}{=} 0$ within the complete temperature range considered (compare to equation 3.142). This approximation can be expressed as:

$$n_{bSTE}^{form\,0}(E_{part}, \mathbf{x}) = \frac{(1 - F_{e^- trap}) \cdot \rho_{ioniz}(E_{part}, \mathbf{x})}{2.35 \cdot E_{gap}}$$

$$n_{bSTE}^{form\,e^- STH}(E_{part}, T, \mathbf{x}, t) \stackrel{!}{=} +\Theta(t) \cdot n_{bSTE}^{form\,0}(E_{part}, \mathbf{x})$$

Hence, as indicated with this formulation, the initially created density distribution of blue STEs is independent of temperature. This approximation already simplifies the system of differential equations as, due to omitting the time-dependency of the external excitation process, the system of differential equations is homogenized (see equations 3.138 and 3.139). In fact, this approximation can be motivated by the fact that, for densely produced ionization for which the quenched model has to be applied, the fraction of electron-STH pairs that recombine immediately can be expected to be larger than for a spatially distributed energy deposition[50] (compare appendix B.2). It should be noted that, for temperatures $T \lesssim 100\text{K}$, this assumptions is, in fact, no approximation, but corresponds to the exact description of the excitation of blue STEs by the primary interacting particle within the model (compare section III/3.1.2).

3. Within the quenched model, the branching ratios for blue STEs are different compared to the unquenched model, as a fraction $F_{b\ d-d}(T, E_{part})$ of the blue STEs recombines non-radiatively due to the Förster interaction. The extent of this fraction depends on the density of the created STE population (the Förster interaction depends on the density) and, hence, on the energy and type of interacting particle. Taking into account this additional recombination channel, the quenched branching ratios of the blue STE have to fulfill the following relationship:

$$\left[F_{b\ rad}^{q}(T) + F_{b\ mig}^{q}(T) + F_{b\ nr}^{q}(T)\right](E_{part}) + F_{b\ d-d}^{q}(T, E_{part}) = 1 \qquad (3.145)$$

where the superscript q indicates that these are the branching ratios of the quenched model. Equation 3.145 expresses that, within the quenched model, a blue STE can either decay radiatively, non-radiatively, migrate to a defect center or interact with another blue STE via the Förster interaction and get quenched. As the sum of all of these branching ratios is unity, it is expressed that no other de-excitation possibilities are considered within the developed model. As indicated by equation 3.145, within the model, it is assumed that the relative partitioning between the radiative, non-radiative and migration processes for blue STEs is not dependent on the type and energy of the interacting particle. This implies that the partitioning between the radiative, non-radiative and migration branching ratios, does not change in comparison to the unquenched model. This assumptions is motivated by the fact that the Förster interaction is described as an additional recombination channel

[50] This conclusion can be drawn, when considering that, for a spatially dense energy deposition, more than one STH can be found in the vicinity of one electron in the conduction band. Hence, the probability for an immediate recombination process of electrons with STHs increases for densely deposited energy compared to spatially distributed electron-STH pairs.

which does not influence the relative probabilities of the intrinsic processes (radiative, non-radiative recombination or migration) of the STEs. This assumption can, e.g., be expressed by the relationship:

$$\frac{F^q_{b\ rad}(T)}{F^q_{b\ mig}(T)} \stackrel{!}{=} \frac{F_{b\ rad}(T)}{F_{b\ mig}(T)} \tag{3.146}$$

From this assumption, it can also be deduced that the intrinsic processes, i.e., the radiative, non-radiative and migration times, in the quenched model are the same as in the unquenched model as they are not influenced by the Förster interaction. Hence, the intrinsic lifetime $\tau_{ltb}(T)$ (equation 3.131 in section III/3.2.3) as well as the unquenched effective lifetime $\tau_1(T)$ of blue STEs (equation 3.106, section III/3.2.3), if calculated for the quenched model, do not change compared to the unquenched model. Therefore, the relationship that $\tau_1(T)$ almost equals to $\tau_{ltb}(T)$ applies for the unquenched as well as for the quenched model. In addition, it can be seen that the number of blue photons produced that escape the crystal, i.e., the fraction of blue STEs that decay radiatively and are not absorbed at defect centers can be expressed by:

$$F^q_{b\ rad} \cdot (1 - F_{abs}) \tag{3.147}$$

where it should be noted that $F^q_{b\ rad}$ is not equal to $F_{b\ rad}$, as the blue STEs can also recombine via the Förster interaction.

4. As can be seen from equations 3.138 and 3.139, within the quenched model, the mathematical description of the green STE population as well as of the mutual excitation processes of the blue and green STE populations stay the same as in the unquenched model (equations 3.101 and 3.102 in section III/3.2.3). It is assumed that the Förster interaction does not influence the intrinsic processes of the STEs (it only delivers an additional decay channel for blue STEs). This implies that the reaction function of the green STE population on external excitations can still be described by an exponential with decay time $\tau_2(T)$, where $\tau_2(T)$ is still defined by equation 3.107 (section III/3.2.3) as in the unquenched model. Thus, it can be deduced that, also in the quenched model, $\tau_2(T)$ is almost equal to $\tau_{ltg}(T)$. This also implies that the branching ratios of green STEs in the quenched and unquenched model stay the same. Additionally, it can be seen that also in the quenched model, the green STEs are excited by the fraction of blue STEs that migrate to and are absorbed at defect centers:

$$(F^q_{b\ mig}(T) + F_{abs} \cdot F^q_{b\ rad}(T))$$

Hence, using the radiative branching ratio of green STEs $F^q_{g\ rad}(T) = F_{g\ rad}(T)$, the fraction of blue STEs that excite green STEs and decay radiatively there, i.e., that produce green photons can be expressed as:

$$F_{g\ rad}(T) \cdot (F^q_{b\ mig}(T) + F_{abs} \cdot F^q_{b\ rad}(T))$$

5. As explained, $\tau_1(T)$ and $\tau_2(T)$ stay the same in the quenched model as in the unquenched model. Hence, also in the quenched model, $\tau_2(T)$ is expected to be small compared to $\tau_1(T)$ (compare equation 3.137 in section III/3.2.3). In addition, $\tau_2(T)$

is short compared to the timescale on which the Förster interaction has to be considered[51] (compare discussion in the next paragraph).

Using approximation 3 and 4, the ratio of the numbers of blue and green photons in the quenched model can be expressed by (compare equation 3.112 in section III/3.2.2 for the unquenched ratio):

$$\frac{F^q_{b\ rad}(T)}{F_{g\ rad}(T)} \cdot \frac{(1-F_{abs})}{(F^q_{b\ mig}(T) + F_{abs} \cdot F^q_{b\ rad}(T))} = \frac{1}{F_{g\ rad}(T)} \cdot \frac{(1-F_{abs})}{(\frac{F^q_{b\ mig}(T)}{F^q_{b\ rad}(T)} + F_{abs})} =$$

$$= \frac{1}{F_{g\ rad}(T)} \cdot \frac{(1-F_{abs})}{(\frac{F_{b\ mig}(T)}{F_{b\ rad}(T)} + F_{abs})} = R_{b-g}(T) \tag{3.148}$$

Hence, using approximations 3 and 4, it can be deduced that the ratio of the number of blue photons (that escape the crystal) to the number of green photons (that escape the crystal) is the same for the quenched as for the unquenched model.

b) Application of the Approximations to the Unquenched Model:

In appendix B.9, a detailed presentation of the application of the explained approximations to the unquenched model solutions and differential equations (see section III/3.2.3) can be found. From this discussion three conclusions for the quenched model can be drawn:

i) Using the approximations 2 and 4 made above, the complete unquenched model can be approximated by the following expressions:

$$\frac{\partial N^{nq}_b(t)}{\partial t} \approx -\frac{1}{\tau_1(T)} \cdot N^{nq}_b(t) + \Theta(t) \cdot (1 - F_{e^- trap}) \cdot N_{eh}(E_{part}) \tag{3.149}$$

$$N^{nq}_b(E_{part}, T, t) \approx \Theta(t) \cdot (1 - F_{e^- trap}) \cdot N_{eh}(E_{part}) \cdot e^{-\frac{t}{\tau_1(T)}} \tag{3.150}$$

$$N^{nq}_g(E_{part}, T, t) \approx \left[\left(\frac{1}{\tau_{\mathrm{mig,\ b\to g}}(T)} + F_{abs} \cdot \frac{1}{\tau_{rb}(T)}\right) \cdot N^{nq}_b(E_{part}, T, t)\right] * \left[\Theta(t) \cdot e^{-\frac{t}{\tau_2(T)}}\right] \tag{3.151}$$

Four observations can be emphasized (for a detailed derivation, see appendix B.9):

- The approximations made, lead to a decoupling of the system of differential equations so that only a simplified differential equation (equation 3.149) for the blue STE population remains: **The excitation term by the green STE population as well as the time-dependent excitation process are no longer included**.
- It should be noted that the (main) influence of the green STE population on the blue STE population is still contained in the differential equation as in equations 3.149 and 3.150 **the effective unquenched lifetime of blue STEs, $\tau_1(T)$, instead of the intrinsic lifetime of blue STEs** $\tau_{ltb}(T)$ is used.

[51] In section III/2.2.3, the results (from [41]) of fits to light-pulse shapes, for γ- and α-particles, with the sum of two exponentials are presented: Within a temperature range from mK up to 300K, the correspondingly fast decay time is determined to be of the order of $\sim 1\mu$s and the correspondingly slow decay-time to be of the order of $\sim 10\mu$s to $\sim 100\mu$s (depending on temperature). As will be explained in the next paragraph, within the model developed here, the slow exponential decay time is assigned to the effective unquenched lifetime of blue STEs, $\tau_1(T)$, and the fast exponential decay time is assigned to the reduction of the STE population due to the Förster interaction. Hence, the Förster interaction can be assigned a "typical" time scale of $\mathcal{O}(1\mu$s). For a more detailed explanation, see the next paragraph.

- Due to the interdependencies of the blue and green STE populations, **the green STE population can be described by a convolution** of the fraction of blue STEs (that excite green STEs) with the response function of the green STE population, $\Theta(t) \cdot e^{-\frac{t}{\tau_2(T)}}$ (see equation 3.151).
- The factor $\left[\frac{1}{\tau_{\text{mig, b}\rightarrow\text{g}}(T)} + F_{abs} \cdot \frac{1}{\tau_{rb}(T)}\right]$ in equation 3.151 corresponds to the fraction of blue STEs that excite green STEs.

It has to be noted that the description of the green STE population in the quenched model is the same as in the unquenched model and that, at no point in the derivation (compare appendix B.9), special features of the blue unquenched STE population were used. Hence, it can be deduced that these observations can directly be transferred to the quenched model. Of course, the differential equation for the quenched blue STE population additionally contains the Förster interaction (compare paragraph *c*).

ii) Using additionally approximation 5, it can be shown that the description of the unquenched model can be simplified further for temperatures $T \gtrsim 20$K:

$$N_g^{nq}(E_{part}, T, t) \approx \left(\frac{1}{\tau_{\text{mig, b}\rightarrow\text{g}}(T)} + F_{abs} \cdot \frac{1}{\tau_{rb}(T)}\right) \cdot N_b^{nq}(E_{part}, T, t) \tag{3.152}$$

$$P_g^{nq}(E_{part}, T, t) \approx \frac{1}{R_{b-g}(T)} \cdot P_b^{nq}(E_{part}, T, t) \tag{3.153}$$

where it was used that $R_{b-g}(T)$ can be expressed by (see equation 3.112 in section III/3.2.2):

$$R_{b-g}(T) := \frac{P_b^{nq}(E_{part}, T)}{P_g^{nq}(E_{part}, T)} = \frac{F_{b\ rad}(T)}{F_{g\ rad}(T)} \cdot \frac{(1 - F_{abs})}{(F_{b\ mig}(T) + F_{abs} \cdot F_{b\ rad}(T))} \tag{3.154}$$

The observation can be made, that approximation 5 leads to **the same pulse shapes of the blue and green scintillation light** (except for a scaling factor) **for temperatures** $T \gtrsim 20\mathbf{K}$. In paragraph *a*, it was shown that the ratio $R_{b-g}(T)$ of the numbers of blue and green photons in the quenched model and the unquenched model agree. Additionally, it has to be noted that no specific feature of the unquenched model was used to derive this result (compare appendix B.9). Hence the relationship given by equation 3.153 can directly be transferred to the quenched model.

iii) Using approximation 3 and 4 it can be shown that (for the complete temperature range) the integral ratio of the number of green photons can be expressed as:

$$P_g^{nq}(E_{part}, T) = \int P_g^{nq}(E_{part}, T, t)dt \approx \frac{1}{R_{b-g}(T)} \cdot P_b^{nq}(E_{part}, T) \tag{3.155}$$

Thus, it can be seen that **the integrated number of green photons is directly proportional to the integrated number of blue photons** (in the complete temperature range). Again, the expression for the ratio of the numbers of blue and green photons was used, but no specific feature of the unquenched model was used (compare appendix B.9) to derive this result. Hence, this relationship (equation 3.153) can directly be transferred to the quenched model.

As a consequence, applying the approximations 2 to 5 to the unquenched model (as well as using the expression for $R_{b-g}(T)$) leads to a greatly simplified differential equation for blue STEs and an expression for the calculation of the decay-time spectrum of the green photons via a convolution. In the next paragraph, these results are transferred to the quenched model.

c) Derived Description of the Quenched Model:

From these considerations it can be deduced that, with the help of the explained approximations, the system of differential equations describing the quenched model (equations 3.138 and 3.139) can be simplified and decoupled. The complete quenched model can then be described by the approximated differential equation for blue STEs and the calculation of the green STE population can be performed via a convolution:

$$\begin{aligned}
\frac{\partial n_b^q(\mathbf{x},t)}{\partial t} &= -\frac{1}{\tau_{ltb}(T)} \cdot n_b^q(\mathbf{x},t) - \frac{2\cdot\pi^{\frac{3}{2}}}{3} \cdot \frac{R_{d-d}^3(T)}{\sqrt{\tau_{ltb}(T)\cdot t}} \cdot (n_b^q(\mathbf{x},t))^2 + \\
&\quad + \frac{1}{\tau_{\text{mig, g}\to\text{b}}(T)} \cdot n_g^q(\mathbf{x},t) + n_{bSTE}^{form\,e^-STH}(E_{part},T,\mathbf{x},t) \\
\Rightarrow \frac{\partial n_b^q(\mathbf{x},t)}{\partial t} &\approx -\frac{1}{\tau_1(T)} \cdot n_b^q(\mathbf{x},t) - \frac{2\cdot\pi^{\frac{3}{2}}}{3} \cdot \frac{R_{d-d}^3(T)}{\sqrt{\tau_1(T)\cdot t}} \cdot (n_b^q(\mathbf{x},t))^2 + \\
&\quad + \Theta(t) \cdot n_{bSTE}^{form\,0}(E_{part},\mathbf{x}) \qquad (3.156)
\end{aligned}$$

$$\Rightarrow N_b^q(E_{part},T,t) = \int\limits_{V_{ex}} n_b^q(\mathbf{x},t)d\mathbf{x} \qquad (3.157)$$

$$\Rightarrow N_g^q(E_{part},T,t) \approx \left[\left(\frac{1}{\tau_{\text{mig, b}\to\text{g}}(T)} + F_{abs}\cdot\frac{1}{\tau_{rb}(T)}\right)\cdot N_b^q(E_{part},T,t)\right] * \left[\Theta(t)\cdot e^{-\frac{t}{\tau_2(T)}}\right] \qquad (3.158)$$

$$\begin{aligned}
\Rightarrow P_b^q(E_{part},T,t) &= (1-F_{abs})\cdot\frac{1}{\tau_{rb}(T)}\cdot N_b^q(E_{part},T,t) \\
&= (1-F_{abs})\cdot\int\limits_{V_{ex}}\frac{1}{\tau_{rb}(T)}\cdot n_b^q(\mathbf{x},t)d\mathbf{x} \qquad (3.159)
\end{aligned}$$

$$\Rightarrow P_g^q(E_{part},T,t) = \frac{1}{\tau_{rg}(T)}\cdot N_g^q(E_{part},T,t) \qquad (3.160)$$

$$\begin{aligned}
\Rightarrow P_{tot}^q(E_{part},T) &= \int\left[P_b^q(E_{part},T,t) + P_g^q(E_{part},T,t)\right]dt \approx \\
&\approx \left(1+\frac{1}{R_{b-g}(T)}\right)\cdot P_b^q(E_{part},T) \qquad (3.161)
\end{aligned}$$

with the initial distribution $n_{bSTE}^{form\,0}(E_{part},\mathbf{x})$ of produced blue STEs and with $\tau_1(T)$ and $\tau_2(T)$ still (compare equations 3.106 and 3.107 in section III/3.2.3) defined as effective

unquenched lifetimes of the blue and green STE population, respectively:

$$\frac{1}{\tau_{1/2}(T)} := \frac{1}{2}\cdot\left(\frac{1}{\tau_{ltb}(T)}+\frac{1}{\tau_{ltg}(T)}\right)\mp \\ \mp\frac{1}{2}\cdot\sqrt{\left(\frac{1}{\tau_{ltg}(T)}-\frac{1}{\tau_{ltb}(T)}\right)^2+4\cdot\frac{1}{\tau_{\text{mig, g}\rightarrow\text{b}}(T)}\cdot\left(\frac{1}{\tau_{\text{mig, b}\rightarrow\text{g}}(T)}+F_{abs}\cdot\frac{1}{\tau_{rb}(T)}\right)} \tag{3.162}$$

where the minus sign corresponds to $\tau_1(T)$ and the plus sign corresponds to $\tau_2(T)$.

It should be noted that within the presented approximations of the quenched model, the temporal behavior of the STEs is described by $\tau_1(T)$ and $\tau_2(T)$ which contain the migration and absorption processes. Hence, the derived description of the temporal evolution of the blue and green STE populations (equations 3.156 and 3.158) **contains the mutual excitation processes of the two STE populations**. In addition, it can be seen that, also for the Förster interaction the time $\tau_1(T)$ is used instead of $\tau_{ltb}(T)$, as $\tau_1(T)$ is interpreted as effective unquenched lifetime of the blue STE population in absence of the Förster interaction[52]. Comparing equation 3.156 to the differential equation for blue STEs for $T \lesssim 5\text{K}$ in the unquenched model (equation 3.115, section III/3.2.3), it becomes clear that equation 3.156 corresponds to the exact description of the density of quenched blue STEs[53] for $T \lesssim 5\text{K}$. For the description of the green STE population (equation 3.158), the number of STEs ($N_g^q(E_{part},T,t)$) instead of their density ($n_g^q(E_{part},T,t)$) can directly be used, as the temporal evolution of the green STE population does not contain processes that depend on the densities of STEs (compare equation 3.139).

From equation 3.161, it can be seen that, if only the total amount of scintillation light $L_{tot}^q(E_{part},T)$ produced (in energy, equation 3.98 in section III/3.2.2), is of interest (e.g., for the calculation of the light yield of an interacting particle), the decay-time spectrum of the green photons does not have to be calculated explicitly:

$$\Rightarrow L_{tot}^q(E_{part},T) = \int\left[\overline{E}_{Pb}(T)\cdot P_b^q(E_{part},T,t)+\overline{E}_{Pg}(T)\cdot P_g^q(E_{part},T,t)\right]dt \approx \\ \approx\left(\overline{E}_{Pb}(T)+\overline{E}_{Pg}(T)\cdot\frac{1}{R_{b-g}(T)}\right)\cdot P_b^q(E_{part},T) \tag{3.163}$$

where $\overline{E}_{Pb}(T)$ and $\overline{E}_{Pg}(T)$ correspond to the mean energies of the blue and green photons, respectively.

If, however, the decay-time spectrum for green photons is of interest, two different cases are distinguished:

- For temperatures $T \gtrsim 20K$, the expression for the green STE population and hence, for the decay-time spectrum of the green photons, can be simplified further (compare

[52] From the definition of the Förster interaction it can be seen that exactly this time $\tau_1(T)$ has to be used for the calculation of the Förster interaction (compare the definition of $R_{d-d}(T)$, equation 3.72 in section III/3.1.3).

[53] At $T \lesssim 5\text{K}$, the complete initial generation of blue STEs is regarded as instantaneously ($F_{dr}(T)=0$), no migration processes are possible and the effective unquenched lifetime $\tau_1(T)$ of blue STEs corresponds to the intrinsic lifetime $\tau_{ltb}(T)$ of blue STEs: $\tau_1(T \lesssim 5\text{K}) = \tau_{ltb}(T \lesssim 5\text{K}) \approx \tau_{L1b}$.

equation 3.153):

$$P_g^q(E_{part}, T, t) \approx \frac{1}{R_{b-g}(T)} \cdot P_b^q(E_{part}, T, t) \tag{3.164}$$

It can be seen that for temperatures $T \gtrsim 20$K, the decay-time spectrum of green photons in the quenched model agrees with the decay-time spectrum of blue photons.

- For temperatures $T \lesssim 20$K, however, $\tau_2(T)$ is assumed to become significantly longer, as the radiative recombination from the higher-lying energy level of the green STEs is expected to become less probable (compare section III/3.1.3). Therefore, equation 3.158 has to be used. Thus, the calculation of the decay-time spectrum of green photons for $T \lesssim 20$K involves the convolution of the decay-time spectrum of blue photons with an exponential. This case is discussed at the end of this section, using an example for a decay-time spectrum of the $CaWO_4$ scintillation light from literature.

d) Derived Solution for Blue STEs:

In the following, the solution of the simplified differential equation for blue STEs $n_b^q(\mathbf{x}, t)$ (equation 3.156) is presented. Several observations that can already be made on this basis, i.e., without introducing a specific expression for the initial ($t = 0$) distribution $n_{bSTE}^{form\,0}(E_{part}, \mathbf{x})$ of the density of blue STEs, are discussed.

Equation 3.156 of the blue STE population can be solved analytically yielding the expression for the temporal evolution of the density of blue STEs within the quenched model for the complete temperature range (mK up to $T \approx 300$K):

$$\begin{aligned} n_b^q(\mathbf{x}, t) = \Theta(t) \cdot n_{bSTE}^{form\,0}(E_{part}, \mathbf{x}) \cdot e^{-\frac{t}{\tau_1(T)}} \cdot \\ \cdot \frac{1}{1 + n_{bSTE}^{form\,0}(E_{part}, \mathbf{x}) \cdot \frac{2}{3}\pi^2 \cdot R_{d-d}^3(T) \cdot erf\left(\sqrt{\frac{t}{\tau_1(T)}}\right)} \end{aligned} \tag{3.165}$$

where erf is the error function.

On the basis of equation 3.165, which describes the temporal evolution of the density of quenched blue STEs, already several important observations can be made:

- Inspecting the exponential term (equation 3.165, exponential with decay time $\tau_1(T)$), it can be seen that this term corresponds to the dominating pulse shape of the unquenched blue scintillation light (in the complete temperature range, compare discussion at the end of section III/3.2.3).
- The last term in the formula for the quenched blue STE population (second line in equation 3.165) corresponds to the impact of the Förster interaction.
- The value of the error function in equation 3.165, at $t = 0$ is $erf(\sqrt{0}) = 0$. For increasing t, the error function increases monotonically towards $\lim_{t\to\infty} erf\left(\sqrt{\frac{t}{\tau_1(T)}}\right) = 1$. The value of the error function at $t = \tau_1(T)$ is $erf(\sqrt{1}) \approx 0.84$. It should be noted that for small t, $t \lesssim 0.2 \cdot \tau_1(T)$, the slope of the error function is larger than unity, whereas for large t, $t \gtrsim 0.2 \cdot \tau_1(T)$, the slope of the error function is smaller than unity. The value of the error function at $t = 0.2 \cdot \tau_1(T)$ is $erf\left(\sqrt{\frac{0.2 \cdot \tau_1(T)}{\tau_1(T)}}\right) \approx 0.47$

- For $t = 0$, the second term of equation 3.165 equals unity. Therefore, at $t = 0$, the expression for the density of the quenched STE population (described by equation 3.165) is directly proportional to the density (and therefore to the number) of initially produced STEs (compare equation 3.141 for $n_{bSTE}^{form\,0}(E_{part}, \mathbf{x})$)[54]. Hence, the number of photons generated at $t \approx 0$ is directly proportional to the number of generated STEs. This means that, at $t = 0$, the height of the produced scintillation-light pulse is directly proportional to the fraction of energy deposited in ionization, $F_{ioniz}(E_{part})$. It has to be noted that $F_{ioniz}(E_{part})$ is different for different interacting particles depositing the same energy (compare section III/3.1.1).

- For all times $t > 0$ after the energy deposition, the error function satisfies $0 < erf(t > 0) < 1$. Hence, the last term of equation 3.165 (second line) depends on the density of generated STEs, $n_{bSTE}^{form\,0}(E_{part}, \mathbf{x})$, and is always smaller than unity. The factor given by the last term, which is always larger than zero and smaller than unity, can be interpreted as a reduction of the value of $n_{bSTE}^{form\,0}(E_{part}, \mathbf{x})$ (in the first line of equation 3.165). A a consequence, the value with which the exponential term with decay time $\tau_1(T)$ is multiplied (first line of equation 3.165) is reduced with time. The extent of this reduction depends on the density of the initially created STE population $n_{bSTE}^{form\,0}(E_{part}, \mathbf{x})$ (in the second term of equation 3.165). This behavior reflects the autocorrelation of the Förster interaction.

- For small times $t \lesssim 0.2 \cdot \tau_1(T)$, the value of the second term decreases comparably fast (slope of the error function larger than 1).

- For large times $t \gtrsim 0.2 \cdot \tau_1(T)$, the value of the second term decreases comparably slowly (slope of the error function smaller than 1).

- Hence, as already discussed in the context of the introduction of the Förster interaction (see section III/3.1.3), it can be seen that, for small times $t \lesssim 0.2 \cdot \tau_1(T)$ after the initial energy deposition, the impact of the second term is large. It describes an additional, non-exponential reduction of the blue STE population and, hence, also of the decay-time spectrum of the produced photons, $P_b^q(E_{part}, T, t)$.

- For large times $t \gg 0.2 \cdot \tau_1(T)$, this second term converges to a constant value (as it no longer depends on t). Therefore, for large times t, the time dependency of the STE population and, hence, of the decay-time spectrum of the produced photons, $P_b^q(E_{part}, T, t)$, is dominated by the purely exponential function with decay time $\tau_1(T)$ independently of $n_{bSTE}^{form\,0}(E_{part}, \mathbf{x})$.

The conclusions that can be drawn from these considerations for the decay-time spectra and for the amount of scintillation light generated for different interacting particles are discussed in the following section.

Decay-Time Spectrum of the Quenched Blue Scintillation Light

In the following, the calculation of the decay-time spectra of the quenched blue scintillation light for an energy deposition by a heavy, charged particle as primary interacting particle in

[54] This proportionality would also remain if a fraction $F_{dr}(T)$ of the STEs was generated in the delayed recombination process, as, in first order approximation, this fraction does not depend on the ionization density, and, thus, does not depend on the interacting particle (compare appendix B.2.1).

$CaWO_4$ on the basis of the derived solution for the blue STE population (equation 3.165) is presented. For this purpose the distribution of the density of blue STEs initially created in the energy-deposition process of the interacting particle, $n_{bSTE}^{form\,0}(E_{part}, \mathbf{x})$, is needed. The model developed within this work to describe this initial blue STE distribution as well as the method to determine the parameters used within this model was introduced in section III/3.1.2: The complete volume, $V_{ex}(E_{part})$, excited by a heavy, charged particle with energy E_{part} within its energy-loss process is divided into the PIT volume and a large number of Rec volumes, where each of these sub-volumes is further sub-divided into an inner and an outer volume containing different densities of initially created STEs (see, e.g., equations 3.24 and 3.26 in section III/3.1.2 for the STE-density distributions within the inner and outer PIT volumes). It should be noted that dividing $V_{ex}(E_{part})$ into several sub-volumes is not in conflict with the calculation of the decay-time spectrum of blue photons, $P_b^q(E_{part}, T, t)$, using equation 3.143: The subdivision of the total volume corresponds to splitting the complete volume integral into several volume integrals over the individual sub-volumes which are disjoint by definition (interval additivity of the integral).

In order to improve the readability of the formulas, in the following, the dependency of the used parameters on the type and the energy of the interacting particle is not explicitly displayed within formulas.

Calculation of the Decay-Time Spectrum of Quenched Blue Photons:

The resulting decay-time spectrum of the blue photons calculated by inserting the initially produced STE density into equation 3.165 is exemplarily presented for the inner volume of the primary ionization track[55], $V_{PIT}^{in}(E_{part})$ (model PIT): The expression for the initially created blue STE density in the inner volume of the PIT (equation 3.24 in section III/3.1.2) is inserted into the solution for the quenched STE density (equation 3.165). This yields the temporal evolution of the blue STE population in the inner volume of the PIT, $V_{PIT}^{in}(E_{part})$. Using equation 3.143, i.e., performing the volume integral of the STE population over $V_{PIT}^{in}(E_{part})$, results in the decay-time spectrum of the quenched blue photons, $P_{b,in,PIT}^{q}(E_{part}, T, t)$, produced by the blue STEs, $N_{bSTE,PIT}^{in}(E_{part})$, in the inner volume of the PIT:

$$P_{b,in,PIT}^{q}(T,t) = \Theta(t) \cdot \frac{(1-F_{abs})}{\tau_{rb}(T)} \cdot N_{bSTE,PIT}^{in} \cdot e^{-\frac{t}{\tau_1(T)}} \cdot \cdot \frac{1}{n_{bSTE,in,PIT}^{form\,0} \cdot \frac{2}{3}\pi^2 \cdot R_{d-d}^3(T) \cdot erf\left(\sqrt{\frac{t}{\tau_1(T)}}\right) \cdot (1 - e^{-\alpha_{PIT} \cdot l_{track}})} \cdot \cdot \ln\left(\frac{1 + n_{bSTE,in,PIT}^{form\,0} \cdot \frac{2}{3}\pi^2 \cdot R_{d-d}^3(T) \cdot erf\left(\sqrt{\frac{t}{\tau_1(T)}}\right)}{1 + n_{bSTE,in,PIT}^{form\,0} \cdot \frac{2}{3}\pi^2 \cdot R_{d-d}^3(T) \cdot erf\left(\sqrt{\frac{t}{\tau_1(T)}}\right) \cdot e^{-\alpha_{PIT} \cdot l_{track}}}\right) \tag{3.166}$$

where the factor $\frac{(1-F_{abs})}{\tau_{rb}(T)}$ (in the first line of equation 3.166) indicates that the fraction F_{abs} of the blue photons produced by the radiative decay of blue STEs (with $\tau_{rb}(T)$) is absorbed at defect centers and does not escape the crystal (compare section III/3.1.3). In addition, it should be noted that the factor $(1 - e^{-\alpha_{PIT} \cdot l_{track}})$ in the denominator of

[55] More details on the calculation of the decay-time spectra for the respective inner and outer volumes described in the two models (PIT and Rec) can be found in appendix B.10.

the second line of equation 3.166 reflects the structure of the argument of the natural logarithm in the third line[56] of equation 3.166.

For comparison, the corresponding final expression for the inner volume of one of the slices of a recoil track (model *Rec*, compare section III/3.1.2) is stated in equation 3.167. The result for the decay-time spectrum of the quenched blue photons generated by the radiative decay of the blue STEs within the inner volume, $V^{in}_{Rec[i]}(E_{part})$, of one of the 1nm long slices of a recoil track, $N^{in}_{bSTE,Rec[i]}$, can be expressed by:

$$P^{q}_{b,in,Rec[i]}(T,t) = \Theta(t) \cdot \frac{(1-F_{abs})}{\tau_{rb}(T)} \cdot N^{in}_{bSTE,Rec[i]} \cdot e^{-\frac{t}{\tau_1(T)}} \cdot \cdot \frac{1}{1 + n^{form\,0}_{bSTE,in,Rec[i]} \cdot \frac{2}{3}\pi^2 \cdot R^3_{d-d}(T) \cdot erf\left(\sqrt{\frac{t}{\tau_1(T)}}\right)} \quad (3.167)$$

This formula exhibits a simpler structure (compared to equation 3.166) as the distribution of the initially created blue STE population within the inner (and outer) *Rec* volumes are modeled as homogeneous distribution within the respective volume. In contrary, in the *PIT* volumes a dependency of the ionization distribution on the position along the track of the primary interacting particle (z-coordinate) is included in the model (compare section III/3.1.2).

It should be kept in mind that the complete volume excited by one interacting particle is composed of at least one volume described by model *PIT* and of many volumes described by the model *Rec* (see discussion in chapter III/3.1.2). In addition, it has to be noted that the parameters describing the geometrical extent of the excited volumes as, e.g., $V^{in}_{PIT}(E_{part})$ or $\alpha_{PIT}(E_{part})$, and the distribution of the density of the initially created STE population, e.g., $n^{form\,0}_{bSTE,in,PIT}(E_{part})$, as well as the initial number of blue STEs, e.g., $N^{in}_{bSTE,PIT}(E_{part})$, are dependent on the type and energy E_{part} of the primary interacting particle. Within the model developed, these parameters exhibit no temperature dependency (for a short discussion of this assumption, see section III/6.3). The temporal parameters within the formulas describing the scintillation-light decay-time spectra (equations 3.166 and 3.167), $\tau_1(T)$ (the effective unquenched lifetime of blue STEs) and $\tau_{rb}(T)$ (the radiative recombination time of blue STEs), as well as the Förster radius, $R_{d-d}(T)$, however, are only, as indicated, dependent on the temperature, and not on the type and energy of the interacting primary particle.

Discussion of the Decay-Time Spectrum of the Quenched Blue Scintillation Light as well as of the Total Amount of Scintillation Light Produced

As discussed above (see equations 3.163 and 3.161), the total amount of scintillation light as well as the total number of photons generated can be described with the decay-time spectrum of blue STEs only (summed up for all individual volumes excited in the energy deposition process of the primary interacting particle, i.e., also by its recoil particles, compare section III/3.1.2). This is due to the fact that the number of green photons produced is directly proportional to the number of blue photons produced, independent of the initial density of blue STEs (see equation 3.161). Therefore, in the following, the impact of

[56] $\ln\left(\frac{1+a}{1+a\cdot e^{-\alpha l}}\right) = \ln(1+a) - \ln\left(1+a\cdot e^{-\alpha l}\right)$.

the Förster interaction onto the amount of produced scintillation light will be discussed without considering the green light pulse-shape.

The expression for the decay-time spectrum of blue photons of the inner volume of a slice of a recoil track (equation 3.167) can be compared with the expression for the temporal evolution of the blue STE population as described by the solution of the quenched model (equation 3.165). It can be seen that the term describing the influence of the Förster interaction (second line in both equations) remains exactly the same whereas, in the respective first term, the *initial density* of blue STEs (equation 3.165) is replaced by the *initial number* of blue STEs (equation 3.167). Nonetheless, the structure of the expressions (dependency on time as well as on the Förster interaction) is exactly the same.

In addition, it has to be noted that the structure of the expressions for the decay-time spectra of blue photons generated by the STE populations in the inner volume of the PIT (equation 3.166) and in the inner volume of $Rec[i]$ (equation 3.167) is also very similar. It can be seen that the terms in the respective first lines of the expressions correspond directly to each other (of course, the respective associated initial numbers of STEs have to be used). The respective other terms, describing the impact of the Förster interaction do not correspond directly to each other. However, their limiting behavior, for very large times $t \to \infty$, for very small times $t \to 0$ as well as the temporal trends in between are the same: For very small times $t \to 0$, both of these terms converge to unity whereas, for very large times t, both of these terms converge to a constant value. For increasing time t (starting at $t = 0$), both of these terms decrease monotonically with a steep slope at the beginning, then this slope decreases with time. The difference between these two expressions is that the slope at the beginning described by the Förster-interaction term of the PIT volume is steeper at the beginning and decreases faster with time than the evolution described in the Rec volume. These differences occur due to the fact that the STE population within the PIT volume is additionally structured in comparison to the STEs within a Rec volume: The STE distribution within the PIT volume is characterized by an increased density at the beginning of the track, decreasing to smaller densities along track[57] (exponential variation in z-direction, for details, see section III/3.1.2).

The same observations can be made concerning the expressions for the decay-time spectra of blue photons generated by the STE populations in the outer volumes of the PIT and the Rec model (see equations B.91 and B.93 in appendix B.10).

Additionally, it should be noted that, for the complete expression of the decay-time spectrum for one primary interacting particle, $P_b^q(E_{part}, T, t)$, (given by the sum of inner and outer volumes of the type PIT and $Rec[i]$, see section III/3.1.2), the factor:

$$\Theta(t) \cdot \frac{(1 - F_{abs})}{\tau_{rb}(T)} \cdot e^{-\frac{t}{\tau_1(T)}}$$

[57]The described decreasing STE-density distribution can be observed for particles with energies smaller than the energy where the maximum energy-loss occurs (Bragg peak, compare discussion in appendix B.3.10). However, also for particles with energies larger than this threshold energy a variation of the STE-density distribution along their track occurs. The only difference is that the produced STE density first increases until the Bragg peak is reached and then starts to decrease. As can be seen from figure B.15 in appendix B.3.10, also for such high-energetic particles, the STE density distribution within the PIT volume is described with an exponential variation along the primary particle track.

(see the respective first lines of the expressions for the decay-time spectra) can be factored out. The remaining terms correspond to the impact of the Förster interaction within the respective sub-volumes and describe the influence of the quenching onto the pulse shape and onto the amount of scintillation light generated.

Hence, it can be deduced that the temporal behavior of the decay-time spectrum of the quenched blue photons (as described by the respective formulas) is basically the same as the temporal behavior of the quenched blue STE population (equation 3.165). Therefore, the discussion of the quenched blue STE population can be qualitatively transferred to the shape of the decay-time spectrum of the quenched blue photons (as already indicated there). Four major observations are repeated in short form:

- At $t = 0$, the pulse height of the total blue scintillation light produced by one primary interacting particle can be expressed by the total number of initially produced blue STEs, $N_{bSTE}(E_{part})$ (see equation 3.10 in section III/3.1.2). This relationship is obtained by considering that all terms describing the Förster interaction are equal to unity at $t = 0$ and that the sum of blue STEs within all excited volumes equals the total number of initially created blue STEs:

$$P_b^q(E_{part}, T, t = 0) = \frac{(1 - F_{abs})}{\tau_{rb}(T)} \cdot N_{bSTE}(E_{part}) = \\ = \frac{(1 - F_{abs})}{\tau_{rb}(T)} \cdot \frac{(1 - F_{e^- trap})}{2.35 \cdot E_{gap}} \cdot F_{ioniz}(E_{part}) \cdot E_{part} \qquad (3.168)$$

  Hence, it can be seen that, within the developed model, it is predicted that the amplitude of the scintillation-light pulse at $t = 0$ is directly proportional to $F_{ioniz}(E_{part}) \cdot E_{part}$, i.e., to the amount of the deposited energy that is converted into ionization.

- **The impact of the Förster interaction is described by the respective second and third terms in the expressions (see, e.g., equations 3.166 and 3.167) for the decay-time spectrum of quenched blue photons. These terms lead to a reduction of the pulse height with time, additionally to the exponential decay** (described by the respective first lines of the expressions).

- For **small times** t $(0 < t \lesssim 0.2 \cdot \tau_1(T))$, **the reduction of the pulse height introduced by the Förster interaction is large** whereas **for larger times** t $(0.2 \cdot \tau_1(T) \lesssim t)$, the **impact of the Förster interaction on the pulse shape decreases** significantly (less variation of the terms corresponding to the Förster interaction with time[58]).

- **For large times** t $(0.2 \cdot \tau_1(T) \ll t)$, **the complete decay-time spectrum of the quenched blue photons converges to a purely exponential decay with decay constant** $\tau_1(T)$, independently of the density of initially created blue STEs. $\tau_1(T)$ corresponds to the effective unquenched lifetime of blue STEs in absence of the Förster interaction and is approximately equal to the intrinsic lifetime[59] $\tau_{ltb}(T)$ of

[58] It should be noted that the same limiting time of $0.2 \cdot \tau_1(T)$ as in the discussion of the quenched blue STE population (equation 3.165) can be used as the dependency of the error function on time is the same in the decay-time spectrum of the blue photons as in the temporal evolution of the blue STEs.

[59] The intrinsic lifetime is determined by the migration time, the radiative and non-radiative recombination times of the blue STEs in absence of the Förster interaction and in absence of the mutual excitation processes of blue and green STEs (compare section III/3.2.4).

blue STEs. **This exponential decay time is the same as for the unquenched decay-time spectrum** (compare section III/3.2.3).

From these conclusions drawn for the decay-time spectrum of the quenched blue STEs, predictions for the total amount of scintillation light generated can be deduced[60]. From the expression and discussion of the decay-time spectrum of the quenched blue scintillation light it can be seen that the different amount of scintillation light produced for different interacting particles is the result of two combined effects:

- As the amplitude of the blue scintillation-light pulse at $t = 0$ is directly proportional to the number of initially generated blue STEs, it can be deduced that the number of blue STEs taking part in the light production process in the first place is directly proportional to the amount of energy deposited in ionization, described by the factor $F_{ioniz}(E_{part})$.
- Due to the dependency of the term describing the Förster interaction on the density of the initially generated blue STE population and due to its effect on the pulse shape of the blue scintillation light, it can be deduced that, for different initial densities of blue STEs, a different fraction of these blue STEs is quenched: This implies that, e.g., for the same number of initially created blue STEs, dependent on their density, different fractions of these STEs recombine non-radiatively via the Förster interaction and, hence, different amounts of scintillation light are produced.

Hence, it can be seen that the decay-time spectrum of the produced blue photons and, thus, also the total amount of the produced scintillation light (blue and green), are dependent on the density of the blue STE population generated in the energy-deposition process. This underlines the importance of the correct determination of the generated ionization density in the energy-deposition process (see section III/3.1.2).

Therefore, within the model developed here, the observed light-yield quenching for different interacting particles in $CaWO_4$ (compare section III/2.2.5) **is ascribed to the combination of the different efficiencies of producing ionization combined with the different distributions of initially generated blue STEs for different interacting particles.**

The **temperature-dependency** of the efficiency of generating scintillation light for different interacting particles that can be deduced from this conclusion is discussed in the context of the complete model with all parameters assigned (in section III/6.1.1).

Illustration of the Decay-Time Spectrum and Amount of the Quenched Blue Scintillation Light Produced

In order to illustrate the described dependencies as well as the general effect of the Förster interaction on the decay-time spectrum of blue photons, examples for decay-time spectra of blue photons are plotted in figure 3.11. As a basis for a comparison, the decay-time spectrum of blue photons calculated for a 100keV Oxygen ion as the primary interacting

[60] It should be noted that the integration over time required to calculate the total amount of scintillation light generated (equation 3.161) can, in general, not be performed analytically, but is performed numerically (compare section III/6.1).

particle in $CaWO_4$ at $T \lesssim 5$K is used. The calculation was performed using the complete model[61] (see section III/5.4). A 100keV Oxygen ion deposits the fraction $F_{ioniz}(E_{part}) = 66.8\%$ of its energy in ionization (compare table 3.2 in section III/3.1.1)) distributed within the excited volume $V_{ex}^{O}(100\text{keV})$. The corresponding decay-time spectrum is displayed as a solid green line in figure 3.11. Additionally, for comparison, four decay-time spectra for hypothetical energy depositions on the basis of varied numbers and/or densities of blue STEs in comparison to the 100keV Oxygen pulse are displayed:

- Dashed green line (pulse 1): The same energy deposited in ionization is assumed (66.8%). Hence, the same number of blue STEs are initially created. However, for this decay-time spectrum, it is assumed that the energy is distributed in a practically infinitely large volume, so that no interaction between the generated STEs is possible. Thus, the unquenched model (equation 3.117) was used for the calculation of the pulse.
- Dashed red line (pulse 2): Half of the energy deposited in ionization is assumed (33.4%). Hence, only half of the number of blue STEs are initially created. Also for this decay-time spectrum, it is assumed that the energy is distributed in a practically infinitely large volume. Thus, the unquenched model (equation 3.117) was used for the calculation of the pulse.
- Solid blue line (pulse 3): The same energy deposited in ionization is assumed (66.8%). A dense distribution of initially created STEs is assumed, hence, as for the original decay-time spectrum (100keV Oxygen ion, solid green line), the quenched model is used for the calculation. However, the volume in which the energy is distributed is reduced by a factor of 2 compared to the 100keV Oxygen pulse[62]. Hence, the density of blue STEs is doubled while the same number of blue STEs is initially created.
- Solid red line (pulse 4): A dense distribution of initially created STEs is assumed and, hence, as for the original decay-time spectrum (100keV Oxygen ion, solid green line), the quenched model is used for the calculation. However, the energy deposited in ionization as well as the volume in which the energy is distributed were each reduced by a factor of 2 compared to the 100keV Oxygen pulse[63]. Hence, the density of initially created blue STEs is exactly the same as for the original 100keV Oxygen pulse, however, only half of the number of blue STEs is generated.

The colored horizontal arrows in figure 3.11 indicate the amplitudes of the respectively colored pulses. The amplitudes of the pulses correspond to the results of the calculations and are not scaled in any manner.

In addition, the significant parameters characterizing the calculated scintillation-light

[61] The calculation was performed on the basis of equations 3.166 and 3.167, using the STE distribution determined for a 100keV Oxygen ion as described in section III/3.1.2 as well as using the model parameters determined as described in section III/5.4.

[62] This was achieved by dividing all radii of the respective sub-volumes by the factor of $\sqrt{2}$. This way to reduce the volume was chosen as a reduction of the track length (which would have been an alternative) would have had an impact on the exponential distribution of blue STEs along the track. The distribution of the blue STEs initially generated between the respective sub-volumes was preserved compared to the original pulse.

[63] Again, the radii were multiplied by a factor of $\sqrt{2}$, while the energy deposited in each individual volume was divided by a factor of 2. The relative distribution of the blue STEs initially generated between the respective sub-volumes was preserved compared to the original pulse.

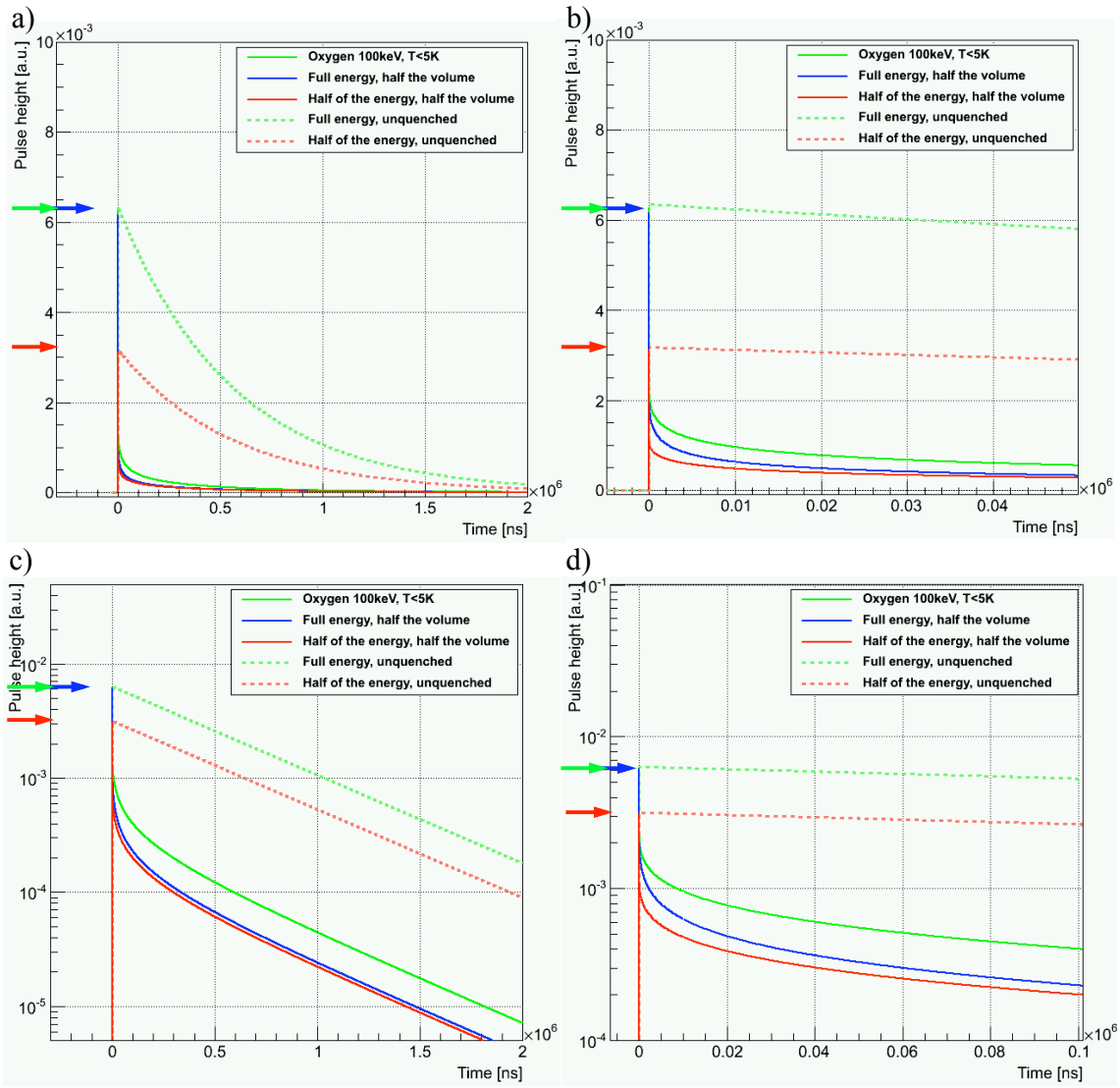

Figure 3.11: Decay-time spectra of blue photons, calculated with the quenched and unquenched model as described in the main text: The solid green line corresponds to the blue scintillation light generated for a 100keV Oxygen ion as the primary interacting particle at a temperature $T \lesssim 5$K. The dashed lines correspond to decay-time spectra calculated with the unquenched model, the solid lines correspond to decay-time spectra calculated with the quenched model. Panel a) and b): Normal y-axis; Panel c) and d): Logarithmical y-axis. Panel b) and d) show close-up views of the beginning of the pulses.

pulses are presented in table 3.6. All values are stated as relative values in comparison to the values of the 100keV Oxygen pulse (for this pulse the absolute values are stated). It should be noted that the number of photons escaping the crystal (last line in table 3.6) can be calculated solely on the basis of the decay-time spectra of the blue photons (compare equation 3.163, which is valid for the quenched and unquenched model as discussed there) and can, therefore, be stated without considering the green light pulse-shape.

From the decay-time spectra plotted in figure 3.11 and the values stated in table 3.6, it can be seen that, as discussed, the amplitudes of the pulses with the same number of initially

pulse	100keV Oxygen	pulse 1	pulse 2	pulse 3	pulse 4
E_{ioniz}	66.8keV	$1 \cdot 66.8$keV	$0.5 \cdot 66.8$keV	$1 \cdot 66.8$keV	$0.5 \cdot 66.8$keV
V_{ex}	V_{ex}^{O}	∞	∞	$0.5 \cdot V_{ex}^{O}$	$0.5 \cdot V_{ex}^{O}$
# STEs	3555	$1 \cdot 3555$	$0.5 \cdot 3555$	$1 \cdot 3555$	$0.5 \cdot 3555$
# photons	234.4	$15.2 \cdot 234.4$	$7.6 \cdot 234.4$	$0.59 \cdot 234.4$	$0.5 \cdot 234.4$

Table 3.6: Parameters calculated for the decay-time spectra displayed in figure 3.11: The second column (100keV Oxygen) indicates the values obtained for the 100keV Oxygen pulse at temperatures $T \lesssim 5$K. The values in the other columns are stated as relative values in comparison to the corresponding value in the second column. In the first line, the amount of energy deposited in ionization, in the second line, the extent of the excited volume, in the third line, the number of STEs initially generated and in the fourth line, the number of photons generated that escape the crystal are indicated.

created STEs are the same. The influence of the Förster interaction onto the pulse shape can clearly be seen when comparing, e.g., the dashed green (unquenched) and solid green (quenched) pulse for which the same number of initially created STEs were used. The impact of the Förster interaction on the amount of generated light can also clearly be seen as the numbers of photons generated for quenched pulses (solid lines) in comparison to unquenched pulses (dashed lines) are strongly reduced. In addition, the non-linear dependency of the Förster interaction on the density of the initially created blue STEs can be identified from the relative number of photons escaping the crystal for pulse 3 in comparison to the original pulse (100keV Oxygen ion): The density of blue STEs for pulse 3 was exactly doubled while the same number of initially generated STEs was used, the amount of photons generated, however is neither the same nor exactly halfed compared to the original pulse.

Decay-Time Spectrum of the Quenched Green Scintillation Light

As discussed above, the decay-time spectrum of green photons at temperatures $T \gtrsim 20K$ is expected to exhibit the same pulse shape as the decay-time spectrum of the blue photons, only with a different amplitude (compare equation 3.164). Hence, the complete discussion regarding the shape of the decay-time spectrum of the blue photons can directly be adopted for the decay-time spectrum of green photons at temperatures $T \gtrsim 20$K.

For temperatures below 20K, however, the influence of the time $\tau_2(T)$, the effective unquenched lifetime of green STEs, is expected to become non-negligible. Hence, the decay-time spectrum of green photons at $T \lesssim 20$K has to be calculated with equation 3.158 (convolution of the blue decay-time spectrum with the response function of green STEs). However, as becomes clear when inspecting equations 3.166 and 3.167 describing the decay-time spectra of the blue scintillation light generated, such a convolution cannot be performed analytically. Nonetheless, an approximate, qualitative description of the decay-time spectrum of the green scintillation light for $T \lesssim 20$K can be obtained when approximating the blue scintillation-light pulse-shape qualitatively by, e.g., three exponentials with respective decay times[64]: $\tau_{d-d}(T)$, a fast decay time of the order of 1μs, reflecting the impact of the quenching at the beginning of the pulse, $\tau_1(T)$, a slow decay

[64]It should be noted that this phenomenological description of the blue scintillation-light pulse-shape almost corresponds to the expression often used to fit whole pulse shapes (blue and green light) of

time, corresponding to the effective unquenched lifetime of blue STEs (of the order of several 10μs to a few 100μs at $T \lesssim 20$K, compare section III/5.4 and the following) and τ_m, an intermediate decay time (or the order of 1μs to several 10μs) to model the transition between the fast and the slow decay. A demonstration of this approach is presented in appendix B.11. The resulting, qualitative description of the blue and green photons in the quenched model can be expressed by:

$$P_b^q(E_{part},T,t) \approx \Theta(t)\cdot P_b^q(E_{part},T)\cdot \\ \cdot\left[\frac{A_{d-d}(T)}{\tau_{d-d}(T)}\cdot e^{-\frac{t}{\tau_{d-d}(T)}}+\frac{A_m(T)}{\tau_m(T)}\cdot e^{-\frac{t}{\tau_m(T)}}+\frac{A_1(T)}{\tau_1(T)}\cdot e^{-\frac{t}{\tau_1(T)}}\right] \tag{3.169}$$

$$P_g^q(E_{part},T,t) \approx \Theta(t)\cdot P_b^q(E_{part},T)\cdot\left(\frac{\tau_{rb}(T)}{(1-F_{abs})\cdot\tau_{\text{mig, b}\to\text{g}}(T)}+\frac{F_{abs}}{(1-F_{abs})}\right)\cdot\frac{1}{\tau_{rg}(T)}\cdot \\ \cdot\left[\frac{A_{d-d}(T)}{1-\frac{\tau_{d-d}(T)}{\tau_2(T)}}\cdot\left\{e^{-\frac{t}{\tau_2(T)}}-e^{-\frac{t}{\tau_{d-d}(T)}}\right\}+\frac{A_m(T)}{\frac{\tau_m(T)}{\tau_2(T)}-1}\cdot\left\{e^{-\frac{t}{\tau_m(T)}}-e^{-\frac{t}{\tau_2(T)}}\right\}+\right. \\ \left.+\frac{A_1(T)}{\frac{\tau_1(T)}{\tau_2(T)}-1}\cdot\left\{e^{-\frac{t}{\tau_1(T)}}-e^{-\frac{t}{\tau_2(T)}}\right\}\right] \tag{3.170}$$

where $A_{d-d}(T)$, $A_m(T)$ and $A_1(T)$ correspond, respectively, to the relative weights of the fast, the intermediate and the slow decaying exponential pulse in the blue scintillation-light pulse-shape (see appendix B.11) and $\tau_{rb}(T)$ and $\tau_{rg}(T)$ correspond, respectively, to the radiative decay times of blue and green STEs. $\tau_{\text{mig, b}\to\text{g}}(T)$ corresponds to the migration time from blue STEs to defect centers and F_{abs} corresponds to the fraction of blue photons absorbed at defect centers. From equation 3.170, it can be seen that, within this approach, the pulse shape of the green scintillation light at temperatures $T \lesssim 20$K is described by the sum of three pulses with exponential rise and decay. The first pulse in formula 3.170 (first curly brackets in the second line) describes a fast rising and fast decaying pulse (i.e., fast in comparison to $\tau_1(T)$) as both decay times involved, $\tau_2(T)$ as well as $\tau_{d-d}(T)$, are expected to be much smaller than $\tau_1(T)$. The second pulse in formula 3.170 (second curly brackets in the second line) describes a fast rising and fast (with $\tau_m(T)$) decaying pulse (i.e., fast rising in comparison to $\tau_1(T)$) as both times involved, $\tau_2(T)$ and $\tau_m(T)$, are expected to be much smaller[65] than $\tau_1(T)$. The third pulse in formula 3.170 (curly brackets in the third line) describes a pulse rising with $\tau_2(T)$ (effective unquenched lifetime of green STEs) and decaying with $\tau_1(T)$ (effective unquenched lifetime of blue STEs). Hence, this third pulse describes the fraction of green scintillation light that exhibits the same slow decay time as the slow decay time of the blue scintillation light (compare equation 3.169). As can be deduced from these considerations, the relative integrals of the respective first pulses (corresponding to fast decaying pulses) of the blue and the green decay-time spectra are both equal to $A_{d-d}(T)$, the relative integrals of the intermediate pulses are both equal to $A_m(T)$ and the relative integrals of the respective third pulses (corresponding to slowly decaying pulses) of the blue and the green decay-time spectra are both equal to $A_1(T)$. Hence, the relative decompositions into fast, intermediately and slowly decaying pulses of the blue and green decay-time spectra are the same, however, the partial pulses of the green scintillation light exhibit rise times.

scintillation-light pulses recorded for $CaWO_4$ under particle excitation (compare section III/2.2.3).

[65] Actually, $\tau_m(T)$ is chosen best of the order of $\sim \frac{1}{10}\cdot\tau_1(T)$ and is, thus, in fact considerably faster than $\tau_1(T)$.

Discussion of the Decay-Time Spectrum of the Complete Quenched Scintillation Light at $T \lesssim 5$K

In order to illustrate the described behavior, a scintillation-light pulse from [54], recorded for a $CaWO_4$ crystal under 18keV Oxygen-ion excitation at 6K is used[66]. This pulse was recorded in [54] without a spectral filter and should, hence, be describable by the sum of the quenched blue and green decay-time spectra (equations 3.169 and 3.170). The scintillation-light pulse from [54] can be seen in figure 3.12.

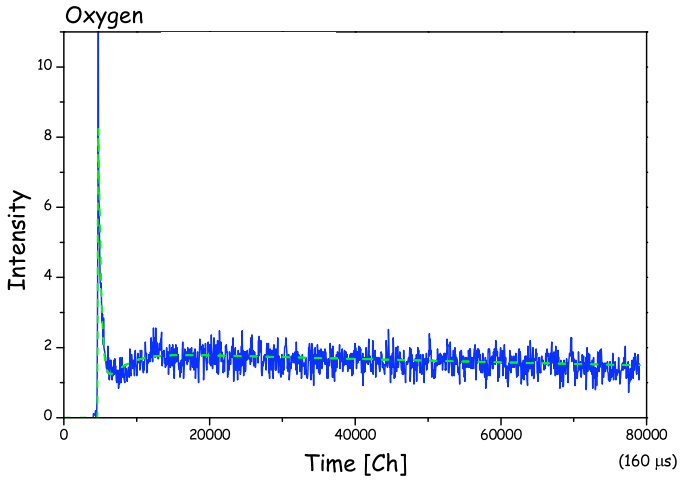

Figure 3.12: Scintillation-light pulse shape recorded for the excitation of a $CaWO_4$ crystal with 18keV Oxygen ions at 6K (figure adopted from[54]). The data points are marked in blue, the dashed green line corresponds to a fit performed in [54] (for details, see discussion before equations 3.176 and 3.177). The pulse shape corresponds to the sum of the blue and the green scintillation light produced.

In order to interpret this pulse shape within the developed model, the decay-time spectra of the blue and green scintillation-light photons (for a temperature of 6K) have to be analyzed. At a temperature of 6K, the description of the blue and of the green scintillation-light pulse shape (equation 3.170) can be further simplified as, for such low temperatures ($T \lesssim 5$K), the migration of STEs has almost ceased (compare section III/3.1.3). Therefore, the only recombination mechanism active should be the radiative decay from the ground level of the respective STE (compare section III/3.2.1). Hence, the following relationships can be applied (compare to the discussion in section III/3.2.3):

$$\tau_1(T \lesssim 5\text{K}) \approx \tau_{ltb}(T \lesssim 5\text{K}) \approx \tau_{rb}(T \lesssim 5\text{K}) \approx \tau_{L1b} \tag{3.171}$$

$$\tau_2(T \lesssim 5\text{K}) \approx \tau_{ltg}(T \lesssim 5\text{K}) \approx \tau_{rg}(T \lesssim 5\text{K}) \approx \tau_{L1g} \tag{3.172}$$

$$\frac{1}{\tau_{\text{mig, b}\rightarrow\text{g}}(T \lesssim 5\text{K})} \approx 0 \tag{3.173}$$

This leads to the following expression for the decay-time spectrum of the blue and the

[66] For recording, a large-area silicon Avalanche Photo-Diode (APD) stabilized at $\sim$ 94K was used in [54].

green STEs at temperatures $T \lesssim 5$K:

$$P_b^q(E_{part},T,t) \approx \Theta(t)\cdot P_b^q(E_{part},T)\cdot \\ \cdot\left[\frac{A_{d-d}(T)}{\tau_{d-d}(T)}\cdot e^{-\frac{t}{\tau_{d-d}(T)}}+\frac{A_m(T)}{\tau_m(T)}\cdot e^{-\frac{t}{\tau_m(T)}}+\frac{A_1(T)}{\tau_{L1b}}\cdot e^{-\frac{t}{\tau_{L1b}}}\right] \tag{3.174}$$

$$P_g^q(E_{part},T,t) \approx \Theta(t)\cdot P_b^q(E_{part},T)\cdot\frac{F_{abs}}{(1-F_{abs})}\cdot \\ \cdot\left[\frac{A_{d-d}(T)}{\tau_{L1g}-\tau_{d-d}(T)}\cdot\left\{e^{-\frac{t}{\tau_{L1g}}}-e^{-\frac{t}{\tau_{d-d}(T)}}\right\}+\frac{A_m(T)}{\tau_m(T)-\tau_{L1g}(T)}\cdot\left\{e^{-\frac{t}{\tau_m(T)}}-e^{-\frac{t}{\tau_{L1g}(T)}}\right\}+\right. \\ \left.+\frac{A_1(T)}{\tau_{L1b}-\tau_{L1g}}\cdot\left\{e^{-\frac{t}{\tau_{L1b}}}-e^{-\frac{t}{\tau_{L1g}}}\right\}\right] \tag{3.175}$$

where the factor $\frac{F_{abs}}{(1-F_{abs})}$ in the first line of equation 3.175 describes the ratio of the amount of green light produced to the amount of blue light produced. Using this relationship it can be shown that the fraction $(1-F_{abs})$ of the total number of produced photons are blue photons, whereas the fraction F_{abs} are green photons (compare to the unquenched model for $T \lesssim 5$K in section III/3.2.3). In addition, it can be seen that the respective third pulses of both decay-time spectra (third term in square brackets in equation 3.174 and 3.175, respectively) exhibit a decay time corresponding to the radiative decay time τ_{L1b} of blue STEs from the ground level of blue STEs. The difference between the blue and the green decay-time spectrum is that, as can be seen from equation 3.175, all pulses of the green decay-time spectrum exhibit rise times, $\tau_{dd}(T)$ or τ_{L1g}, respectively. Hence, it can be deduced that the fraction A_1 of the total number of photons produced (sum of blue and green photons) is expected to exhibit a slow decay time of τ_{L1b}, whereas the fraction $F_{abs}\cdot A_1(T)$ of this slow decaying light should exhibit a rise time of $\tau_{L1g}(T)$.

In order to quantitatively interpret the described scintillation-light pulse-shapes (equations 3.174 and 3.175), data on the fraction of the total amount of scintillation light contained in the blue component as determined in [54] for a typical $CaWO_4$ crystal investigated there (i.e., $(1-F_{abs}) \approx 70\%$ of the total amount of scintillation light produced is blue) can be used. Additionally, from the discussion of qualitative pulse-shape fits (in [41], described in section III/2.2.3), it can be deduced that, for Oxygen recoils, the fraction of scintillation light with faster decaying behavior should be $< 20\%$ (at low temperatures). It should be noted that it is assumed that the "fast decaying fraction" as determined in the qualitative pulse shape fits in [41] (using only two exponentials) comprises the fast and the intermediately decaying fraction of the scintillation light as introduced within the present work (see equations 3.174 and 3.175). Using this information, a rough estimate of the share between the fast and slow decaying blue and green pulse shapes (partial pulses of equations 3.174 and 3.175) of the complete scintillation light decay-time spectrum (sum of blue and green light, as recorded in [54] and shown in figure 3.13) can be gained:

- Fraction *1* of the complete light: Blue light with an immediate rise and slow decay time τ_{L1b}: $\sim 56\%$.
- Fraction *2* of the complete light: Blue light with an immediate rise and faster (compared to τ_{L1b}, i.e., fast and intermediate) decay times $\tau_{d-d}(T)$ or $\tau_m(T)$: $\sim 14\%$.
- Fraction *3* of the complete light: Green light with a slow rise of τ_{L1g} and slow decay time τ_{L1b}: $\sim 24\%$.

- Fraction *4* of the complete light: Green light with a rise time of $\tau_{d-d}(T)$ and $\tau_{L1g}(T)$ and a faster decay time τ_{L1g} or $\tau_m(T)$ (faster compared to $\tau_{L1b}(T)$): $\sim 6\%$.

From these estimations it can be deduced that, most probably the green scintillation light exhibiting a faster decay time (τ_{L1g} and $\tau_m(T)$, fraction *4*) can be neglected compared to all other contributions. Hence, the complete pulse shape should be describable by the main fraction *1*, corresponding to blue light with immediate rise and slow decay with τ_{L1b}, a smaller fraction *2*, corresponding to blue light with an immediate rise and a comparably fast decay with $\tau_{d-d}(T)$ and $\tau_m(T)$, and the fraction *3* corresponding to green light with a slow, observable rise time τ_{L1g} and the same slow decay time τ_{L1b} as fraction *1*.

In figure 3.13, it is illustrated how these predictions can be used to interpret the pulse shape as recorded for 18keV O ions from [54]:

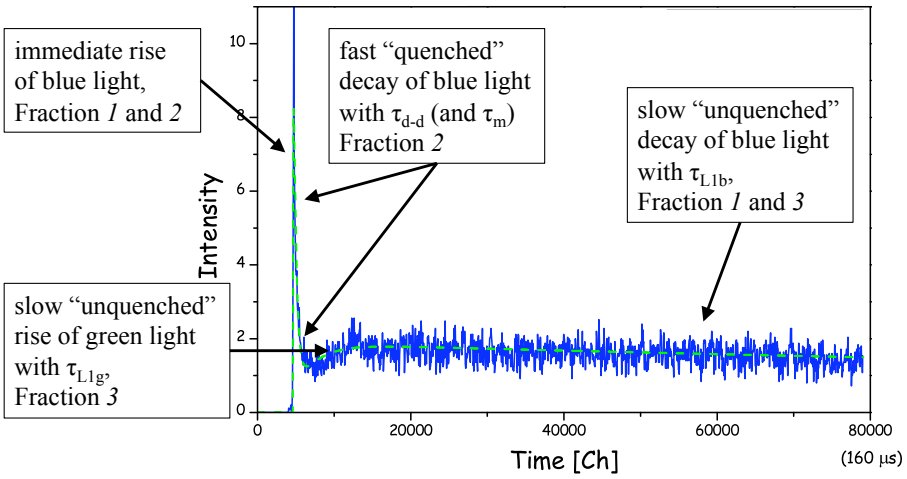

Figure 3.13: Scintillation-light pulse shape recorded for the excitation of a $CaWO_4$ crystal with 18keV Oxygen ions at 6K (figure adopted from[54]). The data points are marked in blue, the dashed green line corresponds to a fit performed in [54] (for details, see discussion before equations 3.176 and 3.177). Additionally indicated and labeled is the interpretation of the observed rise and decay times within the model developed here (for details, see main text).

From figure 3.13 it can be seen that the observed pulse shape of the scintillation light can be fully explained with the developed interpretation of the blue and green scintillation light pulse shapes.

Besides this graphical interpretation, it can be attempted to qualitatively reproduce the pulse shape as recorded in [54] (see figure 3.12) with the sum of the blue and green pulse shapes (equations 3.174 and 3.175). It should be noted, that no quantitative pulse-shape fit was strived for as no information on the ratio of blue to green light contained in the recorded light pulse as well as no information on the response function of the setup utilized in [54] was available. Thus, no attempt was made to quantitatively reproduce of the pulse shape. The result of such a qualitative approach is shown in figure 3.14: In panel a), the black line corresponds to the quenched blue photon decay-time spectrum as calculated with the complete quenched model for an interacting O ion of 20keV at a temperature of $T \lesssim 5$K (see section III/6.1.1). The dashed blue line corresponds to the reproduction of this pulse shape by three exponentials using equation 3.174. In panel b), this approximate

blue light pulse shape is shown as solid blue line. The solid green line corresponds to the green photon decay-time spectrum as calculated with equation 3.175 using this blue light pulse-shape as input. The solid red line corresponds to the sum of both contributions and, hence, should qualitatively reproduce the scintillation-light pulse-shape as recorded in [54] (see figure 3.12).

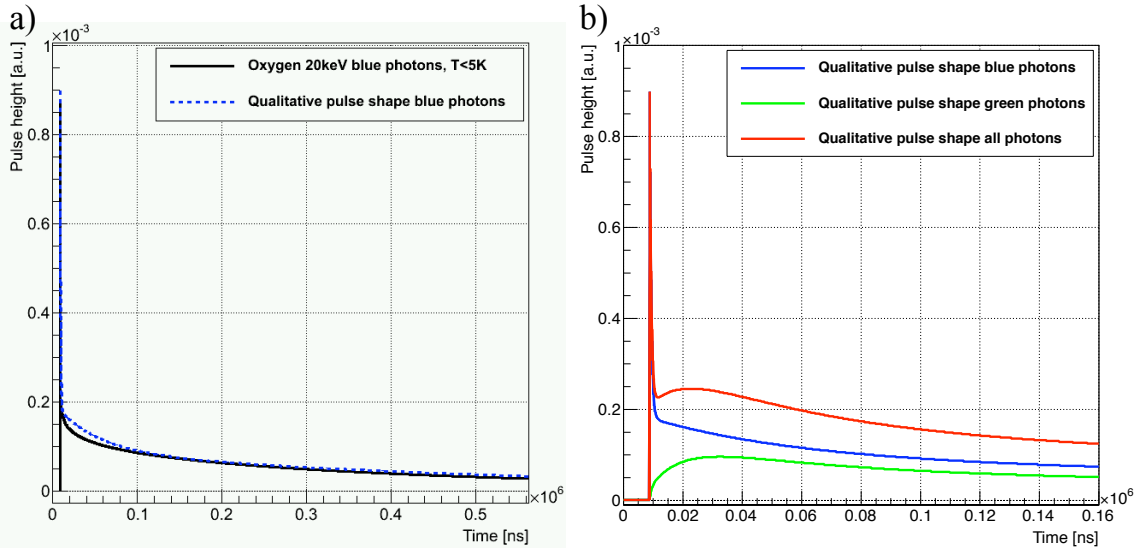

Figure 3.14: Scintillation-light pulse shapes as calculated with the approximations of the quenched model (equations 3.174 and 3.175) for a 20keV O ion as primary interacting particle (for $T \lesssim$ 5K). Panel a): In black, the result for the blue scintillation light pulse shape as calculated with the complete quenched model can be seen (compare section III/6.1.1). The dashed blue line corresponds to the approximation of this pulse shape with three exponentials as described by equation 3.174. In panel b), this approximated blue pulse shape (solid blue line) as well as the green light pulse-shape as calculated with equation 3.175 on the basis of this blue light pulse-shape (solid green line) can be seen. The solid red line corresponds to the total decay-time spectrum, i.e., the sum of the blue and the green light pulse-shapes.

Comparing the complete light pulse-shape as calculated with the approximated model (solid red line in panel b of figure 3.14) to the recorded light pulse-shape (figure 3.13), it can be seen that the model calculation nicely complies with the observed light pulse-shape.

Thus, it can be concluded that, within the developed model, the slow rise time and the slow decay time observed for the recorded scintillation-light decay-time spectrum are identified with the radiative decay times of green and blue STEs from their ground levels, τ_{L1g} and τ_{L1b}, respectively. It should be noted that this interpretation of the light pulse-shape can be used to gain estimates for these radiative recombination times. For this purpose, the qualitative pulse-shape fit of the recorded scintillation-light decay-time spectrum from [54] (shown as dashed green line in figure 3.12 and 3.13) is used: This phenomenological fit was performed in [54] with the sum of two exponentially-shaped pulses: One with immediate rise time and fast decay time and the second one with a non-zero rise time and a slow decay time. Hence, the fit function used in [54] almost complies with the description of the pulse shape within the model developed in the present work. Thus, the values obtained in [54] for the non-zero rise time as well as for the slow decay time of the pulse

are adopted for the radiative decay times of blue and green STEs from their ground levels, τ_{L1b} and τ_{L1g}, respectively (the errors of the fit results are between 1% and 2%). Thus, in the following, τ_{L1b} and τ_{L1g} are assumed to be given by (values from [54]):

$$\tau_{L1b} = 565\mu\text{s} \tag{3.176}$$

$$\tau_{L1g} = 4.98\mu\text{s} \tag{3.177}$$

These values are adopted for the model developed here, as, within the present work, no decay-time spectra were recorded at such low temperatures that allow this straight-forward identification of the decay times from the ground levels of blue and green STEs.

3.3 Summary of the Complete Model and Concept for the Determination of the Model Parameters

In the following, a short summary and review of the predictions of the developed model for the scintillation-light generation and quenching in $CaWO_4$ is presented. This summary is followed by a description of a concept for the determination of the free model parameters.

3.3.1 Summary of the Complete Model

The developed model includes the complete light generation process on a microscopic basis which follows the energy deposition process by an interacting particle in $CaWO_4$. The parameters of the model depend on the temperature T, the energy and type of the primary interacting particle E_{part} as well as on the defect density $C_{\text{defects}} := C_{gC}$ (density of green centers) of the $CaWO_4$ crystal investigated. Within the model, the following processes are described:

- The production of the initial blue STE population and its density distribution within the crystal volume, dependent on E_{part} and C_{gC} and T. This process contains the description of:
  - The different energy deposition processes by different interacting particles, i.e., the fraction of energy deposited in ionization (electrons in the conduction band and STHs in the valence band), $F_{ioniz}(E_{part})$, as well as its spatial distribution within the crystal volume described by $\rho_{ioniz}(E_{part}, \mathbf{x})$. These parameters are determined with the help of a geometrical model developed for the energy-deposition process for different interacting particles using data delivered by the simulations performed as well as by applying the assumed energy- and particle-dependencies of the different geometrical parameters describing the ionization-density distribution.
  - The efficiency and temporal evolution of the creation of the initial blue STE population out of these electrons and STHs, i.e., the immediate and delayed capture processes of electrons by STHs and by electron traps. These processes are represented by the fraction of electrons that get captured by electron traps, F_{e^-traps} (which depends on C_{gC}) as well as by the fraction, $F_{dr}(T)$, of electron-STH pairs recombining in the delayed process (with rise time $\tau_{dr}(T)$) to STEs.
- The coupled temporal evolution of the blue and green STE populations, $n_b(E_{part}, T, \mathbf{x}, t)$ and $n_g(E_{part}, T, \mathbf{x}, t)$, dependent on T and C_{gC} as well as dependent on the density

of the initially created blue STE population, i.e., additionally dependent on E_{part}. This includes the description of:

  - The mutual excitation process of blue and green STEs by migration and absorption of blue photons at defect centers. These processes are described by the migration times of blue and green STEs to defect or intrinsic centers, respectively, as well as by the fraction F_{abs} of blue photons which is reabsorbed at defect centers (and, hence, does not escape the crystal). The probability for these processes to occur depends, of course, on the defect density, C_{gC} and the temperature T.
  - The radiative, non-radiative and migration processes of the blue and green STE populations, respectively. The combination of these intrinsic de-excitation processes of the respective STE populations can be expressed by, $\tau_{ltb}(T)$ and $\tau_{ltg}(T)$, the respective intrinsic lifetime of the blue and the green STE population.
  - The interaction of two blue STEs via the Förster interaction yielding the non-radiative recombination of one of these STEs, i.e., leading to a non-radiative quenching process of the blue STE population. This process is described by the so-called Förster radius $R_{d-d}(T)$ which is a material- and temperature-dependent parameter: The Förster radius is the same for all modes of energy deposition in any $CaWO_4$ single crystals at the same temperature, i.e., the Förster radius is independent of the excitation mode and the defect density. The probability for this quenching process to occur depends non-linearily on the density of the initially created STE population.

- The production of blue and green scintillation light by the interdependent blue and green STE populations dependent on T, C_{gC} and the initial blue STE-density. As the initially created blue STE density depends on E_{part}, also the decay-time spectra, $P_b(E_{part}, T, t)$ and $P_g(E_{part}, T, t)$, of the blue and the green scintillation light created by the radiative decay of the blue and the green STE populations depend on E_{part}. The light creation process is described by:

  - The *unquenched model* for rarely distributed initial blue STE densities that approximate zero, i.e., for spatially separated blue STEs. This model desribes the full analytical solution of the coupled system of differential equations for the temporal evolution of the blue and green STE populations with very low densities, i.e., without the Förster interaction. The unquenched scintillation-light decay-time spectrum is expressed with the help of the initially produced number of created blue STEs, the effective unquenched lifetimes of the blue and green STEs, $\tau_1(T)$ and $\tau_2(T)$, respectively, as well as with the delayed recombination time $\tau_{dr}(T)$ of a fraction of the initially created blue STEs. The initially created number of blue STEs depends on the efficiency of the STE creation process. The effective unquenched lifetimes describe the combined influence on the STE lifetimes by their intrinsic lifetimes, $\tau_{ltb}(T)$ and $\tau_{ltg}(T)$ (containing the radiative, non-radiative and migration processes of blue and green STEs, respectively, in absence of the Förster interaction or any extrinsic excitation processes), and their mutual excitation processes (migration of STEs and reabsorption of blue photons at defect centers). The delayed recombination

time $\tau_{dr}(T)$ accounts for the delayed, diffusion-controlled recombination process of the fraction $F_{dr}(T)$ of the electrons and STHs to STEs.

– The *complete, quenched model* for initially created, dense blue STE populations as, e.g., found in the energy-loss tracks of heavy, charged interacting particles like nuclear recoils. This model describes the approximate solution of the coupled system of differential equations for the temporal evolution of the blue and green STE populations with non-negligible densities, i.e., including the Förster interaction. The quenched scintillation-light decay-time spectrum is expressed by the same parameters as the unquenched scintillation-light decay-time spectrum, however, additionally depends on the initially created blue STE-density distribution, $n_{bSTE}^{form\,0}(E_{part}, \mathbf{x})$ (which also depends on the efficiency of the STE creation process) and the Förster radius $R_{d-d}(T)$.

Hence, with the complete model, the decay-time spectrum of the scintillation light generated for an energy deposition in the $CaWO_4$ crystal (by a rare excitation mode or by an interacting particle) can be derived dependent on the mode of excitation, e.g., the type and energy of the interacting particle, and dependent on the temperature and defect density of the $CaWO_4$ crystal. Thus, with the model, the shape of the decay-time spectrum of the scintillation light as well as the produced amount of scintillation light (integral of the decay-time spectrum) and its decomposition into blue and green scintillation light dependent on all of the parameters mentioned is predicted: For an initially created spatially separated blue STE population, an almost purely exponential decay-time spectrum with the effective unquenched lifetime of the blue STEs as decay time and a high efficiency of creating scintillation light is expected. For an initially created dense STE population, e.g., by an interacting particle like a nuclear recoil, a non-exponential, fast decay of the scintillation-light pulse-shape at the beginning of the pulse followed by an exponential decay with the (same) effective unquenched lifetime of the blue STEs and a decreased efficiency of creating scintillation light (dependent on the density of the initially created blue STEs) is expected.

Thus, the observed light-yield quenching effect for different interacting particles is explained by a combination of the different efficiencies of creating ionization for different interacting particles ($F_{ioniz}(E_{part})$) and the differing impact of the Förster interaction ($R_{d-d}(T)$) on the respectively created STE population $n_{bSTE}^{form\,0}(E_{part}, \mathbf{x})$ due to the different densities of STEs created in the initial energy deposition process.

In particular, it should be noted that the prediction of a purely exponential decay-time spectrum for an unquenched excitation mode only, i.e., for spatially separated STEs, implies that also the light generation process for electrons and γ-particles as primary interacting particles is subjected to the quenching process: It can be observed that the scintillation-light pulse-shape generated for electron and γ-particle interactions in $CaWO_4$ exhibits a non-exponential (fast decaying) shape at the beginning of the pulse (compare, e.g., discussion in section III/2.2.3). Thus, within the developed model, this observation implies that the light yield for electron and γ-particle interactions in $CaWO_4$ is quenched compared to the unquenched scintillation light generation by spatially distributed STEs. An estimation of the impact of this effect onto the light yield for electrons or γ-particles in comparison to the unquenched light yield is presented in appendix B.12.

3.3.2 Free Parameters of the Model and Concept for their Determination

In order to determine the various free model parameters and their respective temperature-dependencies, the fact can be used that, within the developed model, not only the amount of scintillation light created is predicted in dependency of the model parameters, but, that also the pulse shape and spectral composition of the scintillation light is described in dependency of these parameters. Thus, the basic idea to determine as many of the free model parameters as possible from experiments without using information on the generated amount of scintillation light is to record decay-time and wavelength spectra of a $CaWO_4$ single crystal produced by different modes of excitation at different temperatures. The recorded decay-time and wavelength spectra can then be fitted with the corresponding model predictions (light-pulse shapes and wavelength spectra) with the parameters of the model as free fit-parameters. Hence, to determine the parameters of the complete (quenched) model, measurements of the scintillation light of a $CaWO_4$ crystal excited by interacting particles, such as nuclear recoils, producing quenched scintillation light are required. It should be noted that, trying to determine all of the model parameters only by such a quenched measurement could be challenging due to the large number of free model parameters (e.g., the Förster radius or the various contributions to the unquenched effective lifetimes - radiative, non-radiative and migration times, as well as the probabilities for the mutual excitation processes to occur). It should be noted that, in addition to all of these free model parameters, for the prediction of the quenched scintillation-light pulse-shape also the mathematical description of the STE density-distribution initially created by the energy deposition is required. In the description of the initially created STE density, in turn, the radial parameters of the produced ionization-density distribution are remaining undetermined. Thus, these parameters also have to be adjusted using the recorded scintillation-light decay-time spectrum (compare discussion in section III/3.1.2 and appendix B.3.10). Therefore, additional measurements have to be performed that allow to determine most of the model parameters independently of the initially created STE-density distribution, i.e., for example, independent of the quenching effect. An excitation mode fulfilling this requirement is the so-called two-photon excitation technique with which spatially separated STEs can be created. The decay-time spectrum recorded for such a rare excitation mode can then be described by the unquenched model. With such unquenched measurements the determination of many of the model parameters, i.e., the effective unquenched lifetimes of STEs (and their decomposition into radiative, non-radiative and migration times) as well as the defect density and reabsorption probability of blue photons at defect centers in the investigated $CaWO_4$ crystal, independent of the quenching effect, can be performed. The transfer of these parameters determined with unquenched measurement to the quenched measurements is possible as these parameters are predicted to be the same for rare and dense excitation modes. In addition, such unquenched measurements allow to validate the unquenched model and to test several model predictions (e.g., purely exponential decay-time spectrum for spatially separated STEs). Hence, such an independent determination of these parameters offers the advantage of greatly reducing the number of free parameters in the analysis of the quenched measurements. Thus, using the parameters determined with the unquenched measurements, the only free model parameters remaining in the analysis of the quenched measurements are the value of the Förster radius, $R_{d-d}(T)$ as well as the radial parameters of the ionization distribution initially generated.

In order to realize the suggested measurements, within the present work, measurements of the scintillation-light decay-time spectra of a $CaWO_4$ crystal produced by pulsed two-photon excitation with laser light (rare, unquenched exctiation) and pulsed ion-beam excitation (dense, quenched excitation) at the Tandem accelerator of the MLL (Maier-Leibnitz-Laboratorium) were performed. In order to determine the model parameters dependent on temperature and to test and validate various predictions of the developed model, the decay-time and wavelength spectra of the generated scintillation light were recorded for two different wavelengths regions separately (the blue and the green scintillation light), at two different temperatures ($\sim$ 300K and $\sim$ 20K) as well as with two different $CaWO_4$ crystal samples. The conducted experiments are presented in detail in chapter III/4, their analysis in the context of the developed model yielding the determination of most of the model parameters can be found in chapter III/5.

It should be noted that, using the results of these experiments not all of the free model parameters could be determined. However, to determine a complete set of parameters for the developed model, some of the model parameters have to be estimated on the basis of results of measurements presented in the literature and the assumptions made. A list of the respective parameters for which such a strategy had to be used, the utilized assumptions as well as the corresponding values determined are presented in the following (for an explanation of these estimates, see appendix B.13). In section III/6.3, suggestions for experiments that could be performed to determine these parameters independently of any assumptions are described.

Parameters Estimated from Data in the Literature

- The radiative decay times of the blue and green STEs at very low temperatures ($T \lesssim 5$K), i.e., from the respective lower-lying energy levels only: $\tau_{rb}(T \lesssim 5\text{K}) \approx \tau_{L1b}$ and $\tau_{rg}(T \lesssim 5\text{K}) \approx \tau_{L1g}$ (compare section III/3.1.3). These parameters cannot be determined from the experiments conducted within the present work as no measurements below a temperature of $\sim$ 20K were performed. Thus, as already discussed in section I/3.2.4 (see equations 3.176 and 3.177), values for these parameters are adopted from literature:

$$\tau_{L1b} = 565\mu\text{s} \tag{3.178}$$

$$\tau_{L1g} = 4.98\mu\text{s} \tag{3.179}$$

  It should be noted that, as will be shown in section III/5.2.2, the radiative decay times of the blue and the green scintillation light at a temperature of $\sim$ 20K and $\sim$ 300K can be determined from the experiments performed within the present work. Thus, by adopting the values for the radiative decay times at very low temperatures and using the values determined from the experiments, the complete temperature dependencies of the blue and green STE radiative decay times can be determined (compare equations 3.54 and 3.59 in section III/3.1.3).

- The temperature-dependent diffusion coefficients of the blue and green STEs, $D_{\text{bSTE}}(T)$ and $D_{\text{gSTE}}(T)$ (see equations 3.64 and 3.67 in section III/3.1.3): These values have to be adopted from literature as their temperature-dependency could only be determined by decay-time measurements at various temperatures covering the complete temperature range from room temperature to $\sim$ 5K. However, within the present

work, only measurements at $\sim$ 20K and $\sim$ 300K were performed:. Thus, as already indicated in section III/3.1.3, the values for the temperature-dependent diffusion coefficients are adopted from literature:

$$D_{\mathrm{bSTE}}(T) = 1.2 \cdot 10^{-7} \frac{\mathrm{cm}^2}{s} \cdot e^{(-\frac{4.5\mathrm{meV}}{k_B \cdot T})} \tag{3.180}$$

$$D_{\mathrm{gSTE}}(T) = 1.2 \cdot 10^{-7} \frac{\mathrm{cm}^2}{s} \cdot e^{(-\frac{6.9\mathrm{meV}}{k_B \cdot T})} \tag{3.181}$$

It should be noted that, by using these values and equations 3.63 and 3.66 (section III/3.1.3), the temperature-dependent migration time of green STEs, $\tau_{\mathrm{mig,\ g\rightarrow b}}(T)$, and the temperature-dependent hopping time of blue STEs, $t_{h\mathrm{b}}(T)$, are automatically determined. Thus, the only unknown for the determination of the migration time of blue STEs to defect centers is the density of defects, $C_{\mathrm{defects}} := C_{gC}$ (density of green centers) within the investigated $CaWO_4$ crystal.

- The energy barriers for the non-radiative recombination of blue and green STEs: ΔE_b and ΔE_g (see equations 3.57 and 3.61 in section III/3.1.3). As for the diffusion coefficients, the values determining the temperature dependency of the non-radiative process could only be fixed with decay-time measurements for at least two temperatures between (compare discussion in appendix B.7) $\sim$ 200K and $\sim$ 300K (for ΔE_b) and $\sim$ 70K and $\sim$ 300K (for ΔE_g). As, however, within the present work, only measurements at temperatures of $\sim$ 20K and $\sim$ 300K were performed, the values for the energy barriers of the non-radiative recombination processes could not be determined independently. Therefore, the value for ΔE_b is adopted from literature. For the value of ΔE_g, it is demanded that the impact of the non-radiative recombination process of green STEs on the total amount of unquenched scintillation light produced, $L_{tot}^{nq}(T)$, becomes important for temperatures $\gtrsim$ 70K, i.e., that the amount of unquenched scintillation light produced, for temperatures $\gtrsim$ 70K, is reduced due to the non-radiative recombination of green STEs (compare discussion in section III/3.2.1 and the discussion in appendix B.7):

$$\Delta E_b \approx 0.32\mathrm{eV} \tag{3.182}$$

$$\Delta E_g : L_{tot}^{nq}(T \gtrsim 70\mathrm{K}) \lesssim 1 \tag{3.183}$$

It should be noted that these values are only required if the complete temperature-dependency of the blue and green non-radiative decay-times is of interest as well as if temperatures above $\sim$ 200K (for blue STEs) or above $\sim$ 70K (for green STEs) are investigated. Below these temperatures, the non-radiative recombination processes are assumed to be negligible (compare discussion in section III/3.2.1).

- The delayed rise time of the initially created blue STE population at a temperature of $\sim$ 300K: $\tau_{dr}(T)$ (see equation 3.43 in section III/3.1.2). The value for this parameters could be determined with the help of the decay-time measurements for two-photon excitation at room temperature (partial rise at the beginning of the pulse). However, as will be discussed in section III/5.2.1, on the one hand, the response function of the utilized detection system introduces a decay time of roughly of the same order of magnitude as $\tau_{dr}(T)$ and, on the other hand, the simultaneous detection of reflected laser light masks almost the complete rise at the beginning of the pulse, inhibiting

a free fit of the rise time of the scintillation-light pulse. Therefore, the value for $\tau_{dr}(T \approx 300\text{K})$ is adopted from literature:

$$\tau_{dr}(T \approx 300\text{K}) \approx 40\text{ns} \tag{3.184}$$

It should be noted that no conclusions on the temperature dependency of the delayed rise time can be drawn from the results of the present work, as, on the one hand, it is assumed that, for temperatures below $T \approx 100$K, the influence of the delayed recombination of STEs can be neglected (compare equation 3.6 in section III/3.1.2) and as, on the other hand, no measurements at temperatures between 300K and 100K were performed within the present work.

- The fraction of electrons F_{e^-trap} that is captured by electron traps and, thus, lost to the STE-creation process (compare section III/3.1.2): This fraction is estimated with the help of the absolute light yield for electron/γ events at low temperatures as well as using the values assessed for the electron/γ Quenching Factor (compared to the unquenched light output, see appendix B.12) For a deduction and explanation of the applied approximation see appendix B.13. From this discussion, it can be deduced that, within the present work the fraction F_{e^-trap} of electrons captured by electrons traps is assumed to amount to:

$$F_{e^-trap} \approx 37.5\% \tag{3.185}$$

- Minimum values as well as energy- and particle-dependencies for the radial parameters describing the ionization distribution due to particle-induced energy depositions and a value for the radial extent of the ionization distribution for 100keV electrons as primary interacting particles (compare discussion in appendix B.3.8): For the minimum possible values of some of the radial parameters as well as their dependencies on the type and energy of the primary interacting particle assumptions had to be made to allow the determination of these parameters for different particles with different energies (see appendix B.3.10). To determine the radial extent of the ionization distribution of 100keV electrons, the absolute light yield of 100keV electrons at mK temperatures (as determined from the literature) is used (compare discussion in appendix B.3.9 and section III/6.1.1).

- The fraction of blue photons absorbed at defect centers: F_{abs} (see equation 3.46 in section III/3.1.3). As discussed in section III/3.2.1, within the developed model, for temperatures below ~ 5K, the amount of green scintillation light generated only depends on the fraction of blue photons reabsorbed at defect centers F_{abs} and is, thus, a crystal-dependent parameter. However, within the present work, only measurements at a temperature of ~ 20K and ~ 300K were performed. Thus, as explained in more detail in appendix B.13, the ratio of the relative amount of blue light generated at ~ 20K and at ~ 5K is estimated with the help of data from the literature (see [54]). Using this relationship and the relative amount of blue light generated at ~ 20K for the $CaWO_4$ crystals investigated within the present work (crystal Olga and crystal Philibert, see section III/4.1.2), a value of F_{abs}^{Olga} and F_{abs}^{Phil} could be estimated:

$$F_{abs}^{Olga} \approx 18\% \tag{3.186}$$

$$F_{abs}^{Phil} \approx 19\% \tag{3.187}$$

(for details, see appendix B.13).

- The ratio of the unquenched light yield below[67] $\sim$ 50K, $LY^{nq}(T \lesssim 50\text{K})$, to the unquenched light yield at room temperature, $LY^{nq}(T \lesssim 300\text{K})$. As will become clear from the discussion in section III/5.2.2, these values are needed for the determining the values of other model parameters from the analysis of the experiments. As, however, within the present work neither absolute nor relative light yield measurements were performed, values for these parameters have to be determined from data reported in the literature. The most accurate data on the absolute light yield of a typical CRESST $CaWO_4$ crystal is available for γ-interactions for temperatures below $\sim$ 10K and at room temperature (compare section III/2.2.4). It should be noted that, in principle, these values cannot directly be used to determine the ratio of the unquenched light yield (as required) as the light yield for γ events compared to the unquenched light yield is quenched (compare section III/3.3.1 and appendix B.12). Thus, the temperature-dependency of the light yield for γ events is also influenced by the temperature-dependent impact of the Förster interaction (compare discussion in section III/3.1.3). However, as no data on the temperature-dependent unquenched light yield was available, the ratio of the light yield for γ interactions in $CaWO_4$ below $\sim$ 10K and at 300K had to be used (compare table 2.2 in section III/2.2.4):

$$\frac{LY^{nq}(T \lesssim 50\text{K})}{LY^{nq}(T \approx 300\text{K})} := \frac{LY^{\gamma}_{abs}(T \lesssim 10\text{K})}{LY^{\gamma}_{abs}(T = 295\text{K})} \approx \frac{6\%}{3.3\%} \approx 1.8 \tag{3.188}$$

It should be noted that, by changing the values of these parameters, also the values of other model parameters determined on the basis of the experiments performed within the present work change. This is due to the fact that the analysis of the experiments could only be conducted by using some of the estimated values of the discussed parameters (for details, see chapter 5).

In table B.4 in appendix B.14, a list of the most important model parameters can be found - except for the parameters describing the ionization distribution initially generated in a particle-induced energy deposition, these parameters can be found in tables 3.3 and 3.4 (for heavy, charged primary interacting particles, such as ions, in section III/3.1.2) as well as in table B.1 (for electrons as primary interacting particles, in appendix B.3.1).

[67] As discussion in section III/3.2.1, for temperatures below $\sim$ 50K, no process changing the unquenched light yield is included in the model (except for a possible change in the mean green and blue photon energies. However, as discussed in section III/3.2.1, for such low temperatures, the mean photon energies can be expected to be constant. Thus, within the developed model, it is predicted that the light yield for temperatures below $\sim$ 50K remains constant.

Chapter 4

Measurement of Wavelength and Decay-Time Spectra for Different Excitations of $CaWO_4$

As described in chapter III/3, a theoretical model explaining the scintillation-light production as well as the mechanism of the scintillation-light quenching in $CaWO_4$ crystals was developed. With this model, the quenching effect is explained on a microscopic scale on the basis of exciton-exciton self-interactions. This model not only predicts the amount of scintillation light produced by different interacting particles, but can also be used to calculate the shape of the decay-time spectrum and of the wavelength spectrum of the scintillation-light output both depending on the type of interacting particle and on the temperature of the $CaWO_4$ crystal.

In order to confirm and test the model, measurements of the decay-time and wavelength spectra of the scintillation light of $CaWO_4$ crystals were performed, as suggested in section III/3.3.2.

4.1 Design of the Experiments

4.1.1 Basic Concept

The basic concept of the experiments was the measurement of wavelength spectra and wavelength-resolved decay-time spectra of the scintillation light generated in a $CaWO_4$ single crystal under different excitations at different temperatures. The temperature-dependent composition of the wavelength spectra and the pulse shapes of the decay-time spectra recorded could then be used to determine (free) model parameters and to validate the model by comparing measurements to predictions (calculated pulse shapes) of the model (see chapter III/5). As discussed in section III/3.3.2, different pulsed excitation modes leading to rare (spatially uncorrelated, separated) STEs (self-trapped excitons) and dense (spatially correlated, closely distributed) STEs in a $CaWO_4$ crystal were required. With these different excitations, the prediction of the model of differently shaped decay-time spectra for unquenched and quenched scintillation-light output can be tested (see section III/3.2): A purely exponential pulse shape for rare excitation and a strongly non-exponential pulse shape for dense excitation is predicted. To assure comparability of the different experiments, all measurements were performed with the same crystal sample and

under the same conditions, i.e. with the same setup.

In order to assure that the developed model is configured and tested for crystals as employed in the CRESST experiment, the crystal sample chosen for the measurements was cut from a typical CRESST crystal. In addition, a second crystal sample, representing the self-grown $CaWO_4$ crystals produced by the CRESST group at E15 in collaboration with the crystal laboratory at TUM[1], was selected for the measurements. All crystal samples exhibit dimensions of (20x10x5)mm^3 (length x height x width). Properties of the investigated crystals are discussed in section III/4.1.2.

To achieve pulsed, **rare excitation** of a $CaWO_4$ crystal, the special features of the so-called two-photon excitation can be capitalized. This excitation mode can be used to produce non-correlated STEs in the $CaWO_4$ crystal which are randomly distributed over a large volume of the crystal. To realize a pulsed two-photon excitation of the $CaWO_4$ crystal, collimated light pulses produced with a N_2 laser were employed (presented in section III/4.1.3).

To realize pulsed, **dense excitation** of a $CaWO_4$ crystal for which the produced ionization deposition density (IDD) can be determined (see section III/3.3.2), ion-beams of the tandem accelerator of the Maier-Leibnitz-Laboratory (MLL)[2] were used. For the presented measurements, excitations with two different ions, each expected to produce highly different excitation densities and thus light yields as well as light-pulse shapes, were realized: The scintillation-light production in a $CaWO_4$ crystal under excitation with pulsed Oxygen- and pulsed Iodine-beams was investigated (presented in section III/4.1.4).

The experimental setup (presented in section III/4.2) was designed in such a way that it could be used for all performed measurements, i.e. for the different excitation modes and at the different temperatures. For this purpose, an experimental chamber connected to the beam line of the MLL accelerator[3] that could be evacuated to $\sim 1 \cdot 10^{-7}$mbar was equipped with instrumentation for the simultaneous detection of wavelength spectra and decay-time spectra. To enable the measurement of decay-time spectra for the two selected wavelength regions (intrinsic and extrinsic scintillation light, see section III/2.2.2), different spectral filters were used. Additionally, the possibility to cool the investigated $CaWO_4$ crystal to $\sim$ 20K was realized, thus, allowing measurements to be performed at room temperature and at $\sim$ 20K.

4.1.2 Investigated $CaWO_4$ Single-Crystal Samples

Samples of two different $CaWO_4$ single crystals were investigated in the presented measurements: Crystal "Olga", representing the bought CRESST crystals and crystal "Philibert", representing the crystals produced at the crystal laboratory, Technische Universität München. Details on the growth process of crystal Philibert can be found in [100, 101]. Both crystals originally were cylindrical in shape and received an after-growth annealing

[1]Crystal laboratory, Technische Universität München. In collaboration with A. Erb, Walther-Meißner-Institut, Bayerische Akademie der Wissenschaften, Garching, Germany.

[2]Tandem accelerator, Maier-Leibnitz-Laboratorium der Ludwig-Maximilians-Universität München und der Technischen Universität München, Garching, Germany.

[3]The experimental chamber was located in hall II at the position II^{25} of the tandem accelerator.

at high temperature[4] in Oxygen atmosphere them in order to reduce residual stress in the crystal structure and to enhance the light output[5] [102, 54]. For details on the original size of the crystals and the applied annealing processes, see table C.1 in appendix C.1. The characterization of the crystals in the framework of the CRESST experiments is usually performed on the basis of the light yield and resolution (FWHM) of the scintillation light emitted by the crystal under 662keV γ-excitation from a ^{137}Cs source, measured at room temperature with a PMT (see e.g. chapter 5 in [54]). As basis for comparison, the light yield of crystal "Boris" (standard CRESST crystal) is defined as 100% (see chapter 5 in [54]). For both crystals the light emitting properties were determined after the last annealing step when they exhibited their original size. The obtained values can be found in table 4.1. From both crystals two samples each of dimensions (20x10x5)mm^3 were cut from neighboring sites from the inner volume of the crystals. In the following, these samples were treated in the same way: For example, surface treatment of the crystal samples was performed simultaneously for both samples of one crystal. In this way, a replacement sample for each crystal was available. From the values listed in table 4.1, it can be seen,

	Olga	Philibert
sample size [mm^3]	(5x10x20)	(5x10x20)
light yield	95.1%	93.7% [101]
resolution (FWHM)	14.6%	12.7% [101]

Table 4.1: Properties of the investigated $CaWO_4$ crystals.

that both crystals exhibit very similar properties concerning their light yield. Comparing the results of the experiments for both crystals offers the possibility to check the model proposition that the light yield and quenching effect as well as the shape of the wavelength and decay-time spectra observable for one crystal are determined by the impurity density of this crystal. Hence, if the light yield of two crystals is very similar, the model predicts, that also all other measurements should exhibit very similar values.

Tow different **surface treatments** were applied: A surface was either polished to optical quality or roughened with a powder.

- Polishing to optical quality was performed by the crystal laboratory, Technische Unversität München. The quality of the polishing was checked via occurrence of Newtonian rings with a test plate and a Na lamp (wavelength $\sim$ 590nm). On the large surface of the crystals (10x20)mm^2, no rings were observed, indicating that remaining irregularities of the surface were less than half of the wavelength of the employed light, i.e. $\lesssim$ 295nm.
- Roughening of the surfaces was performed with boron carbide[6] (BC_4) powder on a polishing disc for 30 seconds. The size of produced corrugations is expected to be less than 10μm (typical order of magnitude: 1μm) due to the grain size of the powder.

[4]For crystal Olga, this annealing step was performed by the producer [54].

[5]With crystal Olga a second annealing step at lower temperature was performed: This second annealing process is the standardized process used for all bought CRESST crystals. This procedure was identified to be optimal for the bought crystals by several years of investigations within the CRESST group.

[6]TETRABOR®, ESK Ceramics GmbH & Co. KG, Costa Mesa, California, USA. Grain size: $< 10\mu$m.

The polished surfaces can be expected to contain a lower defect density in comparison to the roughened surfaces[7]. However, due to the refractive index of $CaWO_4$, for polished surfaces the probability for internal reflection is large. Roughening of a surface, on the other hand, is expected to create internal diffusive reflection (homogenizing the light output and leading to enhanced light output at other surfaces of the crystal) and to enhance the light transmission through the roughened surface itself [73]. Hence, all surfaces exposed to excitations should be polished, all other surfaces should be roughened.

For the experiments with laser excitation the two large surfaces ((20x10)mm^2) of the samples that were exposed to the laser beam, have been polished whereas all other surfaces have been roughened. For the experiments with ion-beam excitation, all surfaces except one large surface have been roughened. The large surface that has been polished was exposed to the ion-beam and thus used for excitation.

For the determination of the model parameters and for the validation of the model measurements performed with the samples from crystal Olga are used. Results from measurements with samples from crystal Philibert are used as comparison.

4.1.3 Two-Photon Excitation of $CaWO_4$ with a N_2 Laser

To obtain rare, spatially uncorrelated excitations of a $CaWO_4$ crystal the two-photon excitation technique was employed. For this purpose, an intense light source with photon energies below the band gap of $CaWO_4$ is needed. In the performed experiments, a pulsed N_2 laser (see section III/4.3.1) was used to obtain excitation by two-photon absorption.

The photons from the main laser line exhibit a wavelength of $\lambda_L = 337.1$nm corresponding to an energy of $E_L = 3.68$eV which is well below the band gap of $CaWO_4$, $E_{gap} = 5.0$eV (see section III/2.1.2). When the density of the irradiated photons is increased, the probability of simultaneous absorption of two photons by one electron increases. This possibility of excitation is called two-photon excitation (TPE) and was already studied for $CaWO_4$ crystals with photons of, e.g., 2.48eV and 3.49eV [51]. For excitation with the N_2 laser, a resulting energy transfer to one electron of $E_{TPE} = 2 \cdot E_L = 7.36$eV can be calculated. Thus, for TPE with this photon energy, it is expected that electrons and holes in the same electronic states as typically produced by particle interactions are created[8]. Therefore, it can be assumed that electrons and holes created by this TPE process undergo the same relaxation processes to STEs as discussed in sections III/2.1.4 and III/3.1.4.

Although it can be assumed that TPE with 3.68eV photons leads to a comparable STE-production mechanism as particle interaction, using TPE offers special advantages:

- As the direct absorption probability for photons of such energies is small, they can penetrate the whole crystal. Thus, the location in the crystal where STEs are created by TPE can be chosen by positioning of the focal spot of the laser beam. By placing the focal spot, for example, inside the crystal, the luminescence properties of the inner volume of the crystal are probed, almost unaffected by possible surface effects.
- By focussing and defocussing of the laser spot, the excitation density can be influ-

[7] Roughening, in principle, corresponds to a destruction of the crystal structure at the surface.
[8] Electrons in the upper conduction band and holes in the valence band, see section III/2.1.2.

enced. Thus, it is possible to produce different excitation densities (only determined by the level of focussing) in the crystal with the same intensity of incident light. For increasing focussing, the following, qualitative effects should occur with increasing excitation density (density regimes 1 and 2):

1. Increasing the focussing should lead to an increasing probability of two-photon excitation within and close to the focal spot. For not yet extremely focussed and intense excitation, this should lead to a spatially uncorrelated excitation of luminescence centers distributed over a large volume.

2. For extreme focussing and high intensities of the exciting light, it should even be possible to produce high excitation densities which approach densities produced, e.g., in recoil tracks by ion bombardment.

Following the model developed and presented in chapter III/3.1, different temporal evolutions of the created STE populations are expected depending on their density. With excitation densities of regime 2, STEs close to each other are supposed to be created at least in the center of the focal spot. If their density is high enough, they can interact with each other and lead to quenching[9] as described by the model for dense excitation presented in section III/3.2.4. On the other hand, with excitation densities of regime 1 where excitations uncorrelated in space are produced, mainly STEs separated from each other are supposed to be created. These STEs should not be able to interact with each other. Therefore, the evolution of the population of such rarely created STEs should follow the model and differential equation for rare excitation (see section III/3.2.3), leading to a single exponential decay time without any observable quenching. This implies that TPE creating a density of excitations of regime 1 can be used to check the prediction of a single exponential decay for rare excitation.

In order to calculate the induced excitation density for a given setup, not only the emission intensity and the level of focussing of the used photon source, but also the probability for TPE to occur for these photons needs to be known. As especially the last factor is completely unknown, no effort was undertaken to quantitatively determine the realized excitation density in the experiments. However, as the TPE experiments are intended to be used for the confirmation of the rare excitation model (section III/3.2.3), at least a qualitative assignment of the produced excitation density has to be realized. This characterization is presented in section III/4.7.3.

In addition, the fact that the STEs produced by TPE via the laser pulse are not created at exactly the same time, but follow the temporal shape of the exciting laser pulse, is taken into account. The determination of the laser-pulse shape and its width (length) σ_L is presented in section III/4.7.3. The influence of the time dependency of the laser pulse on the expected scintillation-light pulse-shape is discussed in section III/5.2.1.

[9] This effect is in principle the same as described and demonstrated for high density excitation by 90eV photons in [94] (see discussion in section III/6.2). The difference for TPE (discussed here) is that 90eV photons themselves already create more than one STE each and that a beam of 90eV photons is always absorbed in a small region at the surface of the crystal. Thus, it can be expected that the critical density where quenching effects start to be important can be reached much easier with 90eV photons than with TPE, however, mainly at the surface of the crystal.

4.1.4 Pulsed Ion-Beam Excitation of $CaWO_4$ with the Tandem Accelerator

As indicated in section III/4.1.1, to realize pulsed, dense excitation of the $CaWO_4$ crystal, pulsed ion-beams from the tandem accelerator were used.

Employing beams of charged ions from the accelerator to test the validity of the model, implicitly contains an assumption: Excitation with ions incident onto the crystal from the outside leads to the same light-generation mechanisms as excitation produced by recoiling atoms inside the crystal volume. This assumption can be justified as, on the one hand, in general, no local dependencies (at the surface or within the volume) in the generation of scintillation light are expected for $CaWO_4$[10]. On the other hand, no differences are expected due to different original charge states of the interacting particles: Due to the large ionization potential of solid materials, a very effective interaction between incident ions (or recoiling atoms) and electrons of the material occurs. In every collision of an interacting ion (or recoiling atom) with electrons or atomic cores of the crystal, electron stripping or capture processes take place. Thus, already after the first few collisions, the ion is expected to obtain an effective charge state which is no longer influenced by its original charge state. After these first stripping or capture processes, the usual process of adjusting the equilibrium charge state is expected to take place. The final equilibrium charge state is only dependent on the solid material and the velocity and type of interacting ion (or recoiling atom), but not on its original charge state (see, e.g., [87]). Thus, it is expected that virtually the complete energy-loss process of the particle is independent of its original charge state. Hence, for both possibilities discussed, interaction of a charged ion or interaction of a recoiling atom (same species and same energy), it is assumed that the same excitations and light-generation processes take place.

With the tandem accelerator, pulsed mono-energetic beams of various ions with typical energies of some tens of MeV can be produced (see section III/4.4.1). This variability in the projectile choice can be used to demonstrate the validity of the prediction of the model: Independent of the type of exciting particle, always the same parameter R_{dd} describes the interaction strength between created STEs(see section III/3.2.4). For this purpose, ion beams of two different ion types were used in the experiments, a pulsed beam of Oxygen and a pulsed beam of Iodine ions with respective ion energies, both ~ 35MeV. These two ion types were selected due to several reasons: Iodine ions were chosen as they can be expected to deliver quite a small light yield and, thus, a small Quenching Factor. The expected light yield of Oxygen ions, on the other hand, is much larger, i.e. the respective Quenching Factor is much larger. In addition, Oxygen represents a chemical component of $CaWO_4$ and, thus, a typical recoil often observed in this material. Hence, for Oxygen ions, the theoretically calculated prediction of the model (on the basis of the pulse-shape fit of the experimental data) can be compared to experimentally determined Quenching Factors (see section III/2.2.5).

Using pulsed ion beams instead of investigating the interaction of single ions or recoils in $CaWO_4$ crystals provides the important advantage - especially for the decay-time spec-

[10]The scintillation-light production mechanism only depends on the stoichiometry of the crystal structure, i.e., the local distribution of defect centers (see section III/2.2.1). Hence, if no differences in the crystal structure within the volume or at the surface exist, no differences in the light-production mechanism should be observable. For details on the treatment of the crystal surfaces, see section III/4.1.2.

trum measurements - that a signal from the pulsing of the accelerator can be used as trigger source, allowing to determine the beginning of the light pulse independently of the (statistically distributed) arrival time of the first photon. In this way, it can be expected that decay-time spectra with high resolution and good statistics can be recorded.

The use of a defocussed ion beam with a low intensity avoids the creation of ionization tracks of individual ions so closely positioned that the STEs produced by different ions could interact with each other (inter-track quenching). Such an enhanced density of STEs would lead to an increased interaction rate of STEs and thus, to a different scintillation-light pulse shape compared to the model prediction (within the developed model, only the interaction of STEs created by one primary interacting particle is considered). For experimental data and a short discussion of the impact of an enhanced STE density produced by an inter-track quenching effect, see section III/5.3.3.

Thus, for the chosen settings of the accelerator (for details, see section III/4.4.1), the excitation of a $CaWO_4$ crystal by a beam of N_{ion} ions can be regarded as an excitation by N_{ion} independent ions following the temporal pulse shape of the ion beam.

4.2 Experimental Setup

In the following, an overview of the basic experimental setup and the instrumentation as employed in all measurements is presented. Differences in the setup used in the two measurement campaigns (laser and ion-beam excitation) as well as the operational parameters and settings of the laser and the accelerator are presented in sections III/4.3 and III/4.4, respectively.

4.2.1 Basic Setup

In figure 4.1, the basic experimental setup as it was installed in hall II of the tandem accelerator is shown. The upper sketch in figure 4.1 depicts the top view, the lower sketch corresponds to the side view of the setup.
On the right hand side of figure 4.1, the experimental chamber, a CF100 cross with six CF100 and four KF40 flanges, can be seen. The cross has a size of 26cm from one CF100 flange to the other. The $CaWO_4$ crystal (see section III/4.1.2) was positioned exactly in the middle of this chamber. A window with a connector to a glass fiber used as light guide to the spectrometer (see section III/4.2.2) was attached to one of the KF40 flanges. With this spectrometer, the wavelength spectra of the $CaWO_4$ scintillation light were recorded. The photomultiplier (PMT, connected to a storage oscilloscope) employed to measure the decay-time spectra of the scintillation light (see section III/4.2.3) was attached to a CF100 flange with a KF40-CF100 adapter. A holder for the spectral filters (see section III/4.2.4) used to investigate wavelength-specific decay-time spectra was incorporated in the connector of the PMT to the KF40 adapter. The connector of the PMT to the filter and to the chamber was realized in a way that allowed to evacuate the volume in front of the PMT simultaneously with the experimental chamber. On top of the experimental chamber, a cryocooler elongated by a coldfinger and a crystal holder (see section III/4.2.5) was installed at a CF100 flange. With the cryocooler, measurements of the scintillation light of the investigated crystal at $\sim$ 20K were enabled.

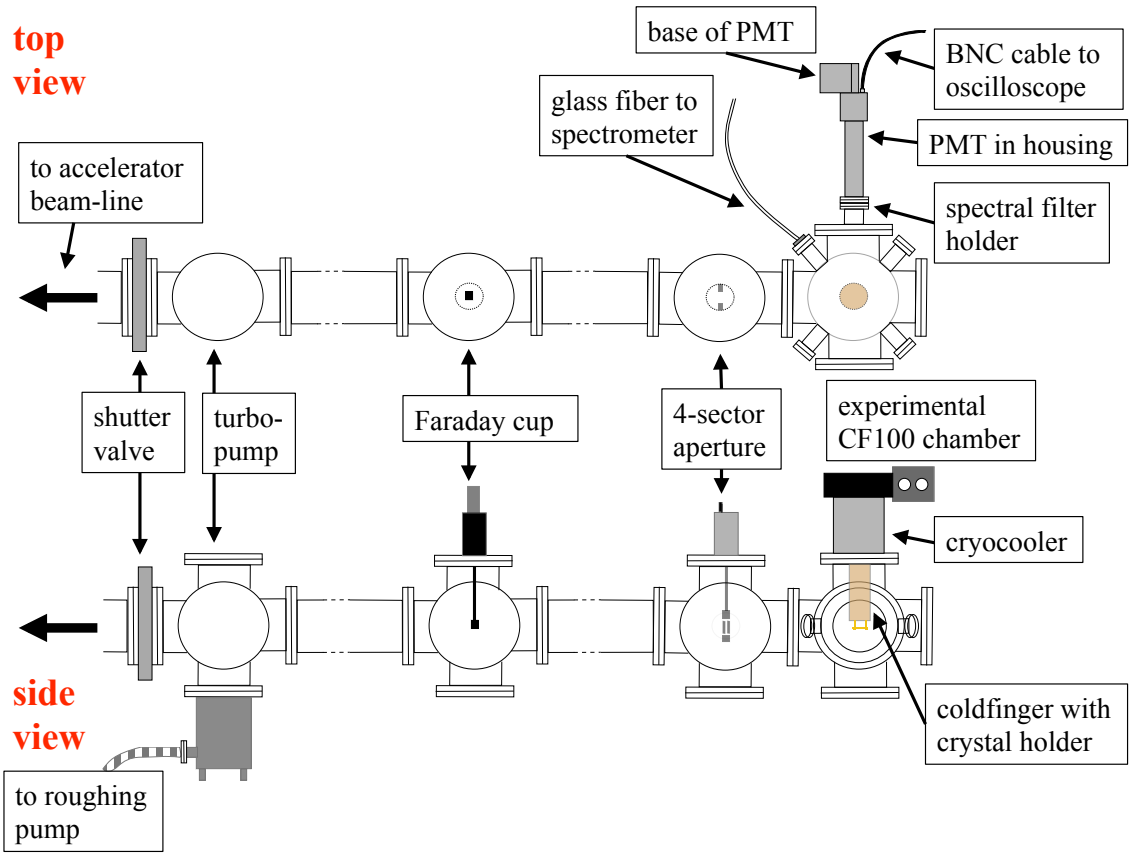

Figure 4.1: Sketch of the basic experimental setup installed in hall II of the tandem accelerator. This setup is connected to the beam line of the accelerator. In the upper sketch the top view, in the lower sketch the side view is shown. For details, see main text.

On the left hand side in figure 4.1, the connection of the setup to the accelerator beam-line is indicated. The setup can be separated from the beam line by a vacuum-tight shutter valve. Evacuation of the setup could be performed independently of the beam line with a pumping unit including a turbo pump[11]. After one hour of evacuating, a pressure of $\sim 1 \cdot 10^{-7}$mbar was reached. To the right of the pumping unit, a Faraday cup that could be positioned in the middle of the beam line and an adjustable 4-sector aperture were installed. Both components were used to characterize the pulsed ion-beam current and geometric profile (see section III/4.7.3). The characterization of the laser pulses is presented in section III/4.7.3.

Further components, the respectively employed trigger sources, positioning of the $CaWO_4$ crystal and geometries of the used excitations are presented separately for the different measurement campaigns in sections III/4.3 and III/4.4.

[11] Turbovac 450, Oerlikon Leybold Vacuum GmbH, Köln, Germany.

4.2.2 The Spectrometer

Wavelength spectra of the scintillation light of excited $CaWO_4$ crystals were measured using a portable UV-VIS spectrometer[12] with an optical glass fiber as light guide. The spectral range covered by the spectrometer ($\sim$ 200nm to 1100nm) fully contains the wavelength region of CaWO4 scintillation light ($\sim$ 300nm to 700nm, see section III/2.2.2). Data acquisition was realized with the spectroscopy software SpectraSuite[13] (details can be found in appendix C.2.1). In the analysis, two results are extracted from the recorded wavelength spectra: They are used for qualitatively comparing the spectral shape of the scintillation-light spectra under different excitations and at different temperatures as well as for drawing quantitative conclusions about the spectral composition of the scintillation light at different temperatures[14]. To allow a quantitative analysis, the recorded spectra were corrected for wavelength dependent non-linearities in the spectrometer and glass fiber response with a calibration measurement (see appendix C.2.2). Additionally, experimental error sources introducing uncertainties were identified and evaluated (see appendix C.2.3). The procedure used for data preparation before the analysis, is presented in section III/4.6.1.

4.2.3 The Photomultiplier Tube and the Storage Oscilloscope

The Photomultiplier Tube

The decay-time spectra of the $CaWO_4$ scintillation light were recorded with a 2" photomultiplier tube[15] (PMT) with a S20 photocathode[16] and a front quartz-window (51mm diameter) optimized for UV-light detection. The quantum efficiency, QE, in the investigated wavelength ranges, 375nm to 425nm and 475nm to 525nm, is 20.76% at 400nm and 14.38% at 500nm according to the manufacturer[17]. For the PMT a gain (photon to electrons), of $G_{\gamma\rightarrow e} = 5.0 \cdot 10^6$ at the typical operating voltage of -1.75kV and $G_{\gamma\rightarrow e} = 1.0 \cdot 10^6$ for an operating voltage of -1.5kV are specified. A typical transit time, t_{TT}, of 46ns and a typical single-electron full width at half maximum, FWHM_{s-el}, of 3ns are given. In the measurements, the PMT was operated in current-mode with a base especially designed for current-mode operation[18]. This operation mode was chosen to allow for an optimized recording of the pulse shape of the $CaWO_4$ scintillation light: At the beginning of the pulse, directly after excitation of the crystal, many photons are generated within a very short time window. To prevent saturation of the PMT signal, due to the (almost) coincident detection of several photons, current-mode operation of the PMT was realized. Read-out and data acquisition was performed with a digital storage oscilloscope (see below). The PMT was 50ΩDC-coupled via a $\sim$ 30cm long BNC cable. Mounting of the PMT to the experimental chamber was realized with a vacuum-tight connector which permitted the evacuation of volume in front of the PMT together with the experimental chamber[19] (see

[12]Maya2000 Pro, Ornet, Seri Kembangan, Malaysia. Read-out is achieved via USB connection to a computer.

[13]Ocean Optics, Dunedin, Florida.

[14]No information on absolute light intensities is extracted as the geometry of the light collection with the glass fiber changed in the different experiments.

[15]PMT type 9426B, ET Enterprises, Uxbridge, United Kingdom.

[16]S20, Thorn EMI Electron Tubes, Middlesex, United Kingdom.
Spectral range with quartz.window: $\sim 180 - 850$nm.

[17]For the S20 photocathode, from Thorn EMI Electron Tubes.

[18]This base was constructed and built by Werner Krötz, TU München [103].

[19]This connector also holds the wavelength filter used.

figure 4.1). The different settings (PMT voltage and trigger configurations) used in the individual experiments, laser excitation and ion-beam excitation, are described in sections III/4.3 and III/4.4, respectively.

In appendix C.4, different measurements that were performed to characterize the signal saturation, response linearity, baseline drift and impulse reaction of the used setup (PMT, base and electronic readout circuit) are presented and discussed. In some of these measurements a fast and highly linear photodetector, a Si-PIN diode (see appendix C.3) was used as reference detector.

Data Acquisition with the Storage Oscilloscope

For the read-out of the PMT signal and the acquisition of the decay-time spectra, a digital 4-channel storage oscilloscope[20] with a bandwidth of 500MHz was used. The typical rise time is specified as 0.75ns and thus faster than all other times considered[21]. The PMT and the respectively used trigger source (see sections III/4.3 and III/4.4) were each 50ΩDC-coupled to input channels of the oscilloscope. Stable triggering was performed with a rising-edge or falling-edge trigger, respectively. To reduce the impact of noise and statistical fluctuations on the data, i.e. to improve the signal-to-noise ratio, for each measurement a large number of individual pulses is averaged to obtain the final, recorded pulse shape. The software installed on the oscilloscope not only allows to save individual pulses but also to perform on-line mathematical operations on the data during acquisition. This software can be used to perform online averaging of N_p pulses ($N_p < 1,000,000$) without storing each individual pulse. Thus, the amount of data that has to be stored and processed is greatly reduced. For each new pulse p_i that is added to the pulse averaged up to the last step $\overline{p_{i-1}}$ a recursive summation is performed[22]. The procedure implemented in the software is described by the recurring operation:

$$\overline{p_i} = \frac{1}{i} \cdot p_i + \frac{i-1}{i} \cdot \overline{p_{i-1}} \tag{4.1}$$

It should be noted, that this recursive-summation procedure can prevent the detection of very long decay times ($\gtrsim$ several 100μs) at very small signal heights ($\lesssim$ a few mV) as discussed in appendix D.2.

In the two types of experiments, laser and ion-beam excitation, highly different maximum pulse heights of the scintillation light were observed. Thus, for an effective signal-to-noise (S/N_{stat}, statistical noise) improvement different numbers of pulses were used for averaging. Typical pulse heights in the ion-beam excitation experiments amount to $\sim$ 5mV. For these experiments, typically 50,000 pulses were averaged, resulting in 1σ widths of the baseline of $\sim 4.0 \cdot 10^{-3}$mV. Thus a typical S/N_{stat} of $\sim 1.3 \cdot 10^3$ was achieved. For the acquisition of 50,000 averaged pulses, $\sim$ 1 hour of measurement time was needed. Typical pulse heights in the laser-excitation experiments amount to $\sim$ 0.5V. In these experiments 5,000 pulses were averaged, resulting in 1σ widths of the baseline of $\sim 0.13 \cdot 10^{-3}$V. Thus a typical S/N_{stat} of $\sim 3.8 \cdot 10^3$ was achieved. For acquisition of 5,000 averaged pulses around five minutes of measurement time were needed. The chosen settings of the vertical and

[20] Waverunner 6050A, LeCroy, Chestnut Ridge, USA.

[21] The influence of this rise time on the signal pulse-shape is included in the determination of the impulse reaction of the used setup (including the oscilloscope), see appendix C.4.4.

[22] See manual of LECROY Waverunner 6000A series oscilloscopes.

timing resolutions in the individual measurements, as well as the resulting measurement uncertainties are presented in appendix C.4.5.

The combination of all measurement uncertainties of the decay-time measurement setup (PMT and data acquisition, statistical and systematical) as well as the corresponding error evaluation are presented in appendix C.4.6.

4.2.4 Optical Filters

Two different optical filters (25mm diameter each) were used in front of the PMT to observe decay-time spectra for selected wavelength ranges of the $CaWO_4$ scintillation light. These filters exhibit central wavelengths (CWL) of 400nm (±5nm) and 500nm (±5nm), respectively, with FWHM of the bandpass regions of 50nm (±5nm) according to the producer[23]. Filters with these CWLs were chosen in order to selectively investigate the $CaWO_4$ scintillation light in the regions dominated by "intrinsic" (blue light, 400nm filter) and "extrinsic" (green light, 500nm filter) light generation (see definitions in section III/2.2.1 and chapter III/3.1). The broad bandpasses were chosen to allow for a maximized light collection with the PMT while still concentrating on the relevant wavelength regions. A maximized light collection efficiency is especially important for the experiments with ion-beam excitation as in these measurements only very small light intensities can be expected (see appendix C.11).

To allow an estimation of the light detection efficiency of the complete setup (used in the data analysis, see chapter III/5), the relative amount of $CaWO_4$ scintillation light passing through the filters has to be determined. For this purpose the relative transmissions of the filters are needed. For a description of the conducted measurements and the procedure used for the determination of the relative transmissions, see appendix C.5. In table 4.2, the determined relative filter transmissions $Tr_{CWL,T}$ for the scintillation light of $CaWO_4$ at two different temperatures T, $T = RT$ (room temperature) and $T = LT \approx 20$K (low temperature) and for the different filters $CWL = 400$nm (400nm filter) and $CWL = 500$nm (500nm filter) are presented.

filter CWL	temperature T	relative transmission Tr
400nm	RT	$Tr_{400nm,\,RT} \approx 32\%$
400nm	LT	$Tr_{400nm,\,LT} \approx 35\%$
500nm	RT	$Tr_{500nm,\,RT} \approx 15\%$
500nm	LT	$Tr_{500nm,\,LT} \approx 15\%$

Table 4.2: Estimated relative filter transmissions for the $CaWO_4$ scintillation-light spectrum at room temperature ($\sim 300K$) and low temperature ($\sim 20K$).

The changes in the relative transmission with temperature roughly reflect the changes in the spectral composition of the $CaWO_4$ scintillation-light spectrum with temperature, e.g., for low temperature more blue light is produced, changing the shape of the spectrum slightly so that, at low temperatures a larger fraction of the scintillation light is within the region of the 400nm filter (see discussion in section III/3.2.3).

[23] 400nm (500nm) CWL, 25mm diameter hard-coated bandpass interference-filter, T84-781 (T84-783), Edmund Optics, Barrington, USA.

4.2.5 Cooling System

For cooling of the $CaWO_4$ crystal, a cryocooler[24] was used. At the head of the cryocooler, two temperature stages can be found. The center stage (cold stage) allows for a connection to the lowest temperatures achievable with the cooler ($\sim$ 20K for the setup used with a cool-down time of $\sim$ 50 minutes). The outer stage (concentric around the center stage) which can be used for the installation of a radiation shield is only cooled to $\sim$ 190K in the setup used. The cooler was installed on top of the experimental chamber as depicted in figure 4.1. The cold stage of the cooler is elongated by a coldfinger (copper with a brass head). The length of the complete coldfinger is chosen such to position the $CaWO_4$ crystal exactly in the center of the experimental chamber. The head of the coldfinger is made out of brass to assure good thermal contact and good mechanical handling and stability[25]. In order to achieve low temperatures and fast cooling times of the coldfinger, a thermal radiation shield (copper) surrounding the coldfinger was introduced. This radiation shield was coupled to the outer stage of the cooler. Thermal and mechanical coupling of the crystal to the head of the cryocooler was achieved with a brass plate fixed to the head of the cryocooler with two screws as depicted in figure 4.2. Contrary to the coldfinger, the

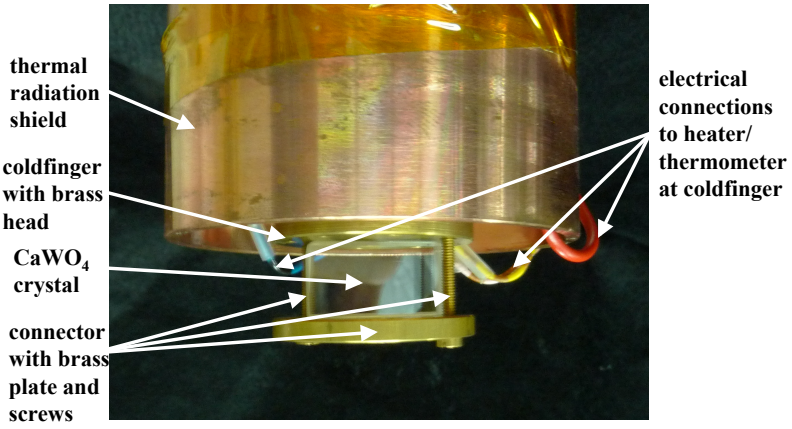

Figure 4.2: Lower part of the coldfinger of the cryocooler: The copper thermal radiation shield surrounding the copper coldfinger with brass head can be seen. The $CaWO_4$ crystal (view onto the largest side of the (20x10x5)mm^3 crystal) is attached to the coldfinger with a brass plate and two screws ensuring thermal contact, mechanical stability and free access to the crystal from almost all directions. In addition, the cables connecting the heater and thermometer (mounted at the coldfinger inside the radiation shield) can be seen.

$CaWO_4$ crystal could not be surrounded by a thermal radiation shield due to several reasons: On the one hand, the $CaWO_4$ crystal has to be accessible to the different excitations (laser-light beam and ion beam) and to the optical observations (PMT and spectrometer). On the other hand, the amount of material in the vicinity of the $CaWO_4$ crystal should be minimized to avoid excitation of other materials (except for the $CaWO_4$ crystal) by the ion beam (possible γ-production, see discussion in appendix C.9) and to reduce surfaces where the laser light could be reflected (see discussion in appendix C.10.2).

[24] Coolstar, Edwards, Crawley, United Kingdom.

[25] In principle, the head of the cryocooler could also have been made from copper, however, brass is harder and thus easier to machine and to handle.

4.2.6 Temperature Measurement

To determine the temperature of the setup during the experiments, a PT100[26] was installed at the head of the cryocooler inside the radiation shield, together with a heater resistor for fast warmup.

Thermometer

The location of the thermometer was chosen to be inside the radiation shield to avoid material close to the $CaWO_4$ crystal that could be excited by the ion beam or reflect laser light. This position, unfortunately, prevents exact determination of the crystal temperature as there could be a temperature gradient between the coldfinger (surrounded by the radiation shield) and the $CaWO_4$ crystal. Thus, this thermometer was used to monitor the temperature reached by the cryocooler and can only be regarded as a rough indicator for the crystal temperature. As inside the thermal radiation shield only limited space is available, a small thermometer, the PT100, was chosen. With the PT100, it could be observed that the low temperature plateau reached by the cryocooler decreased in the course of the first three low-temperature measurements[27]. This can be attributed to the fact that the cryocooler had not been used in a long time before employing it in the presented measurements. For all measurements conducted afterwards, no difference in the temperature indicated by the PT100, i.e. the temperature of the cryocooler, could be observed. However, correct determination of the crystal temperature is desirable in the analysis of the data for the model evaluation.

Temperature Determination

For the determination of the temperature of the $CaWO_4$ crystal, the highly temperature dependent (see section III/2.2.3), slow decay time of the scintillation light of the $CaWO_4$ crystal, $\tau_{\mathrm{meas}}(T)$, can be used, independent of the excitation mode[28]. Especially in the temperature range reached with the cryocooler of around 20K, the decay kinetics is very sensible to small temperature changes: Changes in the decay time by a factor of ~ 1.5 ($\sim 50\mu$s to $\sim 75\mu$s) can be observed for a temperature change from $\sim$ 25K to 20K and, for a change of $\sim$ 1K at 20K, a change in decay time of $\sim 9\%$ has been observed (compare section III/2.2.3). Thus, the scintillation light of the $CaWO_4$ crystal itself can be used as a thermometer. For the temperature dependency of the decay time, a mathematical model as described in section III/2.2.3 (the three-level model from [41]) can be used to

[26] A PT100 is a standardized platinum resistance thermometer.

[27] The first experiment was the excitation of crystal Olga with the Iodine-beam using the 400nm filter at room temperature and low temperature, followed by the the same experiments using the 500nm filter. The third experiment was the excitation of crystal Philibert with the Iodine-beam using the 400nm filter at room temperature and low temperature. In this low-temperature measurement, the PT100 reading showed the same value as in all following low-temperature measurements.

[28] Justification of the assumption that this slow decay time is in fact independent of the excitation used (in the present case: two-photon excitation with the laser light or ion-beam excitation) is given in section III/3.2.4 theoretically and in section III/4.7.2 experimentally. For the procedure used to determine this slow decay time see appendix C.8.

express the relationship between temperature T and observable decay time $\tau_{\text{meas}}(T)$[29]:

$$\frac{1}{\tau_{\text{meas}}(T)} = \frac{k_1 + k_2 \cdot e^{-\frac{D}{k_B \cdot T}}}{1 + e^{-\frac{D}{k_B \cdot T}}} + K \cdot e^{-\frac{\Delta E}{k_B \cdot T}} \tag{4.2}$$

with the following parameters:

$$\begin{aligned} k_1 &= 1.79 \cdot 10^3 \text{s}^{-1} \\ k_2 &= 1.58 \cdot 10^5 \text{s}^{-1} \\ K &= 9.51 \cdot 10^9 \text{s}^{-1} \\ \text{D} &= 4.40 \cdot 10^{-3} \text{eV} \\ \Delta\text{E} &= 0.320 \text{eV} \end{aligned} \tag{4.3}$$

In appendix C.6, the determination of these parameters for the measurements presented here is described. This model allows the determination of the temperature of the $CaWO_4$ crystal during a measurement if the slow exponential decay time of the scintillation light is determined.

4.3 Setup Used for the Two-Photon Excitation: N_2 Laser

In the following, the laser and the setup used for the experiments with two-photon excitation are presented.

4.3.1 The N_2 Laser

A PSX-100 excimer laser[30] was used. The laser is a compact, portable, air cooled light source[31] that can be operated with the usual one phase 230V power grid. Pulses with typical durations of ∼2.5ns, mJ pulse energies and repetition rates of up to 100Hz can be produced. A simplified sketch of the laser and its working principle is presented in figure 4.3.
The gas volume of the laser can be filled and evacuated via a gas in- and outlet. In the presented experiments, the laser was operated at a pressure of ∼ 450mbar of nitrogen 5.0 (purity 99.999%). Photons from the main laser line of nitrogen exhibit a wavelength of 337.1nm with a band width of 0.1nm [99]. The gas volume is enclosed within partially transparent mirrors at both ends[32]. Laser activity is achieved by a high voltage (HV) discharge (across the gas volume) between the two electrodes controlled by a fast switch. This discharge effectively populates the upper lasing level which has an intrinsic lifetime

[29] Note that in this context this model is just used for describing the dependency of the observable decay time on temperature without assigning physical meanings to the model parameters. The "radiative" and "nonradiative" decay times calculated with this three-level model do not correspond to the "radiative" and "nonradiative" decay times in the developed model presented in section III/3.1.

[30] MPB Communications Inc., Montréal, Canada. Specified gases by the producer: F_2, ArF, KrCl, KrF, XeCl and XeF.

[31] Dimensions (length x width x height): (30x26x21)cm^3, weight: 13.4kg.

[32] To obtain laser action in a N_2-gas laser, no repeated passage of the photons through the laser medium is required. The gain for spontaneous and stimulated emission of the N_2 gas is so high that, in principle, no mirrors are needed at all: Already after one passage of the produced photons through the laser volume, the complete material is excited and no more amplification can be obtained [99]. For this reason, a N_2-gas laser is often called a superradiant laser [104].

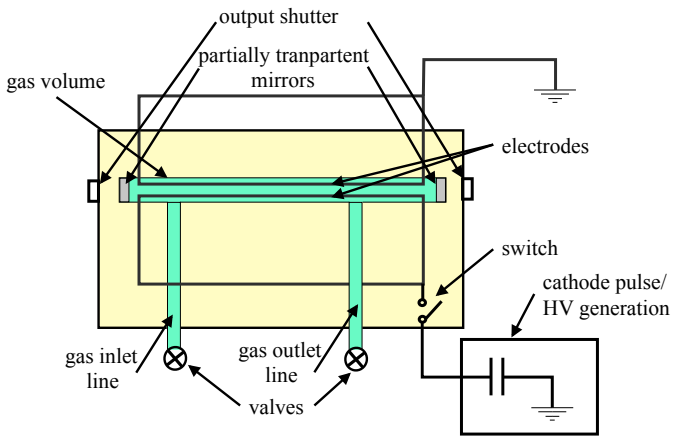

Figure 4.3: Simplified sketch of the laser and its working principle. For details, see main text.

of $\sim$ 20ns [99]. The lower lasing level, a metastable level, exhibits a lifetime of the order of 10μs [99]. Electrons decayed to the lower lasing level are able to absorb the generated laser light and, thus, account for losses growing with time in the lasing process. These increasing losses lead to a decrease in gain with time and, thus, to a termination of the laser pulse for times shorter than the intrinsic lifetime of the upper laser level. This self-terminating effect of the laser activity enables pulse lengths of the order of $\sim$ 2ns [99]. The light produced by the discharge is a composition of coherent, fast light emitted at the laser-line wavelength and spontaneous emission close to the laser line. Nonetheless, the wavelength spectrum as well as the time structure of the emitted light is strongly dominated by the laser line (see discussion in section III/4.7.3). The produced light pulse can escape the laser via the front and back window (apertures). The front window can be closed with a shutter, the back window can be closed with a cap.

Operation of the N_2 Laser

Before operation of the laser, the gas volume was flushed with high-purity nitrogen and evacuated (with a dry membrane pump) several times to assure that no residual impurities remain within the volume. For the measurements, the laser and the photomultiplier were each operated with individual isolating transformers to suppress electric crosstalk of the discharge pulse onto the PMT. For this purpose, iron plates were positioned between the laser and the PMT to serve as additional electromagnetic shielding. While these measures greatly suppressed the noise on the PMT signal[33], nonetheless, some electric crosstalk remained on the PMT signal (see discussion in appendix C.4.3). For the operation of the laser, typical pulse repetition rates of $\sim$ 60Hz to $\sim$ 85Hz were used[34]. The power output for individual pulses varied by an amount of up to $\pm$15% (see section III/5.2). This variability in the signal intensity was already qualitatively visible by eye when watching

[33] A reduction of the amplitude of induced noise by a factor of $\sim$ 5 was achieved.

[34] Pulse-repetition rates of this order of magnitude correspond to pulse intervals of $\sim$ 12 to $\sim$ 17ms. Therefore it is assured that the excitations created in the $CaWO_4$ crystal have decayed before the start of the next pulse (compare to the slow decay-time component for the complete temperature range, as discussed in section III/2.2.3).

the luminescence light produced by laser light incident on a sheet of white paper[35]. By measuring the size of the luminescent spot on the white paper at a distance of 0.15m and 3.5m from the center of the laser, the beam dimension and beam divergence can be estimated: At a distance of 0.15m, the beam exhibits a size of $\sim$ (3x3)mm^2, at a distance of $\sim$ 3.5m the size increases to $\sim$ (20x15)mm^2. From these observations, it can be concluded, that the laser beam possesses a dimension (height x width) of $\sim$ (3x3)mm^2, in accordance with the values stated in the data sheet of the laser. The beam divergence can be estimated to amount to $\sim$ 2.5mrad in each direction, close to the value given in the data sheet (beam divergence (height x width): (3x3)$mrad^2$).

4.3.2 Complete Setup

Overview of the Setup

In figure 4.4, a sketch of the complete experimental setup as employed in the laser-excitation experiments is presented. Simplified light paths are indicated: The laser-light beam is shown in violet whereas $CaWO_4$ scintillation light is shown as blue lines. In the center of figure 4.4, the N_2 laser, emitting in both directions, can be seen. The complete laser-light paths outside of the experimental chamber were enclosed in a black, light-tight housing (not depicted in the figure) to suppress stray light and to prevent laser light escaping the experimental setup.

Trigger Source

On the right hand side of the laser, the setup used for triggering is shown: The laser light escaping the rear exit of the laser is reflected at a sheet of white paper and detected by a fast photodetector (Si-PIN diode, see appendix C.3). The large and the fast signal of the Si diode provided a stable trigger source in all laser-excitation measurements.

Injection of the Laser Light into the Experimental Chamber

The laser light escaping the front (left) exit of the laser entered the experimental chamber via a vacuum-tight flange with a fused quartz window (thickness: 3mm). Fused quartz was chosen to achieve transmission of the UV laser-light into the experimental chamber. The left edge of the laser was positioned at a distance of 55cm from the center of the experimental chamber and, thus, from the $CaWO_4$ crystal. Choosing a large distance of the laser to the crystal has the advantage that less recombination light reaches the crystal due to its larger divergence (see discussion above).

Components Installed in the Experimental Chamber

On the left-hand side of figure 4.4, the experimental chamber with the attached PMT and glass fiber can be seen. A closer view to the experimental chamber and the installed components is shown in figure 4.5, with a zoomed-in view onto the $CaWO_4$ crystal on the right-hand side.

[35]For manufacturing white papers, it is very common to employ optical brighteners. These chemical compounds absorb light in the invisible ultraviolet range and reemit light in the blue range. This technique is used to make white paper appear "whiter" as it emits more visible light than obtained by simple reflection.

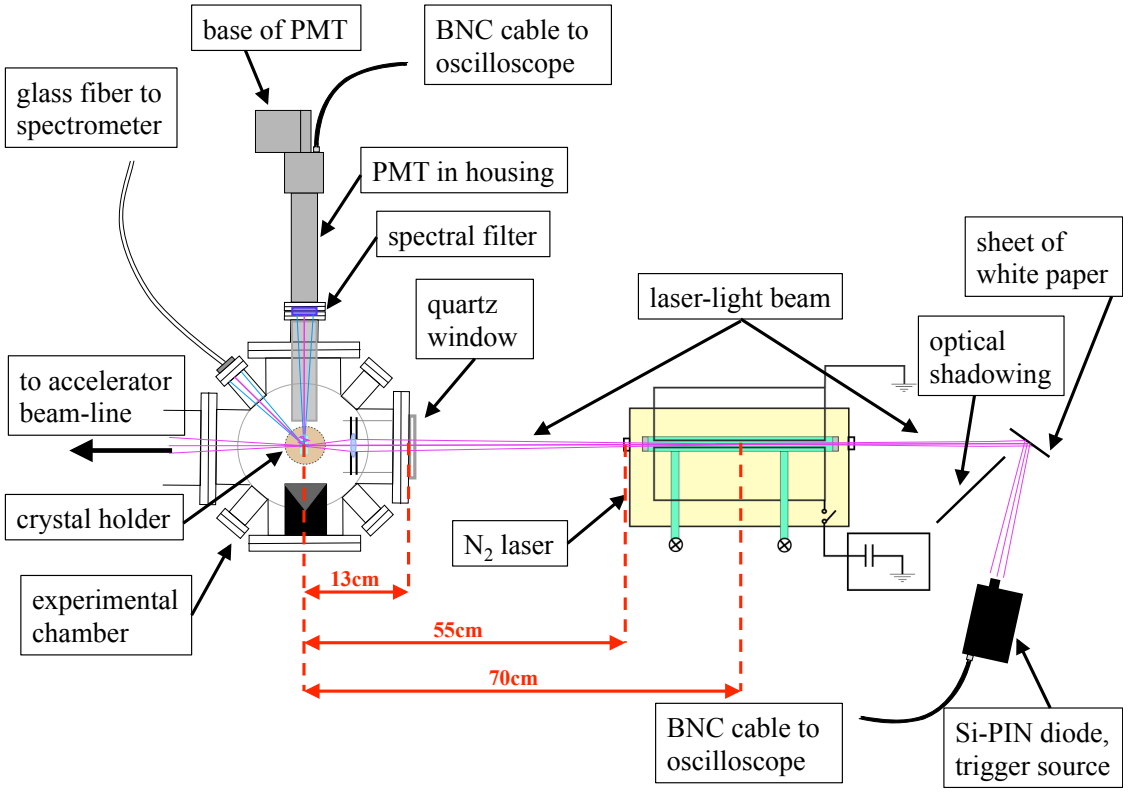

Figure 4.4: Sketch of the setup as used in the laser-excitation measurements (top view). From left to right three main components are shown: The experimental chamber containing the $CaWO_4$ crystal, the N_2 laser, and the Si-PIN diode used for triggering. The UV laser-light path is depicted in violet, the $CaWO_4$ scintillation-light path is shown in blue.

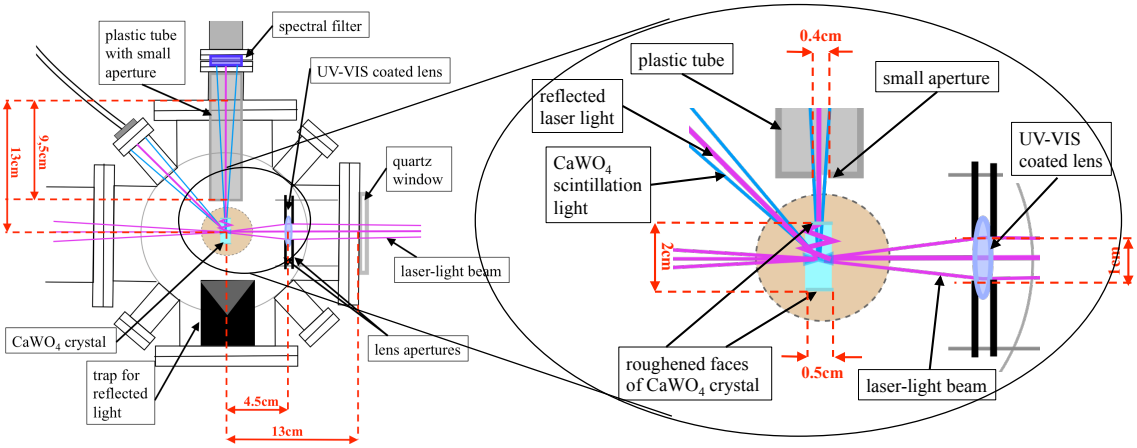

Figure 4.5: Close-up view of the setup. To the left, the experimental chamber and all contained components are shown. On the right hand side a zoomed-in view onto the $CaWO_4$ crystal can be seen. In this sketch the idealized, simplified light path within the crystal can be recognized: The repeated reflection of laser light at the crystal surfaces is indicated as violet zig-zag line.

Focussing of the Laser Light and Anti-Reflectance Installation

In order to obtain two-photon excitation (TPE) with the laser light, it has to be focussed onto the crystal. For this purpose, a UV-VIS (ultraviolet and visible) coated quartz lens[36] was installed inside the chamber between two aluminum discs used as apertures. The lens was positioned at a distance of 4.5cm to the center of the $CaWO_4$ crystal to achieve maximum focussing. (For a detailed discussion of the influence of the lens position on the produced scintillation light, see section III/4.7.3.) The apertures before and after the lens have a diameter of 1cm each. They are installed to restrict the entrance of recombination light without cropping away too much intensity of the laser light[37]. To prevent light from being reflected at the apertures, the aluminum discs were painted with black, antireflective color[38]. To further diminish the amount of laser light directly reaching the PMT, two additional components were installed in the experimental chamber: An aluminum cylinder with cone-shaped groove was installed opposite to the PMT as light trap also painted black[39]. A (dark grey) plastic tube with a small aperture (diameter 4.0mm) was introduced to restrict the observation angle available for the PMT. The aperture was positioned at a distance of only 3.5cm to the center of the $CaWO_4$ crystal so that the free line of sight onto the PMT was virtually reduced to light originating directly from the $CaWO_4$ crystal. Despite these measures, there was still laser light visible on the decay-time spectra recorded with the PMT. As source of this remaining scattered light, the reflection of laser light at the $CaWO_4$ crystal itself could be identified. This process is indicated on the right-hand side in figure 4.5 in the zoomed-in view of the crystal. The repeated reflection of laser light at the inner surfaces of the crystal are indicated as violet zig-zag line. Hence, no further reduction of scattered laser light on the PMT signal could be achieved (see discussion in section III/4.7.3).

Position of the $CaWO_4$ Crystal

In figure 4.6, photographs of a $CaWO_4$ crystal installed in its holder in the center of the experimental chamber are shown. The surfaces (size: (10x20)mm^2) perpendicular to the laser beam were polished to optical quality (see section III/4.1.2) to prevent increased scattering or absorption of the laser light by defects at the surface[40]. In this way, the laser light could penetrate the complete volume of the crystal. The surfaces at the side of the crystal facing the PMT and the opposite side (size: (5x10)mm^2) were roughened (see section III/4.1.2) to enhance the amount of light escaping the crystal in all directions, as discussed in section III/4.1.2. In figure 4.6 b), it can be seen that, indeed, the laser beam penetrates and excites a volume spreading over the complete thickness of the crystal. The fact that the total side-face of the crystal seems to glow, reflects the efficiency of the

[36] UV double-convex lens, T48-844, Edmund Optics, Barrington, USA. Technical data: Diameter 25mm, center thickness 5.52mm, radii 54.14mm, effective focal length 60mm, UV-VIS coated for anti-reflectance.

[37] Due to the beam divergence determined above, a diameter of the laser beam of $\gtrsim$ 5.5mm is expected at the location of the lens. The apertures additionally help to suppress the entrance of light into the chamber that was reflected several times within the lens and would leave the lens in its edge regions under arbitrary scattering angles. In this way the intensity of laser light scattered directly onto the PMT and spectrometer could be diminished.

[38] NEXTEL Velvet-Coating 811-21, Mankiewicz Gbr. & Co., Hamburg, Germany. Ultra-low reflectivity optical paint.

[39] The paint used was also the highly antireflective 3M black velvet paint.

[40] As discussed in section III/2.1.3, defects are expected to exhibit decreased band gaps and could thus act as absorption centers for the laser light. A non-polished or even roughened surface of the crystal could contain an enhanced density of such defects.

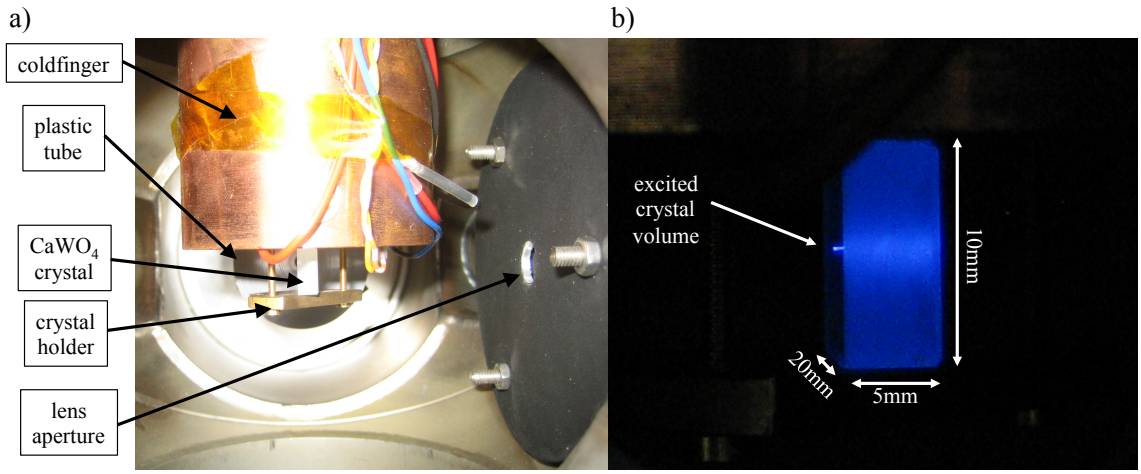

Figure 4.6: Photos of one of the investigated $CaWO_4$ crystals ((5x10x20)mm^3) installed in the setup used for the laser-excitation measurements (view through the flange opposite to the PMT with the trap for reflected light removed). In figure a), the crystal in its holder attached to the coldfinger (center), the lens aperture (right) and the plastic tube (grey circular surface behind the crystal) can be seen. In figure b), a closer view to the crystal installed in the same setup is shown. This photo was not taken perfectly perpendicular to the small side-face of the crystal, but with a small angular misalignment. Hence, also part of the large, polished (left) surface of the crystal can be seen. For this photograph, the $CaWO_4$ crystal was excited by the pulsed N_2 laser-beam. The dark blue, luminous area corresponds to the small side-face of the crystal, the horizontal, lighter blue region in its center corresponds to the track of excitons excited by two-photon absorption of incident laser photons. To the left of the blue-glowing side-face of the crystal a small, intensely blue, sharp line can be recognized. This line depicts a view onto the excited volume through the polished, large face (left side) of the crystal.

roughened surface in scattering the produced scintillation light into arbitrary directions. The thickness of the thin blue line, visible to the left of the side-face of the crystal, corresponds to the real, radial extent of the crystal volume excited by the laser beam. A detailed discussion of the geometry of the laser beam, i.e. its focussing, and the produced excitation can be found in section III/4.7.3 and appendix C.10.2.

Solid Angle of Observation with the PMT

From this description of the geometry of the setup, the solid angle observable with the PMT can be estimated. The value of the solid angle of observation $\Omega_L = 8.2 \cdot 10^{-4}$ (see appendix C.7.1) is used for the analysis of the measurements as it determines the fraction of the generated scintillation light that is detected, i.e. the geometrical detection efficiency of the system (see appendix C.11).

Prior to the measurements, the experimental chamber was always evacuated to allow cool-down of the crystal and to prevent scattering at or excitation of gas atoms by the laser photons. With the described setup, the measurements of the $CaWO_4$ decay-time and wavelength spectra under laser-excitation were performed. An overview of the different performed measurements can be found in section III/4.5.2.

4.4 Setup Used for the Ion-Beam Excitation: Tandem Accelerator

In the following, the working principle and the chosen settings of the tandem accelerator as well as the employed experimental setup used in the ion-beam excitation measurements are presented.

4.4.1 The Tandem Accelerator

To obtain a beam of ions of the desired type, Cs ions (produced by a heated Cs-source) are generated and accelerated towards the source containing the atoms of the desired type in solid form. The Cs ions sputter atoms from the surface of the source that get negatively ionized in the process of escaping the source (pick up of electrons from a Cs layer). These ions are extracted with the help of the so-called extraction voltage. After passing a preselection (typically single-ionized ions are selected), they are subjected to the so-called pre-accelerator voltage ($\sim$ 200keV). Subsequently, they are injected into the accelerator tube where they traverse and get accelerated by the terminal voltage for the first time until they reach the middle of the accelerator where they pass through a stripping foil. Penetrating the foil leads to a loss of several electrons of the ions resulting in multiply charged, positive ions. These are accelerated by the terminal voltage again, concordantly to their charge. By a 90 degree magnet, the desired ions (charge and respective energy) can be selected. With electro-magnetical lenses and deflection magnets installed in the beam-line, the beam of ions can be focussed (or defocussed) and guided through the beam-line to the respective experimental chamber.

Pulsing of the beam is achieved by a chopper (cutting away parts of the originally continuous beam) and a buncher (compressing the excised, surviving ion packages in time) on the low-energy side of the accelerator. Additional pulse shaping and shortening can be achieved with a high-energy chopper cutting away smeared-out tails of the ion pulses left-over by the bunching process. The achieved pulse widths of the ion pulses typically amount to 2 to 3ns [11, 105, 77]. The complete pulsing process is controlled by the pulsing of the low-energy chopper. This pulsing is performed on the basis of a 5MHz frequency generator. Pulse-repetition rates of inverse powers of 2 of this frequency ($\frac{5MHz}{2^n}$, $n \in \mathbb{N}$, $n < 12$) can be chosen. To produce even smaller repetition rates (larger pulse intervals), an external pulsing can additionally be used. For this purpose, a +5V TTL-signal of the desired frequency has to be added as envelope function to the internal pulsing of the low-energy chopper. This envelope function opens a time window for accepting internally created pulses (from the chopper-pulsing) that are allowed to be transmitted to the chopper. In this way, for an external pulsing of, e.g., 1kHz with a pulse width (acceptance-window width) of 50μs and an internal pulsing of $\frac{5MHz}{2^8} \approx$ 19.5kHz, corresponding to 51.2μs, only every 19th or 20th internally created pulse will be transmitted to the chopper. Hence, the created pulsing exhibits a frequency of roughly 1kHz where almost alternately every 19th and 20th internally created pulse leads to the generation of an ion-beam pulse.

A more detailed description of the basic working principle of the tandem accelerator at the MLL as well as of the procedure to produce pulsed ion beams can be found, e.g., in [11, 105, 77] and references therein.

Chosen Settings of the Tandem Accelerator

As discussed in section III/4.1.4, pulsed beams of Oxygen and Iodine ions were used for the dense excitation mode of the $CaWO_4$ crystals. For these measurements, six days of beamtime at the tandem accelerator of the MLL could be used. In the following, the settings of the accelerator for the pulsed ion-beam production and the resulting ion energies are presented.

In principle, ion energies in the range from $\sim$ 5keV up to $\sim$ 100keV would be optimal[41]. However, the ion energies produced by the tandem accelerator cannot be chosen arbitrarily: For small ion energies, on the one hand, the beam production (mainly influenced by the terminal voltage) and the beam guidance get highly unstable. On the other hand, it holds true that the smaller the ion energy, the smaller the light yield and, thus, the possibly achievable statistics for the decay-time measurements and accordingly for the pulse-shape determination. Hence, an ion energy within the accessible range of the tandem accelerator (a few tens of MeV) that is estimated to deliver a large enough amount of detectable light was chosen: For both types of ions an energy of $\sim$ 35MeV was realized (see below). In this context, it has to be noted that the comparably large ion energies are no intrinsic disadvantage for the model test (see section III/3.3).

Sharply defined, fast excitation pulses are needed to determine the pulse shape of the $CaWO_4$ scintillation light, especially at the beginning of the pulse, where the influence of the quenching process is large. In addition, the pulsing frequency has to be adjusted to match the slow decay times of the scintillation light in order to assure that all excitations in the crystal have decayed at the arrival time of the next pulse. In particular, it has to be taken into account that the decay time increases strongly with decreasing temperature. For the temperatures used in the measurements, $\sim$ 300K and $\sim$ 20K (see section III/4.5), the slow decay time of $CaWO_4$ crystals amounts to $\sim 9\mu$s and $\sim 75\mu$s, respectively (see appendix C.8). Hence, pulse repetition rates should be chosen such that several decades of exponential decay before the start of the new pulse are possible.

The corresponding settings of the accelerator[42] that were chosen for the measurements with ion-beam excitation are shown in table 4.3.

4.4.2 Complete Setup

Overview of the Setup

The experimental setup used in the experiments with ion-beam excitation is very similar to the basic setup shown in figure 4.1 (see section III/4.2.1). In contrast to the laser-excitation experiments, no other light source than the $CaWO_4$ crystal was present in the experimental chamber. Hence, no apertures or light traps were needed. An overview of the complete setup is shown in figure 4.7. The pulsed ion beam is indicated as green lines, simplified paths of the generated $CaWO_4$ scintillation light are shown in blue.

[41] These energies are supposed to be used for testing and validating the developed model in the framework of the Dark Matter experiments CRESST and EURECA. The region of interest for the Dark Matter experiments roughly stretches to maximal 100keV recoils, dependent on the theoretical model (see section I/2.2).

[42] For the value of the terminal voltage, the analog measurement - assumed to be more precise than the digital measurement - is taken.

ion species		^{16}O	^{127}I
charge		5+	6+
extraction voltage	[MV]	0.01785	0.01708
pre-accelerator voltage	[MV]	0.1477	0.1290
terminal voltage	[MV]	5.796	4.946
ion energy	[MeV]	34.942	34.768
pulsing frequency ($T \approx 300$K)	[kHz]	9.765625	19.53125
pulse interval ($T \approx 300$K)	[μs]	102.4	51.2
pulsing frequency ($T \approx 20$K)	[kHz]	1	1
pulse interval ($T \approx 20$K)	[ms]	1	1

Table 4.3: Settings of the accelerator and pulsing employed in the different performed experiments with ion-beam excitation: Pulsing for measurements at room temperature ($\sim$ 300K) was performed with the internal pulsing only. Pulsing for the measurements at low temperature ($\sim$ 20K) was performed with the help of an external 1kHz pulsing with 50μs pulse width. In this case, the frequency of the external pulsing is given in the table.

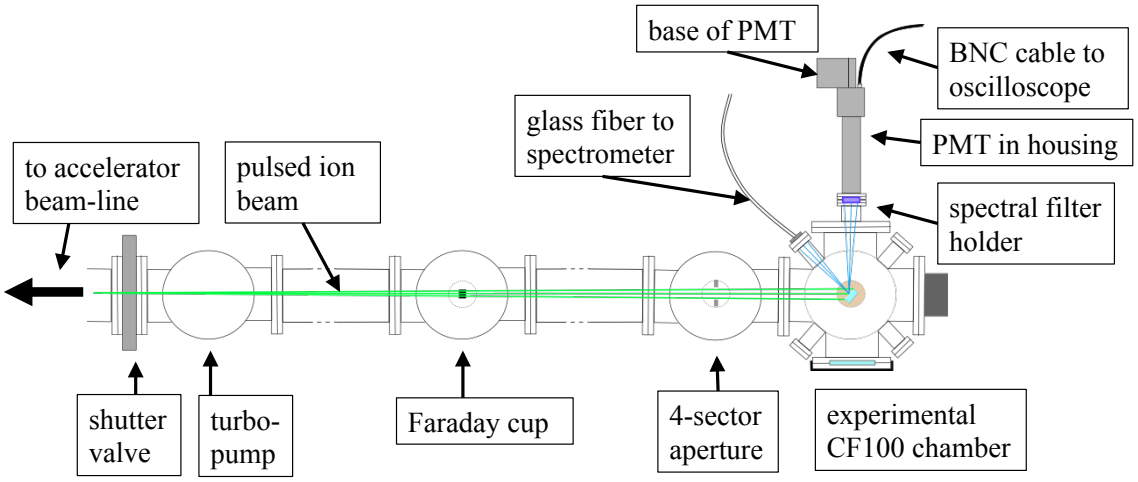

Figure 4.7: Sketch of the setup as used in the ion-beam excitation measurements (top view). From left to right the following main components are shown: The connection to the beam line of the accelerator (shutter valve), the last part of the beam line containing components for beam adjustment and analysis (movable Faraday cup and 4-sector aperture) as well as the experimental chamber containing the $CaWO_4$ crystal installed in its holder. The $CaWO_4$ scintillation light is depicted in blue. The pulsed ion beam is indicated as green lines.

Regulation and Evaluation of the Pulsed Ion Beam

Left to the shutter valve, prior to the experimental setup, an magnetic lens is installed in the beam line of the accelerator (not indicated in figure 4.7). With this lens, final adjustments of the direction of the beam as well as (de-)focussing of the beam can be performed. Before connecting the experimental setup to the accelerator beam-line by opening the shutter valve, the setup was evacuated to $\sim 1 \cdot 10^{-7}$mbar. Rough analysis of the beam current (ions per pulse) could be accomplished via the removable Faraday cup installed in

the beam line. Investigation and evaluation of the direction and geometrical broadening of the beam was achieved by using the 4-sector aperture. This aperture contains four separate sectors surrounding the central beam line. The beam current incident on each sector can be read out individually. Additionally, the spacing between the four sectors, i.e., the dimension of the central beam line, can be adjusted. In this way, the beam direction and its elongation in all directions can be determined. For details on the determined geometrical shape of the ion beam and the analysis of the time structure of the pulses, see section III/4.7.3.

Components Installed in the Experimental Chamber and Position of the $CaWO_4$ Crystal

In figure 4.8 a), a zoom into the experimental chamber, in figure 4.8 b), a photograph of a $CaWO_4$ crystal excited by the ion beam are shown. To obtain enough light intensity to

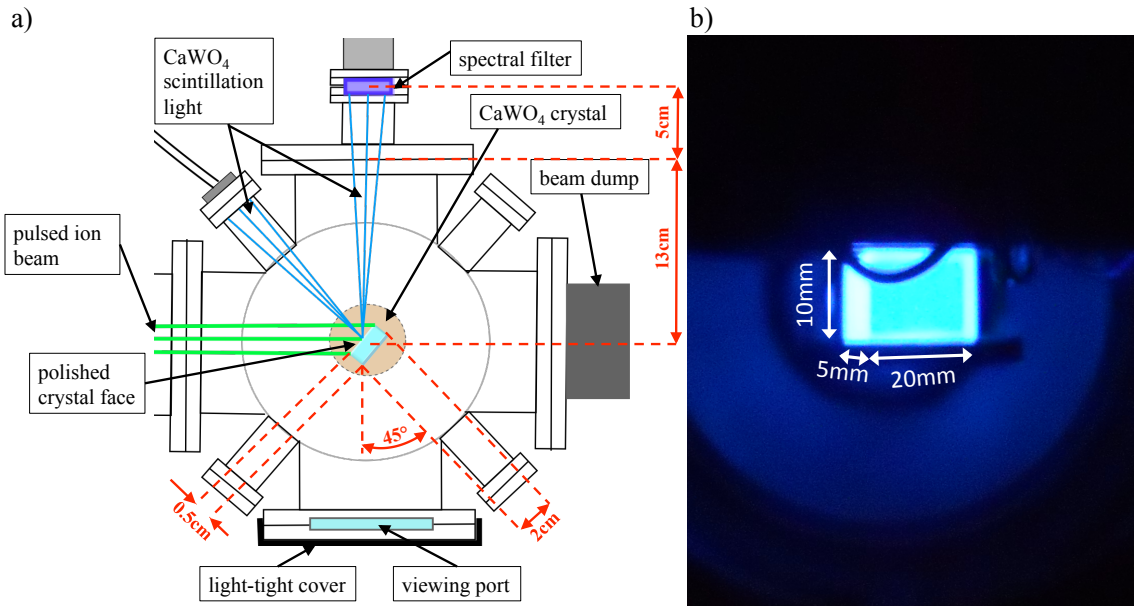

Figure 4.8: Panel a): Zoom into the setup as used in the ion-beam excitation measurements (top view): The experimental chamber and all contained components are shown. The idealized, simplified paths of the scintillation light (blue lines) can be recognized. The complete, large surface of the crystal is exposed to the defocussed ion-beam (green lines). Panel b): Photo of one of the investigated $CaWO_4$ crystals ((5x10x20)mm^3) installed in the setup used for the ion-beam excitation measurements. The photo was taken in side view through the viewing port of the flange opposite to the PMT. The crystal scintillating under ion-beam excitation (blue glowing area) can be seen (angle of view: 45°). The black line visible in the upper region of the crystal is the shadow of a cable of the thermometer connection of the cryocooler (see section III/4.2.5).

take a photo, the pulsing of the ion beam was set to 5MHz so that the crystal was excited every 0.2μs by a pulse of ions. In the close-up view of the setup, the simplified light paths of the generated scintillation light (blue lines) can be recognized. The ion beam incident onto the $CaWO_4$ crystal is depicted in green. In this setup, the $CaWO_4$ crystal is oriented in a 45° angle in relation to the ion beam to enhance the size of the crystal area observed with the PMT. The large, (10x20)mm^2 surface of the crystal facing the ion beam and the

PMT was polished to optical quality, all other surfaces were roughened to enhance the light output of the crystal. For the definition of the surface treatments, see section III/4.1.2. The surface penetrated by the ions was polished in order to avoid enhanced excitation of defects possibly contained in a roughened surface. In figure 4.8 a), it is illustrated that the complete crystal surface facing the incident ions was illuminated by the defocussed beam. Onto the flange to the right of the crystal, a beam dump (made of lead) was installed to shield radiation possibly created by the ion beam. The flange opposite to the PMT was equipped with a viewing port to additionally allow optical analysis of the quality of the beam adjustment, i.e., to inspect the area of the crystal surface hit by the ion beam. During the actual measurements this flange was covered by a light-tight cap to avoid stray light in the setup.

Solid Angle of Observation with the PMT

The solid angle of observation with the PMT in the ion-beam experiments can be estimated from the presented setup. The value $\Omega_{IB} = 1.2 \cdot 10^{-3}$ (see appendix C.7.2) will be used for the determination of the geometrical detection efficiency of the system (see appendix C.11).

Trigger Source

In these experiments, no independent light signal could be used as trigger source (as was possible with the laser). As discussed in section III/4.1.4, it would also be unfavorable to use the generated scintillation light itself as trigger source. However, the pulsing signal of the low-energy chopper can be used as trigger source as it is correlated in time with each produced ion pulse.

With the described setup, the measurements under ion-beam excitation were performed. An overview of the different performed measurements can be found in section III/4.5.1.

4.5 Overview of Measurement Campaigns

In the following, an overview of the performed measurements with the two $CaWO_4$ crystal samples Olga and Philibert installed in the described setups is presented. At first, the experiments with Iodine-beam and Oxygen-beam excitation were performed. Thereafter, the experiments with two-photon excitation were conducted. For each excitation source, a measurement with the 400nm filter at room temperature and at low temperature, respectively, and a measurement with the 500nm filter at room temperature and at low temperature, respectively, were conducted. For each of these constellations, averaged decay-time spectra with the PMT were recorded. For each excitation source and each temperature (independently of the used filter), a respective wavelength spectrum was recorded with the spectrometer. The different measurements are labelled according to the crystal (**O** $\widehat{=}$ Olga, **P** $\widehat{=}$ Philibert) and the instrument (**PMT** $\widehat{=}$ decay-time spectrum recorded with the PMT, **S** $\widehat{=}$ wavelength spectrum recorded with the spectrometer) with which they were performed as well as with a running integer number (see sections III/4.5.1 and III/4.5.2). A wavelength spectrum that was recorded under the same conditions (temperature and excitation) as a decay-time spectrum is assigned the same respective integer number.

With the samples from crystal Olga, all of the described measurements were performed. The resulting data will be used for the determination of the parameters of the developed model and its validation (see chapter III/5). With the samples from crystal Philibert, only some of these measurements were performed as these are only used for comparison of the self-grown crystals with bought ones.

The procedure used for the determination of the slow decay time which was employed for the assignment of the temperature of the $CaWO_4$ crystal during the measurement (see section III/4.2.6) is presented in appendix C.8. The standard temperatures during the measurements were $\sim$ 300K and $\sim$ 20K, respectively.

4.5.1 Ion-Beam Excitation

The following measurements were performed with ion-beam excitation and will be used for the model evaluation and comparison of the crystals. An overview of these measurements can be found in table 4.4.

crystal	ion beam	T_{cryst} [K]	PMT meas. no. PMT	PMT filter	PMT t_{rl} [μs]	spectrometer meas. no. spectrum
Olga	^{127}I	298	**O1$_{PMT}$**	400nm	100	**O1$_S$**
		29	**O2$_{PMT}$**		2000	**O2$_S$**
		298	**O3$_{PMT}$**	500nm	100	-
		27	**O4$_{PMT}$**		500	-
	^{16}O	309	**O5$_{PMT}$**	400nm	100	-
		20	**O6$_{PMT}$**		1000	-
		300	**O7$_{PMT}$**	500nm	100	**O7$_S$**
		21	**O8$_{PMT}$**		1000	**O8$_S$**
Philibert	^{127}I	308	**P1$_{PMT}$**	400nm	100	**P1$_S$**
		20	**P2$_{PMT}$**		1000	**P2$_S$**
	^{16}O	302	**P3$_{PMT}$**	400nm	100	**P3$_S$**
		18	**P4$_{PMT}$**		1000	**P4$_S$**

Table 4.4: Overview of the measurements performed under ion-beam excitation: Displayed are the investigated crystal, the ion type used for excitation, the crystal temperature T_{cryst}, the decay-time spectrum measurement-number, the used optical filter and record length t_{rl} as well as the wavelength spectrum measurement-number.

The employed ion-beam pulse repetition-rates can be found in table 4.3 in section III/4.4.1. All decay-time spectra were recorded with a PMT voltage of -1.75kV. Typically 50,000 individual PMT pulses were averaged for each measurement[43] (see section III/4.2.3). To achieve sufficient light outputs for the recording of the wavelength spectra, the basic 5MHz frequency of the chopper of the accelerator was used, producing a pulse of ions

[43] In the measurement **O6$_{PMT}$**, even more pulses (112,000) were averaged as the additional noise component on the baseline (discussed in appendix C.4.3) was strongly visible and further reduction of the statistical noise was aimed at. In measurement **P5$_{PMT}$**, which was the last run in this beam time only 30,000 pulses were averaged.

every 0.2μs[44]. For the recording of the wavelength spectra with the spectrometer, integration times of 30s (Iodine beam) and 10s (Oxygen beam) were used. As already discussed in section III/4.2.6, in the first two cold measurements (**O2$_{\mathbf{PMT}}$** and **O4$_{\mathbf{PMT}}$**), the cryocooler did not reach its final low-temperature plateau. However, as can be seen from the values for the crystal temperature given in table 4.4, in all following measurements, the realized low temperature was approximately the same. The slightly elevated temperatures (309K and 308K) in the measurements **O5$_{\mathbf{PMT}}$** and **P1$_{\mathbf{PMT}}$**, respectively, can be assigned to an elongated heating procedure of the cryocooler after preceding low-temperature measurements (see discussion in appendix C.8). The comparably small temperature (18K) determined for the measurement **P4$_{\mathbf{PMT}}$** should be treated with care, as this value most probably reflects an artifact of the procedure used to determine the temperature (for details, see appendix C.8).

4.5.2 Two-Photon Excitation

The measurements performed with laser excitation which will be used for the model evaluation and crystal comparison are listed in table 4.5.

crystal	T_{cryst} [K]	PMT			spectrometer
		meas. no. PMT	filter	t_{rl} [μs]	meas. no. spectrum
Olga	298	**O9$_{\mathbf{PMT}}$**	400nm	10/100	-
	20	**O10$_{\mathbf{PMT}}$**		10/100/1000	-
	298	**O11$_{\mathbf{PMT}}$**	500nm	10/100	**O11$_{\mathbf{S}}$**
	21	**O12$_{\mathbf{PMT}}$**		10/100/1000	**O12$_{\mathbf{S}}$**
Philibert	298	**P5$_{\mathbf{PMT}}$**	400nm	10/100	**P5$_{\mathbf{S}}$**
	18	**P6$_{\mathbf{PMT}}$**		10/100/1000	**P6$_{\mathbf{S}}$**

Table 4.5: Overview of the measurements performed under laser excitation: Displayed are the investigated crystal, its temperature T_{cryst}, the decay-time spectrum measurement-number, the respectively used optical filter and the different used record length t_{rl} as well as the wavelength spectrum measurement-number.

The used settings of the laser can be found in section III/4.3.1. The decay-time spectra were recorded with a PMT voltage of -1.5kV. In each measurement, 5,000 individual PMT pulses were averaged (see section III/4.2.3). Due to the large amount of scintillation light observed in these measurements the same settings of the laser could be used for the recording of the wavelength spectra. An integration time of the spectrometer of 20s was used. As can be seen from table 4.5, each decay-time measurement was repeated with multiple record lengths and, hence, different time resolutions (see discussion in appendix C.4.5). For a short discussion of the exceptionally small temperature (18K) determined for the measurement **P6$_{\mathbf{PMT}}$**, see appendix C.8.

[44]In order to avoid the production of radiation damage due to this increased ion intensity, the exposure times were kept short. Decay-time spectra before and after such a measurement were compared to check for changes in the light-emitting properties. No changes could be observed.

4.6 Data Preprocessing

Before analysis, the data (wavelength and decay-time spectra) obtained in the measurements presented above are preprocessed, as described in the following.

4.6.1 Wavelength Spectra

The recorded scintillation-light spectra and dark spectra are imported into a ROOT [106] environment. The data for wavelengths above 800nm where no intensity due to the scintillation light of $CaWO_4$ has to be expected is used for the determination of a possibly remaining DC offset. In the first step of the data preparation, the determined DC offset is subtracted from the data. In the next step, the spectral response of the setup (spectrometer and glass fiber) is corrected by multiplication with the wavelength dependent correction factor $CF(\lambda)$ according to the procedure described in appendix C.2.2. In addition, for each corrected spectrum the position of the maximum of the scintillation light $\lambda_{\max}$ is calculated. This is accomplished with the help of a running average filter over ±4 channels, corresponding to around ±2nm, to suppress the influence of statistical fluctuations. With this running average filter, also the respective value of the maximum intensity (as average of the central value ±4 channels) is determined. This value is used to normalize the maximum of each spectrum to unity to allow for an easier qualitative comparison (see section III/4.7.1). Before analyzing the data, the systematical and statistical errors (as determined in appendix C.2.3) are assigned to the individual data points.

4.6.2 Decay-Time Spectra

The recorded decay-time spectra (typically averages of 5,000 or 50,000 individual PMT pulses) are imported into a ROOT [106] environment. Data points from the baseline before the pulse are used to produce a baseline histogram which is employed to calculate the DC offset of the pulses[45]: A histogram of the voltage values in the selected region is compiled. This histogram is fitted with a gaussian where the mean of this gaussian is identified with the remaining DC offset. This DC offset is subtracted from the data and the voltage coordinate of the pulses is reverted to yield positive pulses. The one-sigma width of the baseline histogram is used to determine the statistical uncertainty of the data points, according to appendices C.4.6 and D.1. In the same routine, the minimum distance of data points in the time and voltage coordinate, i.e., the corresponding resolutions of the data acquisition, as well as the employed record length are automatically detected so that the respective uncertainties can be calculated (see appendix C.4.6). All uncertainties that are considered, as described in appendix C.4.6, are assigned to the individual data points[46].

As described in sections III/4.3.2 and III/4.4.2, the trigger source in the laser excitation experiments was the Si-diode signal whereas in the ion-beam excitation experiments the pulsing signal of the chopper was used as trigger signal. For different settings of the accelerator (e.g., different ion beams or pulsing frequencies), the transmitted pulsing signal from the chopper exhibited different time shifts with respect to the produced ion pulse. Therefore, the decay-time spectra recorded under ion-beam excitation exhibit strongly differing time shifts with respect to the zero of time (time of triggering). As this information

[45] For an overview of the selected regions for each pulse, see table C.6 in appendix C.9.

[46] Before being analyzed, the time base of the pulses is converted from seconds to a ns time base to facilitate fitting of the pulses.

(the time-shift between the trigger-signal and the scintillation-light signal) is, however, not needed in the analysis, the maxima of the decay-time spectra recorded under ion-beam excitation are determined and the pulses are shifted to align the maxima with the zero of time. In this way, an easier selection of starting parameters for the fits of the pulses is obtained as no arbitrary time shift has to be handled. In the laser-excitation experiments, for each realized experimental configuration (crystal, filter and temperature) at least two measurement with different record lengths were performed. The trigger signal of the Si diode used for the measurements with one investigated configuration (e.g., $\mathbf{O9_{PMT}}$ with a record length of 10μs and 100μs) can be regarded as identical as no modifications of the setup or trigger settings were performed in between. Hence, for such measurements, with the same configuration, but different record lengths, it can be expected that the recorded decay-time spectra exhibit the same temporal characteristics, i.e. the same starting time of the pulse. In order to sustain the temporal correlation of the different decay-time spectra recorded for the same configuration, no temporal shifts of the data recorded under TPE are performed.

In these preprocessing steps, also the time regions of the decay-time spectra recorded under ion-beam excitation used for the determination of the pure exponential decay-time fit (required for the calculation of the temperature of the crystal, see appendix C.8) are selected. The procedure used to choose these regions as wells as the respectively chosen time windows can be found in appendix C.9. In addition, a selection of data points used for the fits of the model to the decay-time spectra recorded under ion-beam excitation is performed, as described in appendix C.9. This selection is necessary, to reduce the computing time of these numerically extensive fits (see section and III/5.3.2). For the decay-time spectra recorded under laser excitation, no such selections were required as, on the one hand, the pure exponential decay time is included as a free parameter in the total pulse-shape fit. On the other hand, the fit of the model for the unquenched light-generation to the data is much less numerically extensive (see section III/5.2.1).

4.7 Qualitative Analysis of the Data Recorded for Laser and Ion-Beam Excitation

In this section, a first overview and comparison of the data obtained with the different excitation modes at different temperatures and for different wavelengths regions is given. At first, a qualitative comparison of the different recorded wavelength and decay-time spectra is presented. Thereafter, the pulse shapes and characteristics of the employed excitation pulses (ion-beam and laser) are presented as they greatly influence the pulse-shape of the produced scintillation light, especially within the first few nanoseconds of the decay-time spectrum.

In the following, the term ”room temperature” denotes the measurements recorded without running cryocooler, whereas ”low temperature” denotes all measurements performed with running cryocooler.

4.7.1 Qualitative Comparison of the Measured Wavelength Spectra

At first, some basic features of the recorded wavelength spectra are discussed using as example the wavelength spectra recorded with crystal Olga at room temperature under the

three different excitations. In figure 4.9 these spectra, preprocessed according to section III/4.6.1 (note in particular that the maxima are normalized to unity) are shown. A broad

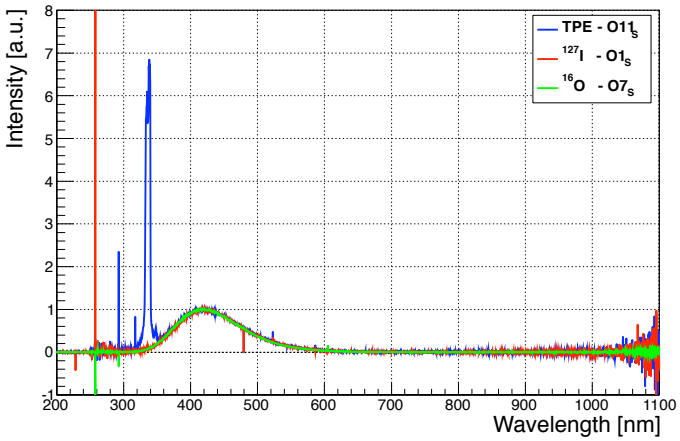

Figure 4.9: Comparison of the wavelength spectra recorded with crystal Olga for the different excitations at room temperature: The spectra are preprocessed according to section III/4.6.1 (no error bars shown) and the complete data range is depicted. In blue, the spectrum recorded under two-photon excitation ($\mathbf{O11_S}$), in red, the spectrum recorded under Iodine-beam excitation ($\mathbf{O1_S}$) and in green, the spectrum recorded under Oxygen-beam excitation ($\mathbf{O7_S}$) are shown.

and featureless spectrum of the $CaWO_4$ scintillation light can be seen roughly between 300nm and 700nm. The spikes at $\sim$ 260nm as well as the noisy regions around 280nm and for wavelengths larger than $\sim$ 950nm which are visible on all spectra are due to the applied spectral correction function (see section III/4.2.2 and appendix C.2.2). On the spectrum recorded under two-photon excitation (blue line in figure 4.9) a dominant structure at around 340nm can be recognized. This peak can be attributed to the detection of laser light reflected at and within the $CaWO_4$ crystal as is shown and discussed in section III/4.7.3. Additionally, it can be seen that the wavelength region which is interesting for the characterization of the scintillation light of $CaWO_4$ can be limited to the region spanning from 300nm to 700nm. Hence, in the following, only this wavelength region of the recorded spectra will be shown and be used for fitting of the data (see section III/5.1).

In figure 4.10 a), a zoom into this wavelength region for the presented wavelength spectra is depicted, in panel 4.10 b) the y-axis is shown in logarithmic scale to allow a better comparison. Four main features can be observed:

- As anticipated by the model (see, e.g., discussion of equation 3.148 in section III/3.2.4), the shapes of the scintillation-light spectra, i.e., the ratios of produced blue-to-green light, recorded under the different excitations are the same: The model predicts, that independent of the location of the volume excited by an energy deposition (possibly different defect densities at the surface (ion beam) or inner volume (TPE) of the crystal), the main contribution of the green light component is produced by reabsorption of created blue photons by defect (green) centers within the complete crystal volume (see discussion in section III/3.2.2).
- The spectra are broad and featureless with a slight asymmetry at the larger wavelength side (for details, see discussion in section III/5.1).

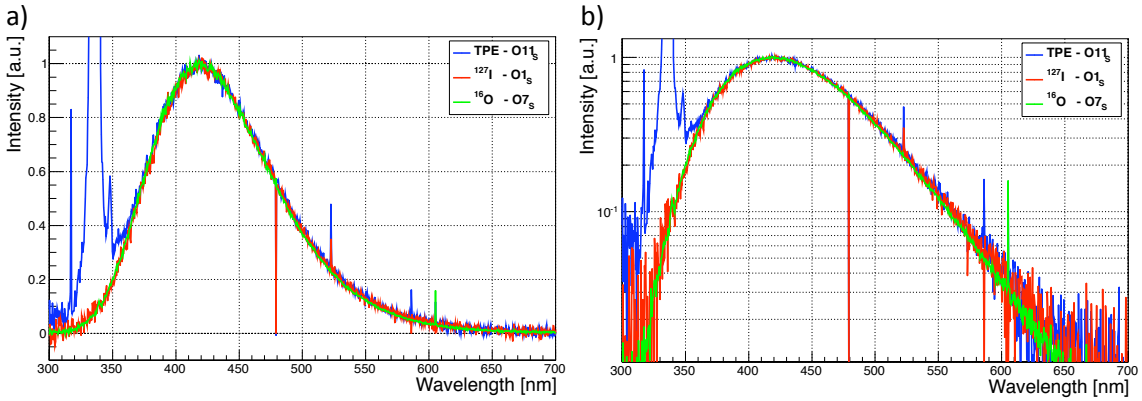

Figure 4.10: Comparison of the wavelength spectra recorded with crystal Olga for the different excitations at room temperature: The spectra are preprocessed according to section III/4.6.1 (no error bars shown). In blue, the spectrum recorded under two-photon excitation (**O11S**), in red, the spectrum recorded under Iodine-beam excitation (**O1S**) and in green, the spectrum recorded under Oxygen-beam excitation (**O7S**) are shown. Figure a): normal y-axis, figure b): logarithmical y-axis. The peak at $\sim$ 340nm visible on the blue spectrum (recorded for TPE) is caused by the detection of laser light reflected within or at the $CaWO_4$ crystal. The sharp spikes on the spectra can be attributed to data outliers due to individual pixels of the spectrometer.

- For the spectrum recorded with TPE (**O11S**) the laser line (at $\sim$ 340nm) as well as a small enhancement of the intensity around this laser line can be seen. This enhancement can be attributed to recombination light from the laser (see section III/4.3.1).

- The spectrum recorded under Iodine-beam excitation (**O1S**) exhibits a larger statistical noise component than the spectrum recorded under Oxygen-beam excitation (**O7S**). This can be attributed to the fact, that the spectrum for Oxygen beam excitation was recorded with much better statistics ($\sim$ 3 to 4 times larger intensities were detected for the Oxygen beam).

The same observations can be made in the comparison of the wavelength spectra recorded for the different excitations for crystal Olga at low temperatures (see figure 4.11 a and b) as well as for the spectra recorded for crystal Philibert at room temperature (see figure 4.11 c and d) and at low temperature (see figure 4.11 e and f), respectively.

Due to these features and the clearly visible and anticipated similarity of the respective spectra (one crystal at one temperature for different excitations), for the analysis of the wavelength spectra in each case only one spectrum is selected. The spectra which will be used in section III/5.1 for the fits of the spectral shape and thus for the determination of the spectral composition are the respective spectra obtained with Oxygen-beam excitation. These spectra are selected as, on the one hand, they offer the advantage, compared to the TPE spectra, that no additional light source was present. On the other hand, they exhibit better statistics and hence, a better signal-to-noise ratio, than the spectra recorded under Iodine-beam excitation. Hence, in the following, only the spectra recorded under Oxygen-beam excitation are discussed as the implications that can be drawn can be expected to be valid also for the corresponding spectra obtained under TPE and Iodine-

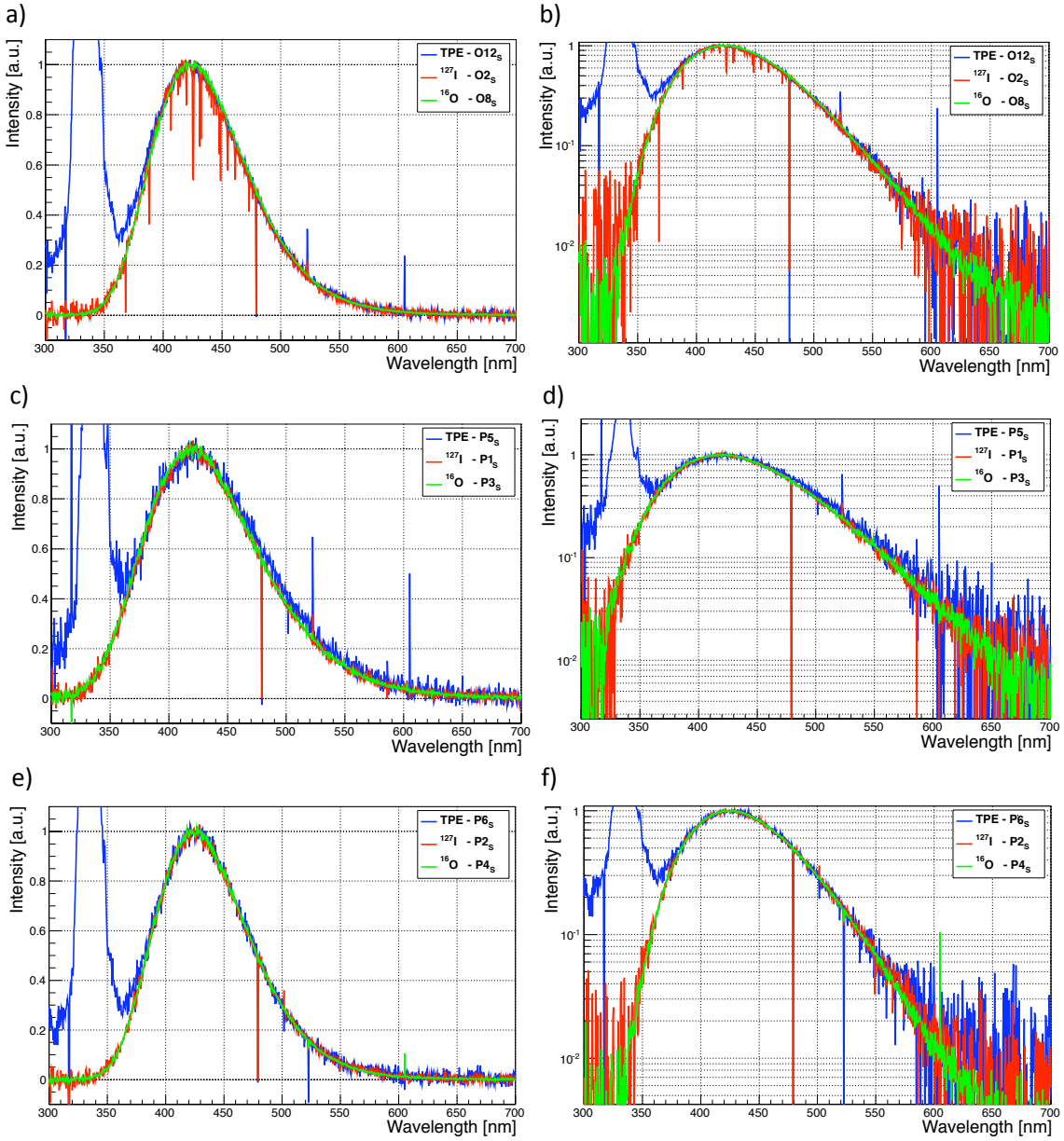

Figure 4.11: Comparison of the wavelength spectra recorded with crystal Olga (panel a and b) and crystal Philibert (panel c, d, e and f) for the different excitations at low temperature (panel a, b, e and f) and at room temperature (panel c and d). The spectra are preprocessed according to section III/4.6.1 (no error bars shown). Spectra recorded with two-photon excitation are shown in blue, spectra recorded with Iodine-beam excitation are shown in red and spectra recorded with Oxygen-beam excitation are shown in green. Figure a), c) and e): normal y-axis, figure b), d) and f): logarithmical y-axis. The peak at $\sim$ 340nm visible on the blue spectra (recorded for TPE) is caused by the detection of laser light reflected within or at the $CaWO_4$ crystal. The sharp spikes on the spectra can be attributed to data outliers due to individual pixels of the spectrometer.

beam excitation.

When comparing the spectra recorded for the same excitation (Oxygen-beam) recorded

at room temperature and low temperature (see figure 4.12 a) for crystal Olga and b) for crystal Philibert) it can be seen, that the spectra obtained at room temperature (red lines) are broadened (compare discussion in section III/2.2.2). This change in the shape of the spectra recorded for different temperatures is discussed in more detail in section III/5.1 within the quantitative analysis of the spectra.

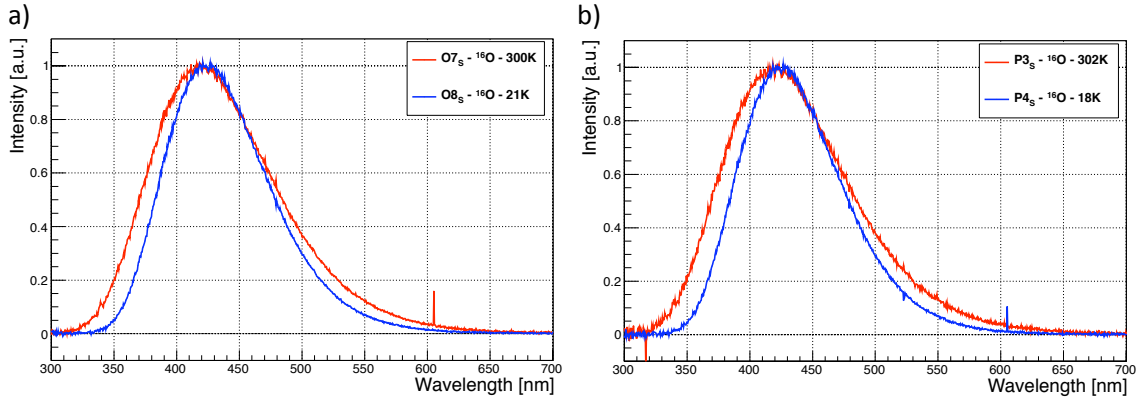

Figure 4.12: Comparison of the wavelength spectra recorded with crystal Olga (panel a) and crystal Philibert (panel b) under Oxygen-beam excitation at room temperature (red line) and at low temperature (blue line): The spectra are preprocessed according to section III/4.6.1 (no error bars shown). In red the respective spectrum recorded at room temperature is shown. The sharp spikes on the spectra can be attributed to data outliers due to individual pixels of the spectrometer.

Additionally, the spectra recorded for the two different crystals under the same conditions can be compared: In figure 4.13 (panel a: normal scale for the y-axis, panel b: logarithmical scale for the y-axis) the spectra recorded under Oxygen-beam excitation at room temperature for crystal Olga (red line) and crystal Philibert (green line) are shown. No significant differences can be seen.

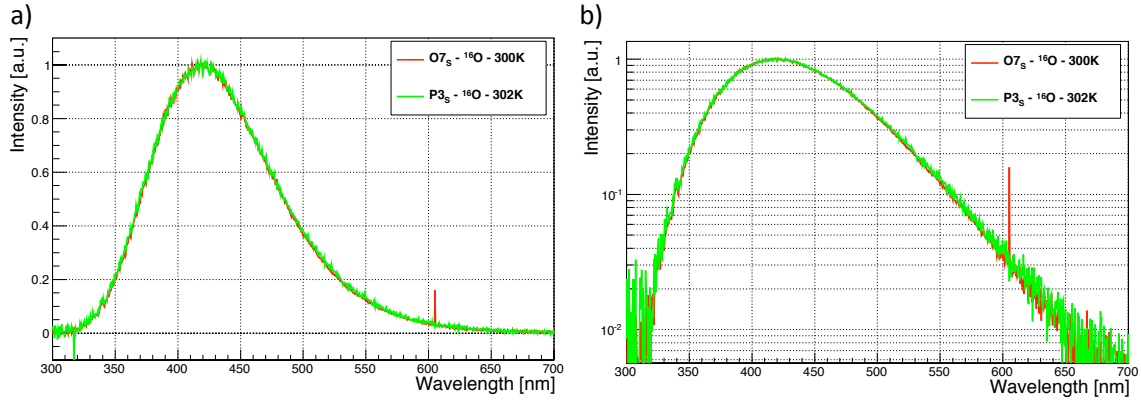

Figure 4.13: Comparison of the wavelength spectra recorded with crystal Olga (red line) and crystal Philibert (green line) under Oxygen-beam excitation at room temperature: The spectra are preprocessed according to section III/4.6.1 (no error bars shown). Figure a): normal y-axis, figure b): logarithmical y-axis. The sharp spikes on the spectra can be attributed to data outliers due to individual pixels of the spectrometer.

As predicted by the developed model, the light yield of a crystal should be coupled to its spectral output (see discussion in section III/5.1.2). The light yield of crystal Olga was determined to 95.1%, the light yield of crystal Philibert was determined to 93.7% (as compared to crystal "Boris" (100%), see section III/4.1.2). Hence, both crystals exhibit approximately the same light yield and thus should also produce approximately the same wavelength spectra, as is observed. In a closer look to figure 4.13 b), it can be seen, that the spectrum recorded for crystal Philibert (green line) exhibits slightly more intensity in the long wavelength range (green light). This observation can also be found as a result of the fits to the spectral shape of the spectra and is in perfect agreement with the slightly lower light yield for crystal Philibert in comparison to crystal Olga (see fits and discussion in section III/5.1).

4.7.2 Qualitative Comparison of the Measured Decay-Time Spectra

The main features that can be observed for the decay-time spectra obtained for the different excitation modes are discussed using the decay time spectra of crystal Olga recorded at low temperature with the 500nm filter as an example[47].

The spectra recorded under TPE, Oxygen-beam and Iodine-beam excitation were preprocessed according to sectionIII/4.6.2. For a better visual comparison no error bars were drawn and the respective maxima of the scintillation light spectra (for the determination of the maxima of the TPE spectrum, see below) were scaled to unity[48] and shifted to the zero of time. In figure 4.14 these spectra recorded for crystal Olga (500nm filter, at low temperature) under TPE ($\mathbf{O12_{PMT}}$), Oxygen-beam ($\mathbf{O8_{PMT}}$) and Iodine-beam ($\mathbf{O4_{PMT}}$) excitation are shown.
The dominant feature that can be seen in figure 4.14, is the fast spike at the beginning of the light pulse recorded under TPE (blue line). This fast rising and decaying part of the light pulse (at 0ns) can be attributed to the detection of laser light being reflected at surfaces of or within the $CaWO_4$ crystal sample (see section III/4.7.3). Due to this identification of the spike with laser light, the maximum of the $CaWO_4$ scintillation light which was used for normalization of the pulse height for this figure was searched in a time window after this spike. As all decay-time spectra are scaled to unity it is obvious, that excitation with a particle beam in comparison to excitation with TPE produces significantly different pulse shapes. In order to obtain a better understanding, in figure 4.15 the same pulses are shown in a zoomed-in view.
This representation shows, that not only the light-pulse shape recorded under laser excitation differs from the pulse shape obtained for particle excitation, but that additionally the pulse shapes recorded for different interacting particles differs. This observation is in perfect agreement with the model predictions (see section III/3.3.1). To further characterize the presented decay-time spectra, in figure 4.16, the same pulses, now with a log-scale for the y-axis, are shown.

[47] These decay-time spectra were chosen for the qualitative comparison as they exhibit small baseline distortions and their respective measurement temperatures are relatively similar. It has to be noted, that for the final analysis different measurement temperatures are no problem, as these are taken into account by using the appropriate exponential decay time.

[48] In order to demonstrate the original pulse heights of the pulses, the scaling factors that were determined and used are given: For the pulse recorded with TPE a scaling factor of $\sim$ 26.2, with Oxygen-beam excitation a scaling factor of $\sim$ 1110 and with Iodine-beam excitation a scaling factor of $\sim$ 2286 were used.

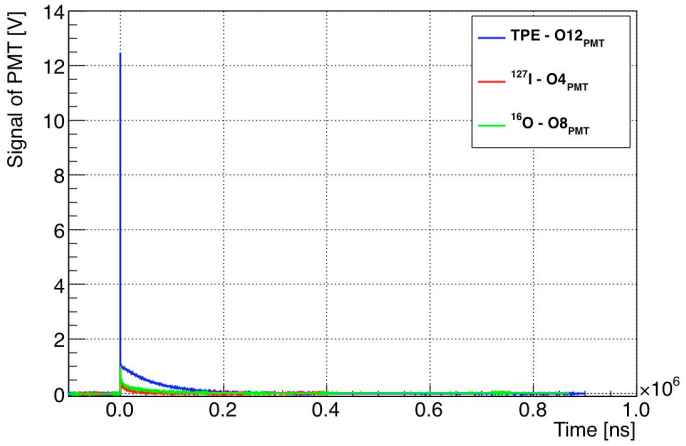

Figure 4.14: Comparison of the decay-time spectra recorded with crystal Olga under TPE (blue line), Oxygen-beam (green line) and Iodine-beam (red line) excitation at low temperature: The spectra are preprocessed according to section III/4.6.2 (no error bars shown). In addition, the respective maxima of the scintillation light are scaled to unity and shifted to the zero of time.

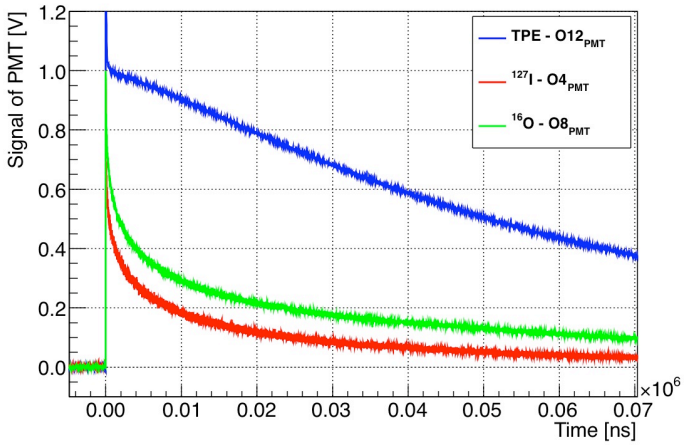

Figure 4.15: Comparison of the decay-time spectra recorded with crystal Olga under TPE (blue line), Oxygen-beam (green line) and Iodine-beam (red line) excitation at low temperature. The spectra are preprocessed according to section III/4.6.2 (no error bars shown). In addition, the respective maxima of the scintillation light are scaled to unity and shifted to the zero of time.

Three central observations can be made:

- For the decay-time spectrum recorded with TPE (blue line) it can be seen, that at late times ($\gtrsim 10\mu$s) the spectrum follows a purely exponential decay. Only for very short times after the start of the pulse deviations from this purely exponential behavior are visible: The spectrum seems to flatten slightly. This can be attributed to a delayed rise time of a fraction of the intensity of the $CaWO_4$ scintillation light, which will be shown and discussed in more detail in the quantitative data analysis (see section III/5.2).

- The decay-time spectra recorded under ion-beam excitation show a clearly non-

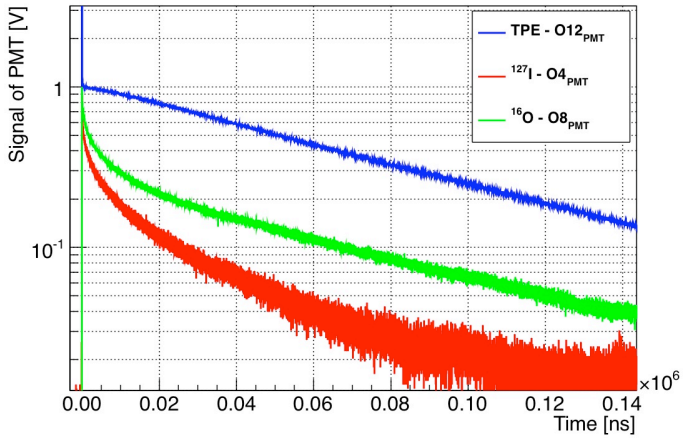

Figure 4.16: Comparison of the decay-time spectra recorded with crystal Olga under TPE (blue line), Oxygen-beam (green line) and Iodine-beam (red line) excitation at low temperature. The spectra are preprocessed according to section III/4.6.2 (no error bars shown). In addition, the respective maxima of the scintillation light are scaled to unity and shifted to the zero of time. The y-axis is plotted as logarithmical scale.

exponential behavior for times $\lesssim 30\mu$s. Even with two exponential decay times this behavior cannot be described appropriately. Only for larger times their shape resembles a purely exponential decay. Exactly such a behavior is predicted by the model (compare section III/3.3.1 and see fits in section III/5.3.2).

- For the pulses recorded under TPE and Oxygen excitation (green and blue line in figure 4.16), this exponential decay for larger times resembles approximately the same decay time (lines are parallel). For the pulse recorded under Iodine-beam excitation, the exponential decay at large times seems to be slightly faster. The developed model predicts that the exponential decay at large times is only dependent on the temperature of the crystal and not on the interacting particle (compare section III/3.3.1). This prediction is in concordance with the observed decay times, as during the measurement of the decay-time spectrum with Iodine-beam excitation, the cryocooler did not reach its final low-temperature plateau (as could be seen on the PT100 reading). During the other two measurements, the PT100 reading showed the same value. Hence, the observation of a slightly shorter exponential decay time for the pulse recorded under Iodine-beam excitation as well as of the same decay time for TPE and Oxygen-beam excitation is in perfect agreement with the predictions of the model (compare section III/3.3.1).

The exact determination of the respective pulse shapes is performed in the framework of the quantitative analysis presented in section III/5.3.

In addition, the decay-time spectra recorded with the same excitation mode at the same temperature for the two different filters can be compared. In figure 4.17, for this purpose the two decay-time spectra recorded at room temperature for crystal Olga under Iodine-beam excitation with the 400nm (blue line) and the 500nm (green line) filter are shown.

It can be seen that, in fact, as proposed by the model (compare section III/3.2.4), the two

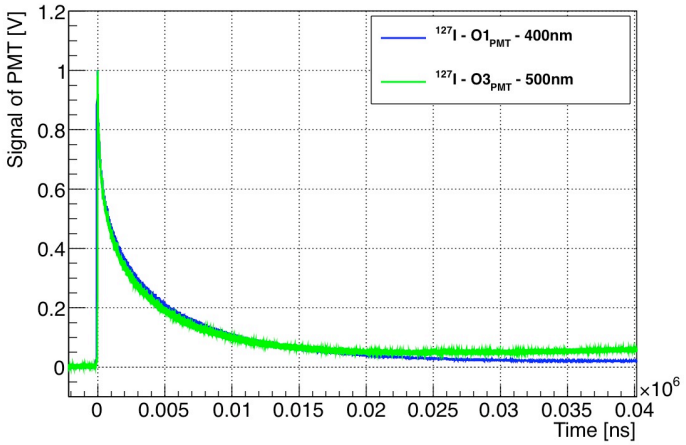

Figure 4.17: Comparison of the decay-time spectra recorded with crystal Olga under Oxygen-beam excitation at room temperature with the 400nm filter (blue line) and the 500nm filter (green line). The spectra are preprocessed according to section III/4.6.2 (no error bars shown). In addition, the respective maxima of the scintillation light are scaled to unity and shifted to the zero of time.

decay-time spectra exhibit in principle the same shape. This observation is very important, as it supports the assumption of the model, that the fast component at the beginning of pulses produced by particle interaction is not due to the green light component as sometimes suggested in literature (see, e.g., [66]). However, as can be seen in figure 4.17, the two decay-time spectra do not exhibit exactly the same shape. This observation can be explained ba the influence of different baseline drifts (see discussion in appendix C.4.3): For the pulse recorded with the 500nm filter, it can clearly be seen that the pulse height starts to rise again for times larger than $\sim 20,000$ns. For the blue pulse, much less impact of the baseline drift is visible. Due to these different influences it is not surprising that the two pulses exhibit slightly different visible shapes.

Additionally, the decay-time spectra recorded for the two different crystals (Olga and Philibert) under the same conditions can be compared: In figure 4.18 (panel a: normal scale for the y-axis, panel b: logarithmical scale for the y-axis) the spectra recorded under Iodine-beam excitation at room temperature for crystal Olga (red line) and crystal Philibert (green line) are shown.

Concerning the impact of different drifts of the baselines the same observations as in the discussion of figure 4.17 can be made. This feature is nicely visible in figure 4.18 b) with the logarithmical y-axis. The baseline of the pulse recorded for crystal Olga (red line) shows a rising drift, whereas the pulse recorded for crystal Philibert exhibits a falling drift. Apart from this influence, no significant differences between the pulse shapes can be seen.

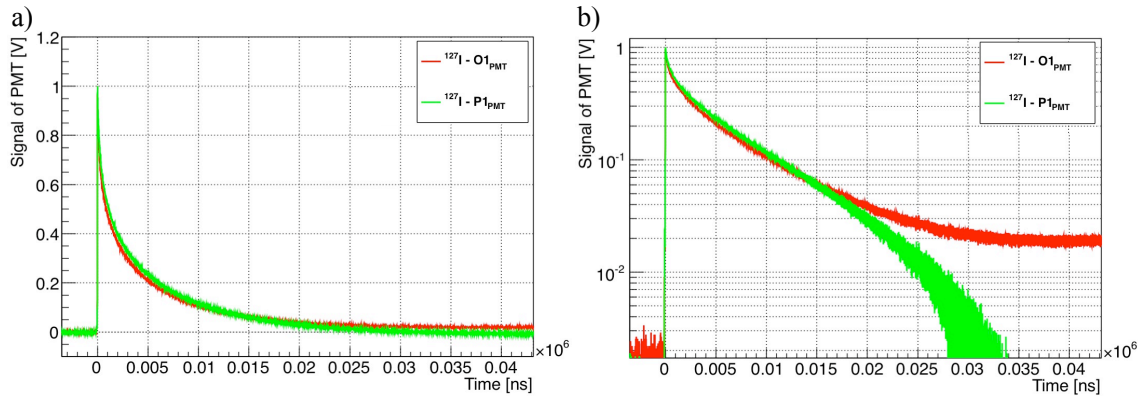

Figure 4.18: Comparison of the decay-time spectra recorded with crystal Olga (red line) and crystal Philibert (green line) with Iodine-beam excitation at room temperature with the 400nm filter: The spectra are preprocessed according to section III/4.6.2 (no error bars shown). In addition, the respective maxima of the scintillation light are scaled to unity and shifted to the zero of time. Figure a): normal y-axis, figure b): logarithmical y-axis.

4.7.3 Characterization of the Excitation Pulses

To characterize the pulse shape (and spectral composition[49]) of the excitation pulses (laser light and ion beam) prior to the actual measurements a BaF_2 crystal of nearly the same size as the investigated $CaWO_4$ crystal was installed in the experimental setup (see sections III/4.3.2 and III/4.4.2). The BaF_2 crystal was exposed to the different excitations and measurements with the PMT and the spectrometer were performed. BaF_2 was chosen for several reasons: Due to its large band gap BaF_2 cannot be excited significantly by the employed laser beam and, additionally, BaF_2 is one of the fastest scintillators known [107]. See appendix C.10.1 for a more thorough discussion.

Characterization of the Laser Pulse

In the experiments with laser excitation, the BaF_2 crystal was used to investigate the temporal and spectral shape of the laser-light pulse independently from the $CaWO_4$ scintillation light. As described in more detail in appendix C.10.2, it could be shown, that in every measurement of the scintillation light of a $CaWO_4$ under TPE, additionally to the scintillation light, laser light reflected at the crystal is detected with the PMT and the spectrometer. Hence, for the analysis of the data recorded with laser excitation of the $CaWO_4$ crystal, the exact pulse shape of the laser pulse has to be determined. In figure 4.19 a), an example of a decay-time spectrum (first 500ns) recorded for crystal Olga (**O10$_{PMT}$**) with the 400nm filter under laser excitation at low temperature is shown in black. In red, the reflected laser-light pulse recorded with the BaF_2 crystal and the 400nm filter (recorded as described in appendix C.10.2) is shown. For better visual comparison of the pulse shapes, the reflected laser-light pulse is scaled to the same maximum height as the pulse recorded with the $CaWO_4$ crystal[50]. In figure 4.19 b), a pulse shape fit (in

[49] The spectral composition of the laser-light pulse is of interest as it is partially reflected at the $CaWO_4$ crystal. Hence, it is detected with the PMT and with the spectrometer simultaneously with the $CaWO_4$ scintillation light.

[50] This figure is only used for illustrative purposes. Of course, the employed scaling does not perfectly display the true contribution of the reflected laser light to the detected decay-time spectrum **O10$_{PMT}$**.

red) to the reflected laser-light pulse (in black) is shown.

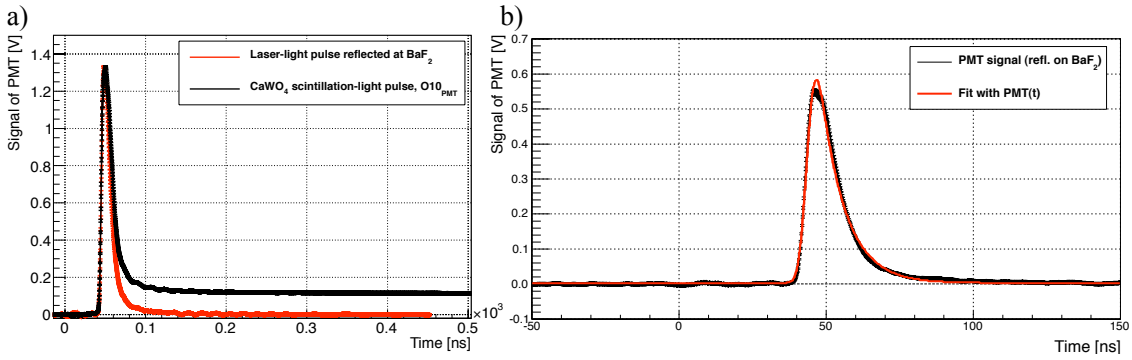

Figure 4.19: Determination of the pulse shape of the reflected laser light: Figure a): Comparison of the pulse shape of the reflected laser light (in red) and the decay-time spectrum recorded for laser excitation of a $CaWO_4$ crystal in the final setup (in black, first 500ns of $\mathbf{O10_{PMT}}$). For easier comparison of the pulse shape, the laser-light pulse is scaled to the same maximum height as the recorded decay-time spectrum for the $CaWO_4$ crystal. Figure b): Pulse-shape fit (red line) of the reflected laser light (in black). For details, see the main text.

From the comparison shown in figure 4.19 a) it becomes clear that the shape of the decay-time spectrum recorded for the excited $CaWO_4$ crystal (black markers) is - within the first $\sim$ 20ns - strongly dominated by the detection of the reflected laser light (red markers). In figure 4.19 b), the determination of a mathematical description of the shape of the laser-light pulse is depicted. For a discussion of the fit function $PMT(t)$, see appendices C.10.2 and C.4.4. As discussed there, for the description of the shape of the laser-light pulse a Gaussian distribution can be employed. In order to perform the fit of the laser-light pulse shape shown in red in figure 4.19 b) also the impulse reaction of the PMT-oscilloscope system (see appendix C.4.4) has to be taken into account. The one-sigma width σ_L of the laser pulse is determined with high accuracy to:

$$\sigma_L = 1.803 \pm 0.044\text{ns} \tag{4.4}$$

In addition to the characterization of the reflected laser light with the help of a BaF_2 crystal, measurements for the investigation of the produced excitation density were performed. For these measurements crystal Olga was installed into the setup and the lens position was varied to induce different degrees of focussing of the laser light at the position of the crystal. These measurements are described in more detail in appendix C.10.2. From these measurements two conclusions can be drawn (see discussion in appendix C.10.2):

- The excitation mode realized by irradiation of a $CaWO_4$ with photons from the N_2 laser is indeed a two-photon excitation process.
- The produced excitation density is not sufficient to produce STEs that are located densely enough to obtain significant interaction between them.

Therefore, the conclusion can be drawn that measurements performed with laser excitation can indeed, as anticipated, be used for the test and validation of the developed model for rare, i.e., spatially uncorrelated excitation.

In reality, the $CaWO_4$ scintillation light produces intensity from the start of the pulse and, hence, the depicted contribution of the reflected light is overestimated.

Characterization of the Ion-Beam Pulse

Also for the characterization of the ion-beam pulse shape, the BaF_2 crystal was used. When irradiating the BaF_2 crystal with an ion-beam pulse, (quenched) scintillation light is generated. The fast rise time of BaF_2 allows to assume that the rising part of the detected decay-time spectrum is dominated by the time structure of the incident ion-beam pulse. In appendix C.10.3, the procedure used to obtain the ion-beam pulse-width $\sigma_{^{127}I}$ and $\sigma_{^{16}O}$ from measurements with a BaF_2 crystal is described. In analogy to the laser-excitation experiments, the shape of the ion-beam is assumed to be Gaussian and has to be convoluted with the function describing the PMT impulse-reaction. The one-sigma widths $\sigma_{^{127}I}$ and $\sigma_{^{16}O}$ for the Iodine and Oxygen-beam pulses are:

$$\sigma_{^{127}I} = 3.94 \pm 0.18\text{ns} \tag{4.5}$$

$$\sigma_{^{16}O} = 3.09 \pm 0.09\text{ns} \tag{4.6}$$

The determined values can be compared to typical pulse widths obtained with the tandem accelerator of, e.g., $\sim$ 2ns for the width of produced neutron pulses [11]. It can be seen that the calculated values for the ion-beam pulse widths are within a reasonable range.

The geometrical shape of the ion-beam pulses and the produced beam current were characterized with the 4-sector aperture and the movable Faraday cup (see section III/4.4.2). With these instruments as well as by visual checks of the luminescing area of the $CaWO_4$ crystal (compare figure 4.8 in section III/4.4.2), it could be achieved that the complete large crystal surface (10x20)mm^2 was illuminated by the respective ion beams. Due to the small beam currents and the correspondingly small Faraday cup readings, large uncertainties are inflicted in the estimation of the number of ions per pulse. The estimated number of ions per pulse amount to:

$$N_{^{127}I} \approx 100...3,000 \frac{\text{ions}}{\text{pulse}} \tag{4.7}$$

$$N_{^{16}O} \approx 100...2,000 \frac{\text{ions}}{\text{pulse}} \tag{4.8}$$

For a more detailed discussion, see appendix C.10.3.

Hence, under the assumption that the complete large crystal surface was illuminated by the ion pulse, a mean area of at least (250x250)μm^2 per ion was available (for the largest estimated value of 3,000 ions per pulse). Thus, due to the rather low number of ions per pulse and the large defocussing, no interaction of the excitations produced in individual ion tracks had to be expected.

Chapter 5

Data Analysis: Determination of the Free Parameters and Validation of the Model

In this chapter, the analysis of the wavelength and decay-time spectra recorded using two-photon excitation by the N_2 laser and ion-beam excitation (oxygen and iodine ions) is presented. The analysis is performed in the context of the developed model for the scintillation-light generation and quenching (see chapter III/3.1) to determine the free model parameters. The employed experimental setups as well as the procedure used for data preprocessing and a qualitative analysis of the data can be found in chapter III/4. In section III/5.1, the quantitative analysis of the recorded wavelength spectra is presented and the results are discussed in the context of the developed model. In section III/5.2, the analysis of the decay-time spectra recorded under laser excitation is presented. The results are employed to determine the free parameters of the unquenched model. The determined values as well as deductions that can be made are discussed. In section III/5.3, the analysis of the decay-time spectra recorded under ion-beam excitation is presented. Within this analysis, reasonable estimates for the free radial parameters of the particle-induced initial STE-density distribution are gained as well as a value for the Förster radius, the only remaining free parameter of the developed model is determined so that the mathematical description of the model is completed (compare discussion in section III/3.3.2). The determined value for the Förster radius is discussed and the complete quenched model is validated. In section III/5.4, a summary of the results and their interpretation in the context of the developed model is presented.

5.1 Wavelength Spectra

As discussed in section III/4.7.1, only the wavelength spectra recorded under oxygen-beam excitation are analyzed quantitatively as the shapes of the spectra recorded using different excitations at the same temperature comply with each other (for crystal Olga and crystal Philibert, respectively). In the following, the analysis of the wavelength spectra is presented. This analysis was performed with the purpose to determine the spectral decomposition of the wavelength spectra into the contribution of the intrinsic (blue) light component and the extrinsic (green) light components (see section III/4.7.1). All wavelength spectra were preprocessed (correction for the spectral response of the spectrometer, normalization of the maxima and error assignment) according to the procedure described

in section III/4.6.1.

5.1.1 Fits of the Wavelength Spectra

In order to determine the relative contributions of the blue and the green scintillation-light components to the generated scintillation light, the wavelength spectra were fitted using the mathematical description of the the wavelength spectrum of the scintillation light of a $CaWO_4$ crystal as presented and discussed in the model developed within the present work (see equation 3.90 in section III/3.2.1): This model describes the total wavelength spectrum, $S_{em,tot}(T,\lambda)$, as the sum of a non-Gaussian sub-spectrum, $S_{em,b}(T,\lambda)$, of the blue scintillation light (equation 3.88 in section III/3.2.1) and a Gaussian sub-spectrum, $S_{em,g}(T,\lambda)$, of the green scintillation light (equation 3.89 in section III/3.2.1).

Equation 3.90 (section III/3.2.1) was used to perform χ^2-fits to the wavelength spectra recorded for crystal Olga ($\mathbf{O7_S}$ and $\mathbf{O8_S}$) and crystal Philibert ($\mathbf{P3_S}$ and $\mathbf{P4_S}$) under oxygen-beam excitation, at room temperature ($\sim$ 300K) and at low temperature ($\sim$ 20K), respectively, in the wavelength region from 300nm to 700nm. In figure 5.1 a) and b), the wavelength spectra of crystal Olga (black markers with error bars, 300K and 21K measurement, respectively) are shown together with the total fit function, $S_{em,tot}(T,\lambda)$, (according to equation 3.90, red line) as well as the individual sub-spectra ,$S_{em,b}(T,\lambda)$ (blue line) and $S_{em,g}(T,\lambda)$ (green line). In figure 5.1 c) and d), the recorded wavelength spectra (black markers with error bars, 302K and 18K measurement, respectively) and the corresponding fits for crystal Philibert are depicted.
It can be seen that the fit function is in very good agreement with the overall shape of the wavelength spectra. Additionally, it can be noticed that - as anticipated by the developed model - the blue scintillation-light component is indeed fitted by an asymmetric shape with a steeper left shoulder (cutoff at shorter wavelengths due to absorption of higher-energetic blue photons by defect centers, compare section III/3.2.1). In table 5.1, the results of these χ^2-fits are presented.

5.1.2 Results and Discussion: Quantitative Decomposition

In order to analyze the obtained fit results in the context of the developed model, the following two parameters, as discussed and introduced in section III/3.2.1, are calculated:

- The respective mean values of the two individual sub-spectra, $m_b(T)$ and $m_g(T)$.
- The widths of the blue and the green sub-spectra, $\sigma_{tot,b}(T)$ and $\sigma_{tot,g}(T)$ (where $\sigma_{tot,g}(T)$ simply corresponds to $\sigma_g(T)$, see section III/3.2.1).

Using these values, several further parameters can be calculated:

- The mean photon energies of the blue and the green scintillation light: $\overline{E}_{Pb}(T) = \frac{h \cdot c}{m_b(T)}$ and $\overline{E}_{Pg}(T) = \frac{h \cdot c}{m_g(T)}$ (derived from the corresponding mean wavelengths of the two sub-spectra, with h corresponding to the Planck constant and c corresponding to the speed of light).
- The relative partial integrals of the blue and green scintillation-light components: $r_b(T) = \frac{I_b(T)}{I_b(T)+I_g(T)}$ and $r_g(T) = \frac{I_g(T)}{I_b(T)+I_g(T)}$.
- The total mean photon energy: $\overline{E}_P(T) = r_b(T) \cdot \overline{E}_{Pb}(T) + r_g(T) \cdot \overline{E}_{Pg}(T)$

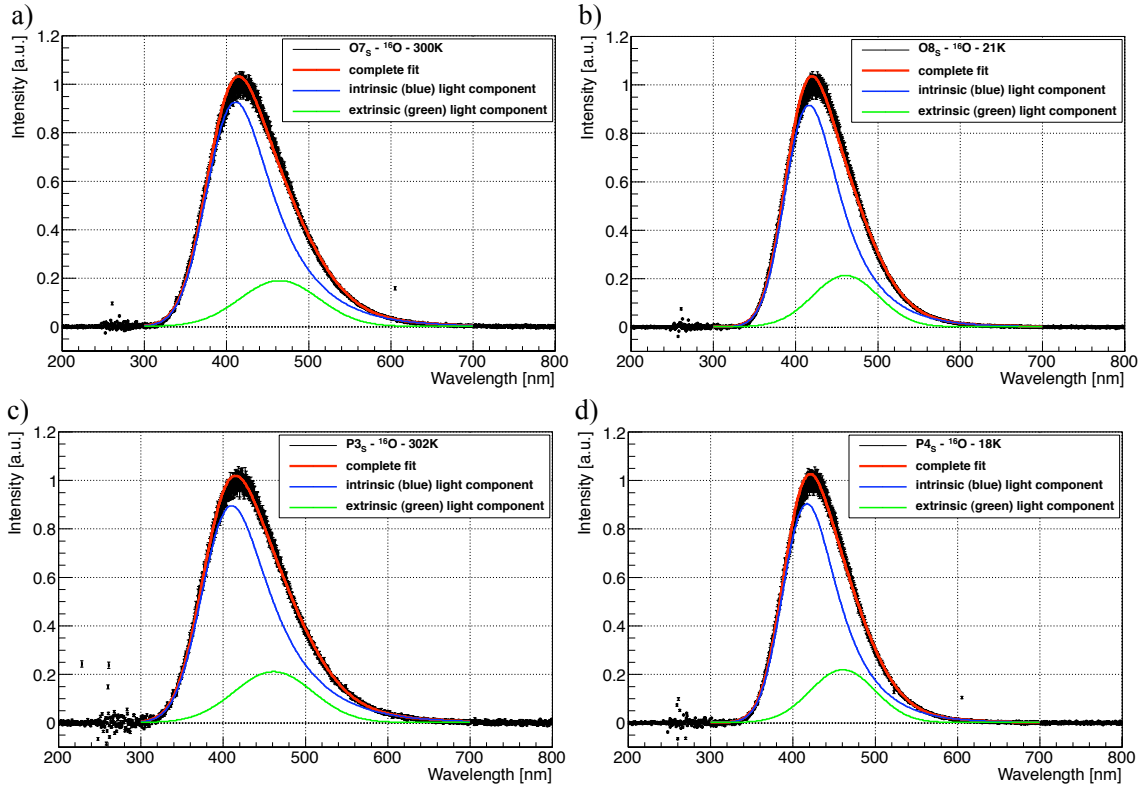

Figure 5.1: Wavelength spectra recorded for crystal Olga (panel a and b) and crystal Philibert (panel c and d) under oxygen-beam excitation: The spectra depicted in panels a) and c) were recorded at room temperature, $\sim$ 300K and $\sim$ 302K, respectively. The spectra depicted in panels b) and c) were recorded at low temperature, $\sim$ 21K and $\sim$ 18K, respectively. The data is depicted as black markers with error bars. The red lines depict the results of the χ^2-fits using the mathematical description developed in the model (equation 3.90). The blue lines correspond to the respective intrinsic light components. The green lines correspond to the respective extrinsic light components.

- The value of the blue-to-green light ratio: $R_{b-g}(T) = \frac{I_b(T)}{I_g(T)}$ (compare equation 3.97 in section III/3.2.2).

The values determined for these parameters are shown in table 5.2.

From these results, several observations and conclusions concerning the light-generation and light-quenching model developed within the present work can be deduced:

- As predicted by the model (compare section III/3.2.1), the blue scintillation light spectrum is represented by an asymmetric shape with a sharper cutoff at the short-wavelength (i.e. high-energy) side. This observation supports the assumption made within the developed model that a fraction of the blue photons - the photons from the high-energetic part of the blue light spectrum with a larger probability - is reabsorbed within the $CaWO_4$ crystal at defect centers and can, hence, not escape the crystal.

- The green sub-spectrum, on the other hand, is well reproduced by a symmetric Gaussian. This observation is in good agreement with the assumption made (compare

	O7$_S$ 300K	**O8$_S$** 21K	**P3$_S$** 302K	**P4$_S$** 18K
red. χ^2	1.79	1.49	1.82	2.06
$A_b(T) = I_b(T)$	102.0 ± 1.1	83.6 ± 1.0	101.7 ± 1.5	81.8 ± 1.1
$\sigma_b(T)$ [nm]	27.8 ± 0.2	23.2 ± 0.2	28.2 ± 0.2	23.4 ± 0.2
$\mu_b(T)$ [nm]	384.5 ± 0.4	394.5 ± 0.3	383.0 ± 0.4	395.4 ± 0.4
$\lambda_{abs}(T)$ [nm]	49.1 ± 0.1	40.3 ± 0.2	51.7 ± 0.4	39.4 ± 0.3
$A_g(T) = I_g(T)$	22.5 ± 1.0	20.9 ± 1.0	24.9 ± 1.5	21.2 ± 1.1
$\sigma_g(T)$ [nm]	47.8 ± 0.5	39.5 ± 0.4	47.4 ± 0.7	38.9 ± 0.4
$\mu_g(T)$ [nm]	464.6 ± 1.3	460.8 ± 1.0	461.3 ± 1.6	460.7 ± 1.1

Table 5.1: Results of the χ^2-fits to the wavelength spectra **O7$_S$**, **O8$_S$**, **P3$_S$** and **P4$_S$** recorded for crystal Olga and crystal Philibert under oxygen-beam excitation at room temperature and at low temperature, respectively: Shown are the intensities, $A_b(T)$ and $A_g(T)$ (which correspond to the partial integrals of the blue and green sub-spectra, $I_b(T)$ and $I_g(T)$, compare section III/3.2.1), the widths, $\sigma_b(T)$ and $\sigma_g(T)$, as well as the mean values, $\mu_b(T)$ and $\mu_g(T)$, of the Gaussians describing the blue and green scintillation-light spectra, respectively. $\lambda_{abs}(T)$ corresponds to the decay constant of the exponential which is used to model the asymmetry of the blue sub-spectrum (compare section III/3.2.1). The errors shown are the statistical errors from the χ^2-fits.

	O7$_S$ 300K	**O8$_S$** 21K	**P3$_S$** 302K	**P4$_S$** 18K
$m_b(T)$ [nm]	433.6 ± 0.4	434.8 ± 0.4	434.7 ± 0.6	434.8 ± 0.5
$\sigma_{tot,b}(T)$ [nm]	56.4 ± 0.1	46.5 ± 0.2	58.9 ± 0.4	45.8 ± 0.3
$\overline{E}_{Pb}(T)$ [eV]	2.861 ± 0.003	2.853 ± 0.003	2.854 ± 0.004	2.853 ± 0.003
$r_b(T)$	(82 ± 1)%	(80 ± 1)%	(80 ± 1)%	(79 ± 1)%
$m_g(T)$ [nm]	464.6 ± 1.3	460.8 ± 1.0	461.3 ± 1.6	460.7 ± 1.1
$\sigma_{tot,g}(T)$ [nm]	47.8 ± 0.5	39.5 ± 0.4	47.4 ± 0.7	38.9 ± 0.4
$\overline{E}_{Pg}(T)$ [eV]	2.670 ± 0.007	2.692 ± 0.006	2.690 ± 0.009	2.693 ± 0.006
$r_g(T)$	(18 ± 1)%	(20 ± 1)%	(20 ± 1)%	(21 ± 1)%
$\overline{E}_P$ [eV]	2.83 ± 0.03	2.82 ± 0.03	2.82 ± 0.04	2.82 ± 0.03
$R_{b-g}(T)$	4.5 ± 0.2	4.0 ± 0.2	4.1 ± 0.3	3.9 ± 0.2

Table 5.2: Values of the mean wavelengths (and photon energies) as well as partial integrated intesities of the blue and the green sub-spectra. Values determined from the results of the χ^2 fits (see section III/5.1.1). All uncertainties stated were determined with Gaussian error propagation.

section III/3.2.1) that for the green scintillation light no absorption centers exist within the $CaWO_4$ crystal, so that all of the green light can escape the crystal.

- From the data in table 5.2, it can be seen that the most significant change of the wavelength spectra from room temperature ($\sim 300K$) down to low temperature ($\sim$ 20K) is a change of the widths of the spectra (comparing the spectra for each crystal separately). As discussed in section III/3.2.1, the widths of the spectra at $\sim$ 20K can be expected to represent the widths the wavelength spectra would exhibit at 0K, $\sigma^{0\,Olga}_{tot,b/g}$ and $\sigma^{0\,Phil}_{tot,b/g}$, respectively (blue and green sub-spectra of crystal Olga

and Philibert):

$$\sigma_{tot,b}^{0\,Olga} := \sigma_{tot,b}^{Olga}(0\text{K}) \approx \sigma_{tot,b}^{Olga}(\sim 20\text{K}) = (46.5 \pm 0.2)\text{nm} \tag{5.1}$$

$$\sigma_{tot,g}^{0\,Olga} := \sigma_{tot,g}^{Olga}(0\text{K}) \approx \sigma_{tot,g}^{Olga}(\sim 20\text{K}) = (39.5 \pm 0.4)\text{nm} \tag{5.2}$$

$$\sigma_{tot,b}^{0\,Phil} := \sigma_{tot,b}^{Phil}(0\text{K}) \approx \sigma_{tot,b}^{Phil}(\sim 20\text{K}) = (45.8 \pm 0.3)\text{nm} \tag{5.3}$$

$$\sigma_{tot,g}^{0\,Phil} := \sigma_{tot,g}^{Phil}(0\text{K}) \approx \sigma_{tot,g}^{Phil}(\sim 20\text{K}) = (38.9 \pm 0.4)\text{nm} \tag{5.4}$$

Within the developed model, the enlarged widths of the spectra at room temperature compared to the widths at 0K are described by the temperature-dependent impact of the electron-phonon coupling present in $CaWO_4$ (compare section III/3.2.1). With this interpretation and the results obtained for the widths of the spectra at 0K (adopting the values for $T = 20$K) and at ~ 300K, the energies of the phonons, E_{phonon}^{Olga} and E_{phonon}^{Phil} (i.e., the phonon mode), primarily interacting with the blue and green light-emitting centers in the $CaWO_4$ crystal can be determined (with equations 3.91 and 3.92, section III/3.2.1) to amount to:

$$E_{phonon,b}^{Olga} = (42.8 \pm 0.6)\text{meV} \tag{5.5}$$

$$E_{phonon,g}^{Olga} = (43.1 \pm 1.9)\text{meV} \tag{5.6}$$

$$E_{phonon,b}^{Phil} = (36.5 \pm 0.9)\text{meV} \tag{5.7}$$

$$E_{phonon,g}^{Phil} = (42.5 \pm 2.3)\text{meV} \tag{5.8}$$

It can be seen that the determined phonon energies, except for $E_{phonon,b}^{Phil}$, nicely comply with each other. It should be noted that the determined phonon energy of ~ 43meV (except for $E_{phonon,b}^{Phil}$) can be assigned to an internal vibration mode of the $[WO_4]^{2-}$ tetrahedra (compare to the result in [51] and the vibrational modes listed in [50]). The reason for the deviation of the value of $E_{phonon,b}^{Phil}$ from all other values, i.e., especially the deviation from $E_{phonon,g}^{Phil}$ which describes the interacting phonon mode within the same crystal, is not conclusively clear: The deviation of this value can mainly be attributed to the comparably large value obtained for $\sigma_{tot,b}^{Phil}(302\text{K})$ and to the comparably small value obtained for $\sigma_{tot,b}^{Phil}(18\text{K})$ (compared to the corresponding values for crystal Olga, see table 5.2), i.e., to the fit values obtained for $\mu_b^{Phil}(T)$ and $\lambda_{abs}^{Phil}(T)$ (table 5.1 in section III/5.1.1). Thus, it can either be speculated that the deviation of $E_{phonon,b}^{Phil}$ can be assigned to the slightly worse quality of the fits of the spectra recorded for crystal Philibert (larger χ^2-values compared to the fits of the spectra recorded for crystal Olga), or, this deviation corresponds, in fact, to a slightly different internal vibration mode of the blue $[WO_4]^{2-}$ tetrahedra in crystal Philibert compared to crystal Olga. Slightly differing internal vibration modes, though, point to, e.g., small differences in the crystal structure which could easily be explained for the two crystals as they have different origins[1]. However, if this possibility would apply, it would remain unclear why the phonon mode interacting with the green scintillation centers exhibits the same frequency for both crystals. It can be summarized that no conclusive statement can be made regarding the origin of the observed deviation of the phonon energy determined for the interaction with

[1]Crystal Olga is a bought crystal, supplied by the General Physics Institute in Russia, whereas crystal Philibert was grown and prepared by the crystal laboratory of Technische Universität München (see table C.1 in appendix C.1 for details).

the blue light-emitting centers in crystal Philibert. To clarify this question, e.g., further measurements of the wavelength spectra at different temperatures could be performed to gain more data for the comparison of the two crystals.

- The values determined for the mean blue, green and total photon energies, $\overline{E}_{Pb}(T)$, $\overline{E}_{Pg}(T)$ and $\overline{E}_{P}(T)$, respectively, at room temperature and at low temperature show almost no variation with temperature (see table 5.2). This result is in good agreement with data from the literature (compare e.g., [51]). When comparing the absolute values determined to values stated in literature (see, e.g., [54]) for the emission maximum of the $CaWO_4$ spectra, it has to be noted that the parameters $\overline{E}_{Pb}(T)$, $\overline{E}_{Pg}(T)$ and $\overline{E}_{P}(T)$ determined within the present work do not correspond to the maxima of the respective wavelength spectra (blue, green and total spectra), but specify the mean blue, green and total photon energies. These values were determined, as the mean energies of the respective sub-spectra, are parameters of the model developed within the present work (see, e.g., equation 3.98 in section III/3.2.2) and are required to calculate the total amount of scintillation light generated (in terms of energy). In addition, it should be noted that, as discussed in section III/3.2.1, at temperatures below $\sim$ 50K, the peak position of the wavelength spectrum of the $CaWO_4$ scintillation light is reported to remain constant [51]. Thus, in the following, the values determined for the blue, green and total photon energies at a temperature of $\sim$ 20K are adopted for all temperatures below $\sim$ 50K, i.e., also for the operating temperature of CRESST detectors of $\sim$ 10mK (compare section III/2.1).

- Regarding the values obtained for the relative amounts of blue and green scintillation light produced, $r_b(T)$ and $r_g(T)$, at room temperature and at $\sim$ 20K, as well as the values determined for the blue-to-green light ratio, $R_{b-g}(T)$, the observation can be made that, at $T \approx$ 20K, slightly less blue scintillation light is produced compared to room temperature. This observation can be explained by the temperature-dependency of the processes involved in the excitation and de-excitation of blue and green STEs as considered within the developed model (compare discussion in section III/3.2.1): At $\sim$ 20K, the amount of green light produced is governed by three processes: On the one hand, the fraction of blue light that is absorbed at defect centers as well as the fraction of blue STEs migrating to defect centers determine how many green STEs become excited during the light-production process. On the other hand, the number of green photons produced by these green STEs is influenced by the relative strengths of the radiative and migration processes of green STEs, i.e., by the size of the radiative branching ratio (compare equation III/3.83 in section III/3.1.4). At elevated temperatures, however, also the non-radiative recombination processes of blue and green STEs are expected to be important. For green STEs already for temperatures $\gtrsim$ 70K all three de-excitation processes (radiative, non-radiative and migration) are predicted to be active. As the temperature-dependency all of the three processes is described by the same mathematical relationship (exponential function of the corresponding energy barrier), it can be expected that at temperatures well above $\sim$ 70K (e.g., above $\sim$ 130K) the contributions of all of these processes remain roughly constant (compare discussion in section III/3.2.1). Thus, the radiative branching ratio of green STEs at temperatures above $\sim$ 130K is expected to maintain roughly the same value. For blue STEs, however, a significant contribution of the non-radiative recombination process is only expected at

temperatures $\gtrsim$ 200K. Thus, for temperatures $\gtrsim$ 200K, the blue STE non-radiative process starts to become important, reducing the number of radiatively decaying and migrating blue STEs and, hence, the number of green STEs that become exited for temperatures above $\sim$ 200K. As the radiative branching ratio of green STEs is expected to stay roughly constant, the described processes (decrease of radiatively decaying and migrating blue STEs) result in a reduction of produced green photons for temperatures $\gtrsim$ 200K compared to $\sim$ 20K. The number of blue photons produced, however, is only influenced by the decrease of the number of radiatively decaying blue STEs and is, hence, expected to be reduced less severely. Therefore, as observed, a relative decrease of the number of green photons produced, i.e., a relative increase of the number blue photons produced, at room temperature down to $\sim$ 20K can be expected. For a confirmation of this interpretation as well as a graphical illustration of the temperature-dependency of the involved processes, see section III/5.2.2.

- To obtain an estimate of the the relative amount of blue scintillation light produced for temperatures below $\sim$ 5K, $r_b^{Olga}(T \approx 20\text{K})$ ($r_b^{Phil}(T \approx 20\text{K})$) can be used: As already discussed in section III/3.3.2 (and appendix B.13), the principle temperature-dependency of $r_b(T)$ can be adopted from the literature (see [54]). For temperatures $T \lesssim$ 5K, however, the relative amount of blue scintillation light produced is assumed to be only dependent on the fraction of blue photons absorbed at defect centers, F_{abs} (compare section III/3.2.1). Thus, $r_b^{Olga}(T \approx 20\text{K})$ and $r_b^{Phil}(T \approx 20\text{K})$ can be used to estimate the fraction of blue photons absorbed at defect centers resulting in the following values for F_{abs}^{Olga} and F_{abs}^{Phil} (compare appendix B.13 for more details):

$$F_{abs}^{Olga} \approx (18 \pm 1)\% \tag{5.9}$$

$$F_{abs}^{Phil} \approx (19 \pm 1)\% \tag{5.10}$$

  where the uncertainties correspond to the quadratically propagated statistical errors from the fit results. It should be noted that the uncertainty introduced by adopting the temperature-dependency of $r_b(T)$ from the literature is most probably larger.

- Comparing the values of the relative amount of green scintillation light produced for crystal Olga to the values determined for crystal Philibert, it can be seen that, for crystal Philibert, slightly more green scintillation light is produced. Within the developed model, this difference is interpreted to be caused by a slightly larger defect density contained in crystal Philibert compared to crystal Olga: A larger defect density leads to an increased fraction of blue photons being reabsorbed at defect centers (compare equations 5.9 and 5.10) and, thus, to an increased number of green STEs excited. This, in turn, leads to the production of an enhanced number of green photons. Thus, the slightly larger relative amount of green scintillation light produced by crystal Philibert is attributed to a slightly larger defect density in crystal Philibert compared to crystal Olga.

- It should be noted that a larger defect density is expected to lead to a decreased total amount of scintillation light produced: As discussed in section III/2.1.3, the defect centers (responsible for the production of green scintillation light) are assumed to account also for the presence of electron traps in $CaWO_4$ crystals. Thus, a larger defect density results in a larger density of electrons traps and, hence, in a larger

probability of electrons getting caught by electron traps instead of recombining to STEs with their STHs (see section III/3.1.2). Therefore, for a larger defect density, less STEs and, hence, less scintillation light are assumed to be produced. Thus, an enlarged defect density is assumed to result in the production of a larger relative fraction of green scintillation light as well as in a reduction of the total amount of scintillation light produced. This prediction of the model is in perfect agreement with the experimental results obtained as for crystal Philibert, for which a slightly larger relative fraction of produced green scintillation light (compared to crystal Olga) is determined, a slightly smaller light yield in comparison to crystal Olga is specified (compare table C.1 in appendix C.1).

Hence, with the experimental results obtained from the analysis of the wavelength spectra of the $CaWO_4$ scintillation light various predictions of the model can be confirmed and several free model parameters can be determined. The values determined for the fraction of blue photons reabsorbed at defect centers, F_{abs} as well as for the mean photon energies, $\overline{E}_{Pb}(T)$, $\overline{E}_{Pg}(T)$ and $\overline{E}_{P}(T)$ (of the blue, green and complete spectra), will be used in the following in the analysis of the recorded decay-time spectra.

5.2 Unquenched Decay-Time Spectra: Data Recorded with Laser Excitation

For the analysis of the decay-time spectra recorded with laser excitation, i.e., with two-photon excitation, the unquenched model is utilized (compare discussion in appendix C.10.2 where it is shown that the scintillation light contained in these decay-time spectra was indeed created by a spatially separated STE population). Hence, as discussed in section III/3.3.2, in order to determine many of the free model parameters, the decay-time spectra as predicted by the unquenched model (for the blue and the green light at room temperature and at $\sim$ 20K) are used to fit the recorded data. In the following, a short discussion of the utilized fit function as well as of the applied fitting procedure is presented. Thereafter, the results obtained are discussed and interpreted in the context of the developed model.

The data analyzed in the following are the decay-time spectra $\mathbf{O9_{PMT}}$, $\mathbf{O10_{PMT}}$ (400nm filter, crystal Olga, $T \approx 298$K and $T \approx 20$K, respectively), $\mathbf{O11_{PMT}}$, $\mathbf{O12_{PMT}}$ (500nm filter, crystal Olga, $T \approx 298$K and $T \approx 21$K, respectively) as well as $\mathbf{P5_{PMT}}$ and $\mathbf{P6_{PMT}}$ (400nm filter, crystal Philibert, $T \approx 298$K and $T \approx 18$K, respectively) recorded under two-photon excitation with the N_2 laser (compare table 4.5 in section III/4.5.2). All decay-time spectra were preprocessed according to the procedure described in section III/4.6.2.

It should be noted that with crystal Philibert only measurements with the 400nm filter were performed. Therefore, as will become clear from the discussion of the parameters that can be determined by the fits, for crystal Philibert, the complete set of model parameters cannot be determined. Thus, the results from the fits to the decay-time spectra $\mathbf{P5_{PMT}}$ and $\mathbf{P6_{PMT}}$ can only be used to compare the two crystals investigated.

5.2.1 Pulse-Shape Fits of the Unquenched $CaWO_4$ Scintillation Light

Fit Function

The excitation in the considered measurements was performed with light-pulses from the N_2 laser via the two-photon effect using either the 400nm optical filter (blue light) or the 500nm optical filter (green light) in front of the PMT. As can be seen from the fits of the wavelengths spectra (see, e.g., figures 5.1 in section III/5.1), the scintillation light passing through each of these optical filters (widths of the bandpass regions of 50nm respectively, compare section III/4.2.4 and appendix C.5) can neither be ascribed to the blue scintillation-light sub-spectrum only nor to the green scintillation-light sub-spectrum only. Nonetheless, in the following, the scintillation light detected with the 400nm filter is assumed to be purely describable by the blue scintillation-light decay-time spectrum from the developed model and the scintillation light detected with the 500nm filter is assumed to be purely describable by the green scintillation-light decay-time spectrum from the developed model. However, it should be kept in mind that, especially for the measurements performed with the 500nm filter, this assumption (i.e., neglecting the influence of the blue scintillation light) most probably only delivers an approximate description of the recorded pulse shape.

As discussed in section III/4.1.3, in the simultaneous absorption process of two photons from the N_2 laser, an energy of 7.36eV is transferred to an electron-hole pair. As this energy is far too small to excite an additional secondary electron-hole pair (band-gap of $CaWO_4$, $E_{gap} = 5.0$eV, see section III/2.1.2), for each two-photon absorption event, exactly one electron is excited into the conduction band. In addition, it has to be taken into account that the electron-hole pairs excited in this process are expected to be spatially separated from each other and the resulting STEs are, thus, not interacting. Hence, the scintillation light produced by one of these individual, spatially separated blue (green) STEs is described by the decay-time spectrum of the unquenched blue (unquenched green) scintillation light, $P_b^{nq}(1\,eh, T, t)$ ($P_g^{nq}(1\,eh, T, t)$), formulated for one electron-hole pair, $N_{eh}(E_{part}) = 1\,eh$. Within the developed model, these decay-time spectra are described by equations 3.104 and 3.105 (section III/3.2.3) for ~ 300K and equations 3.126 and 3.127 (section III/3.2.3) for ~ 20K, respectively, with $N_{eh}(E_{part}) = 1$. The effective unquenched lifetimes of the blue and the green STEs, $\tau_1(T)$ and $\tau_2(T)$ (containing the intrinsic de-excitation processes as well as the mutual excitation processes of the blue and green STE populations), used to express these pulse shapes are defined by equations 3.106 and 3.107 (section III/3.2.3), respectively.

In order to fit the recorded decay-time spectra using the pulse shapes predicted by the unquenched model, several simplification of the expressions for the unquenched decay-time spectra of one electron-hole pair can be performed (compare to the discussion of negligible terms in section III/3.2.3 and appendix B.8). In addition, the excitation by the laser pulse (with a non-negligible temporal width, compare section III/4.7.3 and appendix C.10.2) as well as the impact of the impulse reaction of the utilized detection system (compare appendix C.4.4) on the detected light pulse-shapes have to be considered. Furthermore, it has to be taken into account that, as discussed in section III/4.7.2 (see also appendix C.10), simultaneously to the $CaWO_4$ scintillation light, a fraction of the laser light (reflected at the $CaWO_4$ crystal) is detected by the PMT. The deduction of the final fit functions for the unquenched blue and green scintillation light at $T \approx 300$K and at $T \approx 20$K can be found

in appendix E.1. As discussed there in detail, the complete fit functions, $F_b^L(N_{eh}^L(T),T,t)$ and $F_g^L(N_{eh}^L(T),T,t)$, for the unquenched blue and green scintillation-light decay-time spectra excited by one laser pulse producing $N_{eh}^L(T)$ electron-hole pairs can be described as the sum of the blue or green $CaWO_4$ scintillation light, $P_b^{L\,fit\,final}(N_{eh}^L(T),T,t)$ and $P_g^{L\,fit\,final}(N_{eh}^L(T),T,t)$ (equation 5.11, influenced by the width of the laser-light pulse used for excitation and by the impulse reaction of the detection system) and of the reflected laser-light pulse-shape, $R^L(T,t)$ (equation 5.12, influenced by the impulse reaction of the detection system). In the following, the final fit function obtained for the example of the decay-time spectrum of the blue scintillation light at room temperature is presented (compare appendix E.1):

$$\begin{aligned}
P_b^{L\,fit\,final}(N_{eh}^L(T),T\approx 300\mathrm{K},t) = {} & \frac{I_b^{nq\,fit}(T)\cdot DE_{L,\,400nm,\,RT}}{2}\cdot \\
\cdot\Bigg[& \frac{1}{1-\frac{\tau_{el}}{\tau_1(T)}}\cdot\left(1-\frac{F_{dr}(T)}{1-\frac{\tau_1(T)}{\tau_{dr}(T)}}\right)\cdot e^{-\frac{t-\mu_{tot}}{\tau_1(T)}}\cdot e^{\left(\frac{\sigma_{tot}}{\sqrt{2}\cdot\tau_1(T)}\right)^2}\cdot \\
& \cdot\left\{1+erf\left(\frac{t-\mu_{tot}}{\sqrt{2}\cdot\sigma_{tot}}-\frac{\sigma_{tot}}{\sqrt{2}\cdot\tau_1(T)}\right)\right\}- \\
& -\frac{F_{dr}(T)}{1-\frac{\tau_{dr}(T)}{\tau_1(T)}}\cdot\frac{1}{1-\frac{\tau_{el}}{\tau_{dr}(T)}}\cdot e^{-\frac{t-\mu_{tot}}{\tau_{dr}(T)}}\cdot e^{\left(\frac{\sigma_{tot}}{\sqrt{2}\cdot\tau_{dr}(T)}\right)^2}\cdot \\
& \cdot\left\{1+erf\left(\frac{t-\mu_{tot}}{\sqrt{2}\cdot\sigma_{tot}}-\frac{\sigma_{tot}}{\sqrt{2}\cdot\tau_{dr}(T)}\right)\right\}- \\
& -\left(\frac{1}{1-\frac{\tau_{el}}{\tau_1(T)}}\cdot\left(1-\frac{F_{dr}(T)}{1-\frac{\tau_1(T)}{\tau_{dr}(T)}}\right)-\frac{F_{dr}(T)}{1-\frac{\tau_{dr}(T)}{\tau_1(T)}}\cdot\frac{1}{1-\frac{\tau_{el}}{\tau_{dr}(T)}}\right)\cdot e^{-\frac{t-\mu_{tot}}{\tau_{el}}}\cdot e^{\left(\frac{\sigma_{tot}}{\sqrt{2}\cdot\tau_{el}}\right)^2}\cdot \\
& \cdot\left\{1+erf\left(\frac{t-\mu_{tot}}{\sqrt{2}\cdot\sigma_{tot}}-\frac{\sigma_{tot}}{\sqrt{2}\cdot\tau_{el}}\right)\right\}\Bigg]+c_{BL} \qquad (5.11)
\end{aligned}$$

$$\begin{aligned}
R^L(T,t) = {} & \frac{R_0(T)\cdot DE_{L,\,400nm,\,RT}}{2\cdot\tau_{el}}\cdot e^{-\frac{t-\mu_{tot}}{\tau_{el}}}\cdot e^{\frac{\sigma_L^2+\sigma_{TT}^2}{2\cdot\tau_{el}^2}}\cdot \\
& \cdot\left\{1+erf\left(\frac{t-\mu_{tot}}{\sqrt{2}\cdot\sqrt{\sigma_L^2+\sigma_{TT}^2}}-\frac{\sqrt{\sigma_L^2+\sigma_{TT}^2}}{\sqrt{2}\cdot\tau_{el}}\right)\right\} \qquad (5.12)
\end{aligned}$$

$$\begin{aligned}
F_b^L(N_{eh}^L(T\approx 300\mathrm{K}),T\approx 300\mathrm{K},t) = {} & \\
P_b^{L\,fit\,final}(N_{eh}^L(T\approx 300\mathrm{K}),T\approx 300\mathrm{K},t) & + R^L(T\approx 300\mathrm{K},t) \qquad (5.13)
\end{aligned}$$

where $I_b^{nq\,fit}(T)$ is a scaling factor accounting, e.g., for the number $N_{eh}^L(T\approx 300\mathrm{K})$ of electron-hole pairs produced per laser pulse (see equation E.7 in appendix E.1), $DE_{L,\,400nm,\,RT}$ is the estimated detection and conversion efficiency of the utilized detection system (compare appendix C.11), τ_{el} and $\sigma_{tot} := \sqrt{\sigma_{TT}^2+\frac{\sigma_L^2}{2}}$ are known parameters describing the influence of the laser-light pulse-shape and the impulse reaction (see appendix C.4.4 and section III/4.7.3), $\tau_{dr}(T)$ is the rise time of the scintillation light produced by the delayed created fraction $F_{dr}(T)$ of the STEs, $\mu_{tot} := \mu_L + \mu_{TT}$ corresponds to the combined time shift of the signal relative to the time of triggering (due to the difference of the maximum of the laser pulse and the time of triggering as well as due to the transit-time shift of the

PMT, compare appendix C.4.4), c_{BL} accounts for a possible constant offset of the baseline of the recorded pulse and $R_0(T)$ is the scaling factor of the reflected laser light containing, e.g., the number of photons from the laser pulse reflected at the crystal.

The final fit functions $F_g^L(N_{eh}^L(T \approx 300\text{K}), T \approx 300\text{K}, t)$ for the green decay-time spectra recorded at room temperature as well as $F_b^L(N_{eh}^L(T \approx 20\text{K}), T \approx 20\text{K}, t)$ and $F_g^L(N_{eh}^L(T \approx 20\text{K}), T \approx 20\text{K}, t)$ for the blue and the green decay-time spectra recorded at ~ 20K, respectively, can be obtained in an analogous way from the expressions for the unquenched blue and the unquenched green scintillation light delivered by the model (see, e.g., equations E.2 to E.4 in appendix E.1).

Applied Fit Procedure

Some of the free fit parameters appear simultaneously in the fit functions of the green and the blue scintillation light for the same temperature. Therefore, all of the wavelength spectra recorded for one crystal at one temperature with both optical filters were fitted simultaneously using a global χ^2-fit, e.g., all data recorded for crystal Olga with the 400nm filter, $\mathbf{O9_{PMT}}$ (record lengths of 10μs and 100μs), and the 500nm filter, $\mathbf{O11_{PMT}}$ (record lengths of 10μs and 100μs) were fitted simultaneously. It should be noted that, as the laser was not running with constant power output, the pulse heights of the recorded decay-time spectra differ from each other (even of those recorded under the exact same conditions, i.e., same crystal position, temperature and optical filter). Therefore, in the simultaneous fits of the decay-time spectra recorded, e.g., at room temperature with the 400nm filter, $\mathbf{O9_{PMT}}$ (record lengths of 10μs and 100μs), the exact same fit functions with the identical parameters are used. However, for the 10μs measurement this function is extended for a multiplication factor, $M_{10\mu\text{s}}^b(T)$ (free fit parameter), with which the complete fit function is multiplied. Thus, this factor only scales the total pulse height of the decay-time spectrum recorded with 10μs record length in comparison to the measurement with 100μs record length. The 100μs measurement is not assigned a multiplication factor, but serves as reference. For a more detailed description as well as a list of the respective free fit parameters, see appendix E.2. It should be noted that, by performing the combined fits with parameters common for all decay-time spectra recorded for one temperature, it is implicitly assumed that all of these measurements were performed at exactly the same temperature. This was, as can be seen from table 4.5 in section III/4.5.2, not exactly the case. However, the differences between the temperatures during the measurements are small, so that a mean temperature for all decay-time spectra recorded for crystal Olga under laser excitation at room temperature ($\mathbf{O9_{PMT}}$ and $\mathbf{O11_{PMT}}$) of $T = 298$K and for all decay-time spectra recorded for crystal Olga under laser excitation at low temperature ($\mathbf{O10_{PMT}}$ and $\mathbf{O12_{PMT}}$) of $T = 20$K is assumed[2], in the following.

Outline of the Method for the Determination of the Unquenched Model Parameters from the Fit Results

The goal of these combined fits of the unquenched decay-time spectra recorded is to determine all free parameters of the fit functions with the highest possible accuracy. This

[2]The mean temperature of the low temperature measurement is determined to be 20K as the averaged decay-time of these two measurements is assigned a temperature of 20K (compare to the determination of the crystal temperature in appendix C.8.3).

is strived for as the following parameters of the fits are required to determine the free parameters of the unquenched model[3]. These parameters are:

- The effective unquenched lifetime of blue STEs, $\tau_1(T = 298\text{K})$ and $\tau_1(T = 20\text{K})$, appearing in all of the fit functions (blue and green scintillation light at room temperature and low temperature).
- The effective unquenched lifetime of green STEs, $\tau_2(T = 298\text{K})$ and $\tau_2(T = 20\text{K})$, appearing only in the fit functions of the green scintillation light (at room temperature and low temperature).
- The delayed rise time $\tau_{dr}(T = 298\text{K})$ of the fraction $F_{dr}(T = 298\text{K})$ of the scintillation light, appearing only in the fit functions of the blue and the green scintillation light at room temperature.

If the values for all of these parameters can be determined by the fits, then, the free parameters of the unquenched model at a temperature of $T = 298\text{K}$ and $T = 20\text{K}$ can be determined: As described in appendix E.3, for this purpose, the values determined for the fit parameters and the values for the relative amount of blue and green scintillation light produced at room temperature and at low temperature, $r_b(T \approx 298\text{K}) = 1 - r_g(T \approx 298\text{K})$ and $r_b(T \approx 20\text{K}) = 1 - r_g(T \approx 20\text{K})$, (calculated from the analysis of the wavelength spectra of the scintillation light, see section III/5.1.2) have to be used. The unquenched model parameters for $T = 298\text{K}$ and $T = 20\text{K}$, in turn, can then be used to calculate the temperature-dependency of almost all of the free parameters of the unquenched model: The only process for which no statement on the temperature-dependency can be deduced from the performed measurements is the delayed creation of the fraction $F_{dr}(T)$ of blue STEs with rise time $\tau_d r(T)$. For these parameters, the values at only one temperature are delivered by the fits and no detailed assumptions on their temperature-dependency are made (compare section III/3.1.2). Thus, as is presented in the following, except for this delayed recombination process of a fraction of the STEs (which is, in fact, neglected for the complete quenched model, compare section III/3.2.4), the temperature-dependency of all parameters of the unquenched model can be determined from the values of these parameters at $T = 298\text{K}$ and $T = 20\text{K}$ (obtained from the fits):

- From the fit results, the radiative decay times of blue and green STEs, $\tau_{rb}(T = 298\text{K})$, $\tau_{rb}(T = 20\text{K})$ and $\tau_{rg}(T = 298\text{K})$, $\tau_{rg}(T = 20\text{K})$ are determined. In addition, it is assumed that the radiative decay times of the blue and green STEs at temperatures $T \lesssim 5\text{K}$, i.e., the radiative decay times from the energetically lower-lying emitting levels τ_{L1b} and τ_{L1g}, are known (compare section III/3.3.2). Using this information, all parameters describing the temperature-dependency of the radiative decay times of blue and green STEs can be determined (compare equations 3.54 and 3.59 (section III/3.1.3)):

$$\frac{1}{\tau_{rb}(T)} := \frac{\frac{1}{\tau_{L1b}} + \frac{1}{\tau_{L2b}} \cdot e^{-\frac{D_b}{k_B \cdot T}}}{1 + e^{-\frac{D_b}{k_B \cdot T}}} \tag{5.14}$$

$$\frac{1}{\tau_{rg}(T)} := \frac{\frac{1}{\tau_{L1g}} + \frac{1}{\tau_{L2g}} \cdot e^{-\frac{D_g}{k_B \cdot T}}}{1 + e^{-\frac{D_g}{k_B \cdot T}}} \tag{5.15}$$

[3] All other free fit parameters only account for scaling effects, times shifts, constant offsets or the reflected laser light and do, hence, not influence the model parameters.

i.e., the values for τ_{L2b}, D_b and τ_{L2g}, D_g can be determined.

- From the fit results, the non-radiative decay times of blue and green STEs, $\tau_{nrb}(T = 298\text{K})$ and $\tau_{nrg}(T = 298\text{K})$ are determined. It should be noted that, at $T = 20\text{K}$, the non-radiative recombination of STEs is assumed to be negligible (compare discussion in section III/3.2.1). As discussed in section III/3.3.2, the energy barrier of the non-radiative recombination process of blue STEs is assumed to be known. Therefore, the complete temperature dependency of the non-radiative recombination of blue STEs can be determined using the value of $\tau_{nrb}(T = 298\text{K})$ (compare equation 3.57 in section III/3.1.3):

$$\frac{1}{\tau_{nrb}(T)} := K_{nrb} \cdot e^{-\frac{\Delta E_b}{k_B \cdot T}} \tag{5.16}$$

  i.e., the value of K_{nrb} can be calculated.
  The energy barrier of the non-radiative recombination process of green STEs, however, is not assumed to be known (no values can be adopted from the literature). Thus, the description of the temperature-dependency of the non-radiative recombination time of green STEs contains two unknown parameters, K_{nrg} and ΔE_g (compare equation 3.61 in section III/3.1.3):

$$\frac{1}{\tau_{nrg}(T)} := K_{nrg} \cdot e^{-\frac{\Delta E_g}{k_B \cdot T}} \tag{5.17}$$

  Nonetheless, as discussed in section III/3.3.2, a constraint on the value of ΔE_g is postulated, allowing to estimate ΔE_g if the temperature-dependent total amount of unquenched scintillation light produced can be calculated, i.e., if the temperature-dependencies of all other blue and green STE recombination times are known: The temperature-dependent total amount of unquenched scintillation light can be calculated using equations 3.110 and 3.111 (section III/3.2.3). The size of ΔE_g, however, influences the temperature-dependent radiative and migration branching ratios of the green STEs and, thus, the temperature-dependent amount of green scintillation light produced. Demanding that the total amount of unquenched scintillation light produced decreases for temperature $T \gtrsim 70\text{K}$ (compare section III/3.3.2), allows to adjust a value for ΔE_g. Thus, using this method, also a value for ΔE_g and, hence, for K_{nrg} can be estimated.

- From the fit results, the migration times of blue STEs, $\tau_{\text{mig, b}\rightarrow\text{g}}(T = 298\text{K})$ and $\tau_{\text{mig, g}\rightarrow\text{b}}(T = 20\text{K})$ are determined. It should be noted that the migration time of green STEs, $\tau_{\text{mig, g}\rightarrow\text{b}}(T)$, as well as its temperature-dependency is assumed to be known (compare section III/3.3.2). In addition, it is assumed that the hopping time of blue STEs, $t_{h\text{b}}(T)$, with

$$\tau_{\text{mig, b}\rightarrow\text{g}}(T) = \frac{t_{h\text{b}}(T)}{C_{\text{defects}}} \tag{5.18}$$

  is already known (see section III/3.3.2 and equation 3.63 in section III/3.1.3). Thus, from the determination of the migration time of blue STEs for at least one of the investigated temperatures, the defect density C_{defects} of the investigated crystal can be determined using equation 5.18. With the value of the defect density, in turn, the temperature-dependent migration time of blue STEs can be calculated.

- Using all of these determined recombination and migration times of blue and green STEs (as well as their respective temperature-dependencies), the temperature-dependency of
  - The intrinsic lifetimes, $\tau_{ltb}(T)$ and $\tau_{ltg}(T)$ (equations 3.81 and 3.82 in section III/3.1.4)
  - The effective unquenched lifetimes, $\tau_1(T)$ and $\tau_2(T)$ (equations 3.106 and 3.107 in section III/3.2.3)
  - The different branching ratios, $F_{b/g\,rad}(T)$, $F_{b/g\,mig}(T)$ and $F_{b/g\,nrad}(T)$ (equations 3.83, 3.84 and 3.85 in section III/3.1.4)

  of the blue and the green STEs, respectively, can be calculated.
- Thus, if the number of (spatially separated) electron-hole pairs initially created, $N_{eh}(E_{part})$, is known, then, with all of these determined parameters, the decay-time spectra of the unquenched blue and green scintillation light, $P_b^{nq}(E_{part}, T, t)$ and $P_g^{nq}(E_{part}, T, t)$ (equations 3.104 and 3.105 in section III/3.2.3), as well as the temperature-dependent number of produced (unquenched) blue photons, $P_b^{nq}(E_{part}, T)$, and green photons, $P_g^{nq}(E_{part}, T)$ (equations 3.110 and 3.111 in section III/3.2.3), can be determined. Using additionally that the mean energy of the produced scintillation-light photons is, in good approximation, independent of temperature (compare section III/5.1.2) and known from the fits of the wavelength spectra (compare section III/5.1.2), the complete temperature-dependency of the total amount of produced scintillation light, $L_{tot}^{nq}(E_{part}, T)$ (equation 3.113 in section III/3.2.3), can be calculated. It should be noticed that the parameters F_{abs} and F_{e^-traps} are assumed to be known (compare section III/3.3.2).

Thus, if the values of the parameters $\tau_1(T)$ and $\tau_2(T)$ at the temperatures $T = 298$K and $T = 20$K, respectively, can be determined from the fits of the decay-time spectra recorded under laser excitation, then all of the parameters (and their temperature-dependencies) of the unquenched model for the investigated crystal can be calculated (under the assumption of some values for several model parameters as explained in section III/3.3.2). The only exception is the temperature-dependency of the delayed recombination process of a fraction of the initially created blue STEs. However, it has to be noticed that, as this process is not expected to have any impact on the amount of scintillation light generated, it is neglected in the formulation of the quenched model. Thus, the determination of the temperature-dependency of $\tau_{dr}(T)$ and $F_{dr}(T)$ is not required for the formulation of the complete quenched model as these parameters are not utilized there.

From this discussion, it becomes clear that, for crystal Philibert for which only measurements with the 400nm filter (blue light) were performed, the complete set of parameters cannot be determined as the effective unquenched lifetime of green STEs, $\tau_2(T)$, cannot be assigned a value ($\tau_2(T)$ only appears in the fit function of the green scintillation light). Thus, as already indicated in the introduction to this section, the measurements and results of the fits for crystal Philibert are only used to compare the two crystals investigated.

Limitations and Problems of the Fits

However, it should be noted that, due to the reflected laser light covering the beginning of the scintillation-light pulse as well as due to the (slow) impulse reaction of the detection

system and the non-negligible width of the excitation pulse, features of the recorded pulse shapes at the beginning of the pulses are problematic to describe with the fit. These features are the partial rise time $\tau_{dr}(T)$ of the fraction $F_{dr}(T)$ of the blue scintillation light at $T = 298\text{K}$ and the rise of the green scintillation light with rise time $\tau_2(T)$ (at $T = 298\text{K}$ and at $T = 20\text{K}$). Additionally, it should be taken into account that, as discussed in appendix C.4, for large pulse heights (at least for signal heights $\gtrsim 0.9\text{V}$), the PMT signal starts to saturate and that, for short times t after the excitation pulse, a non-negligible extra noise-component (crosstalk from the laser discharge, compare appendix C.4.3) is observable on the recorded signals. These features as well as their impact on the determination of the rising part of the scinitllation-light pulse are discussed in appendix E.4. From these considerations, it becomes clear that the determination of the parameters $\tau_{dr}(T)$ and $\tau_2(T)$ by fitting the recorded decay-time spectra is challenging or even prevented. In figure 5.2, the addressed problems are illustrated graphically for the example of the scintillation-light decay-time spectra recorded for crystal Olga at room temperature. In figure 5.2 a) and b) (zoom to the beginning of the pulse), the measurement $\mathbf{O9_{PMT}}$ (crystal Olga, laser excitation, $T = 298\text{K}, 10\mu\text{s}$ record length, 400nm filter) is depicted. In figure 5.2 c) and d) (zoom to the beginning of the pulse), the measurement $\mathbf{O11_{PMT}}$ (crystal Olga, laser excitation, $T = 298\text{K}, 10\mu\text{s}$ record length, 500nm filter) is shown. Additionally, the respective results from the performed fits are indicated where the complete fit function (equation 5.13) is represented by the solid red line, the part of the fit function corresponding to the $CaWO_4$ scintillation light (equation 5.11) is shown as a dashed blue or green line and the part of the fit function corresponding to the reflected laser-light pulse (equation 5.12) is shown as a dotted violet line.

The strategy used to obtain values or at least estimates for these parameters by using either predetermined values from the literature or fitting procedures with alternately fixed values for some parameters, in spite of all of these difficulties, is discussed in appendix E.4. From this discussion, it can be concluded that, on the one hand, the value for $\tau_{dr}(T \approx 300\text{K})$, the rise time of the delayed produced scintillation light at room temperature, cannot be determined from the fits. Thus, the value of $\tau_{dr}(T \approx 300\text{K}) = 40\text{ns}$ from the literature [71] is adopted for the model developed within the present work (see also discussion in section III/3.1.2). On the other hand, it is discussed that, for the rise time $\tau_2(T)$, two different methods are applied depending on temperature: For room temperature, the value of this parameter can be determined by iteratively fixing its value or the values of all other free parameters in the fits. Thus, $\tau_2(T = 298\text{K})$ is, in the end, actually determined from the data. The value for $\tau_2(T = 20\text{K})$, however, cannot be determined in this way. The strategy used to obtain a reasonable estimate for this parameter is based on an estimate of the defect density of the investigated $CaWO_4$ crystal from the fit results of the decay-time spectra recorded at room temperature. Using this value and a preliminary result for $\tau_1(T = 20\text{K})$ from a first fit of the unquenched decay-time spectra at low temperatures, a preliminary value for $\tau_2(T = 20\text{K})$ can be calculated. This value can then be inserted as a fixed parameter into the fit function so that a new value for $\tau_1(T = 20\text{K})$ can be determined via a fit which, in turn, can then be used to recalculate the value of $\tau_2(T = 20\text{K})$. It should be noted that, already after one iteration, the results obtained were stable. A more detailed discussion of this method can be found in appendix E.4.

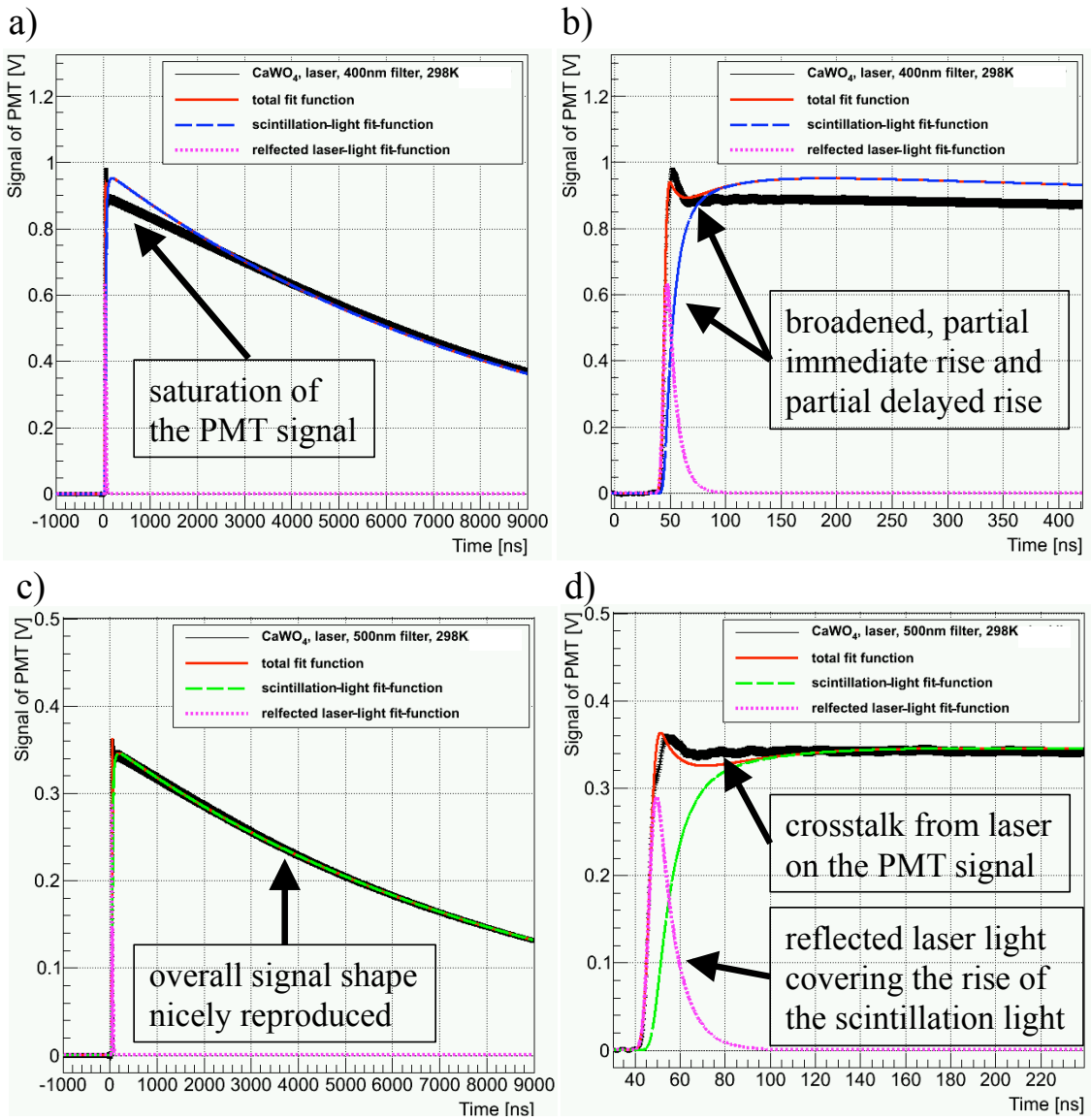

Figure 5.2: Decay-time spectra (black lines and markers with error bars) recorded for crystal Olga under laser-beam excitation at room temperature: In panel a) and b), the spectrum $\mathbf{O9_{PMT}}$ recorded with the 400nm filter (record length of 10μs) is shown. In panel c) and d), the spectrum $\mathbf{O11_{PMT}}$ recorded with the 500nm filter (record length of 10μs) is shown. The spectra were preprocessed according to section III/4.6.2. Panel a) and c) depict the complete record length of these spectra, in panel b) and c), zooms to the beginning of the pulses of panel a) and c), respectively, are shown. The spectra were fitted simultaneously with the fit functions as described in the main text. The complete fit functions are indicated as solid red lines. In addition, the decomposition of the fit functions into the partial pulse representing the reflected laser light (dotted violet lines) and the partial pulse representing the $CaWO_4$ scintillation light (dashed, blue and green lines, respectively) is shown. The different features of the data as well as of the fit functions indicated in the figure are discussed in the main text as well as in appendix E.4 in detail.

5.2.2 Results and Determination of Free Model Parameters

In the following, the results obtained from the fits as well as the determined free parameters of the unquenched model using these results are presented. At first, the results obtained

for the free parameters of the fits of the decay-time spectra recorded for crystal Olga under laser excitation at room temperature ($\mathbf{O9_{PMT}}$ and $\mathbf{O11_{PMT}}$) are presented, followed by the estimation of the defect density of the investigated crystal Olga based on these results. With the value of the defect density determined in this way, the fits of the decay-time spectra recorded for crystal Olga under laser excitation at low temperature ($\mathbf{O9_{PMT}}$ and $\mathbf{O11_{PMT}}$) could be performed, as described in appendix E.4. The results from these fits are presented. At the end of the section, the values and temperature-dependencies determined for the free parameters of the unquenched model for crystal Olga are presented.

The results of the fits of the decay-time spectra of crystal Philibert ($\mathbf{P5_{PMT}}$ and $\mathbf{P6_{PMT}}$, only measurements with the 400nm filter) are presented in appendix E.5. As with the information gained from these fits, a complete set of parameters of the unquenched model for crystal Philibert could not be determined, these values are only used as comparison for the values obtained from the fits of the data recorded with crystal Olga. This comparison is discussed in appendix E.5 and reveals no major differences.

Results of the Fits to the Unquenched Decay-Time Spectra Recorded at Room Temperature

In table 5.3, the results for the free parameters of the combined fits of the decay-time spectra recorded for crystal Olga under laser excitation at room temperature, $\mathbf{O9_{PMT}}$ and $\mathbf{O11_{PMT}}$, can be found. The parameters with superscript b have to be assigned to the decay time spectrum $\mathbf{O9_{PMT}}$ (blue light) and parameters with superscript g have to be assigned to the decay time spectrum $\mathbf{O11_{PMT}}$ (green light).

For figures of examples of these fits, see figure 5.2 in section III/5.2.1. Regarding the results of the fits listed in table 5.3, it can be observed that the value for $\tau_1(T)$ (effective unquenched lifetime of blue STEs) complies with values from the literature for the slow component of the $CaWO_4$ scintillation light under particle excitation (compare, e.g., values stated in table 2.1, section III/2.2.3 from [41]). This observation confirms the prediction of the model that the slow decay time observed under particle excitation essentially corresponds to the undisturbed decay of blue STEs. In addition, the value determined for $F_{dr}(T)$ (fraction of scintillation light with rise time $\tau_{dr}(T)$) can be compared to the value reported in the literature ($\sim 15\%$ [71], see section III/3.1.2). It can be seen that the determination of $F_{dr}(T)$ in the present work yields almost the same value, thus, within the interpretation of this process in the developed model, pointing to a similar defect density of crystal Olga and the $CaWO_4$ crystal investigated in [71]. This observation justifies with hindsight the adoption of the value for $\tau_{dr}(T)$ which is also expected to depend on the defect density of the crystal[4]. In addition, from these fit results, it can be seen that the effective unquenched lifetime of green STEs, $\tau_2(T)$, is much smaller than the effective unquenched lifetime of blue STEs, $\tau_1(T)$, as anticipated by the model (compare, e.g., equation 3.136 in section III/3.2.3).

[4]It has to be noted that, additionally to the fits with the fixed, chosen value of 40ns for $\tau_{dr}(T)$, also fits with values of $\tau_{dr}(T)$ ranging from 10ns to 60ns were tested, neither of them yielding a better description of the pulse shapes, but all of them delivering similar values for $F_{dr}(T)$.

fit parameter		result
$I_b^{nq\,fit}(T = 298\text{K})$	$[10^6\,\frac{\gamma}{s}]$	2.0044 ± 0.0002
$I_g^{nq\,fit}(T = 298\text{K})$	$[10^6\,\frac{\gamma}{s}]$	2.4103 ± 0.0003
$\tau_1(T = 298\text{K})$	$[\mu\text{s}]$	9.0913 ± 0.0004
$\tau_2(T = 298\text{K})$	[ns]	1.4032 ± 0.0279
μ_{tot}^b	[ns]	44.4353 ± 0.0220
μ_{tot}^g	[ns]	46.5953 ± 0.0201
c_{BL}^b	$[\mu\text{V}]$	70.1306 ± 0.6107
c_{BL}^g	$[\mu\text{V}]$	55.2126 ± 0.3090
R_0^b	$[10^{-2}\,\gamma]$	1.7455 ± 0.0074
R_0^g	$[10^{-2}\,\gamma]$	2.6450 ± 0.008
$M_{10\mu\text{s}}^b(T = 298\text{K})$		1.1087 ± 0.0001
$M_{10\mu\text{s}}^g(T = 298\text{K})$		1.0317 ± 0.0001
$F_{dr}(T = 298\text{K})$	[%]	12.9262 ± 0.1137
reduced χ^2		2.10

Table 5.3: Summary of the results of the fits of the unquenched decay-time spectra **O9$_{\mathbf{PMT}}$** and **O11$_{\mathbf{PMT}}$** recorded at room temperature, $T = 298\text{K}$ (compare table 4.5 in section III/4.5.2): The value obtained for the effective unquenched lifetime $\tau_2(T)$ of the green STEs was determined as described in section III/5.2.1. $I_b^{nq\,fit}(T)$ and $I_g^{nq\,fit}(T)$ correspond to the basic scaling factor of the pulse height of the decay-time spectra, respectively, $\tau_1(T)$ is the effective unquenched lifetime of blue STEs, μ_{tot}^b and μ_{tot}^g are the temporal shifts of the detected pulses compared to the respective times of triggering, c_{BL}^b and c_{BL}^g are the DC offsets of the baseline levels, R_0^b and R_0^g correspond to the scaling factors for the pulse shapes describing the reflected laser light, $M_{10\mu\text{s}}^b(T)$ and $M_{10\mu\text{s}}^g(T)$ are the scaling factors of the decay-time spectra recorded with a record length of $10\mu\text{s}$ in comparison to the ones recorded with a record length of $100\mu\text{s}$, and $F_{dr}(T)$ is the fraction of scintillation light exhibiting a delayed rise. In addition, the globally obtained, reduced χ^2-value is shown. The unit $[\frac{\gamma}{s}]$ denotes photons per second, the unit $[\gamma]$ denotes number of photons.

Determination of an Estimate for the Defect Density of the Investigated $CaWO_4$ Crystal

As discussed in appendix E.4, the fit of the decay-time spectra recorded at 20K did not allow to directly determine a reliable value for the effective unquenched lifetime $\tau_2(T)$.

Therefore, the strategy was used that if, the defect density of the instigated crystal is known (or, at least, can be estimated), then the value for $\tau_1(T = 20\text{K})$ obtained from the fit can be used to determine all of the model parameters for a temperature of $T = 20\text{K}$, i.e., also $\tau_2(T = 20\text{K})$ (see appendix E.4 for details). Thus, an estimate for the defect density C_{defects} has to be determined without using a value for $\tau_2(T = 20\text{K})$ (as was originally intended, compare discussion of the determination of the free parameters of the unquenched model in section III/5.2). The derivation of such an estimate is outlined in the following:

By assuming an arbitrary value for the defect density C_{defects}, all values of the model parameters can be calculated from the fit results for $\tau_1(T = 298\text{K})$, $\tau_2(T = 298\text{K})$ and $\tau_1(T = 20\text{K})$ (compare to the discussion of the determination of the free parameters of the unquenched model in section III/5.2). It should be noted that, as all of the model

parameters depend on the choice of the value for C_{defects}, only values of C_{defects} within a certain range, $[C^{min}_{\text{defects}}, C^{max}_{\text{defects}}]$, deliver physically reasonable sets of parameters. In more detail, this can be explained using the following three facts:

- The blue-to-green ratio of the scintillation light produced at room temperature is known (from the fits of the wavelength spectra, see section III/5.1.2).
- The sum of the radiative, non-radiative and migration branching ratios has to equal unity (compare equations 3.83 to 3.85 in section III/3.1.4).
- The migration time of green STEs and the hopping time of blue STEs are assumed to be known from the literature (compare section III/3.3.2).

Using these three facts, the values for the non-radiative branching ratios of blue and green STEs, $F_{b\,nrad}(T = 298\text{K})$ and $F_{g\,nrad}(T = 298\text{K})$), at room temperature are determined for different defect densities using the results from the fits of the decay-time spectra recorded at $T = 298$K. In figure 5.3, the values determined for $F_{b\,nrad}(T = 298\text{K})$ (filled, blue triangles indicating the calculated data points, dotted blue line as guide for the eye) and $F_{g\,nrad}(T = 298\text{K})$ (filled, green circles indicating the calculated data points, dashed green line as guide for the eye) for different defect densities are shown. In addition, two vertical, dashed, red lines are shown, indicating the minimum and maximum value of the defect density for which both of the non-radiative branching ratios exhibit positive values[5].

From figure 5.3, it can be seen that, only for values of the defect density $C_{\text{defects}} \in [C^{min}_{\text{defects}} \approx 30\text{ppm}, C^{max}_{\text{defects}} \approx 275\text{ppm}]$, the values of both non-radiative branching ratios are positive. This observation can be interpreted as described in the following:

- On the one hand, it can be observed that the smaller the defect density, the more efficient the radiative decay of the (few) green STEs has to become in order to produce enough green photons to account for the determined ratio of the blue-to-green light produced. As the migration time of green STEs is fixed, this increased radiative efficiency has to result in a smaller branching ratio for the non-radiative recombination process of the green STEs.
- In fact, if the defect density is chosen too small ($C_{\text{defects}} < C^{min}_{\text{defects}}$), the radiative branching ratio of the green STEs, $F_{r\,g}(T = 298\text{K})$, has to become so efficient that the non-radiative branching ratio of green STEs $F_{nr\,g}(T = 298\text{K})$ would have to become negative, which is, of course, not possible.
- On the other hand, it can be observed that the larger the defect density, the more efficient the migration process of blue STEs to defect centers (compare equation 3.63 in section III/3.1.3). Thus, in order to produce enough blue STEs to account for the determined ratio of the blue-to-green light produced, the more efficient the radiative decay of blue STEs has to become. This, in turn, causes the non-radiative branching ratio of the blue STEs to become smaller.
- Thus, if the defect density is chosen too large ($C_{\text{defects}} > C^{max}_{\text{defects}}$), the radiative branching ratio of the blue STEs has to become so large that the non-radiative

[5]It should be noted that also values for the defect density outside of the plotted region were tested (down to 0ppm and up to 1000ppm). For all of these values, either the non-radiative branching ratio of the blue or of the green STEs was found to be negative.

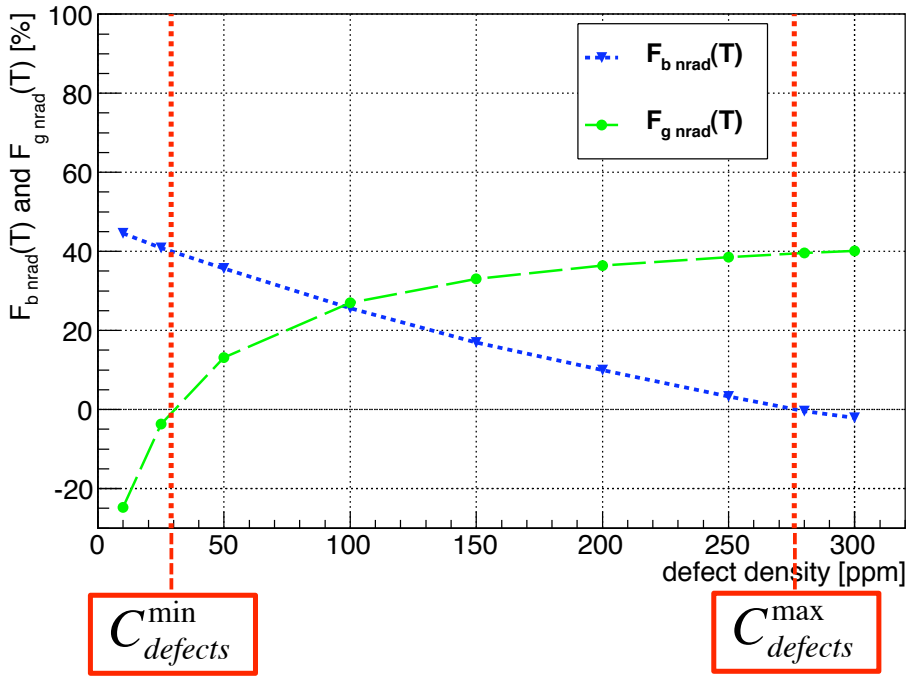

Figure 5.3: Values for the non-radiative branching ratios of blue and green STEs at $T = 298K$ dependent on the defect density, C_{defects}, calculated for crystal Olga on the basis of the results of the fits of the unquenched decay-time spectra recorded under laser excitation: The filled, blue triangles correspond to values calculated for the non-radiative branching ratio of blue STEs, the dotted, blue line only delivers a guide for the eye. The filled, green circles correspond to the values calculated for the non-radiative branching ratio of green STEs, the dashed, green line delivers a guide for the eye. Additionally indicated by the dashed, red lines are the minimum and maximum values of the defect density for which both of the non-radiative branching ratios exhibit positive values.

branching ratio of the blue STEs would need to become negative, which is, of course, not possible either.

From this discussion, it becomes clear that the possible values for the defect density C_{defects} of crystal Olga can be limited to the range [$\sim$ 30ppm, $\sim$ 275ppm]. However, in addition, it should be taken into account that not only negative values for the non-radiative branching ratios of blue and green STEs, but also very small values of, e.g., less than 10%, can be assumed to be not reasonable: It can be observed that the non-radiative decay of blue and green STEs starts to significantly influence the amount of produced scintillation light already for much smaller temperatures than room temperature, i.e., at $T \gtrsim 70$K for green STEs and at $T \gtrsim 200$K for blue STEs (compare section III/3.2.1). Furthermore, due to the observed smaller onset temperature of the non-radiative recombination process of green STEs, it is expected that, for temperatures $T \gtrsim 70$K, the influence of the non-radiative recombination process on the lifetime of green STEs is larger than on the lifetime of blue STEs. Therefore, it is expected that the non-radiative branching ratio of green STEs is larger than the non-radiative branching ratio of blue STEs.

Hence, postulating that, on the one hand, both non-radiative branching ratios have to

be larger than 10% (which is acutally still rather small) and, on the other hand, demanding that the non-radiative branching ratio of green STEs is larger than the one of blue STEs, a stricter restriction of the range of possible values for the defect density C_{defects} can be gained: $C_{\text{defects}} \in [\sim 100\text{ppm}, \sim 200\text{ppm}]$. It should be noted that a defect density within this range seems reasonable when comparing this range to the amount of La added as dopant, e.g., 250ppm La in [59], to improve the optical transmission of $CaWO_4$. Where, within the developed model, a decreased optical transmission of $CaWO_4$ crystals is attributed to the existence of electron traps, i.e., to defect centers (compare section III/2.1.3). Within this interpretation, the amount of La added has to account for the number of defect centers contained in the crystal, i.e., to effectively dope, the added La density has to comply at least to the defect density of the crystal.

In order to proceed further, i.e., to determine the model parameters at $T = 298\text{K}$ and $T = 20\text{K}$, an explicit value for the defect density has to be determined. As no arguments for any further limitation of the possible range for C_{defects} were found, the mean value of the possible range stated was chosen. Hence a value for the defect density of crystal Olga of

$$C_{\text{defects}}^{Olga} := 150\text{ppm} \tag{5.19}$$

is chosen. It should be noted that a possibility to determine the defect density with further measurements (without relying on the determination of $\tau_2(T)$ at low temperatures) is suggested in section III/6.3.

As discussed in section III/5.2.1 and appendix E.4, the (chosen) value for $C_{\text{defects}}^{Olga}$ in combination with a preliminary value for $\tau_1(T = 20\text{K})$ can then be used to determine $\tau_2(T = 20\text{K})$ (as well as all other low-temperature fit parameters) by iteratively performing the fit of the unquenched decay-time spectra recorded at $T = 20\text{K}$, with $\tau_2(T = 20\text{K})$ as a fixed value.

Results of the Fits to the Unquenched Decay-Time Spectra Recorded at Low Temperature

In table 5.4, the results for the free parameters of the combined fits of the decay-time spectra recorded for crystal Olga under laser excitation at low temperature, $\mathbf{O10_{PMT}}$ and $\mathbf{O12_{PMT}}$, can be found where the parameters with superscript b have to be assigned to the decay-time spectrum $\mathbf{O10_{PMT}}$ (blue light) and parameters with superscript g have to be assigned to the decay time spectrum $\mathbf{O12_{PMT}}$ (green light).
As can be seen from table 5.4, for $\tau_2(T = 20\text{K})$, no error is stated, although a Gaussian propagated error from the fit result of, e.g., $\tau_1(T = 20\text{K})$, could, in principle, be determined. No value was stated as, on the one hand, the systematical error due to the uncertainty of the value of $C_{\text{defects}}^{Olga} := 150\text{ppm}$ is very large, so that no attempt was made to propagate this error, and as, on the other hand, the statistical errors from the fits are much smaller (see table 5.4), i.e., negligible compared to the systematical error.

In figure 5.4, two examples of the six decay-time spectra recorded at low temperature that were fitted simultaneously are presented: In panel a) a zoom to the beginning of the pulse of the decay-time spectrum $\mathbf{O10_{PMT}}$ (crystal Olga, 400nm filter, $T = 20\text{K}$, record length of $10\mu\text{s}$) is depicted with black markers and black line (error bars indicated). The

fit parameter		result
$I_b^{nq\,fit}(T = 20\text{K})$	$[10^6\,\frac{\gamma}{s}]$	0.28694 ± 0.00002
$I_g^{nq\,fit}(T = 20\text{K})$	$[10^6\,\frac{\gamma}{s}]$	0.29022 ± 0.00002
$\tau_1(T) = 20\text{K}$	$[\mu\text{s}]$	72.6861 ± 0.0051
$\tau_2(T = 20\text{K})$	[ns]	73.222
μ_{tot}^b	[ns]	46.2137 ± 0.0091
μ_{tot}^g	[ns]	47.6274 ± 0.0096
c_{BL}^b	$[\mu\text{V}]$	222.993 ± 0.426
c_{BL}^g	$[\mu\text{V}]$	68.9873 ± 0.2181
R_0^b	$[10^{-2}\,\gamma]$	5.59748 ± 0.00887
R_0^g	$[10^{-2}\,\gamma]$	7.76057 ± 0.01257
$M_{10\mu\text{s}}^b(T = 20\text{K})$		0.844034 ± 0.000078
$M_{10\mu\text{s}}^g(T = 20\text{K})$		0.97420 ± 0.00009
$M_{1000\mu\text{s}}^b(T = 20\text{K})$		0.84636 ± 0.00011
$M_{1000\mu\text{s}}^g(T = 20\text{K})$		0.91574 ± 0.00013
reduced χ^2		3.17

Table 5.4: Summary of the results of the fits of the unquenched decay-time spectra $\mathbf{O10_{PMT}}$ and $\mathbf{O12_{PMT}}$ recorded at low temperature, $T = 20\text{K}$ (compare table 4.5 in section III/4.5.2): The value obtained for the effective unquenched lifetime, $\tau_2(T)$, of the green STEs, was determined on the basis of the defect density of crystal Olga of $C_{\text{defects}}^{Olga} := 150\text{ppm}$ (as described in section III/5.2.1). $I_b^{nq\,fit}(T)$ and $I_g^{nq\,fit}(T)$ correspond to the basic scaling factora of the pulse heighta of the decay-time spectra, $\tau_1(T)$ is the effective unquenched lifetime of blue STEs, μ_{tot}^b and μ_{tot}^g are the temporal shifts of the detected pulses compared to the respective time of triggering, c_{BL}^b and c_{BL}^g are the DC offsets of the baseline levels, R_0^b and R_0^g correspond to the scaling factors for the pulse shapes describing the reflected laser light, $M_{10\mu\text{s}}^b(T)$ and $M_{10\mu\text{s}}^g(T)$ are the scaling factors of the decay-time spectra recorded with 10μs record length and $M_{1000\mu\text{s}}^b(T)$ and $M_{1000\mu\text{s}}^g(T)$ are the scaling factors of the decay-time spectra recorded with 1000μs record length in comparison to the ones recorded with 100μs record length. In addition, the globally obtained, reduced χ^2-values are shown. The unit $\left[\frac{\gamma}{s}\right]$ denotes photons per second, the unit $[\gamma]$ denotes number of photons.

fit function is depicted as blue line. In panel b), a semi-logarithmical plot (y-axis) of the decay-time spectrum $\mathbf{O12_{PMT}}$ (crystal Olga, 500nm filter, $T = 20\text{K}$, record length of 1000μs) is shown (black markers and line, error bars indicated). The fit fit function is depicted as green line.

From figure 5.4, it can be seen, that the pulse shapes are well reproduced by the model. In panel a) of figure 5.4, it can be seen that, at a temperature of $T = 20\text{K}$, the blue scintillation light exhibits no observable rise time, as predicted by the model (compare, e.g., section III/3.2.3). Concerning the values determined for the effective unquenched lifetimes of the blue and green STEs, it can be seen that, as anticipated by the model, both of these times strongly increase with decreasing temperature (more frequent radiative decay from the lower-lying, longer-living energy level with τ_{L1b} and τ_{L1g}, respectively, compare section III/3.1.3).

The values of the fit parameters determined in this way can now be used to determine the free parameters of the unquenched model. It should be noted that, in this process, the

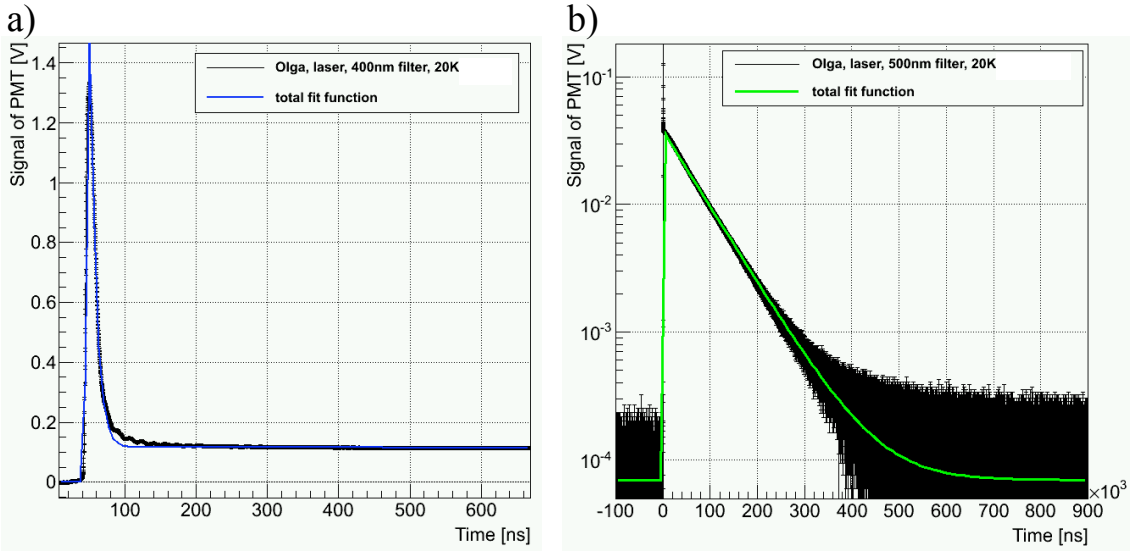

Figure 5.4: Decay-time spectra (black lines and markers with error bars) recorded for crystal Olga under laser-beam excitation at low temperature: In panel a), a zoom to the beginning of the pulse of the spectrum $\mathbf{O10_{PMT}}$ recorded with the 400nm filter (record length 10μs) is shown. In panel b), the spectrum $\mathbf{O12_{PMT}}$ recorded with the 500nm filter (record length 1000μs) is shown. The spectra were preprocessed according to section III/4.6.2. The spectra were fitted simultaneously with the fit functions as described in the main text. The fit functions are indicated as solid blue and green lines, respectively.

statistical uncertainties of the values resulting from the performed fits will be neglected as, on the one hand, they are very small. On the other hand, it has to be kept in mind that all of the low-temperature fit values and, thus, also the model parameters determined on the basis of these fit results contain a rather large, non-negligible uncertainty due to the choice of the value for the defect density of crystal Olga. Hence, those parameters determined in the following which are highly dependent on the defect density (as, e.g., the migration time of blue STEs) should only be regarded as estimates. Nonetheless, it should be noted that, e.g., for the quenched model, only the value for the radiative decay time will be used and this decay time only delivers a scaling factor of the quenched pulses. Thus, the determination of the value for the Förster radius, $R_{d-d}(T)$, is not directly influenced by the choice of $C_{\text{defects}}^{Olga} := 150\text{ppm}$. Nonetheless, the determined value of the Förster radius, of course, indirectly depends on the defect density, as it depends on the number of initially created STEs, which in turn is influenced by the size of the defect density via the fraction of electrons captured by traps, F_{e^-traps}. Within the developed model, it is assumed that electron traps are created by the same centers that are responsible for the green light emission, i.e., by defect centers. As, however, the value of F_{e^-traps} is only estimated within the present work (using values from the literature) and as no explicit expression for the dependency of F_{e^-traps} on C_{defects} is used, the choice of a value for $C_{\text{defects}}^{Olga}$ has no influence on the determined value for $R_{d-d}(T)$.

Determination of the Parameters of the Unquenched Model Using the Fit Results

As discussed in section III/5.2.1 and appendix E.3, the results of the fits for the parameters $\tau_1(T)$ and $\tau_2(T)$ at 298K and at 20K can be used to calculate the values of the free model parameters of the unquenched model at these temperatures. These parameters, in combination with the assumed values for some of the model parameters (compare discussion in section III/5.2.1), can then be used to determine the temperature-dependencies of the parameters of the unquenched model, i.e., the parameters describing the radiative, non-radiative and migration times (except for the temperature-dependency of $\tau_{dr}(T)$ and $F_{dr}(T)$). The determined parameters can be found in table 5.5 (as discussed above, no uncertainties are stated).

model parameter	determined value
$C_{\text{defects}}^{Olga}$ [ppm]	150
τ_{L2b} [μs]	7.67
τ_{L2g} [ns]	3.96
D_b [meV]	3.98
D_g [meV]	6.85
K_{nrb} $\left[\frac{1}{s}\right]$	$6.38 \cdot 10^9$
K_{nrg} $\left[\frac{1}{s}\right]$	$9.20 \cdot 10^8$
ΔE_g [meV]	35.0

Table 5.5: Summary of the results of the determined free model parameters from the fits of the unquenched decay-time spectra: $C_{\text{defects}}^{Olga}$ is the defect density of crystal Olga. As the hopping time of blue STEs is assumed to be known, the migration time of blue STEs can be determined using this value. τ_{L2b} and τ_{L2g} are the radiative recombination times of the energetically higher-lying levels of the blue and the green STEs, respectively. D_b and D_g are the respective energy barriers for the radiative recombination processes. As τ_{L1b} and τ_{L1g} are assumed to be known, the radiative recombination times can be calculated using these values. K_{nrb} and K_{nrg} are the non-radiative rate constants for the blue and green STEs, respectively. ΔE_g is the energy barrier of the non-radiative recombination process of the green STEs. As ΔE_b is assumed to be known, the non-radiative recombination times can be calculated.

Using the parameters determined in the present work (table 5.5) and additionally the parameters predetermined from the literature (see section III/3.3.2), a full set of parameters of the unquenched model (except for the temperature-dependency of $\tau_{dr}(T)$ and $F_{dr}(T)$) is derived. These parameters can be used to calculate the temperature-dependent radiative ($\tau_{rb}(T)$ and $\tau_{rg}(T)$), non-radiative ($\tau_{nrb}(T)$ and $\tau_{nrg}(T)$) and migration times ($\tau_{\text{mig, b}\rightarrow\text{g}}(T)$ and $\tau_{\text{mig, g}\rightarrow\text{b}}(T)$) of blue and green STEs (compare section III/3.1.3). From these values, additionally the intrinsic lifetimes ($\frac{1}{\tau_{ltb}(T)}$ and $\frac{1}{\tau_{ltg}(T)}$) as well as the effective unquenched lifetimes ($\tau_1(T)$ and $\tau_2(T)$) of the blue and green STEs can be calculated (compare sections 3.1.4 and 3.2.3, respectively). It should be noted that $\tau_1(T)$ corresponds to the observable (slow) decay time of the blue and green scintillation light and $\tau_2(T)$ corresponds to the observable rise time of the green scintillation light at least for $T \lesssim 20$K (compare discussion of figure 3.12 in section III/3.2.4). A graphical illustration of the temperature-dependency of the different recombination times of the STEs and their impact on the intrinsic lifetimes

and effective unquenched lifetimes, i.e., the observable rise and decay times of the scintillation light calculated with the determined parameters, can be found in figure 5.5. In figure 5.5 a), the radiative recombination time (long-dashed, dark-blue line), the non-radiative recombination time (dotted, violet line), the migration time (dashed-dotted, blue-grey line), the intrinsic lifetime (short-dashed, blue line) and the effective unquenched lifetime (i.e., the decay time of the blue and green scintillation light, solid, red line) of the blue STEs are depicted. In figure 5.5 b), the radiative recombination time (long-dashed, dark-green line), the non-radiative recombination time (dotted, green-grey line), the migration time (dashed-dotted, dark green-grey line), the intrinsic lifetime (short-dashed, blue line) and the effective unquenched lifetime (i.e., rise time of the green scintillation light, solid red line) of the green STEs are depicted. The different scales of the y-axis in panel a) and b) indicating the different orders of magnitude of the blue STE and green STE processes and lifetimes should be noted.

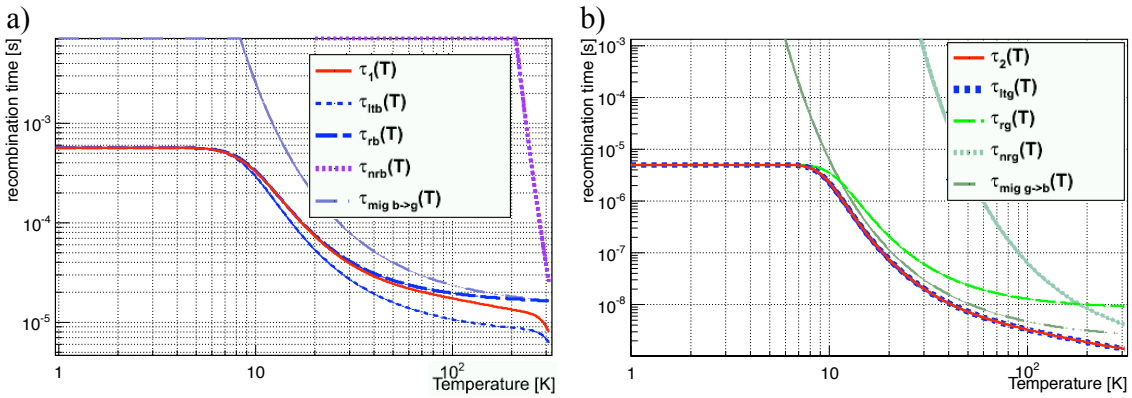

Figure 5.5: Temperature-dependency of the recombination and migration times as well as of the intrinsic and effective unquenched lifetimes of blue (panel a) and green (panel b) STEs: Calculated using the parameters of the unquenched model determined for crystal Olga within the present work.

From figures 5.5 a) and b), the influence of the different recombination and migration processes on the respective intrinsic lifetimes of the blue and green STEs can be seen clearly. As anticipated in the development of the model (compare section III/3.2.3), the lifetimes and process times of the green STEs are much faster than the lifetimes and process times of the blue STEs. In panel a), the effective unquenched lifetime of blue STEs, $\tau_1(T)$, can be compared to the intrinsic lifetime of blue STEs. It can be seen that the influence of the mutual excitation processes of the blue and green STEs (contained in $\tau_1(T)$), leads to a prolongation of the effective lifetime of blue STEs compared to the intrinsic lifetime of blue STEs, $\tau_{ltb}(T)$. This is attributed to the fact that, via the process of exciting green STEs (on the timescale of the effective unquenched lifetime of blue STEs), also blue STEs are re-excited (migration of green STEs to blue centers) on the timescale of the migration time of green STEs. Thus, the population of blue STEs is repopulated by green STEs on a non-negligible timescale leading to a longer observed lifetime of blue STEs as intrinsically present. In panel b) of figure 5.5, the effective unquenched lifetime of green STEs, $\tau_2(T)$, can be compared to the intrinsic lifetime of green STEs. These two times are almost identical (the difference of these two times amounts to maximal $\sim$ 1ps, within

the plotted temperature range) indicating that the impact of the mutual excitation processes on the lifetime of green STEs is almost negligible. This can be attributed to the fact that the intrinsic lifetime of green STEs is much faster than the excitation process by blue STEs. Therefore, the excitation process via the blue STE population determines the observable decay time of the green scintillation light (the light cannot be produced faster than the STEs are excited). The production of the green scintillation light, however, takes place on a timescale almost identical to the intrinsic lifetime of ($\tau_2(T) \approx \tau_{ltg}(T)$) which leads to a rise time of the green scintillation light with $\tau_2(T)$, as observable from experimental data (compare, e.g., figure 3.13 in section III/3.2.4). In addition, the calculated temperature-dependency of the effective unquenched lifetime of blue STEs, $\tau_1(T)$, corresponding to the decay time of the blue and the green scintillation light can be compared to measurements of the "slow" component of the $CaWO_4$ scintillation light under particle-excitation as, e.g., depicted in figure 2.13 (section III/2.2.3) from [41]. A convincing agreement of the model prediction and the measured data can be observed: All features of the temperature-dependency of the measured "slow" decay-time component are reproduced by the calculated effective unquenched lifetime of the blue STEs within the developed model.

With these determined process times and lifetimes of the blue and green STEs, the temperature-dependent number of produced blue and green photons, i.e., also the total number of produced photons, can be calculated (compare equations 3.108 and 3.109 in section III/3.2.3) for a given number of initially produced blue STEs $N_{bSTE}^{form\,e^-STH}(E_{part}) = N_{eh}(E_{part}) \cdot (1 - F_{e^-trao})$: Within the unquenched model, the number of blue STEs initially produced is only a scaling factor of the pulse height of the scintillation light. It does neither influence the pulse shape nor the amount of light produced per STE. Therefore, instead of assuming an arbitrary number of blue STEs initially generated, the number of photons (blue, green and total number) produced per blue STE can be calculated. In addition, the relative amounts of blue and green photons produced can be determined. The results of these calculations on the basis of the parameters of the unquenched model determined for crystal Olga are depicted in figure 5.6. In panel a) of figure 5.6, the temperature-dependent number of blue (blue line) and green (green line) photons as well as the temperature-dependent total number of photons (red line) produced per electron-hole pair as calculated with the model are shown. In panel b) of figure 5.6, the temperature-dependent relative amounts of blue (blue line) and green (green line) photons produced per electron-hole pair, i.e., the ratio of the number of blue and green photons, respectively, and the total number of photons produced per electron-hole pair, are shown.

From panel a) of figure 5.6, it can be seen that, as demanded by the model, at temperatures $\lesssim$ 70K, the total number of photons produced per blue STE in the unquenched model equals unity (compare discussion of the impacts of the different processes considered in the model in section III/3.2.1). At temperatures $T \gtrsim$ 70K, a decrease in the total number of photons produced can be observed, which can be attributed to the onset of the non-radiative recombination process of green STEs. The onset of the non-radiative recombination process of green STEs can also be deduced from figure 5.5 b): At $T \approx$ 70K, the non-radiative recombination time is only about 1 to 1.5 orders of magnitude larger than the radiative and migration times of green STEs. This indicates the contribution of this decay time onto the intrinsic and effective unquenched lifetimes of the green STEs. Further inspecting panel a) of figure 5.6, it can be observed that, at temperatures $T \gtrsim$ 200K,

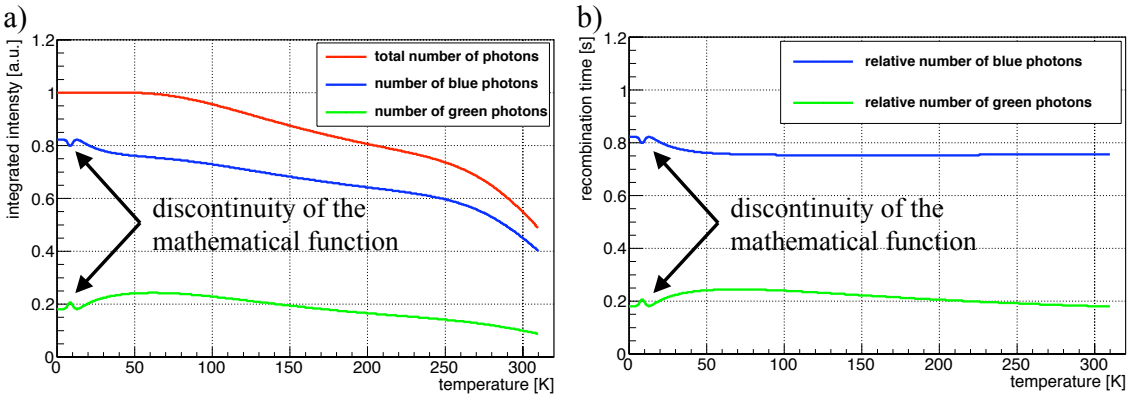

Figure 5.6: Temperature-dependency of the absolute and relative numbers of blue and green photons as well as of the absolute number of all photons produced per blue STE initially created as calculated with the parameters of the unquenched model determined for crystal Olga: In panel a), the total number of photons produced per blue STE (red line) as well as the the numbers of blue and green photons produced (blue and green lines, respectively) can be seen. In panel b), the relative numbers of blue and green photons produced, i.e., the ratio of the number of blue and green photons, respectively, and the total number of photons produced, are shown (blue and green line, respectively). As indicated in the figures, the feature, visible on the graphs of the absolute and relative numbers of blue and green photons produced at $T \approx 10$K, can be attributed to a discontinuity of the mathematical expressions describing these parameters and does not indicate a physical effect.

an additional decrease of the total number of photons can be observed. This effect can be explained analogously with the onset of the non-radiative recombination of blue STEs (compare figure 5.5 a). From panel b) in figure 5.6, it can be seen that the relative amount of blue and green photons produced varies only slightly with temperature. However, as implemented in the model, at low temperatures ($T \lesssim 50$K) the relative number of green photons produced is decreasing which can be attributed to the decreasing efficiency of the migration process of blue STEs (compare migration time and effective unquenched lifetimes of blue STEs in figure 5.5 a) leading to a decreased number of green STEs excited). For very small temperatures ($T \lesssim 5$K), constant values of the relative numbers of blue and green photons produced are reached as in this temperature region, the only excitation process for green STEs is the absorption of blue photons at defect centers which is assumed to be independent of temperature (compare section III/3.1.3). In addition, the calculated temperature-dependencies can be compared to measurements of the relative intensities of the blue and green scintillation light produced, as, e.g, depicted in figure 2.12 (section III/2.2.2, data adopted from [54]). It can be seen that the main features of the temperature-dependencies of both quantities, of the numbers of blue and green photons produced and the total number of photons produced as well as of the relative numbers of blue and green photons produced, are well reproduced by the model. It should be noted that the deviations of calculated and measured temperature-dependencies for intermediate temperatures can most probably be explained by different defect densities of the respectively investigated $CaWO_4$ crystals (crystal Olga within the present work and crystal Conrad within [54], compare discussion in section III/2.2.2) as well as by a potential influence of the quenching effect on the light yield measured in [54] with 30eV photons (compare discussion in section III/3.2.1).

In addition, the values of the parameters of the unquenched model determined in this way can be utilized to determine the relative impact of the different terms of the complete model functions that were neglected in the formulation of the fit functions (compare discussion in section III/5.2.1 and appendix E.1). In order to compare the impact of the terms of the complete unquenched green and blue light model-functions (equations 3.104 and 3.105 for $\sim$ 300K and equations 3.126 and 3.127 for $\sim$ 20K, see section III/3.2.3), the strategy as explained in section III/3.2.3 and appendix B.8 can be used: The integrals of the individual terms can be calculated according to the relationships as derived in appendix B.8 and then be compared to each other. It can be calculated that the ratio of the integrals of the neglected terms and the integrals of the non-neglected terms in the fit functions, amounts at most to $\sim 2.5 \cdot 10^{-4}$. Thus, as anticipated, the impact of the neglected terms onto the pulse shapes of the produced scintillation light is of minor importance. Therefore, the uncertainty introduced due to the performed simplification (negligence of terms) can be regarded as extremely small.

In conclusion, it can be stated that, a complete set of parameters of the unquenched model for crystal Olga could be determined based on

- The results of the analysis of the unquenched decay-time spectra.
- The physically motivated choice of a value for the defect density of crystal Olga.
- Predetermined values for some parameters of the model from the literature.

In the following, the value and temperature-dependendency of the radiative decay time will be used for the analysis of the measurements performed with ion-beam excitation. It should be noted that the values determined are also used for the calculation of the light yield for different interacting particles with the complete quenched model (presented in section III/6.1).

5.3 Quenched Decay-Time Spectra: Data Recorded With Ion-Beam Excitation

As discussed in section III/3.3.2, the decay-time spectra recorded with ion-beam excitation (iodine ^{127}I and oxygen ^{16}O, compare chapter 4), i.e., with an excitation mode creating a dense STE population, are utilized to determine the remaining free parameters of the complete quenched model as well as to validate the complete model. For this purpose, the decay-time spectra recorded with ion-beam excitation are fitted using the pulse shape of the quenched decay-time spectrum as predicted by the model. In the following, at first some basic considerations are presented, followed by a short discussion of the utilized fit function and of the applied procedure to determine the unknown parameters of the quenched model. Thereafter, the results obtained for the remaining free parameters of the complete model as well as the validation of the model are discussed.

The data analyzed in the following are the decay-time spectra $\mathbf{O1_{PMT}}$ to $\mathbf{O4_{PMT}}$ (crystal Olga, iodine-beam excitation, recorded with the 400nm and 500nm filter and at $T \approx 298$K and $T \approx 20$K, respectively) and $\mathbf{O5_{PMT}}$ to $\mathbf{O8_{PMT}}$ (crystal Olga, oxygen-beam excitation, recorded with the 400nm and 500nm filter and at $T \approx 298$K and $T \approx 20$K, respectively) as well as $\mathbf{P1_{PMT}}$, $\mathbf{P2_{PMT}}$ (crystal Philibert, iodine-beam excitation, recorded

with the 400nm filter at $T \approx 298$K and $T \approx 20$K, respectively) and $\mathbf{P3_{PMT}}$, $\mathbf{P4_{PMT}}$ (crystal Philibert, excitation with the oxygen beam, recorded with the 400nm filter at $T \approx 298$K and $T \approx 20$K, respectively) as listed in table 4.4 in section III/4.5.1. All decay-time spectra were preprocessed according to the procedure described in section III/4.6.2.

5.3.1 Basic Considerations

It should be noted that, as discussed in detail at the end of section III/3.2.4, at temperatures $T \gtrsim 20$K, the quenched scintillation-light decay-time spectra of the blue and the green scintillation light predicted by the model exhibit the same shape: The only difference is given by the scaling factor $\frac{1}{R_{b-g}(T)}$ in the mathematical description of the green scintillation light decay-time spectrum (see equation 3.164 in section III/3.2.4). $R_{b-g}(T)$ corresponds to the ratio of blue-to-green light produced. For a discussion and interpretation of a measured quenched scintillation-light pulse-shape from the literature at a temperature $T < 20$K within the developed model, see the discussion of figure 3.12 in section III/3.2.4. In addition, it should be noted that, within the developed model, the mathematical expression for the decay-time spectrum of the quenched blue and green scintillation light produced is the same for all temperatures $T \gtrsim 20$K (up to room temperature which is the maximum temperature considered within the present work).

Thus, as in the conducted experiments only measurements at temperatures $T \gtrsim 20$K were performed, in the following, no differentiation of the pulse shape predicted by the model for the blue and green scintillation light has to be used: In fact, also the scaling factor between the blue and green scintillation-light pulse-shapes does not have to be utilized as, within the developed description of the recorded pulse-shapes (see section III/5.3.2), the amount of scintillation light detected at the PMT for the 400nm or the 500nm filter is not determined by the ratio of blue-to-green-light produced, but by the relative transmissions of the created scintillation light through the filters (compare appendix C.5). By using these relative transmission which account for the shape of the wavelength spectra of the created scintillation light, the relative amounts of blue and green scintillation light produced are already considered.

Therefore, the expression for the decay-time spectrum predicted by the model for the blue and the green scintillation light, respectively (introduced in section III/5.3.2) is assigned no subscript (compare to the unquenched fit function: b or g for blue and green scintillation light, respectively).

In addition, no differentiation of the mathematical expressions of the quenched decay-time spectra at room temperature or at 20K has to be used. However, of course, the temperature-dependent parameters contained in this expression exhibit different values at different temperatures. Therefore, the dependency of the mathematical expression for the decay-time spectrum on temperature needs to be indicated.

5.3.2 Pulse-Shape Fits of the Quenched $CaWO_4$ Scintillation Light

Fit Function

For the fit of the decay-time spectra recorded under ion-beam excitation, the description of the quenched scintillation-light pulse-shape for one primary interacting particle from the

complete model developed is used (see, e.g., equations 3.166 and 3.167 in section III/3.2.4). From the discussion in section III/3.2.4 (and appendix B.3), it can be deduced that, within the developed model, the scintillation-light decay-time spectrum for one primary interacting particle is described by the sum of the expressions for the scintillation light generated by different STE populations: The STE populations created in the inner and outer parts of the $PIT1$ and $PIT2$ volumes (primary ionization track, part one and part two) and by the STE populations initially created in the inner and outer parts of all of the *Rec* volumes (1nm long cylindrical volumes centered around the tracks of the generated nuclear recoil particles as well as of their recoil particles). For details on the modeling of the initially created STE-density distribution, see section III/3.1.2. Hence, the complete decay-time spectrum produced for one primary interacting particle with energy E_{part} can be expressed by:

$$\begin{aligned} P^q(E_{part},T,t) &= P^q_{in,PIT1}(E_{part},T,t) + P^q_{out,PIT1}(E_{part},T,t) + P^q_{in,PIT2}(E_{part},T,t) + \\ &+ P^q_{out,PIT2}(E_{part},T,t) + P^q_{in,Rec}(E_{part},T,t) + P^q_{out,Rec}(E_{part},T,t) \end{aligned} \quad (5.20)$$

where, on the one hand, each of the individual terms depends on the Förster radius $R_{d-d}(T)$. On the other hand, each term depends on the initially created blue STE density-distribution in the respective volume. This implies that each term depends on the amount of energy deposited in ionization within the respective volume, on the spatial distribution of the ionization within this volume as well as on the geometrical description of the extent of the volume (radius and length of the volume, exponential constant of the density distribution and fraction of energy deposited within inner and outer volume, compare section III/3.1.2).

It should be noted that, of course, each ion-beam pulse contained more than one ion. However, as discussed in section III/4.7.3, the number of ions per excitation pulse, $N_{^{127}I}$ or $N_{^{16}O}$, delivers a mere scaling factor of the pulse height of the produced scintillation-light pulse: Due to the low number of ions per pulse and the strongly defocussed beam geometry, each of the ions contained in one pulse can be expected to produce an individual, separated STE population which is not interacting with STEs created by other ions, i.e. it can be assumed that no inter-track quenching took place. Therefore, modeling the scintillation light pulse-shape produced by all ions of in one pulse simply requires to sum the scintillation-light decay-time spectra produced by the individual ions. Of course, the temporal width of the ion pulse needs to be taken into account, as discussed in the following: In analogy to the fit function for the unquenched scintillation light (see section III/5.2), the expression for the decay-time spectrum from the model (equation 5.20) has to be multiplied with the corresponding detection and conversion efficiency as well as to be convoluted with the temporal pulse shape of the respective ion pulse (Gaussian with width $\sigma_{^{127}I} = 3.94$ns and $\sigma_{^{16}O} = 3.08$ns, respectively, compare section III/4.7.3) and the impulse reaction of the utilized detection system (compare discussion in appendix E.1 for the unquenched fit function). However, in contrary to the unquenched fit function, this convolution can no longer be performed analytically, but is implemented numerically within the fit routine[6]. Therefore, the final fit functions, $F^{^{127}I}(E_{^{127}I},T,t)$ and $F^{^{16}O}(E_{^{16}O},T,t)$, cannot be expressed explicitly.

[6]The fits and convolutions were performed using root [106]. In order to enable the numerical convolution of the impulse reaction, the ion-beam pulse and the model function, a Gauss-Legendre-sampling of the parameter space was conducted.

Applied Fit Procedure

The fit function determined for the quenched scintillation-light pulse-shapes contains the following unknown parameters[7]:

- The Förster radius $R_{d-d}(T)$.
- A temporal shift of the recorded decay-time spectrum relative to the time of triggering, μ_{tot}.
- The number of ions per excitation pulse $N_{^{127}I}$ or $N_{^{16}O}$, respectively (scaling factor of the signal height).
- The description of the spatial distribution of the initially produced blue STE density.

This implies that the ionization distribution initially created by the respective primary interacting particles, i.e., the ^{127}I ions and the ^{16}O ions, has to be determined from simulations. For this purpose, simulations with the program SRIM [42] were carried out and the method described in appendix B.3.6 was applied. However, as discussed in detail in appendix B.3.10, the parameters describing the radial distribution of the ionization density around the track of the primary interacting particle (and around the tracks of its recoils) cannot be completely derived by only using the information obtained from the conducted simulations. The strategy developed to obtain estimates for these parameters is discussed in appendix B.3.10: With the help of the decay-time spectrum $\mathbf{O2_{PMT}}$ (crystal Olga, iodine-beam excitation, 400nm filter at low temperature) and a first estimate for the value of the Förster radius of roughly 2 to 4nm (compare values determined in the literature, see section III/3.1.3), the radial parameters of the $PIT1$ and $PIT2$ volumes of the ^{127}I ions are adjusted such that the fit function yields a reasonable reproduction of the pulse shape of the recorded scintillation-light decay-time spectrum. As described in appendix B.3.10, these parameters can then be used to determine the radial parameters of the *Rec* volumes of the ionization distribution created by the ^{127}I ions. It should be noted that a large number of different sets of parameters was tested for the radial parameters as well as for the Förster radius. The values of the parameters chosen in the end were the ones that were found to deliver the best description of the pulse shape. Nonetheless, it should be noted that, as discussed in appendix B.3.10, it is in fact very likely that different combinations of values for the radial parameters and the Förster radius can be found, that reproduce the recorded pulse shape with similar quality. Therefore, the value of the Förster radius determined by the succeeding fit of the decay-time spectrum with the fit function containing the chosen values of the radial parameters as fixed parameters, should only be regarded as an estimate based on the values of the radial parameters.

It should be noted that, in section III/6.3, a method to determine the Förster radius independently from assumptions regarding the radial extent of particle-induced ionization-density distributions is suggested. If such a method is applied, then, in turn, the pulse

[7] For the effective unquenched lifetime $\tau_1(T)$ of the blue STEs, the respective value determined in appendix C.8.3 from a fit of the purely exponentially decaying part of the decay-time spectrum is adopted and used as a fixed parameter in the fits of the quenched decay-time spectra. This strategy was chosen in order to reduce the number of free fit parameters, as these fits involve a numerical convolution that has to be calculated in each step of the fit procedure and are, thus, very extensive with regard to computing time.

shapes of the scintillation-light decay-time spectra for particle interactions could be employed to determine reliable values for the radial parameters.

The values determined of the radial parameters of the ionization distribution of the ^{127}I ions (as used in the experiments, $E_{^{127}I} = 34.768$MeV, compare table 4.3 in section III/4.4.1) by the application of the described method can be found in table 5.6. Additionally, the values of the radial parameters of the ionization distribution of the ^{16}O ions (as used in the experiments, $E_{^{16}O} = 34.942$MeV, compare table 4.3 in section III/4.4.1) as determined with the method described in appendix B.3.10 on the basis of the values of the ^{127}I ions are stated.

radial parameter	determined value for $E_{^{127}I} = 34.768$MeV	determined value for $E_{^{16}O} = 34.942$MeV
$r^{in}_{PIT1}(E_{part})$ [nm]	0.450	2.40
$r^{out}_{PIT1}(E_{part})$ [nm]	11.5	11.5
$r^{in}_{PIT2}(E_{part})$ [nm]	0.225	0.45
$r^{out}_{PIT2}(E_{part})$ [nm]	2.70	11.5
$r^{in}_{Rec}(E_{part})$ [nm]	0.225	0.225
$r^{out}_{Rec}(E_{part})$ [nm]	11.5	11.5
$F^{in}_{PIT1}(E_{part})$	0.91	0.91
$F^{in}_{PIT2}(E_{part})$	0.45	0.91
$F^{in}_{Rec}(E_{part})$	0.48	0.68

Table 5.6: Values of the radial parameters of the ionization distribution of the oxygen and iodine ions determined as described in detail in appendix B.3.10: The highly different values for the $PIT2$ parameters of the oxygen and iodine ions are caused by the different energy-loss processes of these ions within their respective $PIT2$ regions. For a detailed discussion, see appendix B.3.10.

In the following, the parameters stated for the iodine ions in table 5.6 are assumed to be fixed and the radial parameters for all other ions regarded within the present work (see, e.g., section III/6.1) are determined on the basis of these values according to the method described in appendix B.3.10.

With the fixed values for the radial parameters of the ^{127}I ions derived, the decay-time spectra $\mathbf{O1_{PMT}}$ and $\mathbf{O2_{PMT}}$ are fitted with the remaining three parameters ($R_{d-d}(T)$, μ_{tot} and $N_{^{127}I}$) as free parameters, yielding the determination of a value for the Förster radius at room temperature, $R_{d-d}(T = 298\text{K})$, and at low temperature, $R_{d-d}(T = 29\text{K})$. As the Förster radius is only dependent on temperature (compare discussion in section III/3.1.3), i.e. it is independent of the employed excitation mode, the values of the Förster radius determined in this way are assumed to be valid for all other measurements with ion-beam excitation performed within the present work - of course, the respective value for each temperature has to be used. It should be noted that, due to the expected weak temperature dependency of the Förster radius (compare section III/3.1.3), the value determined from the measurement $\mathbf{O2_{PMT}}$ at a temperature of $T = 29$K is adopted for all other measurements performed at low temperature, i.e., also for a temperature of $T = 20$K. Actually, due to the fact that no measurements at temperatures $T \lesssim 20$K were performed, it is assumed that the value determined for $T = 29$K is valid for the complete temperature range below 29K, i.e., for $T \lesssim 29$K.

Thus, in order to test and validate the developed model, the corresponding value of the Förster radius determined for $T = 298$K and $T \approx 20$K, respectively, is adopted as a fixed value for the fits of all other quenched decay-time spectra of crystal Olga at room temperature and at low temperature. In addition, as the Förster radius is expected to be same for every $CaWO_4$ crystal, also the decay-time spectra recorded for crystal Philibert at room temperature and at low temperature are fitted using the determined values for $R_{d-d}(T)$ as fixed values. Hence, all other decay-time spectra - except for the decay-time spectra $\mathbf{O1_{PMT}}$ and $\mathbf{O2_{PMT}}$ - are fitted with only two parameters, i.e., the temporal shift μ_{tot} and the number of ions per pulse $N_{^{127}I}$ or $N_{^{16}O}$, respectively, as free fit parameters. The quality of these fits is assumed to reflect the validity of the developed model. The results obtained are presented in the following.

5.3.3 Results of the Fits and Values Determined for the Förster Radius

In table 5.7, the results of the described fits to the decay-time spectra recorded under ion-beam excitation are presented. In figure 5.7, graphical illustrations of the performed fits for the examples of the decay-time spectra $\mathbf{O2_{PMT}}$ (crystal Olga, ^{127}I, 29K, 400nm filter) and $\mathbf{O5_{PMT}}$ (crystal Olga, ^{16}O, 309K, 400nm filter) are shown. From these examples, it can be seen that the fit function describes the pulse shape of the scintillation light recorded under iodine-beam as well as oxygen-beam excitation reasonably well.

measurement	ion	T [K]	$R_{d-d}(T)$ [nm]	μ_{tot} [ns]	$N_{^{127}I}/N_{^{16}O}$	χ^2
$\mathbf{O1_{PMT}}$	^{127}I	298	2.058 ± 0.004	-26.890 ± 0.109	84.326 ± 0.241	1.35
$\mathbf{O2_{PMT}}$	^{127}I	29	2.84 ± 0.02	-25.26 ± 0.68	163.23 ± 1.72	1.74
$\mathbf{O3_{PMT}}$	^{127}I	298	fixed	-27.01 ± 0.15	79.46 ± 0.07	2.33
$\mathbf{O4_{PMT}}$	^{127}I	27	fixed	-26.26 ± 0.76	96.32 ± 0.16	1.49
$\mathbf{O5_{PMT}}$	^{16}O	309	fixed	-17.48 ± 0.21	69.48 ± 0.065	1.72
$\mathbf{O6_{PMT}}$	^{16}O	20	fixed	-21.61 ± 0.22	70.64 ± 0.12	1.02
$\mathbf{O7_{PMT}}$	^{16}O	300	fixed	-18.56 ± 0.12	345.40 ± 0.22	1.93
$\mathbf{O8_{PMT}}$	^{16}O	21	fixed	-21.50 ± 0.13	300.79 ± 0.42	3.89
$\mathbf{P1_{PMT}}$	^{127}I	308	fixed	-24.91 ± 0.15	103.29 ± 0.06	12.62
$\mathbf{P2_{PMT}}$	^{127}I	20	fixed	-37.34 ± 0.29	88.21 ± 0.17	10.84
$\mathbf{P3_{PMT}}$	^{16}O	302	fixed	-19.56 ± 0.12	187.02 ± 0.12	1.64
$\mathbf{P4_{PMT}}$	^{16}O	18	fixed	-21.53 ± 0.10	138.43 ± 0.02	14.44

Table 5.7: Results of the fits of the decay-time spectra recorded under ion-beam excitation: A description of the applied fit function and procedure can be found in section III/5.3.2. The room-temperature and low-temperature values for the Förster radius were determined with the fits to the decay-time spectra $\mathbf{O1_{PMT}}$ and $\mathbf{O2_{PMT}}$. These values were adopted as fixed values in the fits of all other decay-time spectra. For a discussion of the results, see the main text. The errors stated are the statistical errors from the fits. It has to be kept in mind that, due to the determination of the radial parameters of the ionization densities, corresponding systematical uncertainties are expected to be significantly larger.

From the examples of recorded decay-time spectra (black markers) and their respective fits (red lines) shown in figure 5.7, it can be seen that the fit function reproduces the pulse

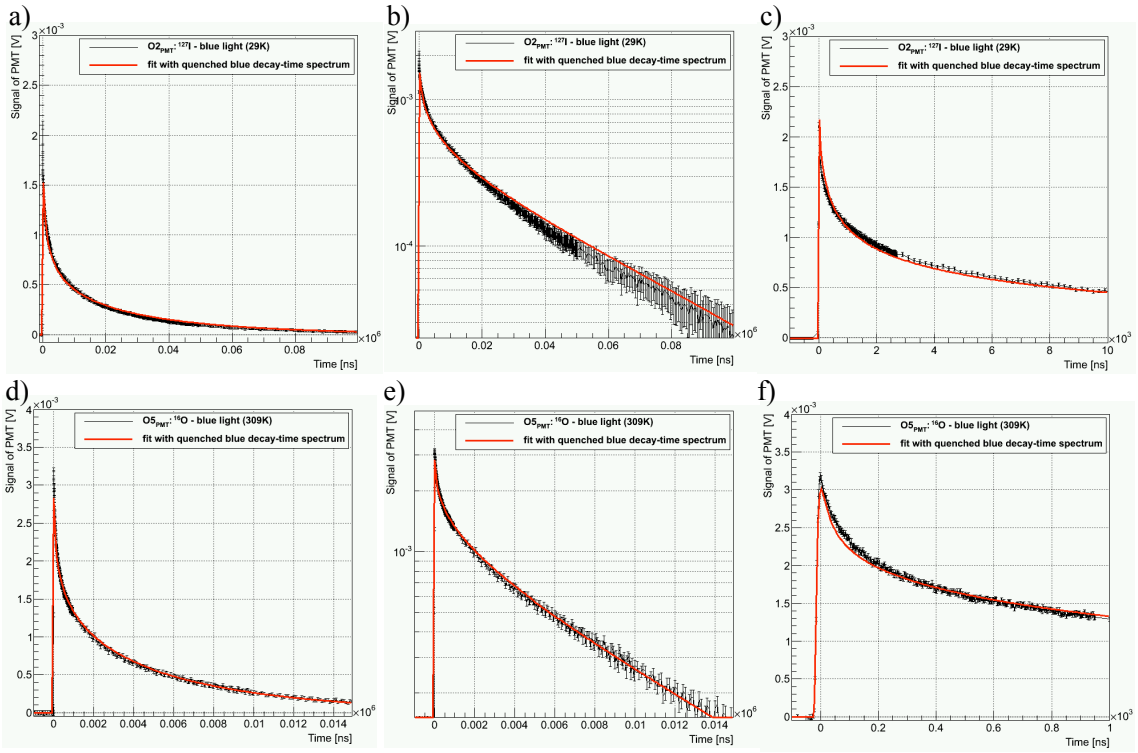

Figure 5.7: Decay-time spectra (black lines and markers with error bars) and corresponding fits with the quenched model fit-function (solid red lines) recorded for crystal Olga under ion-beam excitation: In panel a), b), c), the decay-time spectrum $\mathbf{O2_{PMT}}$ recorded under ^{127}I-beam excitation at $T \approx 29$K with the 400nm filter is shown. In panel d), e), f), the decay-time spectrum $\mathbf{O5_{PMT}}$ recorded under ^{16}O-beam excitation at $T \approx 309$K with the 400nm filter is shown. In panel a) and d), the respective complete ranges used for the fits are shown. In panel b) and e), a semi-logarithmical plot (y-axis) of the same data is shown to illustrate the non-exponentiality of the recorded decay-time spectra at the beginning of the pulses which is nicely reproduced by the fit functions. In panel c) and f), zoomed-in views to the beginning of the pulses are shown, respectively. From these figures, it can also be seen that the respective fit functions describe the data in a satisfying way. The spectra were preprocessed according to section III/4.6.2.

shapes of the decay-time spectra recorded under iodine-beam excitation (panel a to c) at low temperature as well as under oxygen-beam excitation (panel d to f) at room temperature in a satisfying way. Inspecting the zoomed-in view of the respective decay-time spectra depicted in panels c) and d), the observation can be made that at very short times t, the fit function does not perfectly describe the data: In panel c), t can be observed that the fit function slightly exceeds the values of the data points, in panel f), a small underestimation of the data by the fit function can be seen. These small deviations of the fit functions at short times t after the beginning of the pulses from the recorded pulse shapes is attributed to the rather simple description of the ionization-density distribution initially produced: Especially, the fact that the STE-distributions are assumed to exhibit no radial dependency, except for the division into an inner, densely ionized volume and an outer rarely ionized volume is a very simplified model. In fact, by choosing, e.g., a Gaussian profile for the radial ionizaton distribution in the inner part of the PIT volumes, the pulse

shape at the beginning of the pulses can be strongly influenced[8]. The smaller the width of such an Gaussian distribution, i.e., the more enhanced the STE-density distribution directly around the track of the primary interacting particle, the more distinct the initial sharp peak and the faster the light intensity is reduced at the beginning of the pulse. However, such a model would require the introduction of an additional parameter to describe the ionization distribution, i.e., the width of the Gaussian distribution. As is the case for the other radial parameters employed in the model, the width of such a Gaussian distribution could not be determined from the conducted simulations either, but would have to be estimated analogously to the other radial parameters. Due to this uncertainty in the determination of the radial parameters, it was attempted to use as few parameters as possible to describe the initially produced ionization distribution. Thus, the observed deviation of the model function from the recorded decay-time spectra is essentially attributed to the relatively simple modeling of the STE density distribution. Regardless of these small deviations, it can be observed that the overall shape of the decay-time spectra is very well reproduced by the model.

Regarding the results of the fits listed in table 5.7, it can be observed that the fits to three of the decay-time spectra recorded with crystal Philibert yielded quite large χ^2 values. When inspecting the individual decay-time spectra and their fits, it can be deduced that the comparably large χ^2 value for the decay-time spectrum $\mathbf{P4_{PMT}}$ can be attributed to the strongly rising baseline in this measurement which prevents an adequate description of the pulse shape by the model as, within the fit function, a constant baseline is assumed. For the decay-time spectra $\mathbf{P1_{PMT}}$ and $\mathbf{P2_{PMT}}$, it can be observed that, at the beginning of the pulses, an extremely fast decaying fraction of scintillation light was produced (especially well observable for $\mathbf{P2_{PMT}}$). Actually, when comparing the width of this almost Gaussian peak at the beginning of the pulses with the temporal width of the iodine-beam pulse (see section III/4.7.3), it can be seen that the pulse shapes of the scintillation light produced at the beginning of the decay-time spectra $\mathbf{P1_{PMT}}$ and $\mathbf{P2_{PMT}}$ exhibit the same width as the iodine-beam pulse used for excitation: In figure 5.8, the comparison of the pulse shapes of the iodine-beam pulse (panel a) recorded with the BaF_2 crystal (see section III/4.7.3), the decay-time spectrum $\mathbf{P2_{PMT}}$ (panel b) and the decay-time spectrum $\mathbf{O2_{PMT}}$ (panel c) as zoom into the region of the beginning of the pulses is shown. It should be noted that, in all three panels, the length of the x-axis roughly corresponds to 100ns so that the pulse shapes can be compared directly.
The resemblance of the pulse shapes of the iodine-beam pulse (rising part of the BaF_4 pulse in panel a) of figure 5.8, compare discussion in section III/4.7.3) and crystal Philibert is interpreted as being caused by a possibly unstable (temporarily increased) focussing of the iodine beam onto the $CaWO_4$ crystal: An increased focussing of the ion beam leads to iodine ions interacting so closely spaced in the crystal that STEs from tracks of different iodine ions aree produced close enough to each other to interact and quench each other. Such high densities of STEs lead to very fast decaying scintillation light at the beginning of the pulse with a minimum decay time as inherent from the non-negligible temporal

[8]It should be noted that choosing only one Gaussian distribution instead of the division into densely ionized inner and rarely ionized outer volume did not deliver pulse shapes with which the data could be described. For such an ionization distribution, always a much more distinct peak at the beginning of pulses was observed with which the data could not be described, even when strongly reducing the value of the Förster radius, e.g., to 0.6nm, which, partially compensates this effect. Regardless of the value for the Förster radius, the pulse shape produced by such an ionization distribution always exhibited clearly larger values at the beginning of the pulse in comparison to the data.

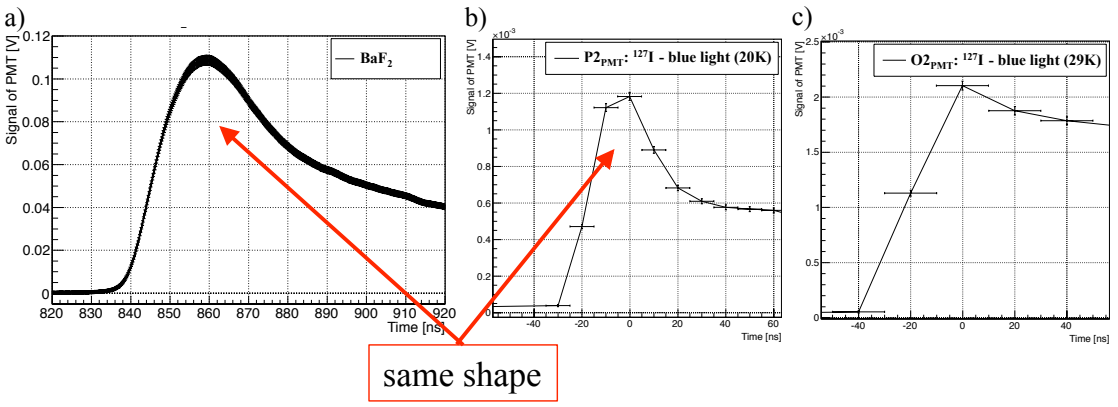

Figure 5.8: Comparison of the pulse shapes for short times t: In panel a), the iodine-beam pulse recorded with the BaF_2 crystal is shown (see section III/4.7.3). In panel b), the decay-time spectrum $\mathbf{P2_{PMT}}$ recorded with crystal Philibert under iodine-beam excitation (400nm filter at low temperature) and in panel c), the decay-time spectrum $\mathbf{O2_{PMT}}$ recorded with crystal Olga under iodine-beam excitation (400nm filter at low temperature) are shown. In each panel, the length of the x-axis roughly corresponds to 100ns so that the pulse shapes can be compared directly. Clearly, the resemblance of the pulse shapes recorded with the BaF_2 crystal and crystal Philibert can be seen. For crystal Olga, a much slower decay at the beginning of the pulse can be observed.

width of the excitation, i.e., the temporal width of the iodine-beam pulse. Thus, the unsatisfactory description of the decay-time spectra $\mathbf{P1_{PMT}}$ and $\mathbf{P2_{PMT}}$ is attributed to the occurrence of inter-track quenching between tracks of different iodine ions.

Apart from the three decay-time spectra discussed, with rather large χ^2 values, it can be seen from table 5.7, that all other decay-time spectra are well described by the developed model, using the same fixed values for the Förster radius (dependent on temperature) as determined by the first two fits to the decay-time spectra $\mathbf{O1_{PMT}}$ and $\mathbf{O2_{PMT}}$ as well as using the same fixed values for the radial parameters (dependent on the type of ion) as presented in table 5.6 (section III/5.3.2). This observation is regarded as an experimental validation of the developed model.

Hence, within the developed model and the performed analysis of the experiments, the values determined for the Förster radius amount to (errors stated correspond to the statistical errors from the fits):

$$R_{d-d}(T = 298\text{K}) = (2.058 \pm 0.004)\text{nm} \tag{5.21}$$

$$R_{d-d}(T = 29\text{K}) = (2.84 \pm 0.02)\text{nm} \tag{5.22}$$

It has to be noted that, as discussed in section III/5.3.2, these values were determined using several assumptions as well as values for several model parameters predetermined with the help of data from the literature. Thus, the values of the Förster radii derived in this way should be considered as estimates on the basis of the applied assumptions. Regardless of this uncertainty, as both values were determined using the same assumptions, i.e., especially, using the same radial distribution of the produced ionization density, it is expected that the relative size of these values can be qualitatively compared: From

these values and their small statistical errors resulting from the fits, it is deduced that the Förster radius at low temperatures is larger than the Förster radius at room temperature. This observation of an increased Förster radius for decreased temperature is in perfect agreement with the prediction of the model (compare section III/3.1.3).

Additionally, these values can be compared to values of the Förster radius for $CaWO_4$ stated in the literature (compare section III/3.1.3): The values determined in literature amount to 2.6nm or 2.93nm (at 300K) in [98] and [94], respectively, as well as to 4.34nm (at 8K) in [94]. It can be seen, that the values for the Förster radius determined within the present work are smaller in comparison to the values from the literature. This could, in principle, result from the discussed uncertainty of the determination of the radial parameters, i.e., possibly another set of parameters could be found, which describes the pulse shapes in an equivalent way, but with larger radial parameters and a correspondingly larger Förster radius. However, it should also be taken into account that, in [94], it is stated that the difference observed between the values obtained there, i.e., between the values of 2.93nm at 300K and of 4.34nm at 8K, is still within the error margins in [94]. Thus, comparable to the present work, also in [94], the absolute values of the Förster radii are afflicted with quite large uncertainties. Therefore, it can be concluded that, within the error margins, a satisfying agreement of the values of the Förster radii determined within the present work and the values from the literature can be observed.

5.4 Summary of the Results

In the following, a short summary of the most important results obtained from the analysis of the wavelength and decay-time spectra recorded under laser excitation as well as under ion-beam excitation in the context of the developed model is presented. It should be noted that, for this summary, also the discussion of the qualitative analysis of the data already performed in section III/4.7 is taken into account.

From the analysis of the wavelength spectra, the following observations and deductions can be made:

- The wavelength spectra recorded under different excitation modes comply with each other as predicted by the model.

- The shape determined for the wavelength spectra of the $CaWO_4$ scintillation light, especially of the blue sub-spectra, support the assumption that blue photons are absorbed at defect centers.

- The mean photon energies of the (blue, green and total) scintillation light of crystal

Olga and crystal Philibert are determined to amount to:

$$\begin{aligned}
\overline{E}_{Pb}^{Olga}(T \lesssim 50\text{K}) &= (2.853 \pm 0.003)\text{eV} & \overline{E}_{Pb}^{Phil}(T \lesssim 50\text{K}) &= (2.853 \pm 0.003)\text{eV} \\
\overline{E}_{Pg}^{Olga}(T \lesssim 50\text{K}) &= (2.692 \pm 0.006)\text{eV} & \overline{E}_{Pg}^{Phil}(T \lesssim 50\text{K}) &= (2.693 \pm 0.006)\text{eV} \\
\overline{E}_{Pb}^{Olga}(T \approx 300\text{K}) &= (2.861 \pm 0.003)\text{eV} & \overline{E}_{Pb}^{Phil}(T \approx 300\text{K}) &= (2.854 \pm 0.004)\text{eV} \\
\overline{E}_{Pg}^{Olga}(T \approx 300\text{K}) &= (2.670 \pm 0.007)\text{eV} & \overline{E}_{Pg}^{Phil}(T \approx 300\text{K}) &= (2.690 \pm 0.009)\text{eV} \\
\overline{E}_{P}^{Olga}(T \lesssim 50\text{K}) &= (2.82 \pm 0.03)\text{eV} & \overline{E}_{P}^{Phil}(T \lesssim 50\text{K}) &= (2.82 \pm 0.03)\text{eV} \\
\overline{E}_{P}^{Olga}(T \approx 300\text{K}) &= (2.83 \pm 0.03)\text{eV} & \overline{E}_{P}^{Phil}(T \approx 300\text{K}) &= (2.82 \pm 0.04)\text{eV}
\end{aligned} \tag{5.23}$$

- The broadening of the wavelength spectra at elevated temperatures can be explained by an interaction of an internal vibration mode of the $[WO_4]^{2-}$ center with the light emitting center.
- The temperature dependency of the blue-to-green ratio of scintillation light produced can be explained by the different temperature-dependent impacts of the radiative, non-radiative and migration processes of blue and green STEs.
- The fraction of blue photons reabsorbed at defect centers in crystal Olga and crystal Philibert can be estimated to amount to (using a scaling factor determined from the literature, compare section II/5.1.2):

$$F_{abs}^{Olga} \approx (18 \pm 1)\% \tag{5.24}$$

$$F_{abs}^{Phil} \approx (19 \pm 1)\% \tag{5.25}$$

- As predicted by the model, a larger relative amount of green scintillation light results in a smaller total amount of scintillation light produced.

From the analysis of the unquenched decay-time spectra, the following observations and deductions can be made:

- The scintillation-light decay-time spectra observed under laser excitation exhibit almost purely exponential pulse shapes.
- At room temperature, a delayed rise of a fraction of the scintillation light can be observed.
- The blue and green scintillation-light decay-time spectra exhibit both the same slow decay time, as predicted by the model.
- The defect density of crystal Olga could be estimated to amount roughly to

$$C_{\text{defects}}^{Olga} \approx (150 \pm 50)\text{ppm} \tag{5.26}$$

where it should be noted that, due to the described problems of determining the low-temperature value of the effective unquenched lifetime of green STEs, $\tau_2(T)$, from the recorded data, this value is afflicted with a large uncertainty.

- On the basis of the estimated value for $C_{\text{defects}}^{Olga}$ and from the fits to the data using the unquenched model prediction (as well as assuming values for some parameters of the unquenched model determined with the help of data from the literature), a complete set of parameters of the unquenched model is obtained for crystal Olga. These parameters describe all decay-time spectra of the blue and the green scintillation light as well as all wavelength spectra recorded for crystal Olga in a consistent way. With these parameters, the pulse shapes of the different decay-time spectra as well as the blue-to-green ratio of the scintillation light (determined from the wavelength spectra for the two temperatures investigated with the experiments) are well reproduced and explained.

- The intrinsic as well as the effective unquenched lifetimes of green STEs are smaller by at least two orders of magnitude than the intrinsic and the effective unquenched lifetimes of blue STEs, as predicted by the model.

- The comparison of various predictions of the complete unquenched model with data from the literature reveals an excellent agreement, validating the developed model (e.g., comparing the temperature-dependency of the amount of scintillation light generated as well as its decomposition into blue and green light or the temperature-dependency of the slow decay time of the $CaWO_4$ scintillation light with the effective unquenched lifetime of blue STEs).

From the analysis of the quenched decay-time spectra, the following observations and deductions can be made:

- As predicted by the model, the slow decay-time observed under particle excitation of $CaWO_4$ complies with the purely exponential decay time of the unquenched scintillation light, $\tau_1(T)$.

- On the basis of the pulse shape of the decay-time spectrum recorded under iodine-beam excitation of crystal Olga at low temperatures with the 400nm filter, the radial parameters of the produced ionization-density distribution were estimated. With these parameters, the determination of the radial parameters of a particle-induced ionization distribution for various particles of different types and with different energies is enabled (compare discussion in appendix B.3.10). Thus, using the values for the radial parameters determined in this way in combination with the results from the simulations with the SRIM program, the ionization-density distribution and, hence, the initially created STE-density distribution for different kinds of heavy, charged particles as primary interacting particles with different energies can be determined.

- From the fits of the decay-time spectra recorded for crystal Olga under iodine-beam excitation at low temperature and at room temperature (with the 400nm filter), values for the Förster radius of $CaWO_4$ were determined:

$$R_{d-d}(T = 298\text{K}) = (2.058 \pm 0.004)\text{nm} \tag{5.27}$$

$$R_{d-d}(T = 29\text{K}) = (2.84 \pm 0.02)\text{nm} \tag{5.28}$$

  where the errors stated correspond to the statistical errors from the fits and do not account for the systematical uncertainties of the determination of the Förster radius.

- The determined values are compatible with values for the Förster radius of $CaWO_4$ stated in the literature.

- As predicted by the model, the low-temperature value of the Förster radius is larger than the room-temperature value. In the following, the value determined for a temperature of $T = 29\text{K}$ is adopted as the value of the Förster radius for all temperatures $T \lesssim 29\text{K}$:

$$R_{d-d}(T \lesssim 29\text{K}) := (2.84 \pm 0.02)\text{nm} \tag{5.29}$$

- Using the determined values of the Förster radii as fixed values in the fits to all other decay-time spectra recorded under ion-beam excitation delivers good descriptions of the pulse shapes - except for two exceptional cases which can be explained consistently within the developed model. Hence, also the decay-time spectra recorded under oxygen-beam excitation or with crystal Philibert or with the 500nm filter (green light) are well described by the model. Thus, the prediction of the model that the Förster radius is a temperature-dependent parameter only and does not depend on the mode of excitation employed (different types of ions) is confirmed. The successful description of the pulse shapes of the iodine- and oxygen-particle induced scintillation-light decay-time spectra using the same fit function and the same Förster radius is, thus, considered as the experimental validation of the complete model for the scintillation-light generation and quenching developed within the present work.

Chapter 6

Application and Discussion of the Complete Model

In this chapter, the application and discussion of the comprehensive model for the scintillation-light generation and quenching in $CaWO_4$ developed within this work (see chapter III/3, including the complete set of parameters as determined in chapter III/5) is presented. In section III/6.1, the model is employed for the prediction of Quenching Factors of different particles interacting in $CaWO_4$ as defined and used in the CRESST experiment for the identification of the type of the interacting particle. The obtained results are discussed and compared to experimental results. In section III/6.2, the comparison of the developed model with existing models for the light generation and quenching in scintillators is presented and differences between the different approaches are pointed out. Limitations of the developed model and the determined set of parameters are referred to in section III/6.3 and possible improvements are suggested. In section III/6.4, the consequences that can be drawn from the complete model as well as its applicability to other scintillating materials are discussed.

6.1 Prediction of Quenching Factors

The model for the light generation and quenching in $CaWO_4$ developed in the present work (see chapter III/3), in combination with the complete set of parameters as determined in chapter III/5, can be employed to calculate Quenching Factors for different interacting particles with different energies in $CaWO_4$. It should be noted that the results of these calculations should be regarded as preliminary as, for the determination of the model parameters (in chapter III/5) and, thus, also for the calculation of the Quenching Factors presented in the following, values from the literature or estimates for important model parameters had to be adopted (compare sections III/3.3.2 and 5.4). For a discussion of possible improvements of this circumstance, see section III/6.3.

In the following, at first, the outline of the calculation of Quenching Factors using the developed model is presented and the important parameters of the model as well as their influence on the amount of generated scintillation light and, thus, on the Quenching Factors are discussed (see section III/6.1.1)). From this discussion, it will become clear that the defect density contained in the crystal not only influences the total amount of scintillation light generated, but also alters the Quenching Factors. Thus, it can be expected that the Quenching Factors for different $CaWO_4$ crystals differ from each other. In order

to investigate this effect, the calculation of the Quenching Factors for different interacting particles is not only performed with the set of parameters as determined for crystal Olga, but is additionally performed for a hypothetical *perfect crystal* containing no defects (at mK temperatures only, see discussion in section III/6.1.1).

Thereafter, the results for the light yields and for the Quenching Factors obtained for electrons, O, Ca and W ions as primary interacting particles in $CaWO_4$, with energies between 10keV and 1MeV, at mK temperatures as well as at room temperature are presented and discussed (for crystal Olga at room temperature and at mK temperatures, for the perfect crystal, at mK temperatures only). These particles were chosen as they represent the intrinsic recoil particles possible in $CaWO_4$ and, thus, account for the vast majority of events that can be observed in dark matter detectors (compare section III/2.1).

6.1.1 Calculation of Quenching Factors

As basis for the calculation of the light yields and Quenching Factors for different interacting particles in $CaWO_4$ in the context of the CRESST experiments, the definitions of these quantities are recalled (compare section I/2.2):

- The light yield of a particle *part* with energy E_{part}, $LY_{det}^{part}(E_{det})$, is defined as the ratio of the energy detected in the light detector, $L_{det}^{part}(E_{det})$ (in the form of scintillation light photons), and the amount of energy detected in the phonon detector, E_{det} (in the form of phonons), where the light yield for a 122keV γ-particle, $LY_{det}^{\gamma}(122\text{keV})$, is defined as unity. Thus, the light yield $LY_{det}^{part}(E_{det})$ can be expressed by the following relationships:

$$LY_{det}^{\gamma}(122\text{keV}) := 1 \tag{6.1}$$

$$LY_{det}^{part}(E_{det}, T) = \frac{L_{det}^{part}(E_{det}, T)}{E_{det}} \tag{6.2}$$

  where, here, in comparison to section I/2.2, a dependency of the light yield on temperature is indicated as, on the one hand, the amount of scintillation light produced for all particles differs for different temperatures and as, on the other hand, also the relative amounts of scintillation light produced for different particles, i.e., also the amount of scintillation light produced for particle *part* compared to a 122keV γ-particle, differs for different temperatures. This variation is due to the non-linearity of the dependency of the produced amount of scintillation light on the initially produced STE density (compare, e.g., equation 3.166 in section III/3.2.4).

- The Quenching Factor of a particle *part* with the energy E_{part}, $QF^{part}(E_{det})$, is defined by the mean light yield of a particle *part* with energy E_{part} relative to the mean light yield of an electron interaction depositing the same energy E_{det} in the phonon channel of a CRESST detector module. The expression *mean* is used to underline that the Quenching Factor is not a quantity that can be assigned to one event caused by one interacting particle in a CRESST detector module, but describes the mean of the light-yield band (in the light-yield energy plane, compare figure 2.2 in section I/2.2) of all events by particles of type *part* relative to the mean of the light-yield band of electron-recoil events. Thus, the Quenching Factor $QF^{part}(E_{det}, T)$ is

expressed by:

$$QF^{part}(E_{det},T) := \frac{\overline{LY_{det}^{part}(E_{det},T)}}{\overline{LY_{det}^{e^-}(E_{det},T)}} = \frac{\overline{L_{det}^{part}(E_{det},T)}}{\overline{L_{det}^{e^-}(E_{det},T)}} \tag{6.3}$$

It should be noted that, due to the method used within the present work to determine the ionization-density distribution of a particle *part* with energy E_{part}, automatically a mean light yield will be calculated: The ionization-density distribution caused by a primary interacting particle is determined as the typical (mean) distribution of several thousands of such interacting particles (on the basis of simulations of several thousands of such primary interacting particles, compare section III/3.1.2 and appendix B.3). Therefore, in the following, the labeling of the mean quantities (overline) for the light yield and the produced amount of scintillation light in the calculation of the Quenching Factors (equation 6.3) will no longer be used explicitly. In addition, from equation 6.3, it can be seen that the *detected* amount of scintillation light in the expression of the Quenching Factor can be replaced by the *produced* amount of scintillation light which can be calculated with the developed model: The factor describing the detection efficiency of the light detector in a CRESST detector module multiplied with the produced amount of scintillation light yields the detected amount of scintillation light[1]. Hence, this factor appears in the nominator and denominator of equation 6.3 and, hence, cancels out[2].

As can be seen from equation 6.3, for the calculation of the Quenching Factor of a primary interacting particle with energy E_{part}, $QF^{part}(E_{det})$, the amount of scintillation light created for the regarded particle, $L_{det}^{part}(E_{det})$, as well as the amount of scintillation light created for an electron recoil event for which the same energy E_{det} is detected in the phonon channel is required. In this context, it has to be noted that, due to the different amounts of scintillation light produced for different types of interacting particles, different fractions of the primarily deposited energy E_{part} escape the crystal in the form of scintillation light. Thus, for different interacting particles depositing the same amount of energy, E_{part}, in the crystal, different fractions of the deposited energy remain within the crystal and can be detected in the phonon channel of a CRESST detector module. This effect is generally referred to as "phonon quenching" (see e.g. [108]) and has to be taken into account if calculated Quenching Factors are to be compared with experimental results.

Thus, in summary, for the calculation of the Quenching Factors, the following expression containing the amounts of scintillation light produced as predicted by the model, $L_{tot}^{q}(E_{part},T)$, can be used:

$$QF^{part}(E_{det},T) := \frac{L_{tot}^{q}(E_{part},T)}{L_{tot}^{q}(E_{el},T)} \tag{6.4}$$

[1] In this context, it should be noted that the produced amount of scintillation light as calculated with the model corresponds to the amount of scintillation light escaping the crystal (compare equation 3.94 in section III/3.2.4).

[2] This can be assumed as no differences in the detection efficiency of the light detector for the scintillation light created by different interacting particles has to be expected: On the one hand, no significant dependencies of the detected amount of light on the position of the particle interaction in the $CaWO_4$ crystal have to be expected (compare section III/2.2.4). On the other hand, the wavelength spectrum of the created scintillation light was shown to be independent of the used excitation mode (compare section III/4.7.1) and, thus, a possibly varying detection efficiency of the light detector for photons of different energies would have no impact.

with the condition that the energy of the particle, E_{part}, and of the electron, E_{el}, are chosen such that the amount of energy deposited in the phonon channel, i.e., the amount of energy not leaving the crystal in the form of scintillation photons, is equal.

In the following, at first, the basic calculation of the amount of scintillation light generated is presented. In this context, a short compilation of the parameters required to perform the calculation of Quenching Factors as well as a short explanation of their impact on the amount of light generated for different interacting particles and, thus, on the Quenching Factors is presented. At the end of this section, the method employed to account for the so-called phonon quenching will be described.

Amount of Scintillation Light Produced

From the discussion of the predictions of the model in section III/3.2.4, it can be seen that the model can be utilized to calculate the decay-time spectrum of the scintillation light, i.e., the sum of the blue and the green decay-time spectra produced by different interacting particles. By integrating the calculated pulse shape over time, the amount of scintillation light generated can be deduced. Actually, as was shown in the deduction of the quenched model description, the total number of photons generated can be calculated on the basis of the blue scintillation-light decay-time spectrum, $P_b^q(E_{part}, T)$, only (compare equation 3.161 in section III/3.2.4 and the corresponding discussion). Utilizing additionally equation 3.163 for the total amount of scintillation light, $L_{tot}^q(E_{part}, T)$, as well as equations 3.148 and 3.154 (all equations from section III/3.2.4) to express the blue-to-green ratio of the light produced, $R_{b-g}(T)$, and the relationship between the total mean photon energy $\overline{E}_P(T)$ and the mean green and mean blue photon energies discussed in section III/5.1.2, the following expression for $L_{tot}^q(E_{part}, T)$ can be derived:

$$L_{tot}^q(E_{part}, T) = \overline{E}_P(T) \cdot \left(1 + \frac{1}{R_{b-g}(T)}\right) \cdot P_b^q(E_{part}, T) \tag{6.5}$$

where $P_b^q(E_{part}, T)$ is defined as the integral of the blue decay-time spectrum $P_g^q(E_{part}, T, t)$ (compare equation 3.161 in section III/3.2.4). The decay-time spectrum of the blue photons, $P_g^q(E_{part}, T, t)$ corresponds to the sum of the decay-time spectra produced by the blue STEs within the various sub-volumes (PIT and Rec volumes) of the complete excited volume (compare, e.g., equation 3.166 in section III/3.2.4). From these expressions, it can be deduced that the total amount of scintillation light produced depends on the following parameters (only major parameters listed):

- $R_{d-d}(T)$, the Förster radius: As discussed in section III/3.2.4, the size of the Förster radius determines the mutual interaction probability of blue STEs and, thus, the impact of the Förster interaction on the amount of light generated. It should be noted that the amount of scintillation light created and, thus, the Quenching Factor does not depend linearly on the size of the Förster radius (compare, e.g., equations 3.166 and 3.167 in section III/3.2.4). Therefore, a different value of the Förster radius results in different values of the Quenching Factor for one particle as the Quenching Factor is defined as a relative quantity depending on the impact of the quenching effect onto the amount of light created for the regarded particle as well as onto the amount of light for electron recoils. From section III/5.4, it can be seen that, within the present work, the following values for the Förster radius of $CaWO_4$

were determined:

$$R_{d-d}(T = 298\text{K}) = 2.058\text{nm} \tag{6.6}$$

$$R_{d-d}(T \lesssim 29\text{K}) = 2.84\text{nm} \tag{6.7}$$

where it should be kept in mind that, for the deduction of these values, several assumptions and estimations were made. In addition, it should be recalled that the Förster radius is assumed to be a temperature-dependent parameter only, i.e. it is supposed to be the same for all $CaWO_4$ single crystals. In fact, the Förster radius could show small variances for different crystals containing highly different defect densities. This can be explained by the fact that, as expressed by equation 3.70 in section III/3.1.3, the Förster radius depends on the emission and absorption spectrum as well as on the radiative branching ratio of the blue STEs. In good approximation, the intrinsic wavelength spectrum of the produced blue photons, i.e., the spectrum of the photons produced before part of them is potentially reabsorbed at defect centers, should be the same for all $CaWO_4$ single crystals, independently of the defect density contained in the crystal. This is assumed as this intrinsic emission spectrum is a feature of the electronic structure of the undisturbed crystal lattice. The same should hold true for the absorption spectrum of blue STEs. However, if a $CaWO_4$ crystal contains a very large number of defects, the radiative branching ratio changes due to the increased probability of migration to defect centers in comparison to the radiative decay (for temperatures at which the migration process is active, i.e., $T \gtrsim 5\text{K}$, compare equations 3.63 and 3.83 in section III/3.1.3 as well as the discussion in section III/3.2.1). Thus, for different $CaWO_4$ crystals with different defect densities, in principle, the Förster radius at $T \gtrsim 5\text{K}$ is different. For $T \lesssim 5\text{K}$, the radiative branching ratio is expected to be unity, independently of the defect density, and, hence, the Förster radius should not depend on the defect density. However, due to the dependency of the Förster radius on the 6th root of the branching ratio, this effect is comparably small, even at room temperature: For example, the 6th root of the radiative branching ratios at 298K for a perfect $CaWO_4$ crystal containing no defects, i.e., 0ppm (which is, of course, not realistic), and for crystal Olga ($C_{\text{defects}}^{Olga} \approx 150\text{ppm}$) only amounts to a factor of ~ 1.1. Thus, in first-order approximation, this effect is expected to be negligible, and, hence, the Förster radius is assumed to be the same for all $CaWO_4$ single crystals.

- $R_{b-g}(T)$, the blue-to-green ratio of the produced scintillation light, and $\overline{E}_P^{Olga}(T)$, the mean photon energy: These quantities reflect the impact of the varying composition of the wavelength spectrum and photon energy on the amount of scintillation light produced (in terms of energy). The knowledge of $R_{b-g}(T)$ allows to calculate the total amount of scintillation light produced without the need to explicitly calculate the decay-time spectrum of the green photons (compare equation 6.5). The values determined for crystal Olga within the present work amount to (compare table 5.2 in section III/5.1.2):

$$R_{b-g}^{Olga}(T = 298\text{K}) = 4.5 \tag{6.8}$$

$$\overline{E}_P^{Olga}(T \approx 300\text{K}) = 2.83\text{eV} \tag{6.9}$$

$$R_{b-g}^{Olga}(T \lesssim 29\text{K}) = 4.0 \tag{6.10}$$

$$\overline{E}_P^{Olga}(T \lesssim 50\text{K}) = 2.82\text{eV} \tag{6.11}$$

- $n_{bSTE}^{form\,0}(E_{part}, \mathbf{x})$, the position-dependent, blue STE-density distribution initially created in the energy-deposition process of the primary interacting particle (and its recoils): As discussed in section III/3.2.4, the spatial distribution of the blue STEs is equally important for the amount of light generated as is the Förster radius (the closer positioned the STEs to each other, the larger the probability that they interact with each other). As is the case for the Förster radius, the amount of scintillation light generated and, thus, the Quenching Factors do not depend linearly on this quantity. As discussed in detail in section III/3.1.2 and appendix B.3, $n_{bSTE}^{form\,0}(E_{part})$ is determined using simulations with the programs CASINO [43] (for electrons) and SRIM [42] (for ions) as well as making use of a geometrical model developed for the ionization-density distribution generated in the energy-loss process of the primary interacting particle. For this description, several parameters are required. It should be noted that the radial parameters of this geometrical model, i.e., the various inner and outer radii as well as the division of the energy deposited in ionization between inner and outer volumes, cannot be determined from the simulations. The method used to determine these quantities can be found in appendices B.3.9 and B.3.10 for electrons and for heavy, charged particles, respectively, and is based on the parameters of the model determined in the analysis of the experiments performed within this work (see section III/5.3):
  - For electrons, only the radius of the ionization distribution $r_{Rec_{el}}(E_{el})$ has to be determined. As discussed in appendix B.3.9, for this purpose, the complete model with all parameters determined is utilized to calculate the amount of scintillation light created for a 100keV electron at mK temperatures. A reference value for $L_{tot}^{q}(E_{el} = 100\text{keV}, mK)$ can be determined with good accuracy from the literature: From [13], the light yield of 100keV electrons at mK temperatures $LY_{det}^{e^-}(E_{el} = 100\text{keV})$ (determined using a CRESST detector module) in comparison to the light yield of 122keV γ-events can be determined to amounts to 1.03. In addition, from the discussion in section III/2.2.4, it can be seen that the absolute amount of scintillation light created for γ particles at mK temperatures amount to 6.0%. Hence, adopting the value of 6.0% for the light yield of 122keV γ-events at mK temperatures, it can be deduced that the absolute amount of scintillation light created for a 100keV electron is given by: $1.03 \cdot 6.0\% \cdot 100\text{keV} = 6.2\% \cdot 100\text{keV} = 6.2\text{keV}$. Using this reference value as well as the complete model, the size of $r_{Rec_{el}}(E_{el} = 100\text{keV})$ can be adjusted such that the calculated amount of scintillation light produced corresponds to 6.2keV. The value determined in this way amounts to:

    $$r_{Rec_{el}}(E_{el} = 100\text{keV}) = 8.44\text{nm} \tag{6.12}$$

    This means that, using this value for the calculation of the total amount of scintillation light produced for a 100keV electron with the developed model at mK temperatures, results in 6.2keV of the energy escaping the crystal as scintillation-light photons. The size of this radius for electrons with different energies is then calculated on the basis of this value and of the assumed dependency of $r_{Rec_{el}}(E_{el})$ on the energy of the primary interacting electron as described in appendix B.3.9.
  - For O, Ca and W ions, the parameters determined from the analysis of the iodine-beam measurements (table 5.6 in section III/5.3.2) as well as the depen-

dency of the radial parameters on the energy and type of the primary interacting particle as described in detail in appendix B.3.10 are employed to calculate the values of these parameters.

- F_{e^-trap}, the fraction of electrons captured by electron traps in the initial creation process of blue STE: The size of F_{e^-trap} determines the number of initially created STEs and, thus, the density of the initially created STEs (compare equations 3.11 and 3.14 in section III/3.1.2). Thus, on the one hand, the smaller F_{e^-trap}, the more STEs are produced that can decay radiatively. Therefore, potentially more light is produced. However, on the other hand, the size of this parameter determines the density of the initially created STEs and, thus, influences the probability of the Förster interaction to occur: The smaller F_{e^-trap}, the larger the density of the initially created STEs, and, thus, the larger the probability for them to interact via the Förster interaction. Hence, as the amount of light produced and, thus, also the Quenching Factors do not depend linearly on the density of initially created STEs, i.e. not linearly on the size of F_{e^-trap}, it can be expected that the size of F_{e^-trap} has an impact on the amount of scintillation light created as well as on the Quenching Factors. In this context, it should be taken into account that the size of F_{e^-trap}, i.e., the fraction of electrons becoming trapped in the initial STE formation process, is ascribed to the density of defects contained in the crystal (electron traps are assumed to be located at defect centers, compare equation 3.8 in section III/3.1.2). Therefore, the parameter F_{e^-trap} and, hence, also the Quenching Factors can be expected to be different for different $CaWO_4$ crystals with different defect densities. Thus, as the parameter F_{e^-trap} is not only expected to influence the quenching process, but also the total amount of scintillation light generated (by changing the absolute number of STEs initially created), it is expected that a relationship between the Quenching Factors and the absolute light yield of $CaWO_4$ crystals exists. The value of F_{e^-trap} utilized within the present work is determined on the basis of am estimate of the impact of the quenching effect on the light yield of electrons/γ-particles in $CaWO_4$ (see appendix B.13). The estimated value amounts to:

$$F_{e^-trap}^{Olga} := 37.5\% \tag{6.13}$$

where it should be taken into account that this value only corresponds to a very rough estimate. In fact, as the impact of this parameter on the amount of scintillation light produced as well as on the quenching effect is quite distinct, it would be very advantageous to obtain a value for this parameter on the basis of independent measurements. For a discussion of such a determination possibility, see section III/6.3.

As can be seen from this discussion, it is expected that the Quenching Factors for different interacting particles in $CaWO_4$ depend on the defect density of the investigated crystal. In order to investigate this prediction, the calculation of the light yields and Quenching Factors were not only performed using the set of model parameters determined for crystal Olga, but also for a hypothetical, perfect crystal containing no defects, i.e., for

$$F_{e^-trap}^{pc} := 0 \tag{6.14}$$

where the superscript *pc* is used as the label for the *perfect crystal*. This calculation was performed for mK temperatures as, for such small temperatures, the only model parameters that have to be additionally adjusted are the blue-to-green ratio of the produced

light

$$R^{pc}_{b-g}(T \lesssim 29\text{K}) \rightarrow \infty \tag{6.15}$$

as no green photons are produced, as well as the mean energy of the created photons,

$$\overline{E}^{pc}_{P}(mK) = \overline{E}^{Olga}_{Pb}(mK) = 2.85\text{eV} \tag{6.16}$$

as only blue photons are produced. The results from these calculations are also presented in section III/6.1.2.

Phonon Quenching

As discussed above, in order to calculate Quenching Factors as they would be determined in the CRESST experiment, the so-called phonon-quenching effect has to be taken into account. This effect is accounted for as explained for the following example:

- It is assumed that the energy deposited by an interacting particle in $CaWO_4$ either is detected in the form of phonons in the phonon channel (PC) or escapes the crystal in the form of scintillation-light photons (not all of these photons are detected with the light detector).

- The produced amount of scintillation light was calculated, e.g, for electrons and W ions, both as primary interacting particles at mK temperatures with an energy of $E_{part} = 100\text{keV}$.

- As the energy calibration of the CRESST phonon detectors is performed with 122keV γ-events in the electron-recoil band, the energy detected in the PC has to be referred to the energy an electron deposits in the $CaWO_4$ crystal in the form of phonons. Therefore, the energy detected in the PC for the 100keV electron is calculated. This can be performed as the amount of scintillation light created (escaping the crystal) is calculated with the model, $L^{q}_{tot}(E_{el} = 100\text{keV}, \text{mK}) = 6.2\text{keV}$. Thus, the energy detected in the PC for a 100keV electron recoil amounts to 93.8keV.

- For a W ion as primary interacting particle with 100keV energy, the fraction of energy detected in the PC, i.e., the fraction that does not escape the crystal as photons, is calculated to amount to 99.8%. This implies that, for a 100keV W ion, only an amount of $L^{q}_{tot}(E_W = 100\text{keV}, \text{mK}) = 0.20\text{keV}$ of the energy is escaping the crystal in form of photons.

- Hence, the energy a W ion would need to have in order to deposit 93.8keV in the PC amounts to $\frac{93.8\text{keV}}{99.8\%} = 94.0\text{keV}$. This means that the W ion for which the same energy is detected in the PC as for a 100keV electron, only has a primary particle energy of $E_{part} = 94.0\text{keV}$.

- As, for a 100keV W ion, the fraction of energy used to produce photons escaping the crystal is known (0.20%) and as it can be assumed that this fraction is the same for the 100keV and the 94.0keV W ion, the amount of energy escaping the crystal as photons can also be calculated for the 94.0keV W ion. This energy amounts to $94.0\text{keV} \cdot 0.20\% = 0.188\text{keV}$.

- Thus, for the Quenching-Factor calculation with equation 6.4, the amount of scintillation light produced for W ions and electrons with the same amount of energy detected in the *PC* (attributed to 100keV particles due to the gauging of the energy axis using electron events), amounts to 6.2keV and 0.188keV for the electron and the W ion, respectively.
- With these values, the Quenching Factor as it would be observed in the CRESST experiment can be calculated: $QF^{part}(E_W = 100\text{keV}, \text{mK}) = \frac{0.188\text{keV}}{6.2\text{keV}} = 3.03\%$.
- For comparison: For the 100keV W ion, an energy of 0.200keV escapes the crystal in the form of photons. The Quenching Factor that would be calculated using this value (i.e., neglecting the phonon-quenching effect) amounts to: 3.23% and, thus, would be $\sim 6.5\%$ larger than the Quenching Factor observed in the experiment.

This method can be applied to all calculated Quenching Factors as, for each energy of primary particles considered within the present work, always the information on the amount of energy of equally energetic electrons that is detected in the phonon channel was calculated.

6.1.2 Results

With the discussed equations and the method introduced to account for the phonon-quenching effect, the Quenching Factors for crystal Olga for electrons, O, Ca and W ions as primary interacting particles with energies between 10keV and 1MeV at mK temperatures and at room temperature were calculated. In addition, as discussed in section III/6.1.1, the calculations were performed for a hypothetical *perfect crystal* at mK temperatures. The results from these calculations are presented and discussed in the following. Considering the results of all of these calculations, it should always be kept in mind that, in order to obtain the full set of parameters of the model, assumptions concerning the values of several model parameters had to be made. However, as the influence of these systematic uncertainties was not determined, no errors are stated in the following.

Absolute Light Yields: Results

As a first result, the absolute light yields of 122keV γ-particles are considered as these values were used for gauging the relative light-yield scale of all other results:

$$L_{tot}^{q\,Olga}(E_\gamma = 122.06\text{keV}, 298\text{K}) = 5.9\% \cdot 122\text{keV} \tag{6.17}$$

$$L_{tot}^{q\,Olga}(E_\gamma = 122.06\text{keV}, \text{mK}) = 5.1\% \cdot 122\text{keV} \tag{6.18}$$

$$L_{tot}^{q\,pc}(E_\gamma = 122.06\text{keV}, \text{mK}) = 7.3\% \cdot 122\text{keV} \tag{6.19}$$

Absolute Light Yields: Discussion

As can be seen from equation 6.17, the absolute light yield of crystal Olga calculated for 122keV γ-particles at mK temperatures nicely complies with the value of 6.0% as determined on the basis of results reported in the literature (compare section III/2.2.4). It should be noted that this agreement is partially caused by the method with which the radial parameters of the ionization distribution of electrons were determined (see equation 6.12 in section III/6.1.1). However, in this method, the radius of the ionization distribution for a 100keV electron was fixed using a value of the absolute light yield for

100keV electrons determined on the basis of data from the literature. Hence, the light yield of 122keV γ events was not used directly as a reference point. Thus, the observed agreement also validates the method with which the ionization distribution of 122keV γ-particle was modeled (compare appendix B.12). However, considering the value determined for the absolute light yields of 122keV γ-particles at room temperature (equation 6.18) and comparing it to the value of 3.3% as determined on the basis of results reported in the literature (compare section III/2.2.4), it can be seen that the model predicts a significantly larger amount of light produced as is observed. This disagreement is attributed to two effects:

- On the one hand, the determination of the parameters of the unquenched model was performed on the basis of the assumption that the unquenched light yield at room temperature is smaller by a factor of 1.8 than the unquenched light yield at low temperatures (compare equation 3.188 in section III/3.3.2). However, the demanded difference exactly corresponds to the difference of the light yields expected for γ-particles at room temperature and at low temperatures. Thus, all model parameters, i.e., also the size of the radiative decay time of blue STEs which determines the unquenched amount of blue scintillation light produced, are determined such that the unquenched light yield changes by a factor of 1.8. However, as, additionally to the radiative branching ratio also the Förster radius changes with temperature, i.e., becomes smaller for increasing temperature (compare section III/3.3.2), the observed change in the amount of scintillation light created for a γ-particle is additionally caused by a decreasing efficiency of the Förster interaction. Therefore, in reality, the change in the amount of unquenched scintillation light is larger than assumed in section III/3.3.2. Introducing a larger change of the unquenched light yield into the model assumptions would lead to a decreased radiative efficiency at room temperature, i.e., also to a smaller amount of scintillation light produced for the 1222keV γ-particle at room temperature.

- On the other hand, it should be noted that the migration of blue STEs to other intrinsic centers was not included in the model (compare section III/3.1.3). However, the diffusion of blue STEs could either result in a weakening of the quenching effect at room temperature compared to low temperatures as the STEs can diffuse away from each other and, in this way, escape the quenching effect. Or, the diffusion could lead to an increased rate of mutual encounter between STEs (in their diffusion process) which would lead to an enlarged probability for the Förster interaction to occur and, therefore, to an enlarged quenching effect at room temperature. Hence, dependent on which one of these effects is more important, the blue STE diffusion could lead to an enhanced quenching probability at room temperature or to a decreased quenching probability at room temperature compared to low temperatures. Such an effect, if its extent and impact was known, could be, in a first step, included into the model by reducing or enlarging the extent of the excited volume at room tempeature compared to the one at low temperatures, i.e. the diffusion effect would be included as an "effective" change of the blue STE density.

However, as the impact of the blue STE diffusion cannot be specified and as the impact of the first effect is expected to be much larger, it is assumed in the following that the disagreement of the room-temperature value is caused by the incorrect assignment of the unquenched light yield. It should be noted that, by attributing the too large value of $L_{tot}^{q\,Olga}(E_\gamma = 122.06\text{keV}, \text{mK})$ to the too efficient radiative decay of blue STEs at room

temperature (incorrect unquenched light yield), this influences the light yields of all particles at room temperature in the same way, i.e., linearly scaled. Thus, as Quenching Factors are relative values of light yields to each other, they are not influenced by this incorrect assignment of the absolute light yields.

The value of the absolute light yield of the hypothetical perfect crystal calculated for 122keV γ-particles at mK temperatures it can be seen that it is larger than the corresponding value of crystal Olga. This reflects the expected increase in light yield due to neglecting the existence of electron traps that could capture electrons.

Relative Light Yields and Quenching Factors: Results

As discussed in section III/6.1.1, the values of the absolute light yields of 122keV γ-particles are used as reference points for the light-yield determination. In table 6.1, the energy-dependent Quenching Factors determined on the basis of the light yields calculated with the model as well as the mean values of the Quenching Factors calculated by averaging over the different values at the different energies are shown.

E_{part} [keV]	crystal Olga 298K			crystal Olga mK			*perfect crystal* mK		
	QF^O	QF^{Ca}	QF^W	QF^O	QF^{Ca}	QF^W	QF^O	QF^{Ca}	QF^W
10	13.51%	7.91%	6.20%	12.58%	7.03%	5.26%	12.08%	6.65%	4.90%
20	13.13%	7.23%	5.78%	11.75%	6.16%	4.74%	11.00%	5.73%	4.31%
50	13.17%	6.82%	4.84%	11.06%	5.50%	3.68%	10.20%	5.01%	3.31%
100	12.53%	6.83%	4.31%	10.04%	5.24%	3.12%	9.07%	4.69%	2.75%
200	11.70%	7.16%	4.15%	9.12%	5.33%	2.91%	8.15%	4.72%	2.54%
500	9.97%	7.10%	4.19%	7.78%	5.06%	2.71%	6.95%	4.43%	2.34%
1000	9.07%	6.43%	4.01%	7.68%	4.42%	2.62%	7.07%	3.82%	2.24%
$\overline{QF^{part}}$	12.53%	7.10%	4.31%	10.04%	5.33%	3.12%	9.07%	4.72%	2.75%

Table 6.1: Results from the Quenching Factor calculations: The values are calculated on the basis of the light yields of the different particles as primary interacting particles relative to the light yield of a 122keV γ-particle. The values presented in columns two to seven correspond to the Quenching Factors as obtained from the calculations with the model and using the set of parameters for crystal Olga. The values in columns two to four correspond to the room-temperature values, the values in the columns five to seven correspond to the values calculated for mK temperatures. The values in columns eight to ten correspond to the values obtained with the model when inserting the parameters as suggested for a perfect crystal without defects, compare (section III/6.1.1).

In figure 6.1, the corresponding light yields of electrons (blue asterisks), O (black circles), Ca (green squares) and W ions (red triangles), relative to the light yield of 122keV γ-particles (violet star) are shown: In panel a) and b), the light yields calculated for crystal Olga at mK temperatures, in panel c) and d), the light yields calculated for crystal Olga at room temperature are depicted and in panel e) and f), the light yields calculated for the *perfect crystal* (without any defects) at mK temperatures are depicted.

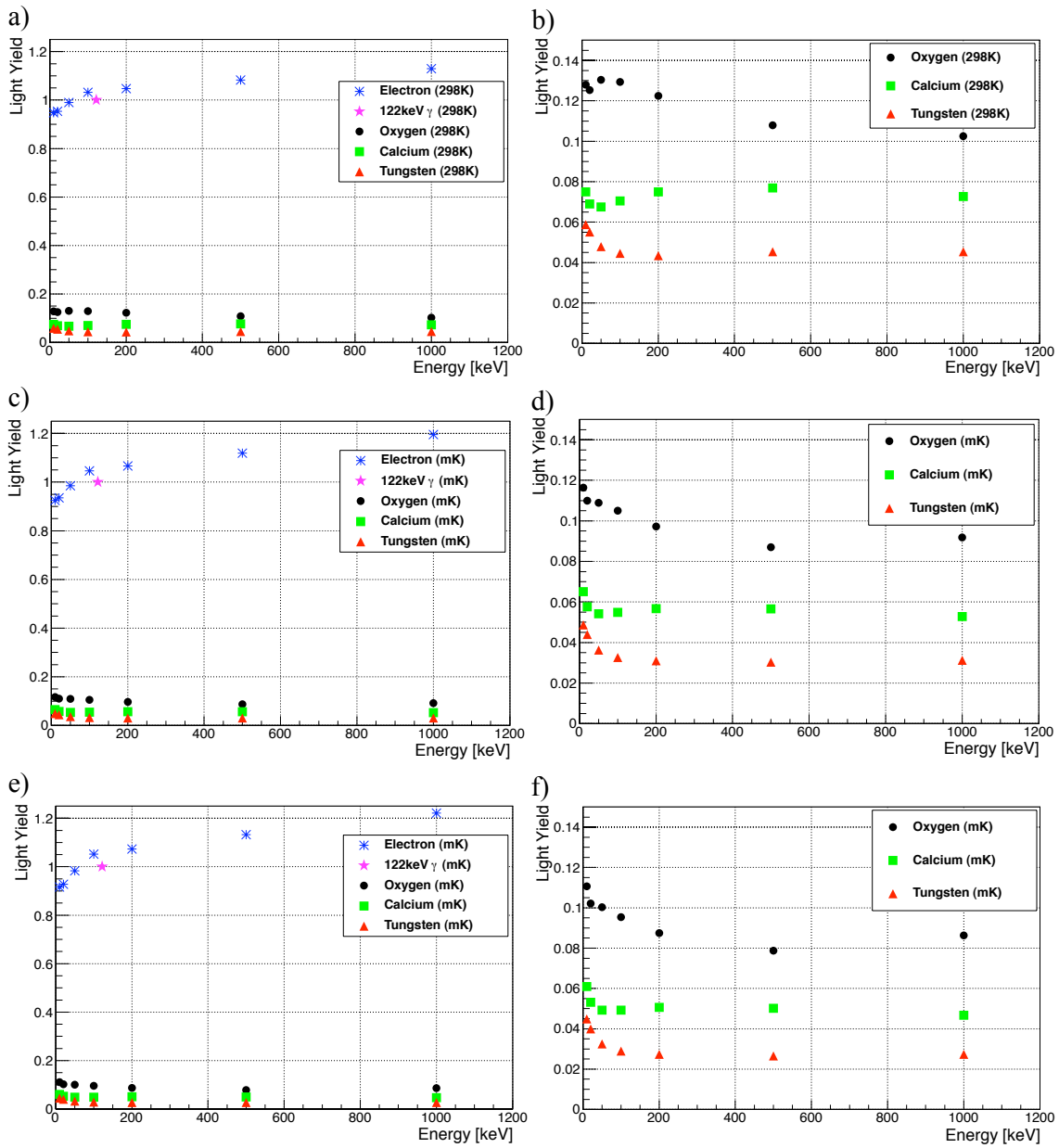

Figure 6.1: Light yields of electrons, O, Ca and W ions with energies between 10keV and 1MeV in the light-yield energy plane relative to the light yields of 122keV γ particles as calculated with the complete model: The phonon-quenching effect was considered in the calculations as described in the main text. In panels a) and b), the light yields calculated for crystal Olga at room temperature can be seen. In panels c) and d), the light yields calculated for crystal Olga at mK temperatures are shown. In panels e) and f), the light yields calculated for a hypothetical, defect-free crystal are shown. In panels a), c) and d) the complete light-yield energy plane is depicted. In panels b), d) and f), a zoom to the light-yield range of the nuclear recoils is shown.

Relative Light Yields and Quenching Factors: Discussion

Considering the light yields and Quenching Factors as calculated with the model (shown in figure 6.1 and table 6.1, respectively) as well as comparing the determined values to

values from the literature, the following observations and deductions can be made:

- The light yield of electrons decreases for decreasing energy of the primary electron. This trend is more significant for electron energies below $\sim$ 100keV than for electron energies larger than 100keV and can be attributed to the method chosen (and motivated) for the modeling of the ionization-density distribution caused by electrons (compare appendix B.3.9). For a comparison of this result, in figure 6.2, the energy-dependent light yield of electrons from [13] as measured in the CRESST experiment (exemplarily for one CRESST detector module) is depicted. The energy-

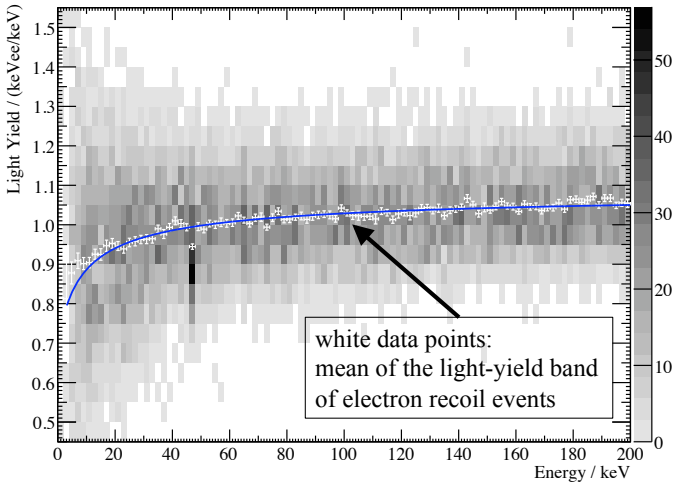

Figure 6.2: Light-yield distribution of electron-recoil events in the energy region from 0keV to 200keV, in (2keV $\times$ (0.05keV$_{ee}$/keV)) bins as recorded with a CRESST detector module in the light-yield energy plane (figure adopted from [13]). For the definition of the unit keV$_{ee}$ (electron equivalent), see section III/2.2. A zoom to the light-yield range of electrons is depicted. The scale on the right-hand side of the figure indicates the number of events in each The white data points mark the weighted mean of the light yield in each 2keV bin, the blue line indicates a fit to the mean light yields as performed in [13].

dependency of the light yield of electron-recoil events as recorded with a CRESST detector module (at mK temperatures) in figure 6.2 has to be compared to the blue asterisks in panel c) in figure 6.1 (in the energy range from 10keV to 200keV) which depicts the (phonon-quenching corrected) light yield as calculated with the model for crystal Olga at mK temperatures. It can be observed that both quantities, the measured light yield as well as the calculated light yield, decrease for decreasing energy. Clearly, a very satisfying agreement of the model prediction with the recorded data can be seen. The decreasing light yield for decreasing energy of electron events is commonly referred to as the scintillator non-proportionality effect (see, e.g., [13] and [109]). Within the developed model, this effect can be explained by the energy-dependency of the ionization-density distribution caused by electrons: The less energetic an electron (or hole), the denser the created ionization-density distribution. For a denser ionization-density distribution, however, the initially produced blue STEs are created closer to each other and can, thus, more efficiently interact via the Förster interaction. This enhanced probability of the STE-STE interaction leads to an increase of non-radiatively recombining STEs and, thus, to a decreased

amount of scintillation light produced.
⇒ **Hence, the energy-dependency of the light yield of electrons is well described by the model and can be explained consistently.**

- From figure 6.1 (panels a), c) and d)), it can be seen that the calculated light yield for 122keV γ-particles (unity by definition) is smaller than the light yield of equally energetic electrons. The observation of a reduced light yield of γ-events compared to equally energetic electron events can also be made when considering experimentally determined data: For example, the 46keV to 48keV energy bin in figure 6.2 can be regarded. This energy bin for which a clearly reduced light yield is measured contains events caused by 46.5keV γ-particles due to an internal ^{210}Pb contamination of the crystal investigated in [13]. The effect of a reduced light yield for γ-events compared to equally energetic electron events is commonly referred to as γ-quenching (see, e.g., [13]). As also deduced in [13], the non-proportionality effect of the electron light-yield is the cause for the observed γ-quenching: As is discussed in appendix B.1, γ-particles deposit their energy by producing at least one electron-hole pair. Thus, the full energy deposited is distributed among at least two "recoil" particles, an electron and a hole. The hole relaxation is expected to occur similarly to the electron relaxation in $CaWO_4$ (compare appendix B.1). Hence, instead of one high-energetic electron carrying the complete energy deposited, several lower-energetic electrons and holes with reduced light yield (see discussion above) are produced. Therefore, for γ-particles, in comparison to equally energetic electrons, less light is produced.
  ⇒ **Thus, as can be seen from figure 6.1, the calculated light yields correctly reproduce the experimentally observed γ-quenching and this effect can fully be explained within the developed model.**
  In addition, it should be noted that this effect is expected to be even more severe for primary γ-energies larger than $\sim$ 500keV. The energy-loss process of γ-particles at these energies is dominated by Compton scattering (see appendix B.1). Thus, an increase in the number of low-energetic recoil particles sharing the deposited energy is expected (several electrons and holes) and, therefore, an increased impact of the non-proportionality effect can be expected.

- In general, for all Quenching Factors and light yields calculated, the observation can be made that these quantities exhibit an energy-dependency. For small energies, the light yield of nuclear recoils increases whereas the light yield of electrons decreases, as discussed and explained above. The increase of the light yield of nuclear-recoil events (O, Ca and W ions) for decreasing energy of the primary particle can be explained, in principle, analogously to the electron light-yield increasing for decreasing energies (only vice a versa) by a decreasing ionization density for decreasing ion energy (as can, e.g., be seen in figure B.12 in appendix B.3.10 or be deduced from the description of the energy-loss process of heavy, charged particles by the Lindhard theory and the Bethe-Bloch formula in section III/3.1.1). As the relative change of the nuclear-recoil light-yields is more severe than the relative change in the electron light-yield, the energy-dependency of the Quenching Factors (of nuclear recoils) follows the trend of the nuclear-recoil light-yield and, therefore, the Quenching Factors decrease for increasing energy. Actually, this energy-dependency of the light yield can, e.g., also be observed for the experimentally determined values of the energy-dependent Quenching Factor of oxygen (measured in [75, 76]) at room temperature, presented

in table 6.2.

E_O [keV]	QF^O ($T = 300$K)
1095	$(8.2^{+0.1}_{-0.1})\%$
1523	$(8.1^{+0.2}_{-0.2})\%$
1684	$(8.0^{+0.4}_{-0.4})\%$
1907	$(7.5^{+0.1}_{-0.1})\%$
2209	$(7.4^{+0.3}_{-0.3})\%$

Table 6.2: Energy-dependent Quenching Factors of oxygen at $T = 300$K, from [75, 76].

From the measured values of the Quenching Factor of oxygen (from [75, 76]), as presented in table 6.2, the same trend for the energy-dependency of the Quenching Factor as predicted by the model can be seen.
⇒ **Thus, the model predicts energy-dependent Quenching Factors with increasing values for decreasing energy. This prediction is confirmed by experimental observations and can be explained consistently.**
In addition, it should be noted that the energy-dependency of the Quenching Factors is predicted to be different for different primary interacting particles and for different temperatures: As can be seen from table 6.1, e.g., at mK temperatures, the light yield of O ions varies over the complete energy range presented whereas the Quenching Factors of Ca and W ions are nearly constant for energies above 100keV and only vary significantly for energies below 100keV. When considering these values, it should be taken into account that, due to the uncertainties in the determination of the model parameters, these values and energy-dependencies should not be regarded as exact. Nonetheless, the trends predicted by the model can be considered as indications of real physical effects.

- Comparing the values of the Quenching Factors calculated for crystal Olga at room temperature and at low temperatures, it can be observed that, for room temperature, larger Quenching Factors are predicted. This is attributed to the smaller Förster radius at room temperature compared to low temperatures: Due to the dependency of the amount of scintillation light produced on the product of Förster radius and STE density as well as due to the fact that this dependency is not linear (compare, e.g., equation 3.166 in section III/3.2.4), it can be deduced that, for a smaller densities, a varying Förster radius has a smaller impact on the amount of scintillation light produced compared to the impact of a varying Förster radius for larger densities. Therefore, the Quenching Factor which depends on the ratio of the light generated for an electron recoil (with a comparably low STE density) and for a nuclear recoil (with a comparably large density) changes for different Förster radii, i.e., for different temperatures.
  ⇒ **Thus, the model predicts and explains a dependency of the Quenching Factors on temperature. It is predicted that the Quenching Factors decrease for decreasing temperature.**
  It should be noted that, even when taking into account that the absolute values for the Förster radius determined within the present work are afflicted with large uncertainties, from the theoretical description of the Förster interaction, it can be

deduced that the Förster radius is expected to increase for decreasing temperature (compare section III/3.1.3). Thus, the described impact of the Förster interaction onto the temperature-dependency of the Quenching Factors as observed for the values in table 6.1 is expected, independently of the determined absolute values of the Förster radius.

- In addition, the light yields and Quenching Factors calculated for crystal Olga and a hypothetical perfect crystal (both calculated for mK temperatures) can be compared. At first, it should be recalled that, on the one hand, the absolute light yield for the perfect crystal is predicted to be larger than the light yield of crystal Olga and that, on the other hand, the calculated Quenching Factors and light yields, as shown in table 6.1 and figure 6.1, are both relative values: The light yield is specified relative to the light yield of a 122keV γ-particle, whereas the Quenching Factor relates the light yield (or absolute amount of light produced) to the light yield (or absolute amount of light produced) of an electron depositing the same amount of energy in the crystal in the form of phonons (compare equations 6.2 and 6.3 in section III/6.1.1, respectively). With these two remarks as basis, the light yields and Quenching Factors of crystal Olga and the hypothetical perfect crystal can be compared: As can be seen, the light yields as well as the Quenching Factors calculated for the perfect crystal are smaller than the respective values for crystal Olga. Within the developed model, this can be explained by the fact that, for the perfect crystal, more STEs are initially created (no electrons are captured by electron traps). However, these STEs are distributed within the same volume. Hence, the density of STEs is larger for the perfect crystal than for crystal Olga. However, the larger the defect density, the more likely the Förster interaction occurs. Again, as already discussed in the context of the temperature dependency of the Quenching Factors, this effect is larger the larger the STE density, i.e., this effect is more pronounced for nuclear recoils than for electron recoils. Therefore, the relative quantities of the light yields and Quenching Factors are expected to change in the predicted way. In addition, it should be noted that, the smaller the defect density, the larger the absolute light yield of the crystal is predicted to be.
  $\Rightarrow$ **Thus, the model predicts and explains a dependency of the Quenching Factors on the defect density of the $CaWO_4$ crystal. An negative correlation between the light yield of a crystal and the Quenching Factors as well as the relative light yields for this crystal is predicted.**

- The absolute values of the Quenching Factors calculated for crystal Olga (at mK temperatures and at room temperature) can be compared to various values of experimentally determined Quenching Factors for $CaWO_4$ crystals from the literature. A list of examples of values from the literature is presented in table 2.3 in section III/2.2.5. Values of different Quenching Factors from experiments (QF_{exp}^{part} from the literature, compare table 2.3 in section III/2.2.5) and the model (QF_{mod}^{part} calculated using the complete model, see table 6.1) can be compared. Examples for such a comparison can be found in table 6.3 where it should be noted that it was attempted to compare values for energies of the primary particle as similar as possible in the experiments and the model calculation. For energy regions where two values are specified from literature as well as from the model, both of these values are stated.

  It can be observed that the Quenching Factors predicted by the model at mK temperatures are in general too small whereas, at room temperature, the predicted

E_{part} [keV]	temperature $[K]$	QF_{exp}^{part}	QF_{mod}^{part}
$100 \lesssim E_O \lesssim 300$	mK	$\sim 10.4\%$	$\sim 9.1\%$
$240 \lesssim E_{Ca} \lesssim 300$	mK	$\sim 6.3\%$	$\sim 5.3\%$
$18 \lesssim E_{Ca} \lesssim 100$	300K	$\sim 6.4\%$ (6.3%)	$\sim 7.2\%$ (6.8%)
$18 \lesssim E_W \lesssim 100$	300K	$\sim 3.9\%$ ($< 3.0\%$)	$\sim 5.8\%$ (4.3%)

Table 6.3: Energy-dependent Quenching Factors of oxygen at $T = 300$K (from [75, 76]).

values are too large. In this context, it should be noted that, on the one hand, of course, the Quenching Factors reported in the literature as well as the the Quenching Factors predicted by the model are both afflicted with uncertainties. On the other hand, it should be noted that, in this comparison, values determined for different crystals are compared and, as discussed, the Quenching Factors for different crystals do not necessarily have to comply with each other. However, it should be noted that the differences observed are most probably larger than it could be explained by the different defect densities of the respectively investigated crystals. In addition, it should be taken into account that the trend of the deviation of the predicted Quenching Factors from the measured values to smaller values at low temperature and to larger values at room temperature cannot be explained with different defect densities. Hence, the observed disagreement of the absolute values is mostly attributed to the large systematical uncertainties of the determination of the model parameters. However, regardless of these large uncertainties, already with the set of parameters of the model as determined within the present work, a satisfying qualitative agreement between the Quenching Factors predicted by the model and reported in literature could be achieved.
$\Rightarrow$ **Thus, it is concluded that, if all of the model parameters could be determined correctly and no assumption or estimations would have to be adopted, it can be expected that the model developed for the light-generation and quenching in $CaWO_4$ could, indeed, be employed to reliably predict Quenching Factors.**

6.2 Comparison with Existing Models for the Light Quenching in $CaWO_4$

In the following, a short comparison of the model for the light generation and quenching developed within the present work and two existing models for the scintillation-light quenching or the light generation from the literature is presented.

Birk's Model

A phenomenological description for the light quenching in scintillating materials frequently used is the so-called Birks' formula (or Birks' saturation law, see, e.g., [95, 13] for examples of the employment of Birks' model for $CaWO_4$ or [110] for an example of the employment of Birks' model for liquid noble gases). Within Birks' model, in principle, a linear dependency (with proportionality constant A) of the number of fundamental excitations (e.g., excitons

or electron-hole pairs) produced in the scintillator by an interacting particle, from the electronic energy-loss of the particle $\frac{dE}{dx}$ is assumed [111]. For those regions with high excitation densities, proportional to $B \cdot \frac{dE}{dx}$ (B corresponding to another proportionality constant), produced in the energy-loss process, some kind of quenching process (which does not have to be specified further within the model) of the fundamental excitations is assumed to occur with probability k. This quenching effect causes a non-radiative recombination or, more generally, a non-radiative loss mechanism of the fundamental excitations [112]. With these considerations, Birks' law can be formulated delivering the following expression for the light output per unit path length, $\frac{dL}{dx}$:

$$\frac{dL}{dx} = \frac{A \cdot \frac{dE}{dx}}{1 + k \cdot B \cdot \frac{dE}{dx}} \tag{6.20}$$

where it should be noted that A, B and k are empirical constants depending on the material. Often, the product $k \cdot B$ is written "kB" and is called Birks' constant. These constants have to be determined from fits of Birks' law to the light-yield data of the investigated scintillator. Hence, for high ionization densities, equation 6.20 describes a reduction of the scintillation efficiency according to $\frac{1}{1+k \cdot B \cdot \frac{dE}{dx}}$. Eventually, for very high densities, equation 6.20 indicates that the light output per unit path length traveled by the interacting particle no longer depends on $\frac{dE}{dx}$, but saturates [111]. Thus, within Birks' model, the quenching effect observed for heavy, charged interacting particles in $CaWO_4$ can either be attributed to a saturation of the light-production mechanism for large values of $\frac{dE}{dx}$, as, e.g., explained in [95], or the quenching effect is attributed to the not yet saturated, but reduced light yield as represented by equation 6.20.

The following main differences of this approach compared to the model developed within the present work can be identified:

- Birk's model is a phenomenological, macroscopic approach in which the description of the energy-loss process of the particle and the quenching process of the excitations is reduced to the quantity of the mean energy-loss rate of the primary particle along its track and to Birks' constant kB.
- The parameters of Birks' model are phenomenological and have to be adjusted using the light yield produced by an interacting particle. They are assumed to be independent of the energy and type of the primary interacting particle.
- In Birks' model, the amount of scintillation light created is only attributed to the path length and the mean value $\frac{dE}{dx}$ of the particle along its path.
- No temperature-dependencies or differences in the energy-loss processes for different interacting particles (e.g., differences in the produced ionization densities or in the amount of energy deposited in ionization) are included in the model.
- In Birks' model, only the amount of scintillation light created is described whereas in the model developed within the present work, in addition, the decay-time spectra of the produced scintillation light are described.

Hence, also in Birks' model, the existence of a non-radiative quenching process is assumed and the basic mathematical dependency of the light output on the parameter describing

the strength of this interaction (the Förster radius $R_{d-d}(T)$ in the model developed in the present work and Birks' constant kB in Birks' model) is actually the same (compare equation 6.20 and, e.g., equations 3.166 and 3.167 in section III/3.2.4). However, within Birks' model, a simple proportionality to the energy loss per unit length is assumed whereas, in the developed model, the comprehensive microscopic description of the time-, temperature-, particle-, energy- and crystal-dependent processes of the energy loss, ionization creation, STE creation and STE-population development is included, leading to the identification of physics parameters describing the light generation and quenching process which are explainable and determinable (by other means than the light yield produced).

Exciton-Exciton Interaction Model for 90eV Photon Excitation

In [94], the decay-time spectra of $CaWO_4$ under differently attenuated photon pulses ($\sim$ 90eV photons from a free-electron laser) are investigated. Due to the high ionization densities utilized, a non-exponential (quenched) decay at the beginning of the pulses is observed. As in the model developed in the present work, this non-exponential decay is attributed to STE-STE interactions (dipole-dipole interaction) resulting in the non-radiative destruction of STEs. Basically, the mathematical formulation of the development of the STE population as in the present work is assumed, however, without considering excitation efficiencies, non-radiative or migration processes or the existence of different (green) luminescence centers. The main two differences of the approach used in [94] and the model developed within the present work are that, on the one hand, the interaction of STEs produced by many interacting photons depositing their energy could be represented by a comparably simple model in [94], in contrary to the description of the ionization-density distribution produced by interacting particles within the present work. On the other hand, in [94], no attempt was made to link the observed and modeled scintillation-light decay-time spectrum to the efficiency of creating scintillation light.

6.3 Limitations of the Developed Model and Possible Improvements

The current major limitations of the model are constituted by the adoptions of values for several model parameters from the literature (compare discussion in section III/6.1.2). Therefore, a set of experiments is suggested with which these uncertainties could be resolved by determining all of the model parameters from experimentally determined quantities. The following experiments would have to be performed to determine all of the model parameters:

1. Unquenched Excitation with the Two-Photon Effect

It is suggested to perform experiments using two-photon excitation with the following requirements regarding the laser, setup and detection system:

- A laser with shorter pulses (less coverage and broadening of the rising part of the pulse) and increased power output (so that, for large focussing, STE densities could be reached for which STE-STE interaction, i.e., quenching would occur).

- Improved suppression of the reflected laser light and improved selection of the investigated wavelength of the scintillation light (e.g., by the employment of a spectrograph instead of optical filters).
- Well defined and controlled focussing/defocussing of the laser beam (e.g., using a beam expander with subsequent focussing optics)
- A measurable excitation density should be realized (e.g., measuring the absorption of laser light as well as the focussing and extent of the excited volume, e.g., optically).
- An absolute light-yield measurement of the unquenched scintillation light (e.g., with an integrating - Ulbricht - sphere and exactly determined detection and conversion efficiency of the setup).
- A measurement of the wavelength spectrum (e.g., using the spectrometer as performed, possibly with improved determination of the response function).
- A decay-time measurement with faster impulse reaction (e.g., employing the single-photon counting mode of the PMT).
- The possibility to perform experiments at well stabilized temperatures from room temperature down to $T \lesssim 5\text{K}$.

With such a setup, measurements of the unquenched light yield, decay-time and wavelength spectra at various temperatures between room temperature and $T \lesssim 5\text{K}$ would have to be performed. Then, the following parameters could be determined:

- F_{e^-trap}, the fraction of electrons excited into the conduction band that becomes captured by traps[3]. This allows to determine the number of STEs initially generated.
- The absolute unquenched light yield per STE and its temperature dependency. This parameter influences the radiative branching ratio for blue and green STEs.
- F_{abs}, the fraction of blue photons absorbed at defect centers.
- All parameters describing the various STE excitation and de-excitation processes (energy barriers, rate constants and radiative decay times from level 1 and 2 of the radiative, non-radiative and migration processes).
- C_{defects}, the defect density of the crystal. This parameter influences the radiative branching ratio for blue and green STEs.
- $\tau_{dr}(T)$ and $F_{dr}(T)$, the delayed rise time of the fraction $F_{dr}(T)$ of the scintillation light.

Using these measurements, the complete set of parameters of the unquenched model could be determined, independently from values adopted from the literature, and, thus, truly corresponding to the respective investigated $CaWO_4$ crystal.

[3]Note that, in principle, also another possibility to determine F_{e^-trap} exists: As discussed in section III/3.2.4, the initial pulse height at $t = 0$ is expected to be directly proportional to the number of blue STEs initially generated, i.e., to $(1 - F_{e^-trap})$. Hence, if all other parameters determining the proportionality factor would be known, F_{e^-trap} could be determined from the initial pulse height of a scintillation-light decay-time spectrum (compare figure 3.11 in section III/3.2.4).

2. Quenched Excitation with the Two-Photon Effect

A second set of measurements, in analogy to the experiments with unquenched excitation is suggested to be performed, with the distinction that, for these measurements, the laser beam is strongly focussed so that a quenched light generation is achieved. As indicated in the description of the setup, the realized excitation density should be determined. Using these measurements and the results from the first set of measurements, the Förster radius could be determined as well as its temperature dependency, without relying on the complex modeling of the ionization-density distribution caused by interacting particles.

With such measurements a full description of the model, except for the description of the particle-induced ionization-density, is achieved without relying on assumptions.

3. Pulsed Electron-Beam Excitation

A third set of measurements is suggested to be performed using pulsed electron-beam excitation. As all parameters of the model, except for the description of the radial distribution of the ionization densities, are known, the pulse shape of the scintillation light which depends on the STE density-distribution can be employed to determined the radius $r_{Rec_{el}}(E_{el})$. In principle, one such measurement at one temperature with one electron energy suffices. However, it is suggested to perform such measurements with different electron energies to test the assumed energy dependency of $r_{Rec_{el}}(E_{el})$ (as described in appendix B.3.9).

In addition, it should be noted that, by performing such an electron-excitation measurement at various temperatures, it can be tested if the assumption made that the parameters describing the ionization distribution as well as the fraction of electrons captured by traps are independent of temperature, is true.

4. Pulsed Ion-Beam Excitation

As a fourth set of measurements, excitation by ions or pulsed ion beams is suggested. In analogy to the electron-beam experiments, the decay-time spectra recorded can be used to determine the radial parameters. Optimally, such an experiment could be performed at lower ion energies as used within the present work ($\sim$ 35MeV) as well as using two ion species to test the assumed particle- and energy-dependencies of the radial parameters.

In addition, it could be attempted to determine the radial distribution of the particle-induced ionization density, e.g., by more elaborate simulations.

It should be noted that, if the energy- and particle-dependencies of the ionization distributions can be clarified, they could most probably be transferred to other target materials by taking into accoutn the different density and mean charge number of the respectively investigated material[4].

Hence, perfroming such a set of experiments, the complete set of parameters of the developed model including the radial dependencies of a particle-induced ionization density

[4]Or, actutally, it could be attempted to use the results obtained from SRIM simulations for both of these materials to derive a scaling factor.

could be determined entirely independently from values stated in the literature.

6.4 Implications of the Developed Model

In conclusion, it should be noted that, if the complete model with all parameters determined and validated is available, this model can, as was presented in section III/6.1, be employed for the calculation of light yields and Quenching Factors for various types of primary interacting particles for the investigated $CaWO_4$ crystal. These Quenching Factors are calculated in dependency on the type and energy of the primary interacting particles as well as on the temperature and defect density of the $CaWO_4$ crystal. Hence, the developed model consistently explains the origin of the different Quenching Factors observed for different interacting particles in $CaWO_4$ and, thus, offers the possibility to predict these parameters which are used for the identification of the type of particles interacting in a CRESST detector module. The model, therefore, helps to understand and potentially optimize the background suppression with the phonon-light technique.

In addition, it should be noted that the developed model can, in principle, be transferred to other scintillators, especially to other types of inorganic (intrinsic) scintillators as, e.g., $CdWO_4$, $CaMO_4$, NaI or BaF_2. However, also a transfer to doped scintillators as, e.g., La:Y_2O_3 or Ti:AL_2O_3 should be possible. In such a case, the quenching effect could perhaps (partially or completely) be attributed to a saturation effect (which could be included into the model). The transfer of the model to another scintillator would offer the possibility to study the background-suppression capabilities of the respective investigated material, by predicting the decay-time spectra, light yields and Quenching Factors for different interacting particles in the context of a possible application for dark matter search or, in more general, for rare event searches.

It should be noted that, with a set of comparably easily performable experiments (experiments 1. to 2. as described in section III/6.3), the complete set of parameters of the model as well as a first validation of the model (with experiment 3. from section III/6.3) can be realized. Using the information gained by these experiments, first predictions of Quenching Factors for the investigated material could be made without performing comparatively extensive experiments with ion beams (experiment 4. in section III/6.3). However, it should be noted that, in order to finally confirm the model and its parameters as determined for the investigated material, also experiments with at least one ion beam at one energy and at one temperature should be performed. Thus, the model offers a comparably simple possibility to investigate scintillators concerning their applicability for the efficient background suppression in rare event searches.

Part IV

Summary and Outlook

Chapter 1

Summary

Experimental evidence from cosmology as well as indications from theoretical particle physics deliver strong hints for the existence of a large amount of matter made up from up to now unknown particles, so-called dark matter particles. Actually, a large fraction of the universe's mass and energy content, $\sim 27\%$, is shown to consist of dark matter. Promising candidates from theoretical particle physics to account for the dark matter are WIMPs, weakly interacting massive particles. The direct detection of WIMPs, potentially possible via the detection of WIMP-nucleus scattering events, is one of the key challenges of present-day astroparticle physics. Due to the small interaction cross section as well as the small energy transfers expected for such WIMP-nucleus scattering events, a large target mass and a low energy threshold of the employed detector as well as a highly efficient background suppression down to ∼keV energy depositions are required to directly detect and identify WIMP interactions within the detector material. In the direct dark matter search experiment CRESST (Cryogenic Rare Event Search with Superconducting Thermometers), cryogenic phonon-light detector modules are employed to fulfill these requirements and to directly detect WIMP-nucleus scattering events. The simultaneous detection of a phonon signal in a transition edge sensor (TES) attached to the scintillating target crystals ($CaWO_4$ single crystals) and of the scintillation-light signal in a separate cryogenic light detector, read out with a TES as well, enables an excellent event-by-event background discrimination down to energies of $\sim$ 15keV. The particle identification is based on the light-quenching effect in $CaWO_4$, i.e., the fact that different interacting particles depositing the same energy in a $CaWO_4$ crystal produce different amounts of scintillation light. This behavior is quantified by the so-called Quenching Factors, corresponding to the relative light yields for different interacting particles in comparison to the light output of e^-/γ interactions in the detector.

For an efficient background suppression with the CRESST detector modules, light detectors with excellent energy resolution at low energies as well as the knowledge of the Quenching Factors for different interacting particles in $CaWO_4$ are required. Within the present work, both of these issues were addressed: On the one hand, the potential of cryogenic composite light detectors with Neganov-Luke amplification for an optimization of the light-detector resolution and, thus, of the background suppression with CRESST detector modules was investigated. On the other hand, a comprehensive, microscopic model for the light generation and quenching in $CaWO_4$ was developed and experimentally validated to provide a theoretical prediction as well as an understanding of Quenching Factors for different interacting particles in $CaWO_4$.

In order to achieve an amplification of the light-detector signal in cryogenic light detectors, the so-called Neganov-Luke effect can be employed. From previous investigations it is already known that a significantly improved signal-to-noise ratio as well as an improvement of the light-detector's energy resolution at comparably large detected light energies can be achieved. However, a decrease of the signal amplification over time was observed which is not optimal with respect to the long-term stability of the detector response required in dark matter experiments as CRESST. On the basis of a detailed understanding of the underlying meachanism of the decrease of the amplification over time, an extended fabrication method for Neganov-Luke light detectors could be developed within the present work. With a Neganov-Luke detector built according to this new fabrication method, it was demonstrated experimentally that, using this new design, the drawback of a decreasing amplification can be overcome: Within the performed experiments, the amplification of the investigated detector could be shown to be constant over time. In addition, the energy-dependent resolution of a Neganov-Luke amplified light detector was investigated at various applied voltages utilizing the LED-calibration method. From the corresponding experiments and their analysis, on the one hand, an understanding of the voltage-dependency of the energy-dependent detector resolution could be deduced. This understanding can be used for a further optimization of the design of Neganov-Luke amplified light detectors. On the other hand, it was demonstrated that, within the low-energy region of the light-detector signal which is important for the dark matter search, already at comparably small applied Neganov-Luke voltages of, e.g, ~ 40V, a significant improvement of the light-detector resolution can be achieved. The impact of the application of the Neganov-Luke effect for light detectors on the background suppression in a CRESST detector module is estimated using the experimentally determined energy-dependent improvement of the light-detector resolution. Thus, the enormous potential of Neganov-Luke detectors for the optimization of the background suppression could be illustrated and it was demonstrated that the derived extended fabrication method allows for a stable, long-term operation of such detectors as required, e.g., in the CRESST experiment.

For the purpose of understanding and quantifying the observed light-quenching effect which is central for the background suppression in the CRESST experiment, a detailed, comprehensive model explaining the light-quenching effect observed for different interacting particles in $CaWO_4$ was developed. This model is based on the microscopic evolution of the population of fundamental excitations produced in an inorganic scintillator by particle interactions. For $CaWO_4$, these fundamental excitations correspond to self-trapped excitons (STEs) at $[WO_4]^{2-}$ complexes. Included in the model are the generation efficiencies of STEs by energy depositions of different interacting particles, the modeling of the particle-induced spatial distribution of the created ionization, the STE-creation and migration-possibilities as well as radiative and non-radiative processes and, in particular, the STE-STE quenching mechanism via the Förster interaction. The combined impact of all of these processes determines the lifetime and light-production efficiency of the STE population in $CaWO_4$. All processes are incorporated as temperature- and energy-dependent parameters. In addition, a dependency of the parameters on the individual crystal due to different defect densities is included in the model. This model not only predicts different light yields, i.e., Quenching Factors, for different interacting particles, but also different shapes of the respective decay-time spectra of the scintillation light. The prediction of differently shaped decay-time spectra was used for the determination of free parameters of the model as well as for its validation. For this purpose, an experiment

at the MLL (Maier-Leibnitz-Laboratorium) tandem accelerator in Garching was set up. Excitation of a $CaWO_4$ crystal was performed at room temperature and at $\sim$ 20K using different ion beams, leading to *quenched* light emission, as well as using two-photon absorption employing a N_2 laser, leading to *unquenched* light emission. With the results from these experiments, most of the free model parameters could be determined as well as various predictions of the model could be tested and confirmed. Applying reasonable estimates as well as using data from the literature to determine the remaining free parameters of the model, a first, preliminary calculation of Quenching Factors for different interacting particles in $CaWO_4$, dependent on the temperature and defect density of the $CaWO_4$ crystal as well as dependent on the energy of the interacting particle, was performed. From a comparison of the preliminary model predictions with values from the literature, already the great potential of the model to correctly predict and explain the light generation and quenching process is demonstrated. Hence, the model developed within the present work delivers a theoretical understanding and predictability of the temperature- and energy-dependent quenching effect. Thus, using the developed model, for the first time, a prediction of Quenching Factors, which are central for the background suppression in the CRESST experiment, on the basis of purely microscopic considerations of the light generation mechanism in $CaWO_4$ is enabled. Moreover, the shapes of the decay-time spectra of the respectively produced scintillation light can be calculated, as, within the developed model, the complete light generation-process is modeled and, hence, the time-dependent production of the scintillation light is described.

Chapter 2

Outlook

From the investigation of light detectors with Neganov-Luke amplification as well as from the model for the light generation and quenching in $CaWO_4$ developed within the present work, several deductions regarding future experiments or applications of the achieved results can be made.

Concerning light detectors with Neganov-Luke amplification, the goal is to capitalize the improved energy-resolution that such detectors offer for the dark matter search with the CRESST experiment or for other rare event searches as, e.g., $0\nu\beta\beta$-decay searches. In order to further improve the achieved results, possibilities to refine the detector design are suggested on the basis of the gained understanding of the physics effects involved. Due to the observed voltage-dependent energy regions for which an increase or decrease of the light-detector resolution has been found, it can be deduced that it would be beneficial to apply voltages above the threshold voltage for complete charge-carrier collection. For this purpose, detectors with high-purity absorber substrates and well-defined ohmic contacts would be advantageous (compare section II/3.3.2). To realize such detectors, on the one hand, a further optimization of the developed fabrication method using p-type Silicon in combination with an alloying/annealing step is suggested. On the other hand, the employment of highly doped contacts, e.g., n^{++} doping with As, for n-type Silicon substrates could deliver well-defined ohmic contacts, even at the low operating temperatures of the light detectors in the CRESST experiment. For a realization of such a design, already a collaboration with the Fraunhofer-Einrichtung für Modulare Festkörper-Technologien, EMFT (München) was started. The process parameters for first tests have been determined and first detectors are to be realized soon.

For the further validation of the developed model for the light generation and quenching in $CaWO_4$, experiments as described in section III/6.3 are suggested to be performed. Actually, an experimental set-up including a new laser with ps pulse-duration, a highly improved and controlled focussing optics for the laser beam as well as a faster detection system is soon started to be realized. With such a laser and detection system, not only two-photon excitation of the $CaWO_4$ crystal can be performed, but also ps-pulsed electron beams will be producible which can, in turn, also be used to excite the $CaWO_4$ crystal. Hence, with such a set-up, an unquenched excitation mode via the two-photon absorption as already utilized within the present work (but with improved timing characteristics) as well as a quenched excitation mode, either by extremely focussing the laser beam (compare section III/6.3) or using the electron pulses, can be produced. Additionally, it is planned

to incorporate a cooling possibility into the set-up which allows to vary the temperature of the crystal from room temperature down to $\sim$ 4K. As discussed in section III/6.3, such a combination of experiments can be utilized to determine the full set of parameters for the developed model and, thus, in the end, enables the prediction of Quenching Factors for various types of interacting particles, dependent on their energy as well as dependent on the temperature and defect density of the investigated $CaWO_4$ crystal. It should be noted that the model can be transferred to other (inorganic) scintillators as, e.g., $CaMoO_4$, Ti:Al_2O_3 or YO_3 which are especially interesting for rare event searches, in particular, with favourable application to light-WIMP searches. For doped scintillators as, e.g, Ti:Al_2O_3 the model can be extended, to account for the limited number and density of scintillation centers (dopants) available. Thus, the developed model, in combination with the planned setup, can be utilized to investigate the light generation and quenching also in other scintillators. Hence, performing experiments as suggested in section III/6.3 as well as potentially material-dependent adjustments of the model, the application of the model allows to predict the background-suppression capabilities of various scintillators in the context of rare event searches employing the phonon-light technique for particle identification.

Part V

Appendix

Appendix A

Supplements to the Scintillation Mechanism in $CaWO_4$

A.1 Diffusion Coefficient of Self-Trapped Excitons in $CaWO_4$

In the following, a discussion of the values of the diffusion constant and the respective activation energies for STEs at regular and disturbed unit cells is presented (see section III/2.1.5).

According to [67], for excitons residing at regular $[WO_4]^{2-}$ groups, $\Delta E_{ex-mobility,\text{reg}}$ can be estimated to be ~ 4.5meV. For exciton transfer from disturbed $[WO_4]^{2-}$ groups (defect states within the band gap) to regular $[WO_4]^{2-}$ a value of $\Delta E_{ex-mobility,\text{dist}} \approx 6.9$meV is determined in [67]. A value for the diffusion constant D_0 is not given in [67]. However, in [68] where the exciton mobility in samarium-doped $CaWO_4$ is investigated, a value for the diffusion constant has been determined. In [68], the efficiency of energy transfer from the Sm levels within the forbidden band gap to higher lying exciton levels of undisturbed $[WO_4]^{2-}$ complexes is investigated. Lattice cells containing Sm can be considered as disturbed $[WO_4]^{2-}$ groups. Thus, it can be assumed that for all migration steps considered in the present thesis or in [68] (STE starting at a regular or a disturbed $[WO_4]^{2-}$) the final state after one migration step is the same (STE at a regular $[WO_4]^{2-}$ group). Additionally, the high temperature limits of the diffusion coefficients can be assumed to be independent of the respective $\Delta E_{ex-mobility}$: $D(T) \approx D_0$ [68]. Hence, the value for D_0 is supposed to be the same for all STEs (at regular or disturbed lattice cells) in pure and Sm-doped $CaWO_4$: $D_0 \approx 1.2 \cdot 10^{-7} \frac{\text{cm}^2}{s}$ [68].

Thus, the temperature-dependent diffusion coefficients of STEs residing at regular $[WO_4]^{2-}$ groups or at distorted $[WO_4]^{2-}$ groups can be estimated to be:

$$D_{\text{STE reg.}}(T) = 1.2 \cdot 10^{-7} \frac{\text{cm}^2}{s} \cdot e^{(-\frac{4.5\text{meV}}{k_B \cdot T})} \tag{A.1}$$

$$D_{\text{STE dist.}}(T) = 1.2 \cdot 10^{-7} \frac{\text{cm}^2}{s} \cdot e^{(-\frac{6.9\text{meV}}{k_B \cdot T})} \tag{A.2}$$

A.2 Diffusion Length of Self-Trapped Excitons in $CaWO_4$

At room temperature (T = 300K), the lifetime of excitons at regular unit cells is $\tau_{\text{STE reg}} \approx 9\mu$s, see section III/2.2 and III/3.2.3). This lifetime and equation 2.6 (section III/2.1.5)

yield a diffusion length $l_{\text{diff reg}}(300\text{K}) \approx 13.5\text{nm}$ for the transfer of a STE from one regular $[WO_4]^{2-}$ to another. This value is in good agreement with the value given in [46]: $l_{diff}(300\text{K}) \approx 12\text{nm}$. Below $\sim 4.6\text{K}$ ($\tau_{\text{STE reg}} \approx 560\mu\text{s}$, see section III/2.2 and III/3.2.3), equation 2.6 (section III/2.1.5) yields diffusion lengths smaller than the distance between two neighboring $[WO_4]^{2-}$ complexes ($d_{\text{W-W}} = 3.87\text{Å}$, see section III/2.1.1). Thus, for $T < 4.6\text{K}$, migration of excitons during their typical lifetime is definitely suppressed.

As the position of $[WO_4]^{2-}$ groups in the crystal structure is highly symmetric (see section III/2.1.1), leading to an almost symmetric electronic band-structure with respect to the Brillouin-zone directions (see figure 2.4), no directional dependency of the exciton mobility in $CaWO_4$ is expected [46]. Contrary to the symmetric sheelite crystal-structure of $CaWO_4$, some other tungstates, e.g., $CdWO_4$, exhibit the non-symmetric wolframite crystal-structure. For such crystals a directional dependency of the exciton mobility accompanied by an overall reduction of the exciton mobility can be expected [46].

A.3 Classification of Inorganic Scintillators

One way to classify scintillators is to distinguish between two rough classes: intrinsic and extrinsic scintillators. These two types of scintillators differ in the way they incorporate their respective luminescence centers. In purely intrinsic scintillators light production is due to self trapping of charges (electrons, holes or excitons) during the excitation of the crystal [70]. The relaxation of these centers (e.g. V_k centers or hole transitions between the upper core and valence bands) leads to the emission of scintillation light. Examples for intrinsic scintillators are CaF_2 (V_k center), CsI (excitonic-like luminescence), BaF_2 (V_k centers and core-to-valence hole transitions) or BGO ($Bi_4Ge_3O_12$, the Bi^{3+}-cation acting as luminescence center) [70]. Doped Scintillators exhibit extrinsic luminescence. In this case activator ions are embedded in the host lattice of the crystal and luminescence is the product of either an electronic transition of the activator itself (e.g. NaI:Tl) or of a transition between the activator and the host lattice (e.g. ZnSe:Te) [70].

A.4 Three-Level Model for the Temperature Dependency of the Slow Decay Time

For the explanation of the temperature dependency of the slow decay-time component of $CaWO_4$, often a three-level model is used [92, 41]. The possibilities for radiative and non-radiative decay of two emitting, interacting, excited energy levels of a luminescence center are included in such a model.

A sketch of the three-level model for $CaWO_4$ is shown in figure A.1. This model describes the de-excitation of emission centers after their excitation (e.g., by particle interaction or phonon absorption) and relaxation to their lowest energetic states. It is assumed that a ground level (labelled 0) and two closely-lying excited energy levels (labelled 1 and 2) of the light emitting center exist. The lower-lying excited level is supposed to be metastable, i.e., to exhibit a very long lifetime. The spacing of the energy levels 1 and 2 corresponds to an energy barrier D. Indicated in the sketch is the possibility for excitations of the upper-lying level 2 to relax (under phonon emission) to the lower-lying level 1 (k_{21}) and the reverse, thermally activated process to populate level 2 via phonon-induced excitation

of level 1 (k_{12}). Both levels can decay radiatively with respective rate constants k_1 and k_2 ($k_2 \gg k_1$) or non-radiatively with the temperature-dependent rate constant $k_{nr}(T)$ to the ground state 0. Its temperature-dependency is described by a corresponding decay rate K and energy barrier ΔE that has to be overcome to realize the non-radiative recombination [41]. The non-radiative decay rate is assumed to be the same for both levels[1].

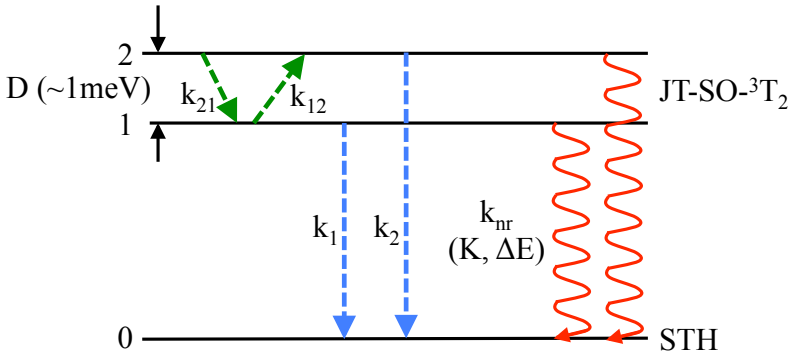

Figure A.1: Sketch of the three-level model for a $CaWO_4$ light-emitting center.

For the application of the model to $CaWO_4$, the emission center is identified with a STE at an excited, regular $[WO_4]^{2-}$ complex (compare figure 2.10). Then, as already indicated in figure A.1, the two JT-SO-$^3T_2$ states (electron states of the STE) can be assigned to be the two (energetically close) emitting energy levels described in the model. Hence, the energy level the electrons relax to under phonon or photon emission can be determined to be the STH level of the STE. The corresponding radiative and non-radiative decay processes as well as their respective energy barriers can also be found in figure 2.10.

In order to calculate the resulting temperature-dependent lifetime of STEs (i.e., the observable decay-time of the scintillation light) within this model, an expression for the temperature-dependent non-radiative decay-rate k_{nr} is needed. Following N.F. Mott et al. [91], the temperature-dependent probability of non-radiative return to the ground state can be described by:

$$k_{nr}(T) = K \cdot e^{-\frac{\Delta E}{k_B \cdot T}} \tag{A.3}$$

where K is the non-radiative rate constant, k_B the Boltzmann-constant, T the temperature and ΔE corresponds to the activation energy that has to be overcome [41]. Assuming thermal equilibrium of the two emitting levels leads to the following condition for the populations n_1 and n_2 of the two levels[2] [41]:

$$n_2(t,T) = n_1(t,T) \cdot e^{-\frac{D}{k_B \cdot T}} \tag{A.4}$$

Hence, the following rate equation for the total population of STEs $n(t,T)$ can be formed

[1] This assumption is justified if the condition $D \ll \Delta E$ is fulfilled. This is the case for $CaWO_4$, as will be shown in the following.

[2] In principle, a factor accounting for possibly different degeneracies of the two emitting levels has to be included. However, the two levels can both be identified with triplet levels and, thus, this factor is unity [41].

and equations A.3 and A.4 can be applied [41]:

$$n(t,T) = n_1(t,T) + n_2(t,T) \tag{A.5}$$

$$\frac{dn(t,T)}{dt} = -k_1 \cdot n_1(t,T) - k_2 \cdot n_2(t,T) - k_{nr}(T) \cdot (n_1(t,T) + n_2(t,T)) \tag{A.6}$$

$$\frac{dn(t,T)}{dt} = -\left(\frac{k_1 + k_2 \cdot e^{-\frac{D}{k_B \cdot T}}}{1 + e^{-\frac{D}{k_B \cdot T}}} + K \cdot e^{-\frac{\Delta E}{k_B \cdot T}} \right) \cdot n(t,T) \tag{A.7}$$

Identifying the first term in the bracket of equation A.7 with the total radiative decay rate $k_r(T)$ and the total recombination rate with $k_{rec}(T)$ leads to the relations:

$$k_r(T) = \frac{k_1 + k_2 \cdot e^{-\frac{D}{k_B \cdot T}}}{1 + e^{-\frac{D}{k_B \cdot T}}} \tag{A.8}$$

$$k_{rec}(T) = k_r(T) + k_{nr}(T) \tag{A.9}$$

$$\frac{dn(t,T)}{dt} = -\left(k_r(T) + k_{nr}(T)\right) \cdot n(t,T) = -k_{rec}(T) \cdot n(t,T) \tag{A.10}$$

The inverse of the total recombination rate corresponds to the lifetime of the complete STE population $\tau_{lt}(T) = \frac{1}{k_{rec}(T)}$ and, thus, to the observed decay time of the produced scintillation light. Of course, the inverse of the non-radiative and radiative decay rates can just as well be identified with the respective decay times $\tau_{nr} = \frac{1}{k_{nr}(T)}$ and $\tau_r = \frac{1}{k_r(T)}$. This yields the following expression for the temperature- and time-dependent total STE population $n(t,T)$ as solution of the rate equation:

$$\frac{1}{\tau_{lt}(T)} = \frac{1}{\tau_r(T)} + \frac{1}{\tau_{nr}(T)} = \frac{k_1 + k_2 \cdot e^{-\frac{D}{k_B \cdot T}}}{1 + e^{-\frac{D}{k_B \cdot T}}} + K \cdot e^{-\frac{\Delta E}{k_B \cdot T}} \tag{A.11}$$

$$n(t,T) = n_0 \cdot e^{-k_{rec}(T) \cdot t} = n_0 \cdot e^{-\frac{t}{\tau_{lt}(T)}} \tag{A.12}$$

with the initial number of STEs $n_0 = n(t=0)$. The scintillation-light pulse $L(t,T)$ is then described by:

$$L(t,T) = k_r(T) \cdot n(t,T) = \frac{n_0}{\tau_r(T)} \cdot e^{-\frac{t}{\tau_{lt}(T)}} \tag{A.13}$$

Hence, the slow component of observed scintillation-light pulses of $CaWO_4$ is described with a single exponential with temperature-dependent decay time $\tau_{lt}(T)$. $\tau_{lt}(T)$ is parameterized by five unknown constants: k_1, k_2, K, D and ΔE, see equation A.11.

This parameterization can be fitted to data obtained for the slow (intrinsic) decay-time of the scintillation light of $CaWO_4$, as shown in figure A.2 [41]: The values of the slow decay time of $CaWO_4$ under α-excitation as determined with a two exponential fit (see table 2.1) are depicted versus temperature (data points as open circles). The red line corresponds to a fit of the three-level model (equation A.11) to the data [41].
As can be seen, this model reproduces the temperature dependency of the slow (intrinsic) decay-time component of the $CaWO_4$ scintillation light nicely. With this fit, the values shown in table A.1 for the unknown parameters were determined in [41].
From these values, and from the data shown in figure A.2, it becomes clear that at very low temperatures ($T \lesssim 10$K), the slow decay time of $CaWO_4$ is completely determined by the radiative decay τ_1 from the energetically lower-lying level 1 leading to the plateau for

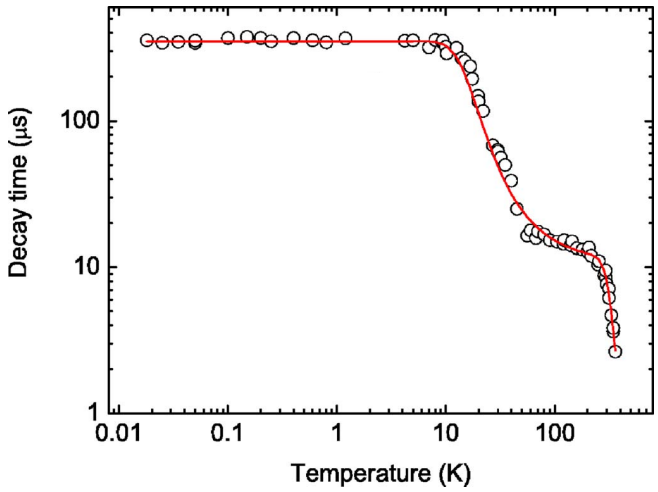

Figure A.2: Temperature dependency of the slow decay time of the scintillation light of $CaWO_4$ under 5.5MeV ^{241}Am α-particle excitation (see values in table 2.1). Circles correspond to data points, the red line to the fit of the three-level model (see equation A.11) to the data. Picture taken from [41].

k_1 [s^{-1}]	$3.0 \cdot 10^3$	$\tau_1 = \frac{1}{k_1}$ [μs]	333
k_2 [s^{-1}]	$1.1 \cdot 10^5$	$\tau_2 = \frac{1}{k_2}$ [μs]	9.1
K [s^{-1}]	$8.6 \cdot 10^9$	$\tau_{non-rad,0} = \frac{1}{K}$ [μs]	$12 \cdot 10^{-3}$
D [mV]	4.4		
ΔE [mV]	320		

Table A.1: Results of the fit with the three-level model to the data shown in figure A.2 (from [41]). Additionally, the decay times corresponding to the fitted rate constants are given in the very right column of the table.

$T \lesssim 10$K in figure A.2. For increasing temperature, radiative decay from level 2 becomes also possible (thermally stimulated) and the resulting decay time decreases, as determined by the temperature-dependent mixture of τ_1 and τ_2 (see equation A.11 with $\tau_{nr}(T) \approx 0\mu$s for $T \lesssim 200$K). For temperatures $T \gtrsim 250$K, the non-radiative decay from both levels $\tau_{nr}(T)$ gains weight and the resulting total decay time is further decreased.

It has to be noted that the model parameters presented in table A.1 which were determined in [41], are afflicted with uncertainties due to the way the slow decay time was determined: The model parameters were derived by a fit with two exponentials to the decay-time data under α-excitation. However, with γ-excitation of the same crystal, the same fit reveals different values for the decay time for the recorded light pulses. Hence, within the presented three-level model, only the temperature dependence of the slow decay-time component is described, but neither the differences of the values obtained under different excitations nor the origin or development of the fast decay-time component are explained. In addition, the possibility and impact of exciton migration is not considered. All these features will be addressed in the model developed in the course of this work, which is presented in chapter III/3.1.

A.5 Rise Time of the Scintillation-Light Pulses

In general, little information about the rise time of scintillation-light pulses of $CaWO_4$ crystals can be found in literature. However, in [65] and [71, 61], investigations of the rising part of the $CaWO_4$ scintillation light - using very fast excitation pulses (280keV electron pulses with a pulse width of 10ns in [65] and photons with energies between 4.65eV to 5.25eV and a pulse width of 100fs in [71, 61]) - were performed. As already discussed in section III/2.1.5, time- and wavelength-resolved, transient optical absorption spectra were measured and discussed in [65] for $CaWO_4$ at 100K. Additionally to the electron and hole absorption-components in the ESA (excited-state absorption) spectra, a third weaker absorption component at 1.3eV with a lifetime of roughly 20ns was observed. This component is assigned to a fraction of electrons that was excited into the conduction band. Before recombination with a (immobile, see section III/2.1.4) STH to a STE, these electrons undergo a migration period until they find a STH [65]. The shortness of the involved decay time of the ESA component points to a high mobility of electrons during this capture process. This assignment is supported by the investigation of the scintillation-light pulse shape presented in [71]: The decay-time spectrum of a $CaWO_4$ crystal (observed at 440nm at room temperature) under excitation by photon pulses of 100fs length was investigated. The pulse shape reveals a dominant fraction of the pulse rising very fast with a time constant of $\sim 200 \pm 50$fs [61], ascribed to virtually direct creation of STEs, and a smaller fraction (amplitude $\gtrsim 15\%$) exhibiting a measurable rise time of ~ 40ns. It is speculated that this component corresponds to a delayed energy transfer-process [71]. Such a delayed energy transfer-process would be delivered by delayed recombination of electrons with STHs due to a migration process, as suggested in [65]. In addition, the order of magnitude of the respective involved times, the decay time of the ESA component and the rise time of the scintillation-light pulse, show good agreement for both experiments.

It can be concluded that the main fraction of STEs in $CaWO_4$ is created very fast, with a rise time of 200 ± 50fs. The partial, delayed rise of the scintillation light of $CaWO_4$ (amplitude $\gtrsim 15\%$) seems to be connected to a delayed recombination of electrons with STHs to STEs. A more detailed interpretation of these measurements and the temperature-dependency of this effect is offered within the developed model in section III/3.1.2.

A.6 Phenomenological Model for the Temperature Dependency of the Light Yield

In the following, a phenomenological model often used to qualitatively describe the temperature dependency of the scintillation-light yield is presented [46]. With such a model, a quantitative description of the efficiency of a scintillator is pursued. In the framework of such a model, the scintillation mechanism is divided into three consecutive steps [46]:

1. Interaction of a particle with the scintillator, deposition of energy and production of low-energetic charge carriers.
2. Energy migration and transfer to the luminescence centers.
3. Production of scintillation photons at the luminescence centers.

Below, the respective efficiencies of these three steps are described quantitively within the phenomenological model (following [46]):

1. The number of electron-hole pairs N_{eh} created by a high-energy quantum of energy E_γ can be estimated to be:

$$N_{eh} = \frac{E_\gamma}{2.35 \cdot E_{gap}} \cdot B \tag{A.14}$$

with E_{gap} corresponding to the energy gap, $2.35 \cdot E_{gap}$ is the mean energy needed to create an electron-hole pair. B is the conversion efficiency defined as the ratio of the number of electron-hole pairs actually created and their maximum possible number.

In [46], the conversion efficiency is assumed to be given by:

$$B = \frac{1}{1 + 0.65 \cdot K_{p-i}} = \left(1 + 0.65 \cdot 0.244 \cdot 10^4 \cdot \left(\frac{1}{\epsilon_\infty} - \frac{1}{\epsilon_0}\right) \cdot \frac{(\hbar\omega_{LO})^{\frac{3}{2}}}{1.5 \cdot E_{gap} \cdot eV^{\frac{1}{2}}}\right)^{-1} \tag{A.15}$$

where K_{p-i} is a material-dependent parameter defined as the ratio of the energy lost to the production of optical phonons and the energy used for ionization. Here, ϵ_∞ and ϵ_0 are the high-frequency and static dielectric constants, respectively, $\hbar\omega_{LO}$ is the energy of longitudinal optical phonons dominating the energy loss to phonons in solids. Calculated values of B for different scintillators can be found in [46].

2. The efficiency of the energy transfer to luminescence centers by free charge carriers is described by a parameter S which usually has to be determined experimentally. In self-activated scintillators as $CaWO_4$ where the luminescence centers are part of every unit cell, the transport efficiency can be assumed to be close to unity. In this case, the parameter S is used to describe the fraction of excitations remaining at intrinsic luminescence centers compared to those excitations that are captured by traps or quenching centers. The migration of these excitations can be modeled by single-step energy transfers from one ion to another via a random walk [46].

3. The luminescence stage is described by the quantum efficiency Q which corresponds to the fraction of excited luminescence centers yielding the production of scintillation photons compared to the ones recombining non-radiatively. At low temperatures, the quantum efficiency is close to unity. For elevated temperatures, it can be described by the classical Mott equation [46]:

$$Q = \frac{1}{1 + C \cdot e^{\frac{-\Delta E}{k_B \cdot T}}} \tag{A.16}$$

where C is the frequency constant characterizing the rate of the non-radiative decay, ΔE is the activation energy, k_B is the Boltzmann constant and T is the temperature. In $CaWO_4$, the quantum efficiency at low temperatures is assumed to be equal to 1.0 [46].

Combining these calculations and definitions gives a quantitative description of the energy efficiency η of scintillators [46]:

$$\eta = \frac{E_\gamma}{2.35 E_{gap}} \cdot B \cdot S \cdot Q = \frac{E_\gamma}{2.35 \cdot E_{gap}} \cdot \left[1 + 0.158 \cdot 10^4 \cdot \left(\frac{1}{\epsilon_\infty} - \frac{1}{\epsilon_0}\right) \frac{(\hbar\omega_{LO})^{\frac{3}{2}}}{1.5 \cdot E_{gap} \cdot eV^{\frac{1}{2}}}\right]^{-1} \cdot S \cdot Q \tag{A.17}$$

which corresponds to the fraction of deposited energy yielding scintillation light production, where the transport efficiency S and the quantum efficiency Q are temperature-dependent parameters.

Values of the model parameters for $CaWO_4$ at room temperature and 9K as used and determined in [46] on the basis of light-yield measurements can be found in table A.2:

	$T = 295$K	$T = 9$K
E_{gap} [eV]	5.2	5.2
E_γ [eV]	2.9	2.9
$\hbar\omega_{LO}$ [meV]	108	108
ϵ_∞	3.5	3.5
ϵ_0	10.4	10.4
B	0.41	0.41
Q	0.76	1.0
S	0.61	0.85
η [%]	4.6	8.3

Table A.2: Parameters of the phenomenological light-yield model for $CaWO_4$ as used and determined in [46].

It can be seen, that the quantum efficiency Q of the scintillation centers at low temperatures is estimated to be unity [46]. This implies, that every excited scintillation center produces one photon at low temperatures. The increase of the value for the energy transfer efficiency S for decreasing temperature (increase from 0.61 to 0.85) is interpreted as a result of the decreasing mobility of excitations, as discussed above [46].

In addition, it should be noted, that in other references (see, e.g., [113] or [79]), the conversion efficiency B is sometimes contained in a combined, phenomenological parameter $\beta = \frac{\alpha}{B}$, where α corresponds to the factor 2.35 in equation A.14. In reference [113], the value of β is estimated to be between 2 and 3. In [79], $\beta \approx 2$ is specified for highly ionic materials as $CaWO_4$. Hence, within such an approach, the value of B is essentially estimated to be unity and the number of created electron-hole pairs can be written as:

$$N_{eh} = \frac{E_\gamma}{\beta \cdot E_{gap}} = \frac{E_\gamma}{2.35 \cdot E_{gap}} \tag{A.18}$$

with $\beta = \alpha = 2.35$ [46], or alternatively, β between 2 and 3 [113, 79].

Within the present work, the second calculation, given by equation A.18, will be used for the estimation of the number of electron-hole pairs created by an electron recoil in $CaWO_4$, as discussed in section III/3.1.1.

It has to be noticed, that within this model, the stated energy efficiency η corresponds to the efficiency of internally *producing* scintillation light for electron recoils in a $CaWO_4$ crystal and *not* to the amount of scintillation light *escaping* the crystal or being *detected* with a light detector. Hence, within this model, the parameter η has to be interpreted as intrinsic light yield LY_{intr} of the $CaWO_4$ crystal.

In order to obtain an estimate of the amount of scintillation light leaving the crystal, the intrinsic light yield has to be multiplied by a factor describing the fraction of scintillation light escaping the crystal, the escape probability EP. This parameter depends e.g., on the shape of the crystal and its surface treatment and cannot be determined directly. An estimation of its value in the context of the CRESST experiment can be obtained from simulations of the light propagation in CRESST detector modules [73]: The calculated values range from 52% to 93%. Thus, according to the simulations a mean value of $EP_{sim} = 73\%$ is assumed. Hence, within the presented phenomenological model, the observable light yield $LY(T)$ (light escaping the crystal at temperature T) of a $CaWO_4$ crystal as employed in the CRESST experiment, can be estimated to:

$$LY(295\text{K}) = LY_{intr}(295\text{K}) \cdot EP_{sim} = 4.6\% \cdot 0.73 = 3.4\% \quad \text{(A.19)}$$

$$LY(T \lesssim 9\text{K}) = LY_{intr}(9\text{K}) \cdot EP_{sim} = 8.3\% \cdot 0.73 = 6.1\% \quad \text{(A.20)}$$

A.7 Position Dependent Detection Efficiency in CRESST Detector Modules

In [114], dependencies of the amount of the detected scintillation light on the position of the energy deposition within the $CaWO_4$ crystal in the CRESST experiment are reported. In a ^{57}Co calibration of CRESST detector modules, it could be observed that less scintillation light was detected if the energy deposition took place at high radial positions (close to the surface) within the crystal. The observed differences of the amount of scintillation light detected in the light detector are, however, not due to different scintillation-light generation yields. The observed differences can be attributed to the impact of the cylindrical shape of the crystals on light trapping and light escaping [114]. Hence, the amount of scintillation light detected in the light detector of a CRESST detector module may exhibit a dependency on the position of the energy deposition, however, the principle light-generation mechanism and its yield can be expected to be the same[3].

[3]This assumption is verified if the defect densities within the crystal volume and at its surface are the same as differences in the defect densities lead to differences in the light generation yield (see discussion in the framework of the model developed in this thesis, see section III/5.2.2).

Appendix B

Supplements to the Model Developed for the Exciton and Scintillation-Light Generation and Quenching in $CaWO_4$

B.1 Deposition of Energy by Different Primary Particles

Taking into account the two energy thresholds defined for electron- and nuclear-recoil production (see section III/3.1.1), the energy-loss processes for different interacting particles are presented in the following. Depending on the type of the primary particle and its energy E_{part}, several (dominant) possibilities for the interaction with the $CaWO_4$ lattice, i.e., the energy deposition process, occur[1]:

- Electromagnetic radiation (photons, x-rays and γ-particles):
  - $E_{gap} \lesssim E_{part} \lesssim E_{i-th}$: Excitation of one electron from the valence band into the conduction band by absorption.
  - $E_{i-th} \lesssim E_{part}$: Dominating scattering partner is the W nucleus and its electrons (cross sections are proportional to Z^n, $n \gtrsim 2$, where Z is the proton number). In figure B.1, the attenuation length of x-rays and γ-particles due to interaction with the W nucleus and its electrons is depicted. The total attenuation length is shown as solid black line, the contributions due to the photoelectric effect (dashed red line), due to Compton scattering (dotted green line) and due to pair production (dashed-dotted blue line) are shown. Attenuation lengths due to Thomson scattering at electrons of the W nuclei as well as the total attenuation lengths due to interactions with O and Ca nuclei and their electrons are at least one order of magnitude larger (see, e.g., figure 4.3 in [75]).

    From the different contributions to the total attenuation length of x-rays and γ-particles in $CaWO_4$ due to interaction with the W nuclei shown in figure B.1, different energy regions can be identified:

[1] Here, only the major interaction mechanisms are given, e.g., for high energetic electrons only the production of ionization is listed. Of course, high energetic electrons can, in principle, also directly produce phonons. However, this process is getting less probable, the higher the electron energy is.

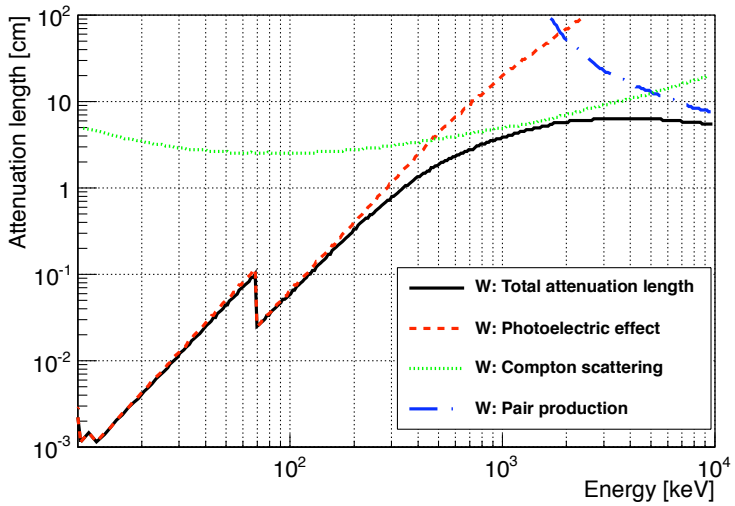

Figure B.1: Attenuation length of x-rays and γ-particles in $CaWO_4$ due to interaction with the W nuclei and their electrons (double-logarithmic scale): The total attenuation length due to interactions with W is shown as solid black line. Additionally, the individual contributions due to the photo-electric effect (dashed red line), Compton scattering (dotted green line) and pair production (dashed-dotted blue line) are shown (data adopted from figure 4.3 in [75]).

    - $E_{i-th} \lesssim E_{part} \lesssim$ 500keV: Production of one high energetic electron in the conduction band and the corresponding hole in the valence band via the photoelectric effect.
    - 500keV $\lesssim E_{part} \lesssim$ 5MeV: Production of several high energetic electrons in the conduction band and corresponding holes in the valence band via the Compton effect.
    - 5MeV $\lesssim E_{part}$: Production of a high energetic particle and its antiparticle (typically an electron and a positron) via pair production.

- Electrons:
  - $E_{gap} \lesssim E_{part} \lesssim E_{i-th}$: Relaxation (thermalization) of the electron to the conduction band edge via longitudinal phonon emission.
  - $E_{i-th} \lesssim E_{part}$: Excitation of electrons into the conduction band (and generation of the respective number of holes in the valence band). The created electrons and holes can excite further electrons into the conduction band (if enough energy was transferred). In total, a mean number of $N_{el} = \frac{E_{part}}{E_{i-th}}$ electrons (and holes) are generated. For high energetic electrons, this process can result in the intermediate generation of, e.g., plasmons, pair production or x-ray production. These intermediate steps, however, are assumed to result in the end in the production of the same number of electrons in the conduction band $N_{el} = \frac{E_{part}}{E_{i-th}}$ (ionization with the same efficiency).

- Holes:
  - $E_{gap} \lesssim E_{part} \lesssim E_{i-th}$: Relaxation (thermalization) of the hole to the valence band edge via longitudinal phonon emission.

  - $E_{i-th} \lesssim E_{part}$: Radiative (x-ray emission) or non-radiative (Auger transitions) relaxation of the atom where the hole resides until the hole is relaxed into the wide valence band (still $E_{i-th} \lesssim E_{part}$). Then the relaxation occurs analogously to the one of high energetic electrons [79].

- Neutrons:

  - $E_{gap} \lesssim E_{part} \lesssim E_{disp}$: Inelastic scattering at a nucleus of the crystal lattice with energy transfer less than the respective displacement energy. The transferred energy is released as phonons.
  - $E_{disp} \lesssim E_{part}$: Inelastic scattering at a nucleus of the crystal lattice with either energy transfer less than the displacement energy (production of phonons) or with energy transfer larger than the displacement energy, which results in the production of a recoiling nucleus and a vacancy in the lattice. The vacancy contains energy stored in the deformation of the crystal lattice.

- α-particles, recoiling nuclei and other heavy, charged particles:

  - $E_{gap} \lesssim E_{part} \lesssim E_{i-th}$: Inelastic scattering at a nucleus of the crystal lattice with energy transfer less than the respective displacement energy. The transferred energy is released as phonons. In the end, the moving particle typically comes to rest at an interstitial lattice site.
  - $E_{i-th} \lesssim E_{part} \lesssim E_{disp}$: Inelastic scattering at a nucleus of the crystal lattice with energy transfer less than the respective displacement energy. The transferred energy is released as phonons. Alternatively or additionally, ionization can be produced, i.e. an electron is excited into the conduction band (hole in the valence band). In the end, the moving particle typically comes to rest at an interstitial lattice site.
  - $E_{disp} \lesssim E_{part}$: Inelastic scattering at nuclei and electrons of the crystal lattice, causing ionization, recoiling nuclei and phonons. Three different cases, corresponding to different amounts of transferred energy, can be distinguished:
    * The transferred energy is less than the displacement energy of the hit nucleus. The transferred energy is released as phonons.
    * The transferred energy is larger than the displacement energy of the hit nucleus and the remaining energy of the primary particle is large enough so that it can leave the produced vacant lattice site: A recoiling nucleus and a vacancy in the lattice are created.
    * The transferred energy is larger than the displacement energy of the hit nucleus and the remaining energy of the primary particle is so small that it cannot leave the produced vacant lattice site. If the primary particle is identical to the produced recoiling nucleus, this collision is called a replacement collision. A recoiling nucleus and a possibly excited particle at the produced vacant lattice site are produced.

    Energy stored in vacancies or replacement collisions is typically released as phonons. The partitioning of the deposited energy into ionization, recoiling nuclei and phonons depends on the type and energy of the primary particle (for details, see section III/3.1.1)

B.2 Details on the Exciton-Formation Process

B.2.1 Diffusion-Controlled Recombination of Electrons and Self-trapped Holes (STHs)

In the following, a simplified model for the diffusion-controlled recombination of electrons and STHs to STEs is presented. Several assumptions are made, simplifying the general model of the diffusion-controlled recombination of two charged particles (see, e.g., [85]). In this way a simple mathematical description of the process can be obtained:

- STHs in $CaWO_4$ are immobile in the considered temperature range, i.e. the diffusion coefficient of STHs, D_{STH}, is assumed to be zero (compare section III/2.1.4).
- In the relaxation process to the band gap of the conduction band, the electrons are uniformly distributed in a volume $V_{e(CB)}^{relax}$ around the corresponding STH. The size of this volume is independent of temperature. This implies that no correlation of initial positions of STHs and electrons within the volume $V_{e(CB)}^{relax}$ is assumed[2].
- The only recombination mechanism for an electron in the conduction band is the recombination with its corresponding STH to form an STE.
- The autocorrelation of the diffusion-controlled recombination rate[3] is neglected. This corresponds to the "steady-state" approximation of a diffusion-controlled reaction (compare, e.g., [115]) and is equivalent to the assumption that the density of available recombination partners does not change with time. As will be shown in section III/3.1.2, a non-negligible number of electrons in the conduction band is captured by electron traps and, thus, removed from the STE-formation process. Therefore, the number of electrons in the conduction band is reduced faster with time than the number of available STHs. In first-order approximation, the number of STHs, N_{STH}^0, compared to the number of electrons can be regarded as constant.

It has to be noted that with the described assumptions, the theoretical model for the recombination of electrons and STHs to STEs as developed here only delivers a first-order approximation of this process.

In a diffusion-controlled recombination process, the existence of a so-called "black sphere" with radius $R_{eSTH}^0(T)$ is assumed (compare to the model of electron-hole pair recombination in [85]). Electron-STH pairs with a distance d_{e^-STH} smaller than this radius experience immediate recombination to a STE. For electron-STH distances d_{e^-STH} larger than this radius, the recombination of electrons with STHs is controlled by a diffusion process of the electron versus the "black sphere" of the STH.

The radius $R_{eSTH}^0(T)$ can be identified with the Onsager radius which is defined as the distance of two charged particles (with charge $q_1 = e$ for the electron and $q_2 = e$ for the STH) for which the energy of the Coulomb interaction (in a dielectric medium with relative electric permittivity ϵ_r) is equal to the thermal energy[4] $k_B \cdot T$ [84]. Then the "black

[2] This is a commonly used approximation (compare, e.g., [85] where it is assumed that no correlation of the particle distribution functions in the initial state exists).

[3] The autocorrelation of the recombination rate describes the decrease of the rate with time due to the reduction of available recombination partners with time (as they have already recombined).

[4] k_B is the Boltzmann constant and T is the temperature.

sphere" (Onsager) radius of immediate recombination is given by:

$$R^0_{eSTH}(T) := \frac{e^2}{4 \cdot \pi \cdot \epsilon_0 \cdot \epsilon_r \cdot k_B \cdot T} \tag{B.1}$$

with ϵ_0 as the vacuum permittivity. It has to be noted that, with this definition of the "black sphere" radius, the influence of the depth of the potential well in the conduction band (induced by the self-trapping process of the hole) is neglected.

Combined with the approximations explained above, the differential equation for the temporal development of the electron population in the conduction band, $N_{e(CB)}(T,t)$ can be described by a total temperature-dependent recombination rate $\beta^{diff}_{e^-STH\rightarrow STE}(T,t)$ (compare [85] for the general case):

$$\frac{\partial N_{e(CB)}(T,t)}{\partial t} = -\beta^{diff}_{e^-STH\rightarrow STE}(T,t) \cdot N_{e(CB)}(T,t) \cdot C_{STH}(T) \tag{B.2}$$

$d_{e^-STH} \leq R^0_{eSTH}$:

$$\beta^{diff}_{e^-STH\rightarrow STE}(T,t) = \frac{4}{3} \cdot \pi \cdot (R^0_{eSTH}(T))^3 \cdot \delta(t) \tag{B.3}$$

$d_{e^-STH} > R^0_{eSTH}$:

$$\beta^{diff}_{e^-STH\rightarrow STE}(T) = 4 \cdot \pi \cdot D_{e(CB)}(T) \cdot R^0_{eSTH}(T) \tag{B.4}$$

where $D_{e(CB)}(T)$ is the diffusion coefficient of electrons in the conduction band and $C_{STH}(T) = \frac{1}{V^{diff}_{e(CB)}(T)}$ is defined as the density of STHs in the volume $V^{diff}_{e(CB)}(T)$ that is probed by the electrons in their diffusion process (for a discussion of a possible temperature dependency[5], see below). The recombination rate described by equation B.3 corresponds to the immediate recombination of electrons and STHs to STEs and the recombination rate described by equation B.4 corresponds to the the diffusion-controlled (delayed) recombination of electrons and STHs to STEs. The initial condition for equation B.2 is that the number of electrons in the conduction band at time $t = 0$ is equal to the number of electrons and holes created in the energy-deposition process $N_{e(CB)}(t = 0) = N_{eh}(E_{part})$ by the primary particle *part* with energy E_{part} (see equation 3.1 in section III/3.1.2).

Inserting equation B.3 into equation B.2, it can be seen that the fraction of immediately recombining electron-STH pairs $F_{im-rec}(T)$ is proportional to:

$$F_{im-rec}(T) \propto (R^0_{eSTH}(T))^3 \cdot C_{STH}(T) \propto \frac{(R^0_{eSTH}(T))^3}{V^{diff}_{e(CB)}(T)} \tag{B.5}$$

Inserting equation B.4 into equation B.2, it can be seen that the recombination rate $k_{dr}(T)$ of the fraction of delayed recombining electron-STH pairs is proportional to:

$$k_{dr}(T) \propto D_{e(CB)}(T) \cdot R^0_{eSTH}(T) \cdot C_{STH}(T) \tag{B.6}$$

In order to clarify the temperature dependency of the recombination process, the temperature dependency of the electron diffusion (or mobility), i.e., the temperature dependency of the volume $V^{diff}_{e(CB)}(T)$ and of the diffusion coefficient $D_{e(CB)}(T)$, has to be reviewed.

[5] If the volume $V^{diff}_{e(CB)}(T)$ probed by the electrons in their diffusion process would increase for decreasing temperature, then the density of STHs in this volume would decrease (under the assumption that one STH per electron is available).

B.2.2 Temperature Dependency of the Electron Diffusion

From the approximations explained above, it can be seen that it is assumed that electrons in the conduction band can only recombine with STHs and that no other recombination process takes place. Therefore, the lifetime of the electrons that do not recombine immediately with STHs is completely determined by their diffusion process. The electrons migrate until they are captured by a STH. As the number of electrons and STHs is assumed to be independent of temperature (compare section III/3.1.2), the diffusion length of the electrons (mean distance travelled until they are captured) is also independent of temperature. Hence, the volume $V_{e(CB)}^{diff}$ as well as the density of STHs available to the electrons for recombination, C_{STH}, are independent of temperature.

The diffusion coefficient of the electrons in the conduction band, $D_{e(CB)}(T)$, on the other hand, is temperature dependent: The mobility $\mu_{e(CB)}(T)$ of the electrons in the conduction band is related to the diffusion coefficient $D_{e(CB)}(T)$ via the Einstein relation $D_{e(CB)}(T) = \frac{\mu_{e(CB)}(T) \cdot k_B \cdot T}{e}$. At elevated temperatures, such as room temperature, the electron mobility in a solid single crystal with a small defect density is dominated by phonon scattering. For decreasing temperature, the mobility increases proportional to $T^{-\frac{3}{2}}$. At low temperatures, the mobility is dominated by impurity scattering and, hence, saturates and even starts to decrease again[6] with decreasing temperature proportional to $T^{\frac{3}{2}}$ [116].

B.2.3 Temperature Dependency of the Electron-STH Pair Recombination

As the volume $V_{e(CB)}^{diff}$ is independent of temperature, the fraction of immediately recombining electron-STH pairs $F_{im-rec}(T)$ is proportional to $(R_{eSTH}^0(T))^3$ (compare equation B.3), i.e., using equation B.1, proportional to T^{-3}. Hence, the fraction of immediately recombining electron-STH pairs increases strongly with decreasing temperature. The recombination rate $k_{dr}(T)$, on the other hand, is proportional to the product of the diffusion coefficient of electrons in the conduction band of $CaWO_4$ and the Onsager radius, $D_{e(CB)}(T) \cdot R_{eSTH}^0(T)$ which is proportional to $\frac{\mu_{e(CB)}(T) \cdot T}{T}$, i.e. $k_{dr}(T) \propto \mu_{e(CB)}(T)$. Hence, for elevated temperatures, a dependency of the recombination rate $k_{dr}(T)$ on temperature of $k_{dr}(T) \propto T^{-\frac{3}{2}}$, at low temperatures, a dependency of $k_{dr}(T) \propto T^{\frac{3}{2}}$ can be expected.

B.2.4 Diffusion-Controlled Recombination of Electrons with Electron Traps

In the following, the capture process of electrons by traps is described in a diffusion-controlled recombination process, in analogy to the electron-capture process by STHs (see equations B.2, B.3 and B.4 in appendix B.2.1). Similarly to the approximations made in appendix B.2.1, it is assumed in the following that the spatial distribution of electron traps with respect to the electrons in the conduction band is uniform, i.e. no correlation of the respective positions is given.

[6] The temperature at which this change in behavior is observed depends on the defect density.

Electron Capture by Electron Traps

The additional recombination processes (in addition to the recombination with STHs), i.e., the immediate and delayed capture of electrons by electron traps, have to be introduced into the differential equation for the electrons in the conduction band with the "black sphere" radius[7] $R^0_{etrap} = R^0_{eSTH}$ (see equation B.1 in appendix B.2.1) and the number density of electron-traps $C_{e^-traps} := C_{\text{defects}}$. Here, C_{defects} is the number density of defect centers producing electron traps, i.e., the number density of green centers (compare definition at the beginning of the chapter). Due to the introduction of the additional recombination partners for electrons, the total diffusion-controlled recombination rate $k_{dr}(T)$ (compare equation 3.4 in appendix B.2.1) is influenced: Qualitatively, it can be assumed that, at room temperature (where the diffusion coefficient can be expected to be dominated by phonon scattering), the recombination rate is accelerated due to the enhanced density of possible recombination partners $C_{STH} + C_{\text{defects}}$. At low temperatures, where also the diffusion coefficient is assumed to depend on the defect density (dominated by scattering at defects, see appendix B.2.2), the influence of the enhanced density of recombination partners can be assumed to be negligible.

Hence, qualitatively it can be expected that, at room temperature, the rise time $\tau_{dr}(T)$ of the delayed produced STE population is decreased due to the enhanced density of available recombination partners (STHs and electron traps) whereas at low temperatures only a minor influence is expected.

Fraction of Electrons Captured by Electron Traps

From the rate equation B.2 (appendix B.2.1), it can be seen that the only difference between the electron-capture processes by STHs and electron traps consists in the different numbers of STHs (one per electron in the approximation applied here) and electron traps within the volume $V^{diff}_{e(CB)}$. These numbers are quantified by the densities C_{STH} and C_{defects}. Hence, the total fraction of electrons captured by electron traps, F_{e^-traps}, or by STHs, $F_{STH} = (1 - F_{e^-traps})$, (in the immediate and delayed processes combined) only depends on the ratio of the relative occurrences of electron taps and STHs in the volume $V^{diff}_{e(CB)}$ probed by the electron in its diffusion process[8]:

$$F_{e^-traps} = \frac{C_{\text{defects}}}{C_{STH} + C_{\text{defects}}} \not\propto T \tag{B.7}$$

$$F_{STH} = (1 - F_{e^-traps}) = \frac{C_{STH}}{C_{STH} + C_{\text{defects}}} \not\propto T \tag{B.8}$$

[7] It can be seen that by neglecting the depth of the potential well in the conduction band in the definition of the "black sphere" radius, the corresponding radii of a STH and an electron trap are assumed to be equal $R^0_{etrap} = R^0_{eSTH}$. This equality corresponds to the assumption that the probabilities of capturing an electron by a STH or by an electron trap located in the same distance to the electron in the conduction band are equal.

[8] The volume $V^{diff}_{e(CB)}$ probed by the electron in its migration process can still be assumed to be independent of temperature as the only recombination processes considered are provided by the recombination with STHs or electron traps. Hence, the electron migrates until it is captured.

B.3 Details of the Determination of the Particle-Induced Ionization Density in $CaWO_4$

In this section, details of the method used to determine the ionization density $\rho_{ioniz}(E_{part}, \mathbf{x})$ and, hence, the initially created blue STE density $n_{bSTE}^{form\,0}(E_{part}, \mathbf{x})$ for different primary interacting particles in $CaWO_4$ are presented. For the outline of the employed method and used models, see section III/3.1.2.

B.3.1 Model for the Ionization-Density Distribution Created by an Electron

As discussed in section III/3.1.2, the energy-loss process of an electron in $CaWO_4$ is regarded to be describable as the excitation of low- and high-energetic electrons in the conduction band and holes in the valence band in individual collisions with the electrons of the target crystal (compare figure 3.3 in section III/3.1.2). Of course, all of the excited electrons and holes possess energies less than or maximally equal to the energy of the primary electron (if the collision was a replacement collision, compare appendix B.1 for the analogous description for the case of interacting ions). Hence, this process is self-similar in the sense that any "secondary" electron generated by an interaction of the "primary" electron with the $CaWO_4$ crystal loses its energy in the same way as the primary electron until, at the end of this chain of created electrons and holes, only particles with energies less than the ionization threshold $E_{i-th} = 11.75\text{eV}$ (corresponding to the mean energy needed to create an electron-hole pair in $CaWO_4$, compare section III/3.1.2) are created. The finally generated distribution of created ionization corresponds to the distribution of these low-energetic electrons produced in the final steps of the energy-loss processes of electrons (and holes). Hence, in analogy to the description of the ionization-density distribution generated by ions, the problem to determine the energy distribution for electrons can, in principle, be reduced to the determination of the ionization distribution generated by electrons and holes with the smallest energies possible, i.e., to the spatial distribution of these low-energetic particles ($E_{e^-/h} \lesssim E_{i-th}$) within the excited volume.

For these low-energetic electrons it can be assumed that their corresponding holes are situated very close (fast self-trapping process of holes and low mobility of holes and STHs in $CaWO_4$, compare section III/2.1.4). Hence, to such a low-energetic electron (together with its corresponding hole) a small sub-volume within the total excited volume is assigned. Each of these small volumes is described as a cylindrical slice around the track of the parent particle by which the low-energetic electron (and its hole) were created. The length of such a slice is chosen to be 1nm, in analogy to the description of the ionization caused by recoil ions created by a heavy charged primary particle with the model *Rec* (compare figure 3.5 in section III/3.1.2). No dependency of the generated ionization density within such a slice on the radial or angular coordinate is assumed, i.e., also no division of this volume into inner and outer cylinders is performed. This choice was made as the ionization created within one of these volumes already corresponds to the ionization by low-energetic electrons only. Hence, no sub-division of the excited volume into a densely ionized "core" and a thinly ionized "penumbra" region is required. In analogy to the *Rec* model for ions, the radial extent of all of these small, excited sub-volumes created by one primary interacting electron is assumed to be the same. Of course, the possibility for two or more of these low-energetic electrons to be generated within the same small volume,

i.e., to be created at roughly the same position, is included. It should be noted that such an overlap is assumed to occur only for low-energetic electrons created by the same parent electron, except for the possibility of an overlap at the position where the higher-energetic, secondary parent electron was created by its respective parent electron: At this position the possibility of an overlap of low-energetic electrons created by the primary parent electron and the secondary parent electron is included in the model (compare figure 3.3 in section III/3.1.2 as well as the description of the overlap region for heavy, charged particles and their recoil ions).

Hence, the ionization density produced by electrons is described using a "simplified" Rec_{el} model only (compare to the model *Rec* model introduced for heavy, charged particles, see discussion above table 3.4 in section III/3.1.2). This model describes the ionization created by low-energetic electrons along the track of the primary electrons as well as along the track of its high-energetic recoil electrons within small volumes $V_{Rec_{el}}$. This model is simple compared to the description of the ionization created by ions as, on the one hand, no "continuously, direct creation of ionization" as for ions (compare model *PIT*) has to be considered and as, on the other hand, no subdivision of one the individually excited volumes $Rec_{el}[i]$ into inner and outer volume has to be taken into account, where the integer number $[i]$ is used to distinguish Rec_{el} volumes with different energy content (compare to the model *Rec* for heavy charged particles in section III/3.1.2).

In analogy to the *Rec* model for ions (compare, e.g., table 3.4 in section III/3.1.2), these individual volumes as well as the STE densities created within these volumes can be described using the following parameters (see table B.1) and relationships:

parameter	meaning
$z \in [0,1]$ [nm]	dimension in z-direction of one of the Rec_{el} volumes, $Rec_{el}[i]$
$\rho = r_{Rec_{el}}(E_{part})$ [nm]	radius of the cylinder of the Rec_{el} volumes
$V_{Rec_{el}}(E_{part})$ [nm^3]	Rec_{el} volume (1nm slice of the primary or recoil electron track)
$E_{ioniz,Rec_{el}[i]}(E_{part})$ [eV]	energy deposited in ionization within the volume $Rec_{el}[i]$ (*by the parent electron* and by its recoil electrons within their "overlap regions")
$N_{bSTE,Rec_{el}[i]}(E_{part})$	number of blue STEs initially created in the volume $Rec_{el}[i]$

Table B.1: Parameters of the model Rec_{el} used to describe the distribution of the energy deposited in ionization and of the initially created blue STE population, within one 1nm long slice $Rec_{el}[i]$ of the track of the primary electron and its recoil electrons.

Using equation 3.13 (section III/3.1.2), the respective initial numbers of blue STEs created in the slice $Rec_{el}[i]$ of an electron track can be expressed by:

$$N_{bSTE,Rec_{el}[i]} = \frac{(1 - F_{e^- trap})}{2.35 \cdot E_{gap}} \cdot E_{ioniz,Rec_{el}[i]} \tag{B.9}$$

One of the $Rec_{el}[i]$ volumes in which the distribution of the initially produced blue STE

populations is described by the model Rec_{el} is defined by:

$$V_{Rec_{el}} := \left\{ \mathbf{x} = \begin{pmatrix} \rho \\ \varphi \\ z \end{pmatrix} \in \mathbb{R}^3; \begin{pmatrix} \rho \\ \varphi \\ z \end{pmatrix} \in [0, r_{Rec_{el}}] \times [0, 2\pi] \times [0, 1] \right\} \tag{B.10}$$

From this expression for the $Rec_{el}[i]$ volumes, it can be seen that the geometrical parameters used are assumed to be the same for all slices of all electron tracks generated by one primary interacting electron (no dependency on i).

Hence, the density of blue STEs produced within the volume $V_{Rec_{el}}(E_{part})$ is assumed to be independent of the position within the volume and can be expressed by:

$$n^{form\,0}_{bSTE,Rec_{el}[i]} := n^{form\,0}_{bSTE,i}(\mathbf{x})\Big|_{\mathbf{x}\in V_{Rec_{el}}} = N_{bSTE,Rec_{el}[i]} \cdot \frac{1}{(r_{Rec_{el}})^2 \cdot \pi \cdot 1\text{nm}} \tag{B.11}$$

$$N_{bSTE,Rec_{el}[i]} = \int\limits_{V_{Rec_{el}}} n^{form\,0}_{bSTE,i}(\mathbf{x})\ \rho\ d\rho d\varphi dz$$

It can be recognized that the STE densities described by equation B.11 do not contain any dependency on the position within the respective volumes besides the limitations of the volumes. This reflects the assumed homogeneous distribution of the ionization within the individual volumes. On the other hand, it can be seen that these densities can differ for different slices of electron tracks ($Rec_{el}[i]$), if the number $N_{bSTE,Rec_{el}[i]}$ of blue STEs deposited in these slices differs, i.e., if a different amount of energy, $E_{ioniz,Rec_{el}[i]}(E_{part})$, was initially deposited within these slices.

A discussion of the determination of the parameters used to described the STE density produced by electrons as primary interacting particles can be found in appendices B.3.7 and B.3.8.

B.3.2 Settings of the Simulation Programs and Data Delivered by the Simulations

In the following, details on the simulations performed with the programs CASINO [43] and SRIM [42] as well as on the delivered data used for the determination of the ionization density $\rho_{ioniz}(E_{part}, \mathbf{x})$ of particles interacting in $CaWO_4$ are presented.

Overview Over the Performed Simulations

- CASINO simulations of electrons: The following energies and number of particles were simulated:
  - 10000 electrons each, with energies of 20eV, 40eV, 60eV, 80eV, 100eV, 120eV, 140eV, 160eV, 180eV and 200eV
  - 10000 electrons each, with energies of 300eV, 400eV, 500eV, 600eV, 700eV, 800eV, 900eV and 1000eV
  - 10000 electrons each, with energies of 2keV, 3keV, 4keV, 5keV, 6keV, 7keV, 8keV, 9keV and 10keV
  - 10000 electrons each, with energies of 20keV, 30keV, 40keV, 50keV, 60keV, 70keV, 80keV, 90keV and 100keV

  - 1000 electrons each, with energies of 200keV, 300keV, 500keV, 700keV and 1MeV

- SRIM simulations of O, Ca and W ions, respectively: The following energies and number of particles were simulated:

  - 10000 ions each, with energies of 20eV, 50eV and 100eV
  - 10000 ions each, with energies of 200eV, 500eV and 1000eV
  - 10000 ions each, with energies of 2keV, 5keV and 10keV
  - 10000 ions each, with energies of 20keV, 50keV and 100keV
  - 10000 ions each, with energies of 200keV, 500keV and 1000keV
  - 2000 ions each, with energies of 2MeV, 5MeV and 10MeV
  - 2000 ions each, with energies of 20MeV and 50MeV

For electrons, a finer binning at low energies was chosen as, within the CASINO simulation, the mean energy of recoiling electrons produced is very small(e.g., for a primary electron of 100keV energy, the mean energy of recoil electrons amounts to only 35.7eV). Therefore, it was attempted to analyze this low-energetic region as accurately as possible.

The Program CASINO and the Utilized Settings

The CASINO program is a Monte Carlo simulation of electron trajectories in solid materials. It was originally designed to calculate many of the signals recorded in a scanning electron microscope [43]. Several features of the CASINO program should be taken into account when using it to simulate the energy-loss process of electrons:

- The simulated electrons always start from outside of the target.

- Hence, a fraction of these electrons can be backscattered and leave the crystal without depositing their complete energy. Such events are particularly marked in the output files. As the situation intended to be investigated within the present work is the interaction of an electron within the volume of a $CaWO_4$ crystal depositing all of its energy there, such backscattered electrons were dismissed in the analysis of the simulated data.

- Within the CASINO simulation, no high-energetic recoil electrons produced by the primary electron are tracked, instead the corresponding low-energetic electrons are directly created [90]. This should be kept in mind when relating any model parameters to the energy of the produced recoil electrons.

- The coordinate system in CASINO is defined as follows: the z-axis corresponds to the direction perpendicular to the target surface and is, thus, parallel to the incident electrons. The target surface is defined by the (x, y)-plane. In the simulations, electrons were always started perpendicular to the target surface.

- For the correct interpretation of the simulated data, at least for electrons with energies $\gtrsim$ 10keV, data on the range and the stopping power (in eV/nm) from the estar database [117] was used for comparison.

utilized version of CASINO*	v2.4.8.1
target parameters	
chemical composition of the material	$CaWO_4$
user defined density $\left[\frac{g}{cm^3}\right]$	6.06
thickness (i.e., depth of the material)*	"substrate"
electron parameters	
simulate multiple energies	no
number of simulated particles	see list of simulations performed
tilt of specimen [°]	0
beam radius [nm]	0
line scan	no
distribution parameters	
for all distributions	"enabled" "collect data logarithmically"
max range parameters	simulated
distribution of energy by position*	
runtime options	
number of displayed trajectories	1000
time between backups [min]	5
minimum electron energy * [keV]	0.01175
conserved electron trajectories	displayed only
physics models*	
Total Cross Section	"Rutherford (Suggested by Murata)"
Partial Cross Section	"Rutherford (Suggested by Murata)"
all other settings	left as automatically set
display options*	
show backscattered electrons	yes
trajectory coloration	by energy
show collisions	all
trajectory resolution*	95%

Table B.2: Settings as used in the CASINO simulations: For settings labeled with *, see comments below.

The relevant settings of the program CASINO can be found in table B.2. These settings were the same in all simulations performed with CASINO.

Comments on the items labeled with * in table B.2:

- Downloaded 05.01.2012 from `http://www.gel.usherbrooke.ca/casino/index.html`
- Thickness of material: the choice of the option "substrate" causes the thickness of the material to be larger than any simulated track so that no simulated electrons can be transmitted through the material.
- Minimum electron energy (in keV): minimal electron energy at which a trajectory is

terminated. The smallest energy that should be considered is the energy required to excite a "secondary" electron into the conduction band, i.e., the ionization threshold energy $E_{i-th} = 2.35 \cdot 5\text{eV} = 11.75\text{eV}$ (see section III/3.1.2).

- Distribution of energy by position: Information collected according to these settings are not used within the analysis.
- Physics models: "Rutherford (Suggested by Murata)". This physics model was used (instead of, e.g., Mott scattering) as especially the behavior of low-energetic electrons is of interest[9].
- Display options: the minimum number of displayed tracks is 25 (as is the minimum number of simulated electrons).
- Trajectory resolution: amount of detail of the trajectory displayed (100% draws all segments of the tracks even if smaller than 1 pixel).

The Program SRIM and the Utilized Settings

With the package TRIM (the Transport of Ions in Matter) of the program SRIM [42], the interactions of an incident atom (called "ion") in a target can be simulated including ion-atom collisions with screened Coulomb potentials, exchange and correlation interactions of the overlapping electron shells as well as long-range interactions of the interacting ion creating electron excitations and plasmons in the target. The calculation comprises target damage, sputtering, ionization and phonon production. The following features of the simulations performed with SRIM should be taken into account:

- SRIM offers the possibility to start ions within the target material. This option was used in order to avoid backscattered ions as the standard condition for, e.g., neutron-induced nuclear recoils is that they take place within the target volume and, hence, do not enter from the outside. Thus, always a starting point deep enough within the target material was chosen to assure that all simulated ions as well as their recoil cascades deposit their total energy within the crystal.
- The only exceptions were the simulations of the ions used in the experiments which had been conducted to determine the model parameters and to validate the complete model (see chapter III/4). These ions were indeed shot onto the crystal from the outside. Therefore, also in the simulations, these ions were started outside of the material.
- In TRIM, the coordinate system differs from the one used in CASINO: In TRIM, the x-axis corresponds to the direction perpendicular to the target surface and the (y, z)-plane defines the target surface. The ions were always started perpendicular to the target surface, i.e., perpendicular to the (y, z)-plane.
- However, in the following, when referring to the coordinate system of the target material, i.e., the crystal, the convention of labeling the axis perpendicular to the target surface with z, as in CASINO, is adopted.

The relevant settings of SRIM are given in table B.3. These settings were the same in all simulations performed.

[9] Mott scattering describes the scattering of electrons off the atomic nucleus with energies large enough so that the electrons start to penetrate the atomic nucleus.

used version of SRIM*	SRIM-2012.03
type of TRIM calculation*	full damage cascades using TRIM.DAT file
ion data	
angle of incidence ([°])	0
target data	
layers	1 ($CaWO_4$)
width* [μm]	2 000
user defined density $\left[\frac{g}{cm^3}\right]$	6.06
compound correction*	1
gas	no
input elements to layer 1 (atomic stoichiometry)	Ca (1), W(1), O(4) all other values left as automatically set
special parameters	
stopping power version*	SRIM-2008
auto save at ion #	10 000
random number seed*	no number set
output disk files	
ion ranges	yes
backscattered ions	yes
transmitted ions/recoils	no
sputtered ions	no
collision details	yes
special "EXYZ File" increment [eV]	0

Table B.3: Settings as used in all SRIM simulations: For settings labeled with *, see comments below.

Comments on the items labeled with *:

- Downloaded 20.04.2012 from `http://www.srim.org/SRIM/SRIMLEGL.htm`
- Type of TRIM calculation: Using the chosen option makes TRIM follow every recoil until its energy drops below the lowest displacement energy of any atom in the target, thus calculating all sub-cascades. The file TRIM.dat contains a list of all of the primary interacting ions to be simulated (type and energy) with their starting positions (x, y, z) and angles of incidence. The starting positions were chosen such that the complete energy of all simulated ions and their recoil cascades was deposited within the material (no backscattered ions or recoils leaving the material). The direction of incidence was always chosen to be normal incidence compared to the target surface.
- Width: The value of 2000μm was chosen to assure that no particles are transmitted through the substrate.
- Compound correction: This value gives the possibility to correct the stopping power

of ions in compound materials compared to the estimate of the stopping power by the sum of the stopping powers of its elemental constituents. A value of unity indicates no corrections as recommended in [42] for compounds containing elements heavier than aluminum (in experiments less than 2% deviation have been determined for many examples of such compounds [42]).

- Random number seed: If no value is given, TRIM uses the number 716381 as starting point (choosing this number will reproduce exactly the same results).

Data Delivered by the Simulations and Used to Determine the Ionization Density Created:

From the simulations with the program CASINO, the output files "Trajectories.dat" containing the following information (only information relevant for the calculations is listed) for each simulated electron trajectory separately were used:

- Backscattered: yes/no
- Position (x, y, z) of a collision within the target leading to the creation of a secondary electron
- $E_{e^-}(x, y, z)$: energy of the primary electron after each collision.

From the simulations with the program SRIM, the output files "COLLISION.txt", "RANGE. txt" and "IONIZ. txt" containing the following information (only information relevant for the calculations is listed) were used:

- "COLLISION.txt" containing information for each simulated ion separately
  - Position (x, y, z) of a collision within the target leading to the creation of a nuclear recoil
  - Type and energy of the created nuclear recoil
  - $E_{ion}(x, y, z)$: energy of the primary ion after each collision.
  - $S_{el}(x, y, z)$: Electronic stopping power in eV/Å of the primary ion at the positions (x, y, z).
- "RANGE.txt" containing information for each simulated ion separately
  - Final position of the simulated ions after their complete energy-loss process $(x_{final}, y_{final}, z_{final})$.
- "IONIZ.txt" containing information already averaged for all simulated ions of one run (one type and one energy of the simulated ions)
  - Energy deposited in ionization in eV/Å by the primary ion and by its nuclear recoils combined at 100 positions z in perpendicular direction into the crystal.
  - Energy deposited in ionization in eV/Å by the primary ion only at 100 positions z in perpendicular direction into the crystal.
  - Energy deposited in ionization in eV/Å by the produced nuclear recoils only at 100 positions z in perpendicular direction into the crystal.

B.3.3 Information Retrieved from the Data Delivered by the Simulations:

From this data the following additional information can be calculated:

- From the production points of the respective recoil particles, the track of the respective primary particle can be calculated. Hence, straggling of the particle track between these collision points is neglected.

- It should be noted that, for ions, as the last step of their track, the difference between the last position where a recoil particle was produced and their final position indicated in the "RANGE.txt" file is added.

- For electrons, the energy they exhibit after their last collision listed is considered and an estimated length corresponding to this energy is added: This length is estimated from a linear extrapolation of the length travelled by a 20eV electron which loses 8.25eV along its track until it is no longer traced (rest energy of 11.75eV). Hence, the length of the track calculated for the 20eV electron corresponds to the length of the track of an electron losing 8.25eV of its energy. This relationship is linearly interpolated to obtain the length of the track traveled by, e.g., a 11.75eV electron.

- For each simulated particle, the length of this track as well as the penetration depth into the target in the direction of their initial movement (z-axis of the crystal) can be determined. These quantities are then averaged over the total number of particles simulated in one run. In this way, the mean length of the track $l_{track}(E_{part})$ as well as the mean maximum penetration depth $d_{max}(E_{part})$ for each particle (type and energy) simulated is determined.

- For ions, additionally, the integrals of the integrated ionization produced (integrating the z-dependent values stated in the "IONIZ.txt files") by the primary interacting particle as well as by all of its recoils is calculated.

Combining these calculated data with the data originally delivered by the simulations, it can be seen that the only information that is delivered in dependency of the position within the material is the production of recoil particles along the track and the electronic stopping of ions along their tracks. It should be noted that for ions no information about the energy of the created electrons is delivered.

B.3.4 Method Developed for the Analysis of the Simulations

In the following the method developed to obtain information on the ionization-density distribution initially created by an interacting particle from the data of the simulations is described for the example of a heavy, charged interacting particle with energy E_{part}. The method applied for electrons as primary interacting particle is, in principle, the same. The only differences result from the fact that for electrons no separately produced direct ionization by the primary particle has to be considered as well as that only one type of recoil particles (secondary electrons) can be produced.

For the analysis of the data delivered by the simulation several basic considerations and assumptions have to be taken into account:

- A smallest unit length Δl_{min} = 1nm as well as a smallest unit volume ΔV_{min} (a cylinder of 1nm length with a radius of 1nm) are defined[10]. These definitions are used to introduce a binned sampling of the volume excited in the energy-loss process of the primary particle as well as of its recoil particles.

- For distances along the track of a particle (of the primary or of a recoil particle) smaller than Δl_{min} = 1nm, all recoil particles generated are assumed to be produced within the same minimal length unit Δl_{min}, i.e., at the same position along the track.

- In addition, in a first step, all energy deposited in ionization directly by the primary ion within Δl_{min} = 1nm along its track is assumed to be deposited within the same minimal volume element ΔV_{min}. It should be noted that this assumption corresponds to neglecting any radial dependency of the produced ionization around the track of the primary particle, i.e., to neglecting the division of the excited volumes into inner and outer cylinder. This choice was made as, on the one hand, directly from the simulations no information on the energy of the produced electrons is available. On the other hand, it can be expected, as discussed above that the major fraction of the produced electrons is low-energetic and, hence, exhibits only a very small range represented by the radius of 1nm of the minimal volume.

- For recoil particles produced along the track of a primary interacting ion it is assumed that, within their energy-loss process, they first have to cross ΔV_{min} (with radius Δl_{min} = 1nm), the volume element excited directly by the primary interacting particle and then start their own, separate tracks where they produce ionization (and recoil particles) of their own. Hence, it can be deduced that the energy deposited by a recoil particle within the first nm along its track (Δl_{min} = 1nm) until it leaves the volume ΔV_{min} overlaps with the ionization created by the primary particle at the position of the recoil production.

- O, Ca and W ions with energies < 50eV have track lengths less than Δl_{min} = 1nm[11]. Hence, if such particles with energies smaller than these energies are created as recoil particles by a primary particle, they do not leave the volume ΔV_{min} excited directly by the primary particle. Therefore, all of the ionization created by such low-energetic recoil particles (directly or by "secondary" recoil particles created by the "primary" recoil particle) overlaps with the ionization created directly by the primary interacting particle.

The method used for the evaluation of the data delivered by the simulations is based on several steps iteratively repeated for each simulated energy starting with the smallest energies considered. Hence, before the application of this method to a primary particle with energy E_{part}, the following information on all possible recoil particles for this primary particle (O, Ca and W ions with energies < E_{part}) is available (due to the earlier application of the same method to all possible recoil particles with energies < E_{part}):

- The amount of energy deposited within the first nm along the PIT_{rec} volume of the respective potential recoil particle (the PIT_{rec} volume of a recoil particle corresponds

[10] It should be noted that this binning was chosen small enough so that the typical length describing the interaction between created blue STEs (the Förster radius, see section III/3.1.3) is larger than the extent of this minimal volume. Hence, it was assumed that variations of the density-distribution within such a minimal volume do not have to be considered.

[11] Electrons with energies ≤ 60eV have track lengths less than Δl_{min} = 1nm.

to the PIT model for a heavy charged particle, see section III/3.1.2). This value is calculated for each supporting-point energy and made available for energies between the supporting points through the continuation of the data points with the help of a cubic spline. These splines are referred to as "overlap splines", $OvS_{rec}(E_{rec})$, for each type of recoil particle rec =O, Ca or W with energy $E_{rec} < E_{part}$.

- The energy depositions (in eV per 1nm bin) of the potential recoil particle within each of the other 1nm bins of its PIT_{rec} volume (except for the first bin). These energy depositions are described by a histogram containing the occurrences of such energy depositions within the PIT_{rec} volume binned in 1eV bins. This histogram is referred to as $NO - PIT_{rec}(E_{rec})$ histogram for a particle of type rec =O, Ca or W with an energy $E_{rec} < E_{part}$ (it contains the information on the ionization within the primary ionization track of the respective, potential recoil exhibiting no overlap with the primary ionization track of the primary particle). At each of the supporting points this histogram is fitted with a Landau distribution using the following five parameters: $\mu(PIT_{rec}, E_{rec})$ (the most probable value), $\sigma(PIT_{rec}, E_{rec})$ (a scale parameter for the width of the distribution), $C(PIT_{rec}, E_{rec})$ (a scaling factor for the integral of the distribution), $Min(PIT_{rec}, E_{rec})$ (the minimum energy deposition within one bin of the PIT_{rec} track) as well as $Max(PIT_{rec}, E_{rec})$ (the maximum energy deposition within one bin of the PIT_{rec} track). Such a description of the histogram is successively made available for each of the supporting point energies. For energies between these supporting-point energies, the values of the parameters of the Landau distribution are made available by describing the energy dependency of each of the five parameters with the help of a cubic spline, respectively. In this way, for each possible recoil particle with energy $E_{rec} < E_{part}$ the calculation of the Landau function describing the $NO - PIT_{rec}(E_{rec})$ histogram and, hence, the calculation of the entries of this histogram, is made possible.

- In analogy, the energy depositions (in eV per 1nm bin) of all of the "secondary" recoil particles for the respective potential "primary" recoil particle are described by a histogram containing the occurrences of these energy depositions binned in 1eV bins. This histogram is referred to as $NO - Rec_{rec}(E_{rec})$ histogram for a particle of type rec =O, Ca or W with an energy $E_{rec} < E_{part}$ (it contains the information on the ionization produced by "secondary" recoils outside of the PIT_{rec} volume of the respective "primary" recoil). In analogy to the $NO - PIT_{rec}(E_{rec})$ histogram, this histogram is described with a Landau function using five parameters $\mu(Rec_{rec}, E_{rec})$, $\sigma(Rec_{rec}, E_{rec})$, $C(Rec_{rec}, E_{rec})$, $Min(Rec_{rec}, E_{rec})$ as well as $Max(Rec_{rec}, E_{rec})$. Also for each of these parameters a continuation between the supporting energies (where the values of these parameters can be determined directly) by a spline is calculated. Hence, also the entries of this histogram can be calculated for any of the potential recoil particles (O, Ca or W ion) with an energy $E_{rec} < E_{part}$.

Hence, the ionization distribution created by a recoil particle (rec = O, Ca or W) with energy $E_{rec} < E_{part}$ is described by the value of the corresponding overlap spline, $OvS_{rec}(E_{rec})$, evaluated for the energy E_{rec}, the Landau distribution corresponding to the $NO-PIT_{rec}(E_{rec})$ histogram described by the values of the splines for the five parameters of the respective Landau distribution, and the Landau distribution corresponding to the $NO-Rec_{rec}(E_{rec})$ histogram described by the values of the splines for the five parameters of the respective

Landau distribution. Before presenting the method used to determine the ionization density distribution of a primary interacting particle with energy E_{part} on the basis of this information, two comments on the described histograms and splines should be made:

- Within the developed description it is implicitly assumed that no overlap between volumes excited by different recoils ("secondary" or "primary") can occur except for a potential overlap within the PIT or PIT_{rec} volumes (production of recoils within the same minimal unit volume V_{min})[12].

- All of the described histograms as well as the amount of energy deposited in the overlap region described by the $OvS_{rec}(E_{rec})$ spline are obtained by averaging over the respective values for all of the simulated particles of one type and energy.

In the following, the five steps of the method (iteratively applied to each simulated supporting-point energy) used to determine the ionization distribution for a primary particle of energy E_{part} on the basis of the data delivered by the simulation of this particle are presented:

1. For the primary particle of energy E_{part}, a binned histogram labelled $PIT(E_{part})$ (1nm binning) of its track is created. This histogram is filled with the data delivered by the simulation:

   - The ionization produced directly by the primary particle (using the electronic stopping power $S_{el}(x, y, z)$ and the information on the total amount of energy deposited in ionization by the primary interacting particle).
   - The ionization created by nuclear recoils within their respective first $PIT(E_{rec})$-histogram bins, i.e., with the energy depositions as described by the overlap splines $OvS_{rec}(E_{rec})$ for O, Ca and W ions.

2. This $PIT(E_{part})$ histogram is fitted with an exponential function (or two concatenated exponential functions) along the primary ionization track of the regarded particle. This fit delivers a simple continuous description of the ionization deposited within the PIT volume by the regarded particle as primary interacting particle.

3. Then, a histogram containing the occurrences of energy depositions (in eV per nm bin) by all recoil particles created outside of the PIT track, i.e., the histogram $NO - Rec_{rec}(E_{part})$ for the primary interacting particle with energy E_{part} is created. This histogram is obtained by summing the $NO - PIT_{rec}(E_{rec})$ and $NO - Rec_{rec}(E_{rec})$ histograms of all produced recoils. The bins and weighted entries of these two histograms for one recoil particle are calculated from the respective Landau distributions describing these histograms for the regarded recoil particle (where the parameters for the Landau distributions are obtained from the respective splines).

4. However, if the regarded primary particle is a potential recoil particle of the $CaWO_4$ lattice, in addition, the entry for the overlap spline $OvS_{rec}(E_{part})$ as well as the histogram $NO - PIT_{rec}(E_{part})$ are determined.

[12] This assumption is justified by the three-dimensional degree of freedom for the direction of movement of the produced recoil particles around the PIT and the PIT_{rec} volume, respectively.

5. Finally, the histograms $NO - PIT_{rec}(E_{part})$ and $NO - Rec_{rec}(E_{part})$ are fitted with Landau distributions and the resulting parameters are used to extend the corresponding splines describing the energy dependency of these parameters. In analogy, the value determined for the ionization density in the overlap region is used to extend the overlap spline, $OvS_{rec}(E_{part})$, for this type of particle.

Hence, using the exponential fit function for the ionization contained in the $PIT(E_{part})$ histogram as well as the histogram $NO - Rec_{rec}(E_{part})$, the complete ionization generated by the considered particle with energy E_{part} is described. A graphical representation of the described method to determine the ionization density of a particle with energy E_{part} from the data delivered by the simulations can be found in appendix B.3.5.

However, in order to use the obtained histogram $NO - Rec_{rec}(E_{part})$ for the calculation of the decay-time spectrum of the scintillation light produced by the primary interacting particle (see section III/3.2.4), a further simplification of the description of the ionization density is aimed at[13]. For this purpose, a rebinning of the histogram $NO - Rec_{rec}(E_{part})$ with larger bin widths is performed to obtain a smaller number of individual bins that have to be taken into account. The edges of the new bins chosen correspond to integer multiples (0, 2^n, $n \in \mathbb{N}_0$) of produced electron-hole pairs, i.e., to $0 \cdot 11.75\text{eV}$, $1 \cdot 11.75\text{eV}$, $2 \cdot 11.75\text{eV}$, $4 \cdot 11.75\text{eV}$, $8 \cdot 11.75\text{eV}$, etc. (compare equation 3.1.2). Of course, in the rebinning process the new weights of the different bins are calculated such that the integral amount of energy contained in the histogram stays the same.

Thus, it can be concluded that, from the described analysis of the data delivered by the simulations the following parameters describing the energy deposition by a primary interacting particle of type *part* with energy E_{part} can be extracted:

- The length of the track of such a particle, $l_{track}(E_{part})$.
- The integral amount of energy deposited in ionization within the PIT volume, $E_{ioniz,PIT}(E_{part})$.
- The exponential decay constant (or two different decay constants for different regions along the track of the primary interacting particle) describing the variation of the ionization density along the PIT, $\alpha_{PIT}(E_{part})$.
- A histogram ($NO - Rec_{rec}(E_{part})$) containing the occurrences of energy depositions (binnend in numbers of created electron-hole pairs, i.e., 1, 2, 4, 8, etc. electron-hole pairs) by recoil particles outside of the PIT volume.

The ionization density within the PIT volume is then described by the model PIT, the ionization density created by all recoils is described as sum of $Rec[i]$ volumes with

[13] In section III/3.2.4, the expression for the decay-time spectrum of photons generated by the STE density distributions described with the $PIT(E_{part})$ fit function and the binnned $NO - Rec_{rec}(E_{part})$ histogram will be presented. For each bin of the $NO - Rec_{rec}(E_{part})$ histogram this expression has to be calculated individually. The resulting decay-time spectrum (sum of all contributions from the continuously described PIT and the binned $NO - Rec_{rec}(E_{part})$ histogram) then describes the complete decay-time spectrum of blue photons generated by the primary interacting particle with energy E_{part}. As will be explained in section III/3.3.2, this function will be used to fit experimentally obtained decay-time spectra of particle-induced scintillation light. Therefore, the mathematical expression for the decay-time spectrum should be as simple as possible.

occurrences as delivered by the $NO - Rec_{rec}(E_{part})$ histogram and energy depositions of 11.75eV, $2 \cdot 11.75$eV, $4 \cdot 11.75$eV, etc., respectively.

B.3.5 Graphical Representation of the Method to Determine the Ionization Density from the Data Delivered by the Simulations

In the following, a graphical representation of the method described in appendix B.3.4, to determine the distribution of the ionization density on the basis of the data delivered by the simulations for the example of a heavy, charged primary interacting particle with energy E_{part} is presented with the help of five figures:

1. Figure (figure B.2): Qualitative, graphical representation of the information obtained from the simulations for a heavy, charged particle as primary interacting particle. The information on the electronic stopping of the primary interacting particle along its track is used to calculate the ionization produced directly along the *PIT* of this particle (in 1nm bins along the track, for the introduction of the *PIT* model, see section III/3.1.2). Additionally, the ionization created by recoil ions within their respective overlap regions is added. The information on the ionization created by recoils is available as energy depositions per excited 1nm long slice along their tracks. It should be noted, that in contrast to the representation in the picture, this information is *not* available as position-depenedent information, but represented by histograms binned according to the energy contained in these small recoil volumes.

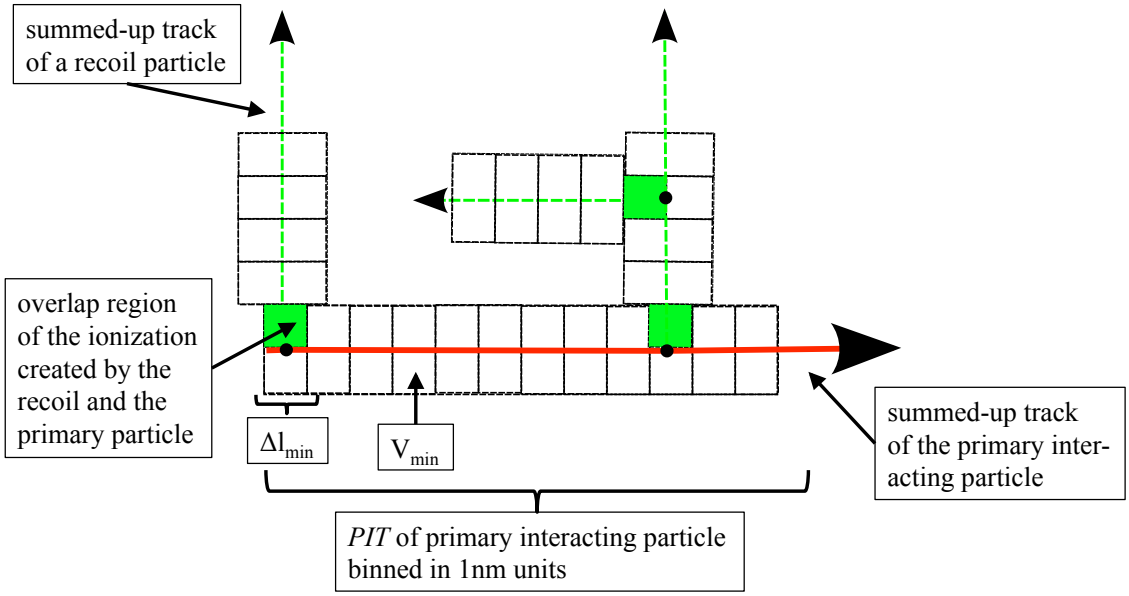

Figure B.2: Qualitative, graphical representation of the information obtained from the simulations for a heavy, charged particle as primary interacting particle. For more information, see text in this appendix.

2. Figure (figure B.3): Mathematical description of the ionization contained in the *PIT* volume and produced by all recoil particles (and their recoil particles) outside of the *PIT* volume. The ionization distribution along the *PIT* (filled red region) is merged into a histogram (1nm bins along the track): Histogram 1. The combined ionization created

by recoil ions outside of the *PIT* volume (filled green region) is summed into another histogram: Histogram 2 ($NO - Rec_{rec}(E_{part})$). This histogram contains the occurrences of energy depositions in 1eV/nm bins of all of the small *Rec* volumes outside of the *PIT* volume (for the introduction of the *Rec* model, see section III/3.1.2).

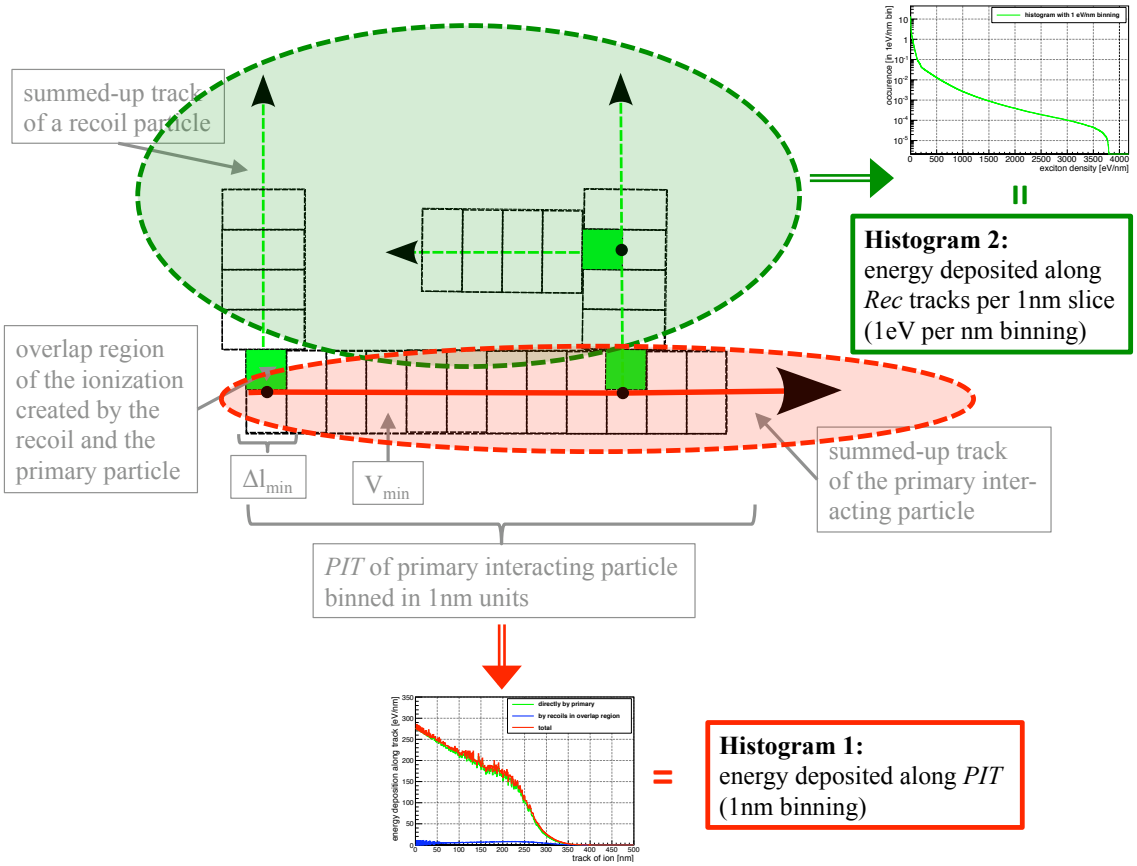

Figure B.3: Mathematical description of the ionization contained in the *PIT* volume and produced by all recoil particles (and their recoil particles) outside of the *PIT* volume. For more information, see text in this appendix.

3. Figure (figure B.4): Simplification of the mathematical description of the distribution of the ionization created: The combined ionization described by the *PIT* histogram (upper left pannel) and by the $NO - Rec_{rec}(E_{part})$ histogram (upper right panel) corresponds to the total ionization produced in the energy-loss process of the primary interacting particle. In order to obtain a simple mathematical description of the complete ionization, on the one hand (lower left panel), the *PIT* histogram (solid green line) is fitted with two concatenated exponentials (solid red line, rescaled to correspond to the correct integral) describing the z-dependency of the ionization within the *PIT* volume. On the other hand (lower right panel), the $NO - Rec_{rec}(E_{part})$ histogram (solid green line) is rebinned to reduce the number of bins that have to be considered. As natural choice, a binning corresponding to integer multiples (1, 2, 4, 8, etc.) of produced electron-hole pairs was performed: The mean energy required to produce an electron-hole pair amounts to 11.75eV. Hence, the entries of all bins with energy depositions $\leq$ 11.75eV are combined into one bin representing an energy deposition of 11.75eV. Of course, the relative weight

of the entry of this bin was adapted so that the integral energy contained still reflects the same value. The new histogram obtained in this way is depicted by the red stars in figure B.4 (lower right panel).

With the fit of the PIT histogram and the rebinned $NO - Rec_{rec}(E_{part})$ histogram, the complete information on the ionization-density distribution of the primary particle as obtained from the simulations is described.

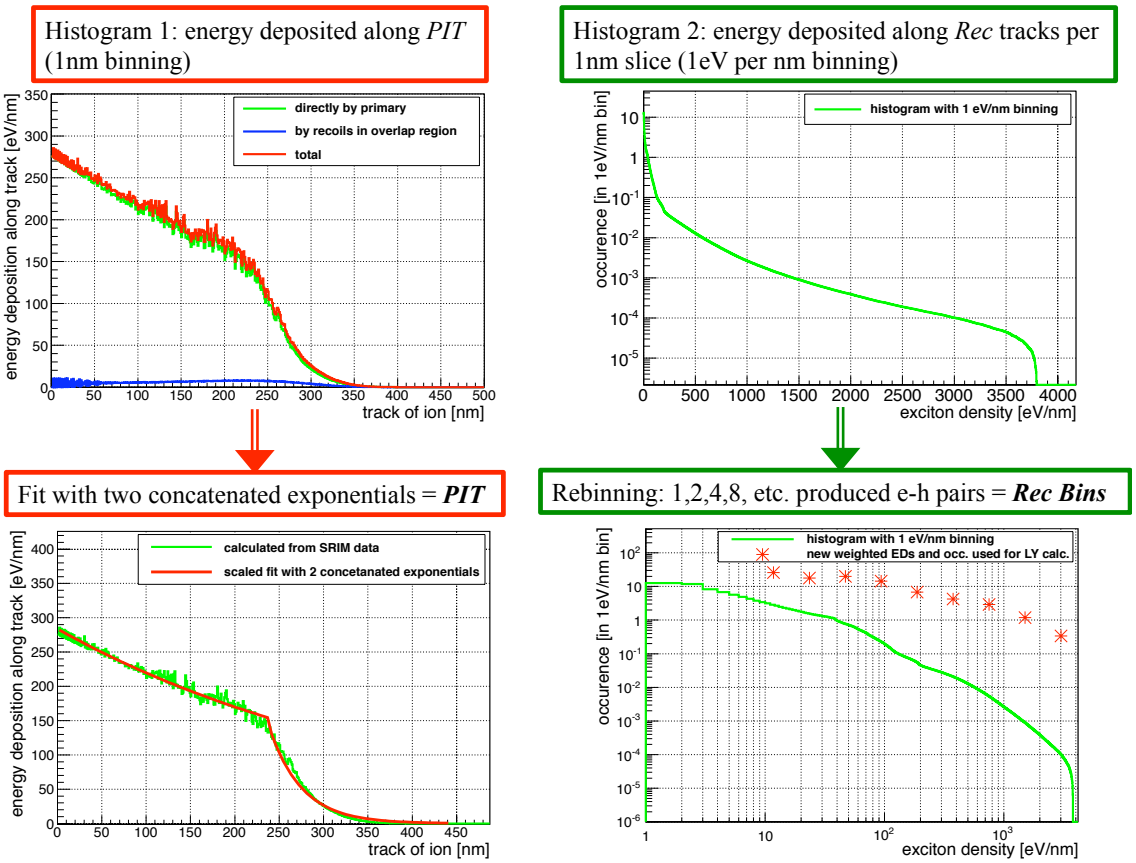

Figure B.4: Simplification of the mathematical description of the distribution of the ionization created. For more information, see text in this appendix.

4. Figure (figure B.5): Considering the regarded particle as recoil particle of a higher-energetic primary. If the regarded particle was a recoil particle produced by a higher-energetic primary particle, the ionization distribution created has to be described in a different way. On the one hand, the energy deposited in the overlap region (first 1nm bin of the PIT of the regarded particle, filled grey region) has to be determined. The ionization distribution created within the rest of the PIT volume (filled pink region) is merged into a histogram: Histogram 3 ($NO - PIT_{rec}(E_{part})$) (with a 1eV/nm binning, in analogy to the histogram $NO - Rec_{rec}(E_{part})$). The newly created histogram $NO - PIT_{rec}(E_{part})$ describes the occurrences of energy depositions (in a 1eV binning) within the PIT volume of the regarded particle (except for the first bin of the PIT). In addition, the Histogram 4, $NO - Rec_{rec}(E_{part})$, is still used to describe the ionization produced by recoils of the regarded particle outside of its PIT volume (filled blue region).

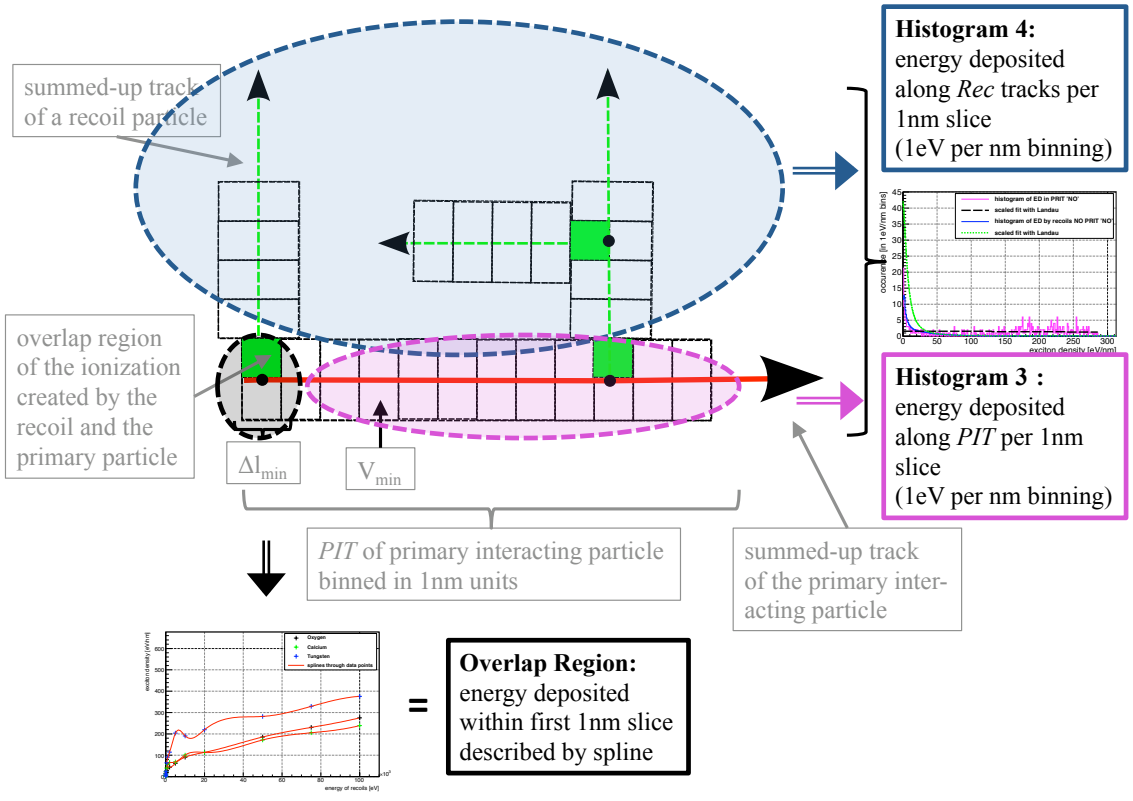

Figure B.5: Considering the regarded particle as recoil particle of a higher-energetic primary. For more information, see text in this appendix.

5. Figure (figure B.6): Energy dependency of the amount of energy deposited in the overlap region: The dependency of the amount of energy contained in the first bin of the *PIT* of an interacting particle on the energy of this particle is described with the help of a spline. In this way, the ionization deposited in the overlap region for a particle of this type with any energy $\leq E_{part}$ can be determined.

6. Figure (figure B.7): Mathematical description of the two histograms, Histogram 3 ($NO - PIT_{rec}(E_{part})$) and Histogram 4 ($NO - Rec_{rec}(E_{part})$) with Landau distributions: As will be discussed in the following, such a description allows a calculation of these histograms for a particle of this type with any energy $\leq E_{part}$. Both of the histograms are fitted with a Landau function, each described by five parameters: the most probable value, the scaling factor of the width, the scaling factor of the integral as well as the minimum and maximum bins with non-zero entries. For each of these ten parameters a spline describing their dependency on the energy of the interacting particle exists (for particles with energies less than E_{part}). The results from the fits of the two histograms for the regarded particle with energy E_{part} are used to extend these splines to higher energies.

It should be noted that exactly these splines of the parameters of the Landau functions as well as the overlap spline extended in this way can be used to calculate the ionization

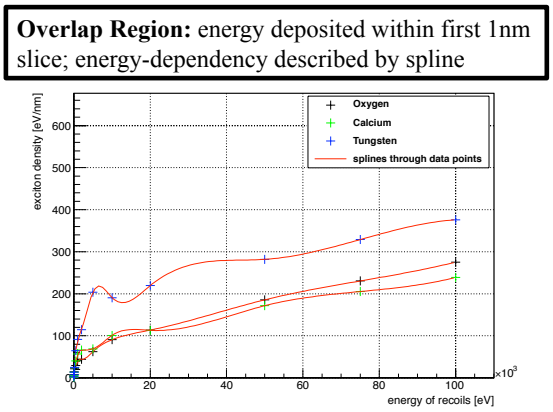

Figure B.6: Energy dependency of the amount of energy deposited in the overlap region. For more information, see text in this appendix.

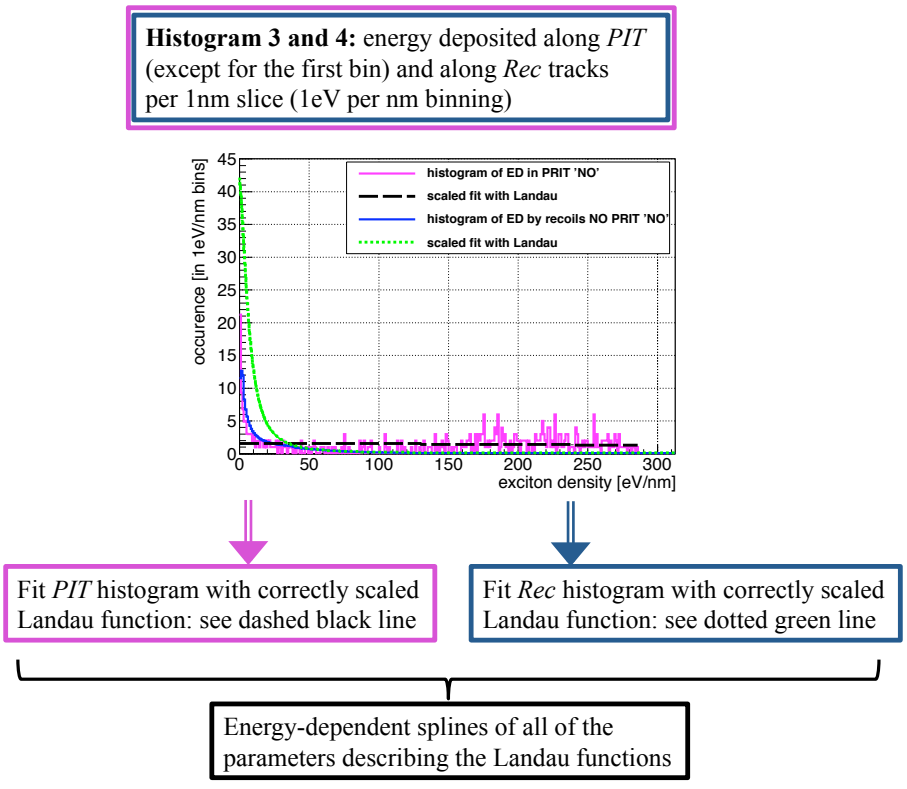

Figure B.7: Mathematical description of the two histograms $NO - PIT_{rec}(E_{part})$ and $NO - Rec_{rec}(E_{part})$ with Landau distributions. For more information, see text in this appendix.

density produced if a particle of the regarded type occurs as recoil ion of a higher-energetic primary particle. Hence, by conversion it can be deduced that the ionization-density distribution by the recoil particles of the regarded primary particle at the beginning of the description (depicted by the filled green region in figure B.3 and by the Histogram 2 in figure B.4) was determined with the help of exactly such splines in combination with

the list of the recoil particles produced for the regarded particle (such a list is delivered by the simulations, compare appendix B.3.2).

B.3.6 Determination of the Ionization-Density Distribution for Heavy, Charged Particles

With the method described in appendices B.3.4 and B.3.5, the data obtained from the simulations for O, Ca and W ions in the energy range from 20eV up to 50MeV were analyzed. In this way, on the one hand, a description of the ionization-density distribution for each of these particles for each supporting point energy was calculated (PIT fitfunction and rebinned $NO - Rec_{rec}(E_{part})$ histogram). On the other hand, simultaneously the database containing the information on the ionization-density distribution by these particles as recoil particles of other heavy, charged particles was created. This database contains, for O, Ca and W ions separately, eleven splines (overlap spline and ten splines for the parameters of the two Landau distributions) describing the dependency of the created ionization distribution on the energy of the recoil particle.

Then, the ionization distribution produced by an arbitrary, heavy, charged particle with energy $E_{part} \leq 50MeV$ (e.g., an α-particle or a Pb nucleus) depositing its energy in a $CaWO_4$ crystal can be determined, by performing the following three steps:

1. A simulation (with the SRIM program) of the energy-loss process of the regarded particle in $CaWO_4$ has to be performed. This simulation delivers the ionization directly produced by the primary particle along its track as well as the list of recoil particles (energy, type and position along the track of the primary particle) produced.

2. A histogram corresponding to the PIT volume is created and filled with the ionization produced directly by the primary interacting particle. Using the database containing the information on the ionization density generated by the potential recoil particles, the ionization produced in the respective overlap regions with the PIT of the primary particle as well as the ionization distribution outside of the PIT can be calculated.

3. The $PIT(E_{part})$ histogram obtained in this way is fitted with an exponential function (or two concatenated exponential functions). The $NO - Rec_{rec}(E_{part})$ histogram is rebinned using the new bin widths (integer number of electron-hole pairs created) introduced above.

B.3.7 Determination of the Ionization-Density Distribution for Electrons and γ-particles

The ionization-density distribution for electrons can be obtained from the simulations performed with the CASINO program in an analogous way as just described for heavy, charged particles (compare to the model for the ionization-density distribution of electrons described in appendix B.3.1). The only difference is that the method applied for electrons is less extensive as, on the one hand, no continuously, directly produced ionization along the particle track has to be considered (the secondary electrons produced are treated as individual recoil particles) and as, on the other hand, only one type of recoil particles (lower-energetic electrons) can be created. Hence, the ionization-density distribution produced by an electron as primary interacting particle is described by a histogram $Rec_{el}(E_{el})$

only. This histogram contains the occurrences of energy depositions (in integer numbers of created electron-hole pairs, in analogy to the histogram $NO - Rec_{rec}(E_{part})$ for ions) within small (1nm long) cylindrical sub-volumes.

As discussed at the beginning of this paragraph, the ionization distribution created by γ-particles is ascribed to the ionization-density distribution of the electron(s) and hole(s) created in the interaction process of the γ-particle with the $CaWO_4$ lattice. Hence, to express the ionization-density distribution produced by a γ-particle, the energies of the electron(s) and hole(s) created have to be estimated. In the following, the result of such an estimate for 122keV γ-particles from a ^{57}Co source is presented as example. This special γ-energy was chosen as within the CRESST experiment, the light yield produced for interactions of such γ-particles in the $CaWO_4$ crystal are used for the normalization of the light-yield scale, i.e., events produced by 122.06keV γs from a ^{57}Co source are assigned a light yield of unity (compare section III/2.1). From figure B.1 in appedix B.1, it can be seen that the interaction process for 122.06keV γ-particles with a $CaWO_4$ crystal is dominated by the production of a photoelectron (from the K-shell of the W nucleus) due to the photoelectric effect at a W nucleus and its electrons. The binding energy of a K-shell electron in a W atom amounts to 69.53keV [118]. Hence, the resulting photoelectron most probably carries an energy of 122.06keV − 69.53keV = 52.53keV. The most probable first step in the relaxation process of the produced hole in the K-shell corresponds to the production of a $K_{\alpha 1}$ x-ray[14] with an energy of 59.32keV [118]. This x-ray will then most probably be reabsorbed by an L-shell electron of the W atom[15] (binding energy $\sim$ 11keV [118]) producing a second photoelectron of $\sim$ 48keV. Hence, the major part of the energy of the 122.06keV γ-particle is shared between two almost equally energetic electrons of roughly 50keV energy.

In order to obtain a simple description of the ionization-density distribution produced by a 122.06keV γ as primary interacting particle, it is assumed that the energy loss process of such a γ-particle can be approximately described by the energy-loss process of two 60keV electrons (multiplied by a factor of $\frac{122.06\text{keV}}{2 \cdot 60\text{keV}} = 1.017$ to obtain the correct total energy deposited)[16].

B.3.8 Radial Distribution of the Ionization-Density Distribution

It should be noted that, as already indicated at the beginning of the discussion of the data delivered by the simulations, from this data no information on the radial distribution of the generated ionization, i.e., for the example of a heavy, charged particle, no information on the radii and partitioning of the ionization between inner and outer *PIT* or *Rec* volumes can be gained. The method used within this work to estimate values for these parameters, i.e., to determine a description of the radial distribution of the created ionization around the track of the primary particle and around the tracks of its recoil particles, as well

[14] The relaxation of the evolving L-shell hole occurs accordingly via the production of less-energetic x-rays and electrons.

[15] The relaxation of the evolving L-shell hole occurs accordingly via the production of less-energetic x-rays and electrons.

[16] An electron energy of 60keV was chosen as, on the one hand, electrons of this energy were already simulated and analyzed for the build-up of the database of the ionization produced by recoil electrons. On the other hand, the summed energy of two of these electrons already roughly corresponds to the total energy of the regarded γ-particle and, hence, only a small correction factor had to be introduced.

as the expected dependency of these parameters on the energy and type of the primary interacting particle is discussed in the following. As the models for the ionization-density distribution for electrons and heavy, charged particles as primary particles differ from each other (e.g., no *PIT* for electrons as primary interacting particle), the radial dependencies have to be discussed separately. Therefore, at first the interpretation and determination of the radial dependencies of the created ionization for electrons is given. Thereafter, the corresponding discussion for heavy, charged particles is presented.

B.3.9 Radial Ionization Distribution for Electrons

As discussed in appendix B.3.1, in the geometrical model describing the spatial distribution of the ionization created by an electron with an energy of E_{el} as primary interacting particle, the complete ionization distribution is represented by small cylindrical sub-volumes (of 1nm length) with a radius $r_{Rec_{el}}(E_{el})$ each. The information on the occurrence and energy content of these small sub-volumes is described by the histogram $Rec_{el}(E_{el})$. It is assumed that the ionization within the individual sub-volumes is distributed homogeneously. From the analysis of the data delivered by the simulations with CASINO, the occurrence of such sub-volumes with respective energy contents (binned in integer multiples of created electron-hole pairs) is retrieved. Hence, for electrons, the only parameter that has to be determined separately is the size of the radius $r_{Rec_{el}}(E_{el})$. The size of this radius should describe the extent of the volume excited by a very low-energetic recoil as well as account for the distribution of the excited sub-volume elements within the crystal, i.e., the distance of the small volumes to each other[17]. As however, this distribution is most probably not modeled realistically in CASINO (no high-energetic electron recoils are produced), an estimation for this parameter cannot simply be extracted from the simulations. Therefore, as will be presented in section III/6.1.1, the radius $r_{Rec_{el}}(E_{el})$ is adjusted for one electron energy, $E_{el} = 100$keV (using the complete light-generation model with all other parameters determined), for which the absolute light yield is known with a high accuracy (from literature). On the basis of this value for a 100keV electron, the size of the radius for electrons with different energies is estimated using the following, proposed estimation of the energy dependency of this radius:

- As discussed, the size of this radius should reflect the extent of the volume excited by the very low-energetic recoils produced in the energy-deposition process.
- From the CASINO simulation, for each simulated primary electron energy E_{el} also the mean number $\overline{N_{rec-el}}(E_{el})$ and mean energy $\overline{E_{rec-el}}(E_{el})$ of the produced recoil electrons are delivered[18].
- The shape of the volume excited by a very low-energetic electron should roughly exhibit the same dimension in each direction, as a low-energetic electrons becomes deflected strongly and stopped quickly. Therefore, the volume excited by such a low-energetic electron is assumed to be describable by a sphere with radius $\overline{d_{max}}(E_{el})$ (mean maximum penetration depth into the material for an electron of energy E_{el}).

[17] The farther away from each other these small sub-volumes are, the lower the density of the created STE population.

[18] This mean energy of recoil electrons is expected to be small due to the shape of the recoil-electron energy spectrum (Landau distribution, compare discussion above figure 3.3). In fact, the mean recoil-electron energies delivered by CASINO are very small, e.g., only $\sim$ 72eV for a 1MeV primary electron. It should be taken into account that this mean recoil energy most probably corresponds to an underestimation as, within the CASINO simulation, no high-energetic recoil electrons are produced.

- Hence, the mean volume, $\overline{V_{ex\,rec-el}(E_{rec-el}(E_{el}))}$, excited per recoil electron with a very small mean energy $\overline{E_{rec-el}}(E_{el})$ is expected to be proportional to $\overline{d_{max}(E_{rec-el}(E_{el}))}^3$:

$$\overline{V_{ex\,rec-el}(E_{rec-el}(E_{el}))} \propto \overline{d_{max}(E_{rec-el}(E_{el}))}^3 \tag{B.12}$$

  It should be noted, that the averaging process indicated by the bar on top of the volume and the penetration depth refers to an averaging determination of the volume and the penetration depth, respectively, for the (already) averaged recoil-electron energy. Thus, with this notation two averaging processes are indicated.

- The mean penetration depth $\overline{d_{max}(E_{rec-el}(E_{el}))}$ for very low-energetic electrons can, e.g., be obtained from the CASINO simulations using primary electron energies from 20eV up to 200eV.

- Using the radius $r_{Rec_{el}}(E_{el} = 100\text{keV})$, the extent of the complete excited volume, $V_{ex}(E_{el} = 100\text{keV})$, for a 100keV electron as primary particle can be calculated (multiplication with the summed number of entries in the $Rec_{el}(E_{el})$ histogram, $\sum_i Occ_{Rec[i]_{el}}(E_{el} = 100\text{keV})$):

$$V_{ex}(E_{el} = 100\text{keV}) = r^2_{Rec_{el}}(E_{el} = 100\text{keV}) \cdot \pi \cdot 1\text{nm} \cdot \sum_i Occ_{Rec[i]_{el}}(E_{el} = 100\text{keV}) \tag{B.13}$$

  Dividing this complete excited volume by the mean number of produced recoil electrons, $\overline{N_{rec-el}}(E_{el})$, the volume excited per mean recoil electron of a 100keV primary electron, $\overline{V_{ex\,rec-el}(E_{rec-el}(E_{el} = 100\text{keV}))}$, can be estimated:

$$\overline{V_{ex\,rec-el}(E_{rec-el}(E_{el} = 100\text{keV}))} = \frac{V_{ex}(E_{el} = 100\text{keV})}{\overline{N_{rec-el}}(E_{el})} \tag{B.14}$$

- Taking now into account that the extent of this volume (per low-energetic recoil electron) is assumed to be proportional to $\overline{d_{max}(E_{rec-el}(E_{el}))}^3$, the extent of the mean volume per recoil electron can be calculated for all other electron energies:

$$\begin{aligned}\overline{V_{ex\,rec-el}(E_{rec-el}(E_{el}))} = \overline{V_{ex\,rec-el}(E_{rec-el}(E_{el} = 100\text{keV}))} \cdot \\ \cdot \left(\frac{\overline{d_{max}(E_{rec-el}(E_{el}))}}{\overline{d_{max}(E_{rec-el}(E_{el} = 100\text{keV}))}} \right)^3\end{aligned} \tag{B.15}$$

- Using the knowledge of the number of recoil electrons, $\overline{N_{rec-el}}(E_{el})$, as well as the number of entries in the $Rec_{el}(E_{el})$ histogram, $\sum_i Occ_{Rec[i]_{el}}(E_{el})$ for a primary electron of energy E_{el}, the volume per one of these entries and, hence, the radius $r_{Rec_{el}}(E_{el})$ can be calculated:

$$r_{Rec_{el}}(E_{el}) = \sqrt{\frac{\overline{N_{rec-el}}(E_{el}) \cdot \overline{V_{ex\,rec-el}(E_{rec-el}(E_{el}))}}{\sum_i Occ_{Rec[i]_{el}}(E_{el}) \cdot \pi \cdot 1\text{nm}}} \tag{B.16}$$

It should be noted that for recoil electron-energies above a certain threshold energy, the volume excited by one of these electrons can no longer be assumed to be describable by a sphere with a radius corresponding to the mean penetration depth, but starts to exhibit

a track-like structure, extended in one direction. However, the increase in the excited volume due to the increase in the track length for such an electron should already be included in the description of the ionization distribution: The track of the electron is divided into 1nm long slices. Hence, if the track length extends 1nm, for this electron two entries in the histogram of energy depositions are produced already taking into account the enlarged excited volume. Therefore, for such electrons, a dependency of the extent of one of the excited sub-volumes only on the square of the mean penetration depth is assumed. In principle, the onset energy of this effect should be recognizable from the mean recoil-electron energy and the corresponding mean penetration depth or track length of electrons of this energy. However, such an identification is prevented by the circumstance that the recoil electrons created in CASINO simulations generally exhibit too small energies. Hence, this onset energy has to be estimated by other means. For example the dependency of the mean recoil-electron energy on the primary electron energy as simulated with CASINO can be considered. The values obtained from the simulations are depicted in figure B.8:

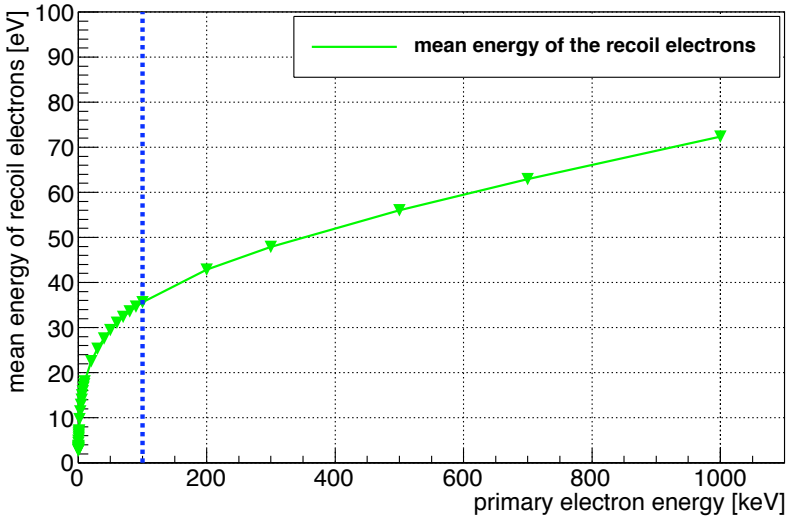

Figure B.8: Mean energy of the recoil electrons produced by a primary interacting electron. Shown are the data obtained from the simulations with CASINO in the primary electron-energy range from 20eV to 1MeV. The dashed blue line indicates the primary electron energy (100keV) which is assumed to separate the two regions of different dependency of the mean recoil energy on the primary electron energy (for details, see explanation below).

Considering the mean energies of the produced recoil electrons shown in figure B.8, it should be noted that, as just discussed, the absolute values of these mean recoil-electron energies should not be taken into account due to the trend of the CASINO simulations to produce low-energetic recoil electrons only. Nonetheless, from figure B.8, it can be seen that the dependency of the recoil-electron energy for primary electrons with an energy of $\gtrsim$ 100keV starts to change (indicated by the dashed blue line in figure B.8). For primary electron energies larger than 100keV, a saturation of the mean recoil-electron energies as determined with CASINO can be observed. Within the developed interpretation of the CASINO simulations, this saturation is interpreted as the primary electron energy above which considerably more higher-energetic recoil electrons are produced. However, within the CASINO program these electrons are represented directly by the low-energetic recoil electrons they produce. In this way, the mean recoil-electron energy does only increase

more slowly.

This observation, on the other hand, can exactly be interpreted as the onset of the efficient production of recoil electrons that possess enough energy to exhibit a track-like excited volume (stretched over two or several of the 1nm slices). Hence, in the following, the dependency of the volume excited by recoil electrons on their mean penetration depth is divided into two regions of different behavior:

- For all primary electron energies $E_{el} \leq 100keV$, the dependency as described by equation B.12 is assumed, i.e., the volume excited per recoil electron is expected to be proportional to $\overline{d_{max}(E_{rec-el}(E_{el}))}^3$. Hence, the volume excited per recoil electron by such a primary electron is determined with equation B.15:

$$\overline{V_{ex\,rec-el}(E_{rec-el}(E_{el}))} = \overline{V_{ex\,rec-el}(E_{rec-el}(E_{el}=100\text{keV}))} \cdot \cdot \left(\frac{\overline{d_{max}(E_{rec-el}(E_{el}))}}{\overline{d_{max}(E_{rec-el}(E_{el}=100\text{keV}))}} \right)^3 \tag{B.17}$$

- For all primary electron energies $E_{el} > 100keV$, it is assumed that the volume excited by one recoil electron is proportional to $\overline{d_{max}(E_{rec-el}(E_{el}))}^2$. Hence, the volume excited by recoil electrons of such a primary electron is determined with the following relationship:

$$\overline{V_{ex\,rec-el}(E_{rec-el}(E_{el}))} = \overline{V_{ex\,rec-el}(E_{rec-el}(E_{el}=100\text{keV}))} \cdot \cdot \left(\frac{\overline{d_{max}(E_{rec-el}(E_{el}))}}{\overline{d_{max}(E_{rec-el}(E_{el}=100\text{keV}))}} \right)^2 \tag{B.18}$$

Hence, by comparing the light yield for 100keV electrons (as calculated with the complete model) to the experimentally determined value from literature (see section III/6.1.1), the value of the radius $r_{Rec_{el}}(E_{el})$ (radius of the ionization-density distribution) for 100keV electrons is determined. Then, assuming the suggested energy dependency of the radius $r_{Rec_{el}}(E_{el})$ (as discussed above), the value for $r_{Rec_{el}}(E_{el})$ can be calculated for electrons with energies ≤ 1MeV (maximum energy considered for electrons within the present work).

B.3.10 Radial Ionization Distribution for Heavy, Charged Particles

As already indicated above, for heavy, charged particles, no information on the radial distribution of the ionization around the track of particles is delivered by the SRIM simulations. Before presenting the method used within the present work to obtain estimates for the parameters describing this radial distribution, the ionization distribution along the track of the primary interacting particle within the *PIT* volume for heavy charged particles as well as the energy dependencies assumed for the radial parameters of the different sub-volumes of the total excited volume for a heavy, charged particle as primary interacting particle are discussed in more detail.

Ionization Distribution within the *PIT* Volume along the Primary Particle Track

It should be noted that for most of the simulated particles, the dependency of the ionization distribution along the track of the primary particle can best be described by a fit

with two concatenated exponential functions. These two different exponential functions correspond to different dependencies of the ionization distribution within the PIT volume, as discussed in the following. The two regions of different dependency of the ionization-density distribution on the position along the PIT are labelled as $PIT1$ and $PIT2$. Their occurrence can be explained by a change in the energy-loss process of the primary interacting particle: At the point where the region $PIT2$ starts, the electronic stopping power for the ion in $CaWO_4$ decreases and the energy-loss due to nuclear recoil production (nuclear stopping) increases. This feature can, e.g., be recognized from the $PIT(E_{part})$ histogram shown in figure B.9. In this histogram, the energy deposited in ionization within the PIT volume (in eV per nm) of an O ion of 100keV energy is depicted.

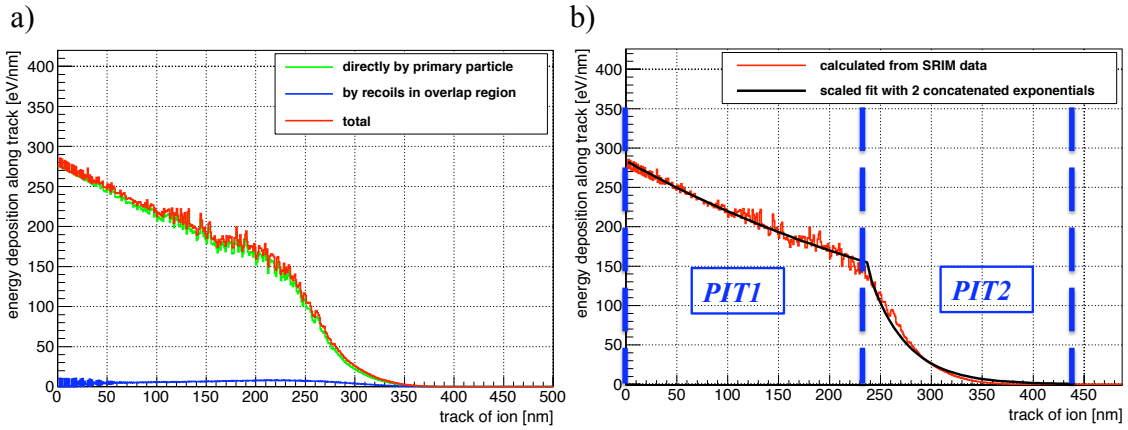

Figure B.9: Ionization distribution in the PIT volume as calculated for a 100keV O ion in the analysis of the data delivered by SRIM. Panel a: In red, the histogram of the total energy (in eV) deposited in ionization (by the primary particle and by its recoil particles within their respective overlap regions) binned in 1nm steps along the track of the primary interacting particle is shown. In green, the contribution due to the ionization created directly by the primary interacting particle is shown. In blue, the contribution due to the produced nuclear recoil particles in the overlap regions along the track is depicted. Panel b: In red, the total energy deposited in ionization is shown. A fit to this histogram with two concatenated exponentials (scaled to the correct integral) can be seen in black. The two regions of different behavior of the energy-loss process of the primary ion are indicated by the dashed blue lines.

From figure B.9, clearly the two regions of the different dependencies of the ionization distribution on the position along the track, i.e., on the energy of the primary interacting ion, can be recognized. In panel a) of figure B.9, it can be seen that this change in the behavior of the ionization distribution coincides with a small increase of the ionization produced by nuclear recoils pointing to an enhanced production of nuclear recoils as explained above. In addition, it should be noticed that the energy of the electrons produced directly by the primary ion (which constitute the main fraction of the ionization produced within the PIT volume) can be expected to differ within the two regions: Within the $PIT1$ region the electrons produced should exhibit a larger average energy, as there, the primary interacting particle still possesses a higher energy. In comparison, within the $PIT2$ region, the primary ion has already lost part of its energy and, thus, the electrons produced can be expected to exhibit a smaller average energy. Hence, within the developed model, for the two regions of the PIT, $PIT1$ and $PIT2$, different parameters for the description of the radial dependency of the produced ionization are used.

Parameters Describing the Radial Dependency of the Ionization Distribution

Thus, for heavy, charged particles the following parameters describing the radial dependency of the created ionization within the two PIT volumes $PIT1$ and $PIT2$, as well as within the Rec volumes have to be determined (compare models PIT and Rec described by tables 3.3 and 3.4, respectively, in section III/3.1.2). These parameters cannot directly be inferred from the performed simulations with SRIM:

- The inner and outer radii of the $PIT1$ and $PIT2$ volumes: $r^{in}_{PIT1}(E_{part})$, $r^{out}_{PIT1}(E_{part})$ as well as $r^{in}_{PIT2}(E_{part})$ and $r^{out}_{PIT2}(E_{part})$.
- The partitioning of the ionization between inner and outer $PIT1$ and $PIT2$ volumes: $F^{in}_{PIT1}(E_{part}) = 1 - F^{out}_{PIT1}(E_{part})$ and $F^{in}_{PIT2}(E_{part}) = 1 - F^{out}_{PIT2}(E_{part})$.
- The inner and outer radii of the Rec volumes: $r^{in}_{Rec}(E_{part})$ and $r^{out}_{Rec}(E_{part})$.
- The partitioning of the ionization between inner and outer Rec volumes: $F^{in}_{Rec}(E_{part}) = 1 - F^{out}_{Rec}(E_{part})$.

It should be noted, that the inner radii of the respective volumes, i.e., the radial extents of the densely ionized regions, are assumed to be mainly characterized by the range of the large number of low-energetic electrons produced. However, it should be taken into account that the fraction of energy deposited in ionization within the inner volume (with a radius characterized by the range of low-energetic electrons) is composed of the ionization created by low-energetic **and** high-energetic electrons (until they high-energetic electrons escape the densely ionized inner region). For the respective outer radii, however, no such direct physical interpretation can be given as they represent the geometrical extent of the mathematically modeled union of the thinly ionized regions excited by the high-energetic electrons after those escaped the densely ionized inner region (compare figures 3.5 and 3.6 in section III/3.1.2). Nonetheless, it seems reasonable to expected that the radius of this outer volume is proportional to the range of the high-energetic electrons depositing their energy there: The larger the range of the high-energetic electrons, the larger the volume where they deposit their ionization. Note, that the larger the range of such a high-energetic electron, the larger also the radial extent of the volume excited by this electron is expected to be. Hence, the larger the range of the high-energetic electron, the larger the radius of the outer volume has to be chosen to represent the extent of the excited volume.

Basic Assumptions for the Energy Dependency of the Radial Parameters

The following basic assumptions concerning the general dependency of the radial parameters on the energy and type of the primary ion are used:

- According to [89], the dependency of the energy E_{el} of the produced electrons on the energy of the primary ion, E_{part}, as well as on the scattering angle of the produced electrons, θ (where $\theta = 90°$ corresponds to a direction of emission of the electron perpendicular to the track of the primary ion), is given by[19]:

$$E_{el} = 4 \cdot \frac{m_e}{m_{part}} \cdot E_{part} \cdot \cos^2(\theta) \tag{B.19}$$

[19] Of course, this formula is only an approximation as, in reality, the target electrons exhibit non-zero energies. Hence, their momentum distribution has to be added to the electron energy as described by formula B.19 [89].

where m_e and m_{part} are the electron and ion mass, respectively. It should be noted that in [89], it is stated that the dependency of the electron energy on the scattering angle of the electron as described by equation B.19 is only valid for high-energetic primary ions. For low-energetic ions, an isotropic emission of the produced electrons, in all directions, is expected.

- As for most of the ion energies considered within the present work, the maximum electron energy described by equation B.19 is less than 10% of the speed of light, in the following a non-relativistic formulation is used. Therefore, equation B.19 can be transformed to:

$$v_{el} = 2 \cdot v_{part} \cdot \cos(\theta) \tag{B.20}$$

with v_{el} and v_{part} corresponding to the electron and the ion velocity, respectively. As the angular dependency of the equation B.20 is expected to be valid only for high-energetic ions and, thus, electrons, the following general dependency of the electron velocity on the particle velocity is expected:

$$\Rightarrow v_{el}(E_{part}) \propto v_{part} \tag{B.21}$$

Thus, in the following, it is assumed that the velocity of the produced electrons is proportional to the velocity of the particle generating these recoil electrons.

- From the CASINO simulations a relationship between the electron energy and their maximum penetration depth into the crystal in the direction of their initial movement can be obtained. Hence, using the CASINO simulations for electrons, an estimate for the dependency of the radial extent of the inner volume of the *PIT* (characterized by the range of the low-energetic electrons, as discussed above) on the energy of the electrons can be obtained. The dependency of the mean maximum penetration depth $\overline{d_{max}}(E_{el})$ on the electron energy is depicted in figure B.10:

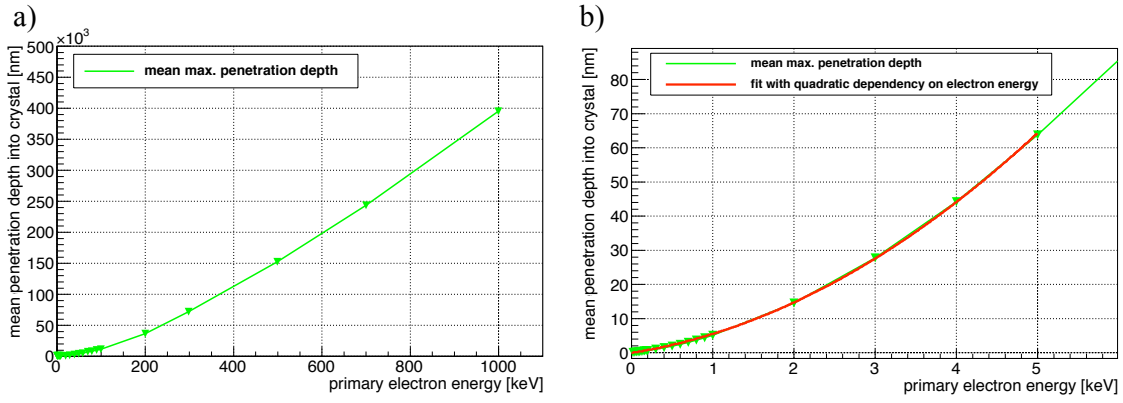

Figure B.10: Dependency of the mean (maximum) penetration depth of electrons in the direction of their initial movement in $CaWO_4$, calculated from simulations with CASINO. Panel a): Complete energy range considered for electrons within the present work (20eV up to 1MeV). Panel b): Zoom into the electron-energy region of interest in the context of the ionization produced by heavy, charged particles (20eV up to 5keV). In addition, a fit with a quadratic dependency of the penetration depth on the electron energy is shown as solid red line.

In panel a) of figure B.10, $\overline{d_{max}}(E_{el})$ as determined from the CASINO simulations for the complete range of electrons (from 20eV up to 1MeV) considered within the present work is depicted. In panel b) of figure B.10 a zoom into the low-energetic part (20eV up to 5keV) is shown as the recoil electrons produced by heavy charged particles exhibit comparably small maximum energies (compare equation B.10). Additionally a fit to $\overline{d_{max}}(E_{el})$ assuming a quadratic dependency of the mean penetration depth on the electron energy is shown (solid red line). It can be seen that the data obtained from the simulations is well described by this fit. Hence, in the following, it is assumed that the range of the low-energetic electrons produced directly by a heavy, charged particle, i.e., the radius $r^{in}(E_{part})$ of the densely ionized inner volume around the track of the primary particle, depends quadratically on the mean energy $E_{el-\text{low-energetic}}$) of the low-energetic electrons:

$$r^{in}(E_{part}) \approx \overline{d_{max}(E_{el-\text{low-energetic}})} \propto \overline{E^2_{el-\text{low-energetic}}} \tag{B.22}$$

- Combining the dependency of the inner radius of the excited volume $r_{in}(E_{part})$ as described by equation B.22 with the dependency of the electron velocity on the velocity of the particle producing the electrons (equation B.21), the following approximate expression can be obtained:

$$\begin{aligned} & r^{in}(E_{part}) \propto \overline{E^2_{el-\text{low-energetic}}} \propto \overline{v^4_{el-\text{low-energetic}}(E_{part})} \propto v^4_{part} \\ \Rightarrow\ & r^{in}(E_{part}) \propto v^4_{part} \end{aligned} \tag{B.23}$$

  Hence, as described by equation B.23, within the developed model, it is assumed that the inner radius of the volume excited in the energy-loss process of a heavy-charged particle (e.g., an oxygen ion as primary interacting particle or its nuclear recoil particles) is proportional to the fourth power of the particle velocity.

- As discussed above, also for the outer radius of the volume excited directly in the energy-loss process of a heavy, charged particle, a direct dependency on the range of the (high-energetic) electrons is assumed. Hence, in analogy to the discussion for the inner radius of the excited volume also for the outer radius the following dependency is assumed:

$$\Rightarrow r^{out}(E_{part}) \propto v^4_{part} \tag{B.24}$$

  It should be noted, that the proportionality factors for $r^{in}(E_{part})$ (equation B.23) and $r^{out}(E_{part})$ (equation B.24) do not comply with each other.

- As discussed in more detail in [89], for high-energetic ions a strongly forward peaked emission of electrons, especially of the high-energetic electrons can be expected (see equation B.19). The smaller the ion energy, i.e., its velocity becomes, the less severe this directional dependency of the emission. Within the developed geometrical model, this effect can be interpreted in terms of the partitioning of the ionization between inner and outer excited volumes: The faster the ion and, hence, the more forward peaked the electron emission, the more energy is deposited within the inner part of the excited volume, i.e., the larger $F^{in}(E_{part})$. As this effect is a volume effect, i.e., influencing the direction of the electron emission in three dimensions,

within the developed model, it is assumed that $F^{in}(E_{part})$ exhibits the following dependency on the velocity v_{part} of the particle producing the electrons[20]:

$$F^{in}(E_{part}) \propto v_{part}^{\frac{1}{3}} \tag{B.25}$$

It should be noted that by assuming this dependency, the fraction of ionization produced within the inner part of the excited volume is predicted to decrease slowly (only a dependency on the third root of the ion velocity is assumed) for smaller ion velocities, i.e., energies. At first sight, this seems to contradict the intuition, however, two factors should be taken into account: On the one hand, the radius of the inner volume, $rin(E_{part})$, is assumed to be strongly decreased for small particle energies (see above). The fraction $F^{in}(E_{part})$ of the ionization which is contained in this inner volume, not only comprises the energy deposited there by the large number of low-energetic electrons, but also the fraction of energy deposited there by high-energetic electrons. On the other hand, the fraction of electrons that are produced with an initial direction almost parallel to the particle track increases for increasing ion energy, i.e., for faster ions. These electrons can be expected to deposit a larger fraction of their energy in the close vicinity of the particle track compared to electrons with initial directions of movements perpendicular to the particle track. A graphical representation of the described interpretation of this effect can be found in figure B.11.

Hence, as depicted in figure B.11, for high energetic ions, a more pronounced structuring of the ionization-density distribution within the excited volume into inner and outer volumes is expected. For low energetic ion, this structuring is assumed to be less severe.

- In addition, minimal values for the fraction of ionization deposited within the inner part of an excited volume, $F^{in}(E_{part})$, as well as for the inner radius of the excited volume, $r^{in}(E_{part})$, are assumed. The assumption of such minimum values possible can be justified by the velocity distribution of the created electrons: Concerning equation B.19, describing the dependency of the energy of the produced electrons on the energy of the primary interacting particle, it should be taken into account, that the target electrons excited by the interacting particle, in reality, exhibit non-zero energies, i.e., a non-vanishing momentum distribution [89]. Hence, this momentum distribution has to be added to the electron energy as described by formula B.19. This intrinsic momentum distribution of the target electrons can be expected to lead to a non-vanishing energy distribution of the created electrons and therefore, to a non-vanishing range distribution of these electrons even for very low-energetic primary interacting particles. Within the developed model, this fact is interpreted as giving rise to a minimum, non-zero value for the inner radius of the ionization distribution within the $PIT2$ volume (which describes the ionization distribution for low-energetic particles). The minimum value for $r^{in}(E_{part})$ is chosen such that it corresponds to the mean penetration depth of 60eV electrons, $\overline{d_{max}}(E_{el} = 60\text{eV})$: Electrons with $E_{el} \leq 60\text{eV}$ exhibit track lengths smaller than 1nm and, hence, are not assumed to start their own ionization tracks within the analysis of the CASINO

[20] It should be noted that the assumed correlation is purely phenomenological and cannot directly be deduced from any relationship stated within the present work.

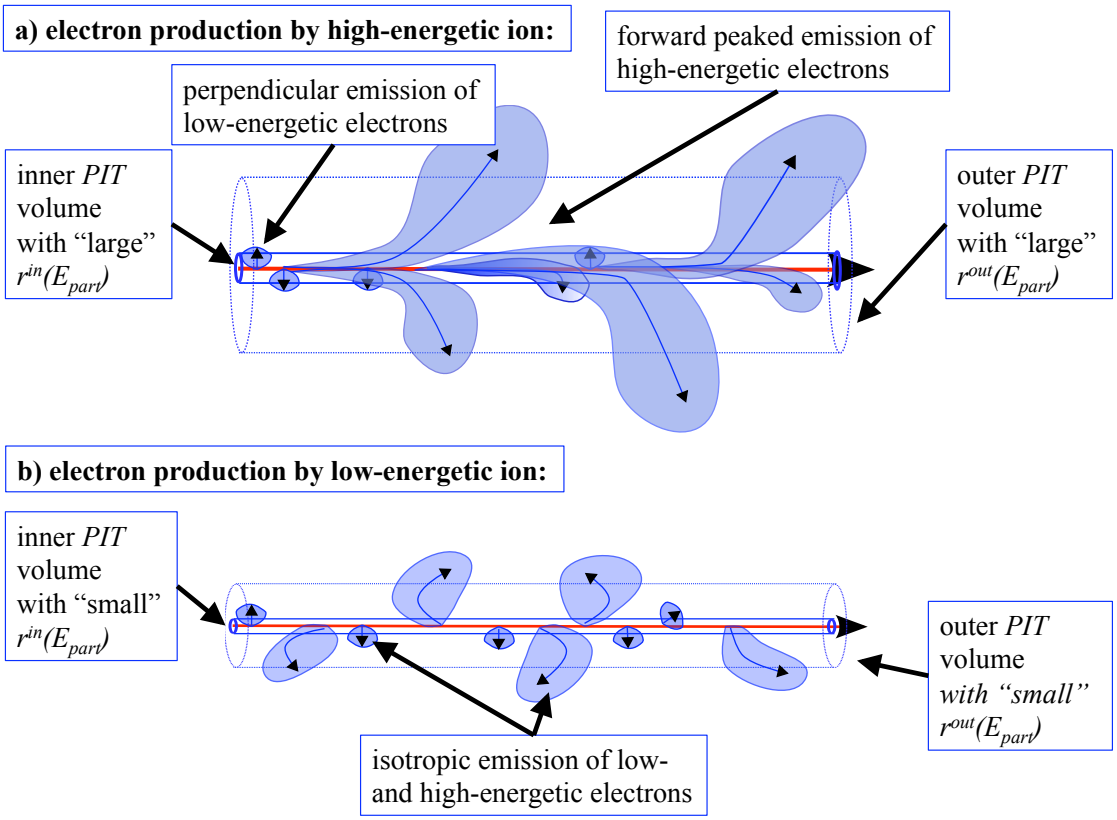

Figure B.11: Qualitative, graphical representation of the dependency of the ionization partitioning between the inner and outer *PIT* volume dependent on the energy of the primary ion. In panel a), the assumed dependency is illustrated for a comparably high-energetic ion, in panel b), this dependency is illustrated for a low-energetic ion: For the high-energetic ion, the radii of the inner and outer volumes of the *PIT* are comparably large compared to the inner and outer radii of the *PIT* volume of a lower-energetic primary ion. In panel a) the assumed forward-peaked emission of high-energetic electrons and the emission of low-energetic electrons perpendicular to the primary ion track are indicated. As depicted, this process is expected to lead to an enhanced deposition of energy within the inner volume of the *PIT* volume. In panel b), the described isotropic emission of electrons of all energies is illustrated. The mean energy of these electrons is smaller, hence, the radii of the inner and outer volumes are smaller compared to a higher-energetic ion.

simulations (compare appendix B.3.4):

$$r_{min}^{in} := \overline{d_{max}}(E_{el} = 60\text{eV}) = 0.225\text{nm} \tag{B.26}$$

As indicated by equation B.26, this minimum value considered for the inner radius is not dependent on the type of the interacting particle as it is a consequence of the momentum distribution of the electrons of the target material. In analogy, a minimum value for $F^{in}(E_{part})$ can be motivated. This minimum value is assumed to be given by:

$$F_{min}^{in} := 0.4 \tag{B.27}$$

The choice of this value will be motivated by a value determined for $F_{PIT2}^{in}(E_{part})$ (see discussion of the method to determine the parameters below).

In the following, the parameters of the different sub-volumes of the complete volume excited by one heavy, charged particle as primary interacting particle using the explained assumptions are discussed in more detail:

The $PIT1$ and $PIT2$ Parameters

The $PIT1$ parameters describe the energy-loss process of the primary ion in the region where it is dominated by the electronic stopping. As discussed in section III/3.1.1, for a primary ion energy of $\gtrsim E_1$ (compare table 3.1 in section III/3.1.1), the electronic stopping power starts to decrease again. Hence, for an energy of the ion smaller than the energy E_1, the electronic stopping power of $CaWO_4$ for this ion can be assumed to start to saturate. Exactly this behavior can be observed when comparing the shapes of the energy deposition along the PIT for one type of ion and different energies. In figure B.12, two examples of the ionization deposition within the PIT volume are shown.

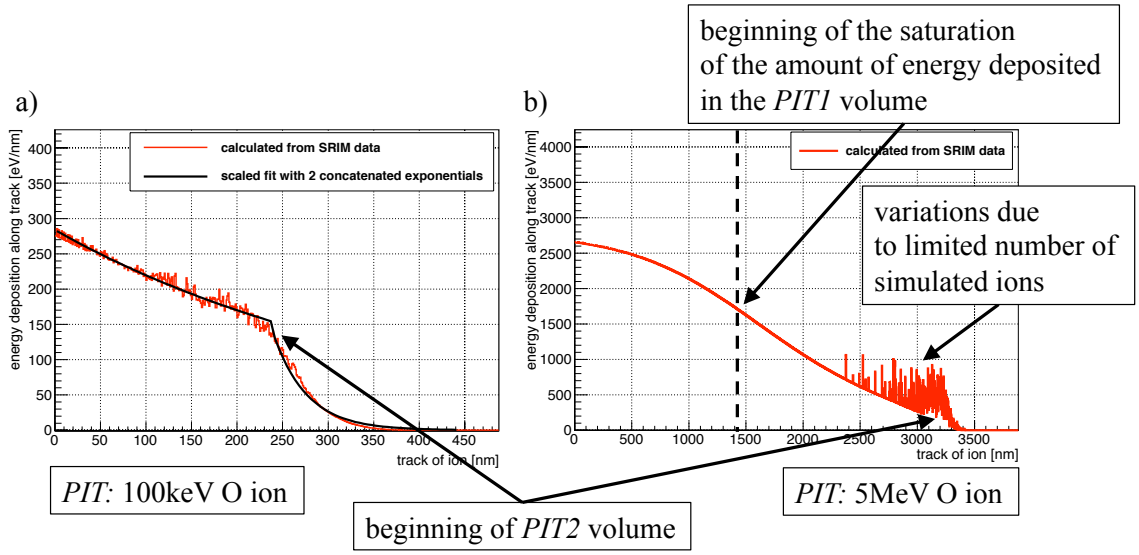

Figure B.12: Ionization distribution within the PIT volume for a 100keV O ion as primary interacting particle (panel a) and for a 5MeV O ion as primary interacting particle (panel b). Indicated are the respective starting points of the $PIT2$ volumes as well as the saturation of the energy deposition within the $PIT1$ volume in the case of the 5MeV O ion. The enhanced noisy structure on the distribution shown for the 5MeV ion within this region can be assigned to the bad statistics gained from the SRIM simulations for such large ion energies. Additionally, in panel b), the approximate starting point of the saturating behavior of the amount of energy deposited in ionization is indicated by the dashed, black line, i.e., for track lengths smaller than this line, the energy deposition starts to saturate.

In figure B.12 a), the ionization distribution within the PIT volume for a 100ekV O ion as primary interacting particle is shown. In figure B.12 b), the ionization distribution within the PIT volume for a 5MeV O ion as primary interacting particle is shown. Clearly the saturating behavior of the amount of energy deposited in ionization for the 5MeV O ion can be seen. This saturating behavior can be determined to be observable for the first time for an O ion energy between 1 and 2 MeV. Within the developed model it is assumed that a saturating amount of energy deposited in ionization can be equated with

a saturating number and energy of the produced electrons[21]. Hence, it is assumed that the electrons produced within the $PIT1$ volume of an O ion as primary particle exhibit a saturating maximum energy for O ion energies above $\sim$ 1.5MeV. In order to obtain a simple mathematical description, a sharp onset of this effect is assumed. Thus, for primary particle energies larger than the threshold energy $E_{part}^{PIT1-sat}$, the energy distribution of the electrons produced within the $PIT1$ volume is assumed to be constant and to exhibit the same shape as the energy distribution of the electrons produced within the $PIT1$ volume at a primary particle energy of $E_{part} = E_{part}^{PIT1-sat}$.

Using these observations, from the SRIM simulations, the corresponding threshold energies for O, Ca and W ion can be determined:

$$E_O^{PIT1-sat} \approx 1.5\text{MeV} \tag{B.28}$$

$$E_{Ca}^{PIT1-sat} \approx 5\text{MeV} \tag{B.29}$$

$$E_W^{PIT1-sat} \gtrsim 50\text{MeV} \tag{B.30}$$

where the observed dependency of the threshold energy on the type of the primary particle can roughly (phenomenologically) be described by:

$$E_{part}^{PIT1-sat} \propto m_{part}^{\frac{3}{2}} \tag{B.31}$$

with m_{part} corresponding to the mass of the primary interacting particle. This observation allows the assignment of a value for $E_{part}^{PIT1-sat}$ for different kinds of heavy, charged particles as primary interacting particle without the necessity of performing simulations with multiple energies for the regarded type of particle. Hence, for a primary interacting particle with an energy larger than the respective threshold energy, $E_{part}^{PIT1-sat}$, it is assumed that the radial parameters of the respective $PIT1$ volumes stay the same. It should be noted that, due to the assumed dependency of the electron velocity **only** on the velocity of the primary interacting particle (and not on the mass or energy of the interacting particle), this implies that the **maximum possible energy transferred to electrons is expected to be independent of the type of the primary interacting particle**. Thus, for a primary particle with an energy larger than its **particle-dependent threshold energy** $E_{part}^{PIT1-sat}$, the radial parameters for the ionization distribution within the $PIT1$ volume are assumed to correspond to the **maximum non-particle dependent radial parameters**. Hence, for $E_{part} \geq E_{part}^{PIT1-sat}$ the following relationships are assumed:

$$r_{PIT1}^{in}(E_{part}) := r_{PIT1}^{in}(E_{part} = E_{part}^{PIT1-sat}) = r_{max\,PIT1}^{in} = const. \tag{B.32}$$

$$r_{PIT1}^{out}(E_{part}) := r_{PIT1}^{out}(E_{part} = E_{part}^{PIT1-sat}) = r_{max\,PIT1}^{out} = const. \tag{B.33}$$

$$F_{PIT1}^{in}(E_{part}) := F_{PIT1}^{in}(E_{part} = E_{part}^{PIT1-sat}) = F_{max\,PIT1}^{in} = const. \tag{B.34}$$

where $r_{max\,PIT1}^{in}$, $r_{max\,PIT1}^{out}$ and $F_{max\,PIT1}^{in}$ correspond to the maximum values of the radial parameters within the $PIT1$ volume.

Concerning a lower limit for these parameters, the $PIT2$ volume and its parameters have

[21] The other possibility to produce a saturating amount of energy deposited in ionization for increasing ion energy would be to allow for increasing electron energies and assume a decreasing number of produced electrons. This possibility was not chosen within the present work.

to be regarded: As discussed above (see discussion below figure B.9), it is assumed that the volume $PIT2$ always describes the energy-loss process of the primary ion starting at the point along the track where the nuclear stopping process increases. Therefore, the parameters describing the $PIT2$ volume are assumed to be the same for one type of ion within the energy range where a splitting of the PIT volume into $PIT1$ and $PIT2$ occurs (compare figure B.9). This is the case for $E_{part} \gtrsim E_{part}^{PIT1-min}$ where $E_{part}^{PIT1-min}$ for O, Ca and W ions corresponds to $\sim$ 1keV (for O and Ca ions) and $\sim$ 2keV (for W ions) as can be determined from the SRIM simulations. Comparing different types of ions, the starting point of the $PIT2$ region is assumed to be characterized by approximately the same velocity of the ions (compare discussion in section III/3.1.1). Using this assumption and the dependencies of the radial parameters on the velocity of the particle producing the electrons, it can be deduced that **the parameters describing the $PIT2$ volume are always the same, independent of the type and energy of the primary ion** producing the electrons there. However, it should be noted that for energies of the primary interacting particle $E_{part} \lesssim$ 1keV, the ionization distribution within the PIT volume can be reproduced by the $PIT2$ volume only. Hence, for primary particles with $E_{part} < E_{part}^{PIT1-min}$, the complete PIT volume is described by the parameters of the $PIT2$ volume only. From this observation several deduction for the PIT parameters can be made:

- For energies of the primary interacting particle $E_{part} \gtrsim E_{part}^{PIT1-min}$, the parameters describing the $PIT2$ volume are always the same, independent of the type and energy of the primary interacting particle:

$$r_{PIT2}^{in}(E_{part} \gtrsim E_{part}^{PIT1-min}) := r_{PIT2}^{in}(E_{part} = E_{part}^{PIT1-min}) = const. \tag{B.35}$$

$$r_{PIT2}^{out}(E_{part} \gtrsim E_{part}^{PIT1-min}) := r_{PIT2}^{out}(E_{part} = E_{part}^{PIT1-min}) = const. \tag{B.36}$$

$$F_{PIT2}^{in}(E_{part} \gtrsim E_{part}^{PIT1-min}) := F_{PIT2}^{in}(E_{part} = E_{part}^{PIT1-min}) = const. \tag{B.37}$$

- For energies $E_{part} < E_{part}^{PIT1-min}$, the $PIT2$ parameters start to change according to the velocity, i.e., the energy, of the primary interacting particle. As will be discussed below (see the description of the method used to determine the radial parameters), within the presented model, for an energy larger than $E_{part}^{PIT1-min}$, the inner radius of the $PIT2$ volume, $r_{PIT2}^{in}(E_{part})$, is estimated to correspond to the minimum value possible for the inner radius r_{min}^{in} (compare equation B.26). Therefore, the inner radius of the $PIT2$ volume is assumed to be constant within the complete energy range considered (as it already approaches the minimum value possible for the largest extent of the $PIT2$ volume for an energy $E_{part} > E_{part}^{PIT1-min}$):

$$r_{PIT2}^{in}(E_{part}) = r_{min}^{in} = const. \tag{B.38}$$

- At an energy of $E_{part} = E_{part}^{PIT1-min}$, the $PIT2$ parameters describe the mean ionization distribution within the complete PIT volume of the primary interacting particle. Hence, the outer radius of the $PIT2$ volume for $E_{part} = E_{part}^{PIT1-min}$, $r_{PIT2}^{out}(E_{part}^{PIT1-min})$, has to reflect the mean of the outer ionization radius for a primary particle at the point where it exhibits **exactly** an energy of $E_{part}^{PIT1-min}$ and the outer ionization radius for a primary particle at the point where it is stopped,

i.e., possesses an energy of 0keV[22]. In analogy, the fraction $F^{in}_{PIT2}(E^{PIT1-min}_{part})$ can be defined, where the minimum value for the value of the fraction (given by equation B.27) has to be considered. As the value of the inner radius of the $PIT2$ volume is assumed to exhibit the same value r^{in}_{min} within the complete energy range considered (several 10eV up to a few 10MeV), it is deduced that the inner ionization radius for a particle of an energy of **exactly** $E^{PIT1-min}_{part}$ also has to correspond to this minimum value.

- At an energy of $E_{part} = E^{PIT1-min}_{part}$, the $PIT1$ parameters correspond to the ionization distribution of the primary interacting particle **with exactly** an energy of $E^{PIT1-min}_{part}$ (if the particle has lost a tiny bit of its energy, the remaining ionization distribution is described by the $PIT2$ volume). Hence, e.g., the outer radius of the $PIT1$ volume, $r^{out}_{PIT1}(E^{PIT1-min}_{part})$, is assumed to correspond to the outer ionization radius for a primary particle **with exactly** an energy of $E^{PIT1-min}_{part}$.

- Thus, at an energy of $E_{part} = E^{PIT1-min}_{part}$, the $PIT1$ and $PIT2$ parameters are correlated with each other, such that the $PIT2$ parameters represent the mean value of the respective 0keV value and the $E^{PIT1-min}_{part}$ value of each parameter, and the $PIT1$ parameters correspond to the respective $E^{PIT1-min}_{part}$ values:

$$r^{out}_{PIT2}(E^{PIT1-min}_{part}) := \frac{r^{out}_{PIT1}(E^{PIT1-min}_{part}) - r^{out}_{PIT2}(0\text{keV})}{2} = \frac{r^{out}_{PIT1}(E^{PIT1-min}_{part})}{2} \tag{B.39}$$

$$F^{in}_{PIT2}(E^{PIT1-min}_{part}) := \frac{F^{in}_{PIT1}(E^{PIT1-min}_{part}) - F^{in}_{PIT1}(0\text{keV})}{2} = \frac{F^{in}_{PIT1}(E^{PIT1-min}_{part}) - F^{in}_{min}}{2} \tag{B.40}$$

$$r^{in}_{PIT2}(E^{PIT1-min}_{part}) := r^{in}_{PIT1}(E^{PIT1-min}_{part}) = r^{in}_{min} \tag{B.41}$$

  where it should be noted that the $PIT2$ parameters for an energy of $E_{part} = E^{PIT1-min}_{part}$ correspond to the values of these parameters for all energies of the primary interacting particle $E_{part} \geq E^{PIT1-min}_{part}$.

- **It should be noted that the $PIT1$ parameters at an energy of $E_{part} = E^{PIT1-min}_{part}$ correspond to the minimal values of the $PIT1$ parameters as for energies below $E^{PIT1-min}_{part}$ no $PIT1$ volume occurs in the description of the ionization distribution along the track of the primary interacting particle.**

- Hence, if the $PIT2$ parameters for one energy and any type of a primary interacting particle with $E_{part} \geq E^{PIT1-min}_{part}$ as well as the minimum values of the $PIT2$ parameters ($r^{out}_{PIT2}(0\text{keV}) := 0\text{nm}$, $F^{in}_{PIT1}(0\text{keV}) := F^{in}_{min}$, $r^{in}_{PIT2}(E^{PIT1-min}_{part}) := r^{in}_{min}$) are determined (or assumed), the minimum values of the $PIT1$ parameters can be deduced.

[22] Such an outer radius for a 0keV particle is not well defined within the presented model as for very low energies the partitioning of the excited volume into inner and outer volume most probably will no longer deliver a good description. Hence, for simplicity it is assumed that the 0keV value of the outer radius of the $PIT2$ volume is given by 0nm.

The *Rec* Parameters

In the following, the dependencies of the *Rec* parameters on the energy and type of the primary interacting ion which are assumed within the present work are discussed. It should be noted that the assumptions made can only be considered as rough first-order approximations. A possibility to improve the utilized estimations is shortly discussed in section III/6.3.

Basic considerations and observations:

The radial parameters of the *Rec* volumes have to reflect the ionization distribution generated by all of the produced nuclear recoils (and their recoils) originating from one primary interacting particle. In figure B.13, an example of the energy spectra of the produced nuclear recoils for an O ion with 100keV energy as primary interacting particle are shown[23].

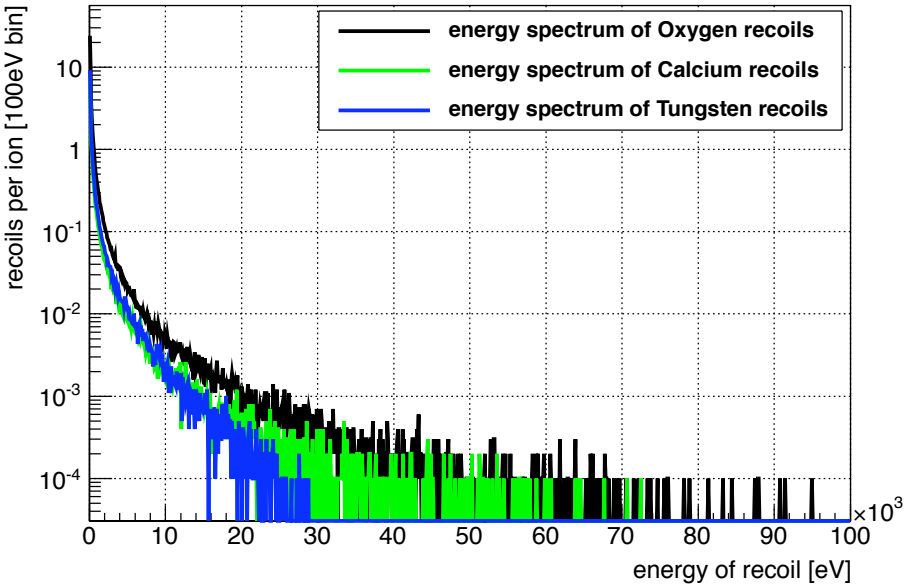

Figure B.13: Energy spectrum of the nuclear recoils (O, Ca and W recoil ions) produced by one O ion with an energy of 100keV as primary interacting particle. These energy spectra were calculated from the SRIM simulations. Shown are the number of nuclear recoils, i.e. O recoils (black spectrum), Ca recoils (green spectrum) and W recoils (blue spectrum), per 100eV bin. It should be noted that the y-axis is depicted logarithmically.

From figure B.13, it can be seen that the majority of the nuclear recoils produced are very low energetic (compare to the expected energy spectrum of electrons - Landau distribution - produced by heavy, charged particles or electrons as primary interacting particles, discussed in section III/3.1.2 and depicted in figure 3.4, section III/3.1.2). It should be noted that this observation can be made independently of the energy and type of the primary interacting particle. However, it can be seen that there is also a non-vanishing probability to produce high-energetic nuclear recoils, i.e., nuclear recoils with energies almost up to

[23]The energy spectrum of the nuclear recoils was calculated from the SRIM simulation as mean energy spectrum obtained by averaging over the 10000 O ions simulated.

the initial energy E_{part} of the primary interacting particle. Thus, the extent of the *Rec* volumes, defined by $r_{Rec}^{in}(E_{part})$ and $r_{Rec}^{out}(E_{part})$, as well as the ionization distributions within these volumes, defined by the partitioning of the ionization between inner and outer volume $F_{Rec}^{in}(E_{part})$, have to describe the ionization distribution created by the large number of low-energetic recoils on the one hand and, on the other hand, the ionization distribution created by the few high-energetic recoils. In this context it should be noted that, as the radial parameters of the *Rec* volumes are no longer only dependent on the energies of the electrons produced by one particle (as is the case for the *PIT* parameters) but also on the energy distribution of the generated nuclear recoils, the meaning of these parameters changes. The following interpretations of the radial parameters of the *Rec* volumes are used:

- The inner radius $r_{Rec}^{in}(E_{part})$ of the *Rec* volumes: The inner radius is assumed to be characterized by the range of the electrons produced by the large amount of low-energetic ions. In this context it should be noted that the mean velocity of all produced recoils is very small and, thus, of course, also the mean energy of all recoils produced is very small: The mean energy of all recoils produced by the ions with the largest energy considered within this work, e.g., a 50MeV O and a 50MeV W ion, only amount to ~ 0.6keV and ~ 4.5keV, respectively. Thus, the mean energy of the recoils in the low-energetic part of the recoil energy spectrum is almost always well below 1keV. Within the presented model, however, for such small particle energies, the inner radius of the excited volume is expected to correspond to the minimum value assumed for inner radii of excited volumes, r_{min}^{in} (compare, e.g. equation B.41). Thus, the following assumption is made (independent of the energy and type of the primary interacting particle):

$$r_{Rec}^{in}(E_{part}) := r_{min}^{in} = const. \tag{B.42}$$

- The outer radius $r_{Rec}^{out}(E_{part})$ of the *Rec* volumes: The outer radius is assumed to be dominantly characterized by the shape of the energy spectrum of the generated nuclear recoils: The more high-energetic nuclear recoils are produced as well as the larger their maximum energy compared to the mean energy of a nuclear recoil, the more high-energetic electrons are generated by the produced nuclear recoils. However, the more high-energetic electrons are produced, the larger the extent of the outer part of the *Rec* volumes has to be chosen to reproduce the increasing extent of the excited volume. Within the developed model, it is assumed that this dependency of the outer radius $r_{Rec}^{out}(E_{part})$ on the shape of the energy spectrum of the generated recoils can be described[24] by the ratio of the maximum velocity of the generated nuclear recoils[25], $v_{rec}^{max}(E_{part})$, and the mean velocity of all generated recoils, $\overline{v_{rec}}(E_{part})$:

$$r_{Rec}^{out}(E_{part}) \propto \frac{v_{rec}^{max}(E_{part})}{\overline{v_{rec}}(E_{part})} \tag{B.43}$$

[24] It should be noted that the assumed dependency of $r_{Rec}^{out}(E_{part})$ on this ratio is purely phenomenological and cannot be deduced from any formula stated within the present work. This dependency was chosen as it is assumed that the shape of the energy spectrum of the nuclear recoils can be characterized by this ratio.

[25] The maximum velocity of a nuclear recoil is, in fact, determined from the simulations as weighted mean maximum velocity of O, Ca and W recoils, i.e., the maximum velocities of a generated O, Ca and W recoil, respectively, are determined and then averaged according to the number of O, Ca and W recoils produced.

- The fraction $F_{Rec}^{in}(E_{part})$ of the ionization generated which is deposited in the inner part of the *Rec* volumes: The fraction of ionization deposited in the inner *Rec* volume is assumed to be characterized by the ratio of the velocity of the low-energetic and of the high-energetic electrons produced. The more low-energetic electrons are produced, that more energy is deposited within the inner part of the excited volume (with a constant radius r_{min}^{in}). However, the fraction of low-energetic electrons produced (with energies so small that they deposit the major fraction of their energy within the inner volume) is assumed to depend on the mean velocity of the produced nuclear recoils, $\overline{v_{rec}}(E_{part})$: The smaller the mean velocity of the produced nuclear recoils, the smaller the energy of the produced electrons, i.e., the larger the relative amount of ionization deposited within the inner part of the excited volume. Following the dependency of the fraction of ionization on the third root of the velocity of the particle producing the ionization (compare F_{PIT}^{in}, "volume effect"), the following dependency of $F_{Rec}^{in}(E_{part})$ on the mean velocity of the produced nuclear recoils is assumed[26]:

$$F_{Rec}^{in}(E_{part}) \propto (-1) \cdot \overline{v_{rec}}^{3}(E_{part}) \tag{B.44}$$

  where the minus sign in equation B.44 has to be noted, expressing that the smaller the mean velocity of the recoils, the larger the fraction of ionization deposited in the inner part of the *Rec* volumes.

Thus, it can be summarized that, to described the dependency of the radial parameters on the energy and type of the primary interacting particle two parameters characterizing the velocity distribution of the generated nuclear recoil particles, i.e., the mean velocity of the produced recoils, $\overline{v_{rec}}(E_{part})$, and the maximum velocity of the produced nuclear recoils, $v_{rec}^{max}(E_{part})$, are used. Both of these quantities can be determined from the SRIM simulations (delivering the list of generated nuclear recoils including the information on the type and energy of the generated recoil). In panel a) of figure B.14, the mean velocity $\overline{v_{rec}}(E_{part})$ of the produced recoils for O, Ca and W ions as primary interacting particle with energies between 1keV and 50MeV as determined from the data delivered by the simulations is presented. In panel b) of figure B.14, the ratio of the maximum velocity to the mean velocity of the produced recoils, $\frac{v_{rec}^{max}(E_{part})}{\overline{v_{rec}}(E_{part})}$, for O, Ca and W ions as primary interacting particle with energies between 1keV and 50MeV as determined from the data delivered by the simulations can be seen.

Hence, using these mean and maximum recoil-velocities (determined separately for each simulated ion type and energy) in combination with equations B.42, B.43 and B.44, in principle, the dependencies of the radial *Rec* parameters on the type and energy of the primary interacting particle are described. However, up to this point no information on the absolute values or proportionality factors is delivered. In order to gain estimates for the proportionality factors of the outer radius, $r_{Rec}^{out}(E_{part})$, and the fraction, $F_{Rec}^{in}(E_{part})$, the ionization distribution for one example of a primary interacting particle is estimated in the following.

[26] It should be noted that the assumed dependency of $F_{Rec}^{in}(E_{part})$ is purely phenomenological and cannot be deduced from any formula stated within the present work.

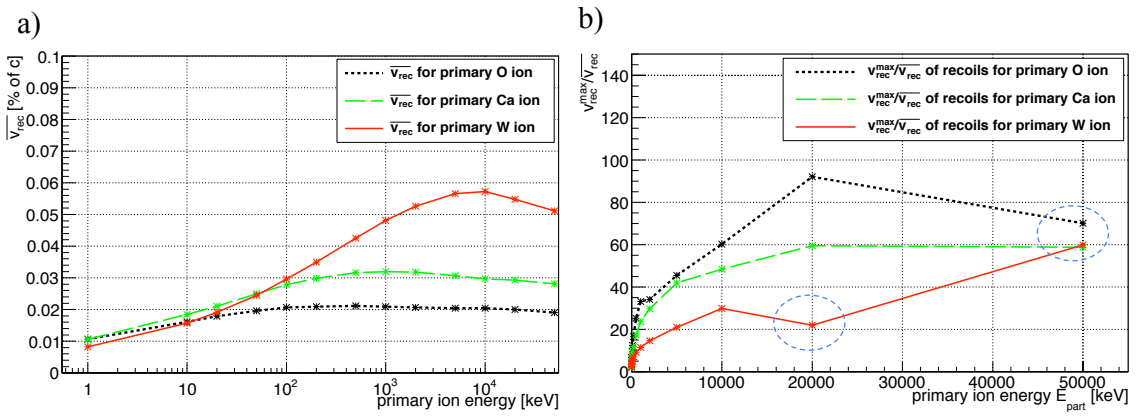

Figure B.14: Panel a: Mean velocities of the nuclear recoils produced by O (dotted black line), Ca (dashed green line) and W (solid red line) ions in $CaWO_4$ with primary ion energies from 1keV up to 50MeV (calculated from the SRIM simulations). The mean velocities $\overline{v_{rec}}(E_{part})$ are shown in percent of the speed of light. The x-axis (primary ion energy) is depicted logarithmically. Panel b: Ratio of the maximum velocities of recoil particles and the mean velocities of recoil particles produced by O (dotted black line), Ca (dashed green line) and W (solid red line) ions in $CaWO_4$ with primary ion energies from 1keV up to 50MeV (calculated from the SRIM simulations). It should be noted that the distinct deviations of the determined ratios for high particle energies from the trends at smaller energies (indicated by dashed blue circles) can be attributed to variations of the simulation results due to the limited number of ions simulated.

Estimation of the Proportionality Factors of $r_{Rec}^{out}(E_{part})$ and $F_{Rec}^{in}(E_{part})$

The method used to obtain an estimate for the proportionality factor is explained for the example of the outer radius $r_{Rec}^{out}(E_{part})$ of the *Rec* volumes, where thereafter only the differences for the method used for the estimation of the proportionality factor for the fraction $F_{Rec}^{in}(E_{part})$ of the *Rec* volumes are presented.

To estimate the proportionality factor of the outer radius, absolute values of $r_{Rec}^{out}(E_{part})$ for a primary interacting particle with two different energies are needed[27] (to determine the gradient and the intersection for zero mean velocity in equation B.43). For this purpose, the value of the outer radius of the *Rec* volumes is estimated for a 10keV and a 100keV O ion as primary interacting particle. In order to allow a simple estimation of the radial parameters of the ionization distribution of the recoils of the O ions as primary interacting particles, two observations are used:

- The recoils produced exhibiting the maximum recoil velocity are always (independent of the type and energy of the primary interacting particle) the oxygen recoils.
- Also independent of the type and energy of the primary interacting particle, always the number of O recoils produced is larger than the number of Ca and W ions produced. This feature is especially pronounced for O ions as primary interacting particles.

[27] It should be noted that due to the assumed dependencies of the parameters on the velocity distributions of the recoils produced by a primary interacting particle, the estimates gained in this way can be easily transferred to different types of primary interacting particles (using the information on the produced recoils delivered by SRIM).

Hence, especially for an O ion as primary interacting particle, the velocity distribution of the produced nuclear recoils is dominated by the O recoils (this is the motivation for the choice of an O ion as primary interacting particle for this method). Therefore, in the following, only the ionization distributions produced by the O recoils of the primary O ion are used to obtain a very rough estimate for the outer radius of the *Rec* volumes.

For the 10keV O ion as primary interacting particle, it is simply assumed that the outer radius of the *Rec* volumes is given by the constant value of the outer radius of the $PIT2$ volume of an O ion:

$$r_{Rec}^{out}(E_O = 10\text{keV}) := r_{PIT2}^{out}(E_O \gtrsim E_O^{PIT1-min}) = const. \tag{B.45}$$

(compare equation B.36). This is assumed to be a reasonable value as, on the one hand, this outer $PIT2$ radius represents the ionization distribution created by an O ion in its energy-loss process for energies between $E_O^{PIT1-min} \approx 1$keV and 0keV and as, on the other hand, the vast majority of the O recoils produced by the primary 10keV O ion possess energies less than 1keV.

However, to obtain a reasonable estimate for the outer radius of the ionization distribution of the O recoils of the 100keV O ion, a more detailed analysis should be used as the energy-spectrum of the produced O recoils stretches from $\sim$ 0keV up to $\sim$ 100keV. To include the influence of the low-energetic and the high-energetic O recoils produced the O recoil-energy spectrum of the 100keV O ion is divided into two parts: One energy interval representing the low-energetic O recoils produced, $E_{O-rec} \in$ [0keV, 10keV], and one energy interval representing the high-energetic O recoils, $E_{O-rec} >$ 10keV. Within both of these intervals the respective mean energy of the contained O recoils, $\overline{E_{O-rec}}$, and their summed energy can be determined. Using the energy-dependent fraction of the energy deposited in ionization $F_{ioniz}(E_{part})$ (see figure 3.1 in section III/3.1.1), the amount of ionization produced by the "low-energetic" and "high-energetic" O recoils for a 100keV O ion as primary interacting particle can be estimated. The values determined in this way can be summarized as follows: The 100ekV O ion as primary interacting particle transfers a total amount $\sim$ 25keV to O recoils, where $\sim$ 18keV are used to produce $\sim$ 47.5 O recoils with energies smaller than 10keV and $\sim$ 7keV are transferred to $\sim$ 0.5 O recoils with energies larger than 10keV[28]. Thus, the mean energies of "low-energetic" and "high-energetic" O recoils amount to $\sim$ 0.54keV and $\sim$ 14keV, respectively. Using the efficiencies for such O ions (with 0.54keV and 14keV energy) to produce ionization (see figure 3.1 in section III/3.1.1) it can be deduced that the "low-energetic" O recoils deposit $\sim$ 4keV into ionization whereas the "high-energetic" O recoils produce $\sim$ 3keV of ionization. Thus, it is assumed that a fraction of $\sim \frac{4\text{keV}}{3\text{keV}+4\text{keV}} \approx 57\%$ of the ionization created by the O recoils of the primary 100keV O ion is produced by the "low-energetic" O recoils whereas a fraction of $\sim \frac{3\text{keV}}{3\text{keV}+\text{keV}} \approx 43\%$ of the ionization by O recoils of the primary O ion is produced by the "high-energetic" recoils. This information can be used in the following way:

- Assuming that the radial parameters characterizing the ionization distribution by the "low-energetic" O recoils as primary interacting particles and by the "high-energetic"

[28] It has to be noted that these values are determined with the help of the energy spectrum of O recoils averaged for 10000 O ions simulated as primary interacting ion (for 100keV and 1MeV each). Due to this averaging process, numbers of recoils (and corresponding mean energies) smaller than one in the high-energetic interval can occur. These numbers reflect the probability of the occurrence of such a high-energetic recoil for one primary O ion. Thus, also the integrated energy within the high-energetic interval can exhibit values less than 10keV.

O recoils as primary interacting particles are known, a weighted mean for the outer radius of the ionization distribution by these O ions as recoils of a primary 100keV O ion can be gained.

- For this purpose, it is assumed that the ionization distribution of the "low-energetic" O recoils can be assigned the same outer radius as the ionization distribution of the O recoils of the 10keV primary O ion: $r^{out}_{Rec-\text{low-energetic}}(E_O = 100\text{keV}) := r^{out}_{Rec}(E_O = 10\text{keV})$.

- For the mean "high-energetic" recoils, it should be noted that from the SRIM simulations (and their analysis) it can be determined that the ionization distribution produced by these particles is dominated by the ionization produced within their respective PIT volumes. Hence, for simplicity, it is assumed that their respective ionization distributions are described by their $PIT1$ parameters only, i.e., for the outer radii, the value of $r^{out}_{PIT1}(E_O \approx 14\text{keV})$ is used.

- Using these two estimates, the outer radius of the Rec volumes of a 100keV O ion can be expressed by the weighted average of the outer radius for the "low-energetic" O recoils and the outer radius of the "high-energetic" recoils:

$$\begin{aligned} & r^{out}_{Rec}(E_O = 100\text{keV}) \approx \\ & \approx 57\% \cdot r^{out}_{Rec-\text{low-energetic}}(E_O = 100\text{keV}) + 43\% \cdot r^{out}_{Rec-\text{high-energetic}}(E_O \approx 100\text{keV}) = \\ & := 57\% \cdot r^{out}_{Rec}(E_O = 10\text{keV}) + 43\% \cdot r^{out}_{PIT1}(E_O \approx 14\text{keV}) := \\ & := 57\% \cdot r^{out}_{PIT2}(E_O \gtrsim E_O^{PIT1-min}) + 43\% \cdot r^{out}_{PIT1}(E_O \approx 14\text{keV}) \end{aligned} \tag{B.46}$$

Thus, an estimate for the outer radius of the Rec volumes of a 10keV O ion and a 100keV O ion as primary interacting particle only on the basis of $PIT1$ and $PIT2$ parameters of O ions is gained. Hence, if the outer radii of the $PIT1$ and $PIT2$ volumes for O ions can be determined, then the outer radii of the Rec volumes of the 10keV and the 100keV O ion as primary interacting particle can be estimated. These values for the outer radii of the Rec volumes for 10keV and 100keV O ions, in turn, can be used, in combination with the assumed dependency of $r^{out}_{Rec}(E_{part})$ on the type and energy of the primary interacting particle (compare equation B.43), to calculate the corresponding proportionality factor in equation B.43.

In principle, the same method is applied for the determination of the proportionality factor for the fraction of ionization $F^{in}_{Rec}(E_{part})$ of the Rec volumes (see equation B.44). However, for $F^{in}_{Rec}(E_{part})$ no reasonable value for the 10keV O ion as primary interacting particle can be estimated on the basis of the informations available. Thus, in addition to the 100keV O ion as primary interacting particle, a corresponding analysis of the O recoil-energy spectrum of a 1MeV O ion as primary interacting particle is performed. Again, it is assumed that the values of the fractions $F^{in}_{Rec}(E_{part})$ of the Rec volumes of the 100keV and the 1MeV O ions as primary interacting particles can be estimated as the weighted average of their "low-energetic" ($E_{O-rec} \leq 10\text{keV}$) and their "high-energetic" ($E_{O-rec} > 10\text{keV}$) recoils. In analogy to the method used for the outer radius of the Rec volumes, the respective high-energetic recoils are assigned the corresponding values of the fraction $F^{in}_{PIT1}(\overline{E_{O-\text{high-energetic}}})$. The low-energetic recoils ($E_{O-rec} \leq 10\text{keV}$) are assigned the same (unknown) value $F^{in}_{Rec}(E_{part} = 10\text{keV})$ (compare equation B.46). The

value of $F_{Rec}^{in}(E_{part} = 10\text{keV})$ can now be adjusted such, that with the resulting proportionality factor and zero-point value for $F_{Rec}^{in}(E_{part})$ in equation B.44, the values for $F_{Rec}^{in}(E_{part})$ and $F_{Rec}^{in}(E_{part})$ are correctly reproduced.

Hence, within the developed description, an estimate for the combined ionization distribution of the *Rec* volumes can be gained if the described dependencies of the radial parameters of the *Rec* volumes are assumed and if the radial parameters of the $PIT1$ and $PIT2$ ionization distribution by the O recoils of an O ion (100keV and 1MeV) as primary interacting particle are known.

It should be noted that, in principle, an analysis of the ionization distribution of the produced nuclear recoils as performed for the O recoils of the 100keV and 1MeV O ions as primary interacting particles could also have been performed for all other types of recoil particles as well as for each of the simulated ion types and energies. In an analogous way as explained for the O ions, an estimate for the radial *Rec* parameters for each ion separately could be gained. However, as, on the one hand, a simple mathematical modeling of the dependency of the radial parameters on the type and energy of the primary interacting particle was strived for and as, on the other hand, the method used to estimate the values of the *Rec* parameters from such an analysis contains large uncertainties (e.g., the choice of the outer radius of the *Rec* volumes for a 10keV O ion as primary interacting particle), this possibility was not pursued. Instead, as described, the assumed recoil velocity-dependencies of the radial parameters (equations B.42, B.43 and B.44) are used to transfer the results for the radial *Rec* parameters obtained for O ions as primary interacting particles to other types of primary interacting particles.

Summary of the Assumed Dependencies and Interdependencies of the Radial Parameters of the PIT and *Rec* volumes

From the above discussions it can be deduced that, with the assumed minimal values for certain radial parameters as well as with the assumed energy dependencies, all of the radial parameters of the PIT and *Rec* volumes can be determined if the $PIT1$ and $PIT2$ parameters are known for one type of a heavy, charged primary interacting particle (e.g., an O ion) at one energy $E_{part} > E_{part}^{PIT1-min}$. From the values of the parameters for such an energy, the following parameters can be deduced:

- The $PIT2$ parameters are determined for all energies $E_{part} \geq E_{part}^{PIT1-min}$ (note that these parameters are assumed to be the same for all types and energies of heavy, charged primary interacting particles with $E_{part} \geq E_{part}^{PIT1-min}$, compare equations B.39, B.40 and B.41). Thus, the $PIT2$ parameters are known for the complete energy range considered, as for smaller energies, $E_{part} < E_{part}^{PIT1-min}$, the assumed energy dependencies of the parameters (as discussed above) and the minimum values of the parameters can be used to determine the values of the $PIT2$ parameters.

- In addition, from the $PIT2$ parameters also the minimum values for the outer radius and for the fraction of the $PIT1$ volume (equations B.39 and B.40) can be determined.

- Using these minimum values for the $PIT1$ parameters as well as the $PIT1$ parameters known for one type and energy of a primary interacting particle, the proportionality factors of the dependencies of the $PIT1$ parameters on the velocity of the

primary particle can be determined (compare equations B.24 andB.25). As these parameters are assumed to only depend on the velocity and not on the type of the primary interacting particle, the $PIT1$ parameters can be calculated for all types of primary interacting particles with energies $E_{part} \lesssim E_{part}^{PIT1-sat}$. For energies larger than $E_{part}^{PIT1-sat}$, the parameters of the $PIT1$ volume are assumed to stay constant (compare equations B.32, B.33 and B.34).

- Using that the $PIT1$ parameters as well as the $PIT2$ parameters can be determined for all types and energies of primary interacting particles, the parameters of the *Rec* volumes can be determined for all types and energies of primary interacting particles as discussed above.

Hence, on the basis of the assumed energy dependencies and minimum values, the values of the radial parameters of the ionization distribution for any type of a heavy, charged particle can be determined with the help of the radial $PIT1$ and $PIT2$ parameters for one type of heavy, charged particle as primary interacting particle with a known energy of $E_{part} > 1$keV.

Method Used to Determine the Parameters Describing the Radial Ionization Distribution for Heavy, Charged Particles

As indicated, the knowledge of the radial $PIT1$ and $PIT2$ parameters for one type of ion at one energy ($>$ 1keV) is required. To gain an estimate for such a set of parameters, the fact is used that, as discussed in section III/3.2.4 (see, e.g., figure 3.11), the values of the radial parameters affect the shape of the decay-time spectrum of the (quenched) scintillation light created. However, it should be noted that, as is also discussed in section III/3.2.4, in addition to the radial parameters of the ionization distribution also the so-called Förster radius affects the shape of the decay-time spectrum of the scintillation light. The dependencies of the pulse shape of the scintillation light on the different radial parameters as well as on the Förster radius are described in the so-called "complete model including quenching" (section III/3.2.4). In order to determine all of the model parameters and to validate the complete model, experiments using different excitation modes for a $CaWO_4$ crystal were performed. The experiments are described in chapter III/4, details on the analysis of the experiments and, hence, on the determined parameters can be found in chapter III/5. Within these experiments, decay-time spectra for ^{16}O ion-beam excitation ($E_O \approx 35$MeV) and ^{127}I ion-beam excitation ($E_I \approx 35$MeV) were recorded. These decay-time spectra are used to determine the free model parameters and to validate the model: The decay-time spectra recorded for the ^{127}I-ion beam are used to adjust and fix all model parameters, the decay-time spectra recorded for the ^{16}O-ion beam are used to validate the model (see sections III/3.3.2 and III/5 as well as the following discussion). This choice can be motivated as discussed in the following:

- In addition to the $PIT1$-saturation threshold-energy discussed for the radial parameters of the $PIT1$ ionization distribution, for such high energetic ions an additional threshold energy should be taken into account: As discussed in section III/3.1.1 (see table 3.1), for energies larger than the energy E_1 defined there, the electronic stopping power for the respective primary interacting particle starts to decrease again. Hence, the threshold energy E_1 characterizing the energy (velocity) of the primary particle for which the maximum energy-loss rate is reached. Therefore, the energy

E_1 can be identified with the primary particle energy for which the so-called Bragg peak occurs.

- Considering the values for E_1 stated in table 3.1 (section III/3.1.1), it becomes clear that a large fraction of the energy-loss process for oxygen (O) ions with 35MeV is characterized by the energy-loss process before the occurrence of the Bragg peak ($E_1 = 6.33$MeV for O ions). This circumstance can, of course, be recognized from the energy deposition (in eV per nm) along the track of the primary interacting particle, i.e., within the PIT volume. It should be noted that the energy of the iodine (I) ions in the experiments (~ 35MeV) is below the respective E_1 energy for I ions. Hence, for I ions of 35MeV, no Bragg peak is expected to occur ($E_1 = 629$MeV for I ions).

- In figure B.15, the energy deposition along the primary particle track for O ions (panel a) and I ions (panel b) with the energies as used in the experiments (~ 35MeV) are shown. In addition to the energy depositions in (eV per nm bin) depicted as solid green line, additionally, the respective fit with two concatenated exponentials is shown as solid red line. It has to be noted that, as indicated in the picture, the division of the PIT into two volumes for 35MeV O ions does no longer correspond to the division of the PIT into $PIT1$ and $PIT2$ as defined above (compare panel b for I ions). Instead, the "new" $PIT1$ volume for O ions is used to describe the energy deposition for energies larger than the Bragg peak, whereas the "new" $PIT2$ volume corresponds to the combined "old" $PIT1$ and $PIT2$ volumes.

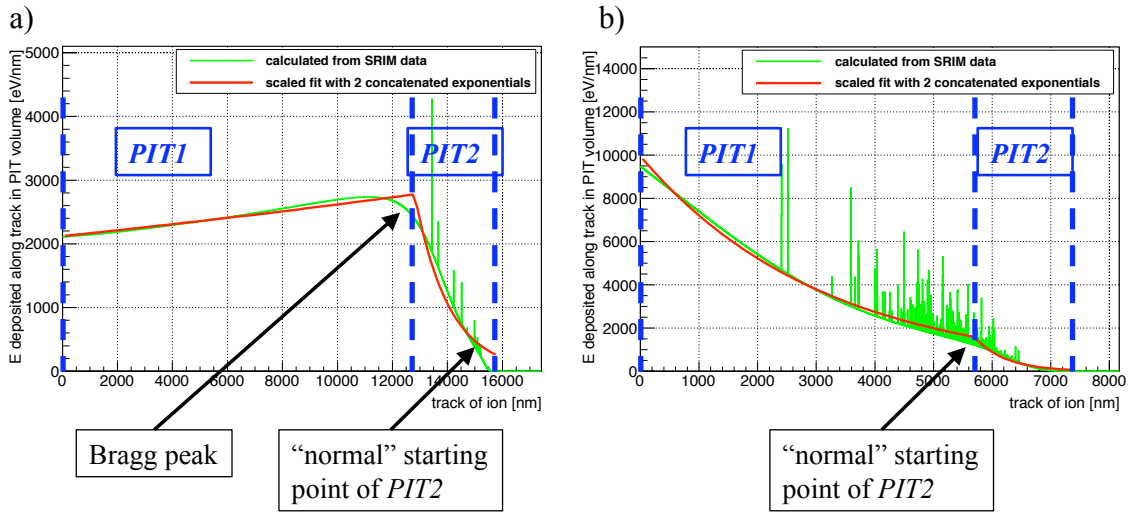

Figure B.15: Energy deposition in ionization (in eV per nm bin) along the track of the primary interacting particle within the PIT volume for O ions (panel a) and I ions (panel b) as used in the experiments (see chapter III/4). The histogram of the energy depositions is shown in green. In addition, the fits with two concatenated exponentials to the PIT histograms, scaled to deliver the correct integrals, are depicted as solid red line. The dashed blue lines indicate the separation of the complete PIT volume into $PIT1$ and $PIT2$ volumes.

- In principle, the energy deposition for the O ion along the primary particle track could have been fitted with three exponentials representing the "new" $PIT1$ and the

"old" $PIT1$ and $PIT2$ volumes, respectively. However, as the "old" $PIT2$ volume only accounts for a very small part of the energy deposited within the total $PIT2$ volume, the radial parameters of this volume could be chosen almost arbitrarily without significantly changing the shape of the decay-time spectrum of the generated scintillation light. Therefore, the PIT volume of 35MeV O ions was modeled by two concatenated exponentials (as depicted in figure B.15 a) where it should be kept in mind that the meaning of the PIT volumes changed. Concerning the radial parameters of these "new" PIT volumes the following assumptions were applied: As discussed, the "new" $PIT2$ volume is dominated by the "old" $PIT1$ volume. Hence, for this region, the radial parameters as calculated for the "old" $PIT1$ volume, i.e., the saturated radial $PIT1$ parameters, are used. Concerning the "new" $PIT1$ volume, describing the ionization distribution for energies before the Bragg peak, three assumptions are made:

1. As the maximum possible energy-transfer to electrons is assumed to have already saturated for energies above $E_{part}^{PIT1-sat} < E_1$, also for the "new" $PIT1$ volume, the velocity of the high-energetic electrons assumed to characterized the outer radius of the excited volume is expected to stay constant. Thus, the outer radius of the "new" $PIT1$ volume is assumed to correspond to the maximum (saturated) value for the outer radius of the "old" $PIT1$ volume.
2. However, due to the much larger velocity of the primary interacting particle within the "new" $PIT1$ region (compared to the velocity within the "old" $PIT1$ region), the mean energy of the produced electrons is assumed to be increased compared to the "old" $PIT1$ volume. This increased mean velocity of the produced electrons can be expected to lead to larger mean penetration depths of the low-energetic electrons produced around the track and, hence, to an enlarged inner radius of the produced ionization distribution. It should be noted that the value of the inner radius within the "new" $PIT1$ volume cannot be predicted on the basis of the assumptions made within the present work. Therefore, the value for the inner radius of the "new" PIT volume for 35MeV O ions (as used in the experiments) has to be adjusted with the help of the shape of the decay-time spectrum of the scintillation light recorded.
3. By increasing the inner radius of the ionization distribution within the "new" $PIT1$ volume compared to the "old" $PIT1$ volume it is assumed that the fraction of energy contained in the inner part of the excited volume stays constant.

Hence, in the description of the ionization distribution produced for a 35MeV O ion as primary interacting particle, no radial parameters of the "old" $PIT2$ volume occur. However, as discussed above, the shape of the recorded decay-time spectra are intended to adjust the $PIT1$ and $PIT2$ parameters. Thus, for this purpose, the decay-time spectrum of the 35MeV O ions cannot be used. In contrary, as can be seen from figure B.15 b, the PIT volume for 35MeV I ions is represented by the two $PIT1$ and $PIT2$ volumes as defined above. Thus, in order to determine the values of the radial parameters of the ionization distribution (and the so-called Förster radius, see discussion below and section III/5.3.2), the decay-time spectra recorded under iodine-beam excitation are used.

In fact, the primary goal of the comparison of the model prediction for the pulse shape of the scintillation light with a recorded light-pulse shape is to determine the value of the

Förster radius.

At this point, it has to be noticed that the mathematical description of the decay-time spectrum described by this model basically contains the dependency on the Förster radius and on the radial parameters in an indistinguishable parametrization: The initially created density of the blue STEs (which is described by the radial parameters of the ionization distribution and the analysis of the SRIM simulations) is always (for every appearance in the mathematical formulation) multiplied with the cubed Förster radius and vice-a-versa (compare equations 3.166 and 3.167 in section III/3.2.4). Hence, in principle, the parameters of these values, the Förster radius and the STE density, are one-to-one correlated and cannot be assigned independently: For any value chosen for the radial parameters, i.e., the STE density, a corresponding value for the Förster radius should be determinable so that the product of the STE density and the cube of the Förster radius yields the same value and, hence, the same shape of the decay-time spectrum of the scintillation light. In principle, this is the case, however, due to the assumed interdependencies of the different radial parameters within the different sub-volumes of the complete excited volume (e.g., the *Rec* volume parameters depend non-linearily on the $PIT1$ and $PIT2$ parameters as discussed in detail above, see, e.g., the Summary of the Assumed Dependencies and Interdependencies of the Radial Parameters of the PIT and *Rec* volumes), deviations from this strict correlation occur.

Thus, in principle, the decay-time spectrum of the scintillation light depends on the radial parameters as well as on the Förster radius, which are both unknown parameters, in a mathematically indistinguishable way. However, this strict correlation is weakened due to the assumed interdependencies of the radial parameters for different sub-volumes. Therefore, within the developed model, it is assumed that reasonable estimates for the radial parameters of the ionization distribution for heavy, charged particles can be obtained for the adjustment of these parameters using the shape of the scintillation-light spectrum recorded for I ions, although this shape is also influenced by the free parameter for the Förster radius. Nonetheless, it should always be taken into account that by using the shape of the decay-time spectrum to determine the parameters describing the radial distribution as well as the Förster radius, most probably, different combinations of solutions for the values of the radial parameters and the Förster radius could be found. In section III/6.3, a different method to determine the value of the Förster radius, independently of the particle-induced ionization distribution is suggested. If such an approach could be realized, the values for the radial parameters of the particle-induced ionization distribution could indeed be determined using the scintillation-light decay-time spectra without correlation with the value of the Förster radius.

Details on the method applied within the present work to adjust the radial parameters with the help of the recorded scintillation-light decay-time spectra as well as on the determined parameters can be found in section III/5.3. From the values of the radial parameters determined in this way, the values for other types of ions and different energies of the ions can be obtained by using the above explained assumptions on the dependencies of these parameters on the velocity, i.e., on the energy and type of the primary interacting particles.

B.4 Energy-Level Scheme and Absorption Spectrum of Defect Centers

B.4.1 Energy-Level Scheme of Defect Centers

Within the model developed in the present thesis, it is assumed that excited defect centers, in principle, exhibit the same energy-level structure at the band edge as intrinsic centers. However, some differences are expected to occur due to the defect contained in the unit cell (e.g., impurity or deformation of the crystal structure). These differences as well as the expected consequences for the energy level scheme of defect centers are discussed in the following.

Electronic Structure of the Ground State of Defect Centers

Defect centers are unit cells containing a distortion. Nonetheless, the lowest-lying energy levels at the conduction band edge are still expected to be formed by the triplet levels $^3T_1/^3T_2$ (see sections III/2.1.3 and III/2.1.6). However, due to the defect contained, their electronic structure can be assumed to already exhibit a deformation, even in the unexcited state, i.e., before the self-trapping process of the hole. Therefore, also without a STH residing at the defect center, a symmetry-breaking process is expected to be present. In analogy to the self-trapping process of the hole, this symmetry-breaking process can be assumed to lead to two changes in the energy-level scheme (compare section III/2.1.4): On the one hand, a reduction of the degeneracy of the energetically lowest-lying levels, and, hence, a splitting of the triplet levels $^3T_1$ and $^3T_2$ is expected. On the other hand, a lowering of the energy levels at the conduction band edge into the band gap is assumed to occur. Due to the reduction of the degeneracy of the triplet levels (even without a STH), transitions from and to the ground level of the unit cell to the generated split states should become partially allowed. Hence, already before the excitation of a defect center, it can be expected that transitions to and from the lowest-lying electron levels (the split triplet states) are allowed. This implies that the deformation of the unit cell due to a defect is assumed to create electron levels (split triplet states) within the band gap for which transitions from and to the ground state are at least partially allowed. It should be noted that the possibility of such transitions can be interpreted as a reduction of the band gap for defect centers in comparison to intrinsic centers (with $E_{gap} \approx 5$eV, see section III/2.1.2): For intrinsic centers only excitation from the ground state to the higher lying singlet states is allowed (compare section III/2.1.4) whereas for defect centers an (at least partially) allowed transition to the lower-lying split triplet-states is expected. As just discussed, these split triplet states are additionally assumed to be shifted to lower energies (within the band gap) by the symmetry-breaking process.

Electronic Structure of the Excited State of Defect Centers

If such a defect center is excited, in principle, exactly the same symmetry-breaking process due to the Jahn-Teller and Spin-Orbit splitting as for STHs at intrinsic centers is assumed to occur (compare section III/2.1.4). Hence, in analogy to the energy-level system of intrinsic centers, the lowest-lying energy levels are expected to be closely spaced Jahn-Teller spin-orbit split states arising from a triplet level. However, no conclusion can be drawn whether these levels arise from the $^3T_1$ or $^3T_2$ level or even a mixture of them. The energy splitting D_g of the two lowest-lying energy levels is expected to be of the same

order of magnitude as for the intrinsic centers (D_b, order of magnitude 1meV, compare, e.g, section III/2.2.1) as in both cases, the reduction of degeneracy is caused by the same underlying effect (deformation of the unit cell, lowering of the point symmetry). Nonetheless, deviations of the total energy level scheme compared to an excited intrinsic center are expected to occur due to the already present distortion and splitting of the triplet levels (for the unexcited defect center):

- In a defect center, the STH delivers only an additional symmetry-breaking process for the already split triplet levels. Hence, the splitting of the triplet levels at an excited defect center, is a combined effect of the principle deformation of the defect center and the self-trapping process of the hole (STH). Therefore, the total reduction of degeneracy can be expected to be larger compared to an excited intrinsic center. This should lead to a larger probability for radiative transitions between the two split levels and the ground level of the system in a defect center compared to an intrinsic center. Hence, the combined deformation effect is supposed to result in an an enhancement of the allowance of radiative transitions in defect centers.

- The combined effect of the distortion of the defect center due to the defect and the STH should also lead to a larger deformation of the excited defect center in comparison to the excited intrinsic center. In a graphical representation of the potential energy curves (compare figure 2.10 in section III/2.2.1 for the excited intrinsic center), this would correspond to an enhanced horizontal shift (configuration coordinate) of the minimum of the electron potential-curve for the defect centers compared to the intrinsic center. As can be seen from figure 2.10 (section III/2.2.1), such an enhanced horizontal shift can be expected to result in a reduced energy barrier $\Delta E_{non-rad}$ for the non-radiative decay, an enlarged energy barrier $\Delta E_{ex-mobility}$ for the exciton mobility and a reduced energy E_{STE} of the STE and, hence, of the produced phonons.

Hence, within the developed model, from these considerations the following predictions for properties of excited defect centers can be drawn:

- The produced scintillation light (radiative decay of the STE) is less energetic than the scintillation light produced at intrinsic centers, i.e., shifted to longer (green) wavelengths. This prediction is supported by experimental observations, see, e.g, section III/2.2.2.

- The energy barrier for the migration of STEs is larger compared to STEs at intrinsic centers. This prediction is supported by experimental observations, see, e.g., equations 3.178 and 3.179 in section III/3.3.2.

- The radiative recombination times for the two split triplet levels is expected to be much shorter than the ones for intrinsic centers (enhanced allowance). This prediction is supported by experimental observations, see section III/5.2.2.

- The energy barrier for the non-radiative recombination of STEs is predicted to be lower compared to STEs at intrinsic centers. This prediction is supported by experimental observations, see section III/3.2.1.

- The energy splitting between the two split triplet levels D_g is assumed to be of the same order of magnitude ($\sim$ 1meV) as for an intrinsic center.

B.4.2 Absorption Characteristics of Defect Centers

In the following, the conclusions that can be drawn for the absorption characteristics of defect centers due to the model developed for the energy level scheme of defect centers (appendix B.4.1) are presented and compared to experimental observations.

Due to the expected reduction of the band gap of defect centers in comparison to intrinsic centers, photons with a significantly lower energy as needed for intrinsic centers should be able to excite defect centers. Hence, within the described model for the electronic structure of defect centers, an absorption edge for defect centers, significantly lower in energy than the one of intrinsic centers (see section III/2.1.2, definition of the band gap as absorption edge), is proposed. This suggestion is in perfect agreement with measurements of the absorption characteristics of defect centers reported in literature:

- In [119], it is reported that defect centers incorporating interstitial oxygen cause absorption at 310nm (4.0eV) and 400nm (3.1eV), i.e., the absorption spectrum overlaps with the emission spectrum of intrinsic luminescence centers.

- In [59], the influence of La doping (250ppm La in the melt before crystallization) on the absorption spectrum of $CaWO_4$ has been investigated. La doping provides additional electrons occupying electron traps in the conduction band which result from defect centers (compare section III/2.1.3). Thus, La doping prevents the excitation of these centers by low energetic photons[29]. It is reported that the transmission of the La-doped sample is significantly increased in the region from 320nm (3.9eV) to 450nm (2.8eV) compared to the undoped sample. This observation indicates, that light in the energy range from 2.8eV (450nm) to 3.9eV (320nm) can be absorbed at defect centers (without filled electron traps).

- Additionally, in [59], the influence of ^{60}Co-radioisotope irradiation (doses between 1 to 230Gy) on the transmission of $CaWO_4$ crystals has been investigated. Such an intense irradiation can be assumed to produce an enhanced defect density in the crystal. It is reported that irradiation leads to a clear increase of absorption in the region from 420nm (3.0eV) to 850nm (1.5eV) with a peak around 520nm (2.4eV).

- In [48], the photoluminescence of disordered $CaWO_4$ films, i.e., not fully crystallized $CaWO_4$ films that contain a large fraction of deformed $[WO_4]^{2-}$ complexes, has been investigated. It is reported that excitation with 488nm (2.5eV) leads to the emission of low-energetic scintillation light (roughly between 450nm and 800nm). It is suggested that this emission can be attributed to the radiative decay of defect centers. This observation indicates that photons with an energy of 2.5eV can be absorbed by defect centers.

It can be deduced that defect centers, in fact, exhibit an absorption (excitation) spectrum at significantly smaller energy than intrinsic centers.

[29] As the electron level within the conduction band is occupied, electrons from the valence band can only be excited into energetically higher-lying levels.

B.5 Radiative Recombination of Blue STEs From Two Emitting Levels

As shown in section III/3.2.3, at very low temperatures ($T \lesssim 5$K), the observed slow decay time (of the order of a few 100μs, in [54]: $\sim 560\mu$s) of the scintillation light of $CaWO_4$ can be identified with the radiative decay time of blue STEs. Therefore, if no variation of the radiative decay time with temperature would occur, also at room temperature the radiative recombination time of blue STEs would have to be of the order of a few 100μs. In section III/3.2.3, however, it is shown that the lifetime of blue STEs at room temperature is of the same order of magnitude as the observed decay time of the scintillation light at room temperature. Hence, the lifetime of blue STEs at room temperature is of the order of 10μs. A radiative recombination time of the order of a few 100μs would imply that, at room temperature, only a fraction of roughly 1% to 10% (given by the ratio of the lifetime to the radiative recombination time) of blue STEs would generate scintillation light (decay radiatively). At low temperatures, however, all of the blue STEs would generate scintillation light as the radiative recombination is the only possibility remaining (see discussion in section III/3.2.1). This would correspond to an increase in scintillation efficiency (fraction of radiatively decaying STEs) of roughly a factor of 10 to 100 from room temperature down to ~ 5K. Such a huge increase is clearly not observed (only a factor of ~ 1.8 is observed, compare section III/2.2.4), indicating that, also at room temperature, more than 1% to 10% of the STEs have to decay radiatively. This, on the other hand, implies that the radiative recombination time of blue STES at room temperature has to be faster than a few 100μs in order to allow more STEs to decay radiatively during their lifetime of $\sim 10\mu$s.

B.6 Details on the Förster Interaction

B.6.1 Derivation of the Time-Dependent Förster Interaction Rate

With the Förster reaction rate $K_{d-d}(T,\rho)$ depending on the distance ρ (equation 3.71 in section III/3.1.3), the impact of the Förster (dipole-dipole) interaction on the temporal evolution of the population (density) of the dipoles $n_j(\mathbf{x},t)$ can be expressed as (compare [85]):

$$\left[\frac{\partial n_j(\mathbf{x},t)}{\partial t}\right]_{d-d} = -\beta_{d-d}(T,t)\cdot n_j^2(\mathbf{x},t) \tag{B.47}$$

$$\begin{aligned}\beta_{d-d}(T,t) &= \int_0^{\infty}\int_0^{\pi}\int_0^{2\pi} K_{d-d}(T,\rho)\cdot g_{jj}(T,\rho,t)\cdot\rho^2\sin(\theta)d\varphi d\theta d\rho = \\ &= 4\cdot\pi\cdot\int_0^{\infty} K_{d-d}(T,\rho)\cdot g_{jj}(T,\rho,t)\cdot\rho^2 d\rho\end{aligned} \tag{B.48}$$

with $\beta_{d-d}(T,t)$ corresponding to the time-dependent interaction rate of two dipoles. As illustrated by equation B.48, $\beta_{d-d}(T,t)$ can be expressed as an integral over space (in spherical coordinates) of the reaction rate $K_{d-d}(T,\rho)$ times the correlation function $g_{jj}(T,\rho,t)$. The correlation function describes the correlation of the interacting dipole positions, i.e.,

of their distances[30] (with the natural condition that for large distances no correlation is present: $\lim_{\rho\to\infty} g_{jj}(T,\rho,t) = 1$ [85]).

With the following approximations, a simple mathematical expression for the Förster interaction rate and the correlation function can be obtained [85]:

- The change of the correlation function of the dipole positions with time due to a diffusion or migration process is neglected[31].
- No spatial dependency of the reaction rate $K_{d-d}(T,\rho)$ is assumed, i.e. the reaction rate does not depend on the absolute positions of the dipoles in the material, but only on their relative distance to each other.
- Three-particle interactions are neglected.
- The dipoles are randomly oriented.
- No correlation of the initial dipole positions exists, i.e., $g_{jj}(T,\rho,t=0) = 1$. It has to be noted that this approximation does not correspond to the assumption of a uniform distribution of dipoles in space[32].

With these approximations, the change of the correlation function with time can be expressed as (for a more general formulation, see, e.g., [85]):

$$\begin{aligned} \frac{\partial g_{jj}(T,\rho,t)}{\partial t} &= -K_{d-d}(T,\rho)\cdot g_{jj}(T,\rho,t) \\ \Rightarrow g_{jj}(T,\rho,t) &= e^{-K_{d-d}(T,\rho)\cdot t} \end{aligned} \tag{B.49}$$

Hence, the change of $g_{jj}(T,\rho,t)$ with time represents the autocorrelation of the reaction rate of the Förster interaction. The larger the reaction rate $K_{d-d}(T,\rho)$, the faster the density of densely positioned dipoles is reduced and, hence, the smaller the resulting recombination rate.

Inserting $g_{jj}(T,\rho,t)$ (equation B.49) and $K_{d-d}(T,\rho)$ (equation 3.71) into equation B.48 and performing the integration over ρ delivers the following expression[33] for the time-

[30] The integral over ρ from 0 to ∞ is well defined, although, in reality the crystal volume is not infinitely large, as the reaction rate $K_{d-d}(T,\rho)$, for very large distances, converges against zero and the correlation function converges against 1. Hence, the integral converges against zero for large distances.

[31] In principle, the dipoles could encounter diffusion determined, e.g., by Coulomb interaction between them, leading to a change in the correlation function.

[32] This approximation only corresponds to the absence of a correlation of the distances of the dipoles, as would, e.g., be given by the following specification: If two dipoles are situated in a distance ρ_0 to each other, then at least a third dipole has to be within the same distance to these two dipoles. Such a correlation is assumed not to exist.

[33] To perform the integration over ρ, the error function $erf(x) = \frac{2}{\sqrt{\pi}} \cdot \int_0^x e^{-y^2} dy$ with $\lim_{x\to\infty} erf(x) = 1$ was used.

dependent Förster interaction rate of two dipoles j:

$$\begin{aligned}\beta_{d-d}(T,t) &= 4\cdot\pi\cdot\int_0^\infty K_{d-d}(T,\rho)\cdot e^{-K_{d-d}(T,\rho)\cdot t}\rho^2 d\rho = \\ &= \frac{4\cdot\pi}{\tau_{lt\,j}(T)}\cdot\int_0^\infty\left(\frac{R_{d-d}(T)}{\rho}\right)^6\cdot e^{-\frac{t}{\tau_{lt\,j}(T)}\cdot\left(\frac{R_{d-d}(T)}{\rho}\right)^6}\rho^2 d\rho = \\ &= \frac{2}{3}\cdot\pi^{\frac{3}{2}}\cdot R_{d-d}^3(T)\cdot\frac{1}{\sqrt{\tau_{lt\,j}(T)\cdot t}}\end{aligned} \tag{B.50}$$

With this expression for the interaction rate, the change in the population of the dipoles j due to the Förster interaction can be described by (compare equation 3.73):

$$\left[\frac{\partial n_j(\mathbf{x},t)}{\partial t}\right]_{d-d} = -\frac{2\cdot\pi^{\frac{3}{2}}}{3}\cdot\frac{R_{d-d}^3(T)}{\sqrt{\tau_{lt\,j}(T)\cdot t}}\cdot n_j^2(\mathbf{x},t) \tag{B.51}$$

Hence, using the introduced approximations, the recombination rate of interacting dipoles due to the Förster energy transfer is determined by the Förster radius $R_{d-d}(T)$, the intrinsic lifetime of the dipoles $\tau_{lt\,j}(T)$ (in absence of the Förster interaction) and the initial distribution of the density of the dipoles $n_j(\mathbf{x}, t=0)$.

B.6.2 Förster Energy-Transfer from Green to Blue STEs

To discuss the possibility of a Förster energy-transfer from a green STE to a blue STE, the overlap integral of the emission spectrum of the green STEs and the absorption spectrum of blue STEs have to be considered. As, however, the emission spectra of the green and blue STEs are within a very similar wavelength region (compare, e.g., figure 2.11 in section III/2.2.2), the overlap integrals of the green and blue STE emission spectra with the blue STE absorption spectrum are assumed to be of the same order of magnitude. Hence, in first approximation, the possibilities of energy transfer from green to blue STEs or from blue to blue STEs are considered to be equally large. However, as will be shown in section III/3.1.3, the intrinsic lifetime of green STEs (determined by radiative, non-radiative and migration processes) within the complete temperature range considered can be determined to be very short, about two to three orders of magnitude smaller than the respective intrinsic lifetime of blue STEs. Therefore, the probability for Förster energy-transfer to occur during the lifetime of green STEs is much smaller than the corresponding probability for blue STEs. Therefore, in the following, the possibility of Förster interaction to occur for green STEs is neglected.

In addition, it can be argued that at least the fraction of green STEs that is produced by reabsorption of blue photons (see discussion in section III/3.1.3) should be distributed over the complete crystal volume, according to the positions of defect centers where blue photons are absorbed. Hence, these green STEs can be expected to be distributed within the total crystal volume and, hence, to be far away from any other STE. Thus, in principle, no interaction partner (another STE) should be available.

B.6.3 Overlap Integral of Emission and Absorption Spectrum of Blue STEs

The emission spectrum of blue STEs in $CaWO_4$ is well known, it corresponds to the blue component of the scintillation-light spectrum, stretching from $\sim$ 300nm (4.2eV) to $\sim$ 600nm (2.1eV) and peaking at roughly 434nm (2.9eV) (these values were determined with measurements within the present work, see section III/5.1.2). As discussed in section III/3.2.1, the most significant change that can be observed with changing temperature is a weakly increasing broadening (i.e., an increasing 1-σ width of the blue spectrum) for increasing temperature by roughly a factor of 1.2 from mK ($\sim$ 46nm) to room temperature ($\sim$ 56nm) (these values were determined with measurements within this work, see section III/5.1.2). It should be noted that, even at low temperatures, the emission spectrum is very broad. The absorption spectrum of blue STEs, on the other hand, is not so well investigated. It has to be kept in mind that, in this context, not the absorption spectrum of an unexcited unit cell is referred to, but the absorption spectrum of an STE, i.e., of the electron (or hole) component of the STE. In [65], a measurement of the transient absorption spectrum of $CaWO_4$ at 100K is discussed. It is reported that the hole component of the STE shows an absorption spectrum peaking at $\sim$ 1.7eV, far away from the emission spectrum. The electron component of the STE, however, shows an absorption spectrum peaking roughly at 2.5 eV (496nm), stretching to at least 3.0eV (which corresponds to the maximum energy tested in [65]). From figure 1 in [65], a 1-σ width of the spectrum of roughly 69nm at 100K can be estimated. The dependency of the shape of the absorption spectrum on temperature cannot be quantified from this reference as only the measurement performed at 100K is available. However, it can be speculated that, in analogy to the emission spectrum, the most significant change with increasing temperature is most probably a broadening of the absorption spectrum[34]. Assuming the same temperature dependency of the width of the absorption spectrum as for the emission spectrum (see discussion in section III/3.2.1), at mK, a 1-σ width of $\sim$ 69nm and, at 300K, a 1-σ width of $\sim$ 83nm can be estimated.

B.6.4 Estimation of the Temperature Dependency of the Förster Radius

In order to obtain a rough estimate of the relative change of the Förster radius with temperature (from mK to room temperature) due to the change in the radiative branching ratio and in the shape of the emission and absorption spectrum, respectively, five assumptions are made:

- Both spectra are gaussian.
- Both spectra exhibit the same temperature-dependency of their widths[35] leading to a 1-σ width of $\sim$ 56nm (300K) and of $\sim$ 46nm (mK) for the emission spectrum and to a 1-σ width of $\sim$ 83nm (300K) and of $\sim$ 69nm (mK) for the absorption spectrum.
- The peak wavelengths of the spectra (434nm for the emission spectrum and 496nm for the absorption spectrum) are independent of temperature (at least for the emission spectrum this is a very good estimate, as is shown in section III/5.1.2).

[34] This broadening is assumed to be caused by the same mechanism as for the emission spectrum, i.e., the interaction of the involved energy levels with phonons from the lattice, compare section III/3.2.1.

[35] This approximation can be supported by the fact that the broadening of both spectra is due to the same mechanism, the electron-phonon coupling in $CaWO_4$.

- The radiative branching ratio of blue STEs at room temperature is equal to 0.41 and at mK temperature is equal to 1.

- The absorptivity of the electron component of the STE exhibits no temperature dependency.

Then, the ratio of the Förster radii at room temperature and at mK can be calculated with equation 3.76:

$$\frac{R_{d-d}(T = 300K)}{R_{d-d}(T \lesssim 5K)} \approx 0.86. \tag{B.52}$$

B.7 Estimation of Parameters of the Non-Radiative Decay of Green STEs

B.7.1 Order of Magnitude Estimate of the Non-Radiative Decay Time

On the basis of the discussion of the temperature-dependencies of the excitation and de-excitation processes of STEs (section III/3.2.1), it can be seen that for temperatures above $\sim$ 70K, the non-radiative decay of green STEs starts to deliver a recombination channel successfully competing to their radiative decay or migration process.

From this interpretation, it can be deduced that, within this temperature region ($T \gtrsim$ 70K), the non-radiative decay time of green STEs has to be roughly of the same order of magnitude as the radiative and the migration processes. Otherwise, the non-radiative decay of green STEs would show no influence onto the amount of light produced (compare section III/3.1.3). Hence, e.g., at room temperature, a non-radiative decay time of green STEs of the order of a few to a few tens of ns is expected (compare discussion of the lifetime of green STEs in section III/3.1.4). Such a short non-radiative decay time is in perfect agreement with the model for the electronic structure of defect centers (see appendix B.4.1). This model predicts a significantly shorter non-radiative decay time for green STEs than for blue STEs[36].

B.7.2 Estimation of the Energy Barrier of the Non-Radiative Decay

In addition, the temperatures at which the impact of the non-radiative recombination processes of blue and green STEs, respectively, start to influence the light generation can be identified as $\approx$ 200K (blue STEs) and $\approx$ 70K (green STEs) (compare section III/3.2.1). As can be seen from the description of the non-radiative processes and the intrinsic lifetimes (see sections III/3.1.3 and III/3.1.3, respectively), these "onset"-temperatures are determined by the size of two parameters: The height of the respective energy barriers $\Delta E_b = 0.32$eV and ΔE_g (not yet determined) and the size of the inverse of the respective non-radiative recombination rate constants K_{nrb} and K_{nrg} relative to the corresponding intrinsic lifetimes of the STEs ($\tau_{ltb}(T)$ and $\tau_{ltg}(T)$, respectively). In order to allow a very rough estimate of the non-radiative energy barrier for green STEs, it can be assumed that the ratio of the intrinsic lifetime and the inverse of the non-radiative rate constants

[36] As discussed in section III/3.2.3, at room temperature, a lifetime and non-radiative decay time of blue STEs of a few to a few tens of μs can be determined.

for blue and green STEs, respectively, are approximately the same[37]. Using this assumption, only the different temperature dependencies of the non-radiative decay times remain. Therefore, the value of ΔE_g can be estimated to amount to: $\Delta E_g \approx \Delta E_b \cdot \frac{70\text{K}}{200\text{K}} = 0.11\text{eV}$.

B.8 Partial Integrals of the Decay-Time Spectra of the Unquenched Model

In the following, the individual integrals of fractions of the blue and green decay-time spectra in the unquenched model, this means, e.g., of the purely exponentially decaying fraction of the blue scintillation light, are calculated and compared to each other. The general expressions for the unquenched decay-time spectra of the blue and green scintillation-light component (valid for the complete temperature range considered) are given by (compare equations 3.104 and 3.105 in section III/3.2.3):

$$\begin{aligned} P_b^{nq}(E_{part},T,t) = \Theta(t)\cdot\frac{(1-F_{abs})\cdot(1-F_{e^-trap})\cdot N_{eh}(E_{part})}{\tau_{rb}(T)}\cdot \\ \cdot\left[\frac{\frac{1}{\tau_{ltg}(T)}-\frac{1}{\tau_1(T)}}{\frac{1}{\tau_2(T)}-\frac{1}{\tau_1(T)}}\cdot\left((1-F_{dr}(T))\cdot e^{-\frac{t}{\tau_1(T)}}+\frac{F_{dr}(T)}{1-\frac{\tau_{dr}(T)}{\tau_1(T)}}\cdot\left\{e^{-\frac{t}{\tau_1(T)}}-e^{-\frac{t}{\tau_{dr}(T)}}\right\}\right)+\right. \\ \left.+\frac{\frac{1}{\tau_2(T)}-\frac{1}{\tau_{ltg}(T)}}{\frac{1}{\tau_2(T)}-\frac{1}{\tau_1(T)}}\cdot\left((1-F_{dr}(T))\cdot e^{-\frac{t}{\tau_2(T)}}+\frac{F_{dr}(T)}{\frac{\tau_{dr}(T)}{\tau_2(T)}-1}\cdot\left\{e^{-\frac{t}{\tau_{dr}(T)}}-e^{-\frac{t}{\tau_2(T)}}\right\}\right)\right] \end{aligned} \tag{B.53}$$

$$\begin{aligned} P_g^{nq}(E_{part},T,t) = \Theta(t)\cdot\frac{(1-F_{e^-trap})\cdot N_{eh}(E_{part})}{\tau_{rg}(T)}\cdot\frac{\frac{1}{\tau_{\text{mig, b}\to\text{g}}(T)}+F_{abs}\cdot\frac{1}{\tau_{rb}(T)}}{\frac{1}{\tau_2(T)}-\frac{1}{\tau_1(T)}}\cdot \\ \cdot\left[(1-F_{dr}(T))\cdot\left\{e^{-\frac{t}{\tau_1(T)}}-e^{-\frac{t}{\tau_2(T)}}\right\}+\frac{F_{dr}(T)}{1-\frac{\tau_{dr}(T)}{\tau_1(T)}}\cdot\left\{e^{-\frac{t}{\tau_1(T)}}-e^{-\frac{t}{\tau_{dr}(T)}}\right\}-\right. \\ \left.-\frac{F_{dr}(T)}{\frac{\tau_{dr}(T)}{\tau_2(T)}-1}\cdot\left\{e^{-\frac{t}{\tau_{dr}(T)}}-e^{-\frac{t}{\tau_2(T)}}\right\}\right] \end{aligned} \tag{B.54}$$

As described in section III/3.2.3, within the model developed, the interpretation of these pulse shapes, i.e., these formulas, can be divided into several terms:

Blue Scintillation Light (equation B.53):

- **First line of equation B.53:**

$$\frac{(1-F_{abs})\cdot(1-F_{e^-trap})\cdot N_{eh}(E_{part})}{\tau_{rb}(T)} \tag{B.55}$$

[37] Although, e.g., the lifetimes of blue and green STEs are predicted to deviate by up to 3 orders of magnitude (see section III/3.1.3), this assumption is expected to deliver an acceptable, very rough approximation: For green STEs in comparison to blue STEs, both, the intrinsic lifetime as well as the non-radiative recombination process, are predicted to be decreased by the same underlying physical process, the deformation of the unit cell due to the contained defect (compare discussion in appendix B.4.1). Therefore, in a very rough approximation, it is assumed that the ratio of both of these times is not afflicted too much by the deformation of the unit cell.

This term reflects that only the fraction $(1-F_{abs})$ of the generated blue scintillation light can escape the crystal. The fraction F_{abs} is absorbed at defect centers. The term $(1-F_{e^-trap})\cdot N_{eh}(E_{part})$ corresponds to the total initially created number of blue STEs (by the energy deposition of an interacting particle). The denominator, $\tau_{rb}(T)$, indicates that only the radiatively decaying fraction of blue STEs is calculated.

- **First term in the square brackets of equation B.53 (second line):**

$$\frac{\frac{1}{\tau_{ltg}(T)}-\frac{1}{\tau_1(T)}}{\frac{1}{\tau_2(T)}-\frac{1}{\tau_1(T)}}\cdot\left((1-F_{dr}(T))\cdot e^{-\frac{t}{\tau_1(T)}}+\frac{F_{dr}(T)}{1-\frac{\tau_{dr}(T)}{\tau_1(T)}}\cdot\left\{e^{-\frac{t}{\tau_1(T)}}-e^{-\frac{t}{\tau_{dr}(T)}}\right\}\right) \quad \text{(B.56)}$$

This term is split into two parts. Both parts exhibit an exponentially decaying pulse shape with decay time $\tau_1(T)$. The first part corresponds to the fraction of STEs created in the immediate electron-STH pair recombination-process, the second part corresponds to the delayed recombination of electron-STH pairs with rise time $\tau_{dr}(T)$. The integral over time of this fraction of blue scintillation light is given by:

$$\int_0^{+\infty}\left[\frac{\frac{1}{\tau_{ltg}(T)}-\frac{1}{\tau_1(T)}}{\frac{1}{\tau_2(T)}-\frac{1}{\tau_1(T)}}\cdot\left((1-F_{dr}(T))\cdot e^{-\frac{t}{\tau_1(T)}}+\frac{F_{dr}(T)}{1-\frac{\tau_{dr}(T)}{\tau_1(T)}}\cdot\left\{e^{-\frac{t}{\tau_1(T)}}-e^{-\frac{t}{\tau_{dr}(T)}}\right\}\right)\right]dt =$$

$$=\frac{\frac{1}{\tau_{ltg}(T)}-\frac{1}{\tau_1(T)}}{\frac{1}{\tau_2(T)}-\frac{1}{\tau_1(T)}}\cdot\tau_1(T)\cdot[(1-F_{dr}(T))+F_{dr}(T)]=\frac{\frac{\tau_1(T)}{\tau_{ltg}(T)}-1}{\frac{1}{\tau_2(T)}-\frac{1}{\tau_1(T)}} \quad \text{(B.57)}$$

where, due to the Heaviside function in equation B.53, the lower limit of the integral corresponds to $t=0$.

As can be seen from equation B.57, the ratio of the integrals of the second part (delayed created blue STEs) to the first part (immediately created STEs) of this term amounts to :

$$\frac{F_{dr}(T)}{1-F_{dr}(T)} \quad \text{(B.58)}$$

- **Second term in the square brackets of equation B.53 (third line):**

$$\frac{\frac{1}{\tau_2(T)}-\frac{1}{\tau_{ltg}(T)}}{\frac{1}{\tau_2(T)}-\frac{1}{\tau_1(T)}}\cdot\left((1-F_{dr}(T))\cdot e^{-\frac{t}{\tau_2(T)}}+\frac{F_{dr}(T)}{\frac{\tau_{dr}(T)}{\tau_2(T)}-1}\cdot\left\{e^{-\frac{t}{\tau_{dr}(T)}}-e^{-\frac{t}{\tau_2(T)}}\right\}\right) \quad \text{(B.59)}$$

This term is also split into two parts. The first part exhibits a purely exponentially decaying pulse shape with decay time $\tau_2(T)$. This part corresponds to the fraction of STEs created in the immediate electron-STH pair recombination-process. The second part exhibits a rise time of $\tau_2(T)$ and a decay time of $\tau_{dr}(T)$ and corresponds to the delayed recombination of electron-STH pairs. The integral over time of this fraction of blue scintillation light is given by:

$$\int_0^{+\infty}\left[\frac{\frac{1}{\tau_2(T)}-\frac{1}{\tau_{ltg}(T)}}{\frac{1}{\tau_2(T)}-\frac{1}{\tau_1(T)}}\cdot\left((1-F_{dr}(T))\cdot e^{-\frac{t}{\tau_2(T)}}+\frac{F_{dr}(T)}{\frac{\tau_{dr}(T)}{\tau_2(T)}-1}\cdot\left\{e^{-\frac{t}{\tau_{dr}(T)}}-e^{-\frac{t}{\tau_2(T)}}\right\}\right)\right]dt =$$

$$=\frac{\frac{1}{\tau_2(T)}-\frac{1}{\tau_{ltg}(T)}}{\frac{1}{\tau_2(T)}-\frac{1}{\tau_1(T)}}\cdot\tau_2(T)\cdot[(1-F_{dr}(T))+F_{dr}(T)]=\frac{1-\frac{\tau_2(T)}{\tau_{ltg}(T)}}{\frac{1}{\tau_2(T)}-\frac{1}{\tau_1(T)}} \quad \text{(B.60)}$$

where, due to the Heaviside function in equation B.53, the lower limit of the integral corresponds to $t = 0$.

Relative impact of these two terms onto the unquenched blue scintillation-light pulse-shape:

With these integrals, the relative relevance of the pulse shapes described by these two terms (second and third line of equation B.53) can be estimated. For this purpose, the ratio of the integrals of these two terms is calculated (integral second term divided by integral first term):

$$\left(\frac{1-\frac{\tau_2(T)}{\tau_{ltg}(T)}}{\frac{1}{\tau_2(T)}-\frac{1}{\tau_1(T)}}\right)\Bigg/\left(\frac{\frac{\tau_1(T)}{\tau_{ltg}(T)}-1}{\frac{1}{\tau_2(T)}-\frac{1}{\tau_1(T)}}\right)=\frac{\tau_{ltg}(T)-\tau_2(T)}{\tau_1(T)-\tau_{ltg}(T)} \tag{B.61}$$

As, within the complete temperature range considered, the following relationships apply (compare to equation 3.137 in section III/3.2.3 and the corresponding discussion)

$$\tau_1(T) \gg \tau_2(T)$$
$$\mathcal{O}(\tau_2(T)) \approx \mathcal{O}(\tau_{ltg}(T))$$

it can be deduced that the integral of the second term is much smaller than the integral of the first term of equation B.53:

$$\left(\frac{1-\frac{\tau_2(T)}{\tau_{ltg}(T)}}{\frac{1}{\tau_2(T)}-\frac{1}{\tau_1(T)}}\right)\Bigg/\left(\frac{\frac{\tau_1(T)}{\tau_{ltg}(T)}-1}{\frac{1}{\tau_2(T)}-\frac{1}{\tau_1(T)}}\right)=\frac{\tau_{ltg}(T)-\tau_2(T)}{\tau_1(T)-\tau_{ltg}(T)} \ll 1 \tag{B.62}$$

Hence, the pulse shape of the unquenched blue scintillation-light component is strongly dominated by the pulse shape described by the first term in square brackets of equation B.53 (within the complete temperature range considered). This term contains exclusively pulse shapes which exhibit a (slow) decay time, $\tau_1(T)$**.** The main fraction $(1 - F_{dr}(T))$ (at 300K $\sim 85\%$, at 100K ≈ 1) of this term rises instantaneously, the fraction $F_{dr}(T)$ (negligible for $T \lesssim 100$K) of this term exhibits a rise time $\tau_{dr}(T)$ (at 300K ≈ 40ns) (compare equation B.58).

In fact, in section III/4.7.2, this conclusion is validated by experimental observations (see also the analysis of the data in section III/5.2). In addition, the validity of this conclusion can be shown by using the complete model with the full set of parameters (determined in section III/5.2.2) to calculate the numerical values of the determined integrals.

Green Scintillation Light (equation B.54):

- **First line of equation B.54:**

$$\frac{(1-F_{e^-trap})\cdot N_{eh}(E_{part})}{\tau_{rg}(T)}\cdot\frac{\frac{1}{\tau_{\mathrm{mig,\ b\to g}}(T)}+F_{abs}\cdot\frac{1}{\tau_{rb}(T)}}{\frac{1}{\tau_2(T)}-\frac{1}{\tau_1(T)}} \tag{B.63}$$

The term $(1 - F_{e^-trap}) \cdot N_{eh}(E_{part})$ corresponds to the total initially created number of blue STEs (in the energy deposition of an interacting particle). The denominator,

$\tau_{rg}(T)$, indicates that only the radiatively decaying fraction of green STEs is calculated. The term $\frac{\frac{1}{\tau_{\text{mig, b}\rightarrow\text{g}}(T)}+F_{abs}\cdot\frac{1}{\tau_{rb}(T)}}{\frac{1}{\tau_2(T)}-\frac{1}{\tau_1(T)}}$ indicates the efficiency with which blue STEs are converted into green STEs.

- **First term in the square brackets of equation B.54:**

$$(1-F_{dr}(T))\cdot\left\{e^{-\frac{t}{\tau_1(T)}}-e^{-\frac{t}{\tau_2(T)}}\right\} \tag{B.64}$$

This term corresponds to the excitation of the green STE population (which, without time-dependent excitation, is characterized by the decay time $\tau_2(T)$) by the immediately created blue STEs (characterized by the decay time $\tau_1(T)$). **Hence, the generated green scintillation light is characterized by two times, $\tau_2(T)$ and $\tau_1(T)$.** The integral over time of this fraction of green scintillation light is given by:

$$\int_0^{+\infty}\left[(1-F_{dr}(T))\cdot\left\{e^{-\frac{t}{\tau_1(T)}}-e^{-\frac{t}{\tau_2(T)}}\right\}\right]dt=[\tau_1(T)-\tau_2(T)]\cdot(1-F_{dr}(T)) \tag{B.65}$$

where, due to the Heaviside function in equation B.54, the lower limit of the integral corresponds to $t=0$.

- **Second term in the square brackets of equation B.54:**

$$\frac{F_{dr}(T)}{1-\frac{\tau_{dr}(T)}{\tau_1(T)}}\cdot\left\{e^{-\frac{t}{\tau_1(T)}}-e^{-\frac{t}{\tau_{dr}(T)}}\right\} \tag{B.66}$$

This term corresponds to the fraction of green photons that is generated by the decay of green STEs which are excited by the delayed fraction of blue STEs (characterized by the times $\tau_{dr}(T)$ and $\tau_1(T)$). **Hence, the generated green scintillation light is characterized by two times, $\tau_{dr}(T)$ and $\tau_1(T)$.** The integral over time of this fraction of green scintillation light is given by:

$$\int_0^{+\infty}\left[\frac{F_{dr}(T)}{1-\frac{\tau_{dr}(T)}{\tau_1(T)}}\cdot\left\{e^{-\frac{t}{\tau_1(T)}}-e^{-\frac{t}{\tau_{dr}(T)}}\right\}\right]dt=\tau_1(T)\cdot F_{dr}(T) \tag{B.67}$$

where, due to the Heaviside function in equation B.54, the lower limit of the integral corresponds to $t=0$.

- **Third term in the square brackets of equation B.54:**

$$\frac{F_{dr}(T)}{\frac{\tau_{dr}(T)}{\tau_2(T)}-1}\cdot\left\{e^{-\frac{t}{\tau_{dr}(T)}}-e^{-\frac{t}{\tau_2(T)}}\right\} \tag{B.68}$$

This term corresponds to the fraction of green photons, that is generated by the decay of green STEs (characterized by the time $\tau_2(T)$) which are excited by the delayed fraction of blue STEs (characterized by the time $\tau_{dr}(T)$). **Hence, the generated**

green scintillation light is characterized by two times, $\tau_{dr}(T)$ and $\tau_2(T)$. The integral over time of this fraction of green scintillation light is given by:

$$\int_0^{+\infty} \left[\frac{F_{dr}(T)}{\frac{\tau_{dr}(T)}{\tau_2(T)} - 1} \cdot \left\{ e^{-\frac{t}{\tau_{dr}(T)}} - e^{-\frac{t}{\tau_2(T)}} \right\} \right] dt = \tau_2(T) \cdot F_{dr}(T) \tag{B.69}$$

where, due to the Heaviside function in equation B.54, the lower limit of the integral corresponds to $t = 0$.

Relative impact of these three terms onto the unquenched green scintillation-light pulse-shape:

With these integrals, the relative relevance of each of these pulse shapes can be calculated. At first, the relative impact of the third term compared to the second term is evaluated. For this purpose, the integral of the third term is divided by the integral of the second term (in square brackets of equation B.54):

$$\left(\tau_2(T) \cdot F_{dr}(T)\right) / \left(\tau_1(T) \cdot F_{dr}(T)\right) = \frac{\tau_2(T)}{\tau_1(T)} \tag{B.70}$$

As, within the complete temperature range considered, the following relationship applies (compare to equation 3.137 in section III/3.2.3 and the corresponding discussion)

$$\tau_1(T) \gg \tau_2(T)$$

it can be deduced that the integral of the third term is much smaller than the integral of the second term (in square brackets of equation B.54):

$$\left(\tau_2(T) \cdot F_{dr}(T)\right) / \left(\tau_1(T) \cdot F_{dr}(T)\right) = \frac{\tau_2(T)}{\tau_1(T)} \ll 1 \tag{B.71}$$

Hence, it can be seen that the impact of the third term (in square brackets of equation B.54) on the pulse shape of the green scintillation light is negligible compared to the second term (in square brackets of equation B.54).

In addition, the relative impact of the second term compared to the first term can be evaluated. For this purpose, the integral of the second term is divided by the integral of the first term (in square brackets of equation B.54):

$$\left(\tau_1(T) \cdot F_{dr}(T)\right) / \left(\left[\tau_1(T) - \tau_2(T)\right] \cdot \left(1 - F_{dr}(T)\right)\right) = \frac{\tau_1(T) \cdot F_{dr}(T)}{\left[\tau_1(T) - \tau_2(T)\right] \cdot \left(1 - F_{dr}(T)\right)} \tag{B.72}$$

As, within the complete temperature range considered, the following relationship applies:

$$\begin{gathered} \tau_1(T) \gg \tau_2(T) \\ \Rightarrow \left[\tau_1(T) - \tau_2(T)\right] \approx \tau_1(T) \end{gathered}$$

it can be deduced that the ratio of the integral of the second term and the integral of the first term (in square brackets of equation B.54) is determined by the fraction of blue STEs created in the delayed formation process, $F_{dr}(T)$:

$$\frac{\tau_1(T) \cdot F_{dr}(T)}{\left[\tau_1(T) - \tau_2(T)\right] \left(1 - F_{dr}(T)\right)} \approx \frac{F_{dr}(T)}{1 - F_{dr}(T)} \tag{B.73}$$

Hence, the pulse shape of the unquenched green scintillation light is strongly dominated by the pulse shape described by the first two terms in square brackets of equation B.54 (within the complete temperatures range considered). These two terms describe exclusively pulse shapes which exhibit a (slow) decay time, $\tau_1(T)$. The first term (fraction $(1 - F_{dr}(T))$) exhibits a rise time $\tau_2(T)$ (with $\tau_2(T)$ being negligibly small for $T \gtrsim 20$K, compare equation B.58). The second term (fraction $F_{dr}(T)$, negligibly small for $T \lesssim 100$K)) exhibits a rise time $\tau_{dr}(T)$ (compare equation B.58).

In fact, in section III/4.7.2, this conclusion is validated by experimental observations (see also the analysis of the data in section III/5.2). Additionally, the deduction that the third term is much smaller than the second term (in square brackets of equation B.54) and, hence, can be neglected, can also be validated by calculations using the complete model with the full set of parameters determined in section III/5.2.2.

Comparison of the Dominating Pulse Shapes of the Blue and Green Light:

Using these considerations, the dominant unquenched green light pulse-shape (described by these first two terms in square brackets of equation B.54) can be compared to the dominant unquenched blue light pulse shape (described by the first term in square brackets of equation B.53). It can be seen that both pulse shapes agree with each other (except for the rise time $\tau_2(T)$ in the green scintillation light). Hence, as long as the rise time $\tau_2(T)$ (green STE population) is very fast ($\mathcal{O}$(1ns)) and as long as it can be neglected compared to the decay time $\tau_1(T)$ (blue STE population), the pulse shapes of the green and blue scintillation light agree with each other. As explained in section III/3.2.3, this is expected to be the case for temperatures $T \gtrsim 20$K.

At temperatures $T \lesssim 20$K, the radiative decay of green STEs becomes dominated by the much slower recombination from the energetically lower-lying energy level (ground state) of the green STEs (compare section III/3.1.3). Hence, for $T \lesssim 20$K, where the intrinsic lifetime of green STEs $\tau_{ltg}(T)$ and, hence, their effective unquenched lifetime $\tau_2(T)$, becomes dominated by the radiative decay, the absolute value of $\tau_2(T)$ is expected to increase significantly with decreasing temperature. Nonetheless, the relationship $\tau_1(T) \gg \tau_2(T)$ is still valid, also for temperatures $T \lesssim 20$K. In addition, it should be taken into account, that for $T \lesssim 100K$, the fractions of scintillation light influenced by the delayed creation of STEs can be neglected.

Hence, for temperatures below 20K, the pulse shape of the blue light is dominated by a purely exponential decay with decay time $\tau_1(T)$ (first part of the first term in square brackets of equation B.53). Whereas the pulse shape of the green scintillation light for temperatures $T \lesssim 20$K is dominated by a pulse shape with a (non-negligible) rise time $\tau_2(T)$ and the same (slow) decay time $\tau_1(T)$ as the blue scintillation light pulse (first term in square brackets of equation III/B.54).

These conclusions will be justified by the inspection of the pulse shape of $CaWO_4$ scintil-

lation light (from [54]) which was recorded at 6K (see section III/3.2.4)[38].

B.9 Application of the Approximations Developed for the Quenched Model to the Unquenched Model

In the following, the application of the five approximations (developed for the quenched model, see section III/3.2.4) to the unquenched model is presented. Such an approach is performed, as for the complete unquenched model analytical solutions are possible, so that the impact of the approximations can be demonstrated explicitly and the respective approximated formulas in each step can be displayed. However, it should be noted, that **all simplifications derived and all conclusions that can be drawn are purely based on the five assumptions and approximations made**. These approximations and assumptions are applied to and are valid for the unquenched as well as for the quenched model: For example inspect a statement of the *assumption 4*, i.e., *that the response of the green STE population can be described by an exponential with decay time* $\tau_2(T)$, is based on the description of the green STE population in the respective models, where this description is the same in the quenched and unquenched model.

Hence, from the results obtained for the unquenched model, direct conclusions for simplification of the quenched model due to the approximations can be drawn (these are presented in section III/3.2.4).

Application of the Approximations on the Unquenched Model and Conclusions Drawn:

- From the discussion of the solution of the general unquenched model (model for 300K, end of section III/3.2.3), it can be seen that the influence of the green STE population (characterized by $\tau_2(T)$) on the pulse shape of the blue scintillation light in the unquenched model is reflected by three features:

  1. The second term in square brackets in equation 3.104 (section III/3.2.3) with two parts, one with $\tau_2(T)$ as rise and and one with $\tau_2(T)$ as decay time.
  2. The scaling factor of the first term in square brackets of equation 3.104 (section III/3.2.3) contains the time $\tau_2(T)$.
  3. The effective unquenched lifetime $\tau_1(T)$ (equation 3.106 in section III/3.2.3) contains the mutual excitation processes of the blue and green STE populations and, hence, is also influenced by the green STE population.

  As discussed within the unquenched model (section III/3.2.3), the second term (in comparison to the first term) can be neglected within the complete temperature range, due to approximation 4. In addition, from approximation 4, it can also be seen that the scaling factor of the first term in equation 3.104 (section III/3.2.3), is approximately equal to unity.

- Applying these two well motivated conclusions as well as approximation 2 ($F_{dr}(T) = 0$) to the solution of the unquenched decay-time spectrum of blue photons in the unquenched model, $P_b^{nq}(E_{part}, T, t)$, (equation 3.104 in section III/3.2.3), the following

[38] This pulse shape is used, as within the presented work, no measurements of the decay-time spectra of $CaWO_4$ scintillation light for temperatures $T \lesssim 20$K were performed.

approximated expressions for $P_b^{nq}(E_{part},T,t)$ (the decay-time spectrum of the blue photons) and for $N_b^{nq}(E_{part},T,t)$ (the temporal evolution of the number of blue STEs) (compare equation 3.99 in section III/3.2.3) are obtained:

$$P_b^{nq}(E_{part},T,t) \approx \Theta(t)\cdot\frac{(1-F_{abs})\cdot(1-F_{e^-trap})\cdot N_{eh}(E_{part})}{\tau_{rb}(T)}\cdot e^{-\frac{t}{\tau_1(T)}} \tag{B.74}$$

$$N_b^{nq}(E_{part},T,t) \approx \Theta(t)\cdot(1-F_{e^-trap})\cdot N_{eh}(E_{part})\cdot e^{-\frac{t}{\tau_1(T)}} \tag{B.75}$$

where it should be noted that the (main) influence of the green STE population on the blue STE population is still contained in this expression as the effective unquenched lifetime of blue STEs, $\tau_1(T)$, and not the intrinsic lifetime of blue STEs $\tau_{ltb}(T)$ is used. It should be noted that the denominator, $\tau_{rb}(T)$, and the numerator, $(1-F_{abs})$, in equation B.74, reflect the fact that $P_b^{nq}(E_{part},T,t)$ is the decay-time spectrum of the produced, unquenched, blue photons that escape the crystal. As can easily be seen, this approximated expression for the unquenched blue STE population (equation B.75) corresponds to the solution of the following approximated differential equation (compare to the general differential equation for the unquenched blue STE population, equation 3.101 in section III/3.2.3):

$$\frac{\partial N_b^{nq}(t)}{\partial t} \approx -\frac{1}{\tau_1(T)}\cdot N_b^{nq}(t) + N_{bSTE}^{form\,e^-STH}(E_{part},t) \tag{B.76}$$

$$N_{bSTE}^{form\,e^-STH}(E_{part},t) = \Theta(t)\cdot(1-F_{e^-trap})\cdot N_{eh}(E_{part})$$

- Applying these approximations also to the solution of the decay-time spectrum of the unquenched green photons[39], $P_g^{nq}(E_{part},T,t)$ (equation 3.105 in section III/3.2.3), the following expressions for the approximated unquenched green photons ($P_g^{nq}(E_{part},T,t)$) and green STEs ($N_g^{nq}(E_{part},T,t)$) (compare equation 3.100 in section III/3.2.3) are obtained:

$$P_g^{nq}(E_{part},T,t) \approx \Theta(t)\cdot\frac{(1-F_{e^-trap})\cdot N_{eh}(E_{part})}{\tau_{rg}(T)}\cdot\frac{\frac{1}{\tau_{\mathrm{mig,\ b\to g}}(T)}+F_{abs}\cdot\frac{1}{\tau_{rb}(T)}}{\frac{1}{\tau_2(T)}-\frac{1}{\tau_1(T)}}\cdot \cdot\left\{e^{-\frac{t}{\tau_1(T)}}-e^{-\frac{t}{\tau_2(T)}}\right\} \tag{B.77}$$

$$N_g^{nq}(E_{part},T,t) \approx \Theta(t)\cdot(1-F_{e^-trap})\cdot N_{eh}(E_{part})\cdot\left(\frac{1}{\tau_{\mathrm{mig,\ b\to g}}(T)}+F_{abs}\cdot\frac{1}{\tau_{rb}(T)}\right)\cdot \cdot\frac{1}{\frac{1}{\tau_2(T)}-\frac{1}{\tau_1(T)}}\cdot\left\{e^{-\frac{t}{\tau_1(T)}}-e^{-\frac{t}{\tau_2(T)}}\right\} \tag{B.78}$$

Comparing the first line of equation B.78 with the approximated expression for the blue STE population (B.75), it can be seen that the factor $\left[\frac{1}{\tau_{\mathrm{mig,\ b\to g}}(T)}+F_{abs}\cdot\frac{1}{\tau_{rb}(T)}\right]$ indicates the fraction of blue STEs that excite green STEs. Using the fact that the temporal evolution of the green STE population in absence of a time-dependent excitation is described by a purely exponential decay with decay time $\tau_2(T)$ (approximation 4), the green STE population can be expressed as a convolution of the

[39]The assumption that the intrinsic lifetime of green STEs, $\tau_{ltg}(T)$, approximately corresponds to the effective unquenched lifetime of green STEs, $\tau_2(T)$, is actually not needed here.

fraction of blue STEs (exciting green STEs) with the exponential $\Theta(t) \cdot e^{-\frac{t}{\tau_2(T)}}$ (for the reaction of the green STE population):

$$\begin{aligned} N_g^{nq}(E_{part},T,t) &\approx \left[\left(\frac{1}{\tau_{\text{mig, b}\to\text{g}}(T)} + F_{abs}\cdot\frac{1}{\tau_{rb}(T)}\right)\cdot N_b^{nq}(E_{part},T,t)\right] * \left[\Theta(t)\cdot e^{-\frac{t}{\tau_2(T)}}\right] = \\ &= \left[\left(\frac{1}{\tau_{\text{mig, b}\to\text{g}}(T)} + F_{abs}\cdot\frac{1}{\tau_{rb}(T)}\right)\cdot(1-F_{e^-trap})\cdot N_{eh}(E_{part})\right]\cdot \\ &\quad\cdot\left[\Theta(t)\cdot e^{-\frac{t}{\tau_1(T)}} * \Theta(t)\cdot e^{-\frac{t}{\tau_2(T)}}\right] \end{aligned} \tag{B.79}$$

- From the derived approximated expressions for the unquenched green STE population and for the differential equation of the unquenched blue STE population, it can be seen that, using the explained approximations, the complete unquenched model can be described by one differential equation for the blue STEs and a calculation specification (convolution) for the green STE population:

$$\frac{\partial N_b^{nq}(t)}{\partial t} \approx -\frac{1}{\tau_1(T)}\cdot N_b^{nq}(t) + \Theta(t)\cdot(1-F_{e^-trap})\cdot N_{eh}(E_{part}) \tag{B.80}$$

$$N_b^{nq}(E_{part},T,t) \approx \Theta(t)\cdot(1-F_{e^-trap})\cdot N_{eh}(E_{part})\cdot e^{-\frac{t}{\tau_1(T)}} \tag{B.81}$$

$$N_g^{nq}(E_{part},T,t) \approx \left[\left(\frac{1}{\tau_{\text{mig, b}\to\text{g}}(T)} + F_{abs}\cdot\frac{1}{\tau_{rb}(T)}\right)\cdot N_b^{nq}(E_{part},T,t)\right] * \left[\Theta(t)\cdot e^{-\frac{t}{\tau_2(T)}}\right] \tag{B.82}$$

Using approximations 3 and 4 ($\tau_1(T) \approx \tau_{ltb}(T)$ and $\tau_2(T) \approx \tau_{ltg}(T)$) and the ratio of the numbers of blue photons to green photons, $R_{b-g}(T)$ (equation 3.112 in section III/3.2.2), it can be easily be shown that the correlation of the integrated numbers of blue and green photons can be expressed as:

$$\begin{aligned} P_b^{nq}(E_{part},T) &= \int P_b^{nq}(E_{part},T,t)dt \approx \\ &\approx (1-F_{abs})\cdot(1-F_{e^-trap})\cdot N_{eh}(E_{part})\cdot F_{b\ rad}(T) \end{aligned} \tag{B.83}$$

$$\begin{aligned} P_g^{nq}(E_{part},T) &= \int P_g^{nq}(E_{part},T,t)dt \approx \\ &\approx \left[(1-F_{e^-trap})\cdot N_{eh}\cdot(F_{b\ mig}(T) + F_{abs}\cdot F_{b\ rad}(T))\right]\cdot F_{g\ rad}(T) = \\ &= \frac{1}{R_{b-g}(T)}\cdot P_b^{nq}(E_{part},T) \end{aligned} \tag{B.84}$$

where the term in square brackets in equation B.84 corresponds to the number of initially created blue STEs that excite green STEs (by migration and absorption of blue photons).

- Using additionally approximation 5 ($\tau_2(T \gtrsim 20\text{K})$ is very small), the expression for the green STE population for $T \gtrsim 20$K can be further simplified, as the reaction time of green STEs is approximated as being instantaneous. Then, the description

of the model for $T \gtrsim 20$K is given by the following expressions:

$$N_b^{nq}(E_{part},T,t) \approx \Theta(t)\cdot(1-F_{e^-trap})\cdot N_{eh}(E_{part})\cdot e^{-\frac{t}{\tau_1(T)}} \tag{B.85}$$

$$N_g^{nq}(E_{part},T,t) \approx \left(\frac{1}{\tau_{\text{mig, b}\to\text{g}}(T)} + F_{abs}\cdot\frac{1}{\tau_{rb}(T)}\right)\cdot N_b^{nq}(E_{part},T,t) \tag{B.86}$$

$$P_b^{nq}(E_{part},T,t) \approx \Theta(t)\cdot\frac{(1-F_{abs})\cdot(1-F_{e^-trap})\cdot N_{eh}(E_{part})}{\tau_{rb}(T)}\cdot e^{-\frac{t}{\tau_1(T)}} \tag{B.87}$$

$$P_g^{nq}(E_{part},T,t) \approx \frac{1}{R_{b-g}(T)}\cdot P_b^{nq}(E_{part},T,t) \tag{B.88}$$

From equations B.87 and B.88 it can be seen that, for $T \gtrsim 20$K, the decay-time spectra of the blue as well as of the green photons are described by the same pulse shape, except for a different scaling factor.

B.10 Calculation of the Decay-Time Spectra of the Blue Photons in the Quenched Model

In the following, the results for the decay-time spectra of blue photons produced by the STEs in the inner and outer volumes of the primary ionization track (model PIT) as well as in the inner and outer volume of a 1nm slice of a recoil track $Rec[i]$ are presented (compare section III/3.2.4 and section III/3.1.2 for the definition of the used parameters). In analogy to section III/3.2.4, the dependency of the parameters on the energy and type of the primary particle is not displayed explicitly within the formulas.

Using equations 3.165 and 3.143 (section III/3.2.4) as well as the initial blue STE densities as defined in section III/3.1.2, the following expressions are obtained:

Model PIT:

The quenched decay-time spectrum of the blue photons, $P^q_{b,in,PIT}(E_{part},T,t)$, produced by the quenched blue STE population in the inner volume, $N^{in}_{bSTE,PIT}(E_{part})$, of the primary ionization track can be expressed as:

$$P^q_{b,in,PIT}(T,t) = \Theta(t)\cdot\frac{(1-F_{abs})}{\tau_{rb}(T)}\cdot e^{-\frac{t}{\tau_1(T)}}\cdot\frac{1}{\frac{2}{3}\pi^2\cdot R^3_{d-d}(T)\cdot erf\left(\sqrt{\frac{t}{\tau_1(T)}}\right)}\cdot$$
$$\cdot\frac{(r^{in}_{PIT})^2\pi}{\alpha_{PIT}}\cdot\ln\left(\frac{1+\frac{N^{in}_{bSTE,PIT}\cdot\alpha_{PIT}}{(r^{in}_{PIT})^2\pi\cdot(1-e^{-\alpha_{PIT}\cdot l_{max}})}\cdot\frac{2}{3}\pi^2\cdot R^3_{d-d}(T)\cdot erf\left(\sqrt{\frac{t}{\tau_1(T)}}\right)}{1+\frac{N^{in}_{bSTE,PIT}\cdot\alpha_{PIT}}{(r^{in}_{PIT})^2\pi\cdot(e^{\alpha_{PIT}\cdot l_{max}}-1)}\cdot\frac{2}{3}\pi^2\cdot R^3_{d-d}(T)\cdot erf\left(\sqrt{\frac{t}{\tau_1(T)}}\right)}\right)$$

Using the position-independent density of blue STEs in the inner volume of the *PIT* (equation 3.24 in section III/3.1.2), $n^{form\,0}_{bSTE,in,PIT}$, this expression can be transformed to:

$$P^{q}_{b,in,PIT}(T,t) = \Theta(t)\cdot\frac{(1-F_{abs})}{\tau_{rb}(T)}\cdot N^{in}_{bSTE,PIT}\cdot e^{-\frac{t}{\tau_1(T)}}\cdot \cdot\frac{1}{n^{form\,0}_{bSTE,in,PIT}\cdot\frac{2}{3}\pi^2\cdot R^3_{d-d}(T)\cdot erf\left(\sqrt{\frac{t}{\tau_1(T)}}\right)\cdot(1-e^{-\alpha_{PIT}\cdot l_{max}})}\cdot \cdot\ln\left(\frac{1+n^{form\,0}_{bSTE,in,PIT}\cdot\frac{2}{3}\pi^2\cdot R^3_{d-d}(T)\cdot erf\left(\sqrt{\frac{t}{\tau_1(T)}}\right)}{1+n^{form\,0}_{bSTE,in,PIT}\cdot\frac{2}{3}\pi^2\cdot R^3_{d-d}(T)\cdot erf\left(\sqrt{\frac{t}{\tau_1(T)}}\right)\cdot e^{-\alpha_{PIT}\cdot l_{max}}}\right) \tag{B.89}$$

The quenched decay-time spectrum of the blue photons, $P^{q}_{b,out,PIT}(E_{part},T,t)$, produced by the quenched blue STE population in the outer volume, $N^{out}_{bSTE,PIT}(E_{part})$, of the primary ionization track can be expressed as:

$$P^{q}_{b,out,PIT}(T,t) = \Theta(t)\cdot\frac{(1-F_{abs})}{\tau_{rb}(T)}\cdot e^{-\frac{t}{\tau_1(T)}}\cdot\frac{1}{\frac{2}{3}\pi^2\cdot R^3_{d-d}(T)\cdot erf\left(\sqrt{\frac{t}{\tau_1(T)}}\right)}\cdot \cdot\frac{((r^{out}_{PIT})^2-(r^{in}_{PIT})^2)\pi}{\alpha_{PIT}}\cdot\ln\left(\frac{1+\frac{N^{out}_{bSTE,PIT}\cdot\alpha_{PIT}}{((r^{out}_{PIT})^2-(r^{in}_{PIT})^2)\pi\cdot(1-e^{-\alpha_{PIT}\cdot l_{max}})}\cdot\frac{2}{3}\pi^2\cdot R^3_{d-d}(T)\cdot erf\left(\sqrt{\frac{t}{\tau_1(T)}}\right)}{1+\frac{N^{out}_{bSTE,PIT}\cdot\alpha_{PIT}}{((r^{out}_{PIT})^2-(r^{in}_{PIT})^2)\pi\cdot(e^{\alpha_{PIT}\cdot l_{max}}-1)}\cdot\frac{2}{3}\pi^2\cdot R^3_{d-d}(T)\cdot erf\left(\sqrt{\frac{t}{\tau_1(T)}}\right)}\right) \tag{B.90}$$

Using the position-independent density of blue STEs in the outer volume of the *PIT* (equation 3.26 in section III/3.1.2), $n^{form\,0}_{bSTE,out,PIT}$, this expression can be transformed to:

$$P^{q}_{b,out,PIT}(T,t) = \Theta(t)\cdot\frac{(1-F_{abs})}{\tau_{rb}(T)}\cdot N^{out}_{bSTE,PIT}\cdot e^{-\frac{t}{\tau_1(T)}}\cdot \cdot\frac{1}{n^{form\,0}_{bSTE,out,PIT}\cdot\frac{2}{3}\pi^2\cdot R^3_{d-d}(T)\cdot erf\left(\sqrt{\frac{t}{\tau_1(T)}}\right)\cdot(1-e^{-\alpha_{PIT}\cdot l_{max}})}\cdot \cdot\ln\left(\frac{1+n^{form\,0}_{bSTE,out,PIT}\cdot\frac{2}{3}\pi^2\cdot R^3_{d-d}(T)\cdot erf\left(\sqrt{\frac{t}{\tau_1(T)}}\right)}{1+n^{form\,0}_{bSTE,out,PIT}\cdot\frac{2}{3}\pi^2\cdot R^3_{d-d}(T)\cdot erf\left(\sqrt{\frac{t}{\tau_1(T)}}\right)\cdot e^{-\alpha_{PIT}\cdot l_{max}}}\right) \tag{B.91}$$

Model Rec:

The quenched decay-time spectrum of the blue photons, $P^{q}_{b,in,Rec[i]}(E_{part},T,t)$, produced by the quenched blue STE population in the inner volume, $N^{in}_{bSTE,Rec[i]}(E_{part})$, of one slice of a recoil track can be expressed as:

$$P^{q}_{b,in,Rec[i]}(T,t) = \Theta(t)\cdot\frac{(1-F_{abs})}{\tau_{rb}(T)}\cdot e^{-\frac{t}{\tau_1(T)}}\cdot\frac{1}{\frac{2}{3}\pi^2\cdot R^3_{d-d}(T)\cdot erf\left(\sqrt{\frac{t}{\tau_1(T)}}\right)}\cdot \cdot(r^{in}_{Rec})^2\pi\cdot 1\text{nm}\cdot\frac{1}{\frac{(r^{in}_{Rec})^2\pi\cdot 1\text{nm}}{N^{in}_{bSTE,Rec[i]}}\cdot\frac{1}{\frac{2}{3}\pi^2\cdot R^3_{d-d}(T)\cdot erf\left(\sqrt{\frac{t}{\tau_1(T)}}\right)}+1} \tag{B.92}$$

Using the position-independent density of blue STEs in the inner volume of one 1nm slice of one recoil track (equation 3.37 in section III/3.1.2)), this expression can be transformed to:

$$P^{q}_{b,in,Rec[i]}(T,t) = \Theta(t) \cdot \frac{(1-F_{abs})}{\tau_{rb}(T)} \cdot N^{in}_{bSTE,Rec[i]} \cdot e^{-\frac{t}{\tau_1(T)}} \cdot \cdot \frac{1}{1 + n^{form\,0}_{bSTE,in,Rec[i]} \cdot \frac{2}{3}\pi^2 \cdot R^3_{d-d}(T) \cdot erf\left(\sqrt{\frac{t}{\tau_1(T)}}\right)} \tag{B.93}$$

The quenched decay-time spectrum of the blue photons, $P^{q}_{b,out,Rec[i]}(E_{part},T,t)$, produced by the quenched blue STE population in the outer volume, $N^{out}_{bSTE,Rec[i]}(E_{part})$, of one slice of a recoil track can be expressed as:

$$P^{q}_{b,out,Rec[i]}(T,t) = \Theta(t) \cdot \frac{(1-F_{abs})}{\tau_{rb}(T)} \cdot e^{-\frac{t}{\tau_1(T)}} \cdot \frac{1}{\frac{2}{3}\pi^2 \cdot R^3_{d-d}(T) \cdot erf\left(\sqrt{\frac{t}{\tau_1(T)}}\right)} \cdot \cdot ((r^{out}_{Rec})^2 - (r^{in}_{Rec})^2)\pi \cdot 1\text{nm} \cdot \frac{1}{\frac{((r^{out}_{Rec})^2-(r^{in}_{Rec})^2)\pi\cdot 1\text{nm}}{N^{out}_{bSTE,Rec[i]}} \cdot \frac{1}{\frac{2}{3}\pi^2 \cdot R^3_{d-d}(T)\cdot erf\left(\sqrt{\frac{t}{\tau_1(T)}}\right)} + 1} \tag{B.94}$$

Using the position-independent density of blue STEs in the outer volume of one 1nm slice of one recoil track (equation 3.38 in section III/3.1.2)), this expression can be transformed to:

$$P^{q}_{b,out,Rec[i]}(T,t) = \Theta(t) \cdot \frac{(1-F_{abs})}{\tau_{rb}(T)} \cdot N^{out}_{bSTE,Rec[i]} \cdot e^{-\frac{t}{\tau_1(T)}} \cdot \cdot \frac{1}{1 + n^{form\,0}_{bSTE,out,Rec[i]} \cdot \frac{2}{3}\pi^2 \cdot R^3_{d-d}(T) \cdot erf\left(\sqrt{\frac{t}{\tau_1(T)}}\right)} \tag{B.95}$$

B.11 Calculation of the Green Decay-Time Spectrum Using a Qualitative Pulse-Shape Description for the Quenched Blue Scintillation Light

In the following, an approach to calculate the decay-time spectrum of green photons in the quenched model at temperatures $T \lesssim 20$K is presented (see section III/3.2.4). As the calculation of the green decay-time spectrum for $T \lesssim 20$K via the convolution of the blue decay-time spectrum with the response function of the green STEs (equation 3.158 in section III/3.2.4) cannot be performed analytically, the following approach is used:

- From the discussion of the decay-time spectrum of the quenched, blue scintillation light, it can be deduced that the pulse shape of the blue scintillation light should be qualitatively describable by the sum of, e.g., three exponentially decaying pulses (compare figure 3.11): The first exponential with a very fast decay-time, labeled as $\tau_{d-d}(T)$, reflects the impact of the Förster interaction on the pulse shape (very efficient reduction of the intensity at the beginning of the pulse). The third exponential with a slow decay time reflects the behavior of the pulse shape at large times for which the Förster interaction becomes negligible. Hence, within the developed model, this second, slow decay time has to correspond to $\tau_1(T)$ (the effective

unquenched lifetime of blue STEs, of the order of several 10μs to a few 100μs for low temperatures, see section III/5.2.2). The second exponential with an intermediate decay time, $\tau_m(T)$ (of the order of 1μs to several 10μs), is used to model the transition between the fast decaying part and the slow decaying part:

$$P_b^q(E_{part},T,t) \approx \Theta(t)\cdot P_b^q(E_{part},T)\cdot \cdot\left[\frac{A_{d-d}(T)}{\tau_{d-d}(T)}\cdot e^{-\frac{t}{\tau_{d-d}(T)}}+\frac{A_m(T)}{\tau_m(T)}\cdot e^{-\frac{t}{\tau_m(T)}}+\frac{A_1(T)}{\tau_1(T)}\cdot e^{-\frac{t}{\tau_1(T)}}\right] \tag{B.96}$$

with

$$A_{d-d}(T)\cdot P_b^q(E_{part},T)=\int_{-\infty}^{+\infty}\Theta(t)\cdot P_b^q(E_{part},T)\cdot\frac{A_{d-d}(T)}{\tau_{d-d}(T)}\cdot e^{-\frac{t}{\tau_{d-d}(T)}}dt$$

$$A_m(T)\cdot P_b^q(E_{part},T)=\int_{-\infty}^{+\infty}\Theta(t)\cdot P_b^q(E_{part},T)\cdot\frac{A_m(T)}{\tau_m(T)}\cdot e^{-\frac{t}{\tau_m(T)}}dt$$

$$A_1(T)\cdot P_b^q(E_{part},T)=\int_{-\infty}^{+\infty}\Theta(t)\cdot P_b^q(E_{part},T)\cdot\frac{A_1(T)}{\tau_1(T)}\cdot e^{-\frac{t}{\tau_1(T)}}dt$$

where $P_b^q(E_{part},T)$ corresponds to the total number of blue photons escaping the crystal (compare equation 3.161 in section III/3.2.4) and $A_{d-d}(T)$, $A_m(T)$ as well as $A_1(T)$ are the relative integrals (weights) of the first, second and third exponential pulse, respectively. Hence, in order to obtain the correct total integral, $A_{d-d}(T)+A_m(T)+A_1(T)\stackrel{!}{=}1$ has to be valid. It should be noted that this phenomenological description of the blue light pulse shape almost corresponds to the expression often used to fit the pulse shape of scintillation-light pulses recorded for $CaWO_4$ under particle excitation (compare section III/2.2.3): Often, only two exponentials are used to represent the complete light pulse shape, where the faster exponential (of the two pulses) roughly corresponds to the sum of the fast and the intermediate exponentials used within the present approach. Hence, as can be seen from the discussion of the data from [41] (where such pulse-shape fits have been performed) in section III/2.2.3, at low temperatures, the relative integral of the first and second exponential, $A_{d-d}(T)+A_m(T)$, should be in the range from $\sim 10\%$ to $\sim 30\%$ (dependent on the type of particle, compare table 2.1 in section III/2.2.3). In addition, from these fits, it can be seen, that $\tau_{d-d}(T)$ should be roughly of the order of 1μs (or faster, as within the approach presented here, additionally an intermediate decay time is used) at low temperatures.

- Using equation 3.159 (section III/3.2.4), the analogous, phenomenological description of the temporal evolution of blue STEs, $N_b^q(E_{part},T,t)$, can be obtained from the decay-time spectrum of blue photons described by equation B.96.

- This phenomenological description of $N_b^q(E_{part},T,t)$ can be convoluted analytically with the response function of the green STEs (compare equation 3.158 in section III/3.2.4),

$$\Theta(t)\cdot e^{-\frac{t}{\tau_2(T)}} \tag{B.97}$$

where $\tau_2(T)$ corresponds to the effective unquenched lifetime of green STEs which is expected to be much smaller than $\tau_1(T)$ (compare discussion in section III/3.2.4).

- With equation 3.160 (section III/3.2.4), an approximate, phenomenological description of the decay-time spectrum of the green scintillation light at $T \lesssim 20$K can be calculated:

$$P_g^q(E_{part},T,t) \approx \Theta(t)\cdot P_b^q(E_{part},T)\cdot\left(\frac{\tau_{rb}(T)}{(1-F_{abs})\cdot\tau_{\mathrm{mig,\ b\to g}}(T)}+\frac{F_{abs}}{(1-F_{abs})}\right)\cdot\frac{1}{\tau_{rg}(T)}\cdot$$
$$\cdot\left[\frac{A_{d-d}(T)}{1-\frac{\tau_{d-d}(T)}{\tau_2(T)}}\cdot\left\{e^{-\frac{t}{\tau_2(T)}}-e^{-\frac{t}{\tau_{d-d}(T)}}\right\}+\frac{A_m(T)}{\frac{\tau_m(T)}{\tau_2(T)}-1}\cdot\left\{e^{-\frac{t}{\tau_m(T)}}-e^{-\frac{t}{\tau_2(T)}}\right\}+\right.$$
$$\left.+\frac{A_1(T)}{\frac{\tau_1(T)}{\tau_2(T)}-1}\cdot\left\{e^{-\frac{t}{\tau_1(T)}}-e^{-\frac{t}{\tau_2(T)}}\right\}\right] \qquad \text{(B.98)}$$

B.12 Estimation of the Impact of the Quenching Effect onto the Light Yield for Electrons and γ-Particles

As discussed in section III/3.3.1, within the developed model, also for electron and γ interactions a quenched light generation is expected, i.e., a reduction of the amount of scintillation light generated in comparison to a completely unquenched light generation. However, this implies that a certain number of the STEs initially created in the energy-deposition process of a γ or electron, are interacting with each other via the Förster interaction. This interaction leads to the non-radiative recombination, i.e., the destruction of STEs and the production of phonons. In analogy to the description of the quenching effect for nuclear recoils which is quantified by the so-called quenching factor (relative to the light yield generated for electron and γ events, compare section III/2.2), in the following, the quenching effect for electrons and γ-particles is described by a quenching factor, $QF_{nq}^{e^-/\gamma}$, relative to the *unquenched light output*. Hence, the size of this quenching factor describes the reduction in light yield for electron and γ particles compared to the theoretically possible maximum amount of scintillation light generated, i.e., without quenching. In order to gain a very rough estimate for $QF_{nq}^{e^-/\gamma}$, the description of the light yield for γ-particles within the phenomenological model for the temperature dependency of the light yield for γ-particles in $CaWO_4$ (from [46]), discussed in appendix A.6, is considered: The only process described within the phenomenological model, that has no counterpart in the model developed within the present work is represented by the factor B (see equation A.15 in appendix A.6). In the phenomenological model, this process is introduced as additional production of optical phonons - besides the relaxation of the electron-hole pairs with mean energies of 11.75eV to the respective band edges (which is also included in the model developed within the present work). Thus, the factor B in the phenomenological model corresponds to the additional production of phonons that cannot be explained by the relaxation of the created electron-hole pairs to the band edges. In the context of the model developed within the present work, these additionally created phonons can be interpreted as being produced in the STE-STE interaction process (which leads to the light quenching proposed to be present also for electron and γ events). Hence, by identifying the impact of the B factor with the quenching effect for electron and γ events, a very rough estimate of the order of magnitude of the reduction of the light yield

for electron and γ events compared to the unquenched light yield can be gained:

$$B \approx Q F_{nq}^{e^-/\gamma} \approx 0.4 \tag{B.99}$$

compare table A.2 in appendix A.6. It should be noted that, this number only corresponds to a very rough estimate. Especially, as the value for the B factor introduced in the phenomenological model is the same for room temperature and 9K (compare table A.2 in appendix A.6), the estimated value for the electron/γ quenching factor compared to the unquenched light yield is the same for room temperature and low temperatures. As can be deduced from the discussion of the temperature dependency of the Förster radius (see appendix B.6.4) as well as of the impact of the Förster radius on the light generation (compare section III/3.2.4), it can be deduced that, in reality, the quenching factor can indeed differ for different temperatures (for a discussion of the temperature dependency of the quenching effect within the developed model, see section III/6.1).

B.13 Estimation of Values for Free Model Parameters From Data in the Literature and Applied Assumptions

In the following, the estimates gained for several free parameters of the model on the basis of data from the literature as well as by applying different assumptions are explained in more detail (compare section III/3.3.2):

- The fraction of electrons captured by electron traps, F_{e^-trap}: As discussed in more detail in section III/6.3, this parameter could, e.g., be determined by an absolute measurement of the efficiency of the scintillation-light production-process for a rare, unquenched excitation mode[40]. However, as no absolute measurement of the light-generation efficiency for the rare excitation mode was performed[41], the value of F_{e^-trap} has to be determined from an estimation based on literature values. The basic idea is, to compare the number of electron-hole pairs created by an interacting particle in $CaWO_4$ (e.g. a γ particle depositing all of its energy in ionization, compare section III/3.1.1) as predicted by the model to the number of photons produced by this interacting particle. It should be noted that, within the developed model, two other processes - besides capturing electrons in traps - lead to a reduction of the number of electron-hole pairs that produce photons. These two processes are the non-radiative recombination of STEs (blue and green STEs) and the destruction of blue STEs via the Förster interaction (quenching). In order to allow for a simpler estimate, the suggested comparison should be performed for values valid at very low temperatures, as then, the non-radiative recombination of STEs can be neglected (compare section III/3.1.3). Thus, e.g., the amount of scintillation light generated for a γ-particle of 122keV at low temperatures can be used as, for this particle, a typical value for the absolute amount of scintillation light created (average for several $CaWO_4$ crystals as used in the CRESST experiment) is available with relative high accuracy (see discussion in section III/2.2.4). Using additionally, that the mean energy of one scintillation-light photon produced at these temperatures is known ($\overline{E_p(T \lesssim 10\text{K})} \approx 2.82$ see, e.g., section III/5.1.2), the number of photons created for

[40] In section III/6.3 also a second possibility for the determination of the fraction F_{e^-trap} is suggested.

[41] For this purpose also the probability for the two-photon process to occur as well as the absolute intensity of the laser-light pulse would have to be known.

a 122keV γ particle interacting in $CaWO_4$ for a temperature of $T \lesssim 10\text{K}$ can be estimated. The number of created electron-hole pairs for a 122keV γ particle can be estimated using the mean energy needed to produce an electron-hole pair ($2.35 \cdot E_{gap}$, with the energy gap $E_{gap} \approx 5\text{eV}$) as well as the efficiency of creating ionization for a 122keV γ particle, $F_{ioniz}(E_\gamma) \approx 1$ (equation 3.1 in section III/3.1.2). In addition, before comparing these two numbers, it should be taken into account that, within the developed model, the light yield of γ events is expected to be reduced due to the quenching effect by a factor of roughly $QF_{uq}^{e^-/\gamma} \approx 0.4$ (compare appendix B.12). Thus, the following relationships for the number of photons, $N_p(E_\gamma)$, and the number of electron-hole pairs, $N_eh(E_\gamma)$, for a γ-particle with $E_\gamma = 122\text{keV}$ are assumed to be valid for temperatures below $\sim 10\text{K}$ (compare equation 3.13 in section III/3.1.1):

$$
\begin{aligned}
LY_{abs}^{\gamma}(T \lesssim 10\text{K}) &\approx 6.0\% \\
N_p(E_\gamma) &\approx \frac{LY_{abs}^{\gamma}(T \lesssim 10\text{K}) \cdot E_\gamma}{\overline{E_p(T \lesssim 10\text{K})}} \\
N_eh(E_\gamma) &\approx \frac{E_\gamma}{2.35 \cdot E_{gap}} \\
\Rightarrow N_p(E_\gamma) &\approx QF_{uq}^{e^-/\gamma} \cdot (1 - F_{e^-trap}) \cdot N_p(E_\gamma) \\
\Rightarrow F_{e^-trap} &\approx 1 - \frac{LY_{abs}^{\gamma}(T \lesssim 10\text{K}) \cdot 2.35 \cdot E_{gap}}{\overline{E_p(T \lesssim 10\text{K})} \cdot QF_{uq}^{e^-/\gamma}} \approx 37.5\%
\end{aligned}
\tag{B.100}
$$

- The fraction of blue photons absorbed at defect centers: F_{abs} (see equation 3.46 in section III/3.1.3). As discussed in section III/3.2.1, within the developed model, for temperatures below $\sim 5\text{K}$, the amount of green scintillation light generated only depends on the fraction of blue photons reabsorbed at defect centers F_{abs}. Hence, in order to determine a value for F_{abs}, the relative amount of blue (or green) scintillation light generated (or the ratio of the blue-to-green scintillation light) for such low temperatures can be used. As, within the present work, no measurements below a temperature of $\sim 20\text{K}$ were performed, the value for the relative amount of generated blue light could not be determined directly from the conducted experiments. However, it has to be noted that the ratio of the produced blue-to-green light is a crystal-dependent parameter as it depends on the defect density of the respectively investigated $CaWO_4$ crystal. Hence, this value could also not be adopted directly from literature. Instead, as the relative amount of blue light generated at $\sim 20\text{K}$ and $\sim 300\text{K}$, $r_b(T \approx 20\text{K})$ and $r_b(T \approx 300\text{K})$ could be determined from the experiments (see section III/5.1.2), information from literature on the temperature dependency of the amount of blue light generated was used to infer a value for $r_b(T \lesssim 5\text{K})$ from the experimentally determined values at 20K and at 300K within this work (see section III/5.1.2 for these results). From the temperature-dependency of $r_b(T)$ (inferred from figure 3.10 b) in section III/3.2.1, values from [54]), the ratio of $r_b(T \lesssim 5\text{K})$ to $r_b(T \approx 20\text{K})$ was determined so that a value for $r_b(T \lesssim 5\text{K})$ for each of the two $CaWO_4$ crystals investigated within the present work (crystal "Olga" and crystal

"Philibert", see section III/4.1.2) could be estimated:

$$\frac{r_b(T \lesssim 5\text{K})}{r_b(T \approx 20\text{K})} \approx \frac{80\%}{78\%} \approx 1.03 \quad \text{(from [54])} \tag{B.101}$$

$$\Rightarrow r_b^{Olga}(T \lesssim 5\text{K}) \approx r_b^{Olga}(T \approx 20\text{K}) \cdot 1.03 \approx 82\% \tag{B.102}$$

$$\Rightarrow r_b^{Phil}(T \lesssim 5\text{K}) \approx r_b^{Phil}(T \approx 20\text{K}) \cdot 1.03 \approx 81\% \tag{B.103}$$

$$\Rightarrow F_{abs}^{Olga} \approx r_g^{Olga}(T \lesssim 5\text{K}) = 1 - r_b^{Olga}(T \lesssim 5\text{K}) \approx 18\% \tag{B.104}$$

$$\Rightarrow F_{abs}^{Phil} \approx r_g^{Phil}(T \lesssim 5\text{K}) = 1 - r_b^{Phil}(T \lesssim 5\text{K}) \approx 19\% \tag{B.105}$$

B.14 Complete List of All Model Parameters

In table B.4, a list of the most important model parameters, their meaning as well as their dependency on the temperature T, the defect density C_{defects} and the type and energy of the primary interacting particle E_{part} as included in the developed model can be found. It should be noted that the geometrical parameters describing the spatial distribution of the ionization-density generated by an interacting particle in the $CaWO_4$ crystal are not shown in this table, but can be found in tables 3.3 and 3.4 (for heavy, charged primary interacting particles, such as ions, in section III/3.1.2) as well as in table B.1 (for electrons as primary interacting particles, in appendix B.3.1). In addition, it should be noted that only the major parameters are listed, i.e., for example, regarding the radiative recombination time of blue STEs, $\tau_{rb}(T)$, only this recombination time is listed, although, within the developed model a parameterization of the temperature-dependency of this decay time using three parameters (τ_{L1b}, τ_{L2b} and D_b, compare equation 3.54 in section III/3.1.3) is performed. These parameterizations of the different model parameters can be found in the respective sections where the model parameters are introduced and explained.

parameter	unit	meaning	dependency on
$part$		type of primary particle	
E_{part}	[eV]	total energy deposited by the primary particle E_{part}	
E_{gap}	[eV]	energy of the band gap	material
C_{defects}	[ppm]	defect density	crystal
C_{gC}	[ppm]	density of green centers	crystal
F_{ioniz}		fraction of E_{part} generating ionization	$part$, E_{part}
$\frac{1}{2.35 \cdot E_{gap}}$	$\left[\frac{1}{\text{eV}}\right]$	mean energy needed to create an electron in the conduction band and a hole in the valence band	E_{gap}
N_{eh}		number of created electrons and holes	$part$, E_{part}
$F_{e^- trap}$		fraction of electrons captured by electron traps	C_{defects}
$N_{STE}^{form\, e^- STH}$		number of initially created blue STEs	$part$, E_{part}, C_{defects}
$N_{im\, STE}^{form\, e^- STH}$		number of immediately created blue STEs	$part$, E_{part}, C_{defects}
$N_{del\, STE}^{form\, e^- STH}$		number of delayed created blue STEs	$part$, E_{part}, C_{defects}
F_{dr}		fraction of electrons captured by STHs in a delayed process	C_{defects}, T
τ_{dr}	[s]	delayed e^--STH recombination time and rise time of the fraction F_{dr} of the scintillation light	C_{defects}, T
$n_{bSTE}^{form\, 0}(\mathbf{x})$	$\left[\frac{\#}{nm^3}\right]$	position-dependent initially created blue STE density	$part$, E_{part}, C_{defects}
F_{abs}		fraction of blue photons absorbed at defect centers	C_{defects}
τ_{rb} (τ_{rg})	[s]	radiative recombination time of blue (green) STEs	T
τ_{nrb} (τ_{nrg})	[s]	non-radiative recombination time of blue (green) STEs	T
$\tau_{\text{mig, b}\to\text{g}}$	[s]	migration time of blue STEs to defect (green) centers	T, C_{defects}
$\tau_{\text{mig, g}\to\text{b}}$	[s]	migration time of green STEs to intrinsic (blue) centers	T
R_{d-d}	[s]	Förster radius: in this distance, the probability of STE-STE interaction is 50% (cp. to other de-excitation processes)	T
τ_{ltb} (τ_{ltg})	[s]	intrinsic unquenched lifetime of blue (green) STEs	T, C_{defects}
R_{b-g}		ratio of blue-to-green light generated	T, C_{defects}
τ_1 (τ_2)	[s]	effective unquenched lifetime of blue (green) STEs (including their mutual (de-)excitation processes	T, C_{defects}
$\overline{E_{Pb}}$ ($\overline{E_{Pg}}$)	[s]	mean energy of blue (green) photons	T

Table B.4: List of the most important model parameters (except for the geometrical parameters describing the particle-induced ionization-density distribution) as well as their meaning and dependencies on temperature T, the defect density C_{defects} and the type and energy of the primary interacting particle E_{part}.

Appendix C

Details of the Experimental Equipment and the Error Evaluation for the Measured Wavelength and Decay-Time Spectra of $CaWO_4$

In the following, details on the components and the setup used in the measurements of the wavelength and decay-time spectra of $CaWO_4$, described in chapter III/4, can be found. The different items and instruments used in the experiments are described and characterized. The respective instrumental uncertainties resulting in measurement uncertainties are discussed and determined.

C.1 Properties of the Investigated Crystals

A summary of the properties of the investigated crystals can be found in table C.1 (see next page).

C.2 Measurement of the Wavelength Spectra: The Spectrometer

C.2.1 Data Acquisition

Data acquisition for the measurements of the wavelength spectra was realized with the spectroscopy software SpectraSuite[1]. Spectra were recorded with a wavelength resolution of 0.48nm, leading to 2068 channels. Depending on the intensity of the surveyed light source, integration times ranging from 13ms up to 30s were used. For some measurements, additionally the averaging over several recorded spectra, provided by the software, was used to improve the data quality[2]. Before performing the actual measurement, each time

[1] Ocean Optics, Dunedin, Florida.

[2] This feature could not always be used as it was attempted to keep the duration of exposure to, e.g., intense ion beam excitation, short in order to avoid radiation damages. For more details, see section III/4.5.

		Olga	Philibert
size			
diameter	[mm]	40.0	40.0
height	[mm]	40.2	40.0
producer		General Physics Institute, Moscow, Russia [54]	crystal laboratory, TUM, Germany [100, 101]
growth procedure		Czochralski	Czochralski
year		2004	2012
post-growth annealing			
gas flow		air [54]	99%Ar, 1%O [100, 101]
temperature	[°C]	1100 [54]	1200 [100, 101]
duration	[h]	not specified	20 [100, 101]
ramping	[°C/h]	not specified	50 [100, 101]
second annealing			
gas flow		pure oxygen	pure oxygen [101, 102]
temperature	[°C]	800	1450 [101, 102]
duration	[h]	48	72 [101]
ramping	[°C/min]	1	50 [101]
light emitting properties			
light yield		95.1%	93.7% [101]
resolution	(FWHM)	14.6%	12.7% [101]

Table C.1: Properties of the $CaWO_4$ crystals that were investigated in the performed measurements.

an individual dark spectrum (light source switched off) was recorded with the exact same experimental setup and software settings. The used software allowed for storage and automatic, online subtraction of this dark spectrum containing residual, ambient stray light.

C.2.2 Calibration of the Spectrometer

The wavelength dependent correction factor of the spectral response of the spectrometer glass-fiber setup was determined in a calibration measurement using a gauged halogen lamp[3]. For operation of the lamp with 6.60A in a distance of 0.7m, the wavelength dependent output of the lamp in the region from $250 - 1100$nm (in 5nm steps) is given in its test certificate[4]. From this data the calibration spectrum of the lamp can be obtained with a resolution of 5nm. To calculate the spectral correction factor $CF(\lambda)$, the spectrum of the lamp (operated with the nominal current of 6.60A) had to be recorded and then be compared to the calibration spectrum of the lamp. For this purpose, the lamp

[3]Halogen lamp, LSB20, serial number LSK113, 100W, 6.60A, L.O.T. Oriel & Co KG, Darmstadt, Germany.

[4]Test certificate number 18332, test facility Heraeus Noblelight GmbH, Hanau, Germany. In principle, the calibration data not only allows spectral correction, but also absolute intensity assignment if the lamp is operated at the specified distance of 0.7m.

and the glass-fiber inlet were set up in a black housing reducing incidence of ambient light.

To establish operation of the lamp with the specified current, a low-ohmic calibration resistor (100.002mΩ) was connected in series to the lamp in the measurement. The voltage was applied with a tunable power supply. The current was determined by a precision voltage measurement[5] at the calibrating resistor to match the nominal 6.60A. Operation of the lamp at a distance of 0.7m to the glass fiber resulted in saturation of the spectrometer response, even for the shortest integration time possible (13ms). Thus, the distance between lamp and glass-fiber inlet was enlarged to 1.80m. At this distance no saturation was observed in the recorded spectrum. In the following, the effect of the enlarged distance on the detected intensity is ignored as in the analysis only the spectral information is used. Hence, as no absolute intensity measurements are pursued, the theoretically expected spectrum can be scaled with an adjustable factor to approximately match the magnitude of the measured spectrum thus allowing for an easier comparison between the two.

The measurement of the halogen lamp spectrum (and the corresponding dark spectrum) was performed using an integration time of 13ms and one scan. In order to eliminate a potentially remaining DC offset of the spectrum[6], the first bins of the recorded spectrum ($\lambda < 250$nm) were used to obtain a background histogram. As the dark spectrum was subtracted online and the lamp spectrum should only show intensities above 250nm, it can be concluded that no light should be detected below 250nm. The background histogram was fitted with a gaussian distribution. The mean value of this gaussian is taken as an estimate for the remaining offset and is therefore subtracted from the measured spectrum. The measured spectrum processed in this way is shown in figure C.1 (red line), together with the scaled calibration spectrum taken from the test certificate (black crosses). Additionally, a third-order spline fit to the data of the calibration spectrum can be seen (green line). This spline is used to calculate a continuation of the calibration spectrum as the measured spectrum is available with much better resolution than the calibration spectrum[7].
The wavelength-dependent correction factor for the spectral response of the spectrometer glass-fiber system can then be obtained by dividing the spline of the calibration spectrum by the measured (DC offset subtracted) spectrum of the halogen lamp[8]. In figure C.2 a), the resulting correction factor for the whole wavelength range can be seen whereas in figure C.2 b) a zoom into the wavelength region of the $CaWO_4$ light output ($300-700$nm) is depicted together with an example of a $CaWO_4$ scintillation-light spectrum (black: as measured with the spectrometer glass-fiber setup, light red: multiplied with the correction factor)[9].
As can already be seen in figure C.1, the detection efficiency of the used setup decreases

[5]Integrating precision voltmeter, type 5020, PREMA Präzisionselektronik GmbH, Mainz, Germany. Input resistance: 10GΩ.

[6]Such a DC background could be induced by temperature drifts of the spectrometer.

[7]A linear interpolation of the data points of the calibration spectrum would have been another possibility to model a continued spectrum. However, a third-order spline fit delivers a more natural continuation.

[8]For wavelengths < 250nm and > 1100nm where no data in the calibration spectrum is available, the correction factor is set to one. This arbitrary assignment is of no importance as no contribution of scintillation light of $CaWO_4$ is existent in these wavelengths ranges. However, as data recorded in these wavelength ranges exists, the correction factor has to be assigned to a value there.

[9]The outlying data point (spike) of the scintillation-light spectrum at ~ 605nm is an artifact due to one pixel of the detector of the spectrometer.

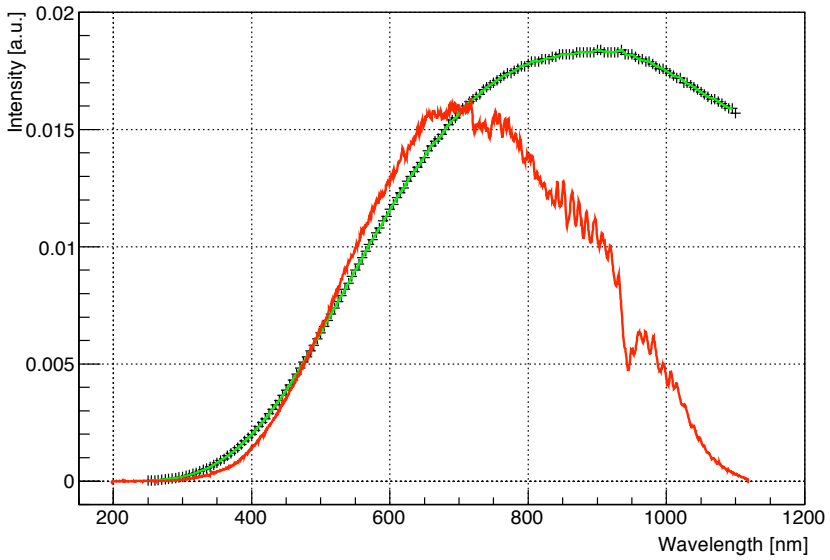

Figure C.1: Spectrum of the halogen lamp measured with the Maya2000 Pro spectrometer (DC offset substracted, red line) and data of the calibration spectrum of the lamp (black crosses) together with a third-order spline fit (green).

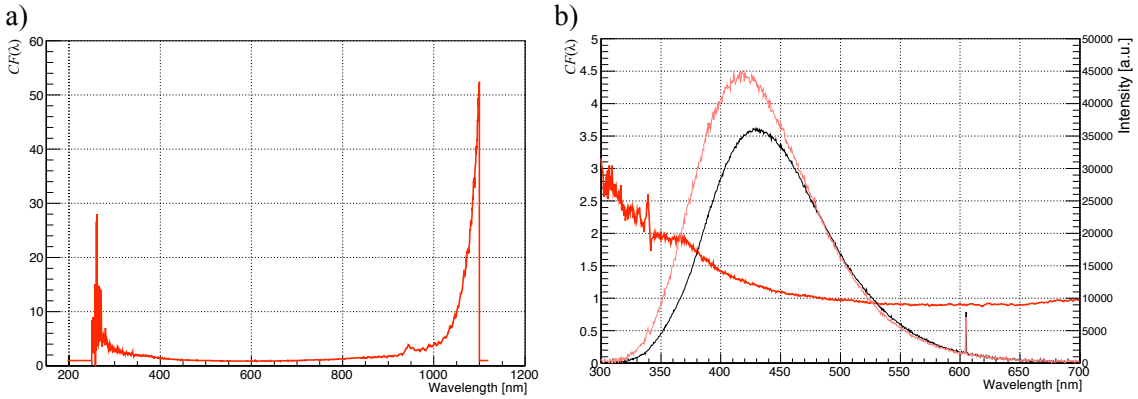

Figure C.2: Correction factor $CF(\lambda)$ (red line) for the wavelength-dependent response of the spectrometer glass-fiber system as calculated from the measured spectrum and the calibration spectrum of the halogen lamp: a) complete wavelength range of the Maya2000 Pro spectrometer; b) zoom into the region $300-700$nm, together with an example of a scintillation-light spectrum of a $CaWO_4$ single crystal: As measured with the spectrometer glass-fiber setup (black) and multiplied by the correction factor (light red). Correction factor: left y-axis, spectral intensity: right y-axis.

continuously for wavelengths $\gtrsim$ 700nm. This behavior is of course reflected in the increasing spectral correction factor for wavelengths $\gtrsim$ 700nm (see figure C.2 a). In the wavelength region of the $CaWO_4$ scintillation light (see figure C.2 b), the correction factor is less wavelength-dependent. Nonetheless, it can clearly be seen that for the wavelength region from $\sim$ 370nm on to lower wavelengths a noisy structure appears on the correction factor. This effect is due to the decreasing intensity of the halogen lamp in this wavelength

region (as can be seen in figure C.1) in combination with a reducing detection efficiency of the setup. However, for the main part of the wavelength region of interest, the correction factor is represented by a smooth dependency on the wavelength. In the following, all measured spectra are multiplied with the determined wavelength-dependent correction factor $CF(\lambda)$ before being analyzed (see section III/4.6).

C.2.3 Wavelength Spectra: Error Evaluation

In the analysis of acquired light spectra with the Maya2000 Pro spectrometer different error sources have to be taken into account. For the systematical error of the measured intensities two features have to be considered: The uncertainty of the response of the Maya2000 Pro spectrometer itself (for a corrected response) and the uncertainty introduced by the correction procedure. For the corrected response of a Maya2000 Pro spectrometer, the manufacturer specifies a remaining non-linearity of $< 1\%$ [120]. Hence, this remaining uncertainty is supposed to correspond to the intrinsic uncertainty of the Maya2000 Pro spectrometer itself. The systematic error introduced by the correction procedure can be estimated with the help of the wavelength-dependent uncertainties of the halogen-lamp calibration-spectrum given in the test certificate. These wavelength-dependent uncertainties range from $8.2 - 12\%$ (on a 95% confidence level), corresponding to one-sigma error intervals of $4.1 - 6\%$. Thus, the systematic error in the wavelength-dependent intensity can be expected to be dominated by the uncertainty due to the correction procedure described above. The statistical error in the intensity measurement is due to fluctuations in the response of different pixels of the Maya2000 Pro spectrometer. Its size can be evaluated with the help of empty dark spectra recorded with the light source turned off (with active background subtraction). These spectra show a straight line with only the statistical fluctuations in the response of different pixels remaining. The measured intensities of a dark spectrum can then be merged into a background histogram. This histogram is fitted with a gaussian where the fitted one-sigma width of the gaussian can be taken as an estimate for the distribution of the fluctuations. Thus, the fitted value for its one-sigma width is identified with the statistical error of the measured intensity (see appendix D.1). Of course, for each used set of spectrometer adjustments (integration time and number of averaged spectra) an individual dark spectrum was acquired. Hence, for the analysis of each individual measurement, the corresponding dark spectrum is used for the determination of the statistical error. As the empty dark spectra were also recorded with active background subtraction, the determined one-sigma width *directly* corresponds to the statistical error on the baseline of the acquired spectra and does *not* have to be multiplied by a factor of $\sqrt{2}$. The absolute systematical and statistical errors can then be added quadratically to obtain the quadratic total uncertainty for the measured intensities.

The absolute uncertainty in the wavelength determination of the measurement is assumed to correspond to the acquired resolution of 0.48nm.

C.3 The Si-PIN Diode

The detector[10] used for the characterization of the PMT and as trigger source for the laser-excitation experiments is a high-bandwidth, fast and highly linear photodetector.

[10] 713A3 Series, Analog Modules Inc., Longwood, USA.

The sensor is a Si-PIN diode[11] with an active area of 2.5mm diameter and a spectral range from $200-1150$nm. Operation of the diode at 90V bias (50ΩDC-coupling) typically results in a rise time $<$ 1ns. This rise time is faster than all other considered times in the conducted experiments (e.g. pulse width of the laser light or PMT electron transit-time spread). Deviation from a linear response of the diode is specified as better than 1% over 7 decades of the signal (peak output swing is 2V). The fast rise time and linear output of the Si diode allow its employment as reference detector. Operating parameters during all experiments were 12V and 0.07A.

The setup used for employing the Si diode as trigger in the laser-excitation experiments can be found in figure 4.4 in section III/4.3.2. The position of the diode and the sheet of white paper (used as reflector for the laser light) as well as the trigger level of the employed rising edge trigger were not exactly the same in all measurements. Hence, the shape and height of the Si diode signal as well as the time jitter between the trigger signal and the $CaWO_4$ scintillation light pulse do not comply with each other in the different measurements. This results in different time shifts of the onset of the scintillation light pulse, detected with the PMT, compared to the time of the trigger signal. Therefore, in the fits of the scintillation light pulses a free parameter corresponding to a shift in time had to be included (see section III/5.2.1).

C.4 Measurement of the Decay-Time Spectra: The Photomultiplier Tube

In the following, different measurements that were performed to characterize the signal saturation, response linearity, impulse reaction and baseline drift of the used setup (PMT, base and electronic readout circuit) are presented. In some of these measurements, the fast Si-PIN diode (see appendix C.3) was used as reference. The same Si Diode was also used as trigger source in the laser-excitation experiments. PMT pulses shown in the following are displayed with reversed voltage coordinate (to yield positive pulses) and baseline subtracted[12].

C.4.1 Qualitative Consideration: Saturation of the PMT Signal

To qualitatively characterize the linearity of the PMT response a comparison of two pulses recorded for a $CaWO_4$ crystal under laser excitation at room temperature is presented in figure C.3. In principle, the same setup as used in the laser-excitation measurements described in section III/4.3 was used. However, the light-collection efficiency was not yet optimized resulting in signal heights smaller by a factor of ~ 2 in comparison to the final laser-excitation experiments. As discussed in section III/4.7.3, not only the scintillation light of the $CaWO_4$ crystal (decay time $\sim 9\mu$s) can be seen, but also laser light being reflected at the crystal (fast structure (spike) at the beginning of the pulse). In black the light signal recorded with the typical operating voltage of the PMT of -1.75kV is shown. The smaller pulse shown in red corresponds to the same signal, however, recorded with a decreased operating voltage of the PMT of only -1.5kV. Both pulses are averages of 1,000 events each (for details on the data acquistion and averaging, see section III/4.2.3 and

[11] FND100Q, EG&G Judson, Montgomeryville, USA.

[12] Baseline subtraction was performed with the help of the pre-trigger region. Details can be found in section III/4.6.

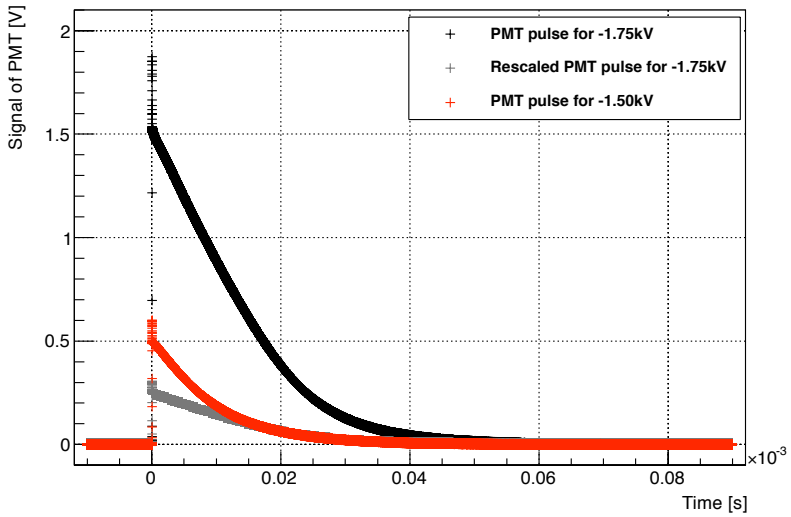

Figure C.3: Scintillation light detected for a $CaWO_4$ crystal under laser excitation: The fast rise and decay at the beginning of all pulses are due to laser light being reflected at the crystal onto the PMT (for details see section III/4.7.3). The signal recorded with an operating voltage of the PMT of -1.75kV is shown as black crosses, the same light pulse recorded with an operating voltage of the PMT of only -1.5kV is shown as red crosses. Pulses in black and red correspond to the data as recorded, only preprocessed according to section III/4.6.2. The black pulse, rescaled to match the pulse height of the red pulse at 20μs is depicted in grey. It can be seen that the PMT output suffers from saturation for signal voltages $\gtrsim 0.9$V (pulse height of black pulse at $\sim 10\mu$s).

appendix C.4.5). In order to detect possible differences in the pulse shapes of the two pulses, they have to be scaled to the same height. However, due to the large pulse height of the signal recorded at -1.75kV, a saturation at the beginning of the pulse is possible. Thus, the factor used for rescaling of the black pulse is determined through the comparison of the signal heights at large times (small signal heights), e.g. at 20μs. Here both signals are expected to be non-saturated. In figure C.3, the signal recorded at -1.75kV, rescaled with this factor, is shown in grey. It can clearly be seen that the pulse recorded with -1.75kV is suffering from saturation from the beginning of the pulse until $\sim 10-15\mu$s. For larger times the two pulses comply with each other. Thus it can be concluded, that for -1.75kV operating voltage, the PMT response starts to saturate for pulse heights larger than ~ 0.9V.

To demonstrate that for signal heights $\lesssim 0.9$V the response of the PMT is linear, another example of pulses obtained under laser excitation is shown in figure C.4. Additionally, it is shown with this example that the PMT delivers the same pulse shape for different operating voltages (signal heights $\lesssim 0.9$V). Again the scintillation light of a $CaWO_4$ crystal under laser excitation was recorded. Two pulses recorded with two different operating voltages of the PMT are shown in figure C.4 a). In this example, however, the maximum signal height of the $CaWO_4$ scintillation light only amounts to[13] ~ 0.35V. The signal recorded

[13]The operating parameters of the laser (purity and pressure of the N_2-gas) were not yet optimized in this measurement. Thus, the excitation intensity of the $CaWO_4$ crystal was decreased resulting in smaller signals than for the measurement presented in figure C.3. However, all other operating parameters were the same.

for an operating voltage of -1.75kV of the PMT is shown in black. The red pulse is the same signal recorded for an operating voltage of the PMT of -1.46kV. In figure C.4 b), both pulses scaled to the same height are shown in a logarithmic plot. As they completely overlap each other, it is apparent that both pulses exhibit the same pulse shape.

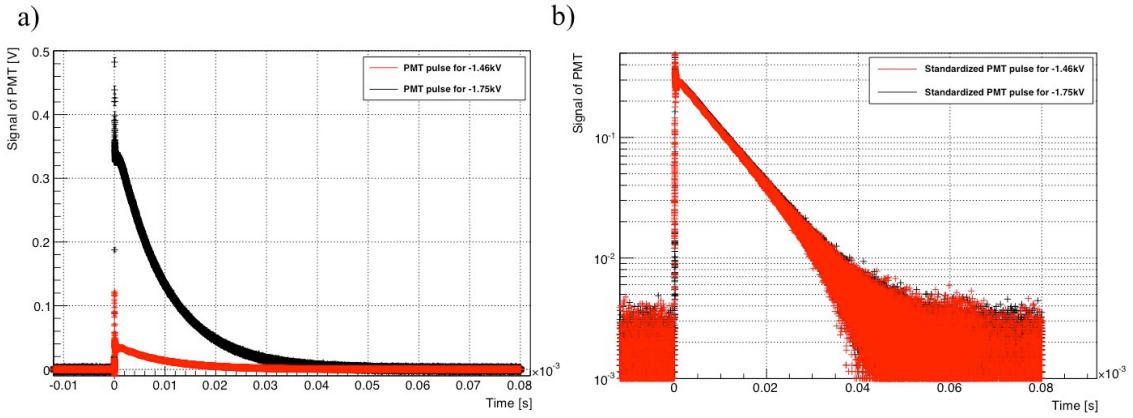

Figure C.4: Scintillation light detected for a $CaWO_4$ crystal under laser excitation: The fast rise and decay at the beginning of all pulses is due to laser light being reflected at the crystal (for details see section III/4.7.3). The signal recorded with an operating voltage of the PMT of -1.75kV is shown in black. The same light pulse as recorded with an operating voltage of the PMT of only -1.46kV is shown in red. Figure a): Signals as recorded (only preprocessed according to section III/4.6.2). The $CaWO_4$ scintillation light (slow decay) shows a maximum of ~ 0.35V. Figure b): Same signals, now scaled to height. For better comparison the y-axis is logarithmic. It can be seen, that the pulses completely overlap each other. Thus, the pulse shapes have to be in very good agreement.

In the ion-beam experiments where the PMT was operated with -1.75kV, typical pulse heights of the PMT signal amount to $\sim 1 - 10$mV (maximum of 100mV for BaF_2). Thus, for the ion-beam experiments, saturation of the PMT signal does not occur. However, in the laser-excitation experiments huge pulse heights were observed. Consequently, the operating voltage of the PMT was reduced to -1.5kV to limit the anode current during the pulse as well as to reduce saturation effects. Nonetheless, still signals with pulse heights of up to ~ 1V were recorded. As explained above, for signal heights $\gtrsim 0.9$V (or even less) an effect of the saturation is expected to occur. In the analysis of the data (see section III/5) no quantitative measures were taken to correct for the effect of saturation. At the respective point in the analysis of the data, the possible saturation effect is referred to and its implications are discussed.

However, a possible uncertainty in the linearity of the PMT response (for signal heights $\lesssim 0.9$V) is taken into account for the error determination. The measurements performed to determine this uncertainty are described in the following.

C.4.2 Uncertainty in the Linearity of the PMT Response

For the determination of the uncertainty of the linearity of the PMT response, light signals with different pulse heights were recorded simultaneously with the PMT and the reference

detector (Si diode). Light pulses from a pulsed blue InGaN-LED[14] with various intensities were recorded with the Si diode and the PMT at the same time. The Si diode signal was used as reference signal. The LED was operated with rectangular voltage pulses of 2μs length from a function generator[15]. The amplitude of the voltage pulse was varied in a range of $3.5 - 4.7$V in 0.2V steps[16]. Data acquisition was performed with both detectors, the Si diode and the PMT, each 50ΩDC-coupled to input channels of the oscilloscope (time base: 1μs per division, resulting in a record length of 10μs, for details on the data acquisition see section III/4.2.3 and appendix C.4.5). Triggering was performed directly on the signal of the function generator fed to a third channel of the oscilloscope with a rising-edge trigger. The light pulses resulted in pulse heights of the PMT and Si diode signals in the range $\sim 0.1 - 0.9$V and $\sim 0.03 - 0.24$V, respectively. Two examples of recorded pulses, for LED voltages of 3.5V (black) and 4.7V (red), are shown in figure C.5 a for the Si diode and in figure C.5 b for the PMT, respectively.

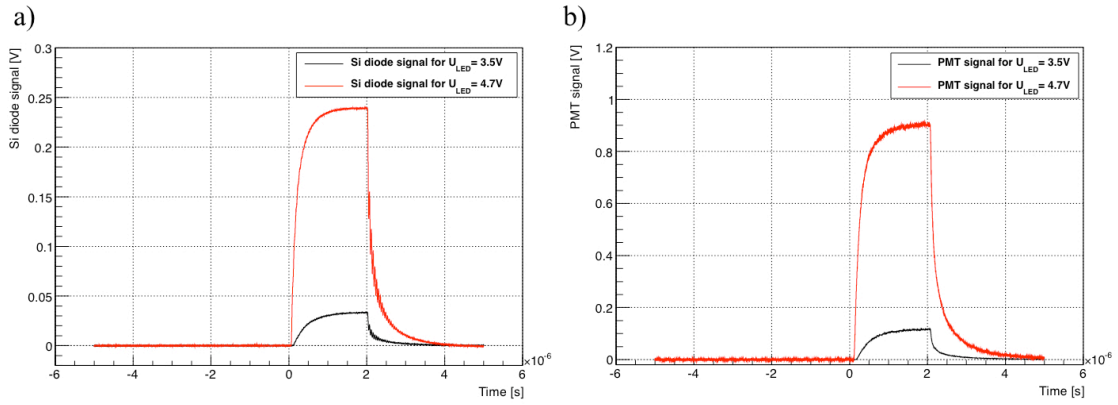

Figure C.5: Light pulses of the blue LED recorded with the Si diode (figure a) and the PMT (figure b). Two examples are shown in each figure: The red pulses correspond to a LED voltage of 4.7V, the black pulses to a LED voltage of 3.5V.

The signal heights of the recorded pulses are determined with the help of the pre-trigger regions (-5μs to 0μs, 25,000 data points) and the signal plateau regions (1.75μs to 2μs, 1,250 data points). For each pulse a histogram of the voltage values of the data points in the respective region is generated. Each histogram is fitted with a gaussian distribution so that the fit value for the mean corresponds to the baseline level and the signal level, respectively. The signal height, i.e. the amplitude, is then the difference between the baseline and the signal level[17]. With these relative amplitudes for each LED voltage i ($i = 1 \ldots 7$), a scaling factor SF_i between the PMT pulse-height and the Si diode pulse-height (taken as reference) can be determined. From these "individual" measurements of

[14] LED430-06, Roithner Lasertechnik GmbH, Wien, Austria. Peak wavelength: 430nm, half width: 20nm.

[15] Dual-Channel Arbitrary/Function Generator AM300, Rhode und Schwarz, München, Germany.

[16] This voltage range was chosen as it allowed proper operation of the LED and resulted in signal heights $\lesssim 0.9$V at the PMT. Uncertainty of the voltage applied to the LED: ±2% according to the data-sheet of the arbitrary function generator. However, this uncertainty is not of importance here, as the signal of the PMT is regarded relative to the Si diode signal and not relative to the absolute LED signal.

[17] Due to the large number of data points in the respective regions the levels are determined with high accuracy.

the scaling factor a mean scaling factor $\overline{SF}$ can be calculated. The relative mean error[18] $\overline{m}$ of $\overline{SF}$ can then be taken as an estimate for the systematic uncertainty of the linearity of the PMT signal $\Delta V_{sys\,Lin-PMT}$ (for non-saturated signals):

$$\begin{aligned} \overline{SF} &= 3.73 \\ \Delta V_{sys\,Lin-PMT} &= \overline{m} = 1.44\% \end{aligned} \tag{C.1}$$

This uncertainty will be used in appendix C.4.6 in the error evaluation of the decay-time measurements.

C.4.3 Drifting Baseline and Crosstalk from the Laser and Accelerator

Another source of uncertainties of the PMT signal are distortions of the baseline, such as statistical fluctuations of the data, time-dependent drifts of the baseline level and electronic crosstalk from noise sources. To reduce the effect of such distortions, many individual light pulses are averaged in the data-acquisition process (for details, see section III/4.2.3 and appendix C.4.5). The statistical uncertainty $\Delta V_{stat-BL}$ introduced by fluctuations on the data is determined using a pre-trigger region before the signal. $\Delta V_{stat-BL}$ is calculated individually for each recorded pulse. The procedure used for the determination of $\Delta V_{stat-BL}$ is described in section III/4.6 and discussed in appendix D.1. The evaluation of the influence of systematic drifts of the baseline and correlated noise due to crosstalk is presented in the following. As in the two measurements, laser and ion-beam excitation, different noise sources emerged, an individual examination for each type of experiment is conducted. For this purpose, typical baselines for each type of experiment are discussed.

Baseline in the Laser-Excitation Experiments

A typical example of an empty baseline recorded with the same settings (PMT, trigger and data acquisition: 5,000 pulses averaged) as used in the laser-excitation measurements is depicted in figure C.6. During this measurement, the laser was operated as usual, however, the shutter in front of the laser was closed to record an empty baseline. In figure C.6 a), the complete signal, in figure b) a zoom into the noise structure on the baseline around 0μs and in figure c) a zoom into the baseline-level region are shown.
The noise structure at $\sim 0\mu$s to 1μs, $V_{noise-pp} \approx 2$mV, shown in figure C.6 b) appears on every signal recorded while the laser is operated. It is correlated with the time of triggering and can be assigned to crosstalk from the discharge of the laser onto the PMT signal. However, its shape and time structure are not identical in each measurement, preventing a simple subtraction of this noise structure from the signal. Given that scintillation-light pulses from the $CaWO_4$ crystal recorded for laser excitation exhibit typical pulse heights of $\sim$ 0.05V up to $\sim$ 1V (much larger than the magnitude of this noise structure), the influence of this noise is neglected in the analysis. In figure C.6 c) a vertical zoom into the baseline is shown. It can be seen that the baseline exhibits a non-negligible drift, despite the 50ΩDC-coupling of the PMT to the oscilloscope. Although this drift is small compared to the maximum signal height of the scintillation-light pulses, it can affect the signal shape at long times where the signal height is small. Thus, this drift can have an impact on fits of slow exponential decay times and has to be considered in the data

[18] The arithmetic mean of the $N = 7$ individual "measurements" of the scaling factor SF_i is $\overline{SF} = \frac{1}{N} \cdot \sum_{i=1}^{N} SF_i$. The variance of the scaling factor is s^2: $s^2 = \frac{1}{N-1} \cdot \sum_{i=1}^{N} (SF_i - \overline{SF})^2$. Finally, the mean error $\overline{m}$ of the arithmetic mean $\overline{SF}$ is given by: $\overline{m} = \frac{s}{\sqrt{N}}$.

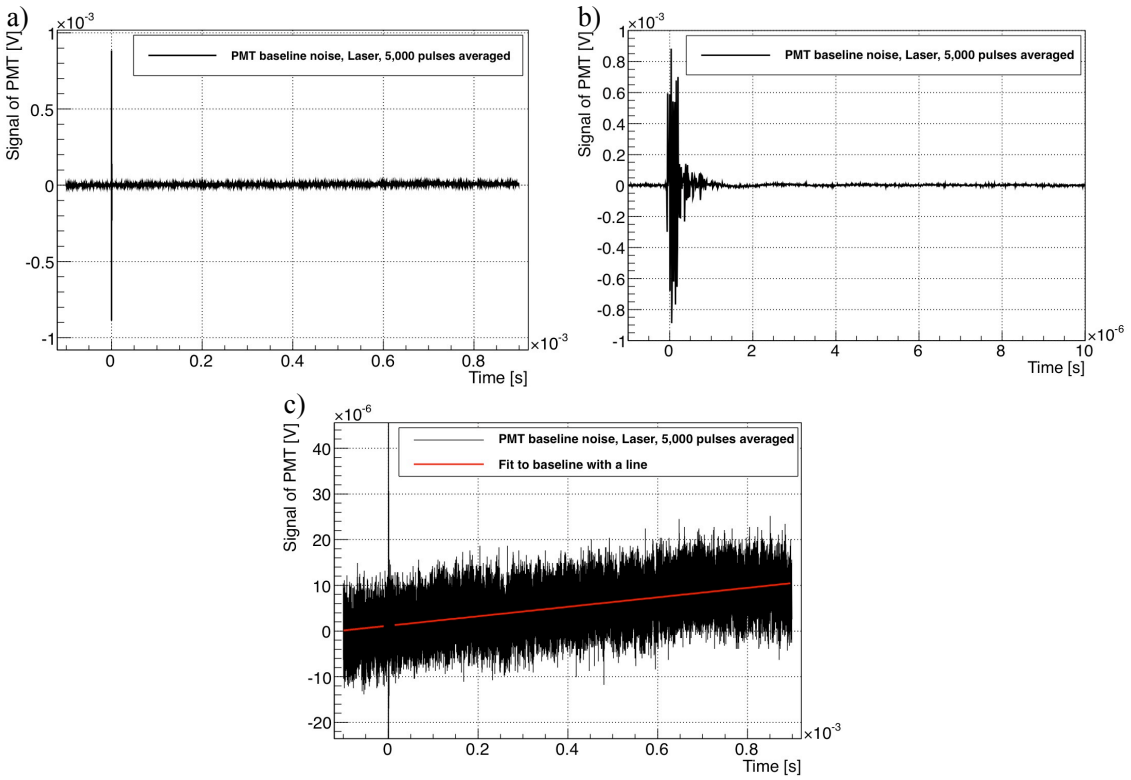

Figure C.6: Empty baseline recorded with the laser-excitation setup (shutter in front of the laser closed) and the PMT operated at -1.5kV. Pulses shown are preprocessed according to section III/4.6.2. Pulses shown in black correspond to the typical baseline recorded in a laser-excitation experiment for 5,000 events averaged. In figure a) the complete vertical (-1mV to $+1$mV) and horizontal axes (-120μs to $+920\mu$s) are shown. In figure b) a zoom (horizontal axis: -1μs to $+10\mu$s) into the noise structure around the time of triggering, $t = 0\mu$s is depicted. In figure c) a zoom (vertical axis: -24μV to $+42\mu$V) into the baseline together with a linear fit to the baseline level (in red) are shown.

analysis. However, the magnitude and trend of the drift varies for each signal recorded (see e.g. figure C.7 b and the corresponding disussion). It can also be observed that this drift does not necessarily follow a linear trend during the recorded time window. In addition, at the end of the recorded time window, the $CaWO_4$ scintillation-light pulses are not necessarily decreased to zero. Thus, an individual determination of the drift of the baseline for each pulse is hardly realizable and would introduce additional uncertainties. Therefore, it is attempted to obtain an estimate of the typical (vertical) magnitude of the drift. Half of this magnitude can then be added to the data as uncertainty of the voltage measurement, $\pm\Delta V_{sys\,BL-PMT\,L}$, due to drifts of the baseline of the PMT[19]. The extent of the drift can be estimated from the gradient m_{BL} of the empty baseline[20] shown in figure C.6. For this purpose, the baseline (data points in a broad region around the noise structure excluded) is fitted with a straight line as shown in figure C.6 c) in red. The

[19]Only half of the total magnitude of the drift is added as error as in the fits of the data in the analysis (section III/5) always a free DC offset level is included. As this parameter is assumed to reflect the correct mean of the drifting baseline, a maximum deflection by half of the total drift magnitude is possible.

[20]This baseline exhibits a typical drift level for measurements conducted with laser excitation.

corresponding uncertainty for each individual pulse can then be determined as half of the fitted gradient $m_{BL-Laser}$ times the respective record length t_{rl} (in s):

$$\begin{aligned} \Delta V_{sys\,BL-PMT\,L} &= \frac{1}{2} \cdot m_{BL-Laser} \cdot t_{rl} \\ m_{BL-Laser} &= 1.036 \cdot 10^{-2} \frac{V}{s} \\ \Delta V_{sys\,BL-PMT\,L} &= 5.182 \cdot 10^{-3} \frac{V}{s} \cdot t_{rl} \end{aligned} \tag{C.2}$$

This uncertainty is used in appendix C.4.6 in the error evaluation of the decay-time measurements for laser excitation.

Baseline in the Ion-Beam Excitation Experiments

A similar examination can be performed for distortions of the baseline in the ion-beam excitation experiments. In these experiments not only different noise conditions were present, but also considerably more pulses were averaged for the data acquisition (typically 50,000 pulses for each measurement). Thus, a different impact of the baseline drift can be expected. For the setup used in the ion-beam experiments, no empty baseline (with active accelerator) was recorded. However, for the qualitative evaluation and quantitative estimation of the baseline drift, data recorded for very small light intensities can be used: The scintillation light of crystal Olga under iodine-beam excitation with the 500nm filter at low temperatures ($\sim$ 25K). The time window chosen for the examination of the baseline ranges from -800μs to 900μs, with the light pulse starting at around 20μs with a (slow) exponential decay time of $\sim 50\mu$s. In this way, there is enough data before and after the light pulse where no signal intensity is expected and thus the baseline level and behavior is visible. The signal was recorded with typical settings as used in all other ion-beam excitation measurements: PMT operating voltage of -1.75kV and 50,000 pulses averaged. In addition, the same measurement was repeated with a reduced number of averaged pulses, 10,000 individual pulses, to clarify the impact of the number of pulses used for averaging. Both pulses are shown together in figure C.7 a) (complete pulses) and b) (zoom into baseline level). In black the signal with 50,000 pulses used for averaging is shown, in red the signal recorded for 10,000 pulses averaged is shown. In figure C.7 c) a fit with a straight line to the baseline of the black pulse (50,000 pulses averaged) is shown in red. In figure C.7 b), clearly the positive influence of the larger number of averaged pulses on the general noise level can be seen: The mean width of the baseline is reduced by a factor of $\sim$ 1.5. Thus, averaging of 50,000 pulses was used in the data acquisition of all other measurements with ion-beam excitation. Besides the statistical fluctuations of the baseline, noise with a frequency of roughly 10kHz can be seen[21]. This noise contribution could be observed for some, but not for all of the ion-beam measurements. The source of this distortion could not be clarified. The impact of this additional noise contribution on the width of the baseline is of course included in the statistical uncertainty of the baseline $\Delta V_{stat-BL}$. Additionally, it can be seen in figure C.7 b) that the trend of the baseline drift can indeed vary - even for the same measurement[22]. Thus, also for ion-beam excitation measurements, the impact of the baseline drift is included into the analysis

[21] In fact, this distortion seems to be a superposition of several frequencies.

[22] The two measurements were performed consecutively. Thus, it is possible, that, e.g. the first 10,000 of the black pulses also exhibited a net downwards drift whereas the other 40,000 pulses showed a net upward drift.

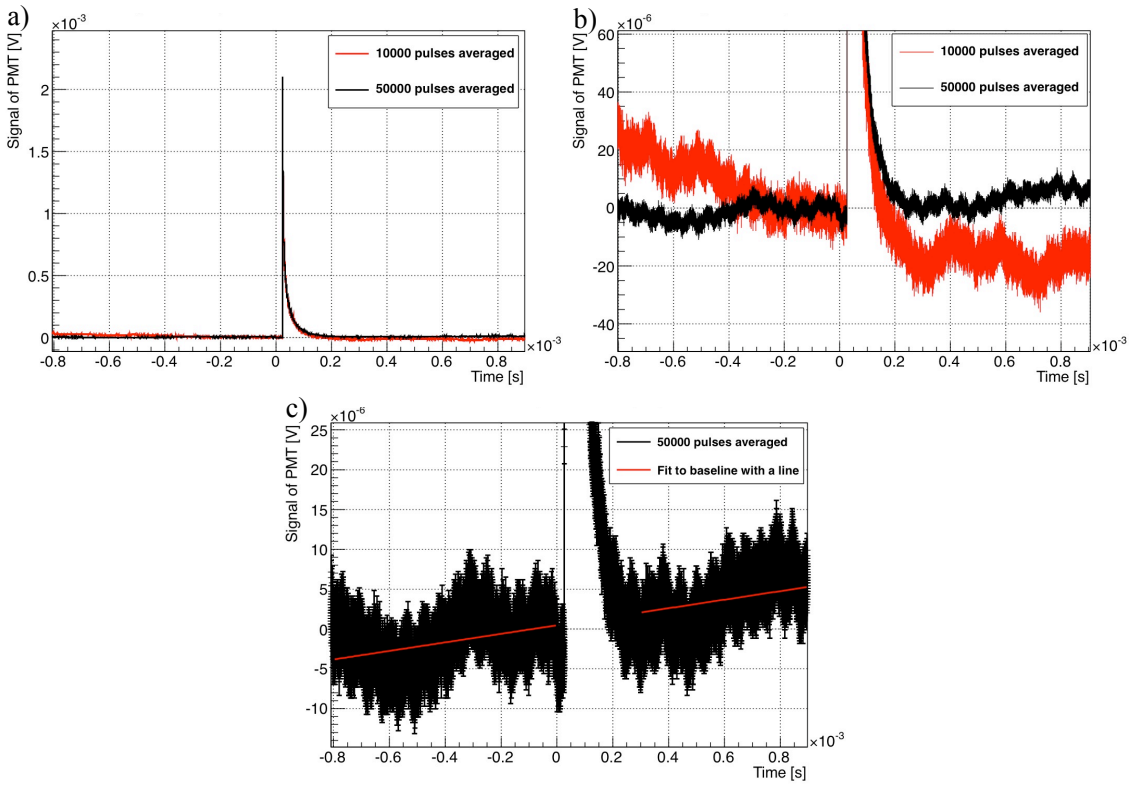

Figure C.7: Scintillation-light pulses of a $CaWO_4$ crystal under iodine-beam excitation recorded with the PMT operated at -1.75kV. Pulses shown are as recorded and preprocessed according to section III/4.6.2. Pulses shown in black correspond to the typical pulses recorded under ion-beam excitation for 50,000 events averaged. Pulses shown in red are averages of only 10,000 events recorded for exactly the same setup. In figure a), the complete vertical (-0.1mV to $+2.4$mV) and horizontal axes (-800μs to $+900\mu$s) are shown. In figure b), a zoom (vertical axis: -46μV to $+61\mu$V) into the baseline of the pulses is depicted. In figure c) a linear fit to the baseline region of the black pulse is shown in red (vertical axis: -15μV to $+25\mu$V).

as an additional systematical error source of the PMT voltage. Determination of the corresponding uncertainty is performed in accordance to the discussion above (for laser excitation). The baseline sample used for this evaluation is the baseline of the measurement shown in figure C.7. This pulse is chosen for two reasons: On the one hand, the baseline is well described (by many samples) due to the small signal height and long record length. On the other hand the magnitude of the baseline drift of this pulse illustrates a typical example for all ion-beam excitation measurements. The corresponding fit with a straight line is shown in red in figure C.7 c). Samples between 0μs and 300μs were excluded due to the non-vanishing light-signal intensity in this region[23]. The resulting uncertainty $\pm\Delta V_{sys\,BL-PMT\,IB}$ for ion-beam measurements (with record length t_{rl}) (in s) is again

[23]This range was chosen as the signal intensity after six decades of decay - calculated for a purely exponential decay - is of the same magnitude as the one-sigma width of the baseline. In reality, the pulse decays a lot faster due to the strong quenching (iodine-beam excitation). Thus, the signal can be expected to be much smaller than the one-sigma width of the baseline for times larger than 300μs.

estimated as half of the gradient m_{BL-IB} of the straight line fit:

$$\begin{aligned} m_{BL-IB} &= 5.364 \cdot 10^{-3} \frac{V}{s} \\ \Delta V_{sys\,BL-PMT\,IB} &= 2.682 \cdot 10^{-3} \frac{V}{s} \cdot t_{rl} \end{aligned} \tag{C.3}$$

The fact that $\Delta V_{sys\,BL-PMT\,IB}$ is smaller than $\Delta V_{sys\,BL-PMT\,L}$ by a factor of ~ 2 is not surprising as ten times more pulses were averaged in the ion-beam experiments. Thus, an enhanced reduction of distortions that are not correlated with the trigger frequency can be expected. $\Delta V_{sys\,BL-PMT\,IB}$ is used in appendix C.4.6 in the error evaluation of the decay-time measurements for laser excitation.

C.4.4 Impulse Reaction and Laser-Pulse Shape

Another source of influence on the detected signal shape is the response function, i.e. the impulse reaction of the detection system, the PMT-base-oscilloscope system. Typically, the impulse reaction $Ir(t)$ can be described by an exponentially modified gaussian distribution, i.e. the convolution of a gaussian with an exponential (see e.g. [121]). The gaussian $G_{TT}(t)$ corresponds to the impact of the electron transit-time t_{TT} of the PMT on the detected signal. This gaussian describes the delay in time t_{TT} of the output signal compared to the input signal (light) and the broadening of the resolution (transit time spread) by σ_{TT} due to variations in t_{TT} for single electrons. The exponential $E_{ER}(t)$ corresponds to the impact of the electronic read-out (ER) circuit on the signal. This exponential describes the exponential decay (or rise[24]) of the output signal by a decay time τ_{el} which is determined by the electronics (the resistance and capacitance) of the output circuit:

$$G_{TT}(t) = \frac{1}{\sqrt{2 \cdot \pi} \cdot \sigma_{TT}} \cdot e^{-\frac{(t-t_{TT})^2}{2 \cdot \sigma_{TT}^2}} \tag{C.4}$$

$$E_{ER}(t) = \Theta(t) \cdot \frac{1}{\tau_{el}} \cdot e^{-\frac{t}{\tau_{el}}} \tag{C.5}$$

$$Ir(t) = G_{TT}(t) * E_{ER}(t) \tag{C.6}$$

where $\Theta(t)$ is the Heavyside function. To determine the impulse reaction of the setup used for decay-time measurements (PMT-base-oscilloscope system), in principle, the detection of a very fast, delta-like light pulse would be optimal. The shape of the recorded signal would be completely determined by the impulse reaction of the system in such a case. However, no light source of such fast, delta-like light pulses was available. Alternatively, a fast light pulse with known time structure can be used. In this case, the shape of the recorded signal is given by the convolution of the light-pulse shape with the impulse reaction of the system. To this end, e.g., the fast laser-light pulses from the N_2 laser employed in the laser-excitation experiments can be used though the pulse shape of the laser-light pulses is not known per se. The shape of the laser-light pulse can be described roughly by a gaussian distribution with a typical width of 1ns $\lesssim \sigma_L \lesssim$ 4ns (compare to the output pulse

[24] Whether τ_{el} corresponds to a rise or decay time depends on the relative magnitude of τ_{el} to the times describing the change in the detected light signal. As an example, a detected light signal with infinitely fast rise and exponential decay time τ_d can be regarded. If $\tau_d > \tau_{el}$, then τ_{el} would correspond to the rise time of the output signal. If, however, $\tau_d < \tau_{el}$, then τ_{el} would correspond to the decay time of the output signal with rise time τ_d.

shape or laser-photon lifetime in [122] and see section III/4.3.1). Thus, determination of the impulse reaction of the system $Ir(t)$ has to be realized simultaneously to the characterization of the laser-pulse shape $L(t)$. Hence, to gain more information about the laser-light pulse-shape, the laser light is not only detected by the PMT, but additionally at the same time by the fast reference detector (Si diode). Due to the characteristics of the reference detector (response time and linearity), the pulse recorded with the Si diode, $SiD(t)$, can be expected to reflect $L(t)$, the laser-light pulse-shape, only. The signal $PMT(t)$ recorded with the PMT is given by the convolution of $L(t)$ with the impulse reaction $Ir(t)$ of the system.

To realize a simultaneous detection of the laser light with the Si diode and the PMT, the setup of the laser-excitation experiments was used. However, instead of a $CaWO_4$ crystal a BaF_2 crystal (of nearly the same size and geometry) was built into the setup. BaF_2 was chosen as the energy of the photons from the laser was not sufficient to produce excitation of the BaF_2 crystal, even in a two-photon excitation process (for details see section III/4.7.3). To completely ensure that only laser light reflected at the BaF_2 crystal is detected with the PMT, the lens focussing the laser beam onto the crystal was removed. Hence, the probability for multiple photon absorption is significantly reduced. In section III/4.7.3 it is shown that in fact only laser light reflected at the BaF_2 crystal reached the PMT. As in the laser-excitation experiments, the Si diode signal was used as trigger signal. However, here this signal is not only used as trigger source, but also for determining the laser-light pulse shape. Hence, special care was taken that the signal of the Si diode did not saturate. For this purpose, the laser light escaping the rear exit of the laser was reflected at two white sheets of paper to reduce its intensity before detecting it with the Si diode. Two measurements with a PMT voltage of -1.5kV and a time-base of 50ns/div (data acquisition) were performed with this setup: The 400nm filter was used in one of these measurements, the 500nm filter was used in the other one. Choosing the high-resolution time-base allows for a detailed examination of the pulse shapes. Like in the laser-excitation measurements, in each measurement 5,000 pulses were averaged. By using the same setup, geometry and settings, it is ensured, that the laser-light pulse-shape and the PMT impulse-reaction determined through this measurement correspond to the pulse shapes and parameters in the $CaWO_4$ decay-time measurements. The data recorded in this way was preprocessed and errors were assigned to the data points according to section III/4.6.2.

The two pulses recorded with the Si diode and the PMT for each filter, can then be fitted simultaneously with the respective functions $SiD(t)$ and $PMT(t)$ using a global χ^2-fit, where the parameters describing $L(t)$ are the same in both functions:

$$L(t) = \frac{L_0}{\sqrt{2\cdot\pi}\cdot\sigma_L}\cdot e^{-\frac{t^2}{2\cdot\sigma_L^2}} \tag{C.7}$$

$$SiD(t) = D_0\cdot L(t-\mu_L)+c_D = \frac{D_0\cdot L_0}{\sqrt{2\cdot\pi}\cdot\sigma_L}\cdot e^{-\frac{(t-\mu_L)^2}{2\cdot\sigma_L^2}}+c_D \tag{C.8}$$

$$\begin{aligned} PMT(t) &= Ir(t)*(P_0\cdot L(t-\mu_L))+c_{PMT} = \\ &= \frac{P_0\cdot L_0}{2\cdot\tau_{el}}\cdot e^{-\frac{t-(\mu_L+t_{TT})}{\tau_{el}}}\cdot e^{\frac{\sigma_L^2+\sigma_{TT}^2}{2\cdot\tau_{el}^2}}\cdot \\ &\quad\cdot\left(1+erf\left(\frac{t-(\mu_L+t_{TT})}{\sqrt{2}\cdot\sqrt{\sigma_L^2+\sigma_{TT}^2}}-\frac{\sqrt{\sigma_L^2+\sigma_{TT}^2}}{\sqrt{2}\cdot\tau_{el}}\right)\right)+c_{PMT} \end{aligned} \tag{C.9}$$

where L_0 is the intensity of the laser-light pulse. The parameters D_0 and P_0 correspond to the detection and conversion efficiencies[25] for the Si diode and PMT, respectively. The parameter μ_L reflects the shift of the laser signal detected with the Si diode relative to the zero of time due to the trigger walk introduced by the rising-edge trigger. The constants c_D and c_{PMT} are included in the fit functions to account for possible remaining DC offsets of the signals. As the absolute light intensity for one laser pulse L_0 is not known, the quantities $(D_0\cdot L_0)$ and $(P_0\cdot L_0)$ are each combined into one respective fit parameter in the fit routine.

The data recorded with the 400nm filter is used for the determination of the parameters describing $L(t)$ and $Ir(t)$. The PMT pulse recorded with the 500nm filter exhibits a considerably smaller pulse height[26] and thus a much worse signal-to-noise ratio. Hence, the latter measurement is only used as a cross-check. The parameters describing the signal shapes in the fit of the 500nm pulses are fixed: The values for τ_{el}, σ_L and σ_{TT} are adopted from the 400nm fit and fixed. Only the parameters describing the amplitudes, timing characteristics and DC offsets, are left as free fit parameters. In figure C.8, the pulses recorded with the 400nm filter are shown in black (upper panel: signal of the Si diode, lower panel: signal of the PMT), the respective fits according to equations C.8 and C.9 are shown in blue and red, respectively.
It can be seen that the diode signal is well described by the symmetric gaussian[27] and that the PMT signal is well described by the exponentially modified gaussian. This is of course

[25] This efficiency includes, e.g., for the PMT signal, the probability of the laser light being reflected at the BaF_2 crystal into the solid angle observed with the PMT, the filter transmissions and all PMT and output-circuit conversion efficiencies for laser-light photons. For a discussion of these efficiencies for $CaWO_4$ scintillation light see appendix C.11. As however, all these parameters are not known and determined for the wavelength of the laser light, they are combined into one free fit parameter.

[26] The wavelength of the laser light (337nm) is farther away from the wavelength window of the 500nm filter (475-525nm) than from the wavelength window of the 400nm filter (375-425nm). For the characterization of the filters and the laser light see sections III/4.2.4 and III/4.7.3. Thus, it is expected that the laser light in the measurement with the 500nm filter is more heavily suppressed and thus leads to a smaller pulse height in comparison to the measurement with the 400nm filter.

[27] This confirms the assumption that the influence of the Si diode impulse-reaction can in fact be neglected: If the impulse reaction of the Si diode would be significant, e.g., a non-symmetric pulse due to a delay introduced by the electronic output circuit of the Si diode should be visible. Due to the fast rise time specified for the Si diode no additional broadening has to be expected.

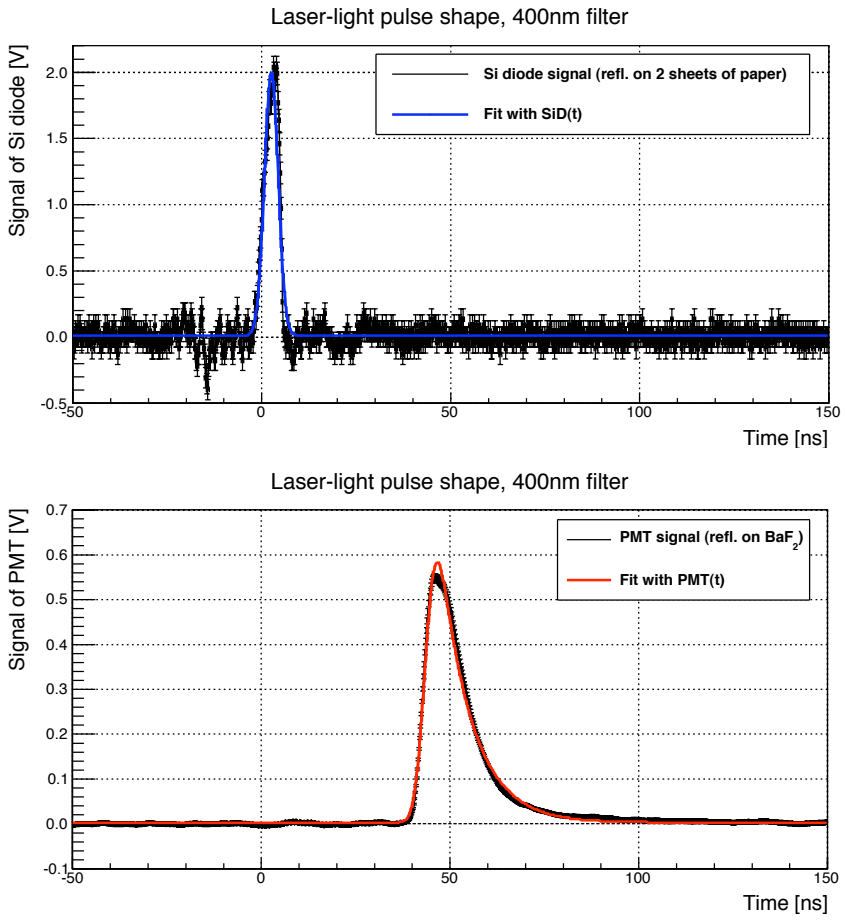

Figure C.8: Pulses recorded in the measurement performed for the characterization of the impulse reaction of the PMT-base-oscilloscope setup and the laser-light pulse shape. Upper panel: Pulse recorded with the Si diode. Lower panel: Pulse recorded with the PMT. In blue and red the respective fits with $SiD(t)$ and $PMT(t)$ are shown.

also reflected in the reduced χ^2 of the combined fit. The results of the fits are presented in table C.2:
From the fit of the data obtained with the 400nm filter, the parameters describing the impulse reaction (σ_{TT} and τ_{el}) and the laser-light pulse shape (σ_L) are determined with high accuracy. As discussed above, the data of the measurement with the 500nm filter has subsequently be used to test the validity of the determined parameter values[28]. As can be seen from the fit data and the achieved $\chi^2 = 0.72$ for the 500nm data (see table C.2), also this fit delivers an excellent description of the recorded pulse shapes.

Additionally, the value of $\sigma_{TT} = 1.278$ns, the transit-time spread determined with the fit to the 400nm data, can be compared to the value for the single-electron FWHM specified

[28]For this test, as well as in the fits of other data recorded with the PMT system (laser and ion-beam excitation), the timing parameters, μ_L and t_{TT}, are not adopted: In the different experiments the settings for the trigger (threshold) as well as the trigger source were not the same (see appendix C.3 and sections III/4.3 and 4.4) and thus different timing characteristics are expected.

fit parameter		400nm results	500nm results
red. χ^2		1.46	0.72
$(D_0 \cdot L_0)$	[Vs]	9.004 ± 0.238	9.061 ± 0.149
μ_L	[ns]	2.606 ± 0.067	2.601 ± 0.059
σ_L	[ns]	1.803 ± 0.044	**1.803**
c_D	[mV]	4.957 ± 1.578	3.022 ± 1.298
$(P_0 \cdot L_0)$	[Vs]	7.751 ± 0.016	0.759 ± 0.004
σ_{TT}	[ns]	1.278 ± 0.069	**1.278**
t_{TT}	[ns]	41.16 ± 0.07	38.54 ± 0.07
τ_{el}	[ns]	8.300 ± 0.024	**8.300**
c_{PMT}	[mV]	1.090 ± 0.036	0.152 ± 0.030

Table C.2: Results of the simultaneous pulse-shape fits to the signals of the Si diode and the PMT.

by the producer of the PMT: $\text{FWHM}_{s-el} = 3\text{ns} \Rightarrow \sigma_{s-el} = \frac{1}{2\cdot\sqrt{2\cdot ln2}} \cdot \text{FWHM}_{s-el} = 1.274\text{ns}$. This value is in excellent agreement with the fit value. Comparing the value for the width of the laser-light pulse, $\sigma_L = 1.803$ns, to typical widths specified in literature (see e.g. [122], laser-photon decay time = 1.21ns) reveals that also the value for this parameter is within a reasonable range. The value determined for $\tau_{el} = 8.300$ns is larger by a factor of 2 to 4 than decay times usually determined for the electronic output-circuit of a typical PMT setup (see e.g. [121]). However, this can be attributed to the fact that the PMT used in this work is operated with a modified base (with larger capacitors) to enable current-mode operation. Thus, also this value can be regarded as being reasonable.

Thus in the following, the parameters describing the impulse reaction and the laser-pulse shape are assumed to be fixed to the values determined in table C.2. These values (numbers in bold in table C.2) are used as fixed parameters in the fits of the scintillation-light pulses of the $CaWO_4$ crystals (see sections III/5.2 and III/5.3):

$$\sigma_{TT} = 1.278\text{ns} \tag{C.10}$$

$$\tau_{el} = 8.300\text{ns} \tag{C.11}$$

$$\sigma_L = 1.803\text{ns} \tag{C.12}$$

C.4.5 Data Acquisition with the Storage Oscilloscope: Settings and Measurement Uncertainties

The vertical resolution of the oscilloscope is specified as 8 bit (with activated enhanced resolution up to 11 bit are possible). The minimum time resolution is specified as 200ps per sample, i.e. 5GS/s (Giga-samples per s). Dependent on the signal to be measured, different settings were used: The vertical range was always chosen such as to maximize the available resolution, i.e. the smallest possible range which still contained the complete signal was used. Hence, the chosen vertical range was not fixed to the same value for all measurements. The horizontal resolution can be chosen in form of standardized times per division where the total record length comprises ten of these divisions. For room temperature measurements where the decay time of the $CaWO_4$ scintillation light is $\sim 9\mu$s, typically recording with a horizontal resolution of 10μs/div was used. For the low-temperature measurements where the decay time of the $CaWO_4$ scintillation light is

between 50μs and 100μs, typically recording with a horizontal resolution of 100μs/div was used. For the laser-excitation measurements, additionally measurements with enhanced horizontal resolutions were performed[29] to allow a more detailed investigation of the pulse shape. At room temperature a second measurement with 1μs/div, at low temperature two additional measurements with 1μs/div and 10μs/div were recorded.

Vertical and timing resolutions of the acquired data, ΔV_{res} and Δt_{res}, depend on the chosen settings, the record length and the vertical range. The corresponding systematic uncertainties due to the finite resolution of the data-acquisition process with the oscilloscope are assumed to amount to:

$$\Delta V_{sys\,Osc} = \frac{1}{2} \cdot \Delta V_{res} \tag{C.13}$$

$$\Delta t_{sys\,Osc} = \frac{1}{2} \cdot \Delta t_{res} \tag{C.14}$$

Determination of the corresponding uncertainties is realized automatically for each recorded signal individually in the data-preprocessing procedure (see appendix C.4.6 and section III/4.6).

The timing resolution, Δt_{res}, of the acquisition for different used record lengths is presented in table C.3.

time per division	total record length	Δt_{res}
1μs/div	10μs	0.2ns
10μs/div	100μs	1ns
100μs/div	1,000μs	10ns
200μs/div	2,000μs	20ns

Table C.3: Timing resolutions of the data acquisition for different settings of the record length.

Due to the different pulse heights obtained for the different excitations and different temperatures, the chosen vertical range was optimized individually in each measurement. In table C.4, examples for typical vertical resolutions ΔV_{res} realized in the different measurements are presented.

excitation	temperature	ΔV_{res}
laser	room temperature	$3.426 \cdot 10^{-5} V$
laser	$\sim 20K$	$1.713 \cdot 10^{-5} V$
ion beam	room temperature	$0.034 \cdot 10^{-5} V$
ion beam	$\sim 20K$	$0.034 \cdot 10^{-5} V$

Table C.4: Typical vertical resolutions of the data acquisition for different excitations and temperatures.

[29] For the ion-beam excitation experiments, this could not be realized due to the limited beamtime at the accelerator.

C.4.6 Decay-Time Spectra: Error Evaluation

In the analysis of the different decay-time spectra recorded with the PMT-oscilloscope system, different error sources have to be taken into account.

For the time-coordinate of the data points, only the systematic uncertainty due to the finite resolution of the data acquisition is considered. Thus, in the following, the error of the the time coordinate Δt is equated with the corresponding systematic uncertainty (see appendix C.4.5):

$$\Delta t = \Delta t_{sys\,Osc} = \frac{1}{2} \cdot \Delta t_{res} \tag{C.15}$$

For the error of the voltage-coordinate of the data points, the following systematical uncertainties, as discussed in appendices C.4, are considered:

- The systematical uncertainty in the linearity of the PMT response[30] for each data point i with amplitude V_i:

$$\Delta V_{sys\,Lin-PMT,\,i} = 1.44\% \cdot V_i$$

- The systematic uncertainty for each data point due to a possible drift of the baseline for a measurement with record length t_{rl} (in s):

$$\begin{aligned} \Delta V_{sys\,BL-PMT\,L} &= 5.182 \cdot 10^{-3} \frac{V}{s} \cdot t_{rl} \quad \text{laser-excitation} \\ \Delta V_{sys\,BL-PMT\,IB} &= 2.682 \cdot 10^{-3} \frac{V}{s} \cdot t_{rl} \quad \text{ion-beam excitation} \end{aligned}$$

- The systematical uncertainty for each data point due to the finite resolution ΔV_{res} of the data acquisition:

$$\Delta V_{sys\,Osc} = \frac{1}{2} \cdot \Delta V_{res}$$

These systematical uncertainties are added linearly (worst-case estimation) to obtain the total systematic error ΔV_{sys} for the voltage coordinate of each data point.

The statistical uncertainty ΔV_{stat} due to statistical fluctuations of the data points can be estimated from an empty pre-trigger region (baseline) and is performed individually for each measurement (see discussion in appendix D.1). For this purpose, care was taken that in all measurements there exists a region before the start of the pulse where the signal intensity of the preceding pulse has decreased to zero. The data points in this region cannot only be used for the estimation of the statistical uncertainty, but also for the definition of the baseline level of the pulse. In the laser-excitation measurements, the position of the trigger in the recorded time window was always fixed to exactly one division, i.e. one tenth of the total record length. In the ion-beam excitation measurements, the length of the pre-trigger region has to be chosen individually for each pulse. In some measurements, the decay of the preceding pulse can be seen at the beginning of the recorded time window. Thus, a baseline region (before the onset of the (triggering) pulse) where no signal

[30] As discussed in appendix C.4.2, this error reflects uncertainties in the PMT response up to voltages of ~ 0.9V.

intensity of the preceding pulse is left is defined individually for each pulse. Typically, the length of this region amounts to $\sim 10\%$ of the total record length.

Thus, the region of the recorded signal chosen for baseline determination always contains $\sim 2,500$ to 10,000 data points. The data points in this region represent the averaged baselines (5,000 or 50,000 pulses were averaged, see appendix C.4.5) of the recorded pulses. By applying the averaging function of the oscilloscope, the statistical fluctuations of the amplitude (voltage) of the data points are already largely suppressed. The remaining fluctuations represent the remaining statistical uncertainty of the voltage measurement. To determine the remaining statistical uncertainty for each recorded signal, a histogram (bins of 0.2μV) of the voltage-coordinates of the baseline is created and fitted with a gaussian distribution. The value determined as 1σ width of this gaussian can be taken as an estimate for the statistical uncertainty ΔV_{stat} for each data point in this measurement[31]. The order of magnitude of the statistical uncertainties obtained in this way is $\sim 1 \cdot 10^{-4}$V for the laser-excitation measurements and $\sim 2 \cdot 10^{-6}$V for the ion-beam excitation measurements.

To obtain the square of the total uncertainty $(\Delta V)^2$ of the voltage measurement, the systematic and statistical uncertainties of each data point have to be added quadratically:

$$\Delta V = \sqrt{(\Delta V_{sys})^2 + (\Delta V_{stat})^2} \tag{C.16}$$

C.5 Optical Filters: Relative Transmissions

To determine the relative amount of $CaWO_4$ scintillation light passing through the filters, the relative transmissions of the filters are needed. The experimental determination of the filter transmissions was realized with the help of the spectrometer and the halogen lamp already used for the calibration of the spectrometer (see appendix C.2.2). After recording the spectrum of the halogen lamp with the spectrometer, as described in appendix C.2.2, the measurement was repeated twice where in each measurement one of the filters was positioned between the lamp and the spectrometer. For all three resulting spectra, the remaining DC offset is determined via a background histogram (as discussed in appendix C.2.2) and subtracted from the data. The spectra obtained in this way are shown in figure C.9 a): The spectrum of the halogen lamp recorded without filter is shown in black, the spectra recorded with the filters are shown in blue (400nm) and green (500nm), respectively. By dividing the spectra measured with filters by the spectrum measured without filter, the respective relative transmissions, as depicted in figure C.9 b), can be obtained: The relative transmission of the 400nm filter is shown in blue, the relative transmission of the 500nm filter is shown in green. From this measurement, the excellent transmission ($\sim 90\%$ to 95%) of the filters in their respective, sharply delimited bandpass regions can be seen. The slightly varying transmission in the bandpass regions can be attributed to the composition of the filters (multi-layer interference filters).

With these relative filter transmissions the relative amount of $CaWO_4$ scintillation light passing through each filter can be estimated. To this end, the scintillation-light spectra

[31] This estimation is well-motivated as the number of data points contained in the histogram of the baseline is large, see appendix D.1.

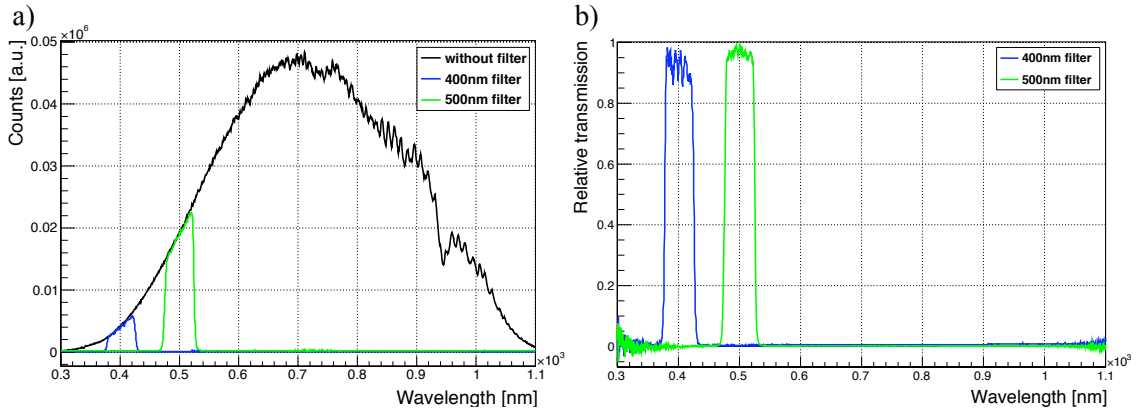

Figure C.9: Determination of the relative filter transmissions: In figure a), the halogen-lamp spectrum without filter (black line), with the 400nm filter (blue line) and with the 500nm filter (green line), each recorded with the spectrometer, are shown. In figure b), the relative transmissions of the 400nm filter (blue) and of the 500nm filter (green) are shown.

of the crystal Olga under oxygen-beam excitation[32] were used. The spectra recorded at room temperature ($\sim$ 298K) and at low temperature ($\sim$ 20K) are preprocessed according to section III/4.6. Spectra at both temperatures are used as the shape of the scintillation-light spectrum of $CaWO_4$ changes with temperature. These spectra are shown as black lines in figure C.10 a) and b), respectively[33]. Multiplying the scintillation-light spectra with the relative transmissions yields the partial spectra that are expected to pass trough the filters. These calculated partial spectra are shown as blue (400nm filter) and green (500nm) lines in figure C.10 a) and b), respectively. The relative amount of scintillation light passing through one of the filters can then be determined (for each temperature) by integrating the corresponding partial and total spectra and normalizing the values using the integral of the respective total spectrum[34].

In the following, the estimates of the relative filter transmissions calculated for 298K are used for all measurements at room temperature. This means that these values are also used if the other $CaWO_4$ crystal was investigated or if the temperature during the measurement was not exactly 298K. Likewise, the values determined for the relative filter transmissions at 20K are used for all measurements at low temperatures. This approach is motivated by the fact that only a rough estimation of the detection efficiency of the setup is pursued. For this reason, no error estimations were performed either.

The values determined with this procedure can be found in table 4.2 in section III/4.2.4.

[32] As shown in section III/4.7.1, the scintillation-light spectra recorded under different excitations at the same temperature exhibit a very similar shape. Thus, for the determination of the relative filter-transmissions of the $CaWO_4$ scintillation light the spectrum exhibiting the best statistics can be used.

[33] The outlying data point (spike) of the scintillation-light spectrum (figure C.10 a, recorded at 298K) at $\sim$ 605nm is an artifact due to one pixel of the detector of the spectrometer.

[34] The range used for integration was 300 to 700nm, representing the wavelength range where scintillation light from $CaWO_4$ crystals can be expected.

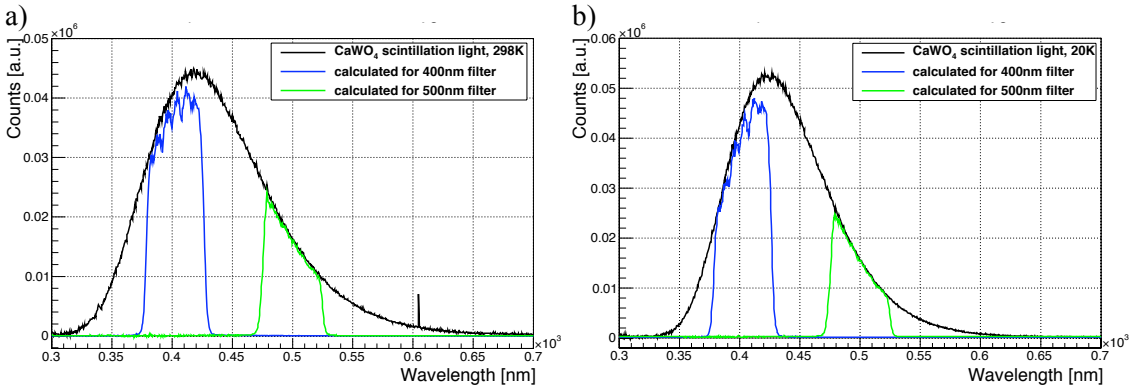

Figure C.10: Scintillation-light spectra of the crystal Olga obtained for oxygen-beam excitation (black lines, spectra are multiplied with the spectrometer correction-function and the DC offset is subtracted, see section III/4.6). Additionally, the respective **calculated** partial spectra expected for light transmission through the 400nm filter (blue line) and the 500nm filter (green line) are shown. Figure a): Spectrum recorded at 298K and respective calculated filter transmissions. Figure b): Spectrum recorded at 20K and respective calculated filter transmissions.

C.6 Parameters used for the Temperature Determination of the $CaWO_4$ Crystal

The $CaWO_4$ crystal used in [41] was of course not the same as that used in the measurements presented here and, even more importantly, the decay times used for the model in [41] were determined by a two-exponential fit to light pulses induced by α particles. Thus, the parameters of the model determined in [41] do not necessarily have to be transferable to the experiments presented here. Nonetheless, the energy barriers ΔE and D determined in [41] should be reliable as they correspond to temperature-related changes in the observed decay time. The temperature where such changes in the decay-time spectrum occur should be comparable even if the decay-time determination is different. In addition, the identification of the parameter k_1 as the radiative decay rate of the energetically lowest-lying level and thus as the observable decay time at very low temperatures ($\lesssim$ 5K) is in accordance with the model developed here[35]. Thus, to compile a three-level model for the used crystal and setup, the model parameters k_1, k_2 and K have to be determined. To achieve this, in principle only three measurements of the (slow) exponential decay time $\tau_{\mathrm{meas}}(T)$ at three different temperatures with "perfectly" determined temperatures are needed. At best three measurements as presented in the following should be performed:

- For the determination of k_1, a measurement at a temperature $T_1 \lesssim$ 5K would be ideal. For such temperatures, only the radiative recombination from the energetically lowest-lying level contributes to the observed decay time:

$$k_1 \approx \frac{1}{\tau_{\mathrm{meas}}(T_1)} \tag{C.17}$$

[35] Just as in the three-level model in [41], also in the model developed in this work, the observable decay time (for blue light) at very low temperatures ($\lesssim$ 5K) is identified with the only remaining possibility for de-excitation of STEs, the radiative decay from the energetically lowest-lying level (see section III/3.1.3).

- For the determination of k_2, a measurement at a temperature T_2 between $\sim$ 5K and $\sim$ 200K would be ideal. For such temperatures only the model parameter k_2 is an unknown for the calculation of the decay time (the magnitude of the contribution by the parameter K is negligible, compare section III/2.2.1 and figure 2.13). Thus, from equation 4.2 (neglecting the second term) follows

$$k_2 \approx \left(\frac{1 + e^{-\frac{D}{k_B \cdot T_2}}}{\tau_{\mathrm{meas}}(T_2)} - k_1 \right) \cdot e^{\frac{D}{k_B \cdot T_2}} \tag{C.18}$$

- For the determination of K, a measurement at a temperature T_3 between $\sim$ 250K and $\sim$ 300K is needed. For such temperatures, the only remaining unknown is then the parameter K:

$$K = \left(\frac{1}{\tau_{\mathrm{meas}}(T_3)} - \frac{k_1 + k_2 \cdot e^{-\frac{D}{k_B \cdot T_3}}}{1 + e^{-\frac{D}{k_B \cdot T_3}}} \right) \cdot e^{\frac{\Delta E}{k_B \cdot T_3}} \tag{C.19}$$

Thus, another possibility to determine the crystal temperature for such measurements has to be found. In the following, the procedure that was used to determine the temperature for the two latter measurements (at $\sim$ 20K and at room temperature) is described.

The basic idea is to conduct two dedicated experiments (warm and cold each), for which it can be assumed that the high temperature during the measurement is the same in both experiments, as well as that the low temperature of the cryocooler is the same in both experiments[36]. For the first measurement, the $CaWO_4$ crystal Olga was installed and excited by the laser (unquenched) at room temperature and at low temperature, so that the respective decay time of the blue luminescence light can be determined to good accuracy. In the second measurement, a thermometer with known calibration[37] was built into the setup instead of the $CaWO_4$ crystal (onto the head of the cryocooler) and read out at room temperature and low temperature. Due to the position of the thermometer, it can be assumed that the temperature of the thermometer corresponds to the temperature of the crystal in the respective first measurement. To achieve concurrent temperatures in both measurements, several hours of cooling and equilibrating were allowed for[38]. With these experiments, the temperature during the two laser-excitation measurements of the crystal Olga with the 400nm filter are determined as 297.7K and 20.2K. Of course, uncertainties in the determination of the temperature are expected due to several factors, e.g. the thermometer calibration, the assumption of the exact concurrent temperatures of the cryocooler or the uncertainty in the resistance measurement of the thermometer. These uncertainties can easily amount to 1 to 2K [39]. In the following, these two temperatures are

[36] Such experiments were performed at the end of the measurement campaign as then the low temperature reached by the cryocooler could be assumed to be the same for every cooldown (see section III/4.2.6).

[37] A speer thermometer (carbon resistance thermometer) with four-point read-out with a resistance bridge was used.

[38] In the ion-beam experiments, such long equilibrating times could not be allowed for due to the limited availability of the accelerator for these measurements.

[39] This error was estimated by comparing the determined temperature of 20.2K to the temperature that would be determined on the basis of the three-level model with the parameters from [41]. For this comparison, the decay time of the scintillation light in the laser-excitation measurement at low temperatures was taken and the corresponding temperature was calculated with equation 4.2 to be 22.83K (parameters of [41]). Of course, this temperature also includes uncertainties due to the temperature and decay-time determination in [41].

considered as fixed-points of the temperature scale and all other temperatures determined with equation 4.2 have to be regarded as relative to these temperatures.

The corresponding decay times of the recorded scintillation-light pulses (crystal Olga, laser excitation with 400nm filter) are determined with high accuracy by fits to the data, as described in section III/5.2: $\tau_{\text{meas}}(297.7\text{K}) = 9.1192 \pm 0.0005\mu\text{s}$ and $\tau_{\text{meas}}(20.2\text{K}) = 75.0197 \pm 0.0071\mu\text{s}$. Errors are statistical errors from the chi-square fit (see section III/5.2). With these results for two temperatures, the decay-time measurement at a third, fixed, preferably very low temperature is the only missing information.

However, in the allotted beam time no temperatures below $\sim 20\text{K}$ could be reached and no third measurement at another precisely determined temperature could be conducted. Therefore, the parameter k_1, specifying the decay time at very low temperatures, has to be adopted from a reference: In [41], the decay time at 20mK is determined with a two-exponential fit to $500 \pm 60\mu\text{s}$ (under γ-excitation) and to $340 \pm 40\mu\text{s}$ (under α-excitation). In [54], a more elaborate fit to a scintillation-light pulse recorded at 6K (under oxygen-ion excitation) is performed, yielding a (slow) exponential decay time of $560 \pm 7\mu\text{s}$. This value is assumed to be more reliable and additionally lies in the upper range of the error margin of the decay time determined in [41] under γ-excitation at 20mK. Thus, it is assumed that the fact, that in [54] the measurement was performed at 6K, compared to the anticipated range of $\lesssim 5\text{K}$, is not of any importance. Hence, in the following for temperatures $\lesssim 5\text{K}$ an exponential decay time of $\tau_{\text{meas}}(T \lesssim 5\text{K}) = 560 \pm 7\mu\text{s}$ is adopted.

With these three decay times and corresponding temperatures, the parameters of the three-level model for the used crystal and setup can be calculated with the equations C.17, C.18 and C.19. With D and ΔE adopted from [41], a complete set of parameters for the model is obtained:

$$\begin{aligned} k_1 &= 1.79 \cdot 10^3 \text{s}^{-1} \\ k_2 &= 1.58 \cdot 10^5 \text{s}^{-1} \\ K &= 9.51 \cdot 10^9 \text{s}^{-1} \\ \text{D} &= 4.40 \cdot 10^{-3} \text{eV} \\ \Delta\text{E} &= 0.320\text{eV} \end{aligned} \tag{C.20}$$

This model allows for the determination of the temperature of the crystal Olga in a measurement if the slow exponential decay time of the scintillation light is determined. However, it also allows to predict the observable (slow) decay time for the crystal Olga at different temperatures. This model, with the parameters as determined for crystal Olga (see equations C.20) is also used for the determination of the temperature of crystal Philibert (for a short discussion, see appendix C.8.3).

C.7 Solid Angle of Observation with the PMT

C.7.1 Two-Photon Excitation: N_2 Laser

In the employed setup for the laser-excitation measurements, the restriction of the solid angle of observation Ω_L is dominated by the size of the aperture (radius $r_{ap} = 2.0\text{mm}$) of the plastic tube in front of the PMT (distance of the aperture to the center of the

crystal $r_{d,ap-c} = 3.5$cm). In order to enable the estimation of the size of the solid angle, the $CaWO_4$ crystal is approximated as point-like light-source. Under this assumption, the solid angle of observation in the laser-excitation experiments is simply given by:

$$\Omega_L = \frac{r_{ap}^2 \cdot \pi}{4 \cdot r_{d,ap-c}^2 \cdot \pi} = \frac{2^2}{4 \cdot 35^2} = 8.2 \cdot 10^{-4} \tag{C.21}$$

C.7.2 Ion-Beam Excitation: Tandem Accelerator

In the setup used for the ion-beam excitation, the limiting component of the solid angle observable with the PMT is the size of the spectral filters (radius $r_{fi} = 1.25$cm). The respective filter was installed at a distance of $r_{d,fi-c} = 18$cm to the center of the crystal. Again, assuming the $CaWO_4$ crystal to correspond to a point-like light source, the solid angle of observation Ω_{IB} under ion-beam excitation, can be estimated to :

$$\Omega_{IB} = \frac{r_{fi}^2 \cdot \pi}{4 \cdot r_{d,fi-c}^2 \cdot \pi} = \frac{1.25^2}{4 \cdot 18^2} = 1.2 \cdot 10^{-3} \tag{C.22}$$

C.8 Crystal-Temperature Assignment: Determination of the Slow Decay Time

To determine the temperature of the crystals during the measurements with ion-beam and laser excitation, the respective purely exponential decay time is needed (see appendix C.6). This time is determined separately for each measurement with a fit to each individual pulse ($\mathbf{O1_{PMT}}$ to $\mathbf{O12_{PMT}}$ and $\mathbf{P1_{PMT}}$ to $\mathbf{P6_{PMT}}$, see section III/4.5).

C.8.1 Measurements with Laser Excitation

For the pulses recorded with laser excitation, the purely exponential decay time is a free parameter of the fits of the *unquenched model* to the pulses (see section III/5.2.1). Hence, the purely exponential decay time is taken from the corresponding fit results (see section III/5.2.2). For a summary of the determined exponential decay times and the corresponding temperatures (derived with equation 4.2 in section III/4.2.6), see table C.5 in appendix C.8.3.

C.8.2 Measurements with Ion-Beam Excitation

For the pulses recorded with ion-beam excitation, in principle, the purely exponential decay time can also be determined as a free parameter of the fit of the *quenched model* to the data (see sections III/5.3). However, as these fits are numerically very extensive, the number of free parameters had to be reduced. Therefore, and to determine the temperature of the crystal without using the quenched model fit, the purely exponential decay time of the pulses recorded for ion-beam excitation was fitted in an independent procedure. The following method and fit function were applied:

- The developed model for the scintillation-light generation and quenching predicts that the purely exponential decay time is independent of the used excitation mode and only dependent on the temperature of the crystal (see section III/3.3.1). This

purely exponential decay is visible at the end of the pulse (i.e. for large times, compare, e.g., figure 4.16 in section III/4.7.2).

- To determine the purely exponential decay time, the same pulse model as used for the pulses recorded with laser excitation (see, e.g., equation 5.13 in section III/5.2.1) is employed to fit the purely exponential part of the pulses recorded for ion-beam excitation[40]. Of course, the part containing the shape of the reflected laser light was not included in the fit.
- The time window for the fits of the unquenched pulse model to the pulses obtained with ion-beam excitation has to be determined: The time window in which the impact of the light quenching is visible (see description and figure C.16 in appendix C.9.2) has to be rejected for this fit.
- As not only the determination of the underlying purely exponential decay time was strived for, but also the determination of the baseline level of the individual pulses with this fit, the **baseline region** (from $\mathbf{t_{min}}$ to $\mathbf{t_{max}}$) and the **exponential fit region** (from $\mathbf{t_{min\,Exp}}$ to $\mathbf{t_{max}}$) were included in the fit (regions as defined and determined in appendix C.9.2).

The following fit function (compare to, e.g., equation 5.13 in section III/5.2.1) was used to fit the different light-pulse shapes $L_{IB,\,CWL,\,T}(t)$ recorded with ion-beam excitation with:
- the two different ion beam: $IB = {}^{127}I$ or $IB = {}^{16}O$
- the two different spectral filters: $CWL = 400\text{nm}$ or $CWL = 500\text{nm}$
- at the two different temperatures: $T = RT$ for the room-temperature measurements or $T = LT$ for the low-temperature measurements

$$
\begin{aligned}
L_{IB,\,CWL,\,T}(t) = {} & \frac{DE_{IB,\,CWL,\,T}\cdot N_{0,\,ex}}{2\cdot\tau_{rad}(T)}\cdot \\
& \cdot\left[\left(1+\frac{R_{dr}(CWL)}{\frac{\tau_d}{\tau_{dr}(T,CWL)}-1}\right)\cdot\frac{1}{1-\frac{\tau_{el}}{\tau_d}}\cdot e^{-\frac{t-\mu}{\tau_d}}\cdot e^{\frac{\sigma_{IB}^2+\sigma_{TT}^2}{2\cdot\tau_d^2}}\cdot\right. \\
& \qquad\left.\cdot\left\{1+erf\left(\frac{t-\mu}{\sqrt{2\cdot(\sigma_{IB}^2+\sigma_{TT}^2)}}-\frac{\sqrt{\sigma_{IB}^2+\sigma_{TT}^2}}{\sqrt{2}\cdot\tau_d}\right)\right\}-\right. \\
& -\frac{R_{dr}(CWL)}{1-\frac{\tau_{dr}(T,CWL)}{\tau_d}}\cdot\frac{1}{1-\frac{\tau_{el}}{\tau_{dr}(T,CWL)}}\cdot e^{-\frac{t-\mu}{\tau_{dr}(T,CWL)}}\cdot e^{\frac{\sigma_{IB}^2+\sigma_{TT}^2}{2\cdot\tau_{dr}(T,CWL)^2}}\cdot \\
& \qquad\cdot\left\{1+erf\left(\frac{t-\mu}{\sqrt{2\cdot(\sigma_{IB}^2+\sigma_{TT}^2)}}-\frac{\sqrt{\sigma_{IB}^2+\sigma_{TT}^2}}{\sqrt{2}\cdot\tau_{dr}(T,\,CWL)}\right)\right\}+ \\
& +\left\{\frac{R_{dr}(CWL)}{1-\frac{\tau_{dr}(T,CWL)}{\tau_d}}\cdot\frac{1}{1-\frac{\tau_{el}}{\tau_{dr}(T,CWL)}}-\left(1+\frac{R_{dr}(CWL)}{\frac{\tau_d}{\tau_{dr}(T,CWL)}-1}\right)\cdot\frac{1}{1-\frac{\tau_{el}}{\tau_d}}\right\}\cdot e^{-\frac{t-\mu}{\tau_{el}}}\cdot e^{\frac{\sigma_{IB}^2+\sigma_{TT}^2}{2\cdot\tau_{el}^2}}\cdot \\
& \qquad\left.\left.\cdot\left\{1+erf\left(\frac{t-\mu}{\sqrt{2\cdot(\sigma_{IB}^2+\sigma_{TT}^2)}}-\frac{\sqrt{\sigma_{IB}^2+\sigma_{TT}^2}}{\sqrt{2}\cdot\tau_{el}}\right)\right\}\right]+c_{BL}
\end{aligned}
\tag{C.23}
$$

[40] This implies that the impact of the rising part of the pulse is also included in the fit of the purely exponential decay time for the pulses recorded with ion-beam excitation (compare pulse model and discussion in section III/5.2.1).

with the free fit parameters:

τ_d	decay time of the scintillation light (corresponding to the lifetime of the excitons)
c_{BL}	possible remaining DC offset of the baseline level
$N_{0,\,ex}$	number of excitons initially produced

and the fixed parameters:

$\tau_{rad}(T)$	radiative decay time of the excitons (see section III/3.3)
$R_{dr}(CWL)$	fraction of scintillation light with a delayed rise (see section III/5.2.1)
$\tau_{dr}(T,\, CWL)$	delayed rise time of the fraction $R_{dr}(CWL)$ of the scintillation light (see section III/5.2.1)
$DE_{IB,\,CWL,\,T}$	detection and conversion efficiency (see appendix C.11)
τ_{el}	decay time of the electronics of the read out circuit (see appendix C.4.4)
σ_{TT}	transit time spread of the PMT (see appendix C.4.4)
σ_{IB}	temporal width of the respective ion beam (see appendix C.10.3)
$\mu := 0$ns	combined time shift of the excitation pulse and the PMT transit time (see section III/5.2.1 and appendix C.4.4)

Equation C.23 is, in principle, equivalent to the unquenched pulse model used for the fits of the pulses recorded with laser excitation, see, e.g., equation 5.13 in section III/5.2.1. However, σ_{IB} substitutes $\frac{\sigma_L}{\sqrt{2}}$ as, in the measurements discussed here, the ion-beam pulse was used for excitation and not the two-photon absorption of laser photons. In addition, the part of the reflected laser light is of course not included in equation C.23.

The values of the fixed parameters are either adopted from the model ($\tau_{rad}(T)$, see section III/3.3), from the results of the fits to the pulses recorded with laser excitation ($R_{dr}(CWL)$ and $\tau_{dr}(T,\, CWL)$, see section III/5.2.2), from the discussion of the detection system ($DE_{IB,\,CWL,\,T}$, see appendix C.11, and τ_{el}, σ_{TT}, see appendix C.4.4) or from the investigation of the ion-beam pulse shape (σ_{IB}, see appendix C.10.3). The parameter μ, determining the temporal shift of the pulse, cannot be fitted as a free parameter as no rising part of the pulse shape was included in the fit. In addition, as explained in section III/4.6.2, the maxima of the decay-time spectra recorded with ion-beam excitation are shifted to zero. Hence, for the fit of equation C.23 to these data, the parameter μ was set to zero[41].

In figure C.11, the fit of equation C.23 to the decay-time spectrum $\mathbf{O5_{PMT}}$ is shown as an example.

For a summary of the fit results for the purely exponential decay times and the temperatures determined with equation 4.2 (section III/4.2.6), see table C.5 in appendix C.8.3.

[41] Several tests have been performed with different fixed values for μ or including μ as a free fit parameter: The result for the decay time τ_d was always the same.

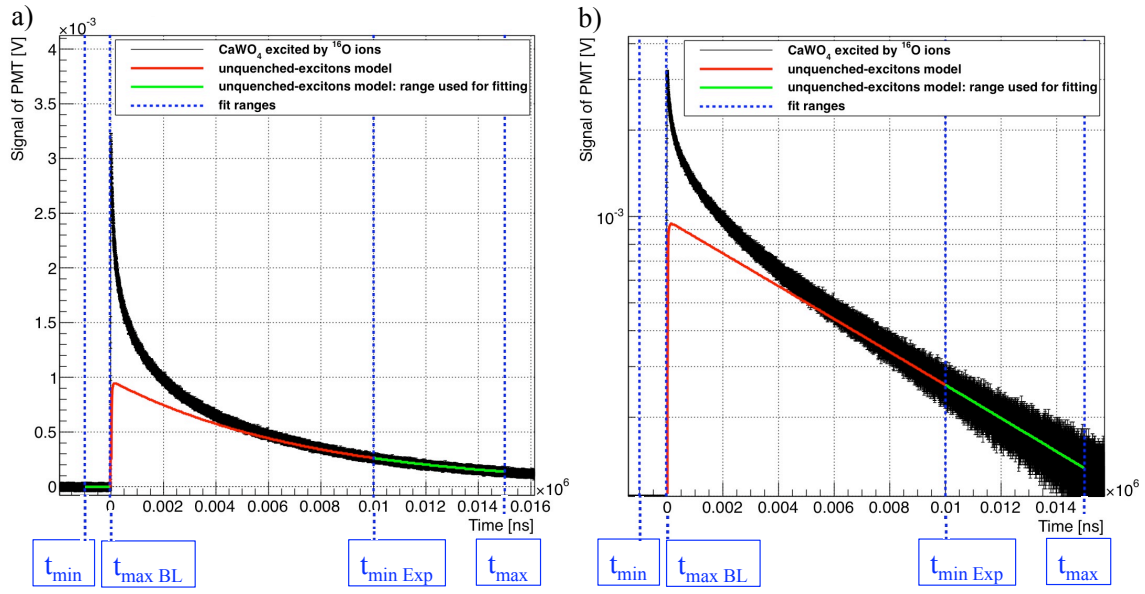

Figure C.11: Example of the fit of the unquenched decay time model to a pulse recorded with ion-beam excitation: In black (markers and error bars), the decay-time spectrum $\mathbf{O5_{PMT}}$ is shown. In green, the fit with the unquenched model to this pulse is shown where the blue dashed lines (and labels) indicate the time windows used for the fit. In red, the complete unquenched model fit can be seen. In figure a), a normal y-axis is shown. In figure b), the y-axis is plotted logarithmically for an easier identification of the purely exponential decay.

C.8.3 Determined Exponential Decay Times and Crystal Temperatures

In table C.5, the fit results[42] obtained for $\tau_d(T_{crystal})$ and c_{BL} are shown together with the achieved reduced χ^2 and the temperature $T_{crystal}$ determined using τ_d with equation 4.2 from section III/4.2.6. In addition, the fit results of the purely exponential decay time of the fits with the unquenched pulse model to the laser pulses (see section III/5.2.2) and the derived crystal temperatures are shown.

The errors of the values of $\tau_d(T_{crystal})$ and c_{BL} shown in table C.5 correspond to the statistical errors from the χ^2 fits. As discussed in appendix C.6, the values for the temperature $T_{crystal}$ calculated with equation 4.2 (section III/4.2.6) and with the parameters given in equations 4.3 (section III/4.2.6) have to be considered as relative to the two reference temperatures determined in appendix C.6. The calculated temperatures are, of course, afflicted with several uncertainties. However, on the one hand, not for all model parameters (of the three-level model used for the calculation of the temperature), a corresponding uncertainty can be determined (ΔE and D are adopted from [41] where no errors are indicated). On the other hand, the procedure used in appendix C.6 to determine the other model parameters includes several error sources not taken into account in detail, e.g., the uncertainty in the calibration of the employed thermometer. Hence, no errors for the values of the determined temperatures are stated. Therefore, it has to be noted that these temperatures represent only estimates of the real crystal temperature.

[42] In these fits, the value of $\mathbf{N_{0,\,ex}}$ is a mere scaling factor of the pulse height. Therefore, the obtained value is not shown in the summary.

measurement number	$\tau_d(T_{crystal})$ [μs]	c_{BL} [μV]	red. χ^2	$T_{crystal}$ [K]
Ion-beam excitation measurements				
O1$_{\mathbf{PMT}}$	9.142 ± 0.012	1.22 ± 0.10	1.23	298
O2$_{\mathbf{PMT}}$	40.19 ± 1.24	-3.21 ± 1.58	0.05	29
O3$_{\mathbf{PMT}}$	9.052 ± 0.042	3.40 ± 0.14	1.10	298
O4$_{\mathbf{PMT}}$	46.08 ± 1.31	2.66 ± 0.28	0.26	27
O5$_{\mathbf{PMT}}$	7.654 ± 0.053	-4.11 ± 0.50	0.89	309
O6$_{\mathbf{PMT}}$	74.58 ± 1.00	2.57 ± 0.63	0.09	20
O7$_{\mathbf{PMT}}$	8.813 ± 0.005	3.86 ± 0.06	1.51	300
O8$_{\mathbf{PMT}}$	70.77 ± 0.68	0.83 ± 0.61	0.20	21
P1$_{\mathbf{PMT}}$	7.765 ± 0.013	-6.48 ± 0.21	0.84	308
P2$_{\mathbf{PMT}}$	76.93 ± 0.69	9.79 ± 0.36	0.21	20
P3$_{\mathbf{PMT}}$	8.504 ± 0.009	3.06 ± 0.30	0.98	302
P4$_{\mathbf{PMT}}$	90.88 ± 0.78	-3.76 ± 0.61	0.33	18
Laser-excitation measurements				
O9$_{\mathbf{PMT}}$	9.1192 ± 0.0005	55.05 ± 0.64	1.81	298
O10$_{\mathbf{PMT}}$	75.020 ± 0.007	172.73 ± 0.47	1.81	20
O11$_{\mathbf{PMT}}$	9.0578 ± 0.0007	0.64 ± 0.34	1.51	298
O12$_{\mathbf{PMT}}$	69.872 ± 0.007	94.86 ± 0.22	1.51	21
P5$_{\mathbf{PMT}}$	9.0685 ± 0.0005	-8.60 ± 0.64	2.48	298
P6$_{\mathbf{PMT}}$	93.119 ± 0.010	457.04 ± 0.51	2.48	18

Table C.5: Summary of the results of the fits of the purely exponential decay time. The values obtained for the purely exponential decay time $\tau_d(T_{crystal})$, the DC offset of the baseline level c_{BL}, the reduced χ^2 and the temperature of the crystal derived from the exponential decay time are shown.

When inspecting the fit results for the decay times and the corresponding temperatures given in table C.5, some values are especially noticeable:

- The decay times of the measurements **O2$_{\mathbf{PMT}}$** and **O4$_{\mathbf{PMT}}$** are considerably smaller than the ones obtained for the other measurements at low temperature. Hence, the determined temperatures (29K and 27K, respectively) are elevated in comparison to the other low temperature measurements. These values are assumed to reflect real conditions (no systematical error) as they can be attributed to the elevated temperature of the cryocooler in these measurements (see discussion in section III/4.2.6).

- The decay times of the measurements **O5$_{\mathbf{PMT}}$** and **P1$_{\mathbf{PMT}}$** are considerably smaller than the ones obtained for the other measurements at room temperature. Hence, the determined temperatures (309K and 308K, respectively) are elevated in comparison to the other room temperature measurements. These values are assumed to reflect real conditions (no systematic error) as they can be attributed to elongated heating procedures of the cryocooler after preceding low-temperature measurements: The slightly elevated temperature (309K) in measurement **O5$_{\mathbf{PMT}}$** can be assigned to the fact that, after the measurement **O6$_{\mathbf{PMT}}$** at low temperature had been performed, the crystal was warmed up with the installed heating resistor. The heating procedure

was not stopped early enough so that the coldfinger as well as the attached crystal were heated to a temperature slightly above room temperature. In this condition, the spectrum $\mathbf{O5_{PMT}}$ was recorded. The same holds true for the elevated temperature of measurement $\mathbf{P1_{PMT}}$. Before this measurement was performed, a measurement at low temperature with crystal Olga was performed. Afterwards, the coldfinger and the crystal were heated up. When changing the crystals (venting the experimental chamber), it was observed that the cryocooler was still at a temperature of only $\sim$ 277K, so that some water condensed on the coldfinger. In order to remove the water, the cryocooler (now with crystal Philibert installed) was heated while the experimental chamber was evacuated. In this condition, the measurement $\mathbf{P1_{PMT}}$ was performed.

- The decay times of the measurements $\mathbf{P4_{PMT}}$ and $\mathbf{P6_{PMT}}$ are considerably larger than the ones obtained for the other measurements at low temperature. Hence, the determined temperatures (18K, for both measurements) are smaller in comparison to the other low temperature measurements. In both of these decay-time measurements an extremely rising baseline level is observed. It can be assumed that the fit results of the exponential decay times are influenced by this rising baseline and tend to exhibit artificially enlarged values. Therefore, the derived temperatures are most probably underestimates of the respective real crystal temperature which can be assumed to be more likely in the temperature region of to the other low temperature measurements, i.e., around 20 to 21K.

In addition, when comparing all decay-times determined for, e.g., crystal Olga at room temperature ($\mathbf{O1_{PMT}}$, $\mathbf{O3_{PMT}}$, $\mathbf{O7_{PMT}}$, $\mathbf{O9_{PMT}}$ and $\mathbf{O11_{PMT}}$, leaving out the measurement $\mathbf{O5_{PMT}}$ due to the elevated temperature), it is evident that these decay times show very good agreement, despite the different excitation modes and different optical filters. This observation is direct evidence for the prediction of the developed model that the underlying exponential decay time of the intrinsic scintillation light of $CaWO_4$ is independent of the used excitation mode (for a more detailed discussion, see section III/5.4).

Furthermore, it can be seen that both investigated crystals, Olga and Philibert, exhibit rather comparable decay times in the different measurements, see, e.g., the decay-time spectra recorded with laser excitation (except the measurement $\mathbf{P6_{PMT}}$). Therefore, it is assumed that the same parameters in the three-level model used for the determination of the crystal temperature can be used for crystal Philibert as for crystal Olga.

C.9 Details on the Data-Preprocessing Procedure Used for the Decay-Time Spectra Recorded with Ion-Beam Excitation

As discussed in section III/4.6.2, for all decay-time spectra, DC offset determination and subtraction, multiplication with (-1) to yield positive pulses, detection of the time- and voltage-resolutions as well as the assignment of uncertainties to the individual data points (see appendix C.4.6) is performed. As already indicated in section III/4.6.2, the decay-time spectra recorded with ion-beam excitation have to be processed further before being analyzed. The necessity for this as well as the applied procedures are described below. The data recorded with laser-excitation do not have to be processed further.

C.9.1 Special Features of the Decay-Time Spectra

In the additional data preparation steps, different features (**feature 1 to 6**) of the decay-time spectra recorded with ion-beam excitation have to be addressed:

1. The influence of the drifting baseline on the baseline level and on the pulse shape at large times (see appendix C.4.3) due to the small pulse height obtained in these measurements (of the order of 5mV, see section III/4.2.3) has to be considered.

2. The influence of the averaging procedure (used in the data acquisition) on the pulse shape at large times has to be considered. This is necessary due to the small pulse heights obtained in these measurements (compare discussion in appendix D.2).

3. The influence of varying trigger settings (trigger level and time shift, see discussion in section III/4.6.2) in the individual measurements has to be considered.

4. In the iodine-beam excitation measurements, an additional small pulse was observed before the beginning of the actual scintillation-light pulse (for details, see appendix C.9.2).

5. The time windows for the determination of the purely exponential decay time (for the calculation of the crystal temperature, see appendix C.8) have to be defined. The exponential decay time determined with this procedure is also used as a fixed parameter in the fit of the quenched decay-time model (see section III/5.3).

6. The fits of the quenched decay-time model (see discussion in section III/5.3) are numerically extensive and require long computation times. In order to limit the necessary computation time, a reduction of data points and free fit parameters is aimed at. Different measures are taken to optimize the fit procedure:

   - Determination of the baseline level (possibly remaining DC offset) independently of the fit of the quenched pulse model (see section III/5.3).
   - Determination of the exponential decay time independently of the quenched pulse model (see section III/5.3).
   - Selection of data points used for the fits (for details, see appendix C.9.3).

C.9.2 Definition of Time Windows for the Analysis of the Data

In order to deal with the above mentioned features (see appendix C.9.1), different time regions (as, e.g., a baseline region) for each measurement have to be defined. This procedure will be explained for the example of the decay-time spectrum $\mathbf{O3_{PMT}}$, recorded for crystal Olga with iodine-beam excitation and the 500nm filter at room temperature, see figure C.12. This measurement was chosen as an example, as the pulse height is rather small ($\sim$ 0.9mV), the baseline drift is large and, hence, disturbances are easily visible. Prior to the definition of the time windows, the maxima of the decay-time spectra are determined and shifted to the zero of time (see discussion in section III/4.6.2).

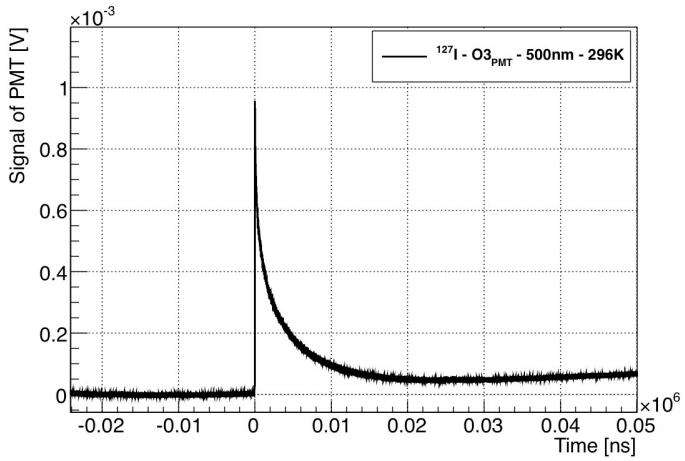

Figure C.12: **O3$_{\mathbf{PMT}}$**: Decay-time spectrum recorded for crystal Olga with iodine-beam excitation and the 500nm filter at room temperature.

- **Features 1 and 2:** For each measurement, an individual time window starting at a point $\mathbf{t_{min}}$ in the baseline before the pulse (where the baseline drift is not dominant) up to a maximum point $\mathbf{t_{max}}$ after which the pulse shape is significantly disturbed (artificially influenced), has to be chosen (see figure C.13):
  Total fit range from $\mathbf{t_{min}}$ to $\mathbf{t_{max}}$.

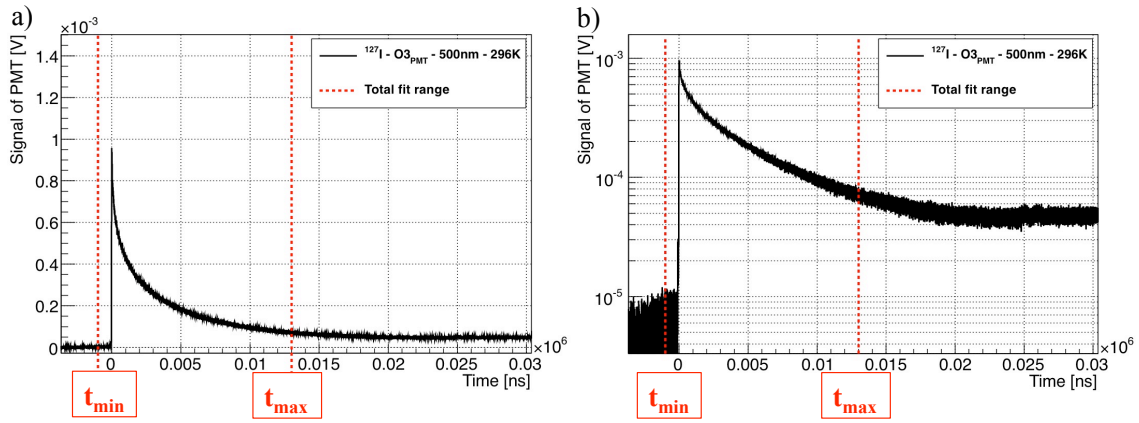

Figure C.13: **O3$_{\mathbf{PMT}}$**: **Total fit range** from $\mathbf{t_{min}}$ to $\mathbf{t_{max}}$. In figure a), a normal y-axis is shown. In figure b), the y-axis is plotted logarithmically to facilitate the identification of the impact of the baseline drift.

- **Feature 3:** For each measurement, an individual pre-trigger region for the baseline definition has to be defined (see figure C.14):
  Baseline range from $\mathbf{t_{min}}$ to $\mathbf{t_{max\,BL}}$.

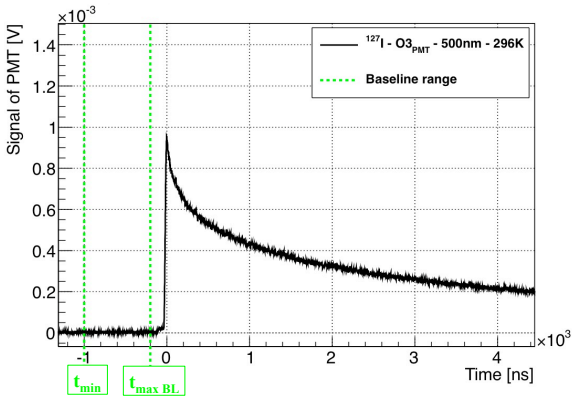

Figure C.14: **O3$_{\mathbf{PMT}}$**: **Baseline range** from $\mathbf{t_{min}}$ to $\mathbf{t_{max\ BL}}$.

- **Feature 4:** For the decay-time spectra recorded with iodine-beam excitation, a small time window directly before the start of the pulse has to be rejected. This is due to the existence of a very small scintillation-light pulse before the actual light pulse, most probably caused by γ particles interacting with the crystal[43]. The data points in the region of this small pulse can simply be rejected as it can be assumed that the small pulse has a negligible impact on the pulse shape of the actual scintillation-light pulse: The ratio of the maximum of the small pulse to the maximum of the actual pulse is only around 1% to 2%. Of course, the rejected data points cannot be included in the baseline region either. Hence, the rejected time region for iodine pulses is defined as (see figure C.15):
  Rejected range (iodine pulses) from $\mathbf{t_{max\ BL}}$ to $\mathbf{t_{rej}}$.

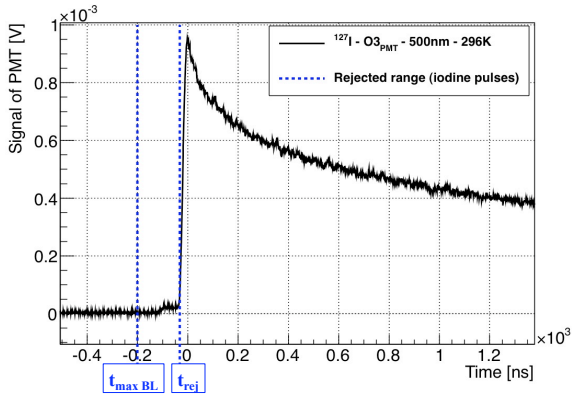

Figure C.15: **O3$_{\mathbf{PMT}}$**: **Rejected range (iodine pulses)** from $\mathbf{t_{max\ BL}}$ to $\mathbf{t_{rej}}$.

[43]It is assumed that the small pulse is caused by γ particles which were produced by the iodine beam hitting (grazing) and exciting parts of the beam line: The time difference between the start of the small pulse and the start of the large pulse can be estimated to be around 50ns. From this time difference and the respective time of flight for the iodine ions and the γ particles, a place of production of the γ particles in a distance of roughly 40cm from the crystal can be estimated. This corresponds roughly to the distance of the 4-sector aperture from the crystal (see figure 4.7 in section III/4.4.2).

- **Feature 5:** The region used for the fit of the purely exponential decay time has to be chosen. The maximum value of this time window corresponds to the maximum value used for fitting $\mathbf{t_{max}}$. The start point of this time window $\mathbf{t_{min\ Exp}}$ is chosen by using a semi-logarithmical plot (logarithmic y-axis) such that the included data points correspond to a straight line (see figure C.16):
  Exponential fit range from $\mathbf{t_{min\ Exp}}$ to $\mathbf{t_{max}}$.

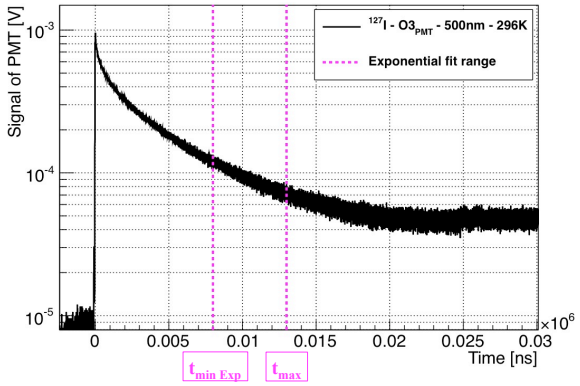

Figure C.16: $\mathbf{O3_{PMT}}$: **Exponential fit range** from $\mathbf{t_{min\ Exp}}$ to $\mathbf{t_{max}}$.

- **Feature 6:** The time window in which the impact of the quenching effect on the pulse shape is visible, the **Quenching range**, can, thus, be defined as ranging from $\mathbf{t_{rej}}$ (for iodine pulses) or from $\mathbf{t_{max\ BL}}$ (for oxygen pulses) to $\mathbf{t_{min\ Exp}}$, which is the starting point of the purely exponential pulse shape. As this time window is still comparably large and contains many data points, e.g., $\sim$ 8000 data points for $\mathbf{O3_{PMT}}$, this window is further divided into two regions:

  1. A first region, the **Quenching dominated range**, including the rise and typically about 1μs of the decaying pulse, ranges from $\mathbf{t_{max\ BL}}$ (oxygen pulses) or $\mathbf{t_{rej}}$ (iodine pulses) to an additionally defined time $\mathbf{t_{max\ Qdom}}$ (for the definition, see below). In this time region, the impact of the quenching effect completely dominates the pulse shape.
  2. A second region, the **Quenching mixed range**, ranges from $\mathbf{t_{max\ Qdom}}$ to $\mathbf{t_{min\ Exp}}$. In this time region, the impact of the quenching effect and of the purely exponential decay time mix.

  To define the time $\mathbf{t_{max\ Qdom}}$ up to which the quenching effect completely dominates the pulse shape, the pulse height difference within the complete **Quenching range** (from the maximum of the pulse to the point where the **Exponential fit range** starts) is determined. Then, the point in time, where the pulse height has reduced from the maximum to $(1 - \frac{1}{e})$ times this pulse height difference[44] is defined as $\mathbf{t_{max\ Qdom}}$. It has to be noted, that this division of the complete **Quenching range** is only an indicator for which times the quenching is dominant. This information is used for the selection of data points (see appendix C.9.3).

[44]The procedure used to estimate the range dominated by quenching, in principle, corresponds to the approximation of the pulse shape at the beginning of the pulse by an exponential decay.

These windows are shown in figure C.17:
Quenching range from $\mathbf{t_{rej}}$ (or from $\mathbf{t_{max\ BL}}$, for oxygen pulses) to $\mathbf{t_{min\ Exp}}$.
Quenching dominated range from $\mathbf{t_{rej}}$ (or from $\mathbf{t_{max\ BL}}$, for oxygen pulses) to $\mathbf{t_{max\ Qdom}}$.
Quenching mixed range from $\mathbf{t_{max\ Qdom}}$ to $\mathbf{t_{min\ Exp}}$.

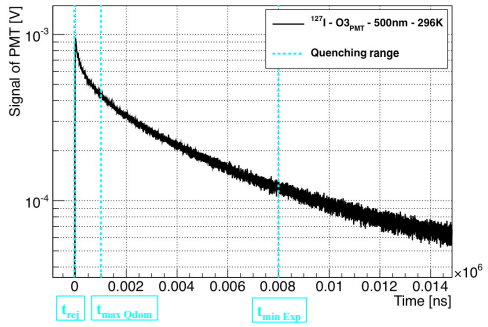

Figure C.17: $\mathbf{O3_{PMT}}$: **Quenching range** from $\mathbf{t_{rej}}$ (for iodine pulses) to $\mathbf{t_{min\ Exp}}$. **Quenching dominated range** from $\mathbf{t_{rej}}$ (for iodine pulses) to $\mathbf{t_{max\ Qdom}}$. **Quenching mixed range** from $\mathbf{t_{max\ Qdom}}$ to $\mathbf{t_{min\ Exp}}$.

A list of the respective determined time windows, i.e. the times $\mathbf{t_{min}}$, $\mathbf{t_{max\ BL}}$, $\mathbf{t_{rej}}$, $\mathbf{t_{max\ Qdom}}$, $\mathbf{t_{min\ Exp}}$ and $\mathbf{t_{max}}$, for all individual measurements with ion-beam excitation can be found in table C.6. It has to be noted that for the decay-time spectra recorded with oxygen-beam excitation no pulse caused by γ particles was visible before the actual pulse. Hence, no value is assigned to the time $\mathbf{t_{rej}}$.

measurement number	$\mathbf{t_{min}}$ [μs]	$\mathbf{t_{max\ BL}}$ [ns]	$\mathbf{t_{rej}}$ [ns]	$\mathbf{t_{max\ Qdom}}$ [μs]	$\mathbf{t_{min\ Exp}}$ [μs]	$\mathbf{t_{max}}$ [μs]
$\mathbf{O1_{PMT}}$	-1	-200	-33	1.3	10	17
$\mathbf{O2_{PMT}}$	-1	-200	-40	2.7	50	100
$\mathbf{O3_{PMT}}$	-1	-200	-32	1.0	8	13
$\mathbf{O4_{PMT}}$	-1	-200	-20	1.5	50	100
$\mathbf{O5_{PMT}}$	-1	-40	-	1.0	10	15
$\mathbf{O6_{PMT}}$	-1	-100	-	2.5	50	100
$\mathbf{O7_{PMT}}$	-1	-40	-	1.0	10	40
$\mathbf{O8_{PMT}}$	-1	-100	-	2.7	50	100
$\mathbf{P1_{PMT}}$	-1	-200	-30	1.5	10	17
$\mathbf{P2_{PMT}}$	-1	-200	-30	1.3	50	200
$\mathbf{P3_{PMT}}$	-1	-40	-	1.1	10	30
$\mathbf{P4_{PMT}}$	-1	-40	-	1.4	30	60

Table C.6: Definition of the different time windows used to characterize the decay-time spectra recorded with ion-beam excitation.

It has to be noted that the decay-time spectra $\mathbf{O3_{PMT}}$ and $\mathbf{P4_{PMT}}$ exhibit strongly drifting baseline levels. Therefore, the respective total fit ranges (as well as the time window used for the fit of the exponential decay time) had to be chosen comparably short.

C.9.3 Selection of Data Points for the Fits

In order to limit the required computation time for the fits of the quenched pulse model to the decay-time spectra recorded with ion-beam excitation (see sections III/5.3), the number of data points used for the fits has to be reduced to around 500 to 1,000 data points[45]. Of course, the selection of data points of the decay-time spectra has to be performed without loosing the pulse-shape information contained in the data: For this reason, different ranges of the recorded decay-time spectra are chosen (within the defined total fit range, see appendix C.9.2) where data points with different frequencies (e.g., every 2nd or every 30th data point) are selected. The applied procedure as well as the frequencies of the selected data points are presented in the following.

- In principle, only data points from the time window defined as **total fit range** ($\mathbf{t_{min}}$ to $\mathbf{t_{max}}$, see appendix C.9.2) are selected.
- In the **baseline range**, $\mathbf{t_{min}}$ to $\mathbf{t_{max\ BL}}$, one data point every 40ns is chosen. In this region, only a few data points are needed as the baseline level is determined independently (see appendix C.8) and used as a fixed parameter in the final fit of the quenched pulse model.
- No samples are chosen from the **rejected range (iodine pulses)** ($\mathbf{t_{max\ BL}}$ to $\mathbf{t_{rej}}$, see appendix C.9.2).
- The most important time window for the fits of the quenched pulse model to the data is the region of the pulses where the quenching effect is dominating the pulse shape: The **Quenching dominated range**, $\mathbf{t_{rej}}$ (iodine pulses) or $\mathbf{t_{max\ BL}}$ (oxygen pulses) to $\mathbf{t_{max\ Qdom}}$. In this region, one data point every 3ns (for room temperature measurements) or every data point (for low temperature measurements) is selected.
- In the region labelled **Quenching mixed range**, $\mathbf{t_{max\ Qdom}}$ to $\mathbf{t_{min\ Exp}}$, the impact of the quenching effect as well as the influence of the purely exponential decay are visible. In order to reduce the amount of selected data points, in this region one data point every 50ns (for room temperature measurements) or every 200ns (for low temperature measurements) is chosen.
- In the **exponential fit range**, $\mathbf{t_{min\ Exp}}$ to $\mathbf{t_{max}}$, one data point every 100ns (for room temperature measurements) or every 500ns (for low temperature measurements) is chosen. In this range, only a few data points are chosen as the exponential decay time which dominates the pulse shape in this time window is determined independently (see appendix C.8) and used as a fixed parameter in the final fit of the quenched pulse model.

With the described procedure, it is achieved that the number of selected data points used for the fits of the quenched pulse model to the decay-time spectra recorded with ion-beam excitation is reduced to around 500 to 1,000 samples while maintaining the information of the pulse shape[46]. An example ($\mathbf{O2_{PMT}}$) of an decay-time spectrum consisting of the selected data points only (red markers) in comparison to the original decay-time spectrum (black markers, including all data points) can be seen in figure C.18.

[45] Still, with such a small number of data points used in the fits, the computation time for one fit took up to 30 hours.

[46] The different choices of the frequencies of selected data points for the measurements at room temperature and at low temperature are a result of the different total window lengths that have to be covered

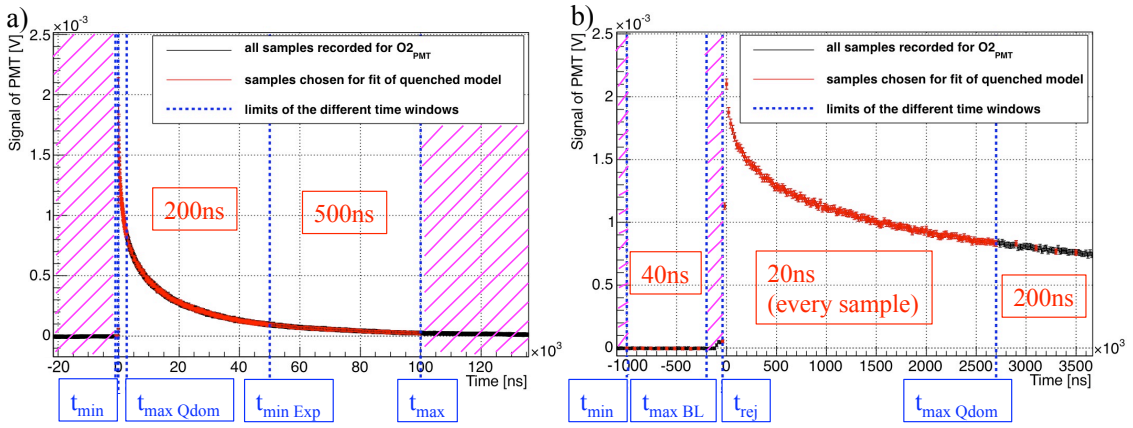

Figure C.18: Decay-time spectrum $\mathbf{O2_{PMT}}$ (black markers): Comparison of the chosen data points (in red) with all recorded data points (in black). In figure a), a time window containing the complete pulse is shown. In figure b), a zoom into the beginning of the pulse is depicted. The blue dashed lines and blue labels indicate the time windows where data points with different frequencies were chosen. The striped areas (pink) correspond to time windows where no data point was chosen. The red labels indicate the time between individual data points chosen for the fit in each time region.

In figure C.18 a), a time range containing the complete pulse(from -20μs to 135μs) is shown. The region of the purely exponential decay ($\mathbf{t_{min\ Exp}}$ to $\mathbf{t_{max}}$) as well as the region of the mixed influence of the quenching and the exponential decay ($\mathbf{t_{max\ Qdom}}$ to $\mathbf{t_{min\ Exp}}$) can be seen. In figure C.18 b), a zoom into the beginning of the pulse (from -1.1μs to 3.6μs) is shown. In this figure, the baseline region ($\mathbf{t_{min}}$ to $\mathbf{t_{max\ BL}}$) as well as the region where the pulse shape is dominated by the quenching effect ($\mathbf{t_{rej}}$ to $\mathbf{t_{max\ Qdom}}$) can be seen.

C.10 Characterization of the Excitation Pulses

C.10.1 BaF_2 as Test Crystal

The band gap of BaF_2 is determined (experimentally and by calculations) to amount to $\sim$ 11eV [107]. Hence, irradiation with laser photons with an energy of $E_L = 3.68$eV (see section III/4.1.3) cannot result in TPE and also absorption of three photons at the same time (11.04eV) would yield only excitation in the absorption tail. To further suppress this excitation possibility, the lens focussing the laser beam onto the crystal was removed during these measurements. In addition, BaF_2, if excited, has the advantage of a very fast light-pulse rise time (rise time $<$ 10ps [123, 124]). In fact, BaF_2 is among the fastest scintillators known [107]. Hence, even if the BaF_2 crystal was excited in the experiments (e.g., by the ion-beam pulse), still the beginning of the produced scintillation-light pulse is much faster than all other times considered in the presented experiments. Hence, these measurements can be employed to determine the temporal (and spectral) characteristics of the used excitation modes.

with the same amount of data points.

C.10.2 Characterization of the Laser Pulse

In the experiments with laser excitation, the BaF_2 crystal was used to investigate the temporal and spectral shape of the laser-light pulse independently from the $CaWO_4$ scintillation light.

Reflection of the Laser Light

In first tests with the laser excitation, very large and fast pulses were detected with the PMT as well as large intensities at and around the wavelength of the main laser line were visible with the spectrometer. In a region of roughly ±50nm around the main laser line, light was detected with the spectrometer. The observed light intensity could be traced to result from the laser light (line at 337.1nm) and recombination light (wavelength region around the central laser line) being reflected at several components within the experimental chamber. In the course of many tests and measurements, the amount of reflected light could be reduced with the help of different measures, as, e.g., the installation of the light trap opposite to the PMT, the introduction of the plastic tube with a small aperture in front of the PMT and the use of apertures before and after the lens (see figure 4.5 in section III/4.3.2). With these measures, the total amount of laser light being detected at the position of the PMT as well as the amount of recombination light were greatly decreased. Further reduction was not possible as was proven by a measurement where no crystal was installed in the experimental chamber. The laser was operated and no measurable light intensity was detected at the position of the PMT. Hence, in all measurements with laser excitation, additionally to the scintillation light generated in the installed crystal, always laser light reflected at or within the crystal is also detected with the PMT and the spectrometer.

Wavelength Spectrum and Qualitative Pulse Shape of the Reflected Laser Light

To characterize the reflected laser light being detected with the PMT, measurements with the BaF_2 crystal installed in the final setup were performed (lens removed). A decay-time spectrum was recorded with the PMT (400nm filter) and a wavelength spectrum was recorded with the spectrometer installed at the position of the PMT (without filter). As indicated above and will be shown in the following, for BaF_2 no (significant) production of scintillation light through irradiation with photons from the N_2 laser has to be expected, especially if the lens focussing the laser light is removed. The wavelength spectrum was recorded with an integration time of 30s. The decay-time spectrum was recorded with the minimal time resolution of 0.2ns and 5,000 pulses averaged, yielding a record length of 500ns. The PMT was operated with a voltage of -1.5kV (standard for the laser-excitation experiments). In figure C.19, the wavelength spectrum (panel a) and the decay-time spectrum (panel b) recorded in this way are shown. From the wavelength spectrum (figure C.19 a), it becomes clear that the dominating light source in this experiment is the laser light itself as only in the wavelength region of the laser line (around 337.1nm) measurable intensity is detectable[47]. Hence, as anticipated, no measurable amount of scintillation light from the BaF_2 crystal was detected in the used setup. In figure C.19 b), the decay-time spectrum of the detected scintillation light as recorded with the PMT and the 400nm filter installed in front of it is shown. Despite the employed 400nm filter, the laser-light pulse

[47] The spikes visible at $\sim$ 318nm and $\sim$ 585nm are outliers of pixels of the detector of the spectrometer.

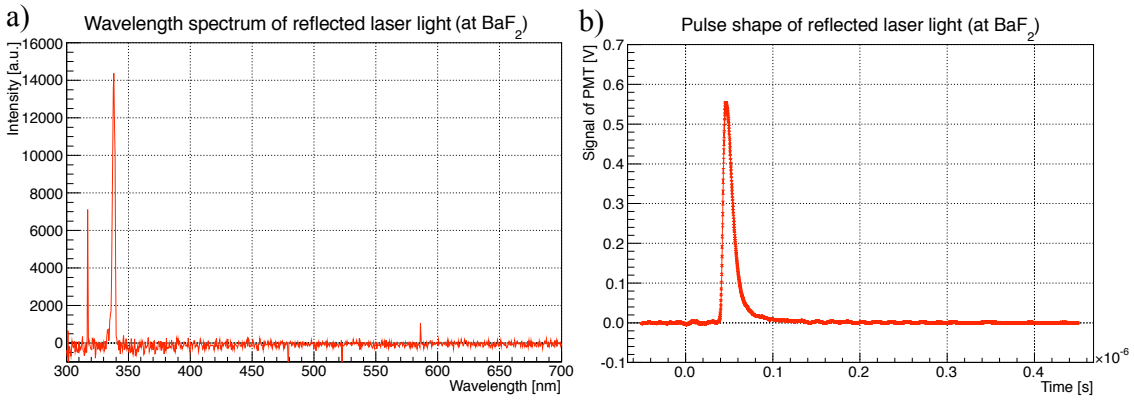

Figure C.19: Laser-light pulse reflected at a BaF_2 crystal installed at the position of the $CaWO_4$ crystal: In figure a), the wavelength spectrum of the reflected light can be seen (preprocessed according to section III/4.6.1, no errors indicated in the picture). In figure b), the decay-time spectrum (preprocessed as described in section III/4.6.2) is shown. Both measurements were performed with the respective detector (spectrometer and PMT) installed at the position of the PMT. For the recording of the decay-time spectrum, the 400nm filter was installed in front of the PMT.

(main line: 337.1nm) is clearly visible. This can be assigned to the fact that the laser-light beam is very intense (up to mJ pulse energies) and that the installed crystal (here: BaF_2 but this implication is also valid for the $CaWO_4$ crystal) acts as reflector and guides the laser light into the direction of the PMT (compare to the light paths indicated on the right-hand side of figure 4.5 in section III/4.3.2).

The recorded wavelength and decay-time spectra additionally show that, in fact, the light generated by the laser entering the experimental chamber is mainly composed of the fast, coherent light originating directly from the laser line. Thus, in the following, possible very small contributions from (slower, non-coherent) recombination light are neglected. Hence, also the temporal distribution of the excitation of the $CaWO_4$ crystal is considered to be completely dominated by the fast laser-light pulse shape (see figure C.19 b).

Quantitative Pulse Shape of the Reflected Laser Light

The fit with the function $PMT(t)$, displayed in figure 4.19 b) (section III/4.7.3), was performed simultaneously to the determination of the impulse reaction of the PMT-base-oscilloscope system: As is shown in appendix C.4.4, for the description of the laser-light pulse a Gaussian distribution can be used. The impulse reaction of the PMT can be described by an exponentially modified gaussian distribution[48]. The recorded pulse shape of the reflected laser light, as depicted in figure 4.19 b), can then be fitted with a convolution of the Gaussian describing the laser pulse $L(t)$ and the exponentially modified gaussian $Ir(t)$ describing the impulse reaction of the PMT. For details on the fit function and fit routine, see equation C.9 in appendix C.4.4. From this fit, the one-sigma width σ_L of the

[48] For the description of the impulse reaction of a system an exponentially modified gaussian distribution, i.e., a convolution of a Gaussian and an exponential function, can be used. In case of the PMT-base-oscilloscope system used here, the Gaussian distribution describes the influence of the transit time spread. The exponential represents the impact of the electronic read-out circuit onto the signal shape.

laser pulse is determined with high accuracy to:

$$\sigma_L = 1.803 \pm 0.044\text{ns} \tag{C.24}$$

Produced Excitation Density with TPE

As already indicated in section III/4.1.3, no absolute measurements of the emission intensity of the laser as well as no quantitative measurements of the focussing quality of the used optics were made. However, in order to characterize the produced excitation density with regard to the interaction possibilities of the produced STEs, dedicated measurements as described in the following were performed.

The basic idea was that the pulse shape of the generated scintillation light should differ for different densities of the STEs, i.e. for different excitation densities (as described in the developed model, see chapter III/3.1). Hence, information on the produced excitation density should be available by comparing the pulse shape of the produced scintillation light for different levels of focussing of the laser light used for the excitation. Variation of the degree of focussing of the laser light was achieved by variation of the lens position with respect to the crystal center. As can be seen in figure 4.5 in sextion III/4.3.2, for the final measurements, the distance of the lens to the center of the crystal was chosen to be 4.5cm. This position was chosen, as in this configuration the focal spot of the laser light was projected into the center of the $CaWO_4$ crystal, i.e. maximum focussing was realized[49]. In figure C.20, the decay-time spectra obtained for different distances between the lens and the crystal ranging from 3.5cm to 6.0cm are depicted[50]. With these variations, it was achieved that still the complete laser beam was incident onto the crystal surface and only the degree of the focussing at the position of the crystal was varied.
In figure C.20 a), the different pulses, as recorded and preprocessed according to section III/4.6.2 are shown (no error bars drawn). It has to be noted that again the fast rising and decaying part at the beginning of all pulses can be ascribed to laser light being reflected and detected. The red pulse corresponds to the position of the lens as chosen for the final measurements. It can be seen that with the lens installed in this position (4.5cm lens-crystal distance) far more scintillation light is generated as compared to the other lens positions. It has to be noted that with the lens positioned, e.g., 6.0cm away from the center of the crystal (black pulse) only a very small scintillation-light intensity was produced although the total incident laser-light intensity did not change. This behavior is proof of the excitation via TPE as it indicates that under unfocussed conditions the density of the incident laser photons was not sufficient to create simultaneous two-photon absorption. In figure C.20 b), the same pulses are shown, however, now scaled to the same height (scaling performed with the pulse heights at 1μs). It cannot only be seen that the signal-to-noise ratio (statistical fluctuations on the baseline) is the best for the lens-crystal distance of 4.5 cm, but also that all pulses cover each other, indicating that the pulse shape is the same independently of the level of focussing.

It can be observed that all pulse shapes - independent from the lens position - exhibit

[49]The position of the focal spot was determined with the help of the visible luminescence light generated on a sheet of white paper.

[50]The data was recorded at room temperature with crystal Olga installed in the final setup, only changing the position of the lens. In every measurement, 5,000 individual pulses were averaged using a record length of 100μs.

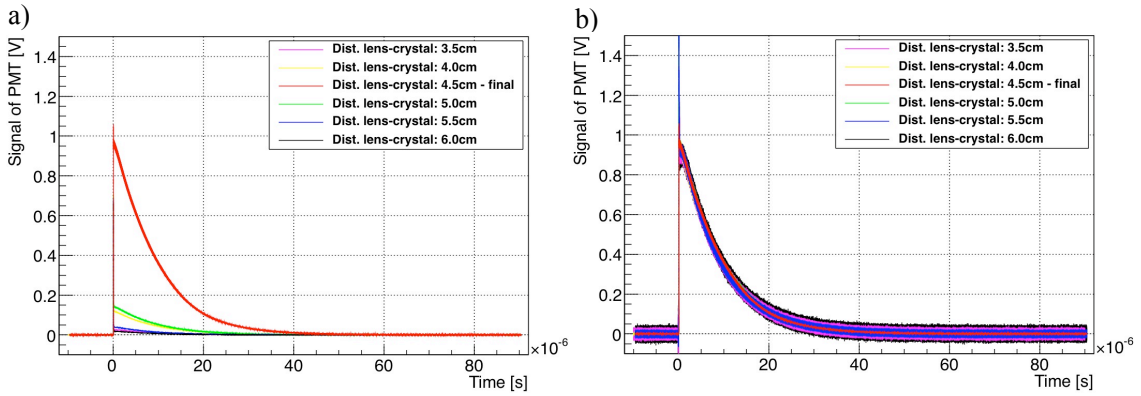

Figure C.20: Decay-time spectra recorded for crystal Olga under laser excitation at room temperature (400nm filter) for different degrees of focussing of the laser light, i.e., different distances between the lens and the crystal. The fast rise and decay at the beginning of all pulses correspond to laser light being reflected at the crystal. Figure a): Pulses as recorded and preprocessed according to section III/4.6.2 (no error bars drawn). Figure b): The same pulses, scaled to the same height using the pulse height at 1μs.

a purely exponentially decaying behavior (see section III/5.2.1 for a detailed discussion of the pulse shapes). Hence, from these measurements it can be deduced that the produced excitation density for all tested positions of the lens was not sufficient to produce STEs that were created densely enough to obtain significant interaction between them[51]. Therefore, the conclusion can be drawn that measurements performed with laser excitation can indeed, as anticipated, be used for the test and validation of the developed model for rare, i.e., spatially uncorrelated excitation.

C.10.3 Characterization of the Ion-Beam Pulse

Also for the characterization of the ion-beam pulse shape, the BaF_2 crystal was used. When irradiating the BaF_2 crystal with an ion-beam pulse, (quenched) scintillation light is generated. In the following, the procedure used to obtain the pulse shape of the ion-beam pulses is presented for the example of the iodine beam. For the oxygen-beam pulse, an analogous procedure can be adopted. Hence, for oxygen only the result of this procedure will be stated.

Pulse Shape of the Ion-Beam Pulses

The BaF_2 crystal was installed in the final setup used for ion-beam excitation, irradiated with the iodine beam and a decay-time spectrum was recorded with the PMT (at room temperature using no optical filter). In the measurement, 10,000 individual pulses were averaged and a record length of 1μs was used. Only the fast rising part of the recorded pulses is used for the determination of the ion-beam pulse shape as, otherwise, the complete time structure of the scintillation light of BaF_2 would have to be considered: The fast rise

[51] In more detail, if sufficient excitation densities (to create interaction between the generated STEs) would have been produced, a non-exponential pulse-shape as well as an increase in the created light intensity for *less* focussing should have been visible. This was not the case.

and fast decay, the two slower decay times and, of course, also the impact of the light-quenching effect on the scintillation-light generation in BaF_2. Hence, the rising part of the recorded light pulse is fitted in analogy to the fit of the reflected laser-light pulses (see equation C.9 appendix C.4.4), i.e. the shape of the ion-beam pulse is assumed to be gaussian and the impact of the PMT impulse reaction is integrated into the fit function by a convolution. The values determining the impulse reaction are adopted from the fits performed in appendix C.4.4, see table C.2. In figure C.21 a), the decay-time spectrum recorded in this experiment is shown. In figure C.21 b), a zoom into the rising part of the pulse (black line and error bars) as well as an example of the fit with the described function (red line) is shown.

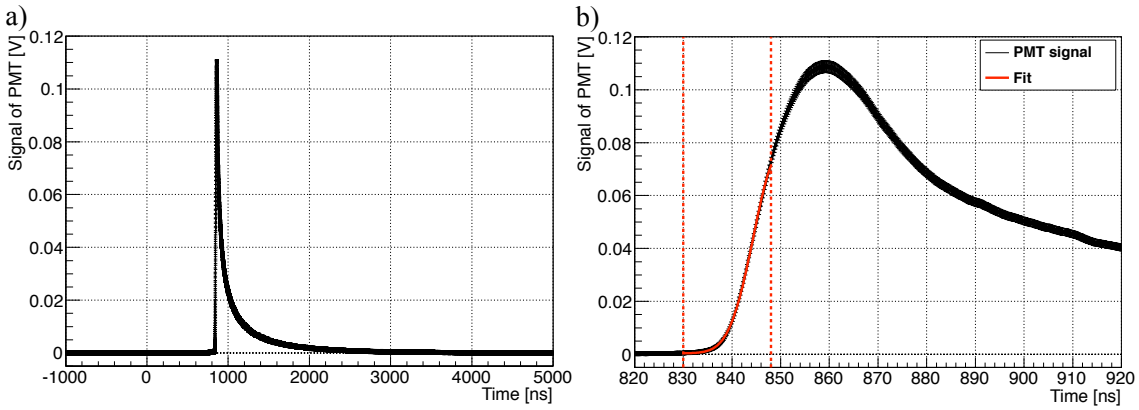

Figure C.21: Decay-time spectra recorded for the BaF_2 crystal under iodine-beam excitation at room temperature (no spectral filter): Figure a): Pulse as recorded and preprocessed according to section III/4.6.2. Figure b): Zoom into the beginning of the pulse (error bars and line drawn in black). In red, an example of a fit to the rising part of the pulse as described above is shown (vertical dashed lines in red indicate the used fit range for this example).

As can be seen in figure C.21 b), around the maximum of the pulse already the different decay times of BaF_2, i.e. also the slower decay times[52]) influence the signal shape. Hence, as indicated by the fit in figure C.21 b), only the rising part of the pulse can be used for the determination of the iodine-beam pulse shape. However, the result of fitting only the rising part of a pulse to determine the width of the excitation pulse is of course dependent on the chosen range for the fit. Therefore, different fit ranges covering different amounts of the rising part were tested and evaluated concerning the achieved reduced χ^2 and their constraint on the value of the ion-beam pulse width $\sigma_{^{127}I}$ (i.e., the uncertainty (error margins) for $\sigma_{^{127}I}$ determined by the fit). The results from the two ranges where by far the best reduced χ^2 in combination with the smallest error margins were achieved were averaged and the corresponding errors were propagated. The results for the one-sigma widths $\sigma_{^{127}I}$ and $\sigma_{^{16}O}$ for the iodine- and oxygen-beam pulses are:

$$\sigma_{^{127}I} = 3.94 \pm 0.18\text{ns} \quad \text{(C.25)}$$

$$\sigma_{^{16}O} = 3.09 \pm 0.09\text{ns} \quad \text{(C.26)}$$

[52]The slower decay times can also be seen in figure C.21 a). If this pulse is fitted with two exponentials in the region from 1000ns to 2000ns, approximately the same decay times as given in reference [124], 430ns and 620ns, are retrieved.

Produced Excitation Density - Inter Track Quenching

In this context, it has to be noted that the ion beam instead of single incident particles was *only* used to create several independent dense excitation tracks (by individual ions) in the crystal and *not* to create one completely excited, connected volume. This was achieved by using small beam currents (number of ions per pulse), low pulsing frequencies (excitation by one pulse has already decayed at the arrival time of the next pulse) and strong defocussing of the beam at the location of the crystal (distributing the small number of ions over the complete surface of the crystal). With these measures, it was achieved that no interaction between excitations created in individual tracks, i.e. no inter-track quenching, had to be expected. Thus, excitation by one pulse of N_{ion} ions from the accelerator can, in principle, be interpreted as a sum of excitations by N_{ion} individual ions. Accordingly, the light output produced by the irradiated crystal (decay-time spectrum) can, in principle, also be interpreted as the sum of light outputs by single ions. However, in reality, the individual ions do not interact in the crystal exactly at the same time due to the non-neglegtable width of the pulse of $\sigma_{ion} \approx 3 - 4$ns. For the calculation of the expected scintillation-light pulse shape due to a pulse of N_{ion} ions, this width σ_{ion} is of course taken into account, as presented in section III/5.3.2.

Beam Current and Geometrical Shape of the Ion Pulse

For monitoring and adjusting of the beam current and its geometrical shape, an electromagnetical lens, a movable Faraday cup and a 4-sector aperture (with adjustable central spacing) installed in the beam line were available (see section III/4.4.2). As discussed in the previous passage, small beam currents with large defocussing were needed. With the lens and the 4-sector aperture, the position and geometry of the ion beam were adjusted to result in a centralized, defocussed beam with a diameter of roughly 15mm at the position of the aperture. Additionally, the part of the area of the crystal illuminated by the ion pulse was checked visually, as indicated by the photo shown in figure 4.8 b). The beam direction and shape was chosen such as to achieve illumination of the complete large crystal area, (20x10)mm^2. To determine the realized beam currents, the movable Faraday cup was used. As, however, the used beam currents were small, the corresponding Faraday cup readings were also very small[53] and the associated uncertainties large. The estimated numbers of ions per pulse $N_{^{127}I}$ and $N_{^{16}O}$ amount to:

$$N_{^{127}I} \approx 100...3,000 \frac{\text{ions}}{\text{pulse}} \tag{C.27}$$

$$N_{^{16}O} \approx 100...2,000 \frac{\text{ions}}{\text{pulse}} \tag{C.28}$$

Hence, under the assumption that the complete large crystal surface was illuminated by the ion pulse, a mean area of at least (250x250)μm^2 per ion was available (for the largest estimated value of 3,000 ions per pulse). Thus, due to the rather low number of ions per pulse and the large defocussing, no interaction of the excitations produced in individual ion tracks had to be expected.

[53] Typical current readings were less than 0.1pA up to to $\sim$ 0.05nA, dependent on the employed pulsing frequency.

C.11 Detection and Conversion Efficiency of the Decay-Time Measurement Setup

In the analysis of the decay-time spectra (see section III/5), the detection and conversion efficiency (amplitude of the voltage signal at the oscilloscope for one photon emitted by the $CaWO_4$ crystal) of the complete setup is used for the fits of the data: The model for the light production and quenching describes the pulse shape of photons escaping the crystal (unit: photons per second, $\frac{\gamma}{s}$). The data recorded in the decay-time measurements correspond to the output voltage of the PMT (V). Thus, the detection and conversion efficiency (unit: $\frac{Vs}{\gamma}$) delivers the conversion factor for the fits of the model to the data.

To gain an estimate of the detection and conversion efficiency DE of the setup used for the decay-time measurements several factors have to be considered. In addition, due to the different setups used for the different excitations ($ex = L$ for laser-excitation or $ex = IB$ for ion-beam excitation) and due to the different temperatures ($T = RT$ or $T = LT$) and different filters ($CWL = 400$nm or $CWL = 500$nm) used in the experiments, different detection and conversion efficiencies $DE_{ex,\,CWL,\,T}$ arise.

For the estimation of the detection and conversion efficiency of photons emitted by the $CaWO_4$ crystal the following factors are taken into account:

- The limited solid angle Ω_{ex} of observation, as determined in sections III/4.3.2 and III/4.4.2, for the laser- and ion-beam excitation measurements, respectively:

$$\begin{aligned} \Omega_L &= 8.2 \cdot 10^{-4} \\ \Omega_{IB} &= 1.2 \cdot 10^{-3} \end{aligned}$$

- The relative transmissions through the filters $Tr_{CWL,\,T}$, as determined in section III/4.2.4, for the 400nm and 500nm filter at room and low temperature, respectively:

$$\begin{aligned} Tr_{400nm,\,RT} &= 32\% \\ Tr_{400nm,\,LT} &= 35\% \\ Tr_{500nm,\,RT} &= 15\% \\ Tr_{500nm,\,LT} &= 15\% \end{aligned}$$

- The wavelength-dependent quantum efficiency QE_{CWL} of the photomultiplier (see section III/4.2.3):

$$\begin{aligned} QE_{400nm} &= 20.76\% \\ QE_{500nm} &= 14.38\% \end{aligned}$$

- The photon-electron gain $G_{\gamma\rightarrow e,\,ex}$ (unit: electron per photon, $\frac{e}{\gamma}$) of the PMT (see section III/4.2.3). This factor varies for different excitations due to the different used operating voltages of the PMT:

$$\begin{aligned} G_{\gamma\rightarrow e,\,L} &= 1.0 \cdot 10^6 \frac{e}{\gamma} \\ G_{\gamma\rightarrow e,\,IB} &= 5.0 \cdot 10^6 \frac{e}{\gamma} \end{aligned}$$

- The conversion of electrons into voltage $C_{e\rightarrow V}$ (unit: $\frac{Vs}{e}$) in the electronic output circuit defined by the 50ΩDC-coupling of the PMT to the oscilloscope:

$$C_{e\rightarrow V} = 1.6022 \cdot 10^{-19} \frac{As}{e} \cdot 50\Omega = 8.011 \cdot 10^{-18} \frac{Vs}{e} \tag{C.29}$$

Thus, the detection and conversion efficiency $DE_{ex,\,CWL,\,T}$ of a measurement with excitation ex at temperature T with the filter CWL is given by:

$$DE_{ex,\,CWL,\,T} = \Omega_{ex} \cdot Tr_{CWL,\,T} \cdot QE_{CWL} \cdot G_{\gamma\rightarrow e,\,ex} \cdot C_{e\rightarrow V} \tag{C.30}$$

In the following, an exemplary calculation to validate the value of the detection and conversion efficiency is presented. With the knowledge of the detection and conversion efficiency of the setup, the number of ions per pulse and the expected light yield for these ions (the quenching factor) the pulse height of the recorded PMT pulse can be estimated and then compared to the measurement. This calculation is performed for the example of the light produced under oxygen-beam excitation at room temperature detected with the 400nm filter:

In the oxygen-beam excitation experiments, one ion-pulse contained around $5 \cdot 10^2$ ions[54] with an energy of $E_{ion} \approx 35MeV$ per ion (see section III/4.7.3). For oxygen recoils in $CaWO_4$, a light yield (photons emitted by the crystal) at room temperature of around $LY^{\gamma}_{abs}(295\text{K}) \cdot QF^{O} \approx 3.3\% \cdot 7.8\% \approx 0.26\%$ can be expected[55]. Thus, taking into account the energy of one photon of ~ 2.9eV, around $1.6 \cdot 10^7$ photons per pulse are expected to escape the crystal. However, due to the restricted angle of observation Ω_{IB}, the limited filter transmission $Tr_{400nm,\,RT}$ and the quantum efficiency of the PMT QE_{400nm}, only $\sim 1.2 \cdot 10^3$ photons are detected with the PMT for one oxygen-pulse. These photons are converted into electrons according to the gain $G_{\gamma\rightarrow e,\,IB}$ of the PMT. These electrons are converted into a voltage by the output circuit of the PMT, as described by the factor $C_{e\rightarrow V}$. However, these photons do not reach the PMT at the same time, but are distributed according to the pulse shape of the scintillation light. At room temperature, the main component of the scintillation-light pulse detected at the PMT exhibits an exponential decay time of $\sim 9\mu$s (see, e.g. section III/2.2.1). Approximating the complete pulse with such an exponential, the maximum pulse height is given by the integral of the pulse divided by the decay time. Thus, the maximum pulse height expected for $\sim 1.2 \cdot 10^3$ detected photons per oxygen pulse amounts to $\sim 5.5 \cdot 10^{-3} \frac{C \cdot \Omega}{s} = 5.5$mV. Comparing this rough estimate[56] to the measured pulse height of ~ 3mV (see section III/5.3), shows a very satisfying agreement.

Thus, it can be concluded, that the values determined for the detection and conversion efficiency $DE_{ex,\,CWL,\,T}$ are within reasonable limits. Hence, when using this parameter as conversion factor in the fits of the measured data (see chapter III/5), reasonable results for the fit parameter of the number of ions per pulse can be expected.

[54] This number is a very rough estimate, see section III/4.7.3.

[55] Values for the light yield of 3.3% and the assumed Quenching Factor for high energetic oxygen recoils of 7.8% from sections III/2.2.4 and III/2.2.5.

[56] The major uncertainty, the uncertainty of the number of ions per pulse might account for a deviation of up to one order of magnitude.

Appendix D

Mathematical Aspects of the Data Acquisition and Analysis

D.1 Determination of Statistical Uncertainties

In the following, a brief discussion of the determination of the statistical uncertainty of individual data points on the basis of baseline samples is presented.

Under the assumption that the amplitudes of the data points are normally distributed around their mean value (white noise), their statistical uncertainty is in principle given by the 1σ width of this underlying gaussian distribution. As, however, this distribution is usually unknown, σ has to be estimated. For this purpose, a histogram of the amplitudes of a large number of i.i.d. data points (independent and identically distributed data points), as, e.g., data points of an empty baseline, can be created and fitted with a gaussian distribution. The fit result $\hat{\sigma}$ for the width of the gaussian distribution represents an estimate for the true underlying value σ. The estimate $\hat{\sigma}$ is of course afflicted with an uncertainty $\Delta\hat{\sigma}$ considering the true value σ. Thus, the statistical uncertainty of one data point should be estimated as a combination of the fitted $\hat{\sigma}$ value and its uncertainty $\Delta\hat{\sigma}$. However, if the number of data points used for the compilation of the histogram is very large, then the impact of the uncertainty $\Delta\hat{\sigma}$ on the determination of the true value σ can be assumed to be very small. Therefore, this uncertainty $\Delta\hat{\sigma}$ can be neglected in such a case and the statistical uncertainty for one data point can be assumed to be given by the value of $\hat{\sigma}$ only.

If the data points are chosen from a baseline sample, i.e. a sample that is expected to contain no signal, then the value of the mean of the fitted gaussian represents an estimate for the DC offset of the signal. If the number of data points is large, similar considerations as for the estimation of the value of σ can be made. Thus, for a large number of data points, the fitted value for the mean represents a very good estimate, with small uncertainty due to the chosen sample of data, for the true DC offset.

D.2 Recursive Summation in the Data Acquisition

As discussed in section III/4.2.3, in the data acquisition process on-line averaging of a large number of acquired pulses was performed in each measurement. The recursive summation

implemented in the software of the oscilloscope used for data acquisition is described by:

$$\overline{p_i} = \frac{1}{i} \cdot p_i + \frac{i-1}{i} \cdot \overline{p_{i-1}}$$

Concerning the data analysis of the averaged data it has to be kept in mind that this recursive summation can lead to artificially influenced pulse shapes of the recorded signals. For data samples with very small signal heights and large numbers of averaged events, this recursive summation can lead to vanishing values of newly added samples:

For example, a signal with a small but constant DC offset ΔV_{DC} and the summation process for one data point with (for simplicity) constant value ΔV_{DC} can be considered. For a large number $i-1$ of already averaged events, the new pulse is divided by a very large number i. If, in this arithmetic operation the accuracy limit of the machine is reached, the value that is added to the old averaged data point is equal to zero. Hence, the new averaged value of this data point is decreased by the factor $\frac{i-1}{i}$ though the real mean value would still be ΔV_{DC}.

In this way it is possible that the pulse shape at large times is artificially influenced, i.e. tends to exhibit too small signal heights for large times:

For the example of a machine accuracy of 1nV (which is the smallest resolution of data points in the output files) and 50,000 samples averaged, for the last pulse in the averaging process the smallest pulse height correctly added is 0.05mV. For a pulse with maximum pulse height of 2mV and a purely exponential decay time of $\tau = 100\mu$s this pulse height is already reached after only 3.7 lifetimes of decay. Hence, for the data point at $t = 3.7 \cdot \tau$ this effect occurs in the last averaging procedure, i.e. in the calculation of the last averaged value $\overline{p_i}$, for $i = 50,000$. However, for data points at times $t > 3.7 \cdot \tau$, i.e. signal heights $< 0.05mV$, this effect occurs already at a correspondingly earlier stage of the averaging procedure at $i < 50,000$. Thus, for data points at larger times this effect gains more and more influence on the averaging procedure.

As can be seen from the example calculation, also for the largest decay times considered here ($\sim 75\mu$s) and the smallest signal heights (~ 0.4mV) this effect should not significantly influence the signal shape for at least three lifetimes of exponential decay. However, the possibility of this effect to occur should be considered and the data range chosen in the analysis of the pulse should thus not be extended to too large times.

Additionally it should be noted that this effect can prevent the detection of very long decay times (of the order of several 100μs up to several ms) which are sometimes reported to be observed for $CaWO_4$ in literature: In some references very slow, weak components of the decay-time spectrum of the $CaWO_4$ scintillation light with decay times of $\sim 200\mu$s at room temperature [53] or even up to hours [66] (and references therein) are reported.

Appendix E

Details on the Analysis of the Unquenched Decay-Time Spectra

E.1 Fit Functions for the Unquenched Decay-Time Spectra

In the following, details on the determination and application of the function used to fit the decay-time spectra recorded for laser excitation (discussed in section III/5.2.1) are presented.

At first, several simplifications of the expressions for such an unquenched decay-time spectra of one electron-hole pair are discussed where thereafter, the complete decay-time spectrum for all electron-hole pairs excited by one laser pulse as well as the consideration of the impulse reaction of the utilized detection system are described. As last feature of the recorded scintillation-light decay-time spectra that has to be considered for the formulation of the fit function, the direct detection of a fraction of the laser light that is reflected at the $CaWO_4$ crystal is discussed.

Simplifications of the Unquenched Decay-Time Spectrum for One Electron-Hole Pair

As discussed in detail in section III/3.2.3 (and appendix B.8), the complete expressions describing the pulse shapes of the blue and green scintillation light contain terms (partial pulses) that are significantly less important (in the sense of their partial integrals) than the leading terms of these formulas. As deduced in section III/3.2.3 and estimated in appendix B.8, the difference between the integrals of the leading terms and those of the smaller partial pulses is larger than three orders of magnitude. Therefore, it cannot be expected that the pulse shapes described by these small partial pulses can be fixed by the fits. Thus, following the argumentation outlined in section III/3.2.3 (in the unquenched model for room temperature as well as in the unquenched model for $T \approx 20$K), the influence of the small partial pulses will be neglected in the fits of the pulse shapes predicted by the model to the decay-time spectra recorded. The following, simplified expressions for the pulse shapes of the unquenched scintillation light generated by individual STEs at ~ 300K (for the original expressions, see equations 3.104 and 3.105 in section III/3.2.3)

will be used:

$$P_b^{nq\,fit}(1\,eh, T \approx 300\mathrm{K}, t) = \Theta(t) \cdot \frac{(1 - F_{abs}) \cdot (1 - F_{e^- trap}) \cdot 1}{\tau_{rb}(T)} \cdot \\ \cdot \frac{\frac{1}{\tau_{ltg}(T)} - \frac{1}{\tau_1(T)}}{\frac{1}{\tau_2(T)} - \frac{1}{\tau_1(T)}} \cdot \left[(1 - F_{dr}(T)) \cdot e^{-\frac{t}{\tau_1(T)}} + \frac{F_{dr}(T)}{1 - \frac{\tau_{dr}(T)}{\tau_1(T)}} \cdot \left\{ e^{-\frac{t}{\tau_1(T)}} - e^{-\frac{t}{\tau_{dr}(T)}} \right\} \right] \tag{E.1}$$

$$P_g^{nq\,fit}(1\,eh, T \approx 300\mathrm{K}, t) = \Theta(t) \cdot \frac{(1 - F_{e^- trap}) \cdot 1}{\tau_{rg}(T)} \cdot \frac{\frac{1}{\tau_{\mathrm{mig,\ b\to g}}(T)} + F_{abs} \cdot \frac{1}{\tau_{rb}(T)}}{\frac{1}{\tau_2(T)} - \frac{1}{\tau_1(T)}} \cdot \\ \cdot \left[(1 - F_{dr}(T)) \cdot \left\{ e^{-\frac{t}{\tau_1(T)}} - e^{-\frac{t}{\tau_2(T)}} \right\} + \frac{F_{dr}(T)}{1 - \frac{\tau_{dr}(T)}{\tau_1(T)}} \cdot \left\{ e^{-\frac{t}{\tau_1(T)}} - e^{-\frac{t}{\tau_{dr}(T)}} \right\} \right] \tag{E.2}$$

The following, simplified expressions for the pulse shapes of the unquenched scintillation light generated by individual STEs at $\sim$ 20K (for the original expressions, see equations 3.126 and 3.127 in section III/3.2.3) will be used:

$$P_b^{nq\,fit}(1\,eh, T \approx 20\mathrm{K}, t) = \Theta(t) \cdot \frac{(1 - F_{abs}) \cdot (1 - F_{e^- trap}) \cdot 1}{\tau_{rb}(T)} \cdot \\ \cdot \frac{\frac{1}{\tau_{ltg}(T)} - \frac{1}{\tau_1(T)}}{\frac{1}{\tau_2(T)} - \frac{1}{\tau_1(T)}} \cdot \left[e^{-\frac{t}{\tau_1(T)}} \right] \tag{E.3}$$

$$P_g^{nq\,fit}(1\,eh, T \approx 20\mathrm{K}, t) = \Theta(t) \cdot \frac{(1 - F_{e^- trap}) \cdot 1}{\tau_{rg}(T)} \cdot \\ \cdot \frac{\frac{1}{\tau_{\mathrm{mig,\ b\to g}}(T)} + F_{abs} \cdot \frac{1}{\tau_{rb}(T)}}{\frac{1}{\tau_2(T)} - \frac{1}{\tau_1(T)}} \cdot \left[e^{-\frac{t}{\tau_1(T)}} - e^{-\frac{t}{\tau_2(T)}} \right] \tag{E.4}$$

where it should be noted, that for equation E.4, describing the pulse shape of the scintillation light at $\sim$ 20K no simplifications were performed. As further justification of these simplification, in section III/5.2.2, the partial integrals of all of the different pulses contained in the original formulas of the pulse shapes will be calculated. The predicted negligibility of the smaller partial pulses will be confirmed. From these equations expressing the main features of the unquenched blue and green $CaWO_4$ scintillation-light decay-time spectra at room temperatures and $\sim$ 20K, it can be seen that the only qualitative difference for these two temperatures is the partial delayed rise (fraction $F_{dr}(T)$ with rise time $\tau_{dr}(T)$) of a fraction of the scintillation light at room temperature due to the partial delayed recombination of electrons and STHs to STEs. Of course, the absolute values of the effective unquenched lifetimes $\tau_1(T)$ and $\tau_2(T)$ are also expected to be different for different temperatures. In addition, it can be noted that in both expressions for the blue decay-time spectrum (equations E.1 and E.3), the effective unquenched lifetime of the green STEs, $\tau_2(T)$, does not appear. The effective unquenched lifetime of blue STEs, $\tau_1(T)$, however, is a parameter of all of the decay-time spectra.

Consideration of the Temporal Shape of the Laser Pulse Used for the Excitation

The pulse shapes as expressed by equations E.1 to E.4 describe the scintillation-light

decay-time spectra produced by one individual electron-hole pair initially created at a temperature of $\sim$ 300K and $\sim$ 20K, respectively. Of course it has to be taken into account that, within the excitation process of one laser pulse not only one electron-hole pair is generated. In addition, the the non-negligible temporal width of the excitation pulse, $L(t)$ (gaussian model of the laser pulse with a pulse width of $\sigma_L = 1.803$ns, compare section III/4.7.3 and appendix C.10.2) has to be considered. In order to include the excitation by the laser pulse into the description of the decay-time spectrum of the scintillation light, the fact is used that in the two-photon excitation the individual electron-hole pairs created do not interact with each other. Therefore, the impact of the temporally distributed excitation (by the laser pulse with a non-negligible width) can be modeled by a convolution of the excitation pulse (laser pulse-shape) with the produced scintillation-light pulse-shape, $P_b^{nq\,fit}(1\,eh,T,t)$ and $P_g^{nq\,fit}(1\,eh,T,t)$, respectively. However, it has to be taken into account that the excitation by the laser pulse is a two-photon absorption, hence, the scintillation-light pulse-shapes have to be convoluted with the squared laser pulse-shape, $L^2(t)$. In addition, it has to be noted that, as discussed in section III/4.1.3, no quantitative statement on the number of electron-hole pairs created in the two-photon absorption process can be made[1]. Thus, the dependency of the decay-time spectra on the intensity of the laser pulse cannot be expressed explicitly. Instead, the integrated number of electron-hole pairs initially created in the absorption process of one laser pulse, labelled as $N_{eh}^L(T)$, is a free fit parameter. As indicated, this parameter could be dependent on temperature as the probability for the two-photon absorption to occur could vary with temperature. From the discussion of the two-photon excitation, it can be deduced that these initially created STEs have to follow the temporal distribution of the squared laser pulse-shape. Thus, for the example of the blue scintillation light at $T \approx 300K$ the scintillation-light pulse shape predicted by the model for the excitation by one light-pulse of the N_2 laser can be expressed by the following equations:

$$L(t) = \frac{L_0}{\sqrt{2\cdot\pi}\cdot\sigma_L}\cdot e^{-\frac{(t-\mu_L)^2}{2\cdot\sigma_L^2}} \tag{E.5}$$

$$P_b^{L\,fit}(N_{eh}^L(T), T\approx 300\text{K}, t) = \\ = \left[N_{eh}^L(T\approx 300\text{K})\cdot\left(\frac{1}{\sqrt{2\cdot\pi}\cdot\sigma_L}\cdot e^{-\frac{(t-\mu_L)^2}{2\cdot\sigma_L^2}}\right)^2\right] * P_b^{nq\,fit}(1\,eh, T\approx 300\text{K}, t) \tag{E.6}$$

where L_0 corresponds to the number of laser photons per laser pulse and μ_L corresponds to the time shift of the maximum of the laser pulse in relation to the trigger signal (delivered by the Si-Diode, as described in section III/4.3.2). In analogy to equation E.6, the blue and green scintillation-light decay-time spectra for the excitation by one laser pulse, $P_g^{L\,fit}(N_{eh}^L(T), T\approx 300\text{K}, t)$, $P_b^{L\,fit}(N_{eh}^L(T), T\approx 20\text{K}, t)$ and $P_g^{L\,fit}(N_{eh}^L(T), T\approx 20\text{K}, t)$ can be expressed as convolution of the single STE decay-time spectra (equations E.2 to E.4) and the laser-light pulse-shape. From equation E.6, it can be deduced that the corresponding numbers of electron-hole pairs created per laser pulse, $N_{eh}^L(T)$, in fact, do not alter the pulse shapes of the scintillation light but simply deliver a multiplication factor.

Inspecting equations E.1 to E.4, it can be observed that the scaling factors of the pulse

[1] For a possibility to realize a determination of the number of electron-hole pairs created in the two-photon excitation process and advantages that could be gained from this information, see section III/6.3. However, in the experiments conducted within the present work, no such assignment could be performed.

shapes of single electron-hole pairs (terms before the square brackets, respectively) contain at least two unknown parameters (e.g., $\tau_{rb}(T)$ and $\tau_{ltg}(T)$ in equation E.1) not appearing in other terms of the equations. Thus, the impact of these parameters on the pulse shape of the produced scintillation light cannot be disentangled by a fit with these equations to data. Taking additionally the unknown number of electron-hole pairs created per laser pulse, $N_{eh}^{L}(T)$, into account, which also only delivers a scaling factor, it can be seen that, in order to use the determined description as fit function for the recorded data, all of these undetermined parameters of the scaling factors have to be united into one fit parameter, $I_b^{nq\,fit}(T)$ and $I_g^{nq\,fit}(T)$, controlling the size of the pulse shapes. It should be noted that these united parameters can be expressed by the same expression for a temperature of ~ 300K and for a temperature of ~ 20K. Nonetheless, of course, these parameters exhibit different values at the different temperatures. These parameters are defined by:

$$I_b^{nq\,fit}(T) := \frac{(1-F_{abs})\cdot(1-F_{e^-trap})}{\tau_{rb}(T)} \cdot \frac{\frac{1}{\tau_{ltg}(T)} - \frac{1}{\tau_1(T)}}{\frac{1}{\tau_2(T)} - \frac{1}{\tau_1(T)}} \cdot N_{eh}^{L}(T) \tag{E.7}$$

$$I_g^{nq\,fit}(T) := \frac{(1-F_{e^-trap})}{\tau_{rg}(T)} \cdot \frac{\frac{1}{\tau_{\mathrm{mig,\ b\to g}}(T)} + F_{abs}\cdot\frac{1}{\tau_{rb}(T)}}{\frac{1}{\tau_2(T)} - \frac{1}{\tau_1(T)}} \cdot N_{eh}^{L}(T) \tag{E.8}$$

Using these parameters and equation E.1 as well as equation E.6 (describing the convolution of the decay-time spectrum for a single electron-hole pair with the excitation pulse), the following expression for the decay-time spectrum of the blue scintillation-light created by one laser pulse at $T \approx 300$K can be obtained :

$$P_b^{L\,fit}(N_{eh}^{L}(T), T\approx 300\mathrm{K}, t) = I_b^{nq\,fit}(T)\cdot\left[\left(\frac{1}{\sqrt{2\cdot\pi}\cdot\sigma_L}\cdot e^{-\frac{(t-\mu_L)^2}{2\cdot\sigma_L^2}}\right)^2 * \right.$$
$$\left. * \left(\Theta(t)\cdot\left[(1-F_{dr}(T))\cdot e^{-\frac{t}{\tau_1(T)}} + \frac{F_{dr}(T)}{1-\frac{\tau_{dr}(T)}{\tau_1(T)}}\cdot\left\{e^{-\frac{t}{\tau_1(T)}} - e^{-\frac{t}{\tau_{dr}(T)}}\right\}\right]\right)\right] \tag{E.9}$$

The expressions for the decay-time spectra of the green scintillation light at $T \approx 300$K, $P_g^{L\,fit}(N_{eh}^{L}(T), T\approx 300\mathrm{K}, t)$, as well as of the blue and green scintillation light at $T \approx 20$K, $P_g^{L\,fit}(N_{eh}^{L}(T), T\approx 20\mathrm{K}, t)$ and $P_g^{L\,fit}(N_{eh}^{L}(T), T\approx 20\mathrm{K}, t)$, respectively, produced by all of the electron-hole pairs excited by one laser pulse can be obtained in an analogous way.

Consideration of the Response Function of the Detection System

As already indicated at the beginning of this paragraph, in addition, the influence of the impulse reaction of the employed detection system, i.e., of the PMT and the oscilloscope, has to be taken into account. This response function, $Ir(t)$, is introduced and determined in appendix C.4.4 and can be described by a convolution of a gaussian shape, $G_{TT}(t)$, corresponding to the transit-time spread and shift introduced by the PMT, and an exponential function, $E_{ER}(t)$, corresponding to the rise or decay times of the signal introduced by the electronic read-out circuit. In addition, to establish the final fit functions, the detection and conversion efficiency, $DE_{ex,CWL,T}$, of the used setup (containing, e.g., the transmissions of the utilized optical filters or the gain of the PMT, see appendix C.11 for details) has to be considered. By multiplying the fit function with $DE_{ex,CWL,T}$,

the unit of the scintillation-light decay-time spectra is converted from photons per second escaping the crystal into volts per second on the oscilloscope. Hence, in order to obtain the final fit function, the decay-time spectrum of the scintillation light produced (equation E.9 for the example of the blue light produced at ~ 300K) has to be convoluted with the response function of the detection system and be multiplied with the detection and conversion efficiency of the utilized setup. The following expression for the fit function describing the recorded data is obtained for the example of the blue scintillation light produced for one laser pulse at a temperature of ~ 300K (executing all of the convolutions analytically):

$$
\begin{aligned}
P_b^{L\,fit\,final}(N_{eh}^L(T), T \approx 300\text{K}, t) = \frac{I_b^{nq\,fit}(T) \cdot DE_{L,\,400nm,\,RT}}{2} \cdot \\
\cdot \Bigg[\frac{1}{1-\frac{\tau_{el}}{\tau_1(T)}} \cdot \left(1 - \frac{F_{dr}(T)}{1-\frac{\tau_1(T)}{\tau_{dr}(T)}} \right) \cdot e^{-\frac{t-\mu_{tot}}{\tau_1(T)}} \cdot e^{\left(\frac{\sigma_{tot}}{\sqrt{2}\cdot\tau_1(T)}\right)^2} \cdot \\
\cdot \left\{ 1 + erf\left(\frac{t-\mu_{tot}}{\sqrt{2}\cdot\sigma_{tot}} - \frac{\sigma_{tot}}{\sqrt{2}\cdot\tau_1(T)} \right) \right\} - \\
- \frac{F_{dr}(T)}{1-\frac{\tau_{dr}(T)}{\tau_1(T)}} \cdot \frac{1}{1-\frac{\tau_{el}}{\tau_{dr}(T)}} \cdot e^{-\frac{t-\mu_{tot}}{\tau_{dr}(T)}} \cdot e^{\left(\frac{\sigma_{tot}}{\sqrt{2}\cdot\tau_{dr}(T)}\right)^2} \cdot \\
\cdot \left\{ 1 + erf\left(\frac{t-\mu_{tot}}{\sqrt{2}\cdot\sigma_{tot}} - \frac{\sigma_{tot}}{\sqrt{2}\cdot\tau_{dr}(T)} \right) \right\} - \\
- \left(\frac{1}{1-\frac{\tau_{el}}{\tau_1(T)}} \cdot \left(1 - \frac{F_{dr}(T)}{1-\frac{\tau_1(T)}{\tau_{dr}(T)}} \right) - \frac{F_{dr}(T)}{1-\frac{\tau_{dr}(T)}{\tau_1(T)}} \cdot \frac{1}{1-\frac{\tau_{el}}{\tau_{dr}(T)}} \right) \cdot e^{-\frac{t-\mu_{tot}}{\tau_{el}}} \cdot e^{\left(\frac{\sigma_{tot}}{\sqrt{2}\cdot\tau_{el}}\right)^2} \cdot \\
\cdot \left\{ 1 + erf\left(\frac{t-\mu_{tot}}{\sqrt{2}\cdot\sigma_{tot}} - \frac{\sigma_{tot}}{\sqrt{2}\cdot\tau_{el}} \right) \right\} \Bigg] + c_{BL}
\end{aligned}
\tag{E.10}
$$

where c_{BL}, is a possible constant offset of the baseline of the recorded pulse, $\tau_{el} = 8.300$ns is the decay time of the electronic read-out system and $\mu_{tot} := \mu_L + \mu_{TT}$ is the total time shift of the maximum of the laser-light pulse compared to the time of trigger due to the shift of the laser-light pulse μ_L and due to the shift μ_{TT}, introduced by the PMT transit-time spread. $\sigma_{tot} := \sqrt{\sigma_{TT}^2 + \frac{\sigma_L^2}{2}} = 1.805$ns is the total broadening of the signal shape introduced by $\sigma_{TT} = 1.278$ns, the transit time spread of the PMT, and $\sigma_L = 1.803$ns, the width of the laser pulse. For the determination of the values of the different parameters, see appendix C.4.4. It should be noted that, as these parameters are determined with high accuracy, in the following, they are assumed to be fixed to the respective values stated (compare discussion in appendix C.4.4). The expressions for the fit functions of the decay-time spectra recorded for the green scintillation light at $T \approx 300$K as well as for the blue and the green scintillation light at $T \approx 20$K can be calculated in an analogous way.

Consideration of the Reflected Laser Light

As discussed in detail in section III/4.7.2 and appendix C.10, a fraction of the laser-light pulse is reflected at and within the $CaWO_4$ and is scattered into the solid angle covered by the PMT. As the laser-light pulses are very intense, part of this reflected laser light

is transmitted through the optical filter positioned in front of the PMT and is directly detected by the PMT. Thus, if the recorded pulse shape is fitted with a function also the directly detected fraction of the laser light has to be considered. For this purpose, the fit function of the detected $CaWO_4$ scintillation light described by equation 5.11 has to be extended for a term describing the light-pulse shape of the reflected laser light, $L(t)$, with an individual scaling factor. Of course also this pulse shape has to be convoluted with the impact reaction, $Ir(t)$, of the employed detection system. It has to be noted that, as the laser light being reflected and then detected with the PMT is, of course, identical with the laser pulse exciting the scintillation light of the $CaWO_4$ crystal, the combined temporal shift $\mu_{tot} := \mu_L + \mu_{TT}$ of the scintillation light-pulse as well as of the reflected laser light pulse are identical. Hence, the following term, $R^L(T,t)$, corresponding to the reflected laser-light pulse has to be added to $P_b^{L\,fit\,final}(N_{eh}^L(T), T \approx 300\text{K}, t)$ (and of course also to the fit functions describing the other decay-time spectra of the produced scintillation light):

$$R^L(T,t) = \frac{R_0(T)}{2\cdot\tau_{el}} \cdot e^{-\frac{t-\mu_{tot}}{\tau_{el}}} \cdot e^{\frac{\sigma_L^2+\sigma_{TT}^2}{2\cdot\tau_{el}^2}} \cdot \left\{ 1 + erf\left(\frac{t-\mu_{tot}}{\sqrt{2}\cdot\sqrt{\sigma_L^2+\sigma_{TT}^2}} - \frac{\sqrt{\sigma_L^2+\sigma_{TT}^2}}{\sqrt{2}\cdot\tau_{el}} \right) \right\} \tag{E.11}$$

where $R_0(T)$ is the only additional free fit parameter introduced and contains all scaling factors that have to be taken into account for the reflected laser light (e.g., the amount of laser light reflected which could possibly be temperature dependent or the transmission of the optical filters for the laser light). It can be seen that, instead of σ_{tot}, the expression $\sqrt{\sigma_{TT}^2+\sigma_L^2}$ is used. This is due to the fact, that for the representation of the reflected laser light, the shape of the laser light does not have to be squared in contrary to the excitation via the two-photon effect.

Summary of the Unquenched Scintillation-Light Fit-Function

Thus, the complete fit functions, $F_{b/g}^L(N_{eh}^L(T), T, t)$, for the unquenched blue and green scintillation-light decay-time spectra recorded with laser excitation can be described as the sum of the blue or green $CaWO_4$ scintillation light, $P_{b/g}^{L\,fit\,final}(N_{eh}^L(T), T, t)$ (equation 5.11, influenced by the width of the laser-light pulse used for excitation and by the impulse reaction of the detection system) and of the reflected laser-light pulse-shape, $R^L(T,t)$ (equation 5.12, influenced by the impulse reaction of the detection system):

$$F_{b/g}^L(N_{eh}^L(T), T, t) = P_{b/g}^{L\,fit\,final}(N_{eh}^L(T), T, t) + R^L(T,t) \tag{E.12}$$

It should be noted that, due to the reflected laser light covering the beginning of the scintillation-light pulse as well as due to the impulse reaction of the detection system and the non-negligible width of the excitation pulse, features of the recorded pulse shape at the beginning of the pulse as, e.g., the partial rise time $\tau_{dr}(T)$ of the fraction $F_{dr}(T)$ of the blue scintillation light at $T \approx 300\text{K}$ or the rise of the green scintillation light with rise time $\tau_2(T)$ (at $\sim 300\text{K}$ and at $\sim 20\text{K}$), are problematic to fix with the fit. Taking additionally into account that, as discussed in appendix C.4, for large PMT signals (latest for signal heights larger than 0.9V), the PMT signal starts to saturate and that additionally, for small times t after the excitation pulse, a non-negligible extra noise-component (crosstalk from the laser discharge) is observable on the recorded signals, it

becomes clear that the determination of these parameters by fits of the recorded decay-time spectra is challenging or even impossible. The strategy used to obtain, nonetheless, values or at least estimates for these parameters is discussed in the following. In addition, a list of the free fit parameters is provided.

E.2 Applied Fit Procedure and Free Fit Parameters

The Parameters $\tau_1(T)$ and $\tau_2(T)$

It should be noted that, in the fit procedure applied, the unquenched effective lifetimes of the STEs, $\tau_1(T)$ and $\tau_2(T)$, are used as fit parameters and not their decomposition into the various process times as expressed by equations 3.106 and 3.107 (section III/3.2.3). Thus, the fits will deliver values for the unquenched effective lifetimes of the STEs, $\tau_1(T)$ and $\tau_2(T)$, where the extraction of the size of the individual process times, as, e.g., the radiative decay time of blue STEs, $\tau_{rb}(T)$, will be performed in the analysis of the fit results. This strategy was chosen as the unquenched effective lifetimes contain a too large number of undetermined parameters resulting in the dependency of the fit function on several of these parameters in a mathematically indistinguishable way (for a further discussion of this fact as well as implications of this observation, see section III/5.2.2).

Simultaneous Fits of All Wavelength Spectra Recorded for the Same Conditions

With these fit functions, features of the decay-time spectra as short as the rise time of the green scintillation light (of the order of 1ns to 10ns) and as long as the decay times of the pulses (several μs up to hundreds of μs) have to be fitted at the same time. In this context, the exact measurements conducted with laser excitation should be recalled: As discussed in section III/4.5.2, for each combination of investigated crystal, temperature and optical filter, several decay-time spectra were recorded. For temperatures of $\sim$ 300K, two measurements under the same conditions were performed, only differing concerning the utilized record length (10μs and 100μs) and, thus, temporal resolution of the recording (high resolution, containing optimized data for the short rise times of the pulses, low resolution, but long record length, containing optimized data for the long decay times of the pulses). For temperatures of $\sim$ 20K, three measurements under the same conditions were performed with record lengths of 10μs, 100μs and 1000μs. In order to utilize all of the information delivered by the different measurements belonging to the same conditions (crystal, temperature and optical filter) at once, all of the respective decay-time spectra are fitted simultaneously: Thus, e.g., for the measurement $\mathbf{O9_{PMT}}$ ($T \approx$ 300K, 400nm filter), the fit function $F_b^L(N_{eh}^L(T), T \approx 300\text{K}, t)$ specified by equation 5.13 with the identical fit parameters inserted is used for both of the measurements performed with 10μs and 100μs record lengths. The only difference between the simultaneously fitted functions is an overall multiplication factor, $M_{100\mu\text{s}}(T \approx 300\text{K})$, of the 100$\mu$s measurement, allowing for a total, overall, different scaling of the size of the fitted pulse shapes. This scaling factor was needed, as the laser was not running with a constant power output resulting in different signal heights even for measurements performed successively under exactly the same conditions. In analogy, for the measurements performed at low temperatures ($T \approx$ 20K), all of the three measurements performed were fitted simultaneously with the same fit function containing the identical parameters, except for the two scaling factors

$M_{100\mu s}(T \approx 20\text{K})$ and $M_{1000\mu s}(T \approx 20\text{K})$ of the fit functions of the 100μs and 1000μs measurements.

Simultaneous Fits of All Wavelength Spectra Recorded at the Same Temperature (for one Crystal)

Furthermore, it should be taken into account that, as discussed above (discussion below equation E.4), e.g., the same unquenched effective lifetime of blue STEs, $\tau_1(T)$, appears in both fit functions for the blue ($F_b^L(N_{eh}^L(T), T, t)$) as well as for the green ($F_g^L(N_{eh}^L(T), T, t)$) decay-time spectra at the same temperature. Thus, in addition to fitting all measurements performed with one crystal, at one temperature with one optical filter simultaneously, all measurements performed with one crystal, at one temperature and both of the optical filters (400nm and 500nm filter) are fitted simultaneously, with all fit parameters ($\tau_1(T)$ as well as $\tau_{dr}(T)$ and $F_{dr}(T)$) appearing in both of the fit functions being identical[2]. This strategy was pursued, on the one hand, to reduce the number of free fit parameters and, on the other hand, to use as much information as possible delivered by the recorded data at once to fix the individual fit parameters.

Performed Fits and Free Fit Parameters

Thus, the following sets of free fit parameters result for the respective combinations of measurements fitted simultaneously:

- The laser-excitation measurements performed with crystal Olga at room temperature ($T = 298\text{K}$) with the 400nm filter, $\mathbf{O9_{PMT}}$ (10μs and 100μs), and the 500nm filter, $\mathbf{O11_{PMT}}$ (10μs and 100μs), were fitted simultaneously. The following set of free fit parameters was used:
  - the same in all fit functions: $\tau_1(298\text{K})$, $\tau_{dr}(298\text{K})$, $F_{dr}(300\text{K})$
  - the same in all $\mathbf{O9_{PMT}}$ measurements: $I_b^{nq\,fit}(298\text{K})$, μ_{tot}^b, c_{BL}^b, $R_0^b(298\text{K})$
  - the same in all $\mathbf{O11_{PMT}}$ measurements: $I_g^{nq\,fit}(298\text{K})$, $\tau_2(298\text{K})$, μ_{tot}^g, c_{BL}^g, $R_0^g(298\text{K})$
  - the scaling factors: $M_{10\mu s}^b(298\text{K})$ and $M_{10\mu s}^g(298\text{K})$

- The laser-excitation measurements performed with crystal Olga at low temperature ($T = 20\text{K}$) with the 400nm filter, $\mathbf{O10_{PMT}}$ (10μs, 100μs and 1000μs), and the 500nm filter, $\mathbf{O12_{PMT}}$ (10μs, 100μs and 1000μs), were fitted simultaneously. The following set of free fit parameters was used:
  - the same in all fit functions: $\tau_1(20\text{K})$
  - the same in all $\mathbf{O10_{PMT}}$ measurements: $I_b^{nq\,fit}(20\text{K})$, μ_{tot}^b, c_{BL}^b, $R_0^b(20\text{K})$
  - the same in all $\mathbf{O12_{PMT}}$ measurements: $I_g^{nq\,fit}(20\text{K})$, $\tau_2(20\text{K})$, μ_{tot}^g, c_{BL}^g, $R_0^g(20\text{K})$
  - the scaling factors: $M_{10\mu s}^b(20\text{K})$, $M_{1000\mu s}^b(20\text{K})$, $M_{10\mu s}^g(20\text{K})$, $M_{1000\mu s}^g(20\text{K})$.

- The laser-excitation measurements performed with crystal Philibert at room temperature ($T = 298\text{K}$) with the 400nm filter, $\mathbf{P5_{PMT}}$ (10μs and 100μs), were fitted simultaneously. The following set of free fit parameters was used:
  - the same in all $\mathbf{P5_{PMT}}$ measurements:

[2]For the low-temperature measurements, no delayed rise time of a fraction of the scintillation light is included in the model, hence, for the low temperature measurements, the only fit parameter appearing in the green and the blue fit function is the decay time $\tau_1(T)$

$I_b^{nq\,fit}$(298K), τ_1(298K), μ_{tot}^b, τ_{dr}(298K), F_{dr}(298K), c_{BL}^b, R_0^b(298K)
- the scaling factor $M_{10\mu s}^b$(298K).

- The laser-excitation measurements performed with crystal Philibert at low temperature (T = 18K) with the 400nm filter, $\mathbf{P6_{PMT}}$ (10μs, 100μs and 1000μs), were fitted simultaneously. The following set of free fit parameters was used:
  - the same in all $\mathbf{P6_{PMT}}$ measurements: $I_b^{nq\,fit}$(18K), τ_1(18K), μ_{tot}^b, c_{BL}^b, R_0^b(18K)
  - the scaling factors $M_{10\mu s}^b$(18K), $M_{1000\mu s}^b$(18K).

As for crystal Philibert, no measurements with the 500nm filter utilized were performed, the effective unquenched lifetime of green STEs $\tau_2(T)$ does not appear in the fits and can, hence, not be determined.

E.3 Determination of the Free Parameters of the Unquenched Model from the Fit Results

In this section, the outline of the method used to obtain the values of the free parameters of the unquenched model at $T \approx$ 300K and $T \approx$ 20K from the results of the fits of the decay-time spectra is described:

The free parameters $\tau_{dr}(T)$ and $F_{dr}(T)$ of the unquenched model are directly included as parameters in the fit functions of the decay-time spectra at room temperature. It should be noted that, as discussed in section III/3.1.2 for temperatures below $\sim$ 100K the delayed creation process of a fraction of the initially created blue STEs is assumed to be negligible. Hence, all informations on the delayed creation process that can be gained from the fits of the unquenched decay-time spectra with the fit functions are the values of $\tau_{dr}(T)$ and $F_{dr}(T)$ for T = 298K.

Concerning the determination of the other free parameters of the unquenched model, in the following, it is assumed that the effective unquenched lifetimes of the blue and the green STEs, τ_1(298K), τ_1(20K) and τ_2(298K), τ_2(20K), respectively, were determined by the fits of the recorded unquenched decay-time spectra with the described fit functions (see appendix E.1).

From equations 3.106 and 3.107 (section III/3.2.3), defining the effective unquenched lifetimes of the blue and the green STEs, $\tau_1(T)$ and $\tau_2(T)$ it can be seen that these parameters depend on several per se unknown STE recombination times: the intrinsic lifetimes $\tau_{ltb}(T)$ and $\tau_{ltg}(T)$ of the blue and green STEs, the radiative decay times $\tau_{rb}(T)$ and $\tau_{rg}(T)$ and the migration time of blue STEs to green (defect) centers $\tau_{\mathrm{mig,\ b\rightarrow g}}(T)$. In fact, it should be noted that the dependency on $\tau_{\mathrm{mig,\ b\rightarrow g}}(T)$ corresponds to a dependency on the defect density C_{defects} (compare, e.g., equation 3.45 in section III/3.1.3) as the diffusion coefficient for blue STEs and, thus, the hopping time of blue STEs, is assumed to be known (compare section III/3.3.2). As additional information, the relative amount of blue photons produced (compared to all photons produced) in the performed measurements is available via the analysis of the wavelength spectra in section III/5.1. This information can be used, when considering the expression for the total amount of blue photons produced $P_b^{nq}(E_{part}, T)$ (for the deposition of the energy E_{part} creating $N_{eh}(E_{part})$ electron-hole pairs) delivered by the unquenched model (see equation 3.108 in section III/3.2.3):

Dividing $P_b^{nq}(E_{part}, T)$ by the number of STEs produced, i.e., by $N_{eh}(E_{part}) \cdot (1 - F_{e-trap})$, an expression for the relative amount of STEs decaying radiatively into blue photons dependent on $\tau_{rb}(T)$, $\tau_{ltg}(T)$, $\tau_1(T)$ and $\tau_2(T)$ is obtained:

$$P_b^{nq}(E_{part}, T) = (1 - F_{abs}) \cdot \frac{(1 - F_{e^-trap}) \cdot N_{eh}(E_{part})}{\tau_{rb}(T)} \cdot \frac{\tau_1(T) \cdot \tau_2(T)}{\tau_{ltg}(T)}$$

$$\Rightarrow \frac{P_b^{nq}(E_{part}, T)}{(1 - F_{e^-trap}) \cdot N_{eh}(E_{part})} = \frac{(1 - F_{abs})}{\tau_{rb}(T)} \cdot \frac{\tau_1(T) \cdot \tau_2(T)}{\tau_{ltg}(T)} \tag{E.13}$$

This quantity, however, the relative amount of STEs decaying radiatively and producing blue photons, is assumed to be known, as on the one hand, the unquenched light yield, i.e., the absolute fraction of STEs decaying radiatively (into blue and green photons) at room temperature and below $\sim$ 50K is assumed to be known (compare equation 3.188 in section III/3.3.2): For a spatially separated STE population as produced in the laser-excitation experiments, for temperatures below $\sim$ 50K, each STE produced is expected to decay radiatively (compare discussion in section III/3.2.1). Thus, the relative amount of STEs decaying radiatively into blue photons at a temperature of $T \approx 20$K is directly given by the ratio $r_b(T = 20\text{K})$ of blue photons produced as determined from the analysis of the wavelength spectra in section III/5.1. For room temperature, the relative amount of STEs decaying radiatively into blue photons can be obtained from the relative number of blue photons produced at room temperature, $r_b(T = 298\text{K})$ (known from the analysis of the wavelength spectra in section III/5.1) and the relative unquenched light yield at room temperature compared to low temperature (compare equation 3.188 in section III/3.3.2). Thus, the value of the left side of equation E.13 is assumed to be known for the investigated crystal at $T = 298$K and $T = 20$K.

In addition, the definitions of the intrinsic lifetimes of the STEs $\tau_{ltb}(T)$ and $\tau_{ltg}(T)$ given by equations 3.131 and 3.132 for $T \approx 300$K and by equations 3.122 for $T \approx 20$K (in section III/3.2.3), have to be taken into account. It should be noted that, for 20K, these equations contain no additional unknown parameters as the lifetimes of STEs at such low temperatures are exclusively determined by the radiative and migration times of the respective STEs where the migration time of the green STEs is assumed to be known (compare section III/3.3.2). For a temperature of $\sim$ 300K, however, in addition, the non-radiative decay-times of blue and green STEs are included in the intrinsic lifetimes.

Thus, if from the fits of the decay-time spectra the values for the parameters $\tau_1(T)$ and $\tau_2(T)$ at $T = 298$K and $T = 20$K can be determined, for each measurement temperature three relationships, $\tau_1(T)$ and $tau_2(T)$ and equation E.13 (containing the information of the fits of the wavelength spectra) can be formulated.

For a temperature of 20K, these three relationships depend on the following three unknown parameters: $\tau_{rb}(T)$, $\tau_{rg}(T)$ and C_{defects}. Hence, for 20K the resulting system of equations can be solved yielding the values for all of the decay times at a temperature of $T = 20$K as well as the for the defect density, C_{defects}, of the investigated crystal.

For a temperature of 298K, these three relationships depend on the following four parameters $\tau_{ltb}(T)$, $\tau_{ltg}(T)$, $\tau_{rb}(T)$ and C_{defects}. Thus, if, from the results of the 20K measurements, the defect density of the investigated crystal is determined, the number of

unknown parameters is reduced to three, so that also for a temperature of 298K the resulting system of equations can be solved. Using that the lifetime of blue STEs is defined by the radiative, the migration and the non-radiative blue STE recombination times and that the migration time of blue STEs is already determined by the value for the defect density, the non-radiative recombination time of blue STEs can also be calculated. In order to calculate the radiative recombination time of the green STEs, equation 3.109 (section III/3.2.3) and the value for $r_g(T \approx 300\text{K}) = 1 - r_b(T \approx 300\text{K})$ (thus, also determined by the fits of the wavelength spectra) are used. Thus, also the radiative recombination time of green STEs at $T = 298\text{K}$ can be determined. Using the lifetime $\tau_{ltg}(T)$ and the migration time $\tau_{\text{mig, g}\rightarrow\text{b}}(T)$ of green STEs, also the non-radiative recombination time of green STEs at $T = 298\text{K}$ can be calculated and, thus, the values for all of the decay times at a temperature of $T = 298\text{K}$ can be determined.

Hence, if the values for $\tau_1(298\text{K})$, $\tau_1(20\text{K})$ and $\tau_2(298\text{K})$, $\tau_2(20\text{K})$ are determined from the fits of the fit functions to the recorded decay-time spectra, then the values for all of the decay-times and lifetimes of blue and green STEs at $T = 298\text{K}$ and $T = 20\text{K}$ can be calculated.

E.4 Limitations of the Fits and Usage of Predetermined Parameters for the Fits

As indicated in section III/5.2.1, it cannot be expected to determine all of the parameters describing the rise of the scintillation light pulses ($\tau_{dr}(298K)$, $\tau_2(298\text{K})$ and $\tau_2(20\text{K})$) by the fits of the unquenched decay-time spectra with the fit functions deduced from the model. In the following, this circumstance will be discussed in more detail and the the method used to determine or estimate, nonetheless reasonable for these three parameters, i.e., for $\tau_{dr}(298K)$, $\tau_2(298\text{K})$ and $\tau_2(20\text{K})$ is deduced.

Example pulses where the described issues can be observed (scintillation-light spectra recorded for crystal Olga at room temperature with the 400nm and the 500nm filter, record length 10μs, respectively) are shown in figure E.1 (together with the final fits according to the fit functions described in appendix E.1 and the strategy as discussed in the following).

- As can be seen from figure E.1, the reflected laser-light pulse shape covers almost the complete region of the rising part of the scintillation-light pulse preventing free fits of the rise times of the recorded scintillation light. It should be noted that for measurements at low temperatures this coverage as well as the influence of the noise on the PMT signal (due to electrical crosstalk from the laser discharge, compare figure E.1 d) are even more severe, due to the fact that at low temperatures, the signal height of the scintillation-light pulses is greatly reduced due to the highly elongated decay times of the scintillation light (several 10μs up to $\sim 100\mu$s). For this reason, the rise time $\tau_2(T \approx 20\text{K})$ of the green scintillation light at low temperatures cannot be determined from the fits. A value for $\tau_2(T \approx 20\text{K})$ is gained using, on the one hand, information obtained from the fits at room temperature and, on the other hand, the fit result for the decay time $\tau_1(T \approx 20\text{K})$, which can be determined with high accuracy. For a more detailed discussion of the this method, see below.

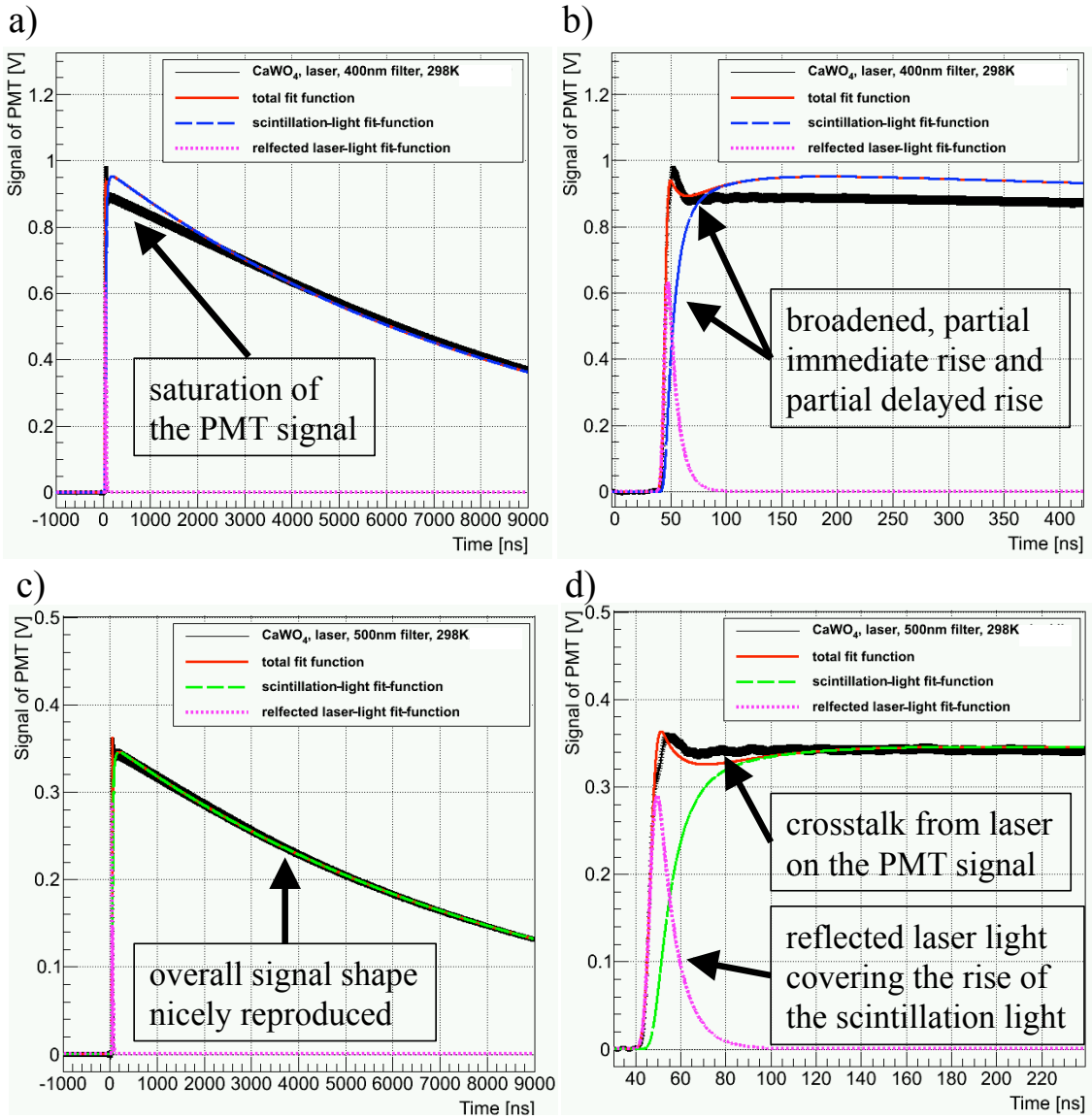

Figure E.1: Decay-time spectra (black lines and markers with error bars) recorded for crystal Olga under laser-beam excitation at room temperature: In panel a) and b), the spectrum $\mathbf{O9_{PMT}}$ recorded with the 400nm filter (record length 10μs) is shown. In panel c) and d), the spectrum $\mathbf{O11_{PMT}}$ recorded with the 500nm filter (record length 10μs) is shown. The spectra were preprocesses according to section III/4.6.2. Panel a) and c) depict the complete record length of these spectra (shortest record lengths with highest resolution recorded), in panel b) and c), zoomed-in views to the beginning of the pulses of panel a) and c), respectively, are shown. The spectra were fitted simultaneously with the fit functions as described in the main text. The complete fit functions are indicated as solid red lines. In addition, the decomposition of the fit function into the partial pulse representing the reflected laser light (dotted violet lines) and the partial pulse representing the $CaWO_4$ scintillation light (dashed, blue and green lines, respectively) is shown. The different features of the data as well as of the fit functions indicated in the figure are discussed in the following.

- As can be seen from figure E.1, at room temperature, the recorded decay-time spectra exhibit large pulse heights (especially for the measurements performed with the 400nm filter, due to the larger intensity of scintillation light in the wavelength region of the transmission of the 400nm filter, compare appendix C.5). First tests with the fit functions revealed that $\tau_{dr}(T)$, the partial delayed rise time, cannot freely be fitted as, unfortunately, the PMT signal starts to saturate for the unquenched pulses so that no reliable fit was possible (compare figure E.1 a and b). Thus, this parameter could not be determined by the fits. Hence, for the rise time $\tau_{dr}(T)$ of the fraction $F_{dr}(T)$ of the scintillation light at room temperature, the value reported in the literature was adopted[3] (compare equation 3.184 in section III/3.3.2 and discussion in section III/3.1.2):

$$\tau_{dr}(T \approx 300\text{K}) = 40\text{ns} \tag{E.14}$$

  Thus, in the following the value as specified by equation E.14 is adopted as fixed value for $\tau_{dr}(T \approx 300\text{K})$. The value for the fraction of scintillation light exhibiting this delayed rise time, $F_{dr}(T)$ is used as a free fit parameter. As can be seen from the fit function also indicated in figure E.1 a) and b) (solid red line, fit performed with the fixed value of 40ns for the delayed rise time $\tau_{dr}(T \approx 300\text{ns})$), clearly the fit function exhibits too large values at small times t after the beginning of the pulse. This "overshoot" of the fit function is, as discussed, attributed to the saturation of the PMT signal at such large pulse heights (compare also discussion and figure C.3 in appendix C.4).

- In figure E.1 b), the impact of the non-negligible width of the laser excitation pulse as well as of the impulse reaction on the actually, partial immediate rise of the blue scintillation light and on the partial delayed rise can be seen: The fit results indicate that about 87% of the blue scintillation light are produced with an immediate rise time, and only $\sim$ 13% are produced with a delayed rise time $\tau_{dr}(T) := 40\text{ns}$. However, as can be seen in figure E.1 b), due to the discussed influences on the detected scintillation-light pulse-shape, the immediately rising fraction of the scintillation light cannot be observed directly and, thus, most probably, can also not be determined very accurately from the fits.

- Apart from these features that can be observed from figure E.1, it has to be kept in mind that the data recorded with the 500nm filter, although fitted with the green scintillation light function only, in reality, contain also a large fraction of blue scintillation light. Tests were made fitting the scintillation light decay-time spectra recorded with the 500nm filter with a sum of green and blue scintillation-light fit functions (the weights were obtained from partial integrals of the fit functions of the wavelength spectra in the bandpass region of the 500nm filter, section III/5.1). However, the results for the different fit parameters from these "combined green" fits were (within the error margins) in accordance with the results obtained for fits of the

[3] It should be noted that the delayed rise time $\tau_{dr}(T)$ actually is assumed to depend of the defect density of the crystal (compare discussion in section III/3.1.2). Thus, in principle, a direct adoption of a value from the literature should not be performed without further knowledge on the defect density of the $CaWO_4$ crystal investigated in the respective reference. However, as this parameter could not be determined accurately from the fits (e.g., different start values resulted in different results), the value stated in the literature had to be adopted in order to perform the fits. Nonetheless, this uncertainty should always be kept in mind.

data recorded with the 500nm filter with the green scintillation-light fit-function only. Thus, it was taken into account that the usage of the weights of the blue and green scintillation light within the bandpass region of the 500nm filter corresponds to the introduction of an additional source of uncertainty into the fit function. Therefore, and as the results of both fits were in agreement with each other, the more simple fit function, containing the green scintillation-light pulse-shape only, was chosen. The resulting fit function containing only the green scintillation light is depicted in figure E.1 c) and d) (dashed green line).

- Concerning the fit of the rise time of the green scintillation light, $\tau_2(T)$, the discussed features also result in a problematic determination of the value of $\tau_2(T)$. In addition, as discussed above, the parameter $\tau_2(T)$, the effective unquenched lifetime of green STEs, only appears in the fit function for the green scintillation light and is, thus, less accurately described by the data compared $\tau_1(T)$, the effective unquenched lifetime of the blue STEs (with major influence on all of the pulse shapes recorded). Furthermore, when trying to determine a value for $\tau_2(T)$ it should be kept in mind that, by fixing the delayed rise time $\tau_{dr}(T)$ most probably also the value determined by the fit for $\tau_2(T)$ is influenced. Tests with the fit function, leaving $\tau_2(T)$ as free parameter resulted in unstable results, i.e., choosing different start values resulted in different fit results (this effect was especially pronounced for the low temperature measurement). Therefore a different strategy to determine values for $\tau_2(T = 289\text{K})$ and $\tau_2(T = 20\text{K})$ had to be developed:

  - For the determination of $\tau_2(T = 289\text{K})$, the following method could be applied successfully: With the help of the relationships of the times $\tau_{ltg}(T \approx 300\text{K})$, $\tau_{\text{mig, g}\rightarrow\text{b}}(T \approx 300\text{K})$ and $\tau_2(T \approx 300\text{K})$ as discussed in sections 3.2.3 and 3.1.4, a reasonable estimate for the value of $\tau_2(T = 298\text{K})$ for the room temperature measurements was determined[4]. This value was then used to iteratively determine the final fit values for the room temperature measurements with crystal Olga by alternately fixing $\tau_2(T = 289\text{K})$ and all of the other fit parameters in the fit functions for room temperature and adopting in each step the values determined for the respective free fit parameters in the preceding step as fixed values in the next step. In this way, a converging fit of the data $\mathbf{O9_{PMT}}$ and $\mathbf{O11_{PMT}}$, recorded for crystal Olga at room temperature, with a reasonable result for $\tau_2(T = 298\text{K})$ was gained (see section III/5.2.2).
  - For the determination of $\tau_2(T = 20\text{K})$, however, this strategy did not result in reasonable values determined. Therefore another method had to be developed: On the one hand, from fits of the low-temperature data with different values fixed for $\tau_2(T = 20\text{K})$, it can be observed that the value obtained for $\tau_1(T = 20\text{K})$ is always very similar. On the other hand, the results of the fits of the room temperature data can be used to determine an estimate for the defect density C_{defects} (see section III/5.2.2). Using this value for C_{defects}, as well as a preliminary value for $\tau_1(T = 20\text{K})$, a value for $\tau_2(T = 20\text{K})$ can be calculated (compare to the discussion of the determination of the free model parameters from the fit results in section III/5.2, the same relationships as indicated there for $T = 20\text{K}$ can be used, however, now, with $\tau_2(T = 20\text{K})$ as unknown variable

[4] This was possible, as it is assumed that the value of $\tau_{\text{mig, g}\rightarrow\text{b}}(T \approx 300\text{K})$ is known, compare section III/3.3.2.

and C_{defects} as known variable). The value for $\tau_2(T = 20\text{K})$ determined in this way is then inserted into the fit function as fixed parameter and the fit of the low-temperature data is performed again yielding a new value for $\tau_1(T = 20\text{K})$. This resulting value can be used to repeat the described method until the values obtained for $\tau_1(T = 20\text{K})$ and $\tau_2(T = 20\text{K})$ do not change any longer. It should be noted that this convergence was already reached after the first iteration. The values of the free fit parameters as well as for $\tau_2(T = 20\text{K})$ obtained in this last iteration step are regarded as final results of the fits of the low-temperature decay-time spectra.

E.5 Results and Discussion of the Fits of the Unquenched Decay-Time Spectra Recorded with Crystal Philibert

In table E.1, the results for the free fitparameters of the fits of the decay-time spectra recorded for crystal Philibert under laser excitation at room temperature, $\mathbf{P5_{PMT}}$ and at $T = 18\text{K}$, $\mathbf{O6_{PMT}}$, can be found, where it should be noted that the analyzed decay-time spectra were all recorded with the 400nm optical filter, so that no values for the green scintillation light, i.e., especially no value for $\tau_2(T)$ could be determined:

	$\mathbf{P5_{PMT}}(T{=}298\text{K})$	$\mathbf{P6_{PMT}}$ $(T{=}18\text{K})$
fit parameter	result	result
$I_b^{nq\,fit}(T)$ $\left[10^6\,\frac{\gamma}{s}\right]$	1.76708 ± 0.00025	0.233098 ± 0.000015
$\tau_1(T)$ $[\mu\text{s}]$	9.06727 ± 0.00051	94.7504 ± 0.0093
μ_{tot}^b [ns]	44.5088 ± 0.0205	45.4298 ± 0.0153
c_{BL}^b $[\mu\text{V}]$	−8.3250 ± 0.6409	429.027 ± 0.511
R_0^b $[10^{-2}\,\gamma]$	1.4736 ± 0.0070	2.98949 ± 0.00574
$M_{10\mu\text{s}}^b(T)$	1.23536 ± 0.00017	1.22947 ± 0.00012
$M_{1000\mu\text{s}}^b(T)$	-	1.01296 ± 0.00014
$F_{dr}(T)$ [%]	18.8986 ± 0.1594	-
red. χ^2	2.53	4.27

Table E.1: Summary of the results of the fits of the unquenched decay-time spectra $\mathbf{P5_{PMT}}$ and $\mathbf{P6_{PMT}}$ recorded at room temperature, $T = 298\text{K}$ and $T = 18\text{K}$ (compare table 4.5 in section III/4.5.2). $I_b^{nq\,fit}(T)$ corresponds to the basic scaling factor of the pulse height of the decay-time spectra, $\tau_1(T)$ is the effective unquenched lifetime of blue STEs, μ_{tot}^b is the temporal shift of the detected pulse compared to the time of triggering, c_{BL}^b is the DC offset of the baseline level, R_0^b corresponds to the scaling factor for the pulse shape describing the reflected laser light, $M_{10\mu\text{s}}^b(T)$ $M_{1000\mu\text{s}}^b(T)$ are the scaling factors of the decay-time spectra recorded with $10\mu\text{s}$ and $1000\mu\text{s}$ record lengths in comparison to the decay-time spectrum recorded with $100\mu\text{s}$ record length (at the same temperature), and $F_{dr}(T)$ is the fraction of scintillation light exhibiting a delayed rise. In addition, the globally obtained, reduced χ^2 is shown. The unit $\left[\frac{\gamma}{s}\right]$ denotes photons per second, the unit $[\gamma]$ denotes photons.

Comparing the determined values for the fit parameters with the corresponding results obtained from the fits of the decay-time spectra recorded with crystal Olga at room temperature and at low temperature (compare tables 5.3 and 5.4 in section III/5.2.2), it can be seen, that no principle differences exit. However, two features of the results obtained

for crystal Philibert have to be noted:

- From table E.1, it can be seen that the fraction of delayed created STEs, $F_{dr}(T)$ for crystal Philibert, is larger than the value obtained for crystal Olga (table 5.3 in section III/5.2.2). In fact, this result could not be explained within the developed model without further information, e.g., the temperature-dependency of the respective value for crystal Olga and crystal Philibert, available. It should, however, be noted that the value of $F_{dr}(T)$ obtained for crystal Philibert is only determined on the basis of the fit of the measurement with the 400nm filter. For crystal Olga, however, also the data from the room temperature measurement with the 500nm filter determines the size of $F_{dr}(T)$ (compare equation E.2 in appendix E.1: $F_{dr}(T)$ is also a parameter of $P_g^{nq\,fit}(1\,eh, T \approx 300\mathrm{K}, t)$). Thus, differences of the determined values could also result from the different amount of information available for the fit. Within the present work, this question cannot be conclusively answered.

- Concerning the fit results obtained for the decay-time spectra $\mathbf{P6_{PMT}}$, a significantly larger reduced χ^2 achieved can be observed. This can be attributed to the exceptionally large slope of the baseline of these decay-time spectra (compare appendix C.8.3). This feature can also be recognized from the noticeably large value determined for the DC offset of the baseline for these measurements. It should be noted, that the slope of the baseline was not accounted for in the description of the scintillation-light pulse shapes with the developed model function. Thus, the worse χ^2 value can be explained with the considerably worse description of the baseline of the pulse and, thus also of the pulse shape itself.

Bibliography

[1] Planck Collaboration, et al., *Planck 2013 results. XVI. Cosmological parameters*, ArXiv e-prints (2013)

[2] D. Clowe, et al., *A Direct Empirical Proof of the Existence of Dark Matter*, Astrophys. J. **648**, L109 (2006)

[3] G. Bertone, et al., *Particle dark matter: evidence, candidates and constraints*, Phys. Rep. **405**, 279 (2005)

[4] J. D. Lewin, et al., *Review of mathematics, numerical factors, and corrections for dark matter experiments based on elastic nuclear recoil*, Astropart. Phys. **6**, 87 (1996)

[5] G. Angloher, et al., *Results from 730 kg days of the CRESST-II Dark Matter Search*, Eur.Phys.J. **C72**, 1971 (2012)

[6] R. Agnese, et al., *Dark Matter Search Results Using the Silicon Detectors of CDMS II*, ArXiv e-prints (2013)

[7] E. Aprile, et al., *Dark Matter Results from 225 Live Days of XENON100 Data*, Phys. Rev. Lett. **109**, 181301 (2012)

[8] M. T. Frandsen, et al., *The unbearable lightness of being: CDMS versus XENON*, JCAP **1307**, 023 (2013)

[9] G. Angloher, et al., *Commissioning run of the CRESST-II dark matter search*, Astropart. Phys. **31**, 270 (2009)

[10] F. Pröbst, et al., *Model for cryogenic particle detectors with superconducting phase transition thermometers*, J. Low Temp. Phys. **100**, 69 (1995)

[11] C. Ciemniak, *Setup of a Neutron Scattering Facility for the Measurement of Scintillation Light Quenching Factors of Low-Temperature Detectors Used in the Direct Dark Matter Search Experiments CRESST and EURECA, Ph.D. thesis, Technische Universität München* (2011)

[12] M. Kiefer, *Improving the Light Channel of the CRESST-II-Dark Matter Detectors, Ph.D. thesis, Technische Universität München* (2012)

[13] R. F. Lang, et al., *Scintillator Non-Proportionality and Gamma Quenching in $CaWO_4$*, arXiv:nucl-ex 0910.4414 (2009)

[14] J. M. Schmaler, *The CRESST Dark Matter Search - New Analysis Methods and Recent Results, Ph.D. thesis, Technische Universität München* (2010)

[15] P. N. Luke, *Voltage-assisted calorimetric ionization detector*, Journal of Applied Physics **64**, 6858 (1988)

[16] B. Neganov, et al., *USSR Patent No. 1037771*, Otkrytia i izobreteniya **146**, 215 (1985)

[17] C. Isaila, et al., *Low-temperature light detectors: Neganov-Luke amplification and calibration*, Phys. Let. B **716**, 160 (2012)

[18] C. Isaila, *Development of Cryogenic Light Detectors with Neganov-Luke Amplification for the Dark Matter Experiments CRESST and EURECA, PhD thesis, Technische Universität München* (2010)

[19] S. Roth, et al., *Cryogenic composite detectors for the dark matter experiments CRESST and EURECA*, Opt. Mat. **31**, 1415 (2009)

[20] S. Roth, *Sputtered Tungsten Thin Films and Composite Detectors for the Application in the Dark Matter Experiments CRESST and EURECA, diploma thesis, Technische Universität München* (2007)

[21] A. Tanzke, *Optimization of Light Detectors for the CRESST Experiment, diploma thesis, Technische Universität München* (2011)

[22] A. Gütlein, *Feasibility Study for a First Observation of Coherent Neutrino Nucleus Scattering Using Low-Temperature Detectors, Ph.D. thesis, Technische Universität München* (2013)

[23] M. Stark, et al., *Application of the Neganov-Luke effect to low-threshold light detectors*, NIM A **545**, 738 (2005)

[24] J. L. Murray, et al., *The Al-Si (Aluminum-Silicon) System*, Bulletin of Alloy Phase Diagrams **5**, 74 (1984)

[25] S. M. Sze, *Physics of semiconductor devices*, A Wiley-Interscience Publication, New York: Wiley, 1981, 2nd ed. (1981)

[26] R. C. Jaeger, *Introduction to Microelectronic Fabrication*, Addison-Wesley Publishing Company, 1988, 2nd ed. (1988)

[27] A. Owens, *Spectral Degradation Effects in an 86cm^3 Ge(HP) Detector*, NIM A **238**, 473 (1985)

[28] M. Paganoni, on behalf of the CMS Electromagnetic Calorimeter Group, CMS Collaboration, *The CMS electromagnetic calorimeter*, IEEE Trans.Nucl.Sci. **54**, 574 (2007)

[29] C. W. E. van Eijk, *Inorganic scintillators in medical imaging*, Phys. Med. Biol. **47**, R85 (2002)

[30] S. Derenzo, et al., *The quest for the ideal inorganic scintillator*, NIM A **505**, 111 (2003)

[31] K. F. Ferris, et al., *Data-Driven Exploration of the Ionization-Phonon Partitioning in Scintillating Radiation Detector Materials*, IEEE Trans.Nucl.Sci. **55**, 1042 (2008)

[32] M. Nikl, et al., *Complex oxide scintillators: Material defects and scintillation performance*, Phys. Stat. Sol. (b) **245**, 1701 (2008)

[33] S. M. Bilenky, et al., *Neutrinoless double-beta decay. A brief review*, Mod. Phys. Lett. A **27**, 1230015 (2012)

[34] B. Schwingenheuer, *Searches for neutrinoless double beta decay*, J. Phys.: Conference Series **375**, 042007 (2012)

[35] I. Ogawa, et al., *Study of ^{48}Ca double beta decay by CANDLES*, J. Phys.: Conference Series **375**, 042018 (2012)

[36] L. Cardani, on behalf of the LUCIFER collaboration, *A Scintillating Bolometer Array for the Search of Neutrinoless Double Beta Decay*, J. Phys.: Conference Series **375**, 042016 (2012)

[37] J. L. Feng, *Dark Matter Candidates from Particle Physics and Methods of Detection*, Annual Reviews in Astronomy and Astrophysics **48**, 495 (2010)

[38] L. Baudis, *Direct Detection of Cold Dark Matter*, arXiv:astro-ph **0711.3788** (2007)

[39] R. O. Paredes, et al., *2010 update on the ROSEBUD project*, PoS(IDM2010) **054** (2010)

[40] V. B. Mikhailik, et al., *Cryogenic scintillators in searches for extremely rare events*, J. Phys. D: Appl. Phys. **39**, 1181 (2006)

[41] V. B. Mikhailik, et al., *Scintillation studies of CaWO4 in the millikelvin temperature range*, Phys. Rev. B **75**, 184308 (2007)

[42] J. F. Ziegler, et al., *SRIM-2011 - The Stopping and Range of Ions in Matter*, `http://www.srim.org/SRIM/SRIMLEGL.htm` (05.01.2012)

[43] A. R. Couture, *under the supervision of Prof. D. Drouin, CASINO v2.4.8.1*, `http://www.gel.usherbrooke.ca/casino/index.html` (05.01.2012)

[44] A. Senyshyn, et al., *Lattice dynamics and thermal properties of $CaWO_4$*, Phys. Rev. B **70**, 214306 (2004)

[45] Y. Zhang, et al., *Electronic band structures of the scheelite materials $CaMoO_4$, $CaWO_4$, $PbMoO_4$, and $PbWO_4$*, Phys. Rev. B **57**, 12738 (1998)

[46] V. B. Mikhailik, et al., *Performance of scintillation materials at cryogenic temperatures*, Phys. Stat. Sol. (b) **247**, 1583 (2010)

[47] R. Grasser, et al., *Optical Properties of $CaWO_4$, and $CaMoO_4$, Crystals in the 4 to 25 eV Region*, Phys. Stat. Sol. (b) **69**, 359 (1975)

[48] E. Orhan, et al., *Towards an insight on the photoluminescence of disordered $CaWO_4$ from a joint experimental and theoretical analysis*, J. Solid State Chem. **178**, 1284 (2005)

[49] R. T. Williams, et al., *Electronic Structure of Pure and Defective PbWO4, CaWO4, and CdWO4*, in V. Mikhailin (editor), *Inorganic Scintillators and their Applications*, Proc. of SCINT99, 118, Moscow State Univ. Press (2000)

[50] L. Gracia, et al., *Presence of excited electronic state in $CaWO_4$ crystals provoked by a tetrahedral distortion: An experimental and theoretical investigation*, J. Appl. Phys. **110**, 043501 (2011)

[51] M. Bacci, et al., *One- and two-photon excited luminescence and band-gap assignment in $CaWO_4$*, Phys. Rev. B **69**, 205110 (2004)

[52] V. Mürk, et al., *A study of electron excitations in $CaWO_4$ and $PbWO_4$*, J. Phys.: Condens. Matter **9**, 249 (1997)

[53] M. Moszyński, et al., *Characterization of $CaWO_4$ scintillator at room and liquid nitrogen temperatures*, NIM Phys. Res. A **553**, 578 (2005)

[54] J. Ninković, *Investigation of $CaWO_4$ Crystals for Simultaneous Phonon-Light Detection in the CRESST Dark Matter Search, Ph.D. thesis, Technische Universität München* (2005)

[55] L. S. Cavalcante, et al., *Electronic structure, growth mechanism and photoluminescence of $CaWO_4$ crystals*, CrystEngComm **14**, 853 (2012)

[56] V. B. Mikhailik, et al., *Radiative decay of self-trapped excitons in $CaMoO_4$ and $MgMoO_4$ crystals* , J. Phys.: Condens. Matter **17**, 7209 (2005)

[57] V. B. Mikhailik, et al., *Luminescence of $CaWO_4$, $CaMoO_4$, and $ZnWO_4$ scintillating crystals under different excitations*, J. Appl. Phys. **97**, 083523 (2005)

[58] V. Nagirnyi, et al., *Emission decay kinetics in a $CaWO_4$:Bi crystal*, NIM A **537**, 61 (2005)

[59] S. Baccaro, et al., *Effect of La Doping on Calcium Tungstate ($CaWO_4$) Crystals Radiation Hardness*, Phys. Stat. Sol. (a) **178**, 799 (2000)

[60] M. Herget, et al., *Reorientation of Hole Centers in $CaWO_4$ Monitored by EPR and Optical Absorption*, Phys. Stat. Sol. (b) **141**, 523 (1987)

[61] V. Nagirnyi, et al., *Relaxation of electronic excitations in wide-gap crystals studied by femtosecond interferometry technique*, Phys. Solid State **50**, 1715 (2008)

[62] R. Grasser, et al., *On the intrinsic nature of the blue luminescence in $CaWO_4$*, J. Lum. **27**, 263 (1982)

[63] M. Bacci, et al., *Structured emission of tetrahedral complexes due to Jahn-Teller and pseudo-Jahn-Teller effects*, Phys. Rev. B **64**, 104302 (2001)

[64] M. Itoh, et al., *Time-resolved luminescence from Jahn-Teller split states of self-trapped excitons in $PbWO_4$*, Phys. Rev. B **73**, 235106 (2006)

[65] V. Pankratov, et al., *Transient Optical Absorption and Luminescence in Calcium Tungstate Crystal*, Phys. Stat. Sol. (b) **225**, R9 (2001)

[66] C. Koepke, et al., *Excited-state absorption in excimer-pumped $CaWO_4$*, J. Lum. **54**, 345 (1993)

[67] M. J. Treadaway, et al., *Luminescence of calcium tungstate crystals*, J. Chem. Phys. **61**, 4003 (1974)

[68] M. J. Treadaway, et al., *Energy transfer in samarium-doped calcium tungstate crystals*, Phys. Rev. B **11**, 862 (1975)

[69] J. van der Laan & Kees Huyser, *DataThief III, Version 1.6 november 2010*, `http://www.datathief.org/` (10.10.2012)

[70] P. A. Rodnyi, *Physical Processes in Inorganic Scintillators*, CRC Press, Boca Raton, FL (1997)

[71] V. Nagirnyi, et al., *Relaxation dynamics of electronic excitations in $CaWO_4$ and $CdWO_4$ crystals studied by femtosecond interferometry technique*, Radiat. Meas. **45**, 262 (2010)

[72] H. Kraus, et al., *Multiple photon counting coincidence (MPCC) technique for scintillator characterisation and its application to studies of $CaWO_4$ and $ZnWO_4$ scintillators*, NIM Phys. Res. A **553**, 522 (2005)

[73] M. v. Sivers, *Optimizing Detectors for Dark Matter Search, diploma thesis, Technische Universität München* (2010)

[74] J. Ninković, et al., *$CaWO_4$ crystals as scintillators for cryogenic dark matter search*, NIM Phys. Res. A **537**, 339 (2005)

[75] T. Jagemann, *Measurement of the Scintillation Light Quenching for Nuclear Recoils induced by Neutron Scattering in Detectors for Dark Matter Particles, Ph.D. thesis, Technische Universität München* (2004)

[76] T. Jagemann, et al., *Measurement of nuclear recoil quenching factors in $CaWO_4$*, Astropart. Phys. **26**, 269 (2006)

[77] S. Wawoczny, *Optimierung des Experimentellen Aufbaus zur Messung der Quenching Faktoren von CRESST/EURECA - Tieftemperaturdetektoren , Diploma thesis, Technische Universität München* (2011)

[78] P. Huff, *The Detector Parameters Determining the Sensitivity of the CRESST-II Experiment , PhD thesis, Technische Universität München* (2010)

[79] P. A. Rodnyi, et al., *Energy Loss in Inorganic Scintillators*, Phys. Stat. Sol. (b) **187**, 15 (1995)

[80] V. Mikhailin, et al., *Study of optical and luminescent properties of some inorganic scintillators in the fundamental absorption region*, NIM Phys. Res. A **486**, 367 (2002)

[81] J. Lindhard, et al., *Integral equations governing radiation effects (notes on atomic collisions III)*, Mat. Fys. Medd. Dan. Vid. Selsk. **33**, 1 (1963)

[82] H. Bethe, *Zur Theorie des Durchgangs schneller Korpuskularstrahlen durch Materie*, Ann. Physik **397**, 325 (1930)

[83] J. F. Ziegler, *Stopping of energetic light ions in elemental matter*, J. Appl. Phys. **85**, 1249 (1999)

[84] K. Wolf, et al., *Dynamics of diffusion-controlled recombination of ions in ionic solutions. Limits of validity of the Debye -Smoluchowski equation*, in P. M. A. Rogaski, K. Adamiec (editor), *Intl. Conference on Solid State Crystals 2000: Growth, Characterization, and Applications of Single Crystals*, volume 4412 of *Proceedings of SPIE, Zakopane, Poland*, 137 (2001)

[85] A. N. Vasil'ev, *From Luminescence Non-Linearity to Scintillation Non-Proportionality*, IEEE Trans.Nucl.Sci. **55**, 1054 (2008)

[86] R. Grasser, et al., *Luminescent sites in $CaWO_4$ and $CaWO_4$:Pb crystals*, J. Lum. **12/13**, 473 (1976)

[87] C. J. Schmitt, *Equilibrium Charge State Distributions of low-Z ions incident on thin self-supporting foils, Ph.D. thesis, Graduate School of the University of Notre Dame, Indiana* (2010)

[88] K. Kiyohara, et al., *Study of angular and energy distribution of secondary electrons emitted by high energy heavy ion impact*, Progress in Nucl. Sc. and Techn. **1**, 222 (2011)

[89] G. Kraft, et al., *LET, track structure and models*, Radiat. Environ. Biophys. **31**, 161 (1992)

[90] A. Morozv, et al., *Spatial distribution of fluorescent light emitted from neon and nitrogen excited by low energy electron beams*, J. Appl. Phys. **100**, 093305 (2006)

[91] N. F. Mott, et al., *On the absorption of light by crystals*, Proc. R. Soc. Lond. A **167**, 384 (1938)

[92] G. B. Beard, et al., *Temperature Dependent Luminescence of $CaWO_4$ and $CdWO_4$*, J. Appl. Phys. **33**, 144 (1962)

[93] V. Yakovyna, et al., *Effect of thermo-chemical treatments on the luminescence and scintillation properties of $CaWO_4$*, Opt. Mat. **30**, 1630 (2008)

[94] S. Vielhauer, et al., *Self-quenching effects of excitons in $CaWO_4$ under high density XUV free electron laser excitation*, Physics of the Solid State **50**, 1789 (2008)

[95] I. Bavykina, et al., *Interpretation of light-quenching factor measurements*, Astropart. Phys. **28**, 489 (2007)

[96] T. Förster, *Zwischenmolekulare Energiewanderung und Fluoreszenz*, Ann. Phys. **437**, 55 (1948)

[97] R. C. Powell, et al., *Singlet exciton energy transfer in organic solids*, J. Lum. **11**, 1 (1975)

[98] S. Vielhauer, et al., *Phosphor materials under high-density XUV FEL excitation: mechanisms of luminescence quenching*, in *(SPIE) Conf. Ser.*, volume 7361 of *SPIE Conf. Ser.* (2009)

[99] M. Csele, *Fundamentals of light sources and lasers*, A Wiley-Interscience publication., John Wiley & Sons, Inc., Hoboken, New Jersey. (2004)

[100] A. Erb, et al., *Growth of high-purity scintillating CaWO4 single crystals for the low-temperature direct dark matter search experiments CRESST-II and EURECA*, CrystEngComm **15**, 2301 (2013)

[101] M. v. Sivers, *Ph.D. thesis, Technische Universität München, in preparation*

[102] M. v. Sivers, et al., *Influence of Annealing on the Optical and Scintillation Properties of $CaWO_4$ Single Crystals*, Optical Materials **34**, 1843 (2012)

[103] A. Ulrich, *Private Communication*

[104] B. S. Patel, *Compact high-power TEA N2 laser*, Rev. Sci. instrum. **49**, 1361 (1978)

[105] R. Strauss, *Quenching Factor Measurements of CaWO4 at mK Temperatures by Neutron Scattering for the Dark Matter Experiments CRESST and EURECA, Diploma thesis, Technische Universität München* (2009)

[106] R. Brun, et al., *ROOT - An Object Oriented Data Analysis Framework, Proceedings AIHENP'96 Workshop, Lausanne, Sep. 1996*, NIM Phys. Res. A **389**, 1188 (1997)

[107] H. Shi, et al., *Ab initio calculations of the BaF_2 bulk and surface F centres*, J. Phys.: Condens. Matter **18**, 8367 (2006)

[108] W. Westphal, *Development and Characterization of Cryogenic Detectors for the CRESST Experiment, Technische Universität München*, `http://www.e15.ph.tum.de/research˙and˙projects/cresst/` (2008)

[109] W. W. Moses, et al., *Scintillator Non-Proportionality: Present Understanding and Future Challenges* , IEEE Trans.Nucl.Sci. **55**, 1049 (2008)

[110] D.-M. Mei, et al., *A model of nuclear recoil scintillation efficiency in noble liquids*, Astropart. Phys. **30**, 12 (2008)

[111] J. B. Birks, *Scintillation Efficiency of Anthracene Crystals*, Proc. Phys. Soc A **63**, 1294 (1950)

[112] J. B. Birks, et al., *Deterioration of Anthracene under α-Particle Irradiation*, Proc. Phys. Soc A **64**, 511 (1951)

[113] M. Nikl, *Scintillation detectors for x-rays*, Meas. Sci. Technol. **17**, R37DR54 (2006)

[114] R. Lang, *Search for Dark Matter with the CRESST Experiment, Ph.D. thesis, Technische Universität München* (2008)

[115] E. Kotomin, et al., *Kinetics of non-steady state diffusion-controlled tunnelling recombination of defects in insulating crystals*, J. Phys. Condens. Matter **1**, 6777 (1989)

[116] S. M. Sze, et al., *Physics of Semiconductor Devices, Third Edition*, John Wiley & Sons, Inc., Hoboken, New Jersey (2007)

[117] NIST - National Institute of Standards and Technology, *estar - stopping-power and range tables for electrons*, `http://physics.nist.gov/PhysRefData/Star/Text/ESTAR.html` (16.07.2013)

[118] R.B. Firestone and L.P. Ekström, *LBNL Isotopes Project Nuclear Data Dissemination Home Page*, http://ie.lbl.gov/toi.html (15.10.2012)

[119] S. Ze-Xu, et al., *First-principles study on electronic structures and absorption bands of $CaWO_4$ crystals*, Phys. Stat. Sol. (a) **204**, 3159 (2007)

[120] Maya 2000, *Ornet, Seri Kembangan, Malaysia*, http://www.ornets.com/Poducts/Specrometer/Maya2000˙and˙2000Pro.html (03.03.2013)

[121] A. J. Parsons, *Photomultipliers - space charge effects & transit time spread*, technical reprint R/P064, http://www.et-enterprises.com/photomultipliers/technical-information-reprints (05.09.2012)

[122] P. Persephonis, et al., *Numerical analysis of the electrical and optical behaviour of a pulsed nitrogen laser through time-dependent resistances and inductances*, Appl. Phys. B **66**, 39 (1998)

[123] C. L. Melcher, et al., *Applicability of Barium Fluoride and Cadmium Tungstate Scintillators for Well Logging*, IEEE Trans.Nucl.Sci. **36**, 1188 (1989)

[124] S. E. Derenzo, et al., *Measurements of the Intrinsic Rise Times of Common Inorganic Scintillators*, IEEE Trans.Nucl.Sci. **47**, 860 (2000)

Acknowledgements

Im Folgenden möchte ich mich bei all Denjenigen bedanken, die zum Gelingen dieser Arbeit beigetragen haben: Mein besonderer Dank gilt meinem Doktorvater, Prof. Dr. Franz von Feilitzsch, für die Möglichkeit diese Arbeit zu verfassen, und zudem für die interessanten Diskussionen und Gespräche.

Genauso sehr will ich mich bei Dr. Walter Potzel, Priv.-Doz. Andreas Ulrich sowie Dr. Jean Lanfrachi bedanken, ohne deren jeweilige Unterstützung diese Arbeit mit Sicherheit nicht zu dem geworden wäre, was sie ist.
Bei Dr. Walter Potzel will ich mich für die schiere Unermüdlichkeit seiner Bereitschaft zu Diskussionen und seinem fortwährenden Interesse an dieser Arbeit danken.
Dr. Andreas Ulrich möchte ich für die tolle Zusammenarbeit und die vielen interessanten Diskussion sowie für die netten Mittagspausen danken.
Bei Dr. Jean Lanfranchi will ich mich -neben vielen anderen Sachen- im Speziellen für seine Unterstützung im letzten Jahr meiner Doktorarbeit bedanken.

Mein außerordentlicher Dank gilt auch Prof. Dr. Schönert und Prof. Dr. Oberauer für das konstruktive Arbeitsumfeld am E15 und das Interesse an meiner Arbeit.

Darüber hinaus gilt mein ganz besonderer Dank Dr. Achim Gütlein, nicht nur für das äußerst angenehme Arbeits- und Büroklima, das wir immer hatten, sondern auch für seine engelsgleiche Geduld, wenn ich dann doch noch eine aller-, aller-, allerletzte Kleinigkeit ... hatte, und ganz besonders für seine Hilfe bei der Datenauswertung.

An dieser Stelle will ich mich auch besonders bei Dipl.-Phys. Domenikus Hellgarthner sowie bei Dipl.-Phys. Andreas Zöller für die offenen Ohren für meine Frage nach der Programmierung in root bedanken. Auch bei allen ehemaligen und derzeitigen Mitgliedern des E15 will ich mich für die tolle Zusammenarbeit, die netten Kaffeepausen und die Unterstützung bei meiner Strahlzeit bedanken. Ganz besonderen Dank möchte ich an dieser Stelle auch dem Werkstatt-Team des E15, Herrn Hagn sowie dem Kristalllabor der TU München aussprechen.

Auch bei unserer Sekretärin Maria Bremberger will ich mich für die tolle Unterstützung und die netten Pausen bedanken.

Ein ganz spezieller Dank gilt meiner Familie für die Geduld und die ermunternden Worte während des Schreibens dieser Arbeit. Außerdem will ich mich bei Dr. Tobias Karspeck bedanken. Du hast mich in so vielerlei Hinsicht unterstützt, dass ich gar nicht weiß, wo ich anfangen soll, daher einfach, Danke für Alles.